

# Toughness and Brittleness of Plastics



# Toughness and Brittleness of Plastics

**Rudolph D. Deanin and  
Aldo M. Crugnola, EDITORS**

*University of Lowell*

A symposium jointly sponsored by  
the Division of Organic Coatings and  
Plastics Chemistry of the American  
Chemical Society and by the Division  
of Engineering Properties and Structures  
of the Society of Plastics Engineers,  
at the 168th Meeting of the American  
Chemical Society, Atlantic City, N. J.,  
September 10–13, 1974.

ADVANCES IN CHEMISTRY SERIES

**154**

AMERICAN CHEMICAL SOCIETY  
WASHINGTON, D. C. 1976



## Library of Congress CIP Data

Toughness and brittleness of plastics.

(Advances in chemistry series; 154. ISSN 0065-2393)

Includes bibliographical references and index.

1. Plastics—Testing—Congresses.

I. Deanin, Rudolph D., 1921– II. Crugnola,  
Aldo M., 1928– III. American Chemical Society.  
Division of Organic Coatings and Plastics Chemistry.  
IV. Society of Plastics Engineers. Division of Engineer-  
ing Properties and Structures. V. Series: American  
Chemical Society. Advances in chemistry series; 154.

QD1.A355 (TA455.P5) 540'.8s  
(620.1'923'6) 76-41267  
ISBN 0-8412-0221-4 ADCSAJ 154 1-411 (1976)

Copyright © 1976

American Chemical Society

All Rights Reserved. No part of this book may be reproduced or transmitted in any form or by any means—graphic, electronic, including photocopying, recording, taping, or information storage and retrieval systems—without written permission from the American Chemical Society.

PRINTED IN THE UNITED STATES OF AMERICA

**American Chemical  
Society Library  
1155 16th St., N.W.  
Washington, D. C. 20036**

# Advances in Chemistry Series

**Robert F. Gould, *Editor***

## *Advisory Board*

Kenneth B. Bischoff

Ellis K. Fields

Jeremiah P. Freeman

E. Desmond Goddard

Jesse C. H. Hwa

Philip C. Kearney

Nina I. McClelland

John L. Margrave

John B. Pfeiffer

Joseph V. Rodricks

Roy L. Whistler

Aaron Wold

## FOREWORD

**ADVANCES IN CHEMISTRY SERIES** was founded in 1949 by the American Chemical Society as an outlet for symposia and collections of data in special areas of topical interest that could not be accommodated in the Society's journals. It provides a medium for symposia that would otherwise be fragmented, their papers distributed among several journals or not published at all. Papers are refereed critically according to ACS editorial standards and receive the careful attention and processing characteristic of ACS publications. Papers published in **ADVANCES IN CHEMISTRY SERIES** are original contributions not published elsewhere in whole or major part and include reports of research as well as reviews since symposia may embrace both types of presentation.

## PREFACE

In many applications of plastics, when products finally fail, they fail because of brittle fracture. Plastics are not unique in this respect; products made of metals, ceramics, and wood also sometimes fail by brittle fracture. Thus the mechanism and understanding of brittle fracture are a major concern of materials scientists and materials engineers.

The prevention of brittle fracture has challenged the ingenuity of polymer chemists, polymer physicists, and plastics engineers. They have made great progress in the past 20 years toward practical solutions of the problem and in the past 10 years toward theoretical understanding as well.

The idea of a symposium on the subject was first suggested five years ago, during a conference on New Plastics Materials at the University of Lowell for the Plastics Institute of America. Noting that many of the new plastics were designed to solve the problem of brittle fracture and that there was much controversy among the conferees on the subject of mechanism and test methods, Albert W. Meyer suggested a symposium on the subject, and the conferees all heartily agreed.

The symposium was organized by the joint efforts of the Organic Coatings and Plastics Division of the American Chemical Society and the Engineering Properties and Structure Division of the Society of Plastics Engineers. The papers were collected from the membership of both societies and through their contacts with other authorities and researchers active in the field. The result is a broad coverage of the present understanding and current research in the field of toughness and brittleness of plastics.

The papers have been collected and arranged in three major classifications dealing with Homogeneous Systems, Multi-Phase Polymer Systems, and Reinforced Plastics. The first group deals mainly with the mechanisms of fracture, while the second and third deal with the two major techniques for preventing fracture and providing toughness. All together they present a thorough coverage of current knowledge and research in the field.

University of Lowell  
Lowell, Mass. 01854  
October 1974

RUDOLPH D. DEANIN  
ALDO M. CRUGNOLA

# Thermodynamic Aspects of Brittleness in Glassy Polymers

S. MATSUOKA

Bell Laboratories, Murray Hill, N. J. 07974

*A shortening in relaxation time in the critically strained region makes some materials tough. The shift of relaxation time is attributed to strain-induced dilatation and can reach as much as five decades. Thermal history, on the other hand, dictates the initial state from which this dilatation starts and may be expressed in terms of excess entropy and enthalpy. The excess enthalpy at  $T_g$  is measurable by differential scanning calorimetry. Brittle to ductile transition behavior is determined by the strain-induced reduction in relaxation time, the initial amount of excess entropy, and the maximum elastic strain that the material can undergo without fracturing or crazing.*

Failure properties are dictated by events in the limited local regions and are more difficult to handle and to interpret molecularly than average properties such as modulus, viscosity, and heat capacity. We propose shortening of relaxation times in material in the critical regions as a mechanism responsible for the toughness of solid plastics. The stress tends to dilate most solids, and the relaxation time can be shortened by several orders of magnitude by this type of dilatation. This process is quantitatively describable in terms of excess entropy. The initial amount of the excess entropy before stress is a function of thermal and mechanical history, *e.g.* annealing and drawing. How much the relaxation time can be shortened is determined by the maximum strain attainable in the material before fracture or craze formation occurs. The shortening of the relaxation time is a local plasticization process, and the mechanical energy is more readily dissipated.



### ***Strain Energy as the Strength Criterion***

In plastics the strength of a material is often unrelated to the average properties such as the modulus. ABS resins, which are essentially rubber-reinforced SAN resins, are stronger in most applications than the unmodified SAN resins, even though both the modulus and the elastic stress limit for SAN are higher than that for ABS. Berry (1) noted that much of the mechanical energy required to propagate a crack through the bulk of a material is dissipated during plastics deformation near the tip of the crack; this energy can be several orders of magnitude greater than the actual surface energy for separating the two surfaces. Thus plastic deformation in microscopic scale is perhaps the most important factor in making a material tough. Tensile elongation indicates the ability of a material to deform before breaking; it is a more important design factor in choosing a proper material than many of the average properties referred to above.

An impact modifier is a rubber phase dispersed in particulate form throughout the matrix of a polymer solid. Unlike plasticizers, the rubber particles retain their intrinsic properties as a separate phase. The glass transition temperature of the parent matrix is not lowered by the addition of an impact modifier. The rubber particles do two things to the parent matrix phase (2, 3, 4): they act as stress concentrators (*i.e.*, a large strain will start in the matrix near the interface) and they enhance the multiaxiality in stress. As multiaxial tensile strength near the interface further enhances dilatation, which shortens the mechanical relaxation time, the otherwise brittle polymer solid of the matrix will undergo plastic deformation in the vicinities of the rubber particles.

### ***Shift of Relaxation Time under Strain***

The concept of stress-induced dilatation affecting the relaxation time or rate has been suggested by others (5, 6, 7, 8). The density of most solids decreases under uniaxial stress because the lateral contraction of the solid body does not quite compensate for the longitudinal extension in the direction of the stress, and the body expands. The Poisson ratio, the ratio of such contraction to the extension, is about 0.35 for many polymeric solids; it would be 0.5 if no change in density occurred, as in an ideal rubber. The volume increase,  $\Delta V$ , accompanying the tensile strain of  $\epsilon$ , can be described by the following equation:

$$\Delta V/V = \epsilon(1-2\mu), \quad (1)$$

where  $V$  is the specific volume, and  $\mu$  is the Poisson ratio (8). The volume increases linearly with the strain up to the elastic limit according to this

equation. However beyond this limit the body either yields, crazes, or fractures, so that deformation beyond this point no longer causes an additional dilatation. The maximum amount of such a strain is about  $3 \times 10^{-2}$  for many polymers. The corresponding fractional volume increase,  $\Delta V/V$ , is about  $10^{-3}$  for many polymer solids.

The WLF equation is an empirical expression for the shift of relaxation time with respect to the temperature change and applies to rubbery materials. It is well known (10) that the WLF equation can be written as a function of the fractional free volume only:

$$\ln a_T = B(1/f - 1/f_g), \quad (2)$$

where  $a_T$  is the normalized relaxation time;  $B$  is a constant and is usually unity;  $f$  is the fractional free volume, and the  $g$  is the glass transition temperature. The fractional free volume reaches  $1/40$  at vitrification where the remaining free volume no longer contributes to the relaxation process and presumably remains constant below  $T_g$ .

If an increase in free volume arising from stress-induced dilatation contributes to the relaxation process in the same manner as dilatation by raising the temperature, we can estimate the shift in relaxation time with Equation 2 by substituting for the fractional free volume,  $f$ ,

$$f = f_g + \Delta V/V = f_g + \epsilon(1-2\mu). \quad (3)$$

(See Curve A in Figure 1.) The maximum possible shift in relaxation time is determined by the limiting elastic strain, beyond which dilatation no longer continues.

### *Effect of Annealing*

Well-annealed polymeric solids tend to be stiffer and more brittle than unannealed solids. For crystalline polymers annealing increases the degree of crystallinity and crystallite sizes (lamellar thickening). These changes are defined and measured thermodynamically as the decrease in enthalpy and entropy.

Annealing of glassy polymers can be thermodynamically treated in a similar way, even though it does not involve crystalline phase transition (11, 12). Annealing a polymer glass will lower the enthalpy. This decrease is approximately equal to the product of the temperature and the corresponding change in entropy since the Gibbs free energy would remain essentially unchanged, as in the case of crystallization of the super-cooled liquid. This excess entropy is associated with the free volume as it becomes available at the glass-to-rubber transition by heating

or by mechanical dilatation. Thus entropy of mixing of the occupied and the unoccupied sites is

$$\Delta S = -R(n_1 \ln v_1 + n_2 \ln v_2), \quad (4)$$

where  $n$  is the mole fraction;  $v$  is the volumetric fraction, and the subscripts 1 and 2 refer to the occupied and unoccupied sites. When the concentration of the unoccupied sites is much smaller than that of the occupied sites, Equation 4 is simplified to the form

$$\Delta S = -Rf \ln f, \quad (5)$$

where  $f$  is the fractional free volume. We stated before that the unoccupied sites in the glass become available as free volume,  $f_g$ , at the point of the glass-to-rubber transition. If the glass is subjected to a thermal history which decreases its excess entropy (annealing), the free volume fraction might be less than the average value,  $f_g$ , for the quenched glass.

Differential scanning calorimetry experiments (10, 11) show that a well-annealed glass would have greater endotherm at the glass-to-rubber transition and conversely would require a greater strain to gain a given amount of fractional free volume by dilatation. A number of curves to account for the different thermal history are shown in Figure 1. These additional curves were calculated for materials with different degrees of

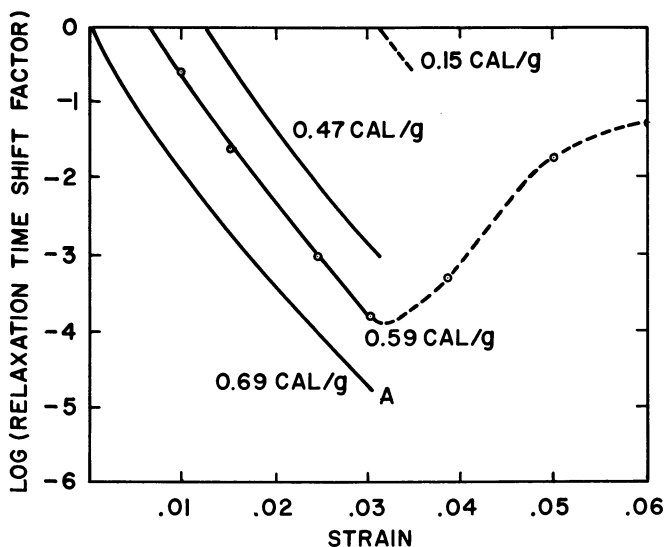


Figure 1. The effect of strain-induced dilatation on relaxation time

annealing. The initial excess enthalpy is a measurable quantity and decreases with annealing. The points are from the experimental data of Ref. 13. The smaller the excess entropy initially, the greater the strain required before the relaxation time begins to shorten. It follows that annealing impedes a strain-induced plasticization.

We have stated that the maximum attainable dilatation is determined by the limiting magnitude of strain; anything above that would cause cracks or crazes. If a sample is well annealed, this maximum strain is reached before a sufficient shift in relaxation time has occurred (*see* Figure 1). The material would not be able to dissipate much strain energy and could fail in brittle manner. How much of a shift in relaxation time is required for the tough behavior depends on the rate of straining pertinent to the particular application or testing method in question. Assuming the average relaxation time at  $f = f_g$  is 1 sec, a shift of two to three decades corresponds to such a requirement.

Our data given here for ABS resins hold for other polymers as well since many exhibit similar values for  $f_g$ , the Poisson ratio, and the limiting stress. For example, the shift of four decades in PVC creep retardation time after annealing was obtained by Turner (13). The maximum excess entropy at  $T_g$  is similar for many polymers and some inorganic glasses (14).

### Literature Cited

1. Berry, J. P., *J. Appl. Phys.* (1963) **34**, 62.
2. Wang, T. T., Matsuo, M., Kwei, T. K., *J. Appl. Phys.* (1971) **42**, 4188.
3. Wang, T. T., Matsuo, M., Kwei, T. K., *J. Polym. Sci. Part A-2* (1972) **10**, 1085.
4. Matsuoka, S., Daane, J. H., *ACS Polymer Preprints* 10-2, 1198 (1969).
5. Ferry, Stratton, *Kolloid-Z.* (1960) **171**, 107.
6. Sternstein, *J. Macromol. Sci. Phys.* (1973) **8**, 557.
7. Kovacs, Stratton, Ferry, *J. Phys. Chem.* (1963) **67**, 152.
8. Struik, *Rheol. Acta* (1966) **5**, 303.
9. Daane, J. H., Matsuoka, S., *Polym. Eng. Sci.* (1968) **8** (4), 246.
10. Ferry, J. D., "Viscoelastic Properties of Polymers," Chap. II, Wiley, New York, 1961.
11. Petrie, S. E. B., *J. Polym. Sci. Part A-2* (1972) **10**, 1255.
12. Matsuoka, S., Aloisio, C. J., Bair, H. E., *J. Appl. Phys.* (1973) **44**, 4265.
13. Turner, S., *Brit. Plast.* (December, 1964), p. 682.
14. Matsuoka, S., Bair, H. E., *Bull. Amer. Phys. Soc.* (1974) **19** (3), 239.

RECEIVED October 18, 1974.

# 2

## Structural Parameters Affecting the Brittleness of Polymer Glasses and Composites

ROGER J. MORGAN and JAMES E. O'NEAL

McDonnell Douglas Research Laboratories, McDonnell Douglas Corp.,  
St. Louis, Mo. 63166

*The degree of brittleness of a polymer glass is related to the amount of flow that occurs during the failure process. Small main-chain glassy state molecular motions, the free volume, and the morphology of polymer glasses all affect these flow processes. The glassy state embrittlement of polycarbonate appears to result from normal free volume changes and not from the growth of ordered regions. The number and size of microvoids affect the amount of molecular flow. Changes in brittleness of polymer glasses induced by fillers in the interfacial region depend mainly on polymer-filler interaction and dilatational stresses.*

The degree of brittleness of a polymer glass depends on the amount of flow that occurs during the failure process, either microscopically *via* crazing or shear banding or macroscopically *via* necking. This flow, which absorbs energy during the failure process, decreases the brittleness of the polymer glass. Flow processes involve both the movement of polymer chain segments past one another and the alignment of ordered nodular regions. The molecular and morphological parameters affecting these flow processes are not entirely understood. There is however growing evidence that small main-chain motions as measured by dynamic mechanical loss, dielectric loss, and NMR techniques enhance the larger scale segmental flow processes (1, 2, 3, 4, 5, 6, 7). The exact nature of these small main-chain motions and the structural parameters that permit their occurrence is incomplete because of the limitations of the experimental techniques. Ordered regions in polymer glasses greatly affect the flow processes involved in the failure mechanisms of these materials. The

size of the nodules, the packing of the intergranular regions, and the nature of any internodular crosslinks will affect flow. There is however considerable controversy on whether polymer glasses (and liquids) consist of ordered regions greater than those associated with normal liquid-like packing (8). Furthermore it is uncertain whether the embrittlement of polymer glasses as a result of annealing below  $T_g$  is a direct consequence of morphological changes or normal liquid-like packing changes in free volume. Other parameters that affect the amount of flow during failure include: (1) molecular weight, (2) degree of crosslinking, (3) low molecular weight additives, (4) number, size and size distribution of microvoids, (5) presence of fillers and proximity of surfaces, (6) fabrication stresses, and (7) type of stress field applied to the polymer glass.

In this paper we discuss (1) small main-chain motions and their effect on the flow processes, (2) the embrittlement of polycarbonate, (3) the formation of microvoids from sample preparation and their effect on the brittleness of polymer glasses, and (4) the modification of the degree of brittleness of polymer glasses at the filler interface in polymer composites.

### **Discussion**

#### **Small Main-Chain Motions and Their Effect on the Flow Processes.**

The factors that govern small main-chain motions in the glassy state are complex. Only units in favorable conformations and surroundings undergo these motions (9) because of distribution in the packing and conformations in the glassy state. All other units are frozen-in until the temperature approaches the main  $T_g$ . The volume swept out by the moving unit in relation to the local free volume available determines the motion if strong intermolecular interactions such as hydrogen bonding are absent. For cooperative torsional motions the smallest volume is swept out by structures containing consecutive trans or extended configurations without side groups. A number of polymers that have secondary glass transitions satisfy this condition, *e.g.*, polyethylene, polytetrafluoroethylene, and *trans*-polybutadiene. Low energy differences between rotational isomers also promote these motions. For example, *trans*-polybutadiene has lower energy differences between rotational isomers than polyethylene (10) and exhibits considerable molecular motion at 50°K lower (9). Collinear bonds in the form of crankshaft structures (9) or phenylene groups may also enhance main-chain motions because these units can rotate without the cooperative motion of bonded neighboring units. However these small main-chain motions are inhibited by strong intermolecular interactions, particularly when such interactions occur short distances from each other along the polymer chain. For example nylon 4 and higher

members of this series have secondary glass transitions (11) whereas nylon 3 does not because it has only two methylene groups between the hydrogen bonding amide units. Crosslinking generally does not significantly affect these small motions—*i.e.*, the secondary glass transition of the liquid epoxy monomer of bisphenol-A-diglycidyl ether is shifted only  $\sim 10^\circ\text{K}$  when incorporated into a crosslinked glass (12).

Small main-chain motions enhance the chances of polymer chain segments associated with flow to pass one another by decreasing the rigidity of the segment. However it seems that these motions are only one of several parameters that affect the flow processes. From studies on the relationships between the dynamic mechanical spectra and the mechanical properties of several glassy polymers we found that the amount of segmental flow during deformation and failure is a function of both the amount of small main-chain motions and the free volume of the glass (6, 9). This indicates that fewer small main-chain motions are necessary to enhance segmental flow as the free volume increases. It was also evident that the small main-chain motions depend on the intra- and intermolecular potential barriers. Indeed recent results indicate that small main-chain motions can be either unaffected (13) or increased despite embrittlement of the glass (14).

**The Embrittlement of Polycarbonate.** Polycarbonate embrittles at  $80^\circ\text{--}130^\circ\text{C}$  ( $T_g \simeq 150^\circ\text{C}$ ) (15, 16, 17, 18); its original properties can be restored by annealing above  $130^\circ\text{C}$ . This embrittlement is accompanied by a small density increase (16, 17, 19) but without detectable changes in short-range order as determined from x-ray diffraction studies (19). We studied the effect of thermal history on the mechanical properties of polycarbonate (Lexan, G. E. Co.) after annealing to constant yield stress. (Solution-cast films and compression-molded specimens attained a constant yield stress, density, and dynamic mechanical  $\gamma$  peak intensity ( $185^\circ\text{K}$ , 1 Hz) after 12 hr annealing at  $145^\circ\text{C}$  and remained unchanged after prolonged annealing—*i.e.*, 17 days). Consecutive glassy state annealing cycles between  $145^\circ$  and  $125^\circ\text{C}$ , produced reversible changes in yield stress, density, and enthalpy of the glass. From plots of the log (strain rate) *vs.* yield stress and fracture topography studies, we showed that the  $125^\circ\text{C}$  annealed glass was considerably more brittle than the  $145^\circ\text{C}$  annealed glass in the impact strain rate region. The linear coefficient of expansion calculated from the reversible density changes had the same order of magnitude as that normally associated with liquid-like packing changes in free volume (*cf.*,  $\sim 2.0 \times 10^{-5}$ ). These observations suggest that the embrittlement of polycarbonate produced by annealing at  $80^\circ\text{--}130^\circ\text{C}$  results from normal free volume changes and not from the growth of ordered regions. However this does not preclude the presence of

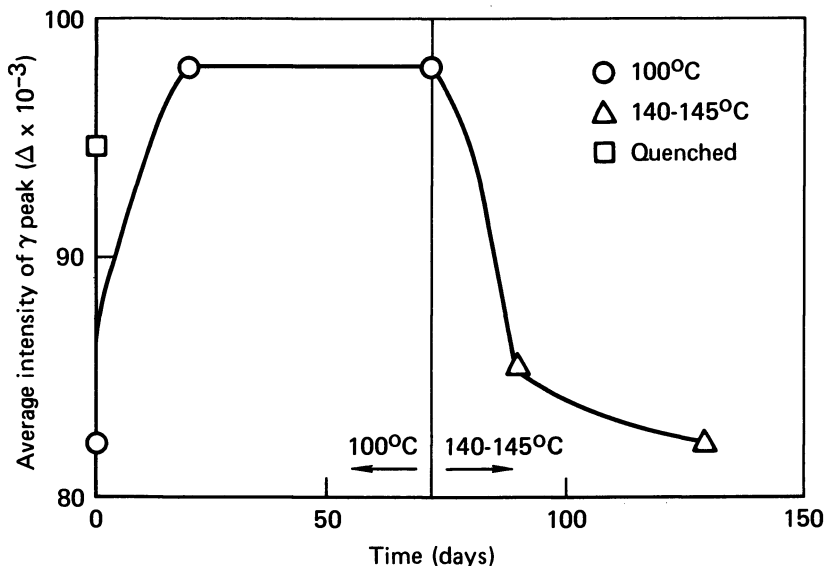
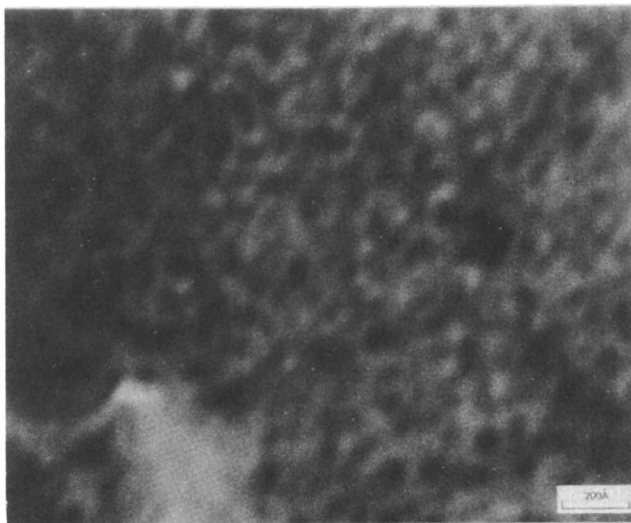


Figure 1. Average intensity of the polycarbonate  $\gamma$  peak vs. time for heat treatments at 100°C and at 140°–145°C

ordered regions in the 145°C equilibrium state glass nor the growth of such regions in a glass with lower order when annealed above 80°C.

Neki and Geil (20) have observed the growth and rearrangement of 100–1400 Å morphological entities on the etched surfaces of quenched polycarbonate on annealing at 145°C. This suggests that ordered regions may exist in the 145°C equilibrium glassy state. Furthermore we found that the dynamic mechanical  $\gamma$  peak exhibits reversible changes in intensity on consecutive thermal annealing cycles between 145° and 100°C. Figure 1 shows a plot of the average intensity of this peak at 120°–250°K vs. time of heat treatment at 100°C and at 140°–145°C. The intensity increases at 100°C in the same time as that necessary to complete the embrittlement (17) and is restored to its original value by annealing just below  $T_g$ . A quenched specimen has a slightly higher intensity than a specimen that has been slowly cooled through  $T_g$ . These results suggest that certain small main-chain motions become enhanced during the embrittlement despite a density increase. We suggest that conformation changes that occur during embrittlement produce poorly packed essentially parallel chain segments, each comprised of consecutive runs of extended configurations. These segments could cause a small density increase but still enhance small main-chain motions by allowing such motions to sweep out smaller volumes than consecutive runs of irregular configurations. Such configurational changes could be caused by ordered





*Figure 2. Nodular structure in polycarbonate with apparent internodular crosslinks (transmission electron micrograph, unshadowed)*

regions consisting of essentially parallel chain segments in the 145°C equilibrium state glass. Small-angle x-ray scattering (SAXS) studies on embrittled and non-embrittled glasses did not reveal any ordered regions below  $\sim 40$  Å, the limit of detection. However transmission electron microscopy of solution-cast thin films did reveal  $\sim 30$  Å nodules (Figure 2) that increased to 50–60 Å on annealing at 125°C. In addition we observed the merging of these nodules and the ordering of the internodular material to form larger structures. The nodules appear to be interconnected by  $\sim 30$  Å internodular crosslinks that are less well-ordered than the nodules themselves. The larger ordered regions were connected by ribbons of interconnected smaller nodules. We suggest that the 30 Å nodules are molecular domains of ordered, single polymer chains that weakly interconnect to form larger structures on annealing below  $T_g$ . Density measurements also suggest that ordered regions may exist in the 145°C equilibrium state glass. The density of polycarbonate increased with increasing annealing temperature above 145°C, indicating the further growth of ordered regions.

Hence for a polycarbonate glass that has a lower state of order than the 145°C equilibrium state, we suggest that annealing at 80–130°C causes simultaneous normal free volume changes and the ordering and interconnection of molecular domains. Although the free volume changes are the primary factor controlling the mechanical properties of the glass, the nature of these changes is modified by ordered regions.

**Microvoid Formation during Sample Preparation of Polymer Glasses.** Flow initiation on a microscopic basis depends on the local stress concentrations present in the form of flaws. The distribution of the magnitudes of the stress intensity factors associated with all flaws smaller than the primary flaw has a significant effect on the amount of flow that occurs during the deformation and failure of a polymer glass. Generally there are more imperfections on the surface of a glass because of its exposure during fabrication. However for epoxy resins (12) and polymers cast from solution (21), surface and internal microvoids can result from the clustering of one of the constituents during sample preparations. For epoxies the tendency of the epoxy monomer of bisphenol A diglycidyl ether to crystallize partially in the liquid monomer (mp  $\sim 35^{\circ}\text{C}$ ) and to crystallize in a partially cured resin introduces different sized microvoids into these glasses by melting the crystals in the resin and subsequently volatilizing the resultant liquid. Results to date show differences in the brittleness of these resins for different sizes of the original crystalline regions. For solution-cast polymer glasses dynamic mechanical studies indicate that part of the diluent exists in small clusters, as evidenced by characteristic absorption peaks (21, 22). This phenomenon can be used to produce microvoids in the glass. Figure 3 shows a transmission electron micrograph of a strained film of a solution-cast polyimide copolymer (Upjohn PI 2080) which has a strong dielectric absorption peak charac-

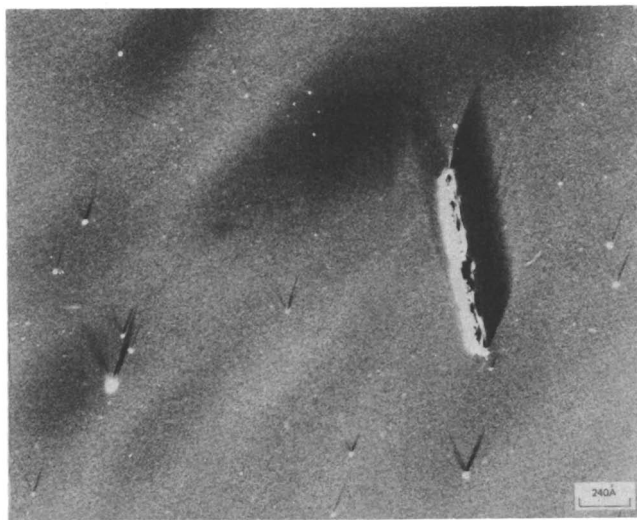


*Figure 3. Strained solution cast polyimide exhibiting microvoids and shear bands (transmission electron micrograph, unshadowed)*

teristic of solvent clustering (21). Microvoids of 10–150 Å, some of which may have resulted from solvent clusters, are visible and act as stress-intensity points as indicated by the dark shear lines associated with each void. The dark lines indicate denser packing of the polymer chains resulting from molecular flow and orientation. It is evident from this electron micrograph that the number and size of microvoids affect the amount of molecular flow. (The resolution and contrast of this micrograph, we believe, result from the film collecting a charge and electrons accumulating at its top surface when on the microscope grid. We are investigating this phenomenon in our laboratories.)

**Modification of the Properties of Polymer Glasses in the Polymer-Filler Interfacial Region in Composites.** In composites the properties of the glass are modified at the interfacial region of the filler. The nature of the interface in fiber composites affects the failure criteria, particularly in the growth of early damage regions *via* interfacial failure from the high shear stresses associated with fiber ends. The fracture process often occurs within the resin adjacent to the interface when there is strong interaction between the matrix and fiber. Hence in glassy polymer composites the strength of interaction between the polymer and filler and the nature of the adjacent polymer layers are important parameters that affect the ease of crack growth along the interface. Amorphous but crystallizable glasses such as polycarbonate will crystallize at the surface of fillers (14, 23). However there are indications that even non-crystallizable glasses such as epoxies order at the filler surface (24).

We studied the effect of high surface area carbon black and fused silica fillers on the large, secondary glass transition of non-crystallizable SBR (31.6% styrene) copolymer which is associated with small main-chain motions of *trans*-polybutadiene units (25). Figure 4 shows plots

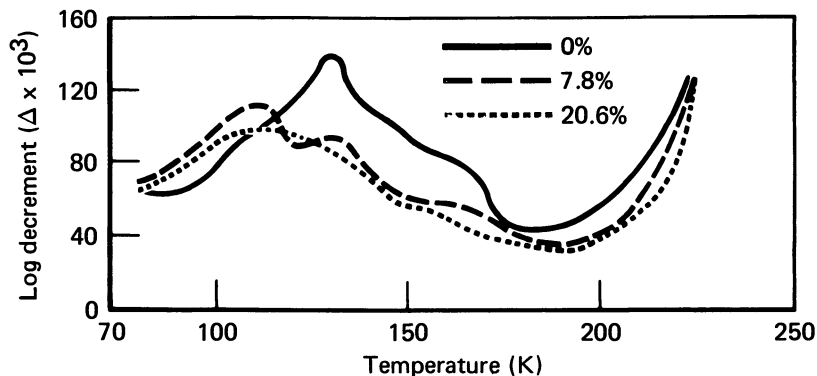


Figure 4. Damping ( $\Delta$ ) vs. temperature for SBR (31.6 mole % styrene) containing 0, 7.8, and 20.6 vol % fused silica

of the cryogenic dynamic-mechanical relaxation spectra of the SBR-fused silica composites at different filler volume fractions. Additional damping mechanisms from filler-filler and polymer-filler frictional effects and a polymer-rich skin effect (26) were negligible for these composites, and hence these data could be analyzed for volume additivity of the matrix damping. From these analyses the amount of molecular motion eliminated from the glassy state by carbon black was greater than that found with fused silica; this indicated stronger polymer-filler interaction. The degree of interaction between polymer and filler at the interface affected polymer layers further removed from the filler surface *via* entropic restrictions of polymer conformations. The dilatational stresses resulting from the mismatch in the coefficients of expansion of filler and matrix caused the relaxation spectra to shift to lower temperatures; this effect was more pronounced when polymer-filler interaction was weak. Changes in the brittleness of the polymer glass matrix induced by the filler in the interfacial region primarily depended on shifts in the polymer relaxation spectra. These shifts depended on the polymer-filler interaction and dilatational stresses. It was concluded that as the interaction between the matrix and the filler becomes stronger, thereby inhibiting dewetting under applied stress, the adjacent polymer matrix becomes more brittle.

### *Literature Cited*

1. Boyer, R. F., *Polym. Eng. Sci.* (1968) **8**, 161.
2. Heijboer, J., *J. Polym. Sci.* (1968) **C16**, 3755.
3. Sauer, J. A., "Molecular Order—Molecular Motion," H. H. Kausch, Ed., p. 69, Interscience, New York, 1971.
4. Garbuglio, C., Ajroldi, G., Casiragni, T., Yittadini, G., *J. Appl. Polym. Sci.* (1971) **15**, 2487.
5. Bauwens, J. C., *J. Mater. Sci.* (1972) **7**, 577.
6. Morgan, R. J., *J. Polym. Sci. Polym. Phys. Ed.* (1973) **11**, 1271.
7. Kastelic, J. R., Baer, E., *J. Macromol. Sci., Phys.* (1973) **B7** (4), 679.
8. "Symposium on Physical Structure of the Amorphous State," *Amer. Chem. Soc., Div. Polymer Chem., Preprints* (1974) **15** (2).
9. Morgan, R. J., Nielsen, L. E., Buchdahl, R., *J. Appl. Phys.* (1971) **42**, 4653.
10. Morgan, R. J., Treloar, L. R. G., *J. Polym. Sci. A2* (1972) **10**, 51.
11. Lawson, A. H., Sauer, J. A., Woodward, A. E., *J. Appl. Phys.* (1963) **34**, 2492.
12. Morgan, R. J., O'Neal, J. E., "Structure-Property Relationships of Epoxy-Amine Systems," unpublished data.
13. Moore, R. S., Petrie, S. E. B., *Amer. Chem. Soc., Div. Poly. Chem., Preprint* **15** (1), 70 (1974).
14. Morgan, R. J., O'Neal, J. E., "The Embrittlement of Polycarbonate," unpublished data.
15. Peilstocker, G., *Kunststoffe* (1961) **51**, 509.
16. Golden, J. H., Hammant, B. L., Hazell, E. A., *J. Appl. Polym. Sci.* (1967) **11**, 1571.
17. LeGrand, D. G., *J. Appl. Polym. Sci.* (1969) **13**, 2129.
18. LeGrand, D. G., *J. Appl. Polym. Sci.* (1972) **16**, 1367.

19. Wignall, G. D., Longman, G. W., *J. Mater. Sci.* (1973) 8, 1439.
20. Neki, K., Geil, P. H., *J. Macromol. Sci., Phys.* (1973) B8(1-2), 295.
21. Morgan, R. J., O'Neal, J. E., "Structure-Property Relationships of Polyimides," unpublished data.
22. Morgan, R. J., Nielsen, L. E., *J. Polym. Sci. A-2* (1972) 10, 1575.
23. Kardos, J. L., Cheng, F. S., Tolbert, T. L., *Proc. Annu. Tech. Conf. SPE, 39th, Chicago, 1972*, 154.
24. Manson, J. A., Chiu, E. H., *Amer. Chem. Soc., Div. Polym. Chem., Preprint* 14 (1), 469 (1973).
25. Morgan, R. J., *J. Mater. Sci.* (1974) 9, 1219.
26. Nielsen, L. E., Lee, B. L., *J. Compos. Mater.* (1972) 6, 136.

RECEIVED October 18, 1974. Research conducted under the McDonnell Douglas Independent Research and Development program.

# Complex Formation and Fracture Surface Morphology of a Highly Doubly Oriented Nylon 66 Rod

J. H. MAGILL and M. KOJIMA

Department of Metallurgical and Materials Engineering,  
University of Pittsburgh, Pittsburgh, Pa. 15261

S. S. POLLACK and M. N. HALLER

Mellon Institute of Science, Carnegie Mellon University, Pittsburgh, Pa. 15213

*Nylon 66 was highly doubly oriented by drawing a necked unoriented rod under pressure between heated metal bars maintained at elevated temperatures (below the polymer melting temperature). The resulting flat strips were examined intact and were microtomed and/or fractured in the three mutually perpendicular directions. The doubly oriented samples were also complexed with aqueous iodine-potassium iodide solutions. The mode of fracture was consistent with the textural features of the strip wherein the hydrogen bonded planes act to maintain sample integrity. V-shaped deformation bands are observed. The original hydrogen bonding network is disrupted to accommodate the voluminous linear  $I_3^-$  ions which line up along the polymer chain backbone direction, forming a new unit cell with one  $K^+I_3^-$  associated with each nylon 66 monomer repeat unit. The complexed system seems relatively stable.*

Ever since the pioneering work of Carothers and his associates (1) in the 1930's which lead to the discovery and subsequent commercial production of nylon 66, this material has occupied a prominent position among other polymers. Although cursory x-ray investigations were carried out in the early stages of technological development to assess orientation and crystallinity, it was the classic work of Bunn and associates (2, 3,

4) that furthered our understanding of the structure of nylon 66 and the nature of crystalline polymers in general. Models of the polymeric solid state were based on this early work. Ideas concerning fracture (rupture by shearing and tearing) were formulated by Bunn and others (2, 5). The concept of tie molecules was invoked at an early date. With the advent of chain folding in the late 1950's—an unexpected revolutionary event in polymer physics—new notions of the arrangement and nature of polymeric molecules evolved (6). Some early concepts of the morphogenesis of the nature of the crystalline state were completely discarded only to be reinvented to a varying degree to account for the mechanical behavior of oriented polymeric systems. The role of tie molecules and microfibrils is still believed to be significant in this regard (8). Not only are fibrillar morphologies a dominant feature in crazing of non-crystalline polymers, but they also appear to be the load-bearing members which help to maintain the integrity of the crystalline domains of semicrystalline plastics. Statton (8, 9) recently demonstrated that the structure and morphology of highly oriented fibers of nylon 66 are modified by thermal treatment at varying tensions. The fiber texture was characterized by several techniques. From these results it was concluded that refolding of molecules is a major contributor to shrinkage and shrinkage tension in an oriented fibrous systems and that tension during high temperature annealing disrupts the crystalline perfection within the sample. Other work on the mechanical behavior of doubly oriented nylon 66 claims that the (001) is really a higher order of discrete, meridional, small-angle reflections. Low frequency infrared results (11, 12) provide valuable insights into our understanding of the structural details of molecular groups in nylon 66 and other polyamides in their original and complexed states with iodine-potassium iodine. Calorimetric measurements (13) made on fibers in diverse moisture environments helped us to comprehend the interaction of water with polyamides which it plasticizes. X-ray scattering measurement from bulk samples and fibers have been made by several investigators (2, 3, 4, 5, 14). A useful compendium of knowledge which deals with many chemical and physical properties is given in a recent book (3) devoted exclusively to the properties of polyamides.

Although much of the work referred to in this paper was done several years ago, it was not reported previously. The content and implications are sufficiently novel to merit mention even at this time. The fracture surface morphology of doubly oriented nylon 66 was studied in its untreated and  $I_2$ -KI complexed state. All the work reported here was done on doubly oriented samples made from an unoriented nylon 66 rod according to the techniques outlined below.

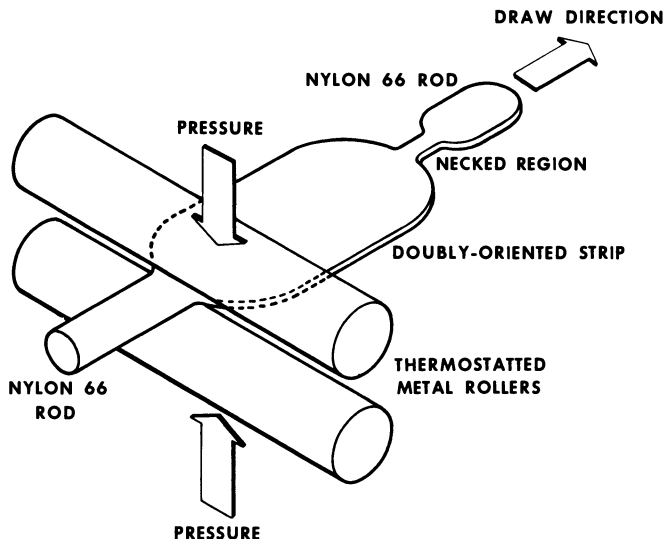


Figure 1. Schematic of the deformation procedure for nylon 66

### Experimental

An unoriented nylon 66,  $\frac{1}{4}$  and  $\frac{3}{8}$  inch diameter rod provided by Imperial Chemical Industries Ltd., U.K. was drawn to form a neck which was then located between carefully positioned metal rods and was doubly oriented by drawing the necked rod through heated metallic bars which were adjusted to keep the sample compressed during the deformation operation. A schematic of the procedure is given in Figure 1. The temperature of the bars was maintained at *ca.* 200°C, and the rod underwent several passes until it showed no significant changes in thickness or length. Through this procedure, attributed to B. C. Stace, the rod was converted into a flat strip at least 1 cm wide and no greater than 0.1 cm thick. The length increased three- to sixfold approximately, depending on the treatment. The doubly oriented specimen was transparent through its thin direction (perpendicular to the deformation plane). Orientation within the main body of the strip was uniform except perhaps close to the edges. About 1–2 mm of the sample was discarded at this location in the work described below.

Thin slices were microtomed from the flat ( $5\text{--}50\ \mu$ ) strip (Figure 2) in the three mutually perpendicular directions. Fractured surface replicas were also made of the three different directions for samples precooled to liquid nitrogen temperature. The specimens fractured most readily between the (010) planes (Figure 2), exhibiting layered cleavage somewhat akin to mica flakes. Traverse to this plane, fracture was less well defined and less facile. However no difficulty was experienced in microtoming the material in all three directions.

The thin sections were examined with the polarizing microscope, infrared spectroscopy, laser light scattering, differential scanning calo-



rimetry, scanning and electron microscopy, and wide and small angle x-ray scattering. Fractured surfaces were studied by optical and scanning electron microscopy and by replication-transmission electron microscopy. Complexes of nylon 66 strips and sections in the doubly oriented state were formed with iodine in potassium iodide solution according to procedures outlined previously (11, 12).

### Results and Discussions

**Morphology of Double-Oriented Samples.** More than a decade ago one of the authors noted that nylon 6 and nylon 66 rods exhibited enhanced transparency in the  $[010]$  direction when they were drawn and doubly oriented in a single operation. The clear nature of the deformed sample arises because the large polycrystalline spherulitic entities and their interspherulitic regions are destroyed during the processing of the rod and are converted into well-ordered, much smaller crystalline domains oriented along the draw direction of the nylon strip (*see* Figure 5). Consequently the intensity of the scattered light is considerably reduced, and the orientation overrides the influence of crystallinity. In doubly oriented polyethylene terephthalate of relatively high crystallinity, enhanced transparency has also been reported. Microtomed sections of this material cut from the nylon strip in the three mutually perpendicular directions had three distinct morphologies. Figure 3A–C illustrates the patterns obtained in directions perpendicular, parallel, and transverse to the rolling direction. In a highly oriented specimen these correspond to the three crystallographic planes  $(001)$ ,  $(010)$ , and  $(100)$  of the sample.

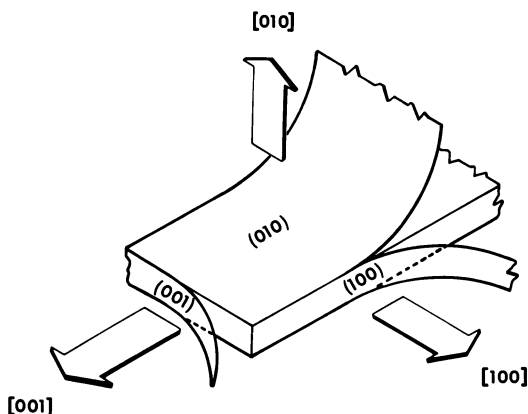


Figure 2. Schematic of a section of deformed nylon rod which may be regarded as a pseudocrystal. The hydrogen bonded  $(010)$  planes and their corresponding directions are indicated.

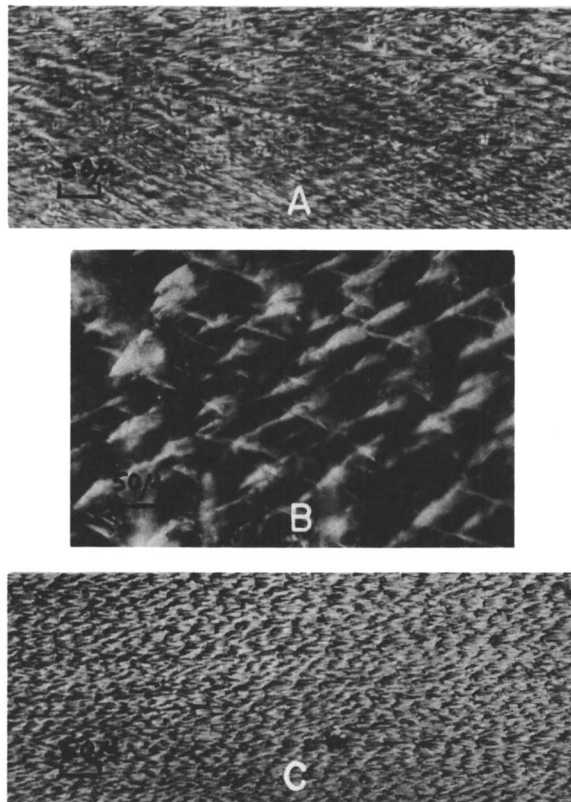


Figure 3. Optical micrograph of sections through a doubly oriented nylon 66 rod taken: (A) perpendicular to the roll direction, (001) of Figure 2; (B) parallel to the roll direction, (010) of Figure 2; and (C) transverse to the rolling plane, (100) of Figure 2.

The most regular deformation habit occurs in the (010) plane, and this is further substantiated by both scanning and electron microscopy.

The nature of the samples is consistent with a well-defined biaxial figure observed in conoscopic light between crossed polars. Light scattering measurements in  $H_v$  and  $V_v$  scattering modes are in accord with highly oriented texture depleted of spherulites in accordance with optical observation. Figure 4 (A and B) illustrates the  $H_v$  and  $V_v$  scattering patterns obtained from microtomed section viewed perpendicular to the (100) plane of Figure 2. (The notation  $H_v$  denotes that the radiation incident on the sample is polarized in the vertical plane; the analyzer is situated horizontal to this direction.) Note that the  $V_v$  pattern is at least an order of magnitude more intense than the  $H_v$  scattering of the same geometry. The  $H_v$  and  $V_v$  scattering perpendicular to the (010)

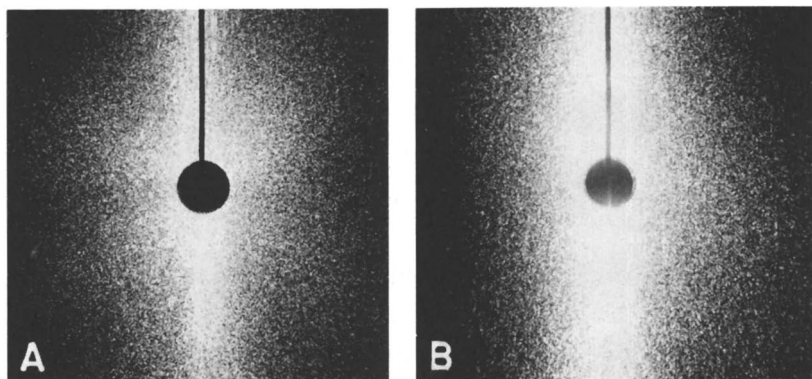


Figure 4. Laser scattering pattern of microtomed section parallel to the [100] direction: (A) is  $H_v$ , exposure 1/10 sec and (B) is  $V_v$ , exposure 1/250 sec. The subscript denotes the polarization of the incident radiation. Sample to film distance, 11.5 cm in (A) and (B); layer beam 0.25 mm diameter.

direction show similar intensity relationships except that there is a contribution from the  $-(CONH)-$  dipoles lying within the plane of the sample which cause some broadening of the pattern across the molecular chain direction.

Differential scanning calorimetry of the unoriented and doubly oriented nylon 66 reveals subtle differences. The doubly oriented samples display two peaks and melt at a higher temperature than the unoriented material. This pattern of behavior is consistent with that previously noted for the melting behavior of oriented nylon 66 fibers. Also note that the morphology of Figure 5 is consistent with a "shiskebob" type texture which may be responsible for the double melting peak. This point will be reported when a definite study substantiates or refutes this suggestion.

X-ray diffraction studies of these samples showed them to be well oriented along as well as perpendicular to the draw direction. The unit cell corresponded to the  $\alpha$  form described by Bunn and Garner (4) in their original paper although we did obtain a few more reflections than they reported. In the virgin rod the small-angle period was about 90 Å. In the doubly oriented sample it was found to be  $100 \pm 10$  Å by small angle x-ray scattering. This value agrees with the dimensions deduced from a platinum shadowed replica of a (010) fracture surface by transmission electron microscopy. Figure 5 illustrates rows of crystallites of this dimension within this surface having their long dimensions oriented transversely to the draw direction (arrowed). The short direction corresponds to the molecular chain directions. Lower magnification micrographs show V-shaped deformation bands (Figure 6) disposed as illustrated in the optical micrographs (*see* Figure 3B for the same plane).

This well-developed pattern is not superficial but procreates through the entire sample; the point of the V is aligned along the draw direction. Optical observations by Zaukelies (15, 16) seem to be consistent with the cavity formation at the tip of the V-shaped deformation bands in Figure 6. Although Zaukelies did not examine the fracture surface in his nylon 66 and nylon 610 samples by electron microscopy, optical observations provided a spotty image with features consistent with the formation of surface cavities having dimensions capable of scattering light. He made similar observations on doubly oriented polyethylene terephthalate and a polyolefin polymer (15, 16). One of us (J. H. M.) noted behavior similar to that shown in this paper for nylon 6 which will be reported at a later date.

It seems plausible to assume that the fracture deformation behavior presented here may be characteristic of all polymers that are readily doubly orientable and that have an easy slip plane. Also note that the V-shaped fracture tip is absent in the other orientation geometries (Figure 3A and 3C). The morphological details of the deformation seem to be affected somewhat by environmental conditions, but it is too early to make precise comments on this point.

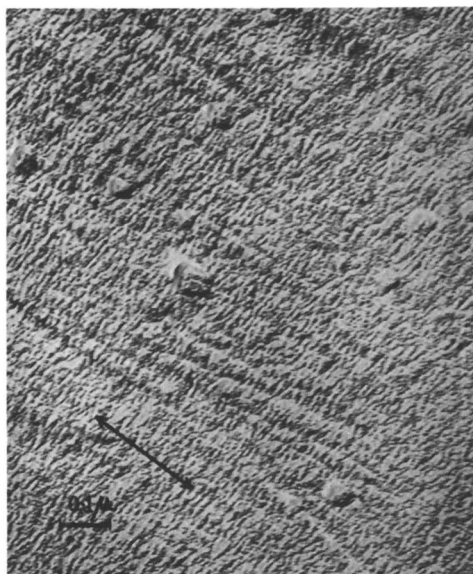
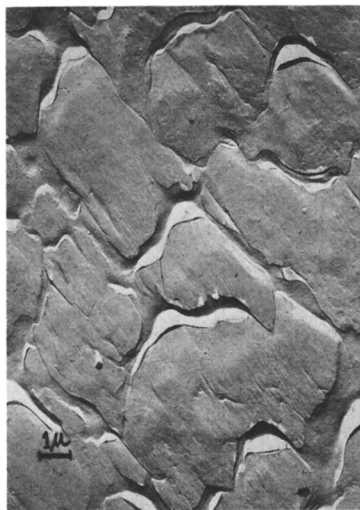


*Figure 5. Replica of platinum shadowed, fractured, (010) hydrogen-bonded surface showing chain folded crystallites aligned with their molecular axis along the draw direction arrowed*

*Figure 6. Electron micrograph illustrating V-shaped deformation bands within the hydrogen-bonded (010) planes of fractured nylon 66. Micron marker insert, an edge view of fracture surface running from (010) plane through the thin direction of the strip (Figure 2).*



Scanning electron micrographs of specimens fractured at liquid nitrogen temperatures and metal shadowed with Pd/Au alloy also exhibited unique deformation patterns which revealed a layered fracture morphology reminiscent of the sheet-like morphology of mica in appearance. Figure 7 shows the terraced texture of a specimen fractured at  $45^\circ$  through the (010) plane in the [100] direction. The angle of the V-shaped fracture in the scanning electron micrograph corresponds to  $58^\circ \pm 2^\circ$  and agrees with that seen in the optical micrographs (Figure 3B). By way of comparison for the unoriented rod, the scanning electron

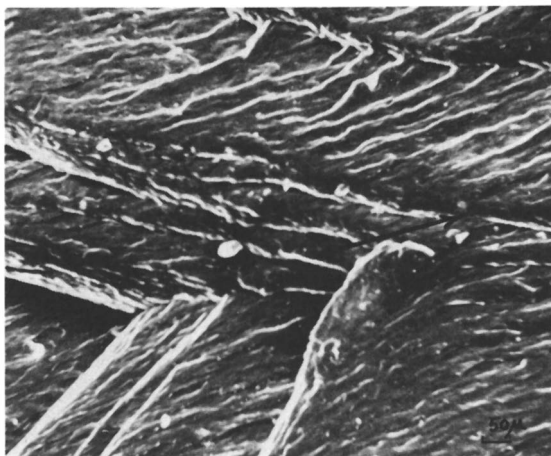


*Figure 7. Scanning electron micrograph of (010) sample shadowed with Pd/Au alloy*

micrograph (Figure 8) displays a spherulitic texture with no preferred orientation exhibited within the rod. The undeformed rod fractured equally well along or transverse to its long axis, whereas in the doubly oriented material fracture occurred most readily between the tenaciously held, hydrogen bonded, sheet-like layers separated by the weaker van der Waals forces. This fracture mode is hardly unexpected when one recalls that the  $-\text{CONH}-$  interchain dipole-dipole interactions contribute 4.8 kcal/mole to the lattice energy of the polyamide crystal (17). About 93% of this interaction energy arises in the "a" axis dipole arrays in nylon 66 and is a controlling structure determining factor which manifests itself in the mode of fracture. Both the x-ray structure and infrared spectroscopic measurements support a texture comprised of hydrogen-bonded sheets. The symmetry of the monomer repeat within the nylon 66 unit cell facilitates H-bond formation in a folded or chain extended confor-

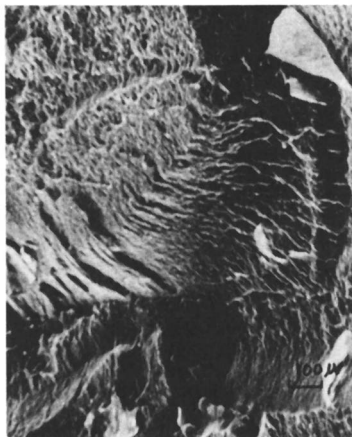


*Figure 8. Scanning electron micrograph of the unoriented nylon 66 rod fractured at 45° to the longitudinal axis*

mation without disruption of the structure. Chain folds where they exist must be regarded as defects which, like chain ends, contribute to the observed amorphous x-ray scattering patterns. Undoubtedly voids and dislocations are numerous in nylon 66, and their overall contributions during drawing are significant. Tie molecules connecting crystalline domains also contribute substantially to the ultimate properties. In polymer fibers these are generated during the orientation procedure. Peterlin (18, 19) noted that a crystalline fiber may have a high crystalline orientation factor (approaching unity) close to its melting point where its mechanical strength is severely impaired; this signifies that the state of the system clearly cannot be defined uniquely in terms of one or two parameters if the environmental conditions are altered. Remember this illustration when attempting to establish simplistic property-texture models which may have questionable validity. At elevated temperatures the

increased mobility in oriented fibers assessed by NMR is likely to be associated with the intercrystallite regions (folded and comprised of tie connections) formed as a consequence of the drawing and deformation that occur within the nylon 66 rod. Since the mobile fraction of the polymeric fibers increases as the sample temperature is raised (9), there is every reason to believe that the conditions used in our double-orientation experiments are consistent with nylon 66 of high crystallinity. In our preliminary x-ray measurements on well-oriented bulk samples, we do not have results to support coherence between the small and wide angle scattering on the meridian—a condition which is claimed to exist in mats of nylon 66 single crystals (10). Still, the topographical features of our samples are consistent with deformation occurring predominantly between kink and slip planes in crystalline material at a well-defined angle  $\theta$  given by the Orowan (20) relation:

$$\cot \theta = 2 md/nc \quad (1)$$

where  $m$  is the number of lamellae involved in the deformation process,  $d$  is the interplanar spacing,  $c$  is the crystal lattice spacing along the slip plane, and  $n$  denotes the number of  $c$  spacings per slip plane. Zaukelais (21) noted that the shear forces for nylon 66 were predominately in the (010) plane and in the [1,3,14] direction—a finding not inconsistent with our observations.

Cursory birefringent measurements made with a Berek compensator indicate some degree of distortion or non-uniformity throughout the deformed nylon 66 strips. This is most predominant at the edges of the doubly oriented sample which were not involved in this study. Currently, there appears to be little doubt that the mode of fracture is consistent with deformation and concomitant textural changes in the unoriented nylon 66 rod during its transformation into a flat doubly oriented strip. Voids and stress raisers cause the crack initiation and its step-like propagation as the fracture moves through the sample predominately along crystallographic directions.

**Doubly Oriented Complexed Samples.** The dimensional changes which oriented samples undergo when complexed with  $I_2$  in KI solutions are a function of film thickness, solution concentration, and time. From previous work (11, 12) appropriate conditions were established for complexing nylon 66. Infrared work on thin sections is invaluable in establishing that a new structure is formed with the triiodide ion ( $I_3^-$ ) strongly interacting with the oxygen and nitrogen atoms of the amide group forming a bridge between an amide nitrogen and a protonated carbonyl group in adjacent sheets. To accommodate this large anion aligned along the molecular chain directions a contraction of the zig-zag chain occurs

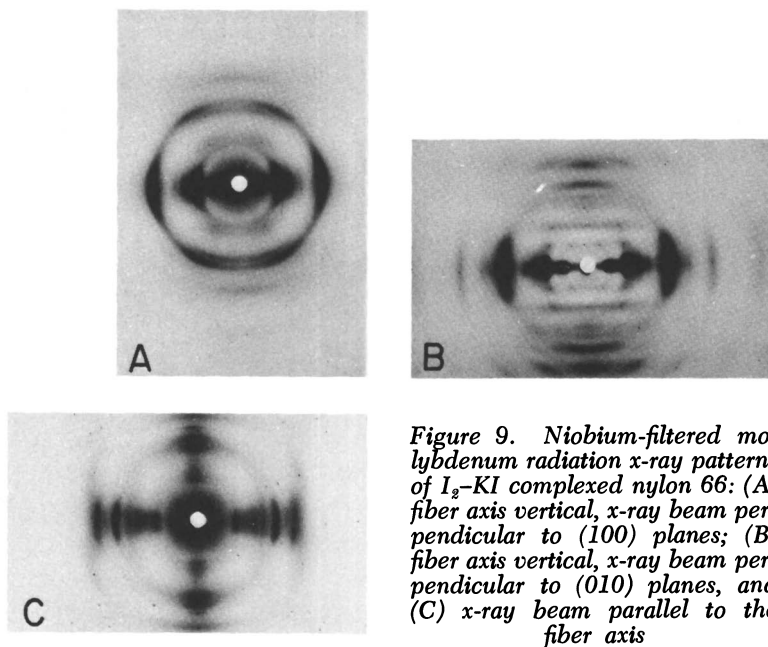


Figure 9. Niobium-filtered molybdenum radiation x-ray patterns of  $I_2$ -KI complexed nylon 66: (A) fiber axis vertical, x-ray beam perpendicular to (100) planes; (B) fiber axis vertical, x-ray beam perpendicular to (010) planes, and (C) x-ray beam parallel to the fiber axis

around the  $-\text{CONH}-$  group in the chain direction. The effect of molecular iodine on polyamides has already been noted by one of us (*see Ref. 11*), and it has been clearly demonstrated that the  $I_3^-$  form is most effective in complex formation.

The infrared spectra (*11, 12*) can be used advantageously to provide a facile procedure to characterize polyamides in the untreated and treated states. Structure-frequency correlations have been established which indicate that the  $\alpha$  form and  $\gamma$  form can be clearly distinguished using two amide bands characteristic of the structure of the polyamide. These are:

	$\alpha$ Form	$\gamma$ Form
amide V	ca. 690 $\text{cm}^{-1}$	ca. 710 $\text{cm}^{-1}$
amide VI	ca. 580 $\text{cm}^{-1}$	ca. 620 $\text{cm}^{-1}$

The amide VI band is associated with  $\text{C}=\text{O}$  out-of-plane bending, and the amide V band corresponds to the  $\text{N}-\text{H}$  out-of-plane bending. Both modes are associated with the changes in crystal modification as we (*11*) and others (*21*) noted by x-ray diffraction in polyamides. For nylon 66 the spectra of the untreated and iodine-potassium iodide desorbed samples are identical although that of the complexed polyamide (*12*) differs significantly. Evidence from polarized low frequency, particularly of the 140 and 100  $\text{cm}^{-1}$  bands of the ion is also definitive on this point and has



been successively used to characterize many polyamide structures (11, 12).

X-ray evidence (Figure 9) with niobium-filtered molybdenum radiation has established that well-defined novel patterns are obtained in the three mutually new perpendicular directions of the complexed sample. Previous workers (22, 23) hinted at a new structure and mentioned that copper radiation was strongly absorbed by the abundance of iodine in the sample. Using 25 unique reflections from the complex, we propose a tentative orthorhombic unit cell for the complex where  $a = 9.33$ ,  $b = 15.95$ , and  $c = 16.30$  Å with a calculated density of 2.52 g/cc based on six molecules per cell. There appears to be one  $K^+I_3^-$  associated with each nylon 66 monomer unit within the complex. Although this x-ray density is higher than that determined by the flotation method (2.4 g/cc in this work), it can be readily rationalized with the current experimental evidence. Figure 9C suggests a degree of chain twisting consistent with this new conformation in the complexed polymer. Note that the nylon 66 reverts to its original  $\alpha$  structure when the iodine is desorbed with warm thiosulfate solution, indicating that this  $\alpha$  structural form was preferred over the chain contracted  $\gamma$  conformation commonly associated with many other polyamides (11). Indeed the route to the  $\gamma$  phase in nylon 6 is conveniently reached through complex formation followed by iodine desorption.

The small angle x-ray scattering results obtained from the nylon 66 complex show a substantial increase in the small angle spacing from 110 Å in the doubly oriented strip to  $160 \pm 20$  Å in the complexed state depicted in Figure 10 along with the rich pattern of collagen that is used as a reference sample. The marked increase in the small-angle spacing is in

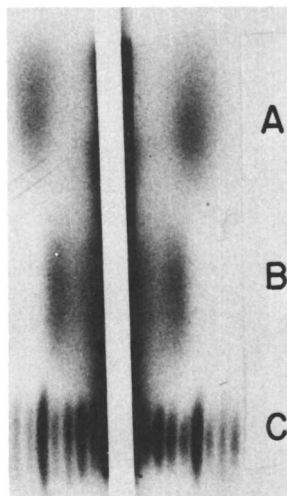


Figure 10. Small angle x-ray pattern of: (a) untreated nylon 66 perpendicular to (010) face; (b)  $I_2$ -KI treated nylon 66 perpendicular to (010) face, and (c) collagen



*Figure 11. Scanning electron micrograph of a freshly fractured sample of complexed nylon 66 showing the distorted layers corresponding to Figure 7. Sample was unshadowed and fractured at liquid nitrogen temperature.*

accord with the geometrical changes of the sample itself attributed to the ingress of  $K^+I_3^-$  into the amorphous and crystalline regions of the sample. The increase in the dimension transverse to the rolling direction is about double that of the original sample with some perceptible void space sometimes occurring in the middle of the swollen section.

Unfortunately the surface of the complexed sample cannot be replicated and examined by electron microscopy because the solvents normally used perturb the complex by introducing artifacts. However scanning electron micrographs of these fracture surfaces indicate that the morphology of the original polymer is modified considerably by the  $I_2$ -KI treatment—a fact consistent with the wide angle x-ray and other evidence. It has been pointed out elsewhere (11) that thin films and fibers of complexed polyamides are very pliable and often putty-like when first removed from the complexing solution; this fact is consistent

with the substantial property changes associated with this new state of the material. The stretchability (11) of the sample is also greatly improved because of the increased plasticization afforded by the moisture complex formation. In thicker samples of the type encountered in this work this plasticity is less apparent, although the structural evidence (infrared and x-ray) should be independent of sample thickness if sufficient time is allowed for all the hydrogen bonds to interact with  $K^+I_3^-$ . We recently noted that the ingress of  $I_2-KI$  into a thick rod is diffusion limited.

Figure 11 shows a scanning electron micrograph of a (010) surface of the complexed nylon that has been fractured at liquid nitrogen temperature. There is some semblance of the layered texture depicted in the original Figure 7. Parenthetically, it is worth pointing out that the stability of the sample surface to the electron beam is greatly enhanced by the  $I_2-KI$  complexing agent so that metal shadowing (with Pd/Au) was unnecessary to prevent surface charging in these materials, thereby permitting more surface detail. However most of the samples reported here were coated to enable a direct comparison with the untreated nylon 66. Many variations in surface texture ranging from a seemingly glassy to an almost faceted appearance have been noted for nylon 66. For example Figure 12 A and B illustrates some of these surfaces, and Figure 13 A and B shows the composition of the back-scattered x-rays from these samples respectively. In both specimens iodine ( $L\alpha$ ), iodine ( $L\beta$ ), potassium ( $K\alpha$ ), and gold ( $L\alpha$ ) are noted. In the case of the "glassy" texture the potassium ( $K\alpha$ ) peak from Figure 12 A was only about one-third the intensity of the value noted in Figure 12 B; this indicated a compositional change between these two areas of the same sample. However, a

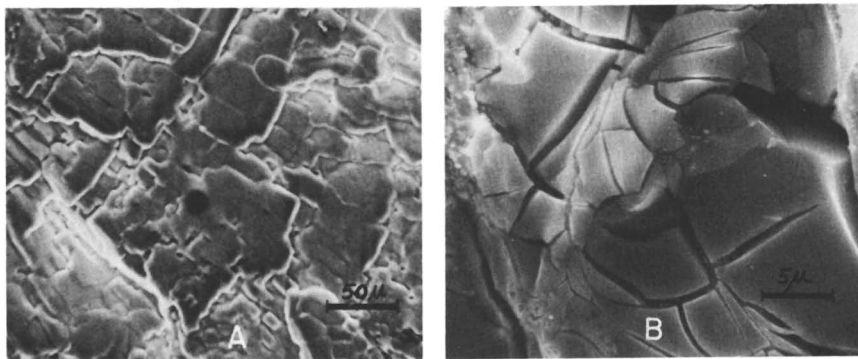


**Figure 12.** Scanning electron micrograph of: (A) another area of the Figure 11 sample displaying a glassy texture, and (B) another structural ramification of the same sample

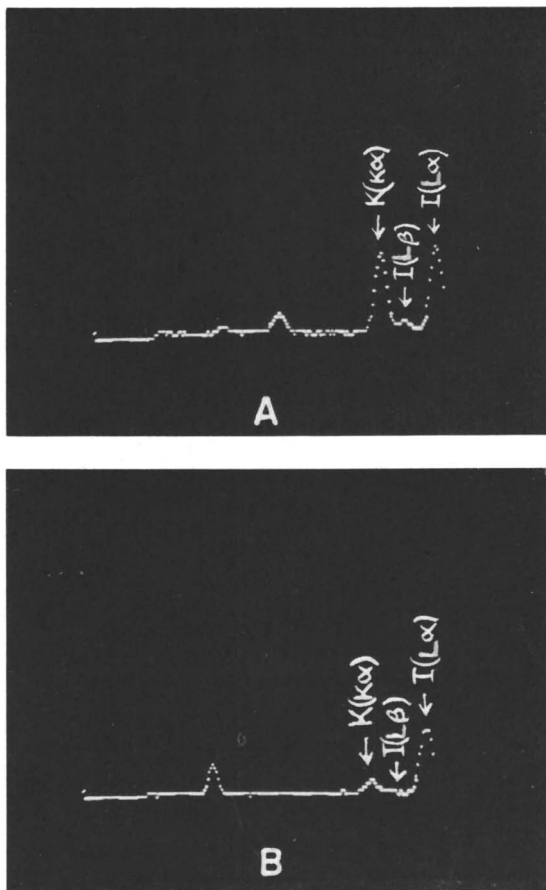
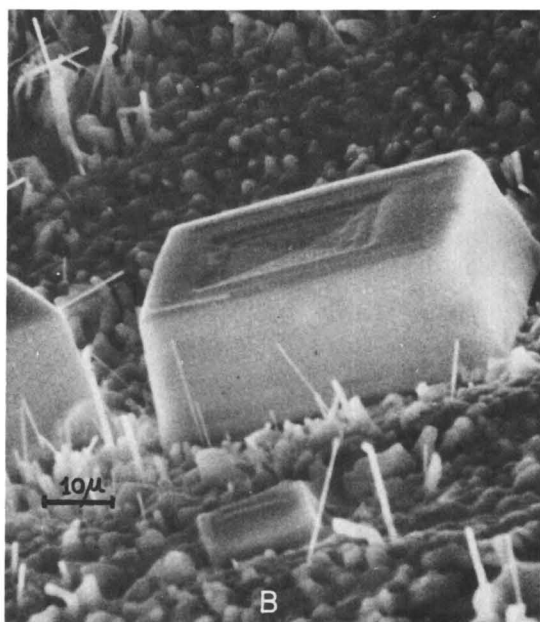
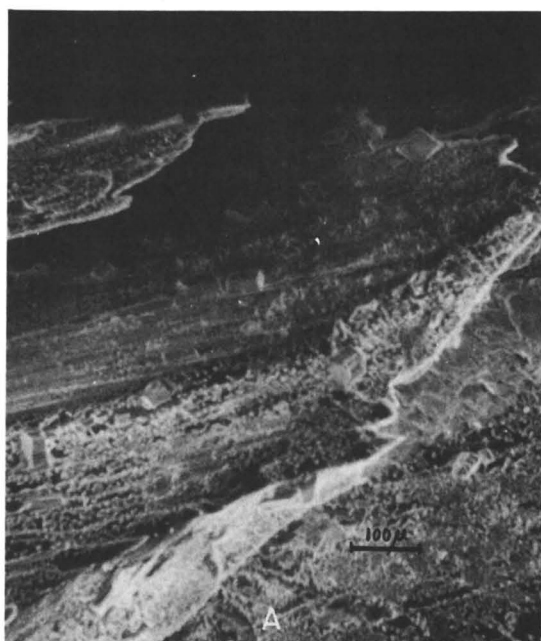


Figure 13. Back scattered x-rays obtained from Figures 12A and 12B

more recent observation on freshly prepared complexed samples does not show significant variations in peak intensities.

It has been noted elsewhere (7, 18, 19) that microfibrils are generated when polymer monofilaments are highly drawn uniaxially. Microfibrils also form here and emerge from the lathe-like sheets comprising the (010) texture in nylon 66 when these materials are drawn to failure. However a lathe-like morphology is very predominant. Although the textures described above have not been completely elucidated in this work, they do reveal a fruitful field for further study—namely, that of complex formation and morphology of highly textured polymers, even though polyamides and nylon 66 have received much attention over several decades. The “shiskebob” texture of Figure 5 requires that it be



**Figure 14.** Scanning electron micrograph of a fracture exhibiting crystalline entities between the (010) layers of a fractured sample after storage at room temperature for eight years at (A) low magnification ( $\times 100$ ), and (B) higher magnification. No metal shadowing was used in these micrographs.

probed more deeply using suitable etchants. Furthermore the treatment of the nylon 66 surface with a complexing agent such as  $I_2$ -KI, which functions as a potential etcher, can be used to modify and to improve the morphology and hence the adhesion between these polymers and other surfaces as reported recently for nylon 6 (25). Certainly this general area of investigation merits a more detailed study from many points of view. We hope that this preliminary report will stimulate interest.

### **Conclusions**

(a). Opaque nylon 66 rod can be readily transformed into relatively thick transparent doubly oriented strip.

(b). The doubly oriented material displays a different fracture morphology in the three major sample directions in the doubly oriented strip.

(c). The V-shaped deformation pattern with a cavity at its tip seems to be characteristic of many polymers which have an easy slip plane in accord with the predictions of Zaukelais. Observations made by optical, scanning, and electron microscopy are self-consistent.

(d). Complex formation of nylon 66 with  $I_2$ -KI in solution gives rise to a new crystal structure where one  $K^+I_3^-$  is coordinated with each monomer repeat unit of nylon 66. A marked density increase is noted. Complex formation occurs in both the crystalline and amorphous regions of the sample with the halogen ion,  $I_3^-$ , aligning itself with the molecular chain direction.

(e). The untreated and complexed doubly oriented samples have been characterized by several complementary experimental techniques which indicate that the morphology is well developed in each instance although the ingress of the large linear  $I_3^-$  ion causes disorientation transversely to the hydrogen-bonded direction in the complexed state.

(f). Difficulties are experienced in making a direct comparison of the fractured and complexed fractured surface by high resolution, electron microscopic techniques because of the interaction of replicating solvents with the complex.

(g). The  $I_2$ -KI solution when mildly applied can be a useful etcher for nylon 66 and other polyamides surfaces since it changes the morphology of the surface and hence its ability to adhere to other surfaces. Details of the surface structure in this regard need further elucidation.

### **Acknowledgments**

The assistance of K. Goebel is gratefully acknowledged in the preparation of the light scattering patterns. Thanks are also given to the Office of Naval Research and the National Science Foundation for partial support of this project.

### **Literature Cited**

1. Mark, H., Whitby, G. S., Eds., "Collected Papers of W. H. Carothers," Interscience, New York, 1940.

2. Hill, R., "Fibres from Synthetic Polymers," Elsevier, Amsterdam, 1953.
3. Cohen, M. J., "Nylon Plastics," S.P.E. Monograph Series, Wiley, 1973.
4. Bunn, C. W., Garner, E. V., *Proc. Roy. Soc. (London)* (1947) **A189**, 39.
5. Bunn, C. W., *Trans. Faraday Soc.* (1939) **35**, 482.
6. Clarke, E., Chapter 8 of reference 3.
7. Peterlin, A., *Amer. Chem. Soc., Div. Polym. Chem., Preprint* **15** (1), 42 (1973).
8. Statton, W. D., *Polym. Sci. Symposium*, #32, 219 (1971).
9. Sattou, W. O., *J. Polym. Sci., Part A2* (1972) **10**, 1587.
10. Aitkins, E. D. T., Sadler, D. M., Keller, A., *J. Polym. Sci., Part A2* (1972) **10**, 863.
11. Matsubara, I., Magill, J. H., *Polymer* (1966) **7**, 199.
12. Matsubara, I., Magill, J. H., *J. Polym. Sci., Phys. Ed.* (1973) **11**, 1173.
13. Jones, C. R., Porter, J., *J. Textile Inst.* (1965) **56**, T498.
14. Beresford, D. R., Bevan, H., *Polymer* (1964) **5**, 247.
15. Zaukelies, D. A., *J. Appl. Phys.* (1962) **33**, 2797.
16. Zaukelies, D. A., private communication (1974).
17. Arridge, R. G. C., Cannon, C. G., *Proc. Roy. Soc. (London)* (1964) **A278**, 91.
18. Glenz, W., Peterlin, A., *Kolloid Z., Z. Polym.* (1971) **247**, 786.
19. Glenz, W., Peterlin, A., *Appl. Polym. Symp.* (1973) **20**, 269.
20. Orowan, E., *Nature* (1942) **149**, 643.
21. Kinoshita, Y., *Makromol. Chem.* (1959) **33**, 1.
22. Ford, E., Warwicker, J. O., *J. Textile Inst.* (1960) **51**, T90.
23. Tranter, T. C., Collins, R. C., *J. Text. Inst. Trans.* (1961) T88.
24. Bell, J. P., Slade, P. E., Dumbleton, J. H., *J. Polym. Sci., Part A2* (1968) **6**.
25. Abu-Isa, I. A., *Polym. Plast. Technol. Eng.* (1973) **2** (1), 29.

RECEIVED October 18, 1974.

# A Flaw Spectrum Theory for Multiple Flaw Failure in Solid Polymers

## I. Effects of Orientation

S. S. STERNSTEIN and J. ROSENTHAL

Materials Engineering Department and Chemical Engineering Department,  
Rensselaer Polytechnic Institute, Troy, N. Y. 12181

*Failure processes in solid polymers often involve multiple local fracture, yield, or craze events. To account for such phenomena a flaw spectrum theory is proposed which considers the distribution of stress concentration factors arising from adventitious distributions of flaw sizes, shapes, and orientations. The theory is used to predict the decrease in transverse tensile strength and increase in axial tensile strength arising from the uniaxial orientation of a glassy polymer. Applications of the theory to multiaxial loading situations and to failure properties of highly oriented fibers and rubber-modified glassy polymers are also considered.*

Fracture processes in polymeric solids are difficult to analyze because of the complicated rheological behavior of these materials. For example, the creep and relaxation behavior of polymers is generally a nonlinear viscoelastic process which is stress or strain state dependent (1, 2, 3). Also the criteria for shear yielding and crazing processes are dependent on both the isotropic and deviatoric components of the stress tensor (4, 5, 6, 7, 8, 9). A mechanical strain history results in a thermomechanical shift of the relaxation time spectrum for metastable glassy polymers which is analogous to time-temperature superposition. This results in far more rapid aging of the glass than that which occurs spontaneously without external stress or strain (10).

The incorporation of nonlinear, history dependent, and stress or strain state dependent deformation processes into a rigorous stress analysis for crack or flaw tip behavior is a formidable task which may never be accomplished in complete detail. However, since flaw instability and



crack growth are never uniaxial, low stress or strain processes locally, the relative significance of various nonideal rheological processes should be assessed as they relate to the fracture process.

Solid polymers may contain various stress concentration sources (hereafter referred to as flaws) which are either continuum defects (such as cracks, holes, inclusions, and the like) or quasimolecular flaws (such as regions of orientation, packing defect, crystallinity, or excess free energy) in an otherwise homogeneous and ostensibly structureless glassy polymer.

Many failure-related processes require consideration of the entire flaw population rather than a single critical flaw. For example, the failure of a sample by the propagation of a single crack, *i.e.*, the classic Griffith problem, is a single flaw problem whereas the formation of numerous shear bands and subsequent ductile drawing of a sample or the formation of enormous numbers of crazes in a dart drop impact test are examples of multiflaw phenomena. The toughness of rubber-modified glassy polymers such as high impact polystyrene is another example where it is convenient to view the material response as being caused by a large number of flaws (the rubber phase) which produce copious amounts of small and beneficial crazes.

The population of flaws can be characterized by a flaw spectrum which is defined by (a) the distribution of flaws in terms of their characteristic dimensions (for example, their lengths and radii of curvature); (b) the distribution in terms of mean spacing or distance between flaws; and (c) the distribution in terms of anisotropy or directional preference with respect to some sample reference axis (*e.g.*, an axis of orientation or draw direction). The interactive and collective probabilities which describe distributions (a), (b), and (c) comprise the flaw spectrum and through suitable analysis serve to determine, in principle, the distribution of stress concentration factors (SCF) in a given material.

In this paper, we present a preliminary treatment of the concept of flaw spectra as related to certain aspects of material behavior. The treatment is limited to non-interacting flaws which is tantamount to considering each flaw as being acted upon by the external stress or strain state without perturbation by nearest neighbor flaws. This is a first approximation which nevertheless gives rise to several interesting predictions in reasonable agreement with observed behavior.

A flaw may be considered active if its stress concentration factor gives rise to local conditions suitable for craze, shear band, or failure initiation. Similarly the activity of the flaw spectrum may be considered as the collective fraction of all flaws that are active for a given set of conditions. The activity (or active fraction of flaws) depends on the external state of stress or strain and on sample orientation or anisotropy

as induced by drawing. Furthermore, the predicted decrease in tensile strength in the direction transverse to the orientation axis agrees well with experimental findings on drawn polystyrene. This is an intriguing result since the calculation is based solely on the idea that changes in the distribution of SCF arise from the changes in ellipticity and orientations of flaws accompanying the drawing process.

While the presence of molecular orientation and its effect on intrinsic fracture toughness (*i.e.*, crack propagation resistance) cannot be denied, our analysis strongly suggest that flaw reorientation and ellipticity changes are equally important. In other words, changes in tensile strength associated with changes in sample anisotropy may be partially caused by changes in the flaw spectra. From this viewpoint, a material's failure properties are determined by the flaw spectrum, and changes in the spectrum must be considered before invoking molecular arguments or changes in failure mechanism.

The flaw spectrum approach may be capable also of correlating failure data obtained under conditions which appear to give different material behavior. For example, tensile, Izod, and dart drop impact tests all give different impact energies or toughness measures. In part, this may be explained by the simple idea that a different fraction of flaws is active in each test. Equal biaxial loading (as in dart drop) and uniaxial tension (as in tensile impact) give rise to different flaw activities; thus it is to be expected that the number of crazes produced in each test will be different.

Flaw activity and the resultant stress concentration factors can also be expected to depend on the material's rheology. The sample loading history and path play a major role in determining the behavior of a given flaw as described elsewhere (6, 11, 12, 13), and these ideas are currently being extended to account for recent developments in constitutive equation theory for solid polymers and the idea of a flaw spectrum. In this paper, time and path dependence are not considered further, and the calculations are based on elastic stress concentration factors associated with elliptic flaw geometries.

### *Stress Concentration from an Elliptic Flaw*

In this section the maximum stress concentration developed by an elliptic hole at arbitrary orientation in an infinite elastic sheet subjected to general biaxial stress loading is considered. In Figure 1, consider an elliptic hole of major axis  $a$ , minor axis  $b$ , and orientation angle  $\beta$  with respect to an axis of applied uniaxial tension  $S_1$ . If the sheet is isotropic, elastic, and infinite, then the major principal stress ( $\sigma$ ) at the surface of the ellipse (14, 15, 16) is given by:

$$\frac{\sigma}{S_1} = \frac{\sinh 2\xi_0 + \cos 2\beta - e^{2\xi_0} \cos 2(\beta - \eta)}{\cosh 2\xi_0 - \cos 2\eta} \quad (1)$$

where  $\xi_0 = \tanh^{-1}(b/a)$ , and the variable  $\eta$  determines the particular point on the elliptic surface (Figure 1) at which the stress is computed, e.g.,  $\eta = 0$  corresponds to the major axis, and  $\eta = \pi/2$  corresponds to the minor axis. The unit tangent on the ellipse surface at the point defined by  $\eta$  is the principal axis direction for the principal stress  $\sigma$ . A second principal axis is the normal to the ellipse surface, and the corresponding principal stress is zero since a free surface is considered.

Consider now that  $S_1$  is zero, and the external stress is given by  $S_2$  as shown in Figure 1. The value of  $\sigma$  generated at the point defined by  $\eta$  can be obtained from Equation 1 provided that  $S_1$  is replaced by  $S_2$ , and  $\beta$  is replaced by  $\pi/2 + \beta$ . The value of  $\eta$  is unchanged since this variable is measured with respect to the major axis. The value of  $\sigma$  generated by the simultaneous application of  $S_1$  and  $S_2$  is obtained simply by adding the two independent contributions from  $S_1$  and  $S_2$ . This is permissible since the principal axes generated by each external load are

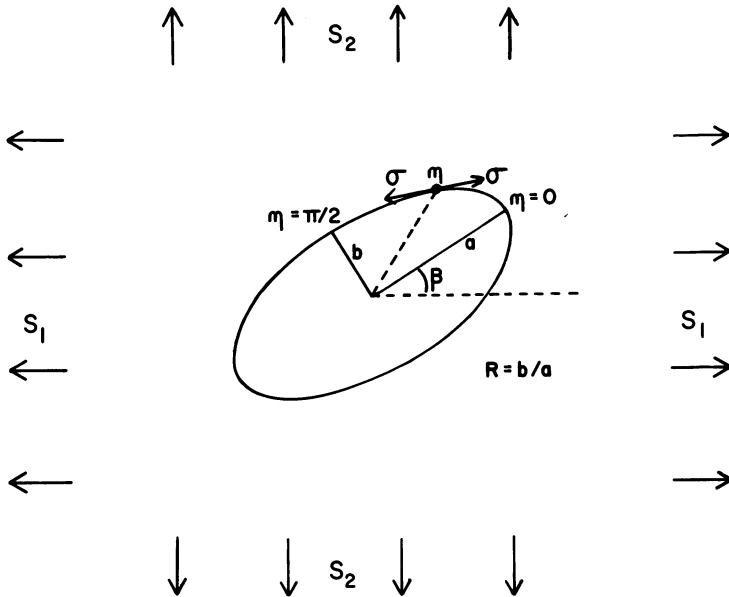


Figure 1. An elliptic flaw in an infinite, isotropic, and elastic medium subjected to uniform biaxial stresses  $S_1$  and  $S_2$ . The major axis of the ellipse is  $a$ , minor axis  $b$ , ellipticity  $R = b/a$ , and orientation angle with respect to  $S_1$  is  $\beta$ .  $\sigma$  is the major principal stress acting at the surface at a point designated by elliptic angle  $\eta$ .

coincident at all points on the elliptic surface. The procedure for superposition at points off the surface is more complicated because the principal axis directions generated by each load individually and by the simultaneous loads will all be different. Only stresses at the surface are considered here.

Superposition of the combined effects of  $S_1$  and  $S_2$  gives rise to a principal stress,  $\sigma$ , at the elliptic surface which is given by:

$$\frac{\sigma}{\sqrt{2}|S|} = \frac{K_1 \sinh 2\xi_0 + K_2 [\cos 2\beta - e^{2\xi_0} \cos 2(\beta - \eta)]}{\cosh 2\xi_0 - \cos 2\eta} \quad (2)$$

where:

$$|S| = \sqrt{S_1^2 + S_2^2}$$

and:

$$K_1 \equiv \frac{S_1 + S_2}{\sqrt{2}|S|}, \quad K_2 \equiv \frac{S_1 - S_2}{\sqrt{2}|S|}$$

from which it follows that  $K_1^2 + K_2^2 = 1$ .  $K_1$  and  $K_2$  are measures of the isotropic (volumetric) and deviatoric (distortional or shear) components of the applied stress state, respectively.

A more convenient means of representing general biaxial stress states is obtained by introducing a variable  $\Psi$  defined as:

$$S_1 \equiv |S| \cos \Psi \text{ and } S_2 \equiv |S| \sin \Psi \quad (3)$$

from which it follows that:

$$\tan \Psi = S_2/S_1 \quad (4)$$

$$\sqrt{2} K_1 = \cos \Psi + \sin \Psi \quad \sqrt{2} K_2 = \cos \Psi - \sin \Psi \quad (5)$$

The stress state variable  $\Psi$  is depicted in Figure 2 and has the following important special values:  $\Psi = 45^\circ$  represents equal biaxial tension;  $0^\circ$  and  $90^\circ$  uniaxial tension;  $-90^\circ$  and  $180^\circ$  uniaxial compression;  $-45^\circ$  and  $135^\circ$  pure shear; and  $-135^\circ$  equal biaxial compression. All biaxial stress states can be represented by a range of  $\Psi$  values from  $45^\circ$  to  $-135^\circ$ .

It is emphasized that  $\Psi$  defines the state of stress and should not be confused with the orientation angle  $\beta$ . For example,  $\Psi = 45^\circ$  and  $\beta = 45^\circ$  represents equal biaxial tension acting on a sheet whose ellipse is at  $45^\circ$  to one of the chosen external principal stress axes. This is not equivalent to  $\Psi = 0$  and  $\beta = 0$ , which represents uniaxial tension parallel to the elliptic major axis (which is equivalent to  $\Psi = 90^\circ$  and  $\beta = 90^\circ$ ). Because of symmetry considerations, all possible combinations of elliptic

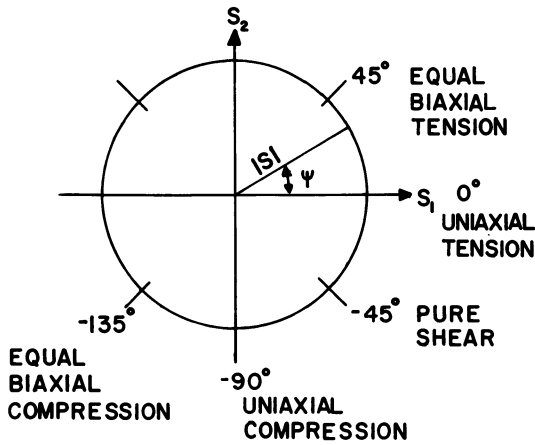


Figure 2. Designation of general biaxial stress states in terms of a stress state angle variable  $\Psi$  and magnitude  $|S| = \sqrt{S_1^2 + S_2^2}$ .  $\Psi$  is defined by  $\tan^{-1}(S_2/S_1)$ .

orientations and stress states are included in the ranges of  $0 \leq \beta \leq 90^\circ$ ,  $-135^\circ \leq \Psi \leq 45^\circ$ .

The principal stress  $\sigma$  (per unit  $|S|$ ) acting at the ellipse surface and given by Equation 2 is a function of several variables, that is:

$$\frac{\sigma}{\sqrt{2}|S|} = f(R, \beta, \Psi, \eta) \quad (6)$$

where the ellipticity ratio  $R$  has been introduced in place of  $\xi_0$  and is defined by  $R = b/a = \tanh \xi_0$ . For fixed ellipticity  $R$ , orientation  $\beta$ , and stress state  $\Psi$ , the value of  $\sigma$  will depend on the elliptic angle  $\eta$  (see Figure 1). ( $R$  is actually an inverse measure of ellipticity, that is,  $R = 1$  represents a circle and  $R = 0$  a line crack.) Of particular interest are the maximum and minimum values of  $\sigma$  for the given  $R, \beta, \Psi$ . To obtain these values conveniently, Equation 2 is differentiated to obtain  $d\sigma/d\eta$  which is set equal to zero to obtain the stationary values. After some algebra and trigonometry, the following equation is obtained:

$$2(\eta + \phi) = \sin^{-1}(C_3/C_4) \quad (7)$$

where  $2\phi \equiv \tan^{-1}(C_2/C_1)$ ,  $C_1 = (K_1 - \mu K_2 \cos 2\beta)(\mu^2 - 1)$ ,  $C_2 = \mu K_2(\mu^2 + 1) \sin 2\beta$ ,  $C_3 = 2\mu^2 K_2 \sin 2\beta$ ,  $C_4 = \sqrt{C_1^2 + C_2^2}$ , and  $\mu = e^{2\xi_0}$ .

There are two distinct roots for  $\eta$  in Equation 7 which represent two positions on the ellipse at which the maximum and minimum values of

$\sigma$  occur. The second principal stress at each of these positions is zero. Consequently the maximum and minimum shear stresses are given by  $|\sigma|/2$ . Depending on the particular values of  $R$ ,  $\beta$ , and  $\Psi$ , the two  $\sigma$  values can both be positive or negative, or of opposite sign. The maximum algebraic  $\sigma$  value (*i.e.*,  $\sigma_1 > \sigma_2$ ) is of interest when local processes governed by a critical tensile stress are being considered as, for example, in crack initiation. On the other hand, the maximum absolute  $\sigma$  value (*e.g.*,  $|\sigma_2| > |\sigma_1|$ ) is of interest when shear-controlled processes are involved as, for example, in shear band formation. The maximum absolute root may or may not correspond to the maximum algebraic root for  $\sigma$ . In the remainder of this paper all values of local stress concentration have been obtained by eliminating  $\eta$  between Equations 2 and 7 and therefore involve only the maximum or minimum values of  $\sigma$  on the elliptic surface.

A particular well known solution to Equations 2 and 7 is uniaxial tension ( $\Psi = 0$ ) applied to a sample containing an ellipse at right angle to the tensile axis ( $\beta = \pi/2$ ). In this case, the roots of Equation 7 are given by  $\eta = 0$  and  $\eta = \pi/2$ . From Equation 2 one obtains a maximum tensile stress for  $\eta = 0$ , corresponding to the major axis of the ellipse (Figure 1), which is given by:

$$\frac{\sigma}{|S|} = 1 + \frac{2}{R} \quad (8)$$

and since  $\Psi = 0$ ,  $|S| = S_1$ .

The more general case where either  $\beta \neq \pi/2$  or  $\Psi \neq 0$ , or both, does not give  $\eta = 0$  and  $\pi/2$  as the maximum and minimum points for  $\sigma$ . Thus, the maximum stress is not given by Equation 8 and does not occur at the major ellipse axis.

It is convenient to define a stress concentration factor based on Equation 6 (after eliminating  $\eta$  by use of Equation 7) as follows:

$$Q = \frac{\sigma}{|S|} = \sqrt{2} f(R, \beta, \Psi, \eta^*) \quad (9)$$

where  $Q$  is the maximum algebraic or maximum absolute stress concentration depending on which root ( $\eta^* = \eta_1$  or  $\eta_2$ ) from Equation 7 is used. These values of  $Q$  can range over many decades depending on the ellipticity  $R$ , and it is therefore useful to scale them by the uniaxial tension values of Equation 8.

This is shown in Figure 3 where scaled maximum algebraic stress concentration factors are shown for uniaxial tension ( $\Psi = 0$ ) and various elliptic orientations  $\beta$ . For  $R = 1$  there is no effect from  $\beta$  since this represents a circle (isotropic when rotated). The case  $R = 0$  represents

a line crack (since  $b/a = R = 0$ ) which is very sensitive to orientation changes. All ellipses display behavior between the upper and lower bounds represented by  $R = 1$  and  $R = 0$ , respectively.

For the case  $R = 0$ , we have obtained a simple analytical solution to Equation 9 (*i.e.*, to Equations 2 and 7) which is given by:

$$\frac{Q}{1 + 2/R} = \frac{\sqrt{2}}{2} (K_1 - K_2 \cos 2\beta) \quad (10)$$

where  $K_1$  and  $K_2$  are defined by Equation 5 in terms of stress state variable  $\psi$ . The curve shown in Figure 3 represents the case  $\psi = 0$  for which  $\sqrt{2}K_1 = \sqrt{2}K_2 = 1$ . Equation 10 is exact for  $R = 0$  but is a good approximation for all ellipticities  $R < 0.1$  and is valid in general biaxial stress states.

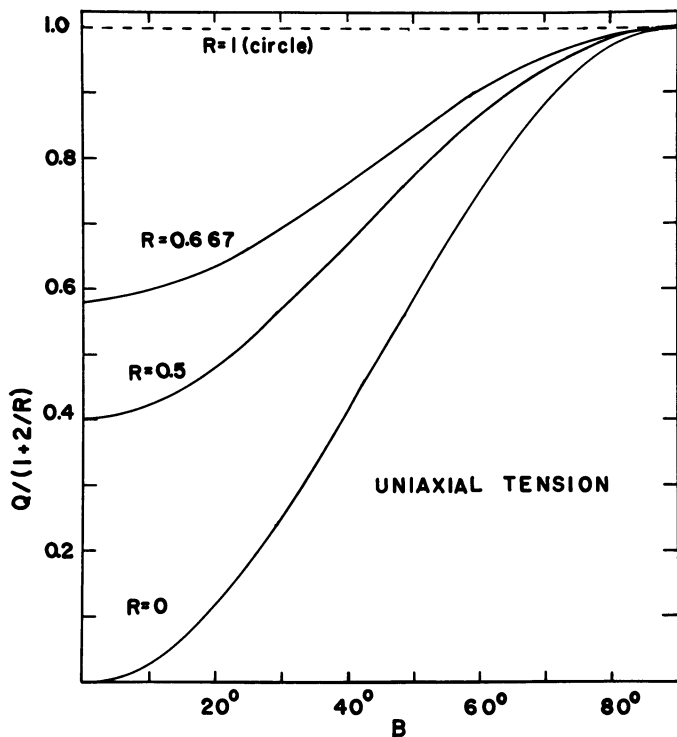


Figure 3. Maximum algebraic stress concentrations ( $Q$ ) developed by elliptic flaws, of various ellipticities  $R$  and for various orientations  $\beta$  with respect to the applied uniaxial tension, relative to the perpendicular orientation value ( $Q = 1 + 2/R$ ).  $R = 0$  represents a line crack.

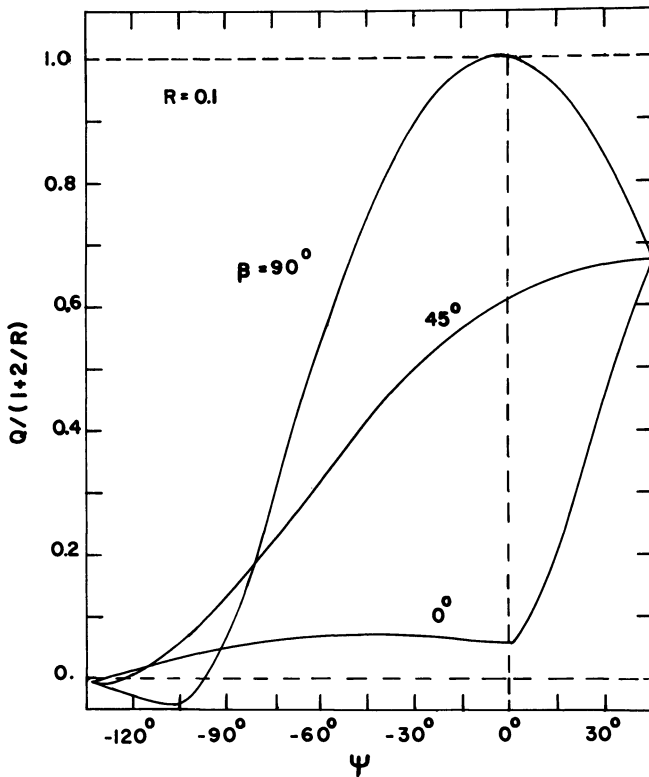


Figure 4. Maximum algebraic stress concentrations developed in general biaxial stress states defined by  $\Psi$  of Figure 2

The effect of stress state on the maximum algebraic stress concentration for various orientations of the ellipse ( $\beta$ ) is shown in Figure 4 for an ellipticity  $R = 0.1$ . The uniaxial tension condition ( $\Psi = 0$ ) generates the highest stress concentration. Equal biaxial tension ( $\Psi = 45^\circ$ ) generates the same stress concentration for any ellipse orientation  $\beta$ . This is because the stress state is planar isotropic, and any pair of orthogonal axes can be chosen as the external principal axes. Consequently the orientation  $\beta$  is without effect.

Maximum absolute stress concentration factors are shown in Figure 5, again for an ellipticity  $R = 0.1$ . As before, all orientations  $\beta$  give the same stress concentration for equal biaxial tension ( $\Psi = 45^\circ$ ). In addition equal biaxial compression ( $\Psi = -135^\circ$ ) gives the same stress concentration since absolute stress concentration is being considered. The shear stress concentration is given by  $|Q|/2$ . The curves shown in Figure 5 are symmetrical about the pure shear condition ( $\Psi = -45^\circ$ ).



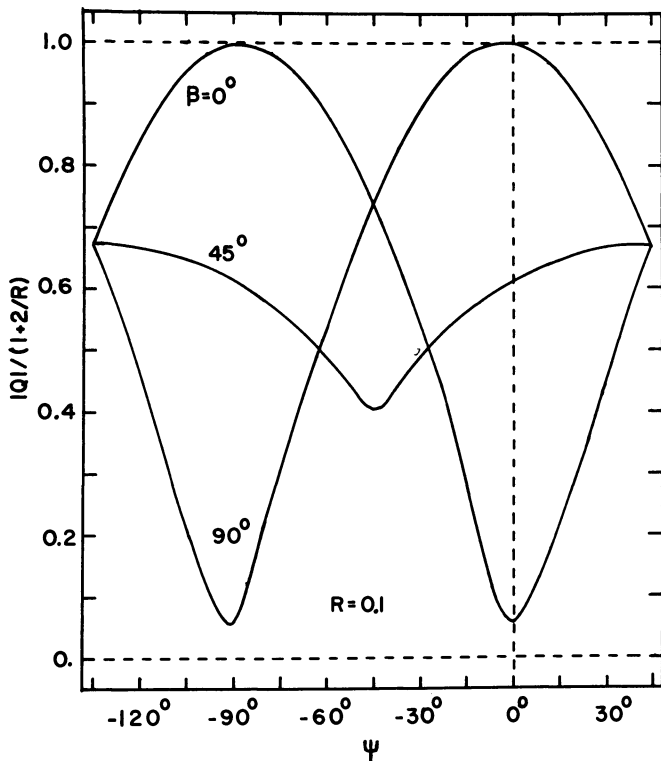


Figure 5. Maximum absolute stress concentrations developed in general biaxial stress states

Figure 3 shows that the fraction of flaws of given ellipticity  $R$  which develop a given or higher level of stress concentration depends on the ellipticity. Thus circular flaws ( $R = 1$ ) are all equally effective in their stress concentrating ability, whereas the fraction of line flaws ( $R = 0$ ) achieving a given level of stress concentration depends markedly on their orientation  $\beta$ . Similarly, Figure 4 shows that stress state has a major effect on the stress concentrating ability of a flaw at a particular orientation. For example, the stress concentration from flaws at orientation  $\beta = 45^\circ$  with respect to the external principal axis ( $S_1$ ) are least affected by a change in stress state from equal biaxial tension ( $\psi = 45^\circ$ ) to uniaxial tension ( $\psi = 0$ ). Conversely, the flaws at  $\beta = 90^\circ$  and  $\beta = 0^\circ$  are strongly affected. Thus, while these flaws all develop the same stress concentration in equal biaxial tension, they differ markedly as the stress state is changed.

The preceding ideas suggest that any material property related to the stress concentrating ability of a distribution of flaws will depend

strongly on the ellipticity and orientation distributions of those flaws and the applied stress state. If the flaw spectrum is described by a distribution function  $P(R, \beta)$ , then the number of flaws having ellipticities between  $R$  and  $R + dR$  and orientations between  $\beta$  and  $\beta + d\beta$  is given by:

$$\delta N = P(R, \beta) dR d\beta \quad (11)$$

If  $N^*$  is the cumulative fraction of active flaws having stress concentration factors equal to or greater than a given value  $Q^*$ , for a given stress state  $\Psi$ , then:

$$N^*(\Psi, Q^*) = \int_{\beta=0}^{2\pi} \int_{R=0}^1 P(R, \beta) H(R, \beta, \Psi, Q^*) dR d\beta \quad (12)$$

where  $H$  is a unit step function defined by:

$$H(R, \beta, \Psi, Q^*) \equiv 0 \text{ if } \frac{\sqrt{2} f(R, \beta, \Psi, \eta^*)}{Q^*} < 1$$

$$\text{and } H(R, \beta, \Psi, Q^*) \equiv 1 \text{ if } \frac{\sqrt{2} f(R, \beta, \Psi, \eta^*)}{Q^*} \geq 1$$

where the function  $f$  is defined by Equation 9. Thus,  $H$  serves to truncate the flaw distribution by rendering the integrand of Equation 12 zero for all flaws having less than the required stress concentrating ability.

The evaluation of Equation 12 for various flaw distributions is currently in progress and will be reported on shortly (17). However, it is clear from Figures 3, 4, and 5 that the number of active flaws for a given  $P(R, \beta)$  will be a strong function of stress state  $\Psi$  and orientation and ellipticity distributions. The dependence of  $N^*$  on  $\Psi$  and  $Q^*$  may be a key factor in evaluating different types of impact tests and sample preparation techniques. In the next section, a simple example is presented in which the effect of a drawing operation on an initially isotropic flaw spectrum is used to predict changes in axial and transverse failure strengths.

### ***Orientation Effects by Drawing***

Consider a master sheet of a given material from which tensile specimens can be cut at various directions as shown in Figure 6A. The master sheet is assumed to be both macroscopically homogeneous and isotropic insofar as its failure properties are concerned. The tensile samples will display no changes of statistical failure properties with their orientation

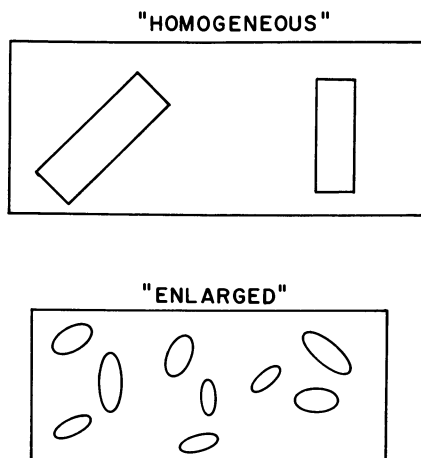


Figure 6. Top: schematic of a homogeneous and isotropic master sheet containing individual samples showing no directional preference of failure properties. Bottom: an enlarged view of a section of an individual sample showing a distribution of flaw ellipticities and orientations.

in the master sheet provided that they are of sufficient size to contain the same flaw spectrum  $P(R, \beta)$  as the master sheet. An enlarged section of one of the tensile samples is depicted in Figure 6B and contains a distribution of both ellipticities and orientations of flaws.

If the master sheet is now subjected to an orientation process, for example, hot stretching followed by cooling, then it can be expected that the flaw spectrum is changed insofar as both the distribution of ellipticities and orientations are concerned. It follows that tensile samples cut from the oriented master sheet will now display different failure properties with respect to their orientation in the master sheet. While molecular orientation and relaxation processes undoubtedly play a role in determining the intrinsic fracture toughness at the high stress concentration regions of each elliptic flaw, it is also necessary to consider the consequences of a change in the flaw spectrum. Thus, anisotropic failure properties and changes in tensile strength may be caused, in part, by changes in the orientation distribution and ellipticities of the flaws, both of which serve to alter the stress concentration factors which result from these flaws. In what follows, the effects of molecular orientation, *per se*, are ignored, and the changes in tensile strength associated with drawing are calculated solely on the basis of flaw spectrum changes.

The effect of an orientation process on an isolated elliptic flaw is depicted in Figure 7A. Let  $\alpha_1$  and  $\alpha_2$  be the permanent stretch (or draw) ratios (ratio of drawn to undrawn length) to which the master sheet is subjected in two orthogonal directions. If an elliptic flaw is originally at right angles to the  $\alpha_1$  direction (*i.e.*,  $\beta = \pi/2$ ) and  $\alpha_2 = 1$ , then  $R$  will increase with  $\alpha_1$  until a particular value of  $\alpha_1$  is reached at which  $R = 1$ . For larger values of  $\alpha_1$ ,  $R$  will then decrease but the major axis of the ellipse is now at  $\beta = 0$ . The critical draw ratio at which the orientation  $\beta$  jumps from  $\pi/2$  to 0 and for which the ellipse is circular ( $R = 1$ ) is described later.

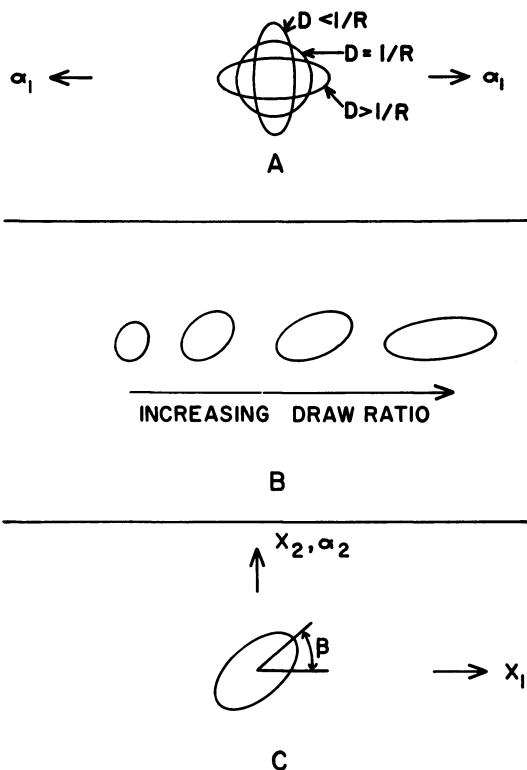


Figure 7. A. Schematic of an elliptic flaw initially at right angles to the draw direction. For a uniaxial draw, the draw ratio  $D = \alpha_1$ . At a critical draw ratio  $D = 1/R$  the ellipse becomes circular. For higher draw ratios ( $D > 1/R$ ), the ellipse forms with a  $90^\circ$  change in its orientation. B. Schematic of the effect of increasing draw ratio on an ellipse initially at some angle other than  $90^\circ$  to the draw direction. C. A general biaxial draw ( $\alpha_1, \alpha_2$ ) acting on an ellipse at initial orientation  $\beta$  to the major draw direction ( $\alpha_1 > \alpha_2$ ).

American Chemical

Society Library

1155 16th St., N.W.

Washington, D. C. 20036

An elliptic flaw which is not perpendicular to the major draw direction (i.e.,  $\beta \neq \pi/2$ ) is depicted in Figure 7B. This ellipse will rotate toward the draw axis and change ellipticity as  $\alpha_1$  increases. Such an ellipse does not exhibit an  $R = 1$  condition. This is shown in more detail below.

An ellipse at arbitrary angle  $\beta$  to the  $\mathbf{x}_1$  axis (Figure 7C) may be described by the equation for a quadric surface:

$$\mathbf{x}^T \mathbf{A} \mathbf{x} = 1 \quad (13)$$

$$\text{where } \mathbf{x} = \begin{bmatrix} \mathbf{x}_1 \\ \mathbf{x}_2 \end{bmatrix} \text{ and } \mathbf{A} = \begin{bmatrix} \mathbf{A}_{11} & \mathbf{A}_{12} \\ \mathbf{A}_{12} & \mathbf{A}_{22} \end{bmatrix}$$

The column vector  $\mathbf{x}$  represents the original (undrawn) coordinate system to which the ellipse is referred,  $\mathbf{x}^T$  is the transpose of  $\mathbf{x}$ , and  $\mathbf{A}$  represents the ellipse. The components of  $\mathbf{A}$  are easily shown to be given by:

$$\left. \begin{aligned} \mathbf{A}_{11} &= 1 + (R^2 - 1) \cos^2 \beta \\ \mathbf{A}_{22} &= 1 + (R^2 - 1) \sin^2 \beta \\ \mathbf{A}_{12} &= (R^2 - 1) \sin \beta \cos \beta \end{aligned} \right\} \quad (14)$$

Had the coordinate system been chosen to coincide with the major and minor axes of the ellipse (or the angle  $\beta = 0$ ), then the matrix  $\mathbf{A}$  would take canonical form given by:

$$\overline{\mathbf{A}} = \begin{bmatrix} R^2 & 0 \\ 0 & 1 \end{bmatrix} \quad (15)$$

The ellipse described by Equations 13, 14, and 15 has no dimensions *per se*, but rather a form factor given by  $R$ . It follows that an ellipse with  $b = 1$  unit of length and  $a = 4$  units ( $R = 0.25$ ) and an ellipse of  $b = 0.1$  and  $a = 0.4$  ( $R = 0.25$ ) are assumed to be indistinguishable in their behavior. Indeed, their stress concentration factors are the same, within the limitations described in the previous section.

The master sheet is now subjected to a uniform biaxial stretch defined by stretch ratios  $\alpha_1$  and  $\alpha_2$ . This plastic-like deformation is describable to a first approximation by the coordinate transformation  $\mathbf{y}_1 = \alpha_1 \mathbf{x}_1$  and  $\mathbf{y}_2 = \alpha_2 \mathbf{x}_2$  or:

$$\mathbf{y} = \mathbf{Q} \mathbf{x} \text{ where } \mathbf{Q} = \begin{bmatrix} \alpha_1 & 0 \\ 0 & \alpha_2 \end{bmatrix} \quad (16)$$

The matrix  $\mathbf{Q}$  is the deformation matrix, and the matrices  $\mathbf{A}$  and  $\mathbf{Q}$  cannot both be diagonal in general. The only case for which this is true is when  $\beta = 0$  or  $\beta = \pi/2$ . We have arbitrarily chosen the coordinate system to make  $\mathbf{Q}$  diagonal in which case  $\mathbf{A}$  is not (*see* Equations 13 and 14).

The inverse deformation is given by:

$$\mathbf{x} = \mathbf{P}\mathbf{y} \text{ where } \mathbf{P} = \mathbf{Q}^{-1} = \begin{bmatrix} 1/\alpha_1 & 0 \\ 0 & 1/\alpha_2 \end{bmatrix} \quad (17)$$

which can be combined with the quadric surface description, Equation 13, as follows:

$$\mathbf{x}^T \mathbf{A} \mathbf{x} = (\mathbf{P}\mathbf{y})^T \mathbf{A} (\mathbf{P}\mathbf{y}) = 1 \quad (18)$$

Since  $(\mathbf{P}\mathbf{y})^T = \mathbf{y}^T \mathbf{P}^T$  and  $\mathbf{P}$  is symmetric ( $\mathbf{P} = \mathbf{P}^T$ ), it follows that:

$$\mathbf{y}^T \mathbf{B} \mathbf{y} = 1 \text{ where } \mathbf{B} = \mathbf{P}\mathbf{A}\mathbf{P} \quad (19)$$

Thus, the original ellipse defined by  $\mathbf{A}$  has transformed to an ellipse defined by  $\mathbf{B} = \mathbf{P}\mathbf{A}\mathbf{P}$  as a result of the permanent biaxial stretch defined by  $\mathbf{Q}$ .

The eigenvalues and eigenvectors of the matrix  $\mathbf{B}$  can be used to directly compute the new ellipticity  $R^*$  and orientation  $\beta^*$  in the stretched state. Carrying out the matrix multiplication  $\mathbf{B} = \mathbf{P}\mathbf{A}\mathbf{P}$ , the components of  $\mathbf{B}$  are found to be given by:

$$\left. \begin{aligned} \mathbf{B}_{11} &= \mathbf{A}_{11}/\alpha_1^2 & \mathbf{B}_{22} &= \mathbf{A}_{22}/\alpha_2^2 \\ \mathbf{B}_{12} &= \mathbf{B}_{21} = \mathbf{A}_{12}/\alpha_1\alpha_2 \end{aligned} \right\} \quad (20)$$

The eigenvalues ( $\lambda$ ) are obtained by the solution to the secular equation  $\det(\mathbf{B} - \lambda\mathbf{I}) = 0$  where  $\mathbf{I}$  is the identity matrix. The results are given by:

$$\lambda_2 = \frac{J + K}{2\alpha_1^2} \text{ and } \lambda_1 = \frac{J - K}{2\alpha_1^2} \quad (21)$$

where  $J \equiv \mathbf{A}_{11} + \mathbf{A}_{22}D^2$ ,  $K \equiv \sqrt{J^2 - 4D^2(\mathbf{A}_{11}\mathbf{A}_{22} - \mathbf{A}_{12}^2)}$ , and  $D \equiv \alpha_1/\alpha_2$  and the components of  $\mathbf{A}$  are given in terms of the original ellipticity  $R$  and orientation  $\beta$  by Equation 14.

The new minor axis  $b^*$  is given by  $(1/\lambda_2)^{1/2}$  and the new major axis  $a^*$  by  $(1/\lambda_1)^{1/2}$ . Therefore, the new ellipticity is given by:

$$R^* = b^*/a^* = (\lambda_1/\lambda_2)^{1/2} \quad (22)$$

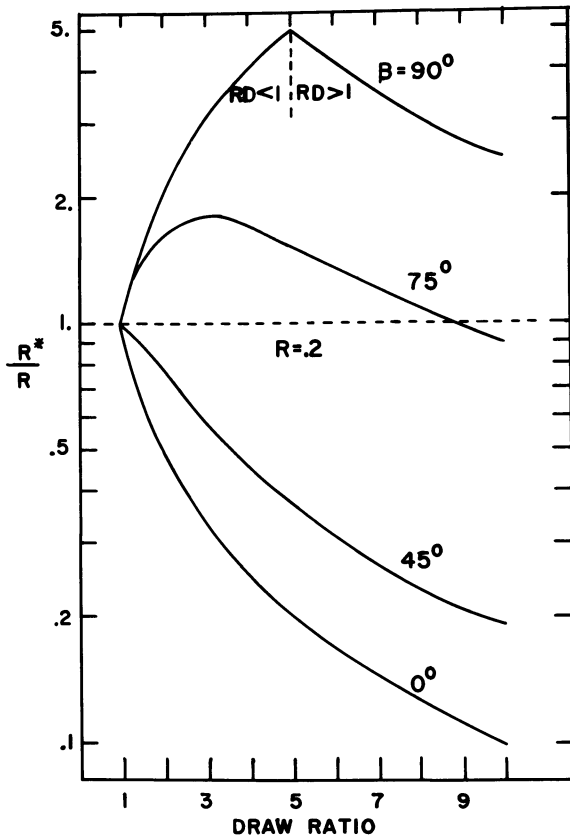


Figure 8. Ellipticity ratios  $R^*/R$  as a function of draw ratio  $D = \alpha_1/\alpha_2$  for ellipses at various initial orientations  $\beta$ . The initial value of  $R$  for all ellipses is 0.2.

The new orientation  $\beta^*$  is given by the eigenvector to  $\mathbf{B}$  corresponding to the  $\lambda_1$  eigenvalue, and the result is:

$$\beta^* = \tan^{-1} \left( \frac{\mathbf{A}_{11} - \lambda_1 \alpha_1^2}{-\mathbf{A}_{12} D} \right) \quad (23)$$

Numerical solutions to Equations 22 and 23 have been obtained for various values of  $R$ ,  $\beta$ ,  $\alpha_1$ , and  $\alpha_2$ . The changes in ellipticity ( $R^*/R$ ) developed by various draw ratios  $D = \alpha_1/\alpha_2$  are shown in Figure 8 for several initial ellipse orientations  $\beta$  and an initial ellipticity  $R = 0.2$ . The curve corresponding to  $\beta = 0$  is given by  $R^*/R = 1/D$  as can be readily obtained from Equations 14, 21, and 22. For all other orientations, that

is  $\beta \neq 0$ , the ratio  $R^*/R$  will depend on the initial value of  $R$  as well as  $\beta$  and  $D$ .

The cusp in the curve corresponding to  $\beta = 90^\circ$  occurs at the condition  $RD = 1$  and represents a critical draw ratio at which the ellipse has transformed to a circle, *i.e.*,  $R^* = 1$  or  $R^*/R = 5$ . For draw ratios lower than the critical value ( $RD < 1$ ), the shape of the  $\beta = 90^\circ$  curve is given by  $R^*/R = D$ . At draw ratios higher than the critical value ( $RD > 1$ ), the flaw becomes elliptic again, and the shape of the curve is given by  $R^*/R = 1/R^2D$ .

The new orientation angles  $\beta^*$  associated with the ellipticities given in Figure 8 are shown in Figure 9. The behavior of the flaws with  $\beta = 90^\circ$  requires some explanation. For draw ratios below the critical value ( $RD < 1$ ),  $\beta^* = 90^\circ$  regardless of  $D$ , whereas for draw ratios higher than the critical value ( $RD > 1$ ),  $\beta^* = 0^\circ$  for  $\beta = 90^\circ$  regardless of  $D$ . In the example shown,  $R = 0.2$  and the critical draw ratio is therefore  $D = 5$ . Thus, when  $D$  is exactly 5, the flaws with  $\beta = 90^\circ$  are circular and may be assigned any value of  $\beta^*$  since a circle is isotropic when rotated. Since  $\beta^*$  is discontinuous when  $D = 5$  (the left hand limit is  $\beta^* = 90^\circ$  and the right hand limit is  $\beta^* = 0^\circ$ ), the value of  $\beta^* = 45^\circ$  at  $D = 5$  is the mean value of  $\beta^*$  when  $D = 5$  is approached from below and above. The value of  $45^\circ$  is continuous with the remainder of the  $\beta^*$  values for values of  $\beta \neq 90^\circ$  on the  $D = 5$  curve. The sequence of events for  $90^\circ$  flaws is illustrated in Figure 7A.

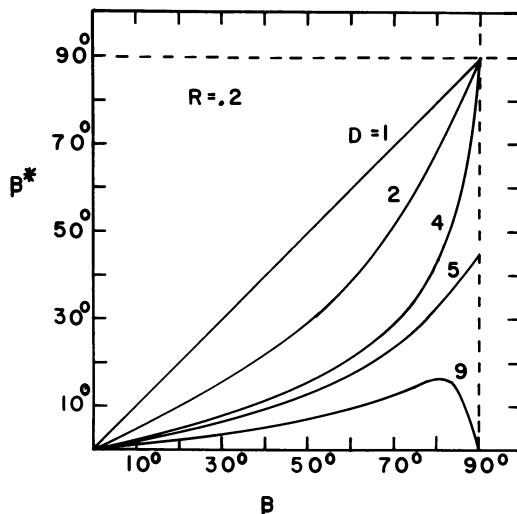


Figure 9. Final orientation  $\beta^*$  vs. initial orientation  $\beta$  for various draw ratios  $D$ . All ellipses have initial  $R = 0.2$ .



The situation for a flaw initially at  $75^\circ$  to the draw direction is similar in that  $R^*$  achieves a maximum value as shown in Figure 8. However, the new orientation  $\beta^*$  of this flaw is continuous with draw ratio as shown in Figure 9 and does not display a jump discontinuity as does the flaw with  $\beta = 90^\circ$ . Furthermore, the flaw never becomes circular regardless of draw ratio ( $R^*/R \neq 5$  in Figure 8).

Flaws at  $\beta = 45^\circ$  to the draw direction display no maximum in  $R^*/R$  as shown in Figure 8. All flaws with  $\beta \leq 45^\circ$  behave similarly in this regard. At draw ratios equal to or greater than the critical value ( $D \geq 1/R$ ), Figure 9 shows that all flaws have orientations  $\beta^* \leq 45^\circ$ ; in other words, no flaws remain oriented at more than  $45^\circ$  to the draw direction.

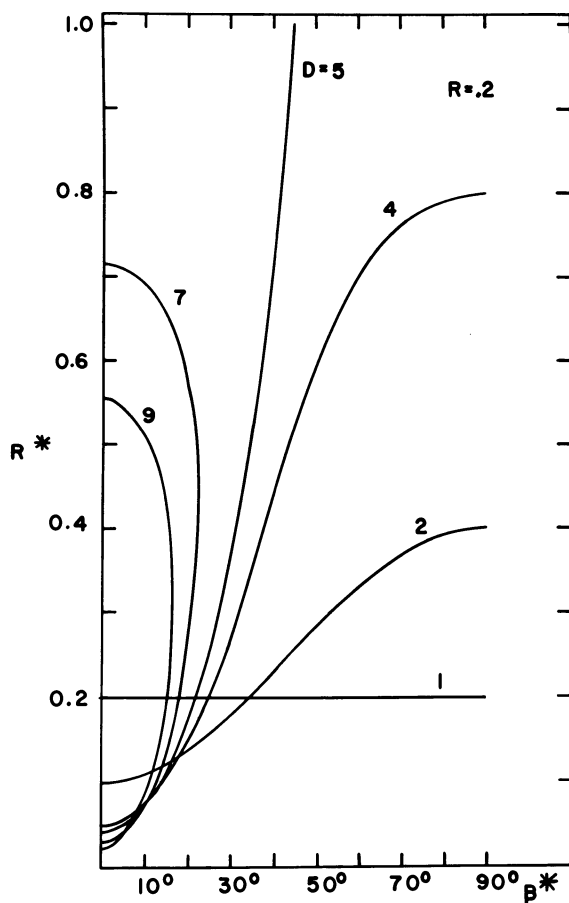


Figure 10. Final ellipticity  $R^*$  vs. final orientation  $\beta^*$  for various draw ratios  $D$ . An isotropic distribution of flaws all of  $R = 0.2$  exists in the undrawn state ( $D = 1$ ).

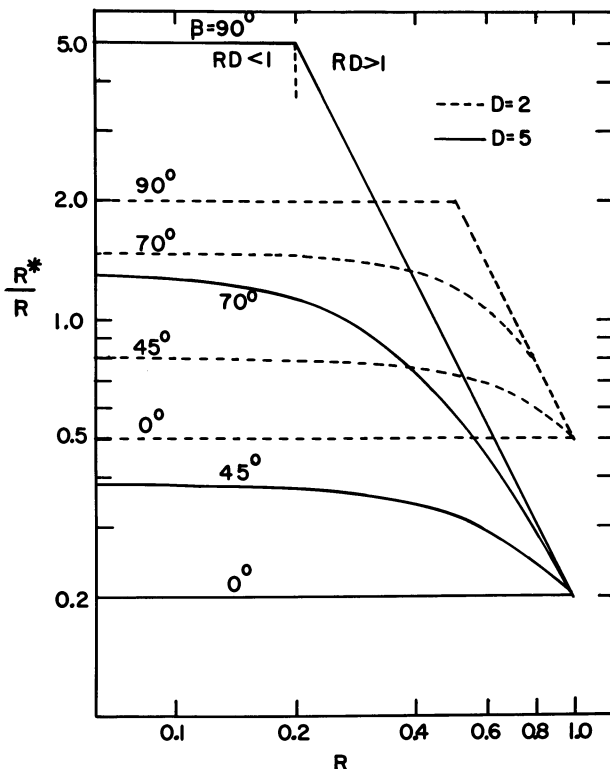


Figure 11. Ellipticity ratio  $R^*/R$  vs. initial  $R$  developed by various draw ratios  $D$  and for various initial orientations  $\beta$

These results have important implications to an analysis of anisotropic tensile strengths as indicated in the next section. For this purpose, it is useful to present the results of Figures 8 and 9 in terms of new ellipticity  $R^*$  vs. new orientation  $\beta^*$  for various draw ratios as shown in Figure 10. The curve  $D = 1$  represents the undrawn, initially isotropic distribution of flaws all of the same ellipticity  $R = 0.2$ . The ellipticity dispersion and orientation distribution anisotropy produced by drawing are apparent. For draw ratios higher than the critical value,  $R^*$  is multiple valued with respect to  $\beta^*$ . The reason for this, as can be seen in Figure 9, is the multiple values of  $\beta$  with respect to  $\beta^*$ . For example, for a draw ratio of  $D = 9$ , the flaws with  $ca. 80^\circ \leq \beta \leq 90^\circ$  have orientations  $\beta^*$  ranging over the same values as do the flaws having  $0^\circ \leq \beta \leq 80^\circ$ .

Physically, the flaws with  $\beta > 80^\circ$  are more effectively blunted than are flaws at a lower angle to the draw direction. Above the critical draw ratio, they are oriented close to the draw direction (low  $\beta^*$ ) and account

for the higher of the two  $R^*$  values for each  $\beta^*$  in Figure 10. The lower  $R^*$  is caused by the flaw having an initial orientation  $\beta < 80$  which is less effectively blunted by drawing but develops the same orientation  $\beta^*$  (Figure 9).

The effect of a fixed draw ratio on a flaw spectrum containing distributions of both  $\beta$  and  $R$  is shown in Figure 11. For the case  $\beta = 0^\circ$  the ratio  $R^*/R$  is independent of  $R$  and is given by  $1/D$ , as noted earlier. For all values  $\beta \neq 0^\circ$ ,  $R^*/R$  depends on the initial value of  $R$ . Considering the curve for  $\beta = 90^\circ$ , all flaws having  $R < 1/D$  change ellipticity according to  $R^*/R = D$  whereas all flaws having  $R > 1/D$  change according to  $R^*/R = 1/R^2D$ .

The ratio  $R^*/R$  vs. initial orientation  $\beta$  is shown in Figure 12 for various initial values of  $R$ . For the case  $R = 1$ , a circle, all orientations

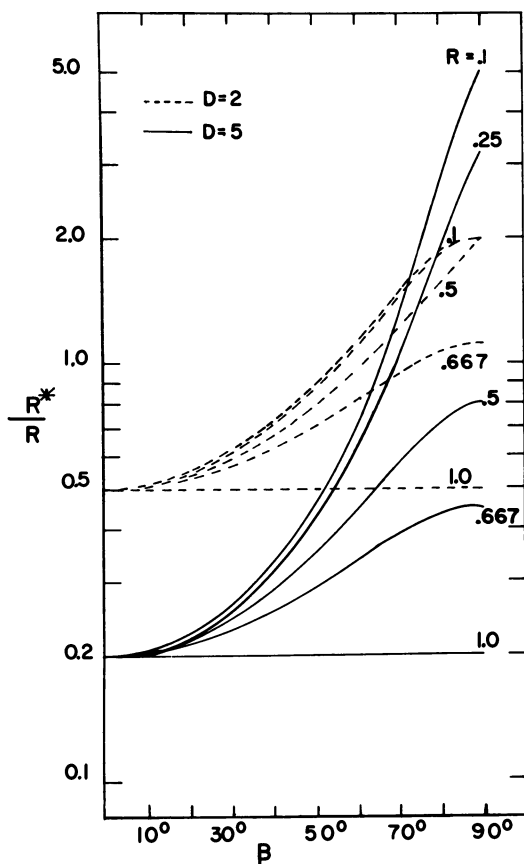


Figure 12. Ellipticity ratio  $R^*/R$  vs. initial orientation  $\beta$  for two draw ratios  $D$

$\beta$  behave the same and  $R^*/R = 1/D$ ; in addition, all ellipses form with their major axes parallel to the draw direction, that is,  $\beta^* = 0^\circ$  regardless of the draw ratio  $D$ . The effect of  $\beta$  is increasingly pronounced as the initial flaws become more slender ( $R \rightarrow 0$ ).

It follows from the results given in Figures 8–12 that, given an initial flaw spectrum  $P(R, \beta)$ , it is possible to compute a new spectrum  $P^*(R^*, \beta^*)$  associated with an anisotropy producing drawing operation. This new spectrum can then be used to characterize anisotropic multiple flaw failure phenomena. Such calculations are currently in progress and will be reported on at a later date (17). For the present purpose, Figures 8–12 show that major changes in the ellipticity and orientation distributions of the flaw spectrum will accompany the drawing process. The results given here are sufficient to estimate the transverse and axial tensile strengths of a drawn sample as described in the next section.

### Anisotropic Tensile Strengths

Stress concentration factors associated with elliptic flaws in an anisotropic matrix are generally unavailable. In the absence of such information, the results presented in Figures 3–5 are a first approximation to the stress concentrations developed by the flaws in the drawn material. It follows that Equation 9 can be written as:

$$Q^* = \sqrt{2} f^*(R^*, \beta^*, \Psi, \eta^*) = \sqrt{2} f(R^*, \beta^*, \Psi, \eta^*) \quad (24)$$

where the function  $f^*$  is the same as  $f$  for the isotropic matrix. Thus, changes in stress concentration factors from drawing are associated with changes in  $R^*$  and  $\beta^*$  and not with the functionality of the stress concentration, *per se*. Thus, Figure 3 is assumed to be valid for the drawn material, in which case  $Q$ ,  $R$ , and  $\beta$  are to be interpreted as  $Q^*$ ,  $R^*$ , and  $\beta^*$ . It is further assumed that molecular orientation does not enhance fracture resistance, *per se*, but rather causes changes in observed tensile strength by modification of the flaw spectrum. This implies that observed tensile strength ( $S_b$ ) is simply inversely proportional to the critical stress concentration factor, that is, local tensile strength is constant, or:

$$S_b^*/S_b = (Q/Q^*)_c \quad (25)$$

where the asterisk refers to some drawn state, and the absence of an asterisk to the undrawn (isotropic) state. The critical stress concentration factors to be used in Equation 25 depend on the flaw spectrum and the loading direction of the tensile strip relative to the draw direction. These are illustrated below.

The simplest example is the case where changes in tensile strength relative to the undrawn, isotropic tensile strength are calculated for samples whose tensile axes are parallel to and perpendicular to the major draw direction ( $\alpha_1$ ). These will be referred to as the axial and transverse directions, respectively. For the present purpose, it is assumed that the undrawn master sheet contained an isotropically distributed set of flaws all of the same ellipticity  $R$ . The problem is then deterministic. Con-

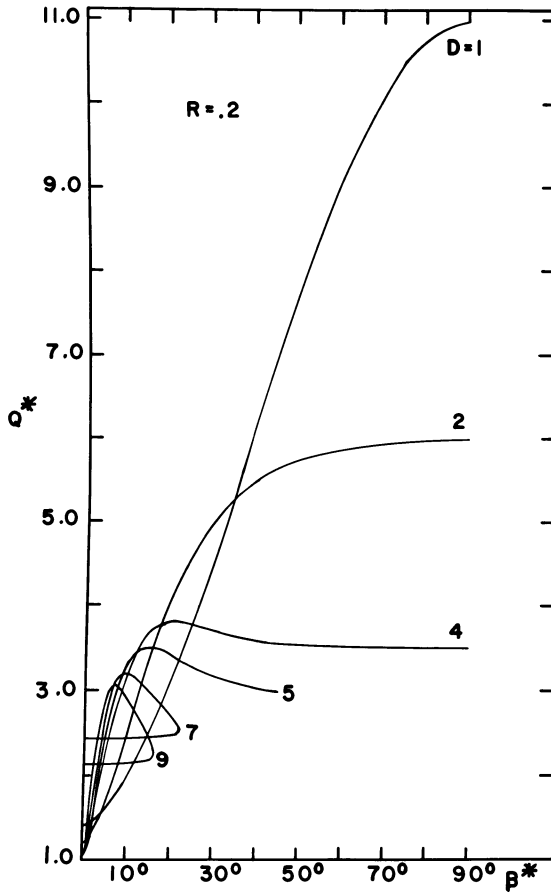


Figure 13. Stress concentrations  $Q^*$  developed by flaws at various final orientations  $\beta^*$  for various draw ratios  $D$ . The direction of stress application is parallel to the major draw direction, that is, in the  $\beta^* = 0^\circ$  direction. These curves account for the new ellipticities  $R^*$  and orientations  $\beta^*$  given in Figure 10 for an initially isotropic and uniform ( $R = 0.2$ ) set of flaws.

sideration of failure probability curves requires analysis of an  $R$  distribution, and this will be considered later.

Consider the axial samples of drawn material. From Figure 3, stress concentration factor decreases with an increase in  $R$  or with a decrease in  $\beta$ . Referring to Figure 8, the flaws at  $\beta = 90^\circ$  always undergo more blunting from drawing (*i.e.*,  $R^*/R$  is greater) than do flaws at lower angles, *e.g.*,  $\beta = 75^\circ$ . However, the flaws with  $\beta = 90^\circ$  remain at  $\beta^* = 90^\circ$  until the critical draw ratio is reached after which  $\beta^* = 0^\circ$  for higher draw ratios, whereas the flaws with  $\beta < 90^\circ$  always have  $\beta^* < 90^\circ$  regardless of draw ratio. The lower stress concentration from  $\beta^* < 90^\circ$  and higher stress concentration from lower  $R^*$  suggest that the critical stress concentration to be used in Equation 25 may arise from flaws whose initial orientation  $\beta$  is not at  $90^\circ$  to the draw direction.

The ellipticity-orientation distribution for the drawn material is given in Figure 10 (for the particular case  $R = 0.2$ ) which can be combined with Figure 3 (to a first approximation) to obtain the drawn state stress concentrations  $Q^*$  vs. orientation  $\beta^*$ . The results are shown in Figure 13. The critical stress concentration to be used in Equation 25 is the maximum value of  $Q^*$  for each draw ratio. It is somewhat surprising to find that the maximum  $Q^*$  for high draw ratios does not arise from flaws originally at  $\beta = 90^\circ$  but rather from lower orientation flaws. This is a consequence of both the enhanced blunting of  $\beta = 90^\circ$  flaws and their reorientations at high draw ratios to  $\beta^* = 0^\circ$ . However, even below the critical draw ratio, for example  $D = 4$  in Figure 13 (the critical value is  $D = 5$  for  $R = 0.2$ ), the opposite effects of lower  $R^*$  and lower  $\beta^*$  on stress concentration combine to give a higher stress concentration from flaws with  $\beta < 90^\circ$ .

Using the critical stress concentrations found in Figure 13 for the drawn material and Equation 8 for the undrawn material, the relative tensile strength ratio is obtained from Equation 25 for axial samples. The results are shown in Figure 14.

The transverse tensile strength is computed by now considering the critical stress concentration which arises from the application of a tensile strength parallel to the  $\beta^* = 90^\circ$  direction, that is, perpendicular to the major draw direction. From Figure 8, the flaws having  $\beta = 0^\circ$  have the lowest value of  $R^*$ . From Figure 9, these flaws have  $\beta^* = 0^\circ$ . Consequently these flaws ( $\beta = 0^\circ$ ) develop the highest stress concentration factor for stresses applied transversely to the draw direction. Since the ellipticity ratio for these flaws is given by  $R^*/R = 1/D$ , Equation 8 gives a stress concentration of:

$$Q_c^* = 1 + \frac{2}{R^*} = 1 + \frac{2D}{R} \quad (26)$$

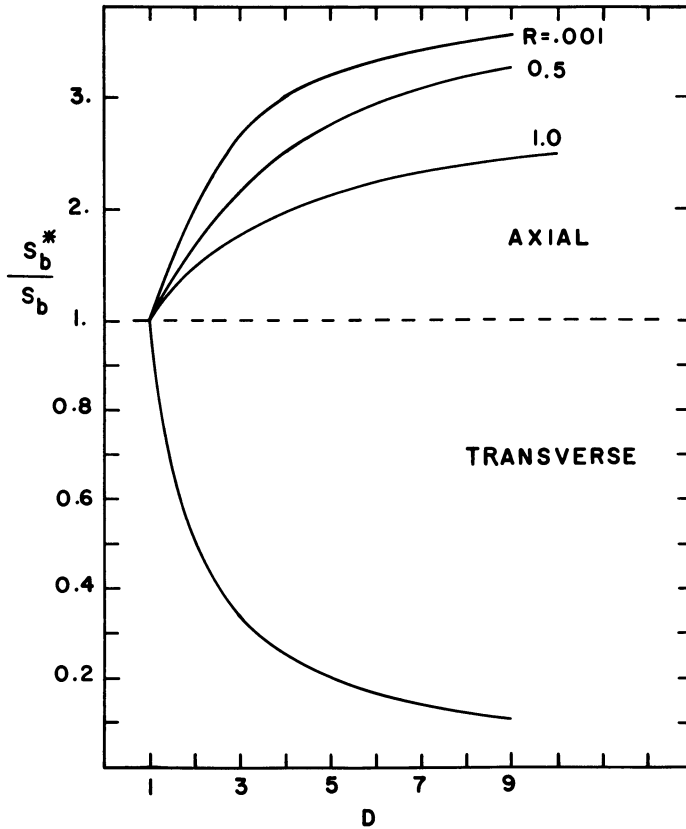


Figure 14. Relative axial tensile strength improvement and transverse tensile strength reduction resulting from the effect of a drawing process on the flaw spectrum. The transverse curve is the limiting curve defined by Equation 29 for  $R = 0$ .

The undrawn samples have an isotropic distribution of flaws; consequently there exists a flaw at  $\beta = 0^\circ$  which is perpendicular to the applied stress and whose stress concentration is given by:

$$Q_c = 1 + \frac{2}{R} \quad (27)$$

The relative tensile strength ratio (Equation 25) for transverse samples is therefore:

$$S_b^*/S_b = (1 + 2/R)/(1 + 2D/R) \quad (28)$$

which for small  $R$  (sharp flaws) approximates to: .

$$D(S_b^*/S_b) = 1 \quad (29)$$

and is shown in Figure 14 for the transverse strength reduction.

Experimental data on the tensile strengths of drawn polystyrene sheets have been obtained by Retting (18) as part of an I.U.P.A.C. study on the effects of orientation on the properties of plastics. Retting's data for transverse tensile strengths of drawn polystyrene are presented in Tables I and II for a low and high molecular weight polymer, respectively. As seen from Table I, the relative transverse tensile strengths for several draw ratios and strain rates agree well with Equation 29. The agreement is not as good for the high molecular weight data in Table II, which indicates that Equation 29 tends to overestimate the reduction in transverse tensile strength. Also, there is an obvious trend toward higher overestimation as the draw ratio increases. For example, at the lowest strain rate, the observed transverse tensile strength is 70% higher than the theory value at a draw ratio of 3.9, but only 20% higher at a draw ratio of 1.5. By comparison no such trend with draw ratio occurs for the low molecular weight polymer.

It seems quite plausible, therefore, that the transverse tensile strength reduction in drawn low molecular weight polymer is governed primarily by flaw spectrum changes as described in the theory presented, with

**Table I. Transverse Tensile Strength of Polystyrene A<sup>a</sup>**

<i>Strain Rate</i> (cm/sec)	<i>Nominal</i> <i>Draw Ratio</i> (D)	<i>Stress to</i> <i>Rupture</i> (N/mm <sup>2</sup> )(S <sub>b</sub> )	D[S <sub>b</sub> */S <sub>b</sub> ]
~ 400	1	42.9	(1.000) <sup>b</sup>
	1.5	31.7	1.1
	2.6	10.6	.64
	3.9	11.4	1.0
.5	1	44.5	(1.000) <sup>b</sup>
	1.5	32.9	1.1
	2.6	18.8	1.1
	3.9	17.3	1.5
8.3 × 10 <sup>-3</sup>	1	40.0	(1.000) <sup>b</sup>
	1.5	24.5	.9
	2.6	16.4	1.1
	3.9	10.4	1.0
8.3 × 10 <sup>-5</sup>	1	30.5	(1.000) <sup>b</sup>
	1.5	16.6	.8
	2.6	13.0	1.1
	3.9	8.66	1.1

<sup>a</sup>  $\bar{M}_n = 52,000$ ,  $\bar{M}_w = 230,000$ , and  $T_g = 98^\circ\text{C}$ .

<sup>b</sup> These values are unity by definition.



Table II. Transverse Tensile Strength Polystyrene B<sup>a</sup>

Strain Rate (cm/sec)	Nominal Draw Ratio (D)	Stress to Rupture (N/mm <sup>2</sup> ) (S <sub>b</sub> )	D[S <sub>b</sub> <sup>*</sup> /S <sub>b</sub> ]
~ 400	1	58.5	(1.000) <sup>b</sup>
	1.5	38.8	1.0
	2.6	25.9	1.2
	3.9	18.4	1.2
.5	1	46.1	(1.000) <sup>b</sup>
	1.5	44.1	1.4
	2.6	26.8	1.5
	3.9	23.8	2.0
8.3 × 10 <sup>-3</sup>	1	45.2	(1.000) <sup>b</sup>
	1.5	37.8	1.3
	2.6	25.6	1.5
	3.9	19.6	1.7
8.3 × 10 <sup>-5</sup>	1	33.8	(1.000) <sup>b</sup>
	1.5	28.0	1.2
	2.6	19.2	1.5
	3.9	15.0	1.7

<sup>a</sup>  $\bar{M}_n = 130,000$ ,  $\bar{M}_w = 300,000$ , and  $T_g = 105^\circ\text{C}$ .

<sup>b</sup> These values are unity by definition.

little or no effect from molecular orientation. Conversely, the high molecular weight polymer undergoes less transverse strength reduction as a result of flaw spectrum changes because of improved local failure strength (or fracture toughness) caused by molecular orientation at the flaw tips. The effect of molecular orientation is increasingly effective at higher draw ratios.

### Discussion

We have intended to demonstrate that a flaw spectrum analysis presents a plausible and useful approach to the problem of multiple flaw failure phenomena in solid polymers. Effects of orientation and stress state may be explained by such an approach, but much additional theory and experiments are required to establish the validity of the method. Several obvious shortcomings of the theory can be overcome, in principle, by a more rigorous analysis. The more serious assumptions or limitations which we intend to either remove or justify in future work are as follows.

(1). The calculation of stress concentration factors arising from flaws in an anisotropic matrix has been obtained from the isotropic results. Much additional work in this general area is required as a large

number of materials problems require knowledge of stress concentration factors for anisotropic media.

(2). The analysis of flaw reorientation in the drawn material is rudimentary. However, it is not obvious that greater detail such as a general formulation using the equations of stress equilibrium and compatibility (several partial differential equations are called for) would significantly enhance the model. This question will be resolved experimentally.

(3). The effects of molecular orientation on local failure properties have been neglected. The simultaneous effects of flaw orientation and molecular orientation should be accounted for in the model and delineated experimentally.

(4). A two-dimensional treatment has been presented. The model is currently being extended to three dimensions to account for surface flaws in a three-dimensional material subjected to a drawing process and bulk flaws or dispersed phase particles in a three-dimensional matrix.

There are some additional applications of the theory which are presently under investigation. These are the effects of drawing on fibers for which the three-dimensional theory with transverse symmetry is applicable and the toughening mechanism in high impact polystyrene for which the flaw spectrum may be viewed as caused by the size, orientation, and spacing distributions of the rubber particles.

### *Acknowledgments*

We are grateful to Wolfgang Retting of B.A.S.F. for making available his I.U.P.A.C. reports prior to publication.

### *Literature Cited*

1. Onaran, K., Findley, W. N., *Trans. Soc. Rheol.* (1965) 9, 299.
2. Benham, P. P., McCammond, D., *Plast. Polym.* (1971) 130.
3. Sternstein, S. S., Ho, T. C., *J. Appl. Phys.* (1972) 43, 4370.
4. Sternstein, S. S., Ongchin, L., Silverman, A., *Appl. Poly. Symp.* (1968) 7, 175.
5. Sternstein, S. S., Ongchin, L., *Amer. Chem. Soc. Div. Chem. Polym. Preprints* (Sept. 1969) 10(2), 1117.
6. Sternstein, S. S., Myers, F. A., *J. Macromol. Sci. Phys.* (1973) B8, 539.
7. Ward, I., *J. Mater. Sci.* (1971) 6, 1397.
8. Bauwens, J. C., *J. Polym. Sci.* (1967), A-2, 5, 1145.
9. Argon, A. S. "Plastic Deformation in Glassy Polymers" in "Polymeric Materials," 1973 Amer. Soc. Mat. Seminar, Amer. Soc. Mat., Metals Park Ohio, 1975.
10. Cama, F. J., "Stress Relaxation of Plasticized and Unplasticized Polyvinylchloride in the Glassy State," Ph.D. Thesis, Rensselaer Polytechnic Institute, Troy, New York, May (1974).
11. Cessna, L. C., Jr., Sternstein, S. S., *Polym. Lett.* (1965) 3, 825.
12. Kinder, D. F., Sternstein, S. S., *Trans. Soc. Rheol.*, in press.

13. Sternstein, S. S., "Yielding Modes in Glassy Polymers," in "Polymeric Materials," 1973 Amer. Soc. Mat. Seminar, Amer. Soc. Mat., Metals Park, Ohio, 1975.
14. Timoshenko, S., Goodier, J. N., "Theory of Elasticity," 2nd ed., p. 201, McGraw Hill, Inc., New York, 1951.
15. Sokolnikoff, I. S., "Mathematical Theory of Elasticity, 2nd ed., McGraw Hill, Inc., New York, 1951.
16. Muskhelishvili, N. I., "Some Basic Problems of the Mathematical Theory of Elasticity," J. R. M. Radolt, translator, 4th ed., P. Noordhoff Ltd., Groningen, Netherlands, 1954.
17. Sternstein, S. S., unpublished data.
18. Retting, W., Orientation in Polymers Programme, Polystyrene, Report on the Results of B.A.S.F., 2nd part, Macromol. Division, I.U.P.A.C., March 1972.

RECEIVED October 18, 1974. Work supported by National Science Foundation Grant No. NSF GH-37249 and carried out in the Materials Research Center which is supported by the National Aeronautics and Space Administration under Grant No. NGL 33-018-003. Additional support by the Shell Foundation and B. F. Goodrich Chemical Co.

## Strain in a Polystyrene Craze Layer

M. J. DOYLE and J. G. WAGNER

Department of Mechanical Engineering, University of Pittsburgh,  
Pittsburgh, Pa. 15261

*From observations of interference patterns and interferometric measurements of the refractive index, the profile of a craze preceding a crack in polystyrene has been determined. The strain along the length of the craze was calculated and found to increase toward the crack tip. The opening displacements across the craze boundaries show a deviation from those predicted for the simple Dugdale yield zone.*

A crack propagating in a glassy polymer is usually preceded by a wedge-shaped layer of craze, an expanded form of the polymer with a density very much less than that of the bulk. Where the length of the craze layer is comparable with the length of the crack, the Griffith theory and linear elastic fracture mechanics cannot be expected to apply (1, 2). Such relatively great amounts of plastic yielding have been recognized in the analysis of the mechanics of fracture based on a model proposed by Dugdale (3) to describe the spread of thin planar yield zones from the ends of a slit in a metal plate and has been applied to the fracture of polymers (2, 4, 5). The analysis assumes a constant stress on the yield zone or craze layer.

In Figure 1 a plate contains a narrow slit of length  $2a$ , and a stress,  $\sigma$ , is applied at some distance from and in a direction perpendicular to the slit. In metals, if the height of the slit is comparable with the thickness of the plate, yielding may occur in thin zones of length  $R$  spreading from the ends of the slit as shear yielding occurs on oblique planes through the thickness; similar effects have been observed also for polycarbonate (6). In many glassy polymers, however, crazing—apparently a dilatational yielding—occurs in thin, planar, wedge-shaped layers which physically appear to conform very closely to the model proposed by Dugdale. In Figure 2 a plate contains a line crack of length  $2c$ , equal to the combined length  $2(a + R)$  of the crack and yield zones shown in Figure 1. The yield zone (or craze) is replaced by a uniform tensile stress,  $\sigma_0$ , equal

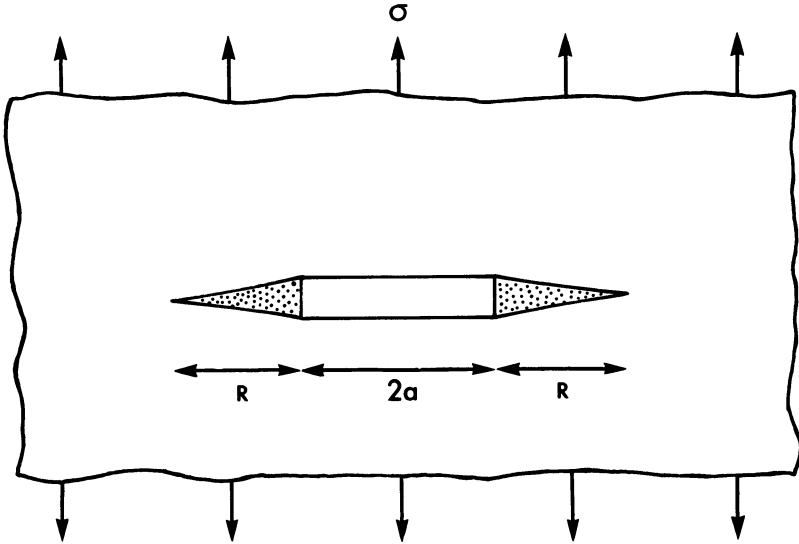


Figure 1. Yielding from the ends of a narrow slot in a plate (schematic)

to the tensile yield stress (or craze stress) of the material which acts on the surfaces of the crack in the region  $0 < x < R$ . The physical elastic-plastic condition is replaced by an equivalent elastic model. Closed form solutions have been derived relating plastic zone length to the opening displacement at the crack tip (3) and also for the displacements across the yield zone along its length (7). The crack opening displacement

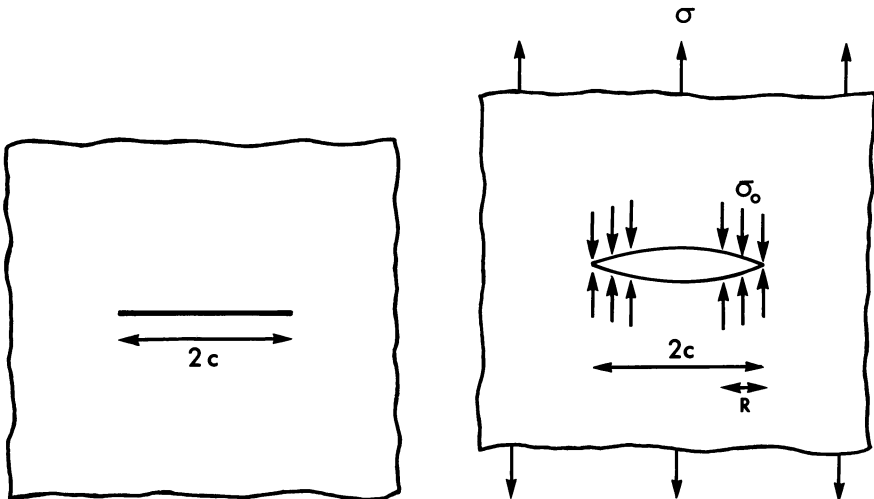


Figure 2. Dugdale model

reflects the stress and strain environment at the crack tip. A constant value of this parameter has been considered as a useful criterion for fracture (8) and has been successfully used to correlate observed fracture load data on cracked specimens of several polymers (2, 4).

In the present work the variation in stretch ratio or strain along a craze in polystyrene has been determined experimentally using methods related to those recently described by Brown and Ward (5) for poly-(methyl methacrylate), and the elastic displacements across the craze zone were compared with the values predicted for the Dugdale model (7).

In their experiments Brown and Ward (5) observed the interference patterns in the craze wedge ahead of a crack in poly(methyl methacrylate) when viewed in monochromatic light from a direction perpendicular to the plane of the craze. By loading and unloading a micro compact tension specimen, interference patterns were obtained for the craze layer in the loaded and unloaded state. Observing that the interference pattern of the fully extended craze was exactly proportional to that in the unloaded state, they concluded that the refractive index and the extension ratio along the craze was constant in each state. From a value of the craze refractive index of 1.32 in the unloaded state the geometric thickness profile of the craze was calculated; when compared with that predicted (7) for the Dugdale model, excellent agreement was found for poly(methyl methacrylate).

In our work direct measurements were made of the refractive index of a polystyrene craze at different positions along the wedge. This was made possible by a change in fracture mechanism in which the craze wedge could be induced to spall off the bulk along one boundary. The detached craze wedge lay stress free on one of the fracture surfaces and its geometric thickness was determined interferometrically. From this data and the observed interference order of the layer, the refractive index was calculated. Although the results show a fairly large scatter, the refractive index of polystyrene apparently decreases from the craze edge toward the crack tip and the strain in the fully stretched craze is not constant but increases toward the crack tip.

#### *Measurement of the Refractive Index in a Craze Wedge*

When a crack propagates in polystyrene at low crack velocities, the craze ruptures close to its median plane by a mechanism having the approximate characteristics of viscous flow. Each fracture surface is then covered by a thin layer of craze. At higher crack velocities, however, failure occurs along the boundaries between the craze and the adjacent bulk polymer by practically brittle fracture (1). The change in fracture

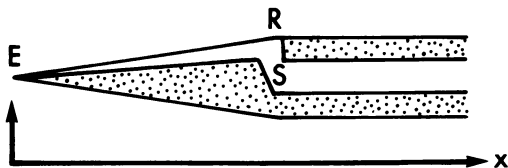


Figure 3. Fracture of the craze wedge along one craze-bulk boundary (schematic)

mechanism, shown schematically in Figure 3, permits a direct determination (9) of the density of the craze layer at S by comparing the geometric thickness of the craze layer before and after thermal collapse (to the bulk density). Where there are patches of craze in the wedge firmly attached to the bulk and adjacent to areas where the craze layer has been stripped away, the refractive index of the craze layer is obtained by comparing the optical thickness (as determined by counting the fringe interference order in monochromatic light) with the geometric thickness (obtained by direct measurement of the silver-coated surface using a double-beam interferometer). The results are shown in Figure 4. It was only possible to measure the thinner leading portion of the craze wedge. Toward the back of the wedge, fracture occurred at both craze boundaries and prevented any reliable interferometric determination of the geometric thickness of the craze layer. The considerable scatter in the measurements arises for the most part from the uncertainty in assigning fractional interference fringe orders. Nevertheless, the values all lie within the range 1.3–1.5; the value of the bulk refractive index is 1.6 and that

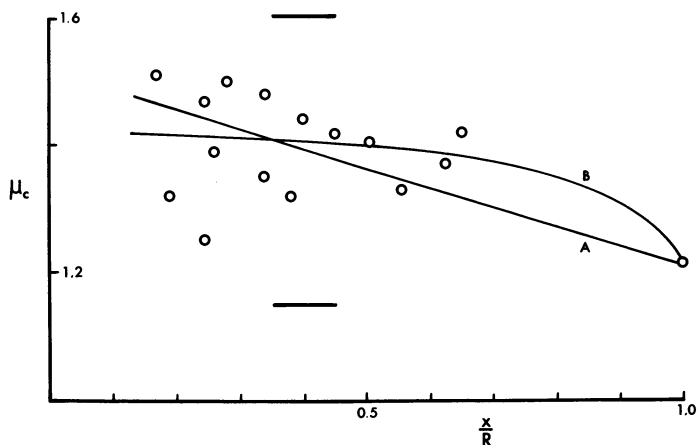


Figure 4. Refractive index of craze vs. distance from edge of craze E

for the fracture surface craze layer at S is usually about 1.15. An estimate of the refractive index of 1.2 at the rear of the craze wedge was obtained by measuring the step height of the top of the wedge above the median plane fracture surface level. This value is also consistent with the observation that the total number of interference fringes in the craze wedge lying between R and E was less than double the interference order of the fracture surface immediately following it. The craze refractive index must decrease toward the crack tip but the data would be consistent, for example, with a linear decrease along the craze length or a constant value over most of the craze length and a rapid drop close to the crack tip ( $x/R = 1$ ). For the purposes of the preliminary investigation reported here, the craze strains have been calculated for both possibilities.

### Strain in the Craze Layer

If the craze layer extends with complete lateral constraint, the strain in the craze is related to the change in its density. From a relationship between density and refractive index, an equation between strain in the craze and its refractive index can be derived. Although it is usual to start with the Lorenz–Lorentz equation, this may not be the correct relationship for a material having the structure of the craze (9). For the present purposes a linear relationship is assumed. The error introduced is at most 10% and only a few percent for the stretched craze with a high void content.

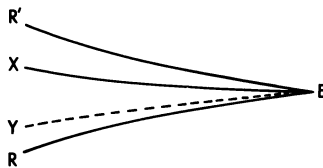


Figure 5. Schematic of stretched craze, detached craze, and equivalent bulk thickness

Figure 5 shows, schematically, the stretched craze attached to the adjacent bulk along the boundaries ER and ER'; after the change in fracture mechanism the craze is shown split away from the bulk along one boundary (ER') and in the absence of any applied tractions the free surface of the craze wedge contracts until it lies along EX. These two wedges of craze, the stretched and unstretched, are both derived from the same layer, EYR, of bulk material. At some point, P, in the craze wedge, let the stretched, unstretched, and equivalent bulk thickness of the craze be  $d_s$ ,



$d_c$ , and  $d_b$ , and their refractive indices  $\mu_s$ ,  $\mu_c$ , and  $\mu_b$ , respectively, and let their orders of optical interference be  $k_s$ ,  $k_c$ , and  $k_b$ . Assuming a linear relationship between volume fraction,  $p_c$ , and refractive index, then

$$\mu_c = 1 + (\mu_b - 1)p_c$$

and since the craze expands with lateral constraint,

$$\mu_c = 1 + (\mu_b - 1) \frac{d_b}{d_c} \quad (1)$$

and

$$\mu_s = 1 + (\mu_b - 1) \frac{d_b}{d_s}$$

From the interference equations for the stressed and unstressed (detached) craze layers:

$$2\mu_s d_s = k_s \Lambda$$

and

$$2\mu_c d_c = k_c \Lambda$$

and

$$\frac{\mu_s d_s}{\mu_c d_c} = \frac{k_s}{k_c} \quad (2)$$

From Equations 1 and 2:

$$\frac{d_s - d_c}{\mu_c d_c} = \frac{k_s - k_c}{k_c}$$

so that

$$\frac{d_s}{d_c} = 1 + \mu_c \left( \frac{k_s}{k_c} - 1 \right) \quad (3)$$

The ratio  $d_s/d_c$  may be defined as a stretch ratio  $\lambda'$ . By similar derivation, the stretch ratio  $\lambda$  of the stressed craze based on the equivalent bulk thickness may be derived:

$$\lambda = 1 + \mu_b \left( \frac{k_s}{k_b} - 1 \right) \quad (4)$$

Equation 3 is identical in form with that derived by Brown and Ward for the stretch ratio of the craze wedge in the loaded and unloaded states. In

their experiment, the unloaded state was that of the craze wedge without the applied loads on the cracked specimen. In that state, however, the craze should be in compression if the bulk material outside the craze zone remains elastic. Since the comparison of strains at different positions in the craze layer is only useful if the unloaded material state is the same—*i.e.*, the craze material has identical structure along the length of the craze—the definition of strain used here is that defined in Equation 4 (based on the initial thickness of the bulk layer from which the craze was produced.) Brown and Ward used the Lorenz–Lorentz equation to derive an equation similar to Equation 3 after an algebraic simplification equivalent to our assumption of the linear weight fraction–refractive index relationship used above. They observed that the ratio equivalent to  $k_s/k_c$  in a PMMA craze was constant along the length of the craze wedge.

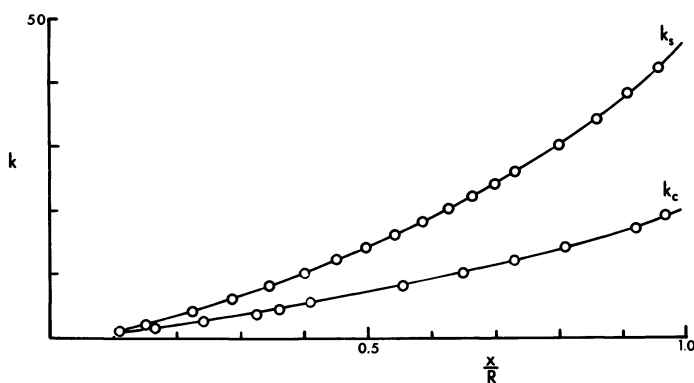


Figure 6. Interference order of the stretched craze  $k_s$  and of detached craze  $k_c$ .

It follows that for a constant refractive index the craze strain is also constant. Our observations on polystyrene indicate that neither the craze refractive index nor the ratios  $k_s/k_c$  and  $k_s/k_b$  are constant along the length of the craze (Figure 6). The values of  $\lambda$  calculated from Equation 4 are shown in Figure 7. That the craze strain is not constant does not preclude the possibility that the craze stress is still constant, as might be the case for an ideal plastic material. However, the experiments on craze stress–strain properties by Kambour (10) and Hoare and Hull (11) indicate that this is not the case.

From these same observations the equivalent bulk thickness was calculated from the equation:

$$d_b = \frac{k_c}{2\mu_c} \left( \frac{\mu_c - 1}{\mu_b - 1} \right) \quad (5)$$

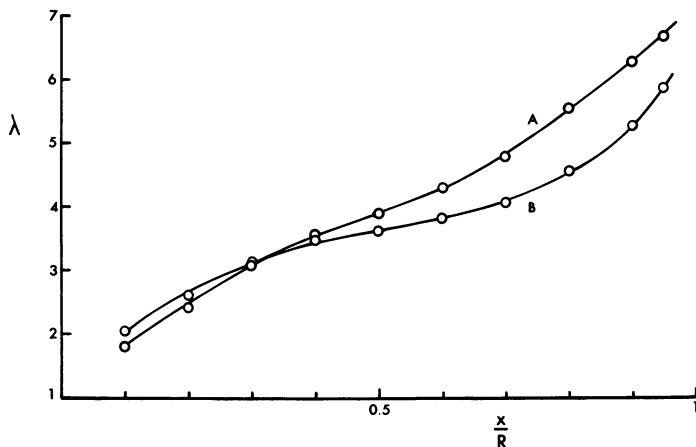


Figure 7. Variation of stretch ratio  $d_s/d_b$  in craze wedge

and is shown in Figure 8 together with the calculated values of  $d_s$ . The curves shown correspond to the variation of craze refractive index shown as curve B in Figure 4; values of  $d_s$  and  $d_b$  calculated for curve A lie very close to and slightly below the curves shown in Figure 8. The amount of bulk polymer drawn into the craze appears to be approximately proportional to the distance from the edge of the craze until near the crack tip where it increases only slightly. These results would be consistent with a craze stress,  $\sigma_0$ , which is constant over most of the craze length and decreases close to the crack tip.

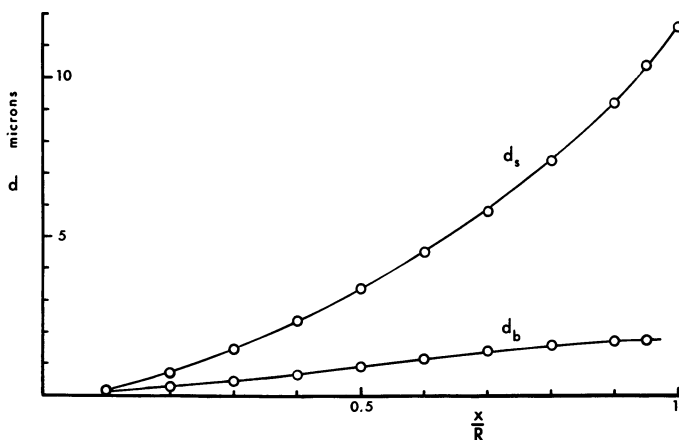


Figure 8. Craze thickness,  $d_s$ , and equivalent bulk layer thickness,  $d_b$

The normalized opening displacement,  $\delta$ , has been calculated along the length of the craze and compared in Figure 9 with that from the equation:

$$\delta = \left[ \xi + \frac{1}{2} \left( 1 - \frac{x}{R} \right) \log \left( \frac{1 + \xi}{1 - \xi} \right) \right],$$

where

$$\xi = \left( \frac{x}{R} \right)^{\frac{1}{2}},$$

derived for the Dugdale model (7). The deviation is similar to that observed by Brown and Ward for a craze in plasticized poly(methyl methacrylate).

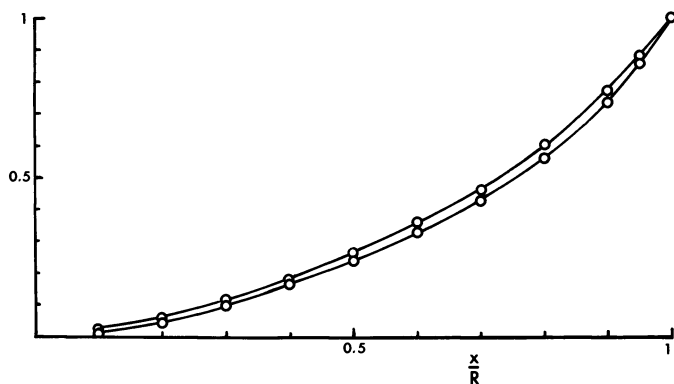


Figure 9. Normalized opening displacement for the Dugdale model (upper curve) and for polystyrene craze (lower curve)

#### Literature Cited

1. Doyle, M. J., Maranci, A., Orowan, E., Stork, S. T., *Proc. Roy. Soc.* (1972) **A329**, 137.
2. Ferguson, R. J., Williams, J. G., *Polymer* (1973) **14**, 102.
3. Dugdale, D. S., *J. Mech. Phys. Solids* (1960) **8**, 100.
4. Ferguson, R. J., Marshall, G. P., Williams, J. G., *Polymer* (1973) **14**, 451.
5. Brown, H. R., Ward, I. M., *Polymer* (1973) **14**, 469.
6. Brinson, H. F., *Proc. Soc. Expt. Stress Anal.* (1970) **27**, 72.
7. Rice, J. R., "Fracture," Chap. 3, Vol. 2, H. Liebowitz, Ed., Academic, New York, 1968.
8. Wells, A. A., *Brit. Weld. Res. Assoc. Rep.* (1963) M13.
9. Doyle, M. J., *J. Mater. Sci.* (1973) **8**, 1185.
10. Kambour, R. P., *Poly. Eng. Sci.* (1968) **8**, 281.
11. Hoare, J., Hull, D., *Phil. Mag.* (1972) **26**, 443.

RECEIVED October 18, 1974.

## Laser Diffraction of Polymer Crazes

### A. CERS

Department of Aerospace Engineering and Mechanics, University of Minnesota, Minneapolis, Minn. 55455

### C. Y. YUAN HSIAO

Department of Biochemistry, Medical School, University of Minnesota, Minneapolis, Minn. 55455

### C. C. HSIAO

Department of Aerospace Engineering and Mechanics, University of Minnesota, Minneapolis, Minn. 55455

*A laser diffraction technique is used to study crazed polystyrene at room temperature. Biaxially oriented polystyrene sheets were stressed and crazed before laser diffraction patterns were photographically recorded. Corresponding micrographs and diffraction patterns from crazing under different environmental conditions are presented. Both chemically induced crazing of a stressed specimen as well as mechanically produced crazes were studied and compared. Laser diffraction was very sensitive to crazes of different qualities. Thin diffraction lines attributed to fine parallel crazes and rough diffraction patterns resulting from distorted crazing were observed. The intensity variation of the diffraction pattern suggests that not only the shape but also the quantity of crazing may be interpretable. The extension of the diffraction technique into quantitative analyses of the kinetic accumulation of crazing distribution is one of the possibilities.*

The complex nature of fracture strength as affected by crazing of a glassy, amorphous polymer is well recognized. Processes leading to the formation and growth of a system of crazes and subsequent nucleation and propagation of cracks must be fully understood before a valid fracture theory can be formulated. Among many influencing factors the

inception and distribution of crazing plays a major role in analyzing the statistical strength behavior of a polymer exposed to stress. The present work is a preliminary attempt to observe crazing through the application of a laser diffraction technique (1). Laser diffraction is extremely sensitive to crazing. Under different environmental conditions stressed polystyrene specimens reveal corresponding diffraction patterns. The diffraction patterns qualitatively characterize the distribution of the crazes together with other features. Several photomicrographs and corresponding laser diffraction patterns are illustrated in this report. Quantitative data on the kinetics of the accumulation of crazing development are being collected to continue this research.

### *Experimental*

Test specimens were cut from biaxially oriented polystyrene sheets supplied by Monsanto Commercial Products Co. The cut specimen,  $8\frac{1}{2} \times 1 \times 0.010$  inches was stressed in an Instron universal tester to 4800 psi before various environmental conditions were introduced locally to induce crazing and to generate the corresponding laser diffraction patterns. Mechanically stressed specimens without chemical applications were either bent or stressed in tension to near failure to produce crazing. All diffraction patterns were obtained with a He-Ne gas laser 0.7 mm in diameter having a 6328-A wavelength. The laser beam was normally about 12 inches in front of the specimen. A screen parallel to the specimen was erected 68 inches from the other side of the specimen to reflect the normal transmission diffraction pattern from each specimen. The diffracted patterns were recorded photographically under identical exposure time and aperture opening about 80 inches from the screen. These distances were constant during the recording process. The accompanying photomicrograph for each diffraction pattern shows the approximate specimen area from which laser diffraction patterns were obtained. The linear horizontal or vertical dimension of the micrographs equals 0.7 mm which is comparable with the diameter of the laser beam.

### *Results and Discussion*

The diffraction patterns reported here reveal quantitative features. As indicated earlier, exact quantitative data are being collected to continue this research. However some preliminary observations and interpretations on the relations between chemical groups and their influence in crazing development are given for possible future reference.

Many chemical compounds that react with polystyrene can initiate crazing if the material is subjected to high stress. On this basis several series of chemicals have been used. Both photomicrographs and their corresponding laser diffraction patterns are recorded side by side for clarity. Table I also lists the chemical formulations and an indication of the intensity of crazing for each of the compounds used.

**Table I. Effects of Environmental Conditions on Crazing**

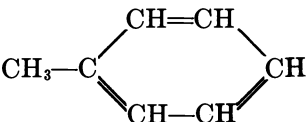
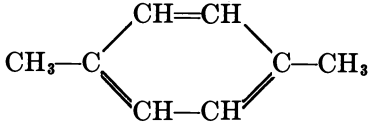
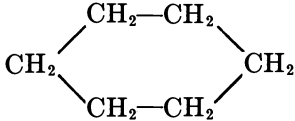
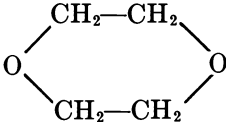
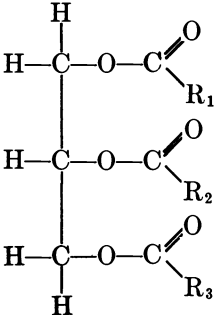
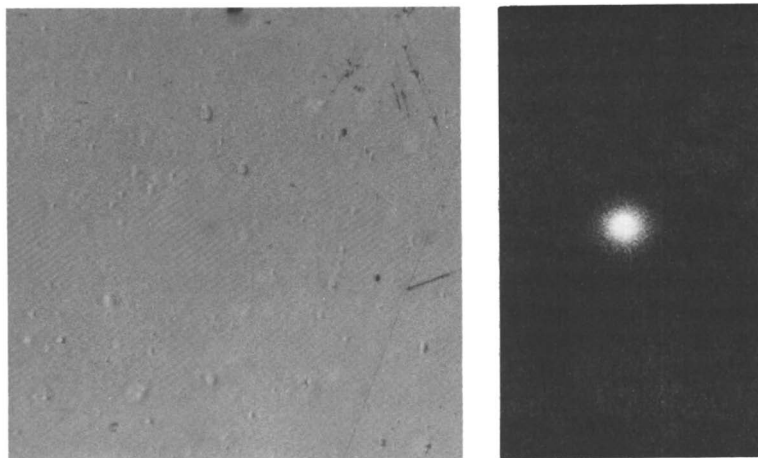
Figure	Environment	Chemical Formula	Intensity of Crazing
<i>Compounds Containing OH Groups (Reagent Grade)</i>			
1	Glycerin	$\begin{array}{c} \text{CH}_2-\text{CH}-\text{CH}_2 \\   \quad   \quad   \\ \text{OH} \quad \text{OH} \quad \text{OH} \end{array}$	none
2	Water	H—OH	weak sharp
3	Ethanol (100%)	CH <sub>3</sub> —CH <sub>2</sub> —OH	moderate well defined
4	Polyethylene glycol	$\begin{array}{c} \text{CH}_2-\text{CH}-\text{CH}-\text{CH} \dots \\   \quad   \quad   \quad   \\ \text{OH} \quad \text{OH} \quad \text{OH} \quad \text{OH} \end{array}$	moderate
5	Propanol	CH <sub>3</sub> —CH <sub>2</sub> —CH <sub>2</sub> OH	strong
6	Isopropyl alcohol	$\begin{array}{c} \text{CH}_3-\text{CH}-\text{CH}_3 \\   \\ \text{OH} \end{array}$	strong
7	Propylene glycol	$\begin{array}{c} \text{CH}_3-\text{CH}-\text{CH}_2\text{OH} \\   \\ \text{OH} \end{array}$	strong
<i>Compounds Containing Chlorine (Reagent Grade)</i>			
8	Methylene dichloride	CH <sub>2</sub> Cl <sub>2</sub>	weak
9	Chloroform	CHCl <sub>3</sub>	moderate
10	Carbon tetrachloride	CCl <sub>4</sub>	moderate
<i>Esters of Fatty Acids (99%)</i>			
11	Methyl linoleate	$\begin{array}{c} \text{CH}_3-(\text{CH}_2)_4-\text{CH}=\text{CH}-\text{CH}_2- \\ \text{CH}=\text{CH}-(\text{CH}_2)_7-\text{COOCH}_3 \end{array}$	moderate
12	Methyl oleate	CH <sub>3</sub> —(CH <sub>2</sub> ) <sub>7</sub> —CH=CH—(CH <sub>2</sub> ) <sub>7</sub> —COOCH <sub>3</sub>	moderate
<i>Hydrocarbons (Reagent Grade)</i>			
13	Toluene (methylbenzene)		moderate

Table I. Continued

Figure	Environment	Chemical Formula	Intensity of Cracking
14	Xylene (dimethylbenzene)		moderate
15	Cyclohexane		moderate well defined
16	<i>p</i> -Dioxane		moderate well defined
17	Pentane	$\text{CH}_3\text{—CH}_2\text{—CH}_2\text{—CH}_2\text{—CH}_3$	moderate well defined
<i>Glycerides</i>			
18	Sesame oil (commercial)		moderate
19	Pure lard (commercial)		moderate
20	Leaf lard (commercial)		moderate
21	Butter (commercial)		moderate
(R <sub>1</sub> , R <sub>2</sub> , and R <sub>3</sub> are fatty acid radicals— saturated or unsaturated)			
22	Finger mark (oil, moisture, etc.)		weak well defined
<i>Mechanical Stressing</i>			
23	Pure bending	—	strong
24	Simple tension	—	strong





*Figure 1. Stressed polystyrene after application of glycerin*

Figure 1 illustrates the stressed polystyrene film without crazing. A thin layer of glycerin has been applied to this area with little or no change in the diffraction pattern as shown on the right. The same laser diffraction pattern of a circular halo was also obtained when distilled water was used. However if a big blot of distilled water were introduced and allowed to dry, minute but perfect parallel crazes developed, and a sharp vertical diffracted light was observed (*see* Figure 2). The possible absorption of atmospheric contaminants by the water or water molecules that entered the polystyrene molecular system and eased the nucleation

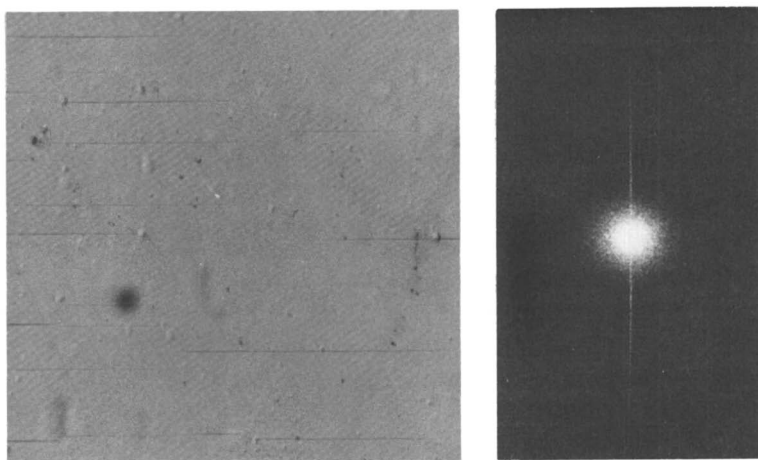


*Figure 2. Stressed polystyrene after application of distilled water*

of crazing may have caused this result. This is only a problem of reaction kinetics. Depending on the concentration of polystyrene in aqueous suspension, its structures or molecular arrangements can be quite different (2). However the bearing of this particular phenomenon on the present problem is not clearly correlated yet.

Several compounds having methylene and hydroxyl groups such as ethanol, polyethylene glycol, propanol, isopropyl alcohol, and propylene glycol have been used. All greatly affected crazing development. Note

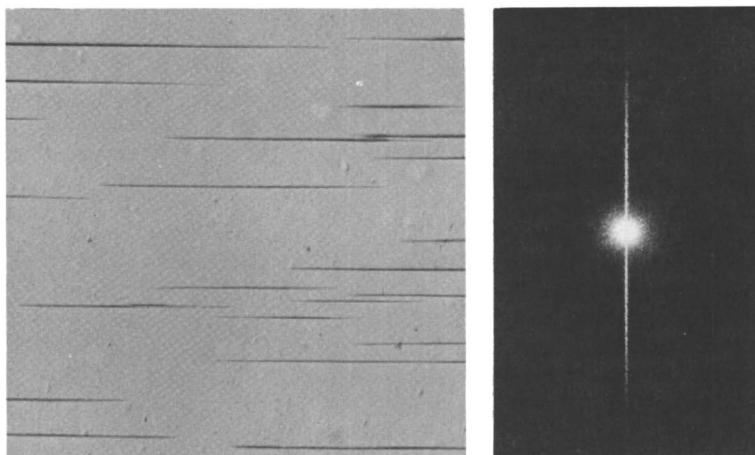


*Figure 3. Stressed polystyrene after application of 100% ethanol*

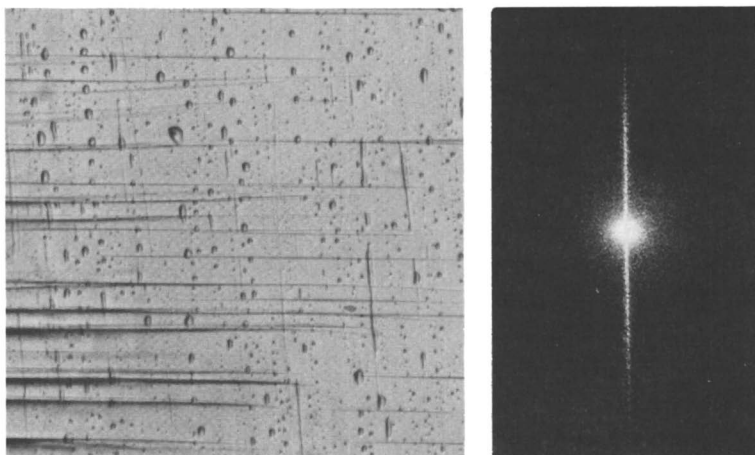


*Figure 4. Stressed polystyrene after application of polyethylene glycol*

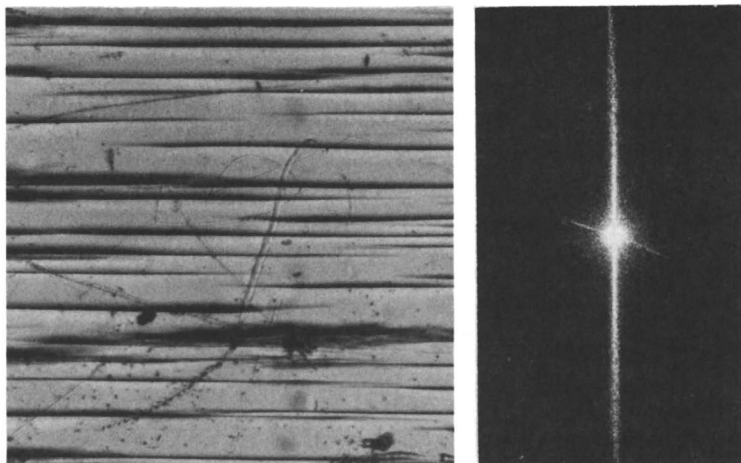


*Figure 5. Stressed polystyrene after application of propanol*

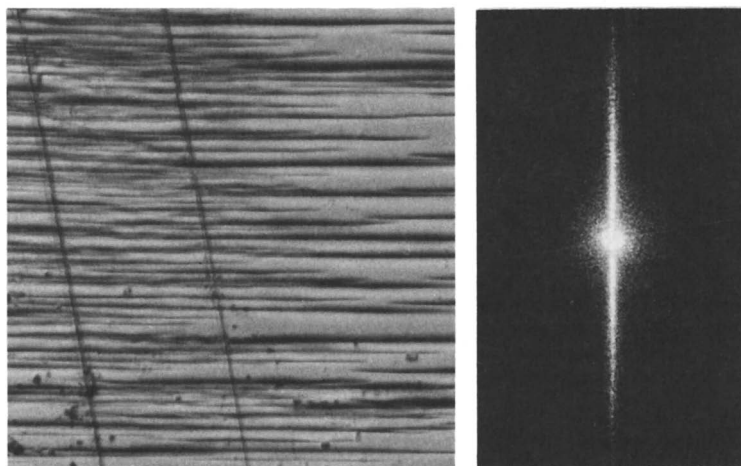


*Figure 6. Stressed polystyrene after application of isopropyl alcohol*

that polyethylene glycol, a polymer containing the same number of hydroxyl and methylene groups similar to those of glycerin, also caused crazing, whereas glycerin did not. Figures 3–7 show an increasing influence on the development of crazing by ethanol, polyethylene glycol, propanol, isopropyl alcohol, and propylene glycol in that order. Methanol greatly affected the initiation and development of crazing. The quantitative effect was comparable with that of propanol in crazing occurrence. The relatively diffused scattering of the laser diffraction reflects the higher degree of irregularity in the craze as compared with previous cases. Again

scratches on the sample appeared as thin diffraction lines across the picture.

Compounds containing chlorine had less influence on craze size and shape than compounds with hydroxyl groups, except glycerin and water. Figures 8–10 show the increasing degree of fine crazes developed from the application of methylene dichloride, chloroform, and carbon tetrachloride. The exact mechanism of the effects of certain chemical groups on the nucleation and propagation of crazes is not understood.

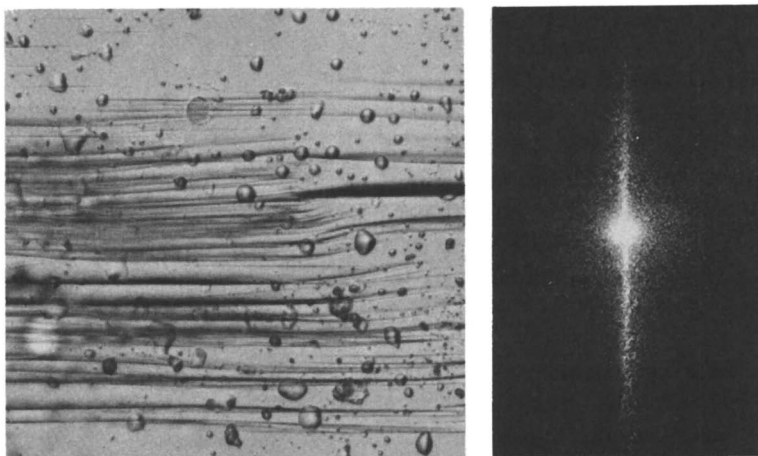


*Figure 7. Stressed polystyrene after application of propylene glycol*

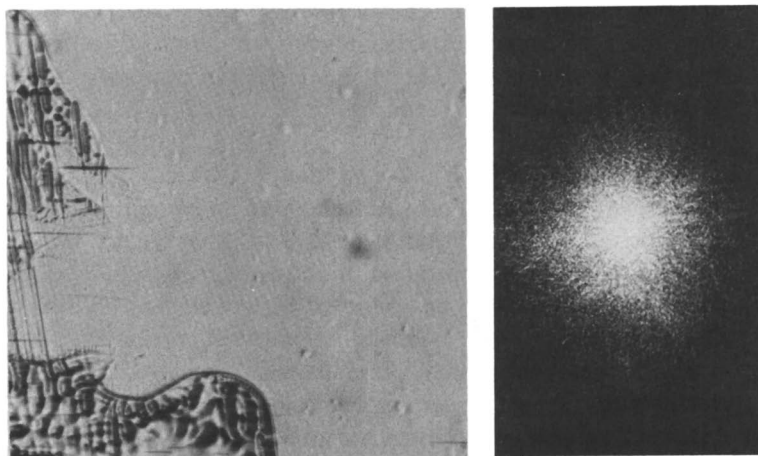


*Figure 8. Stressed polystyrene after application of methylene dichloride*

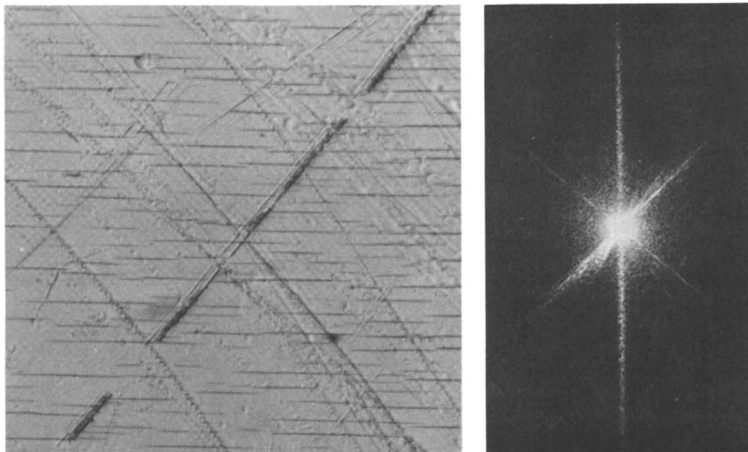


Figure 9. Stressed polystyrene after application of chloroform

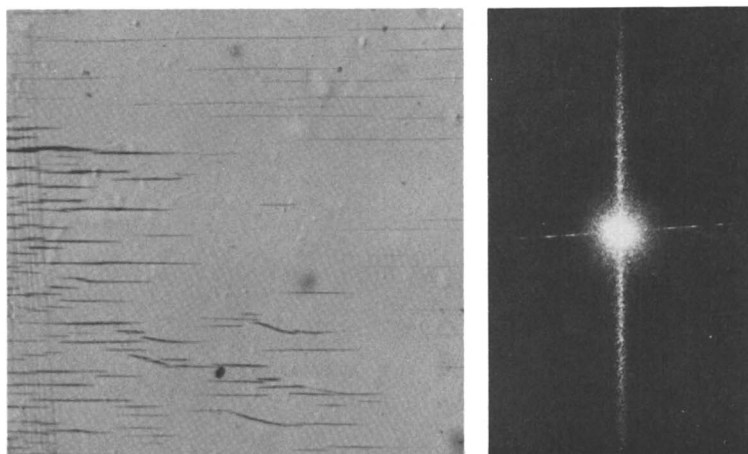
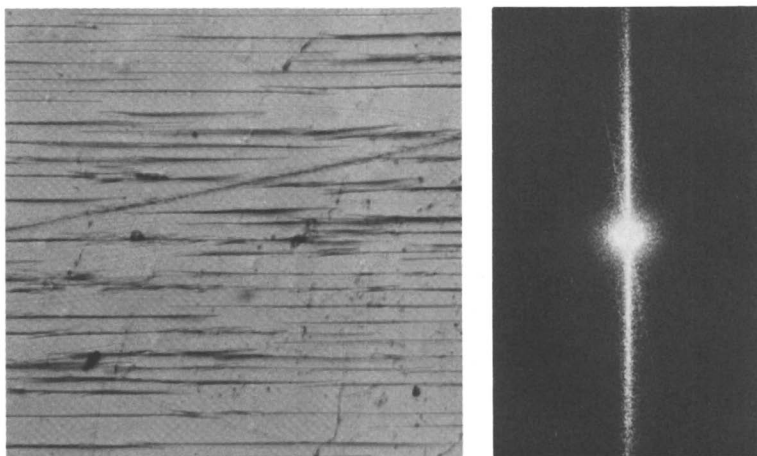


Figure 10. Stressed polystyrene after application of carbon tetrachloride

The esters of fatty acids and hydrocarbons (Table I, 11-17 with corresponding micrographs and laser diffraction patterns) have all assisted moderately to develop crazes in a stressed polystyrene. The effect of methyl linoleate helped to initiate more crazes than that of methyl oleate (*see* Figures 11 and 12). As shown in Figures 13 and 14 toluene and xylene assisted in developing more dense but finer crazes as compared with the first two. Note that these chemicals tend to cover the surface of the polystyrene and cause the central region of the diffraction

pattern to become non-uniform. In contrast with the results shown in Figures 15 and 16 for cyclohexane and *p*-dioxane, also note the fine, long crazes created with these two chemicals, whereas pentane in Figure 17 generated shorter but heavier crazes without clouding the surface of polystyrene.

Glycerides of the commercial quality commonly used in the food industry apparently have different effects on crazing development than



*Figure 11. Stressed polystyrene after application of methyl linoleate*

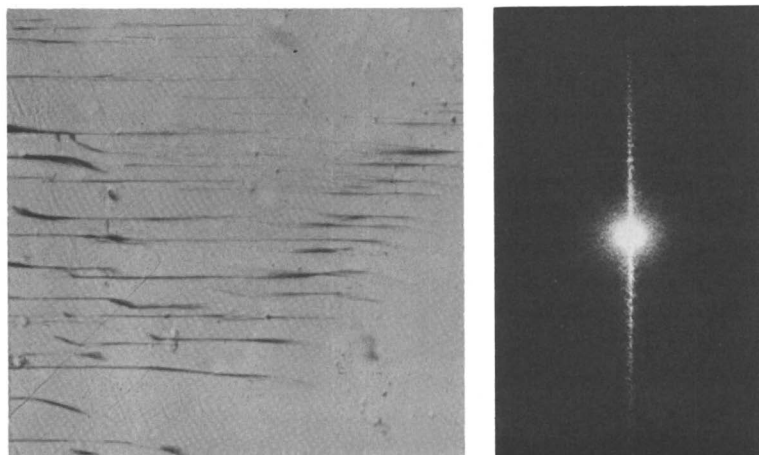


*Figure 12. Stressed polystyrene after application of 99% methyl oleate*

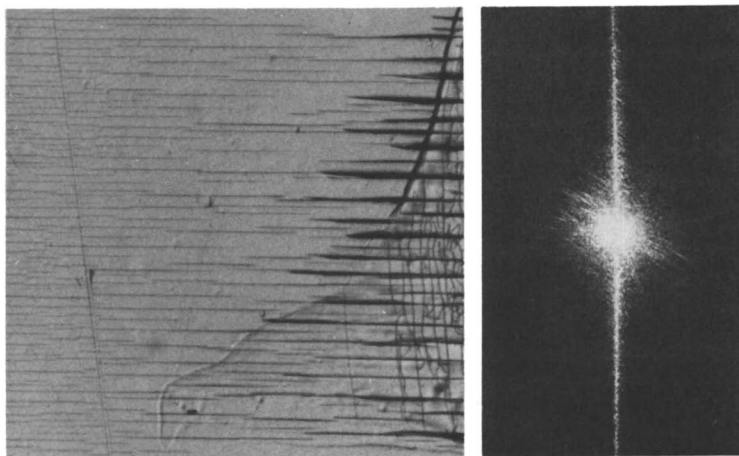


*Figure 13. Stressed polystyrene after application of toluene*

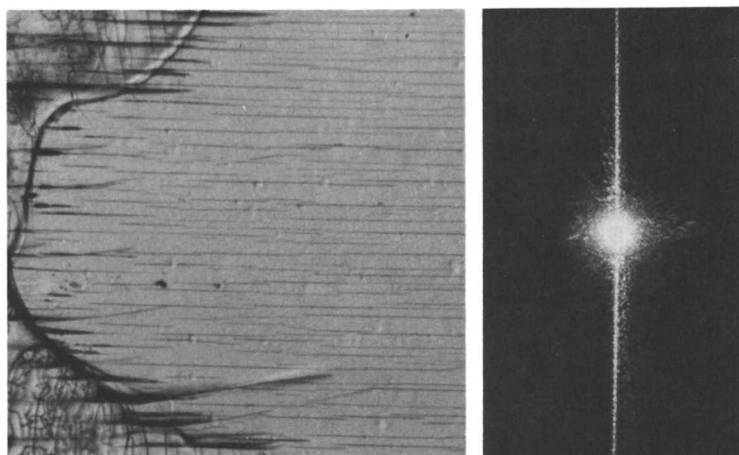


*Figure 14. Stressed polystyrene after application of xylene*

hydrocarbons and esters of fatty acids. All of the glycerides used including sesame oil, pure lard, leaf lard, and butter are less able to produce dense crazes than hydrocarbons and esters of fatty acids (*see* Figures 18–21). With solid lard at room temperature the diffused small angle scattering of the laser by the lard molecules is clearly evident (*see* Figures 19 and 20). A somewhat similar, but less evident, situation occurred when ordinary butter (triglycerides) was brushed on the polystyrene surface (*see* Figure 21).

During this investigation we handled the specimens carefully since finger marks affect the crazing property of polystyrene. Figure 22 shows the crazing marks and their corresponding laser diffraction pattern that resulted from touching the surface of a stressed specimen. Probably the contaminants on fingers are primarily types of glycerides since they produced loose crazes on the surface of specimens similar to those shown in Figures 19–21. The nearly horizontal diffraction lines in both diffrac-

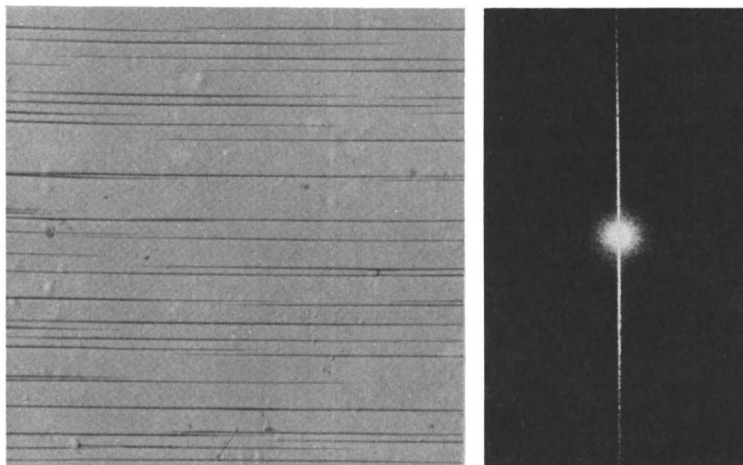


*Figure 15. Stressed polystyrene after application of cyclohexane*

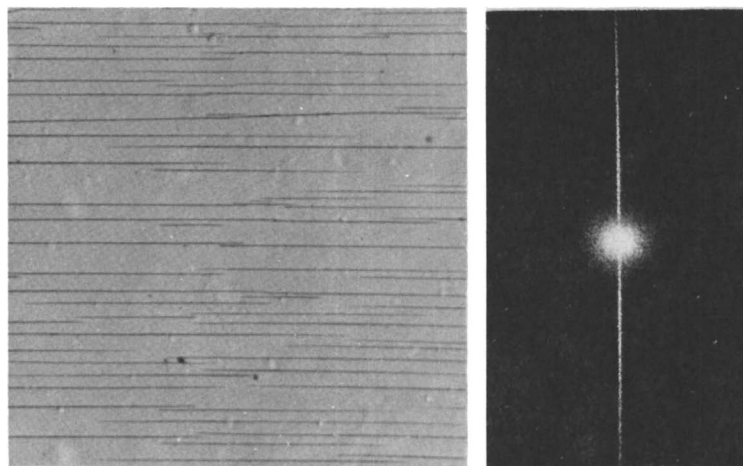


*Figure 16. Stressed polystyrene after application of p-dioxane*



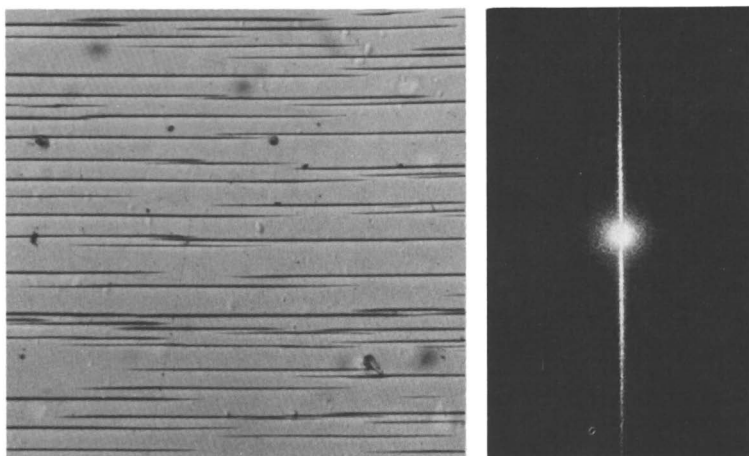


Figure 17. Stressed polystyrene after application of pentane

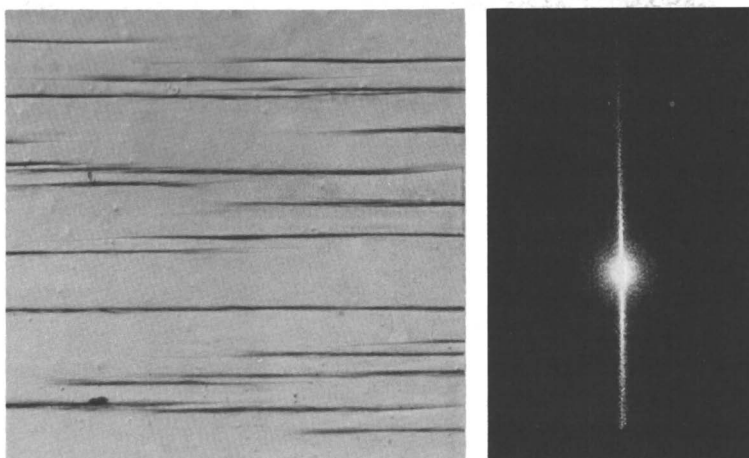


Figure 18. Stressed polystyrene after application of sesame oil

tion patterns probably arise from the surface scratches that appeared on both micrographs (Figures 21 and 22).

Mechanically stressed polystyrene without the application of any chemical compound can also produce crazing. Figure 23 shows crazing and its diffraction pattern attributed to bending the polystyrene sheet; surface crazing appears on only one side. This contrasts the development of crazing in depth by simple tensile stress (*see* Figure 24) where crazes developed on both sides of, and sometimes in between, the surfaces.

The diffraction pattern registers the volume effect regarding the distribution of crazing. In principle if the distribution of crazing is random, the measurements of the diffracted laser intensity should yield the kinetic information on the accumulation of crazing.

Generally all crazes developed perpendicular to the direction of the maximum applied principal stress, which in this case is the vertical direction. The vertical laser diffraction pattern indicates that all horizontal crazes are essentially parallel. According to the theory of light diffraction

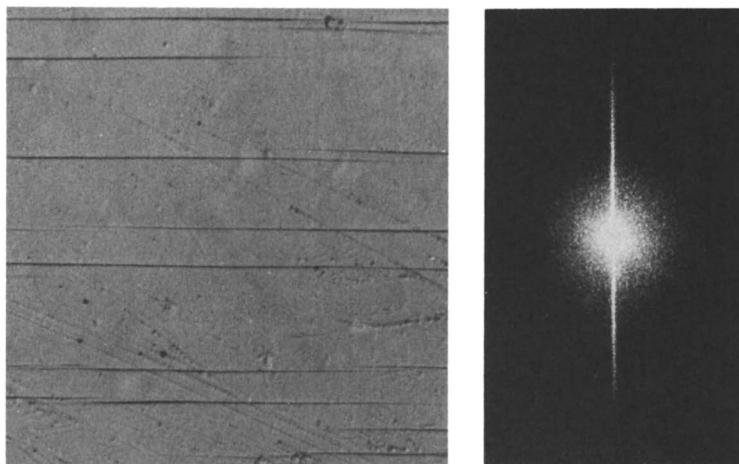


*Figure 19. Stressed polystyrene after application of pure lard*

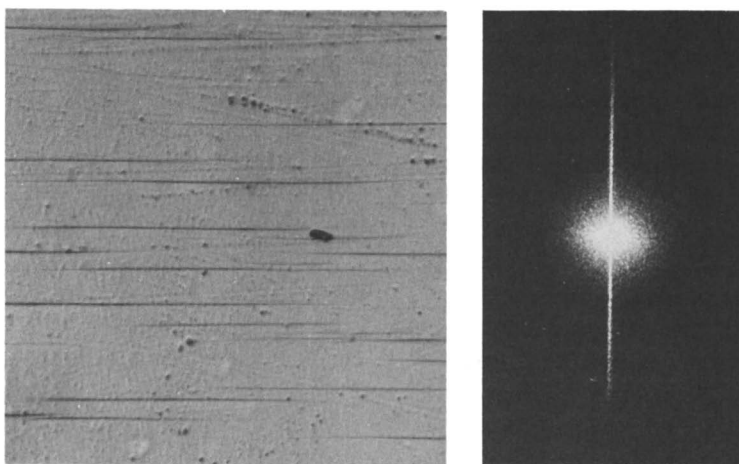


*Figure 20. Stressed polystyrene after application of leaf lard*

(3) if the crazes consist of many apertures irregularly distributed, the total intensity of the light diffracted will be multiples of that diffracted by one. Thus proper quantitative information may be obtainable. However complications will develop if regular distribution of crazing occurs. In addition a slight deviation from parallelism in the plane of crazing arises from the broadening of the vertical diffraction line. Thus the shape of a craze or possibly the slope of the crazing envelope near the

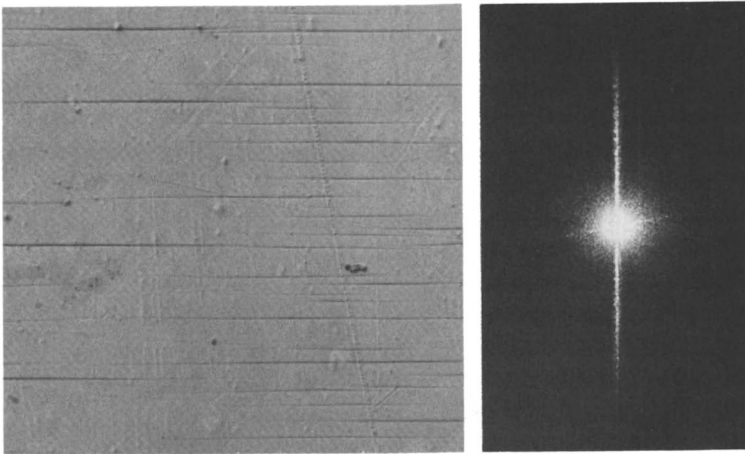


*Figure 21. Stressed polystyrene after application of butter*

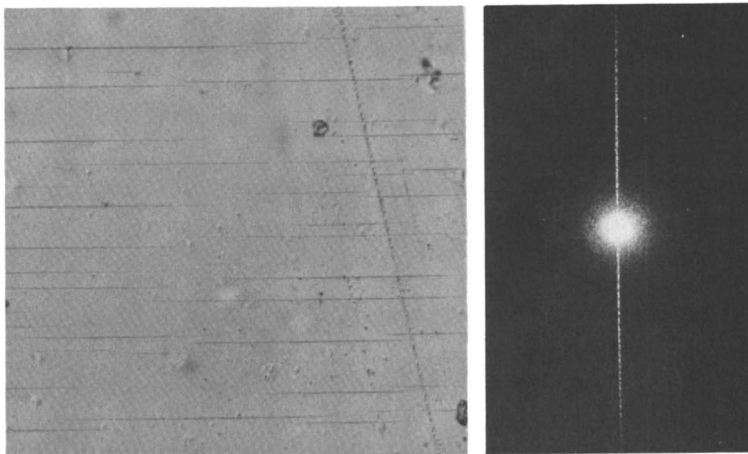


*Figure 22. Stressed polystyrene after contamination by finger marks*

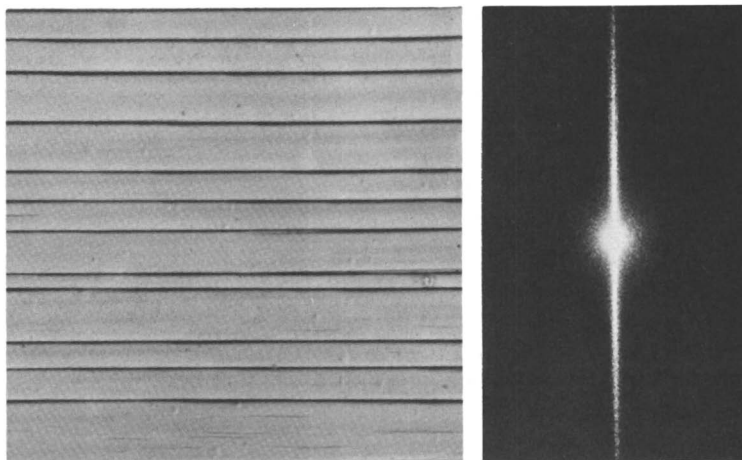


*Figure 23. Craze patterns in crazed polystyrene by mechanical bending*

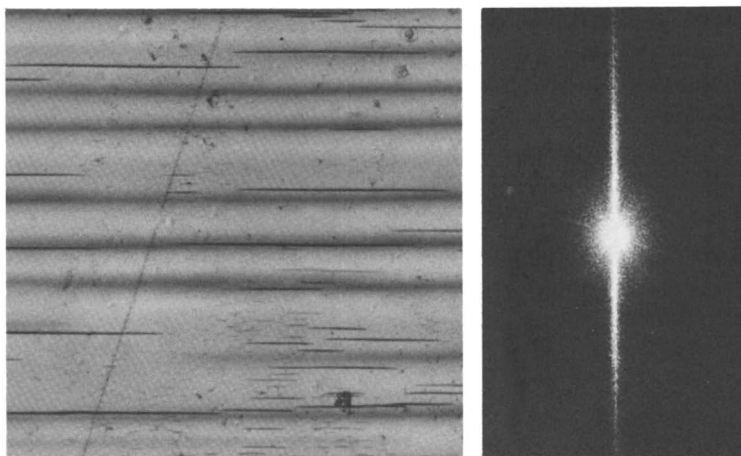


*Figure 24. Craze patterns in crazed polystyrene in simple tension*

edge of the craze may also be associated closely with the diffraction pattern.

### **Conclusions**

Most chemicals including water, but excluding glycerin, will weaken some locations of a polystyrene molecular system and will initiate parallel crazes perpendicular to the applied tensile stress field. The density

distribution of craze development depends on the composition of the chemical compounds. Mechanical stressing, without chemicals, produces crazes, but both the shape and density of the crazes are different from those produced in a chemical environment. Laser diffraction seems to be quite sensitive to the shape and distribution of crazing. The use of the diffraction technique in a quantitative analysis of crazing processes is feasible. A careful systematic study to this end seems highly desirable.

### *Acknowledgment*

The authors thank R. J. Collins and J. A. Corruthers of the Department of Electrical Engineering, University of Minnesota, for their many helpful suggestions and discussions on the application of laser diffraction techniques. They also thank W. T. Peria of the same department for loaning some laser equipment. The various services provided by the Department of Aerospace Engineering and Mechanics of the University of Minnesota are gratefully acknowledged.

### *Literature Cited*

1. Hsiao, C. C., *Appl. Phys. Lett.* (1973) 23, 20.
2. Williams, R., Crandell, R. S., *Phys. Lett.* (1974) 48A, 225.
3. Born, M., Wolf, E., "Principles of Optics," 4th ed., Pergamon, New York, 1970.

RECEIVED October 18, 1974.

# The Fracture Energy of Low Molecular Weight Fractions of Polystyrene

RICHARD E. ROBERTSON

Scientific Research Staff, Ford Motor Co., P. O. Box 2053,  
Dearborn, Mich. 48121

*The fracture energies ( $G_{1c}$ ) of narrow fractions of low molecular weight polystyrene were measured. The fracture energy of the highest molecular weight fraction (111,000) depends on the nature of the crack formed, a phenomenon thought to arise from subsidiary crazing. The lowest fracture energy for this fraction was 27.4 J/m<sup>2</sup> which is lower than obtained previously on similar materials and may represent the absence of subsidiary crazing. The fracture energy of the lowest weight fraction studied (3550) was still about four times that needed to create the surfaces of the crack, though the energy seems to extrapolate to this value at monomeric molecular weights. Only a thin layer of the material is needed—particularly advantageous when only small amounts (< 1 g) of polymer are available.*

An important strength characteristic of all brittle materials is the fracture energy. This is the energy required to propagate the already formed cracks or crack nuclei which always exist in real materials. The fracture energy is obtained from an energy balance with the strain energy available to initiate crack growth. Because the fracture energy is independent of crack or flaw size, unlike the tensile strength, it describes strength better than the tensile strength does for new experimental materials, for example, where large flaws may arise from impurities or from unrefined molding and shaping procedures. Until now, however, the techniques for measuring the fracture energy required larger amounts of material than are usually available with a new material. In this report we describe a method of measurement that requires less than 1 g of material (often much less) and that can also be used for very brittle polymers.

To illustrate the advantages of the technique, we apply it to narrow molecular weight fractions of low molecular weight polystyrene.

The technique involves sandwiching the material between two pieces of a different polymer. The general requirements for the second polymer are: (a) that it be incompatible with the first, (b) that it have a similar thermal expansivity over the temperature range for which the two polymers are glassy to avoid shrinkage stresses, and (c) that there exist for the two a good, low-boiling, common solvent. Also, a clear sandwiching material would enhance measuring the layer thickness and viewing the crack. Poly(methyl methacrylate) is eminently suitable as the sandwiching material for studying narrow molecular weight fractions of polystyrene, and methylene chloride is an appropriate common solvent.

### Experimental

**Specimen Preparation.** The polystyrenes examined are described in Table I. Each was tested and found to be incompatible with the poly(methyl methacrylate); another polystyrene of molecular weight *ca.* 2000 was not incompatible and could not be used. The poly(methyl methacrylate) (PMMA) used for sandwiching the polystyrene was Acrylite cast sheet (American Cyanamid Co.) of molecular weight 3.1 million. The cast sheet has a surface roughness that is much less than the thickness of the polystyrene layers (about 10  $\mu\text{m}$ ). A  $\frac{1}{4}$ -inch thick sheet was used, but later it had to be thinned to improve the accuracy of the measurements. After cutting to  $2\frac{1}{4} \times 2\frac{1}{4}$  inch and removing burrs, the protective paper was removed, and the pieces were washed in two changes of methanol—each with 2 min of ultrasonic agitation to ensure complete removal of the pressure sensitive adhesive used to bond the protective paper. Then the pieces were rinsed in distilled water, and the water droplets were removed by a stream of Freon gas.

The sandwiches were made by dissolving the polystyrene (PS) in methylene chloride and by squeezing a layer of this solution between two pieces of PMMA. The final polystyrene layer was approximately 10  $\mu\text{m}$  thick. To ensure that a ternary solution did not develop between the PS, PMMA, and methylene chloride, which might phase separate to leave PMMA particles in the PS, solution concentrations were used for which the expanded polystyrene molecules tended to overlap. The overlap of the PS coils seems to avoid a ternary solution because even the two parts of PS-PMMA block copolymers seem to avoid each other in solution (1). An estimate of the concentration at which the polystyrene coils in methylene chloride overlap and essentially fill the entire solution space can be obtained by assuming that the radius of the coil is approximately equal to the radius of gyration of the molecule in a Flory or theta solution. The radius of gyration equals  $(\langle r_o^2 \rangle / 6)^{1/2}$ , where  $\langle r_o^2 \rangle^{1/2}$  is the mean end to end distance. The latter for polystyrene is 0.670  $M^{1/2}$  A, where  $M$  is the molecular weight (2). The concentration at which the coils of molecular weight  $M$  fill the whole solution space in a Flory solution is

$$x_{t_0} = 19.4/M^{1/2} \quad (1)$$

**Table I. Polystyrene**

<i>Molecular Weight</i>			$x_{t_0}$ , g/ml	<i>Conc.</i> , g/ml	<i>Fracture Energy</i> , J/m <sup>2</sup>	<i>Source</i> <sup>a</sup>
<i>Peak</i>	$M_w$	$M_N$				
3,550	4,000	3,100	0.325	0.360	0.34	WA
10,300	(10,300 $\pm$ 3%)		0.191	0.248	0.60	AL
20,500	20,800	20,200	0.135	0.149	0.94	WA
34,500	36,000	33,000	0.104	0.132	1.64	WA
111,000	111,000	111,000	0.0581	0.0664	27.4–166.	WA

<sup>a</sup> WA = Waters Associates; AL = ArRo Laboratories.

The values for  $x_{t_0}$  for each molecular weight are given in Table I. Concentrations lower than these will still give complete overlap in a good solvent like methylene chloride because the coils are more expanded. In our previous work with this technique for measuring fracture energy (3), we found that a growing crack would not stabilize within layers less than about 1  $\mu\text{m}$  thick. Hence, to ensure that the crack would grow only within the layer, a thickness of around 10  $\mu\text{m}$  was desired; it also required solution concentrations of 0.1 g/ml. For measuring the layer thickness, 0.12 mg/ml of rhodamine B dye was added to each solution. At 460 nm, 1  $\mu\text{g}/\text{ml}$  of rhodamine B in methylene chloride has an absorbance of 0.19 in a 1-cm thick cell.

After assembling, the PMMA-PS-PMMA sandwiches were dried for one week at room temperature and then for 4 days at 60°C. There was a tendency for the lower molecular weight polystyrene sandwiches to fracture from shrinkage while drying. These were rebonded in a vacuum oven. The specimens were clamped between glass plates with spring loaded clamps and placed in the oven. The oven was evacuated and then heated to approximately 150°C for ½ hr before air was readmitted. After another 15 min at this temperature, the oven was allowed to slowly return to room temperature.

After drying (and rebonding when necessary), the 2¼ × 2¼ inch sandwiches were cut into specimens approximately ½-inch wide. A groove 1.4 mm wide and 6 mm deep was machined in one end, which removed the PS layer and adjacent PMMA, to allow insertion of the cleavage wedge. The other end was machined flat to act as a base. The specimens were clamped across the PS layer during the machining to avoid fracture.

**Mechanical Tests.** The method for measuring fracture energy is shown in Figure 1. The cleavage wedge is driven into the top of the double-cantilever-beam specimen, forcing the two ends apart. Until a critical separation between the ends is reached, which depends on the length of the crack,  $c$ , the crack remains stationary. On reaching this separation, the crack begins to grow, but will come to rest again, or is arrested, at a new length  $c'$  if the separation of the ends is constant. By driving the wedge further into the specimen a new critical separation is reached, and the crack grows again; this is followed by growth arrest. In this way a series of measurements of critical separation and crack length corresponding to both crack growth initiation and arrest can be obtained



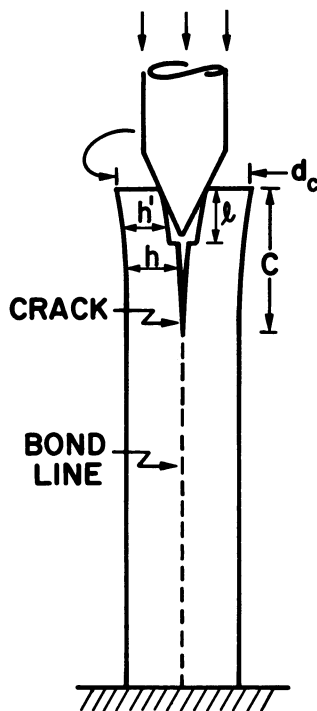


Figure 1. Cleavage experiment: the wedge is driven downward into the specimen and the crack is initiated before the experiment begins. Parameters to compute the fracture energy:  $c$ , the length of the crack below the application of the stress at the top;  $d_c$ , the distance between the outside edges of the specimen at the top as the crack begins to grow.

from the same specimen. This method of cleavage superimposes a compressive stress parallel with the crack path which helps to keep the crack from running off to the side of the specimen. The critical separation is determined by measuring with a micrometer the total distance across the top of the specimen,  $d_c$ , and by subtracting the thickness of the beams,  $2h$ . The crack length,  $c$ , from where the stress is applied at the top of the specimen is measured with a cathetometer.

The fracture energy can be obtained from these measurements of  $d_c$  and  $c$  by using an expression derived by Kanninen (4). When the crack tip is no closer to the end of the specimen than the thickness,  $2h$ , a suitable approximation, which also accounts for the groove in the top of the specimens, is (3)

$$G_{I_0} = \frac{3}{16} \frac{(d_c - 2h)^2 E h^3}{c^4 [1 + 0.64 h/c]^4} \cdot \left\{ 1 + \left[ \left( \frac{h}{h'} \right)^3 - 1 \right] \left( \frac{l}{c} \right)^3 \right\}^{-2} \quad (2)$$

where  $h$  is the thickness of the beam on each side of the crack;  $h'$  is the thickness on each side of the groove;  $l$  is the depth of the groove, and  $E$  is Young's modulus of the beam material (the PMMA). The subscripts of  $G$  refer to mode I fracture, to the mode characteristic of cleavage, and to the condition of crack growth. The symbol  $G_I$  without the subscript  $c$  refers to the rate, with respect to crack growth, at which the strained specimen releases strain energy which may or may not be sufficient to

initiate crack growth. Note that the dimension perpendicular to the plane of Figure 1, the width, does not enter the expression; it is assumed to be constant for the full length of the specimen.

The characteristic of fracture conveyed by  $G_{Ic}$  is sometimes expressed in two other ways. The first is the fracture toughness,  $K_{Ic}$ , which is related to  $G_{Ic}$  by the equation

$$K_{Ic} = (E G_{Ic})^{1/2} \quad (3)$$

For bulk specimens,  $K_{Ic}$  and  $G_{Ic}$  convey the same information. However, for adhesively bonded structures, such as the specimens described in this report,  $K_{Ic}$  and  $G_{Ic}$  differ.  $E$  in Equation 3 is the modulus of the adherend (the PMMA) rather than the adhesive, and so  $K_{Ic}$  is not characteristic solely of the PS layer but of the composite as a whole. The other expression for fracture behavior is the effective fracture surface energy,  $\gamma$ . It is related to the fracture energy by

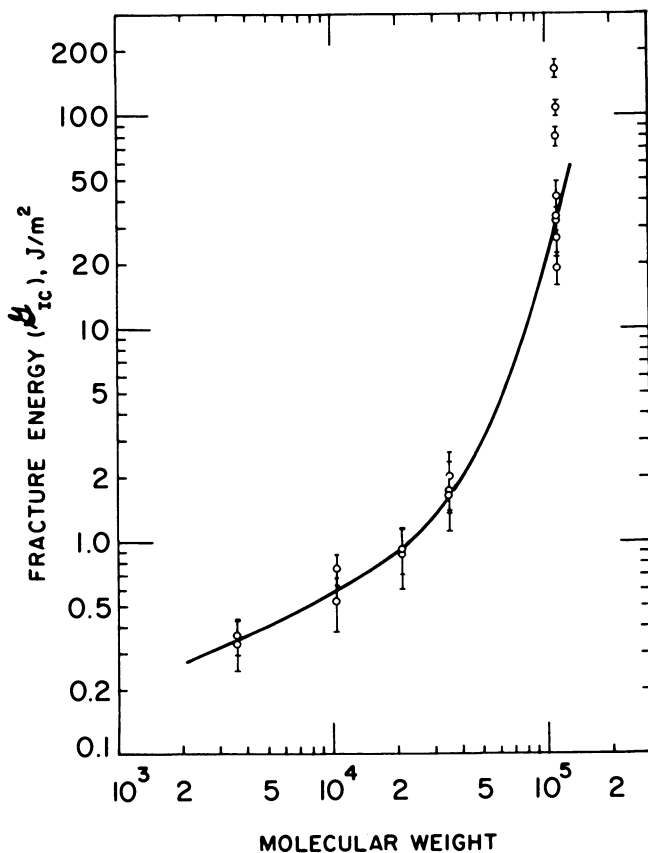


Figure 2. Measured fracture energy ( $G_{Ic}$ ) vs. molecular weight (distribution peak) for narrow molecular weight fractions of polystyrene

$$\gamma = G_{Ic}/2 \quad (4)$$

The factor of 2 arises from the fact that as the crack advances, the exposed surface area increases twice as rapidly as the area of the crack because each side of the crack is counted separately. The use of  $\gamma$  is mainly historical and is significant only in the rare instance when the crack growth criterion is dominated by the energy required to create new surface.

### Results

The fracture energies for polystyrene computed from the measurements of  $c$  and  $d_c$  with Equation 2 are shown in Figure 2 as a function of molecular weight. All of the individual fracture energies obtained from propagating a single crack in a specimen (as many as 14) were averaged; they are plotted in Figure 2. Also shown by line segments are plus and minus one standard deviation. Once a crack was formed in a specimen, approximately the same energy was required to advance it further each time. Hence, the standard deviation for the set of measurements was generally little more than 10% of the mean fracture energy, and this variation arose in part from the following two experimental problems: (a) with the more brittle polymers, where the cleavage pressure needed for crack growth is small, just the measurement of the distance across the top with the micrometer can change the separation; (b) the increases in cleavage pressure to initiate crack growth sometimes could not be made in small enough increments, especially with the more brittle polymers. On the other hand, crack propagation can vary over the specimen; this was reflected in subtle changes in the almost featureless fracture morphology. The average fracture energies are included in Table I.

### Discussion

For the four lower molecular weight materials in Figure 2, the two or three specimens that were tested gave essentially the same fracture energy. For the highest molecular weight, however, different cracks gave different fracture energies; though within 99% confidence limits, the five data points in the range 20–40 J/m<sup>2</sup> are consistent with the average fracture energy of 27.4 J/m<sup>2</sup>. The eight data points for this molecular weight were obtained from five specimens. In the specimens used for more than one datum, the crack was healed between tests by heating above 100°C for ½ hr and then reinitiated. It is not uncommon for different cracks to yield different fracture energies (5, 6). Marshall *et al.* (6) note that the fracture energies obtained by various workers, including themselves, on various styrene homopolymers of commerce have varied from approximately 200 to 7200 J/m<sup>2</sup>. Though some of this

variation may arise from material difference, much of it depends on the multiplicity of crazing that accompanies crack growth (5, 6).  $27.4 \text{ J/m}^2$  is the lowest fracture energy reported for a polystyrene molecular weight above  $10^5$ . Hence it may represent the minimum fracture energy that occurs in the absence of subsidiary crazing. The three data points at higher energy may then represent the inclusion of some subsidiary crazing. It is possible that the occurrence of subsidiary crazing requires a minimum polystyrene layer thickness. The layer thickness of the specimens giving the three highest fracture energies was around  $10 \mu\text{m}$ ; for those giving smaller energies, it was around  $7.5 \mu\text{m}$ .

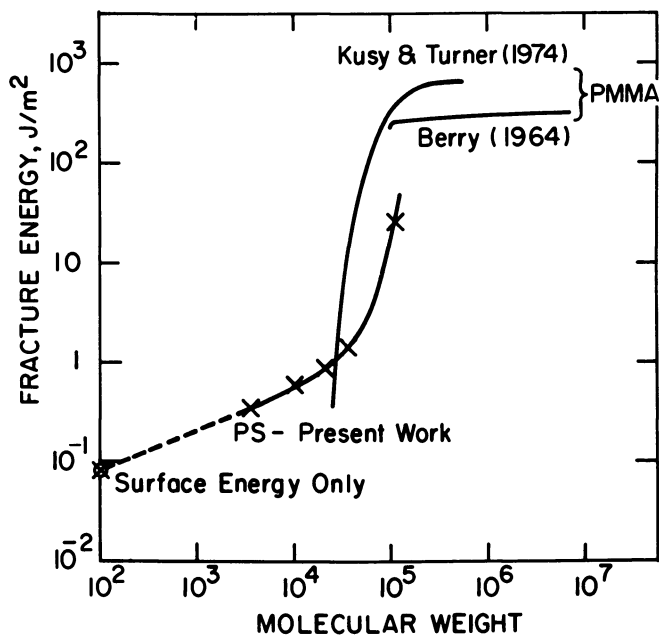


Figure 3. Fracture energy vs. molecular weight of polystyrene and poly(methyl methacrylate)

In the only other studies of fracture energy vs. molecular weight known to us, Berry (7) and Kusy and Turner (8) examined poly(methyl methacrylate) (see Figure 3). The rapid fall in fracture energy below a molecular weight of  $10^5$  is characteristic of both polymers.

The fracture energy of polystyrene is a combination of the plastic energy needed to form crazed material from uncrazed material, the energy to create the exposed surface in the craze, the elastic strain energy stored in the craze, and the energy to create new surface when the craze ruptures (5, 9). As the molecular weight decreases, the amount of crazing and

each of the contributions to the fracture energy decrease, except that needed to form the surface of the crack. We estimated the energy required to form new surface by using the surface energy extrapolated to 20°C from that for molten polystyrene obtained by Wu (10), which is 0.0407 J/m<sup>2</sup>. Our lowest molecular weight specimen, with a contour length of approximately 85 Å, has a fracture energy that is still approximately four times that needed to form the surface area of the crack. However, the fracture energy for polystyrene seems to extrapolate to the energy needed to form the crack surface (0.082 J/m<sup>2</sup>) at monomeric molecular weight (see Figure 3).

### Literature Cited

1. Utiyama, H., Takenaka, K., Mizumori, M., Fukuda, M., *Macromolecules* (1974) 7, 28.
2. Kurata, M., Stockmayer, W. H., *Fortschr. Hochpolym.-Forsch.* (1963) 3, 196.
3. Robertson, R. E., *J. Adhesion* (1975) 7, 121.
4. Kanninen, M. F., *Int. J. Fracture* (1973) 9, 83.
5. Murray, J., Hall, D., *J. Mater. Sci.* (1971) 6, 1277.
6. Marshall, G. P., Culver, L. E., Williams, J. G., *Int. J. Fracture* (1973) 9, 295.
7. Berry, J. P., *J. Polym. Sci.* (1964) A2, 4069.
8. Kusy, R. P., Turner, D. T., *Polymer* (1974) 15, 394.
9. Kambour, R. P., *J. Polym. Sci., Part A-2* (1966) 4, 349.
10. Wu, S., *J. Adhesion* (1973) 5, 39.

RECEIVED October 18, 1974.

## Plane Strain and the Brittleness of Plastics

A. F. YEE, W. V. OLSZEWSKI, and S. MILLER

Synthesis and Characterization Branch, Chemical Laboratory,  
General Electric Corporate Research and Development Center,  
Schenectady, N. Y.

*Double-grooved specimens were used to study the failure of PC, PC/PE, PET, ABS, and HIPS during transitions from plane stress to plane strain. The yield behavior of PC is consistent with a von Mises-type yield criterion; plane strain reduces its elongation. The yield behavior of PC/PE is consistent with a Tresca-type yield criterion; plane strain appears to be relieved by voiding around the PE particles. PET undergoes a ductile-to-brittle transition; its behavior is consistent with a von Mises-type yield locus intersected by a craze locus. The yield behavior of ABS and HIPS is not significantly affected by the plane-stress-to-plane-strain transition. Plane strain alone does not necessarily cause brittleness.*

When notched polymer specimens are subjected to rapid tension or flexure, brittle failure frequently occurs. Whether or not a notched specimen fails brittlely at a given temperature depends on the sharpness of the notch, the thickness of the specimen, and the speed of deformation. Sharpness, thickness, and speed are all relative and interdependent terms. The particular combination of these three variables that causes a ductile-to-brittle transition depends on the polymer and the thermal-mechanical history of the specimen being tested. For example, the notched Izod impact strength of polycarbonate has been investigated by systematically changing only the following variables: notch sharpness (1), specimen thickness (1, 2), speed (3), degree of annealing (1, 4), etc. In each case a ductile-to-brittle transition has been observed.

In the notched Izod impact test, with the exception of some rubber modified plastics, the fracture surface of a specimen that has failed ductilely exhibits significant inward collapsing on the sides of the impact bar near the notch, indicating that a large amount of plastic flow has

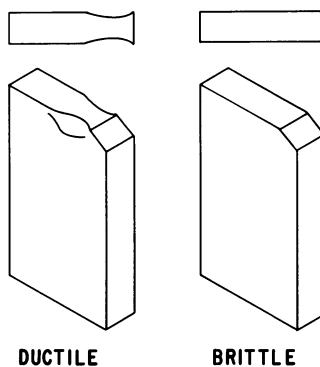


Figure 1. Typical appearances of failed notched Izod impact specimens

taken place. In contrast, the fracture surface of a specimen that has failed brittlely has sides that remain straight and is relatively flat and featureless on a macroscopic scale (Figure 1). Therefore, the ductile-to-brittle transition is thought to be caused by a plane-stress-to-plane-strain transition (5).

The stresses near the root of a notch are extremely complex; and the stress analysis becomes exceedingly difficult when the strain is large, as is the case when yield or failure is imminent. A sharp notch causes constraints and introduces a state of triaxial tension behind the root of the notch (5). This state of stress is consistent with LeGrand's observation of the growth of a flaw behind a notch in a bar of polycarbonate (4). A blunt notch causes constraints when the thickness of the specimen is large. Such a notch can also introduce a state of triaxial tension. While it is desirable to investigate the behavior of polymers in a well-defined state of triaxial tension, it is difficult to accomplish experimentally. However, as we demonstrate below, a state of plane strain is relatively easy to produce. The relationship between plane strain and brittleness of plastics is the subject of our investigation.

Consider a body in the Cartesian coordinates  $x_1$ ,  $x_2$ , and  $x_3$ . Plane strain is defined as the state the body is in when the displacement vector  $\mu_1$  vanishes and when the orthogonal displacement vector components  $\mu_2$  and  $\mu_3$  are functions of  $x_2$  and  $x_3$  only (6). Although not rigorously correct, we will substitute strain  $\epsilon$  for displacement  $\mu$  in the above definition to simplify the following discussion.

The yield criteria of polymers have been reviewed by Ward (7) and more recently by Raghava *et al.* (8). Except for the craze yield criteria of Sternstein and Ongchin (9) and Bowden and Oxborough (10), most of the yield data can be described by a pressure-modified, von Mises-yield criterion. The corresponding yield surface is everywhere convex. A typical yield locus on the  $\sigma_1$ - $\sigma_2$  plane is shown in Figure 2. If the assump-

tion of the normality rule is correct for polymers (11, 12), then the strain vector  $\epsilon$  is normal to the yield locus. [Strain is a tensor; however, for convenience it will be treated here as a vector.] The plane strain point of  $\epsilon_1 = 0$  on this locus can then be located by drawing a tangent to the locus such that it is perpendicular to the  $\sigma_2$  axis; this is because the strain vector at the tangential point has zero component in the  $x_1$  direction. This point is interesting because here  $\epsilon_1$  changes from tensile(+) to compressive(-). Consequently the region of the yield locus in the first quadrant bound by the two plane strain points ( $\epsilon_1 = 0$  and  $\epsilon_2 = 0$ ) is where both  $\epsilon_1$  and  $\epsilon_2$  are  $\geq 0$ . For a hypothetical, two-dimensional material, the stress states in this region could lead to voiding. For a real three dimensional material, a volume dilatation takes place when  $\epsilon_1 + \epsilon_2 + \epsilon_3 > 0$ , thus  $\epsilon_3 > -\epsilon_2$  must be satisfied for dilatation. This can come about as a result of the contraction ratio being smaller than  $\frac{1}{2}$  or as a result of geometric constraints or rigid particle inclusions. [Contraction ratio is the ratio of lateral contraction to axial elongation in a tensile test.] For a viscoelastic material, one other effect that must be considered is the time dependence of Poisson's ratio (13). For example, lateral contraction can lag behind longitudinal stretching when such stretching takes place rapidly, thus producing time dependent dilatation. Dilatation presumably causes voiding and finally crazing (14, 15) and brittle fracture.

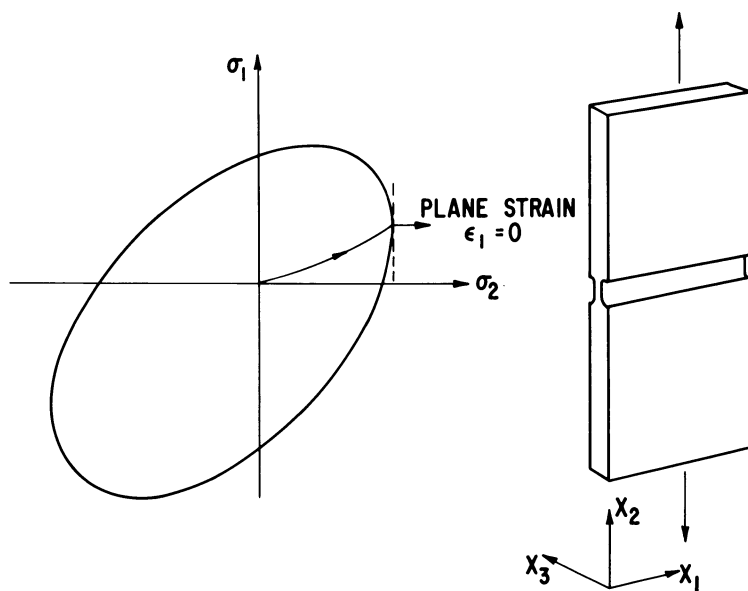


Figure 2. Von Mises-type polymer yield locus with tensile plane strain ( $\epsilon_1 = 0$ ) indicated. Convention for coordinates is also shown.



However, not being able to independently control  $\epsilon_3$ , our investigation is limited only to observations of yield behavior made during a controlled plane-stress-to-plane-strain transition.

### Specimen

Tensile plane strain can be created by pressurizing a fixed-end thin-walled tube or, more simply, by imposing elastic constraint on the edges of a wide strip tensile specimen. Corrigan *et al.* used a specimen with grooves machined on both sides of a weldment to test the biaxial strength of welds in steel (16). Whitney and Andrews tested PMMA in tensile plane strain by clamping a wide thin sheet in wide grips (17). However, the distance between the two grips was so large that it is doubtful that plane strain was obtained. Recently, Lee tested wide HIPS strip specimens with grooves at oblique angles to the tensile axis to vary the biaxiality, including plane strain (18). The stress distribution in a biaxial strip test for polymeric materials has been theoretically analyzed by Cost and Parr (19). Their results can be used to aid in the design of the specimen geometry and the interpretation of the results.

The specimen we used is illustrated in Figure 3. The ideal specimen profile dimensions have been found to be  $T \sim 3t$  and  $b \sim 3t$  to  $5t$  (16,

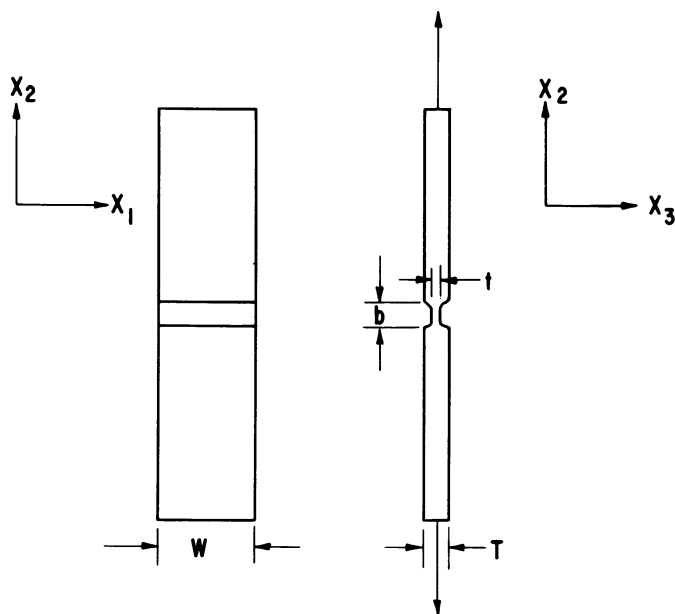


Figure 3. Shape of the specimens. Notations for the dimensions and coordinates are also shown.

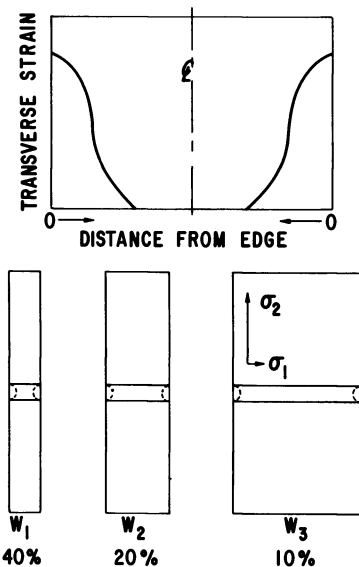


Figure 4. Schematic of the transverse strain distribution and the percent of specimen width not in plane strain ( $\epsilon_1 = 0$ )

18, 20). Elastic constraint is effected when the strip width  $W$  is large compared with  $b$ , but non-zero transverse strains exist (*i.e.*,  $\epsilon_1 \neq 0$ ) at the groove edges regardless of  $W$ . If the specimen is narrow, these finite transverse strain zones overlap and the stress in the specimen is nearly uniaxial. If the specimen is wide, plane strain ( $\epsilon_1 = 0$ ) is realized in a substantial portion of the specimen. This situation is schematically illustrated in Figure 4. Cost and Parr have shown that  $W/b$  has to be five in order that 80% of the specimen will be within 10% of the axial stress that an ideal infinitely wide specimen would have. They have also shown that differences in Poisson's ratio can be accounted for by a simple scaling factor (19). Since most rigid polymers have Poisson's ratio between 0.3 and 0.4, we expect substantial plane strain when  $W/b > 5$ . In these experiments  $b$  was fixed in all cases. However the thickness  $t$  was more difficult to control because of machining accuracy limitations. In plotting the data, smaller scatter was obtained by plotting yield stress against  $W/t$ .

The tensile yield stress variation as a function of  $W$  for a material which has a von Mises-type yield locus is illustrated schematically in Figure 5. This variation is caused by the fact that as the width of the specimen increases, the biaxiality also increases toward the asymptotic value at plane strain. If the material obeys the von Mises yield criterion exactly, the plane strain yield stress should be 15% higher than it would be for simple tension. On the other hand, if the material obeys the Tresca yield criterion, the plane strain yield stress should be identical

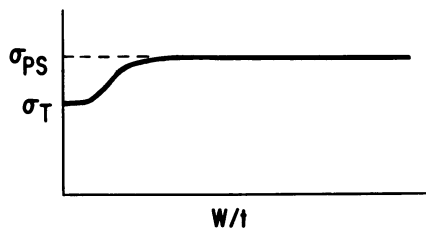


Figure 5. Schematic of yield stress (in the  $x_2$  direction) vs.  $W/t$  for a von Mises-type polymer

to that of simple tension, and no variation in yield stress with respect to  $W$  is to be expected.

At large  $W/b$ , the stress path, *i.e.*, the ratio of  $\sigma_1/\sigma_2$  as  $\sigma_2$  increases, is calculable (21), provided that the Poisson's ratio along the path is known. Since Poisson's ratio (if indeed it can be defined for finite strain) varies from about 0.4 typically to about 0.5 at yield, the stress path is not radial, *i.e.*,  $\sigma_1/\sigma_2$  is not constant. This situation is illustrated schematically in Figure 2. Since accurate values for Poisson's ratio of the polymers tested are not available, the path dependence of our results will have to await further investigation.

### Experiment and Results

We have tested the following polymers: polycarbonate (PC), polycarbonate/4% polyethylene blend (PC/PE), poly(ethylene terephthalate) (PET), ABS, and impact modified polystyrene (HIPS). All materials except PC were compression molded into nominal  $1/8$ -inch sheets. The PC used was an  $1/8$ -inch extruded sheet heat-treated in a manner previously described (22). These PC specimens were considered to be

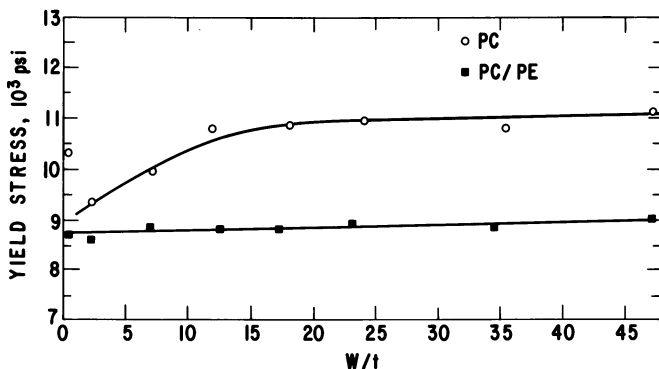


Figure 6. Yield stress ( $\sigma_2$ ) vs.  $W/t$  for PC and PC/PE

isotropic since the tensile strengths taken along and perpendicular to the extrusion direction were identical within experimental error. Observation of birefringence also indicated a satisfactory degree of macroscopic homogeneity in the plane of the sheet. All sheets were milled to 0.100-inch thick. The grooves were machined to  $b = 0.125$  inch and  $t = 0.045 \pm 0.005$  inch. The corners at the base of the grooves are rounded off to a radius of  $1/64$  inch. Ten specimens each of  $W = 0.1, 0.3, 0.5, 0.75, 1.0, 1.5,$  and  $2.0$  inches were tested for each material.

The specimens were stretched in a floor model Instron between 2-inch wide grips at a crosshead rate of 0.5 inch/min. Temperature was  $23 \pm 1^\circ\text{C}$ , but humidity was not controlled. Proper alignment was very important for the wide specimens.

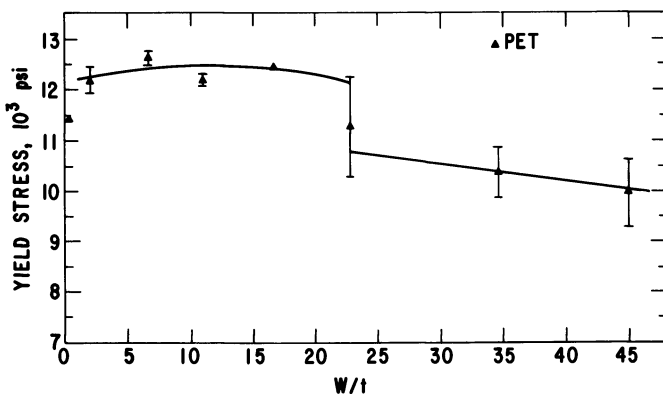


Figure 7. Yield stress ( $\sigma_2$ ) vs.  $W/t$  for PET

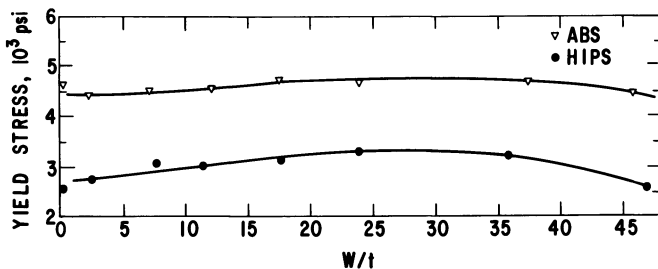


Figure 8. Yield stress ( $\sigma_2$ ) vs.  $W/t$  for ABS and HIPS

Yield stress vs.  $W/t$  curves are plotted for PC and PC/PE in Figure 6, PET in Figure 7, and ABS and HIPS in Figure 8. Unless otherwise indicated, the average deviations are about the size of the symbols. The data near  $W/t = 0$  are from testing conventional dog-bone type tensile specimens.

At  $W/t \sim 20$  ( $W/b \sim 7$ ), the PC specimen was essentially at plane strain because the yield stress approached an asymptotic value, as de-

picted in Figure 5. The ratio of this asymptotic yield stress and the extrapolated  $W/t = 0$  yield stress, which is the ratio of plane strain yield stress to simple tension yield stress ( $\sigma_{ps}/\sigma_t$ ), is about 1.2. Data taken from the work by Raghava *et al.* (8) indicate a ratio of about 1.1. The difference can be attributed to three possible factors: anisotropy, stress concentration, and precision. While the PC sheets have planar isotropy, they may still have normal anisotropy undetectable by the methods used. Normal anisotropy is expected to increase the  $\sigma_{ps}/\sigma_t$  ratio. Cost and Parr found severe stress concentrations near the groove edges (19) which may drop the overall yield stress to a lower value, thus increasing the  $\sigma_{ps}/\sigma_t$  ratio. The average deviation of the data is about 1%, and it cannot account for the magnitude of the difference.

At the speed of testing used, none of the PC specimens, including those at plane strain, failed brittlely. However, the specimens at plane

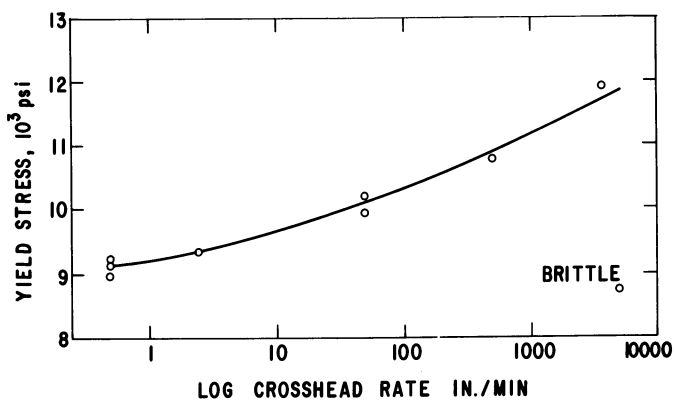
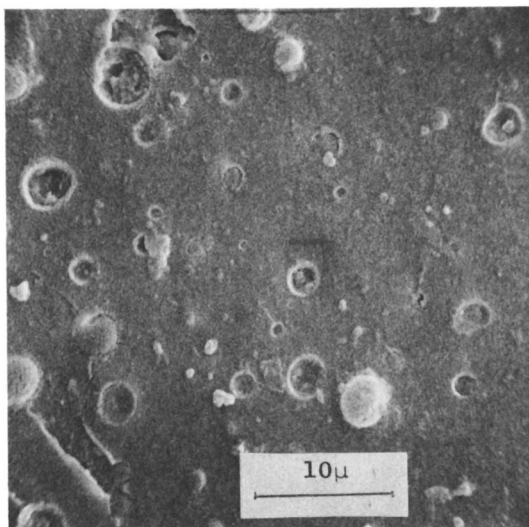
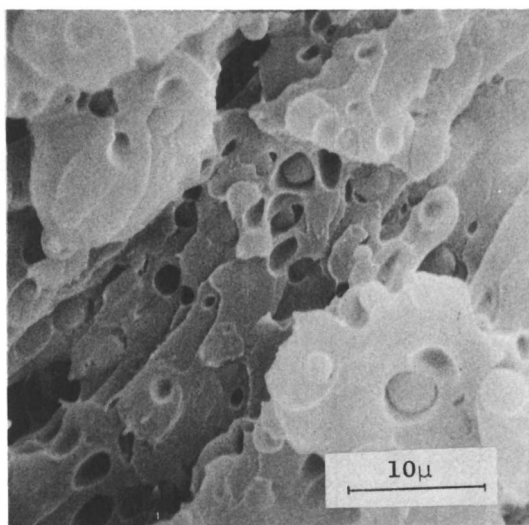


Figure 9. Yield stress ( $\sigma_y$ ) vs. crosshead rate for PC/PE with  $W/b = 8$

strain failed at consistently smaller elongations than those not at plane strain. We were not able to determine with precision the difference in elongation between the two cases since at small  $W/t$  the specimens were rather small and the scatter in measured elongation was quite large, probably because of artifacts introduced during specimen preparation. We subsequently tested 1-inch wide ( $W/b = 8$ ) specimens at speeds up to 6000 inches/min, but none failed brittlely. In contrast, during preliminary experiments using compression molded  $\frac{1}{4}$ -inch thick PC sheet, two specimens at  $W/b = 16$  failed in a completely brittle manner (23). Examination of the fracture surface revealed regions of mirror-like appearance typical of slow crack growth. Interference fringes were also observed, indicating the presence of a broken craze layer. With the exception of these two specimens, the preliminary set and the present



*Figure 10. Scanning electron micrograph of brittle fracture surface in PC/PE. PE is in the form of light-colored spherical particles.*



*Figure 11. Scanning electron micrograph of ductile fracture surface in PC/PE. PE is in the form of light-colored spherical particles.*

set of data are identical. The brittleness of the former set at plane strain is doubtless the result of its thermal history.

The yield stress of PC/PE appears to be a very weak function of width. None of the specimens failed brittlely. However, in the region beyond  $W/t = 20$  ( $W/b = 7$ ), the specimens failed by voids which formed and coalesced in the groove. The appearance of the voids in the groove separated by thin strands of the polymer is similar to photomicrographs of thin crazes. We tested additional 1-inch wide ( $W/b = 8$ )

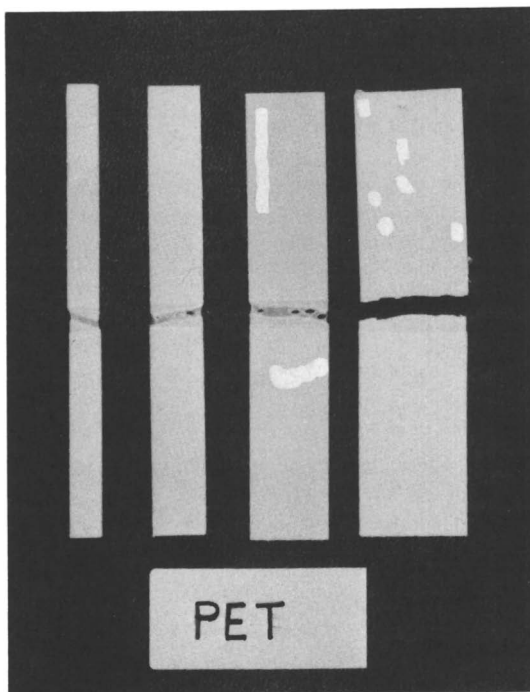


*Figure 12. Four PET specimens of increasing width. First three failed ductilely. Fourth one at larger  $W/t$  was brittle.*

specimens of this material at 0.5, 2.5, 50, 500, 3750, and 5000 inches/min. The yield stress increased monotonically until 5000 inches/min where the specimen failed in a completely brittle manner (Figure 9). An SEM micrograph of this specimen failure surface shows that the matrix has failed cohesively (Figure 10). The spherical PE particles appear to have simply been pulled out. By comparison, an SEM micrograph of a ductile failure surface (Figure 11) shows that voids have formed around the PE spheres and that there is extensive plastic flow in the matrix. Con-

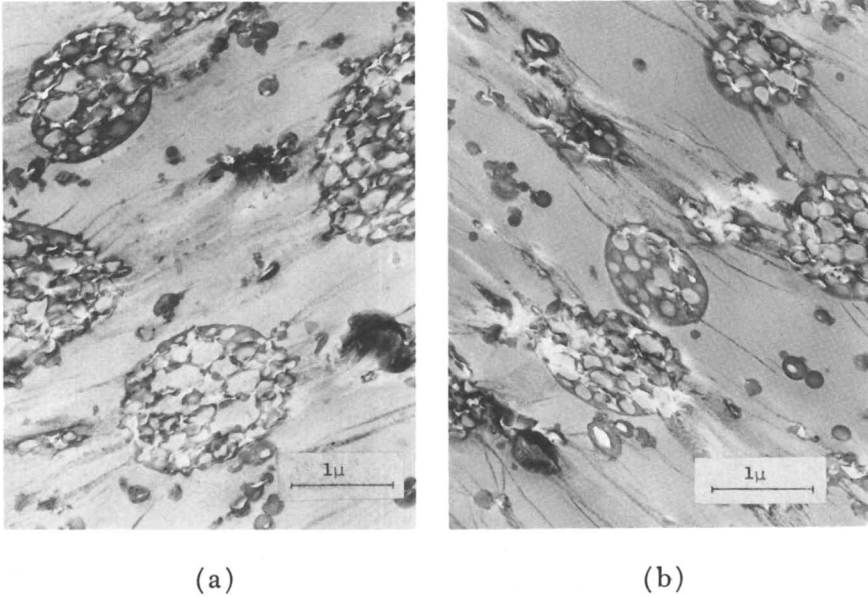


**Figure 13.** Transmission electron micrographs of ABS: (a) narrow specimen ( $W/b = 2$ ); (b) wide specimen ( $W/b = 14$ ). Stretching direction is perpendicular to the crazes.

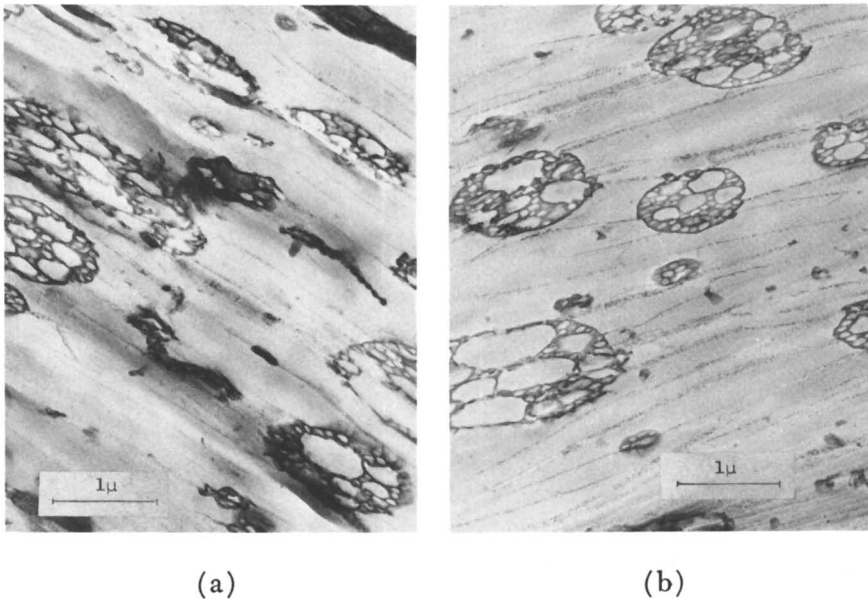


**Figure 14.** Transmission electron micrographs of HIPS: (a) narrow specimen ( $W/b = 2$ ); (b) wide specimen ( $W/b = 14$ ). Stretching direction is perpendicular to the crazes.



ventional dog-bone type specimens of this material do not fail brittlely even at a cross-head rate of 6000 inches/min (3). Thus, a combination of plane strain and high deformation rate brought about brittle failure.

As a result of the compression molding conditions used the PET specimens were highly crystalline. Up to  $W/t \sim 20$  ( $W/b \sim 7$ ) PET failed ductilely, forming well defined shear bands within the grooves. Where the bands intersected, voids eventually appeared. These voids then coalesced and finally caused the specimen to fail. At  $W/t > 20$  ( $W/b > 7$ ) all failures were brittle (Figure 12). This fact is reflected in the much larger scatter of the yield stress of the three widest specimens. In contrast to PC, PET does not go through a high yield stress region but enters directly into a completely brittle region. Examination of the fracture surfaces revealed areas of cohesive failure.

The yield stresses for ABS and HIPS increase with  $W/t$  up to about  $W/t \sim 25$  ( $W/b \sim 9$ ) and then decrease. The failure characteristics—*i.e.*, stress whitening, fracture surface morphology, etc.—do not change appreciably throughout the range of  $W$  tested. We have taken transmission electron micrographs of osmium tetroxide stained specimens of fractured samples of ABS and HIPS. Figures 13a and 14a are micrographs taken near the edge of narrow ( $W/b = 2$ ) specimens of ABS and HIPS, respectively. Figures 13b and 14b are micrographs taken near the center of wide ( $W/b = 14$ ) specimens of ABS and HIPS, respectively. The two micrographs of each material are indistinguishable from each other.

### Discussion

We have observed four distinct types of plane stress/plane strain yield behavior: (a) PC, (b) PC/PE, (c) PET, and (d) ABS and HIPS. These are discussed separately.

**PC.** Plane strain not only increases the yield stress of PC, in agreement with published data (8) and theoretical predictions, but also brings on reduced elongation. The latter observation appears to be consistent with the fact that notched Izod impact strength is lowered when plane strain sets in because of notch width (1, 2), temperature, or notch radius (1), or annealing (1, 4). However, even though total elongation at plane strain is reduced, there is still some plastic flow after yield which appears to be inconsistent with the relatively featureless fracture surface of a PC specimen that has failed brittlely. This apparent inconsistency may be caused by strain rate and/or triaxiality. At a test speed of 6000 inches/min, the strain rate in the grooved section is in the order of  $10^4 \text{ min}^{-1}$ , probably orders of magnitude lower than the local

deformation rate ahead of a flow in a notched specimen in impact flexure. Such high strain rates may cause brittle fracture. Triaxial tension may also create voids which can lead to fracture. Thus, even though plane strain is always associated with brittle fracture in PC, it alone is not sufficient to cause the brittleness.

**PC/PE.** In the case of PC/PE, plane strain alone does not produce significant changes in the yield stress and the deformation behavior. Its yield locus in the tension-tension quadrant is therefore either very nearly a quarter circle or similar to a Tresca locus. The exact shape of the locus can be determined only by much more elaborate biaxial tests. This material is not very notch sensitive compared with PC. The energy to break in a notched Izod impact test is 15 ft-lb/inch for  $\frac{1}{8}$ -inch thick bars and 11 ft-lb/inch for  $\frac{1}{4}$ -inch bars whereas for PC the latter figure is about 2 ft-lb/inch. This reduction in notch sensitivity over pure PC appears to be related to the material's ability to void internally, probably relieving the plane strain.

**PET.** The behavior of crystalline PET at plane strain can be explained if its yield locus is similar to that of PS and PMMA (9, 10) where a craze locus intercepts the shear yield locus. The transition at plane strain to a craze locus would account for the brittleness. This transition, which takes place quite sharply at  $W/t = 23$  ( $W/b = 8$ ), is probably the cause for the low impact strength ( $< 1$  ft-lb/inch) of the  $\frac{1}{8}$ -inch thick notched bars. The plane strain brittleness can be avoided if the geometric constraints can be removed, such as making the notch less sharp or making the test bar thinner. In fact, unnotched bars of PET, equivalent to having an infinite notch radius, are quite tough. The notch sensitivity of PET is typical of crystalline polymers.

**ABS and HIPS.** The yield stress *vs.*  $W/t$  curves of ABS and HIPS are very similar. They are somewhat surprising because the yield stresses reach their respective maximum values near the  $W/t$  (or  $W/b$ ) where plane strain predominates. This behavior is not predicted by either the von Mises-type or the Tresca-type yield criteria. This also appears to be typical of grafted-rubber reinforced polymer systems. A plausible explanation is that the rubber particles have created stress concentrations and constraints in such a way that even in very narrow specimens plane strain (or some stress state approaching it) already exists around these particles. Consequently, when plane strain is imposed on the specimen as a whole, these local stress state are not significantly affected. This may account for the similarity in the appearance of fracture surface electron micrographs (Figures 13a, 13b, 14a, and 14b), but the yield stress variation is still unexplained.

### Conclusion

We have used double-grooved specimens to study systematically the yield behavior of the polymers PC, PC/PE, PET, ABS, and HIPS as they undergo transitions from plane stress to plane strain. Four distinct types of behavior have been observed:

(a) PC: The yield stress increases to an asymptotic value as plane strain predominates. Total elongation is reduced by plane strain. The yield stress variation as a function of biaxiality is consistent with a von Mises-type yield criterion.

(b) PC/PE: The yield stress is a very weak function of biaxiality. It is consistent with a Tresca-type yield criterion. Brittleness in plane strain occurs only at very high strain rates. In ductile failure the PC matrix voids around the PE particles. This appears to be the mechanism that relieves plane strain.

(c) PET: The yield stress increases to a maximum with increasing extent of plane strain. After the maximum the material fails brittlely. This behavior is consistent with a von Mises-type yield locus that is intersected in the tension-tension quadrant by a craze locus.

(d) ABS and HIPS: The yield stress increases to a maximum but then decreases with increasing extent of plane strain. The amount of stress whitening, crazing, and the fracture surface morphology are unaffected by the biaxiality.

We conclude that plane strain alone does not necessarily cause brittleness even though brittle fracture surfaces can always be characterized as having failed in plane strain. One possible way to relieve plane strain is to include rubbery materials.

### Acknowledgment

We thank Daeyong Lee for stimulating discussions and for providing us with valuable references. We also thank J. Vacca, R. Russell, and M. Gill for their work on microscopy.

### Literature Cited

1. Allen, G., Morley, D. C. W., Williams, T., *J. Mater. Sci.* (1973) 8, 1449.
2. Wolstenholme, W. E., Pregun, S. E., Stark, C. F., *J. Appl. Polymer Sci.* (1964) 8, 119.
3. Yee, A. F., unpublished data.
4. LeGrand, D. G., *J. App. Polymer Sci.* (1969) 13, 2129.
5. Bucknall, C. B., Gotham, K. V., Vincent, P. I., in "Polymer Science," p. 666, A. D. Jenkins, Ed., North Holland, 1972.
6. Sokolnikoff, I. S., "Mathematical Theory of Elasticity," pp. 250-253, McGraw Hill, New York, 1956.
7. Ward, I. M., *J. Mater. Sci.* (1971) 6, 1397.
8. Raghava, R., Caddell, R. M., Yeh, C. S. L., *J. Mater. Sci.* (1973) 8, 225.
9. Sternstein, S. S., Ongchin, L., *Amer. Chem. Soc. Polymer Prep.* (1969) 10, 1117.

10. Bowden, P. B., Oxborough, R. J., "A Critical Strain Criterion for Craze Formation in Polystyrene," paper presented at British Plastics Institute, Research Meeting on the Effect of Structure on the Fracture of Plastics—The Role of Craze in Fracture, Univ. of Liverpool, Liverpool, England (April 14, 1972).
11. Ward, I. M., "Mechanical Properties of Solid Polymers," p. 289, Wiley, New York, 1971.
12. Williams, J. G., "Stress Analysis of Polymers," p. 77, Wiley, New York, 1973.
13. Rigbi, Z., *Appl. Polymer Symp.* (1967) 5, 1.
14. Kambour, R. P., *J. Polymer Sci.: Macromolecular Rev.* (1973) 7, 1.
15. Rabinowitz, S., Beardmore, P., *CRC Crit. Rev. Macromol. Sci.* (1972) 1, 1.
16. Corrigan, D. A., Travis, R. E., Ardito, V. P., Adams, L. M., Jr., *Welding Res. Sup.* (1962) 1235.
17. Whitney, W., Andrews, R. D., *J. Polymer Sci., C* (1967) 16, 2981.
18. Lee, D., *J. Mater. Sci.* (1975) 10, 661.
19. Cost, T. L., Parr, C. H., *J. Mater.* (1969) 4, 312.
20. Lee, D., Backofen, W. A., *Trans. Met. Soc., AIME* (1966) 236, 1077.
21. Hill, R., "The Mathematical Theory of Plasticity," p. 78, Oxford University Press, Oxford, 1950.
22. Yee, A. F., deTorres, P. D., *Polymer Sci. and Eng.* (1974) 14, 691.
23. Yee, A. F., Olszewski, W. V., *Amer. Chem. Soc. Org. Coating Plastic Preprints* (1974) 34, 235.

RECEIVED October 18, 1974.

## The Transition from Ductile to Brittle Behavior of a Semicrystalline Polyester by Control of Morphology

CHARLES L. BEATTY and WALTER J. STAUFFER

Xerox Corp., Webster Research Center, Webster, N.Y. 14580

*Significant variation of the ultimate mechanical properties of poly(hexamethylene sebacate), HMS, is possible by control of thermal history without significant variation of percent crystallinity. Both banded and unbanded spherulite morphology samples obtained by crystallization at 52°C and 60°C respectively fracture in a brittle fashion at a strain of  $\sim 0.01$  in./in. An ice-water-quenched specimen does not fracture after a strain of 1.40 in./in. The difference in deformation behavior is interpreted as variation of the population of tie molecules or tie fibrils and variation of crystalline morphological dimensions. The deformation process transforms the appearance of the quenched sample from a creamy white opaque color to a translucent material. Additional experiments are suggested which should define the morphological characteristics that result in variation of the mechanical properties from ductile to brittle behavior.*

The brittle-ductile transition of metals as reported by Orowan (1) is explained on the basis that brittle fracture occurs when the yield stress exceeds a critical value. This is based on the Ludwik-Davidenkov-Orowan hypothesis that brittle fracture and plastic flow are independent processes yielding separate curves as a function of temperature and strain rate. Therefore, the operative deformation process is the one occurring at the lower stress. The intersection of the brittle stress and yield stress curves therefore defines the brittle-ductile transition.

About the same time Flory (2) proposed that the tensile strength of polymers is related to the number average molecular weight. Vincent followed with an analysis of polymer mechanical property behavior as a

function of molecular weight similar to that used by Orowan (3). The brittle strength of the polymers studied (polystyrene, polymethyl methacrylate and polyethylene) was determined at  $-180^{\circ}\text{C}$  (4). This analysis aided in the classification of polymers as brittle or ductile and suggested factors affecting the brittle-ductile transition (*e.g.*, notching, side-group size, crosslinking, plasticizers, orientation, etc.).

Recently Moore and Petrie (5) have demonstrated that control of sample thermal history can result in transition from ductile to brittle behavior for polyethylene terephthalate. This transition in behavior was related to volume relaxation of the glassy state.

The effects of morphology (*i.e.*, crystallization rate) (6, 7, 8) on the mechanical properties of semicrystalline polymers has been studied without observation of a transition from ductile to brittle failure behavior in unoriented samples of similar crystallinity. Often variations in ductility are observed as spherulite size is varied, but this is normally confounded with sizable changes in percent crystallinity. This report demonstrates that a semicrystalline polymer, poly(hexamethylene sebacate) (HMS) may exhibit either ductile or brittle behavior dependent upon thermal history in a manner not directly related to volume relaxation or percent crystallinity.

The synthesis (9, 10), dynamic mechanical (11), rheological (12), dielectric (13), electrical (14), NMR (15), and thermal (16) behavior of HMS and its isomeric analog, poly-2-methyl-2-ethyl propylene sebacate (MEPS), and copolymers of HMS and MEPS have been reported.

### Experimental

The poly(hexamethylene sebacate), HMS, used for these studies had the following molecular weight characteristics:  $\overline{M}_w = 44,000$ ,  $\overline{M}_n = 20,000$ ,  $\overline{M}_w/\overline{M}_n = 2.2$ .

Crystallization at  $52^{\circ}$  and  $60^{\circ}\text{C}$  was performed between polished steel plates in an air oven following compression molding in a laboratory press. The filament specimen used in the quenching experiments was fabricated by (1) inverting a capillary tube into the HMS powder, (2) evacuating the capillary and sample in a vacuum oven, and (3) admitting air pressure after the sample melted to force the sample into the evacuated capillary tube. Note in Figure 1 that this produces a uniform  $\sim 1$  mm diameter unoriented specimen that is easily quenched.

A Leitz Ortholux microscope was used for the optical micrographs. Electron micrographs were obtained by conventional techniques using an International Scientific Instrument Co. minielectron microscope. Crystallinities were determined calorimetrically from the ratio of the heats of fusion of the semicrystalline samples measured (17) experimentally on a Perkin Elmer DSC-1B to the heat of fusion for 100% crystalline HMS of 32 cal/g reported by O'Malley (9, 16). Wide and small angle x-ray diffraction were obtained using a G.E. XRD-5 x-ray diffractometer.

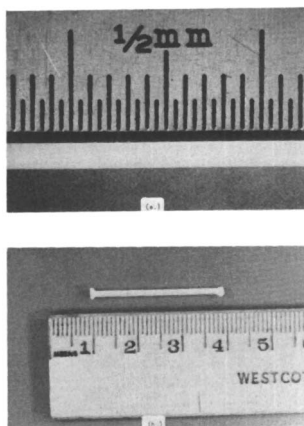


**Figure 1.** Uniform, unoriented, quenched HMS specimens made by the capillary vacuum melt technique

Laue and Warhus cameras were used for the side-angle and small-angle photographs respectively. The stress-strain data were obtained on an electrohydraulic deformation apparatus especially built for Xerox by MTS Systems Corp. (18). Tensile engineering stress-strain data was obtained at 30°C and a strain rate of 0.1 in./in./min.

### Results and Discussion

The existence of tie molecules and/or tie fibrils was initially demonstrated by Keith and Padden (19, 20) *via* electron microscopy. The relationship of these morphological structures to the mechanical strength and deformation behavior of polymers has been demonstrated by Peterlin (21) and by Becht, DeVries, and Kausch (22). Fracture during low strain rate tensile failure can be expected to occur along a path of mini-

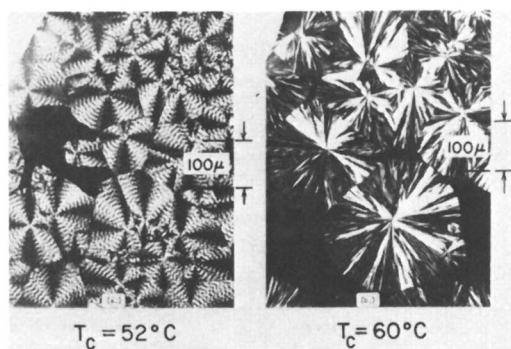


**Figure 2.** Optical micrographs of the (a) banded and (b) unbanded spherulitic morphologies obtained under different crystallization conditions

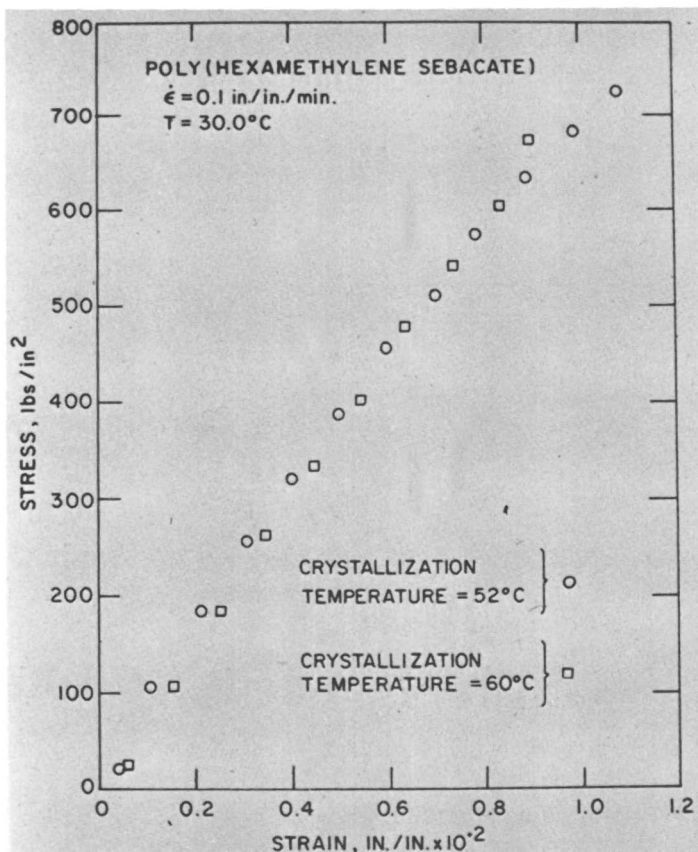
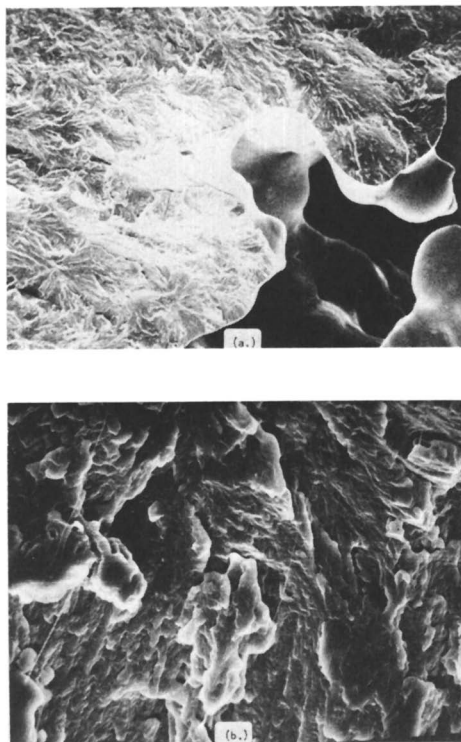


Figure 3. Engineering stress-strain curves for HMS banded and unbanded spherulitic specimens crystallized at 52°C and 60°C respectively

num resistance, avoiding as much as possible the rupture of molecular chains. That is, failure of a semicrystalline polymer above its glass transition appears to occur with decreasing frequency at spherulite boundaries, lamellae boundaries and intralamellae boundaries (*e.g.*, Peterlin's mosaic blocks) (21). This tendency parallels the expected frequency of interactions between these structural units *via* tie molecules and or tie fibrils. Therefore, if crystallinity is invariant, the effect of changing the population of tie molecules can be studied directly.

HMS can crystallize in either banded or nonbanded spherulitic morphologies as illustrated in Figures 2a and 2b respectively (14). Banding is typical of HMS crystallized below 56°C whereas nonbanded spherulites are formed by crystallization above 56°C (14). Banding of polymer spherulites is thought to be related to the periodic twisting of





*Figure 4. Failure surfaces of HMS crystallized at 60°C. Scanning electron micrograph magnifications are 100X and 1000X for (a) and (b) respectively.*

lamellae radiating from the center of the spherulite (23, 24, 25). Consequently, little difference in bulk ultimate deformation behavior would be expected if the interactions between crystalline entities were approximately the same. This is true as deformation of both banded and non-banded spherulitic morphologies demonstrate essentially similar engineering stress-strain curves, as illustrated in Figure 3. Both types of spherulitic morphologies fail in a brittle fashion on the bulk scale with the plane of failure delineating spherulitic and lamellar structural units

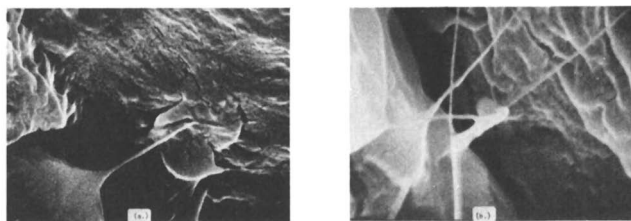


*Figure 5. Scanning electron micrographs of drawn HMS fibrils on fracture surface. Magnifications are 10,000X and 15,000X for (a) and (b) respectively. The HMS sample was crystallized at 60°C.*

shown in Figure 4. However, the scanning electron micrographs (Figures 4 and 5) show that fibrils are formed during the failure process, indicating that extensive local deformation occurs even during bulk brittle failure.

Assuming that these fibrils are related to the existence of tie molecules and or tie fibrils in the unoriented specimen, then an increase in the number of tie molecules and or tie fibrils should change the deformation behavior roughly in the manner described in Figure 6, where the shape, location and magnitude of the curves are arbitrary. It is assumed that percent crystallinity is relatively invariant.

This hypothesis is based on the following reasoning. Single crystal mats of ductile materials like polyethylene are extremely brittle and fragile. In this morphological structure, the crystalline regions are separated from each other. Therefore this combination of properties corresponds to the right half of Figure 6 (*i.e.*, brittle behavior). However, as the single crystal mat anneals, it becomes less fragile. Band and Krimm

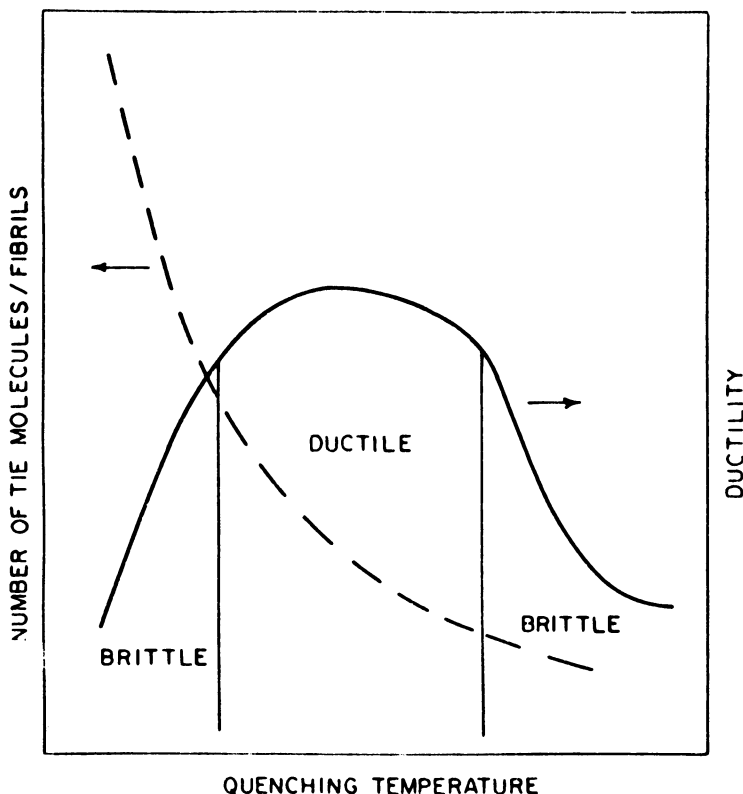


Figure 6. Postulated variation of the population of the tie molecules and/or tie fibrils and ductility with quenching temperature

(26) have demonstrated by infrared studies that interpenetration of chains in different lamellae occurs during the annealing process, indicating that the increase in strength is related to interaction between crystalline and amorphous regions.

Finally, when the material is melted and crystallized, the material is tough and ductile compared with the single-crystal material. Therefore, this analogy is useful to understand the hypothesized transition from brittle to ductile behavior based on increased crystalline–amorphous interactions.

The analogy for brittle behavior, if the number of crystalline–amorphous linkages becomes sufficiently large, is taken from the behavior of cold-drawn semicrystalline polymers. The deformation process consists of separation and rotation of regions of lamellae with respect to their original orientation in the bulk. However, these regions retain their folded chain characteristics and are interconnected by tie molecules as illustrated in Figure 7 (27). The number of effective load-bearing tie molecules increases with increasing deformation (*i.e.*, draw ratio) resulting in a higher fracture stress and less ductile fracture (28).

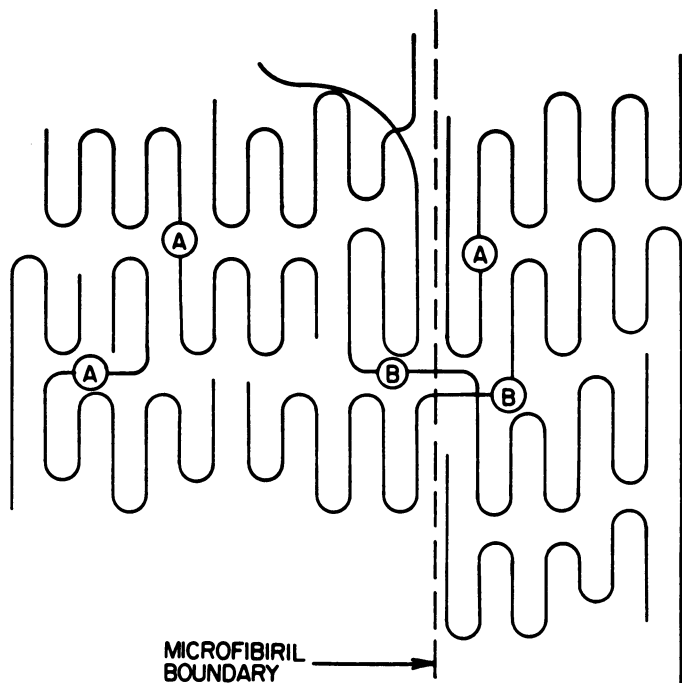
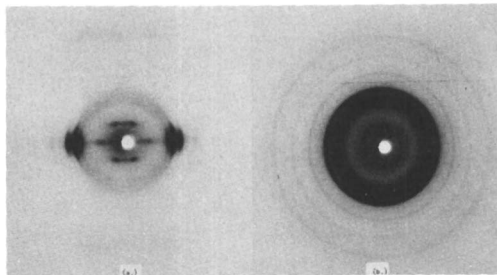


Figure 7. Schematic representation of microfibrils composed of folded chain mosaic block units, tie molecules between blocks (A) and between fibrils (B)



*Figure 8. Wide-angle x-ray diffraction patterns of the (a) oriented and (b) unoriented portions of the quenched sample*

This hypothesis was tested qualitatively by varying the temperature of quenching from the molten state. To aid in uniformity of heat transfer, a small ( $\sim 1$  mm) diameter cylindrical sample was quenched into ice water. Subsequent deformation resulted in necking and cold drawing in excess of 40% of the initial length without failure. As illustrated by the wide angle x-ray patterns in Figure 8, the unnecked portion of the specimen is essentially unoriented whereas the cold drawn portion is highly oriented. Concurrent with the necking was a change in optical appearance. The deformed portion was translucent compared with the opaque-unoriented material (Figure 9).

Southern and Porter (29) and Kwei *et al.* (30, 31) have reported the production of transparent polyethylene from normally translucent polyethylene by a variety of deformation processes. The deformation process results in crystalline entities with dimensions less than the wavelength of light in size, thereby not causing light scattering and consequently the resultant transparency. Similar changes in crystalline morphological dimensions may be responsible for the transformation in optical proper-



*Figure 9. Optical micrograph illustrating the neck between the oriented and unoriented portion of the quenched specimen*

Table I. Heats of Fusion of HMS Polymer

Material Treatment/ <i>i.d.</i>	Runs	$\Delta H^\circ F \pm S^a$ , cal/g	% DSC	%C NMR
HMS filament undrawn	1	24.9 <sub>1</sub>	78	68
HMS filament drawn	1	22.5 <sub>8</sub>	70	—
HMS sample 1, $T_c = 52^\circ\text{C}$ , strained .1 ipm	4	24.9 <sub>7</sub> $\pm$ 1.03	78	—
HMS sample 1, $T_c = 60^\circ\text{C}$ , strained .1 ipm	3	27.5 <sub>0</sub> $\pm$ 0.19	86	70

<sup>a</sup> S is standard deviation.

ties of quenched HMS as a result of deformation. The spherulitic dimensions of the specimens crystallized at 52°C and 60°C are in the 100 $\mu$  range. The highly deformed material is nonspherulitic.

As indicated earlier, the relationship of mechanical properties with the population of tie molecules and or tie fibrils can be achieved providing that (1) the crystallinity is invariant and (2) the crystalline unit cell and crystalline morphological dimensions do not change significantly. Crystallization at different temperatures (*i.e.*, quenching) normally results in changes in both crystallinity and morphological dimensions (*i.e.*, lamellae thickness and spherulite diameter). Fortunately, the crystallinity of HMS is relatively independent of crystallization temperature and deformation as illustrated in Table I. The crystallinity estimated from pulsed NMR measurements (15) was obtained on a sample of HMS of different molecular weight ( $\bar{M}_n = 3165$ ,  $MWD = 1.52$ ) although crystallized under identical conditions. The crystallinity determined by DSC for HMS of another molecular weight ( $\bar{M}_n = 11,400$  and  $MWD = 3.13$ ) was 70% and 66% for samples crystallized at 52°C and 60°C respectively (16). O'Malley and Stauffer's measurements of crystallinity of these samples by density was 66% and 74% for crystallization at 52°C and 60°C respectively. Therefore the results from several techniques and investigators indicate that the crystallinity of HMS is relatively independent of crystallization conditions.

Both banded ( $T_c = 52^\circ\text{C}$ ) and unbanded ( $T_c = 60^\circ\text{C}$ ) spherulitic morphologies had essentially identical stress-strain curves despite a difference in crystallinity of 8% and variations in spherulite size for these two crystallization conditions. These changes in crystallinity and spherulite size might compensate sufficiently to allow similar bulk deformation behavior. However, the sample crystallized at 52°C should have smaller spherulites and thinner lamellae than the sample crystallized at 60°C because of a greater probability of tie molecules. This, combined with its lower crystallinity, should allow more ductile behavior for the 52°C crystallized sample. The fact that both specimens deform similarly indi-

cates that the number of interactions between crystalline structures is approximately independent of morphology and crystallinity differences. The same arguments hold in comparing the deformation behavior and morphology of the ice-water-quenched and 52°C-crystallized samples. However, in this case the crystallinity of both samples are identical, indicating that only the number of tie molecules are increased, probably by formation of thinner lamellae and smaller diameter spherulites.

Future experiments are planned to resolve the interrelationship of crystalline morphological dimensions and the population of tie molecules. This can be accomplished by control of crystallization conditions and the use of nucleating agents. That is, the size of spherulites can be varied without variation of lamellar thickness by addition of nucleating agents followed by crystallization at one temperature. Crystallization at different temperatures followed by annealing will allow comparison of samples having approximately the same lamellar thickness but different spherulitic diameters. Comparison of properties of samples prepared at different temperatures but with similar dimensions (obtained experimentally or by extrapolation) will allow estimation of the effect of tie molecules.

In conclusion, the deformation behavior of poly(hexamethylene sebacate), HMS, can be altered from ductile to brittle by variation of crystallization conditions without significant variation of percent crystallinity. Banded and nonbanded spherulitic morphology samples crystallized at 52°C and 60°C fail at a strain of 0.01 in./in. whereas ice-water-quenched HMS does not fail at a strain of 1.40 in./in. The change in deformation behavior is attributed primarily to an increased population of tie molecules and/or tie fibrils with decreasing crystallization temperature which is related to variation of lamellar and spherulitic dimensions. This ductile-brittle transformation is not caused by volume or enthalpy relaxation as reported for glassy amorphous polymers. Nor is a series of molecular weights, temperatures, strain rates, etc. required to observe this transition. Also, the quenched HMS is transformed from the normal creamy white opaque appearance of HMS to a translucent appearance after deformation.

### Literature Cited

1. Orowan, E., *Rept. Prog. Phys.* (1949) **12**, 185.
2. Flory, P. J., *J. Amer. Chem. Soc.* (1945) **67**, 2048.
3. Vincent, P. I., *Polymer* (1960) **1**, 425.
4. Vincent, P. I., *Plastics* (1964) **29**, 79.
5. Moore, R.S., Petrie, S. E. B., *Polymer Preprints* (1974) **15**, 70.
6. Ohlberg, S. M., Roth, J., Raff, R. A. V., *J. Appl. Polymer Sci.* (1958) **1**, 114.
7. Starkweather, H. W., Brooks, R. E., *J. Appl. Polymer Sci.* (1958) **1**, 236.
8. Kleiner, L. W., Radloff, M. R., Schultz, J. M., Chou, T. W., *J. Polym. Sci., Phys. Ed.* (1974) **12**, 819.

9. O'Malley, J. J., Stauffer, W. J., *J. Polymer Sci., Chem. Ed.* (1974) **12**, 865.
10. O'Malley, J. J., *J. Polymer Sci., B* (1974) **12**, 381.
11. Sanchez, I. C., I.U.P.A.C. Internat. Symp. Macromol., Aberdeen, Scotland, p. 473, Sept., 1973.
12. O'Malley, J. J., Erhardt, P. F., *Bull. Amer. Phys. Soc.* (1975) **20**, 371.
13. Pochan, J. M., Hinman, D. D., accepted for publication, *J. Polym. Sci., Phys. Ed.*
14. O'Malley, J. J., unpublished results.
15. Froix, M. F., Goedde, A. O., unpublished data.
16. O'Malley, J. J., accepted for publication, *J. Polym. Sci., Phys. Ed.*
17. Gill R., Pilato, P., private communication.
18. Beatty, C. L., Stauffer, W. J., to be published.
19. Keith, H. D., Padden, Jr., F. J., Vadimsky, R. G., *J. Polymer Sci. A-2* (1966) **4**, 267.
20. Vadimsky, R. G., Keith, H. D., Padden, Jr., F. J., *J. Polymer Sci., A-2* (1969) **1**, 1367.
21. Peterline, A., *J. Polymer Sci., A-2* (1969) **1**, 1151.
22. Becht, J., DeVries, K. L., Kausch, H. H., *European Polymer J.* (1971) **7**, 105.
23. Keller, A., *J. Polymer Sci.* (1959) **39**, 151.
24. Keith, H. D., Padden, Jr., F. J., *J. Polym. Sci.* (1959) **39**, 101.
25. *Ibid.* (1959) **39**, 123.
26. Bank, M. I., Krimm, S., *J. Appl. Phys.* (1969) **40**, 4248.
27. Peterlin, A., *J. Macromol. Sci., Phys. B6* (1972) 583.
28. VanKrevelen, D. W., Hoftyzer, P. J., Eds., "Properties of Polymers," p. 316, Elsevier, New York, 1972.
29. Southern, J. H., Porter, R. S., *Amer. Chem. Soc. Preprints, Div. Polymer Chem.* (1969) **10**, 1028.
30. Kwei, T. K., Wang, T. T., Bair, H. E., *J. Polymer Sci., C* (1970) **31**, 87.
31. Wang, T. T., Chen, A. S., Kwei, T. K., *J. Polymer Sci., B* (1970) **8**, 505.

RECEIVED October 18, 1974.

# Ductile Failure of Brittle Polymers under Compressive Shear Stresses

SHAUL M. AHARONI

Chemical Research Center, Allied Chemical Corp., Morristown, N.J. 07960

*An explanation is presented according to which ductile failure of brittle polymers occurs when  $\gamma + (\Delta H_a^* - U_o)/\sigma < \omega$ , where  $\gamma$ ,  $\omega$  are the stress concentration coefficients for brittle or ductile failure, respectively,  $\Delta H_a^*$  is the activation energy for the onset of long-range segmental mobility,  $U_o$  is the activation energy for covalent bond scission, and  $\sigma$  is the total stress operating orthogonally to the tip of a propagating crack. Experimental data from friction and impact loading tests, in the presence or absence of high orthogonal stresses demonstrate the validity of the theoretical explanation.*

The literature is replete with examples showing that the application of hydrostatic pressure enhances the ductile behavior of strained amorphous polymers. In this paper we present a possible explanation of this effect and two experiments demonstrating the enhanced ductility of polymers under compressive shear stresses applied orthogonally to the plane of shear.

The ultimate strength of ductile and brittle polymers at room temperature depends linearly on the activation energy for the onset of long-range segmental mobility,  $\Delta H_a^*$  (1). This is shown graphically in Figure 1. Most polymers follow the same dependence of the ultimate stress  $\gamma$  on  $\Delta H_a^*$ , the activation energy for the glass transition:

$$\Delta H_a^* (\text{kcal/mole}) = \sigma (\text{kg/mm}^2) \cdot \omega (\text{mm}^2/\text{kg}) (\text{kcal/mole}) \quad (1)$$

where  $\omega$  is the stress concentration factor for ductile failure. A smaller group of linear polymers, all with aromatic structures in the backbone and high ductility far below  $T_g$ , shows a different dependence of  $\sigma$  on  $\omega$ :

$$(\Delta H_a^* - 70) (\text{kcal/mole}) = (\sigma - 7) (\text{kg/mm}^2) \omega (\text{mm}^2/\text{kg}) (\text{kcal/mole}) \quad (2)$$



From the slopes of the corresponding lines one finds that in Equation 1, the numerical value of  $\omega$  is 10 while in Equation 2,  $\omega = 43$ . This factor in reality has the dimensions of volume, and to express  $\omega$  in  $\text{\AA}^3$  one must multiply the numerical values by  $7.1 \times 10^2$  ( $1 \text{ kcal} = 4.27 \times 10^5 \text{ kg/mm}$  and Avogadro's number is  $6.02 \times 10^{23}$  (2)). Consequently, for Equation 1,  $\omega = 7,100 \text{ \AA}^3$ , and for Equation 2,  $\omega = 30,500 \text{ \AA}^3$ . For polymers obeying Equation 1, the stress concentration factor encompasses the volume of one

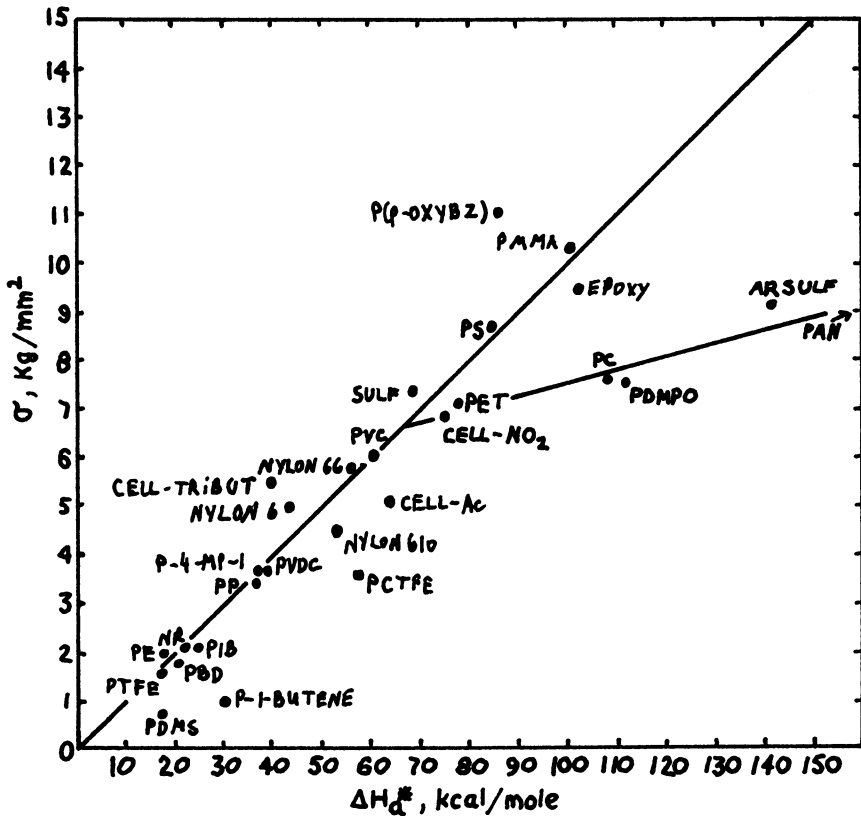


Figure 1. Relationship between ultimate stress,  $\sigma$ , and activation energy for glass transition,  $\Delta H_a^*$ , for 28 polymers. References for stress values are listed in Appendix I.

or two dozen repeat units, but for polymers following Equation 2,  $\omega$  encompasses several hundred repeat units. Ductility below  $T_g$  seems, therefore, to arise from the ability of many segments to undergo cooperative motion simultaneously.

The ductile *vs.* brittle behavior depends on the relationship between the equations

$$\ln \tau = \ln \tau_0 + (U_0 - \gamma\sigma)/RT \quad (3)$$

and

$$\ln \tau_r = \ln \tau_{or} + (\Delta H_a^* - \omega\sigma)/RT \quad (4)$$

where  $\tau$  and  $\tau_r$  are lifetimes for brittle or ductile failure of a sample under the applied stress  $\sigma$ ;  $\tau_0$  and  $\tau_{or}$  are material constants of the same magnitude,  $10^{-12}$  to  $10^{-13}$  sec;  $\gamma$  is the factor of stress concentration for brittle failure;  $U_0$  the activation energy for mechanical bond rupture;  $R$  the gas constant and  $T$  the absolute temperature (3). A comparison of Equations 3 and 4 reveals that when  $\tau > \tau_r$ , the failure will be in a ductile manner, and when  $\tau < \tau_r$ , the fracture will be brittle in character.

Under isothermal conditions, the fracture mode of amorphous polymers, or of the amorphous component in semicrystalline polymers, depends on the relationship between  $(\Delta H_a^* - \omega\sigma)$  and  $(U_0 - \gamma\sigma)$ . Combination of Equations 3 and 4 leads to the following relationships. If

$$(\Delta H_a^* - \omega\sigma) < (U_0 - \gamma\sigma) \quad (5)$$

the fracture will be ductile, and if

$$(\Delta H_a^* - \omega\sigma) > (U_0 - \gamma\sigma) \quad (6)$$

the fracture will be brittle. Rearrangement leads to two corresponding equations. For ductile fracture

$$\gamma + (\Delta H_a^* - U_0)/\sigma < \omega \quad (7)$$

and for brittle fracture

$$\gamma + (\Delta H_a^* - U_0)/\sigma > \omega. \quad (8)$$

At the brittle-ductile transition point

$$\gamma + (\Delta H_a^* - U_0)/\sigma = \omega. \quad (9)$$

This equation indicates that under isothermal conditions in instances where  $\Delta H_a^* < U_0$ ,  $\omega < \gamma$ , and the polymer will experience ductile failure. Recognizing that the brittle stress concentration coefficient  $\gamma$  is nearly constant (4), the requirements for brittle amorphous polymers, whose  $\Delta H_a^* > U_0$  and  $\omega > \gamma$ , to fail in a ductile fashion are to minimize  $(\Delta H_a^* - U_0)/\sigma$  or to maximize  $\omega$ , or both.

If the component  $T$  of an applied compressive shear stress orthogonal to the plane of fracture combines with the normal component  $\sigma_{yy}$  of the local stress at the tip of a crack, then the combined higher stress will minimize  $(\Delta H_a^* - U_0)/\sigma$  and a more ductile failure ensues. This can occur if the orthogonal compressive stress is locally inhomogeneous. Hence, a polymer can fail in a more ductile fashion under orthogonal compressive shear stresses than in their absence.

In recent experiments, the application of stress orthogonally to a shearing surface caused a ductile failure of brittle polymer (5, 6). In the first series (5), a variety of plastomers and elastomers were made to slide one on the surface of another, at a constant velocity of 215 cm/sec, under increasing normal loads. The wear characteristics of polymers, including several brittle ones such as PMMA and PS, depend on the applied normal stress. At relatively low pressure, almost no wear was observable, even under magnification; the little observed was apparently brittle, ill-defined, microparticulate debris. At intermediate normal loads, 3 to 20 kg/cm<sup>2</sup>, roll formation was the dominant mode of wear. Such rolls appear on the surfaces of all uncrosslinked polymers whose  $T_g$  is below the test temperature and on amorphous and semicrystalline polymers whose  $T_g$  is above

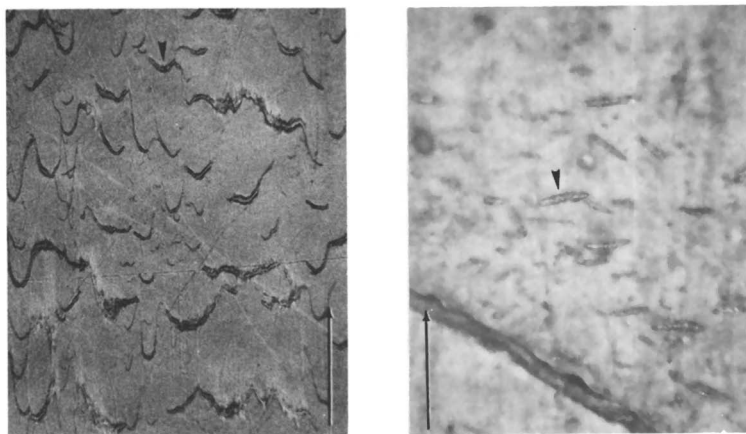


*Figure 2. Wear pattern of PMMA against carbon black-reinforced polybutadiene rubber of 70 Shore A hardness. Left: PMMA surface ( $\times 50$ ); Right: PMMA rolls on rubber surface ( $\times 100$ ).*

the test temperature. Among the latter one finds nylon 6, PET, PMMA and even cured PAI (polyamideimide). For example, Figure 2 shows the ductile wear characteristics of the brittle PMMA surface.

Under heavy normal loads, about 20 kg/cm<sup>2</sup>, ductile shear of whole surfaces takes place. This occurred for such diverse uncrosslinked polymers as the ductile polypropylene and the brittle polystyrene. Layers several thousands angstroms thick were removed from the friction surfaces of these polymers and deposited on their corresponding counter surfaces.

In the second series of experiments (6) brittle samples were fractured under heavy impact in the presence or absence of stress orthogonally applied onto the propagating crack tip. Three modes of fracture can exist. In the first, when no lateral stress exists, the normal component of

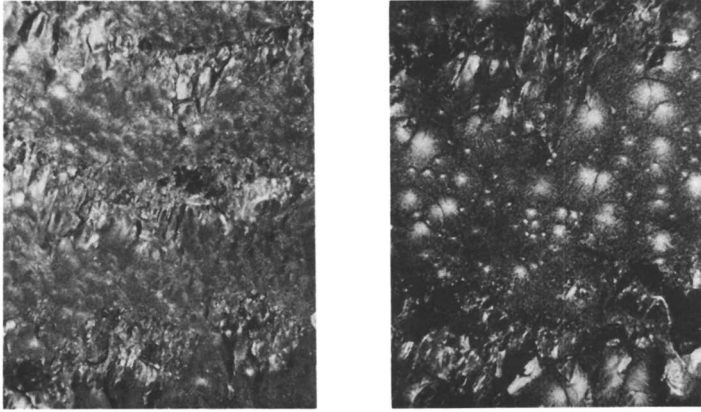


*Figure 3. Fracture surface of PMMA impacted under compressive shear stress. Left: Magnification  $\times 18.5$ , fracture direction from top to bottom. Right: The same spot, magnification  $\times 50$ .*

the impact stress,  $\sigma_{yy}$ , is in the brittle stress range  $\sigma_B$  where the fracture is brittle in nature. This range roughly corresponds to the Hookean part of the stress-strain curve of brittle polymers. Under very high orthogonal stress, when  $T = \sigma_{yy}$  reaches the region of ductile stress  $\sigma_D$ , with  $\sigma_D > \sigma_B$ , then the fracture surface will be fully ductile. These two fracture surface types were observed under the corresponding conditions. If, however, the combination of  $T + \sigma_{yy}$  is between  $\sigma_B$  and  $\sigma_D$ , then brittle and ductile fracture characteristics can coexist. This is usually not observed, but under

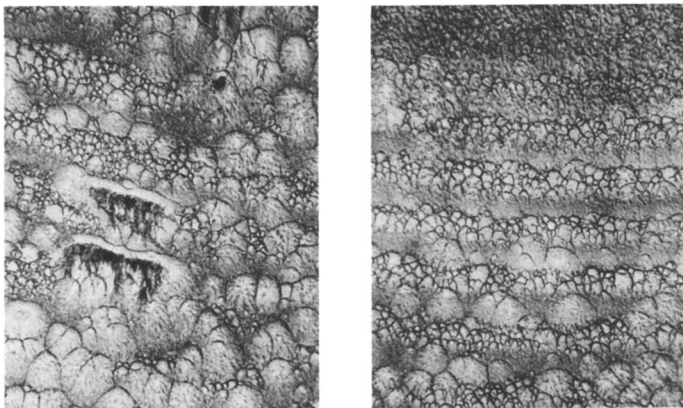


*Figure 4. Fracture surface of PS impacted under compressive shear stress. Crack propagated from top to bottom. Left: magnification  $\times 50$ . Right: a different point on same fracture surface, ( $\times 50$ ).*

impact conditions, at appropriate  $T + \sigma_{yy}$ , a train of impact stress waves conceivably can cause alternating bands of brittle and ductile fracture surface features. This will happen when  $T + \sigma_{yy}$  at the wave peaks reaches the  $\sigma_D$  range, while  $T + \sigma_{yy}$  at the wave troughs will be in the  $\sigma_B$  region. Figures 3 and 4 show, respectively, the alternating wave patterns formed under impact in the presence of a compressive shear stress on the fracture surfaces of PMMA and PS.

In agreement with Equation 7, 8, and 9, the brittle-ductile alternations can be written as

$$\gamma + (\Delta H_a^* - U_o)/(T + \sigma_{yy} \text{ (trough)}) > \omega \quad (10)$$

and

$$\gamma + (\Delta H_a^* - U_o)/(T + \sigma_{yy} \text{ (peak)}) < \omega \quad (11)$$

Actual fractures obtained in PMMA and PS verify not only the common instances of brittleness when

$$\gamma + (\Delta H_a^* - U_o)/\sigma_B > \omega \quad (12)$$

and ductility when

$$\gamma + (\Delta H_a^* - U_o)/\sigma_D < \omega \quad (13)$$

but also the rarely observed case where  $T + \sigma_{yy}$  cyclically fluctuates from  $\sigma_B$  to  $\sigma_D$ .

The alternating wave patterns were not Wallner lines (6) and were insensitive to temperature changes below  $T_g$ . For example, alternating patterns were generated in PMMA at several temperatures covering the range  $-38^\circ$  to  $+85^\circ\text{C}$ . Finally under the stress conditions conducive to the generation of alternating wave patterns in the uncrosslinked PMMA and PS, no alternations were created in the crosslinked epoxy and polyester polymers.

### Appendix I.

#### PDMS.

#### PTFE.

Meals, R. N. and F. M. Lewis, "Silicones," p. 54, Rheinhold, New York, 1959.

Speersneider, C. J. and C. H. Li, *J. Appl. Phys.* (1962) 33, 1871.

Speersneider, C. J. and C. H. Li, *J. Appl. Phys.* (1963) 34, 3004.

#### P-1-Butene.

Rohn, C. L. and H. G. Tinger, *SPE Tech. Papers (28th Ann. Tech. Conf.)* (1970) 16, 638.

#### PE.

Vincent, P. I., *Polymer* (1960) 1, 7.

Vincent, P. I., *Plastics* (1964) 29, 79.

- Laka, M. G. and A. A. Dzenis, *Mekhanika Polimerov* (1967) 3, 1043.  
 Haward, R. N. and G. Thackray, *Proc. Royal Soc. (London)* (1968) A302, 453.  
 Mears, D. R., K. D. Pae, and J. A. Sauer, *J. Appl. Phys.* (1969) 40, 4229.  
 "Handbook of Chemistry and Physics," 52nd Edition, Chemical Rubber Co.,  
 Cleveland, Ohio, 1971, pp. C765-C771.  
 Ward, I. M., *J. Mater. Sci.* (1971) 6, 1397.  
 Meinel, G. and A. Peterlin, *J. Polym. Sci. Pt. A-2* (1971) 9, 67.  
 West, G. H. and J. M. Senior, *Wear* (1972) 19, 37.  
 Bowers, R. C., *J. Appl. Phys.* (1971) 42, 4961.  
 Van Krevelen, D. W., "Properties of Polymers, Correlations with Chemical  
 Structure," Elsevier, Amsterdam, 1972, p. 181.  
 Bowden, F. P. and D. Tabor, "The Friction and Lubrication of Solids, Part II,"  
 Clarendon Press, Oxford, 1964, pp. 214-241.  
 Shooter, K. V. and D. Tabor, *Proc. Phys. Soc.* (1952) 65B, 661.  
 Shooter, K. V., *Proc. Royal Soc. (London)* (1952) 212A, 488.

**PBD.**

- Simonds, H. R., "Source Book of The New Plastics," p. 47, Vol. 2, Reinhold,  
 New York, 1961.  
 Rybalov, S. L. and I. V. Kragelskii, *Mekhanika Polimerov* (1965) 1, 120.  
 Sizikov, N. N. and M. M. Reznikovskii, *Soviet Rubber Tech.* (1970) 29, 25.

**Natural rubber.**

- Anthony, R. L., R. H. Caston, and E. Guth, *J. Phys. Chem.* (1942) 46, 826.  
 Denny, D. F., *Proc. Phys. Soc.* (1953) B66, 721.  
 Eckelmann, W. and H. Wesche, *Kaut. Gummi Kunst.* (1971) 24, 451.  
 Simonds, H. R., *Op. cit.*, *loc. cit.*  
 Sizikov, N. N. and M. M. Reznikovskii, *Op. cit.*

**PIB.**

- G. G. Winspear, Ed., "The Vanderbilt Rubber Handbook," p. 92, R. T. Vander-  
 bilt Co., New York, 1958.

**PP.**

- Ludema, K. C. and D. Tabor, *Wear* (1966) 9, 329.  
 Lancaster, J. K., *Proc. Instn. Mech. Engrs. 1968-69* (1969) 183, Pt. 3P, 98.  
 Bowers, R. C., *op. cit.*  
 Van Krevelen, D. W., *op. cit.*, *loc. cit.*  
 "Handbook of Chemistry and Physics," 52nd Edition, *loc. cit.*  
 Mears, D. R., K. D. Pae, and J. A. Sauer, *op. cit.*  
 1971-1972 *Modern Plastics Encyclopedia* p. 568ff, McGraw-Hill, New York,  
 1971.

**PVDC.**

- Bowden, F. P. and D. Tabor, *op. cit.*, *loc. cit.*  
 "1971-1972 Modern Plastics Encyclopedia," *loc. cit.*

**P-4-MP-1.**

- Mater. Eng.*, (1967) 66, 23.  
 Hase, Y. and P. H. Geil, *Polym. J.* (1971) 2, 581.  
 "Engineering Properties of Thermoplastics," p. 136f, R. M. Ogorkiewicz, ed.,  
 Wiley-Interscience, London, 1970.  
 "1972-1973 Modern Plastics Encyclopedia," McGraw-Hill, New York, 1972.  
 P. I. Vincent, *Nature Phys. Sci.* (1971) 233, 104.

**CELL-TriBUT.**

- Nielsen, L. E., "Mechanical Properties of Polymers," p. 118, Reinhold, New  
 York, 1962.

**Nylon 6.**

- Van Krevelen, D. W., *op. cit.*, *loc. cit.*  
 Bowden, F. P. and D. Tabor, *op. cit.*, *loc. cit.*

"1971-1972 Modern Plastics Encyclopedia," *loc. cit.*  
Savkin, V. G., V. A. Belyi, T. I. Sogolova, and V. A. Kargin, *Mekhanika Polimerov* (1966) **2**, 659.

#### Nylon 66.

Vincent, P. I., *Plastics* (1964) **29**, 79.  
Banevichyus, R. B. and A. N. Machyulis, *Mekhanika Polimerov* (1968) **4**, 402.  
"Engineering Properties of Thermoplastics," *loc. cit.*  
"1971-1972 Modern Plastics Encyclopedia," *loc. cit.*  
"Handbook of Chemistry and Physics," 52nd Edition, *loc. cit.*  
D. W. Van Krevelen, *op. cit.*, *loc. cit.*  
Lancaster, J. K., *op. cit.*  
Shooter, K. V. and D. Tabor, *op. cit.*  
Shooter, K. V., *op. cit.*

#### Nylon 610.

Kramer, E. J., *J. Appl. Polymer Sci.* (1970) **14**, 2825.  
Kramer, E. J., *J. Appl. Phys.* (1970) **41**, 4327.

#### PCITFE.

Van Krevelen, D. W., *op. cit.*, *loc. cit.*  
Brenner, W., D. Lum, and M. W. Riley, "High-Temperature Plastics," pp. 153-154, Reinhold, New York, 1962.  
Ludema, K. C. and D. Tabor, *op. cit.*

#### PVC.

Vincent, P. I., *Polymer* (1960) **1**, 7.  
Vincent, P. I., *Plastics* (1964) **29**, 79.  
Haward, R. N. and G. Thackray, *op. cit.*  
"Engineering Properties of Thermoplastics," *loc. cit.*  
"1971-1972 Modern Plastics Encyclopedia," *loc. cit.*  
Shooter, K. V. and D. Tabor, *op. cit.*  
Shooter, K. V., *op. cit.*  
Bowden, F. P. and D. Tabor, *op. cit.*, *loc. cit.*  
Oberst, H. and W. Retting, *J. Macromol. Sci.* (1971) **B5**, 559.

#### CELL-Ac.

A. Tager, "Physical Chemistry of Polymers," pp. 213, 223, 473, Mir Publishers, Moscow, 1972.  
Carswell, T. S. and H. K. Nason, *Mod. Plastics*, (1944) **21**, 121.

#### CELL-NO<sub>2</sub>.

Tager, A., *op. cit.*, *loc. cit.*  
Haward, R. N. and G. Thackray, *Proc. Royal Soc. (London)* (1968) **A302**, 453.

#### PET.

Vincent, P. I., *Plastics* (1964) **29**, 79.  
Allison, S. W. and I. M. Ward, *Brit. J. Appl. Phys.* (1967) **18**, 1151.  
Roe, J. M. and E. Baer, *Intern. J. Polym. Mater.* (1972) **1**, 133.  
Spivack, M. A., *Rev. Sci. Instr.* (1972) **43**, 985.  
E. I. Du Pont de Nemours Co., Technical Bulletin No. M-1A (PET), undated.  
Van Krevelen, D. W., *op. cit.*, *loc. cit.*  
Shooter, K. V. and D. Tabor, *op. cit.*

#### PS.

Vincent, P. I., *Plastics* (1964) **29**, 79.  
Borisenko, V. N., A. B. Sinani, and V. A. Stepanov, *Mekhanika Polimerov*, (1968) **4**, 787.  
Brady, T. E. and G. S. Y. Yeh, *J. Appl. Phys.* (1971) **42**, 4622.  
Ward, I. M., *op. cit.*

- Dale, W. C. and C. E. Rogers, *J. Appl. Polym. Sci.* (1972) **16**, 21.  
Shooter, K. V. and D. Tabor, *op. cit.*  
Shooter, K. V., *op. cit.*  
Bowden, F. P. and D. Tabor, *op. cit.*, *loc. cit.*  
Lancaster, J. K., *op. cit.*

#### PMMA.

- Laius, L. A. and E. V. Kuvshinskii, *Mekhanika Polimerov* (1966) **2**, 435.  
Elkin, A. I. and V. I. Titov, *Mekhanika Polimerov* (1968) **4**, 90.  
Vincent, P. I., *Plastics* (1964) **29**, 79.  
Borisenko, V. N., A. B. Sinani, and V. A. Stepanov, *op. cit.*  
Ward, I. M., *op. cit.*  
Shooter, K. V. and D. Tabor, *op. cit.*  
Shooter, K. V., *op. cit.*

#### Epoxy.

- Moehlenpah, A. H., A. T. DiBenedetto, and O. Ishai, *Polym. Eng. Sci.*, (1970) **10**, 170.  
Lee, H. and K. Neville, "Handbook of Epoxy Resins," pp. 7-6, 7-8, McGraw-Hill, New York, 1967.  
Suzuki, Y. and K. Shibayama, *Repts. Progr. Polymer Phys. Japan* (1972) **15**, 331.  
"1971-1972 Modern Plastics Encyclopedia, *loc. cit.*

#### PC.

- Robertson, R. E., *J. Appl. Polym. Sci.* (1963) **7**, 443.  
Ogibalov, P. M. and V. I. Moroz-Shobolova, *Mekhanika Polimerov* (1967) **3**, 46.  
Vsevolodov, N. N., G. P. Itinskaya, V. N. Kotrelev, N. P. Novikov, and Yu. I. Yudin, *Mekhanika Polimerov* (1968) **4**, 288.  
Pampillo, C. A. and L. A. Davis, *J. Appl. Phys.* (1971) **42**, 4674.  
Roe, J. M. and E. Baer, *op. cit.*  
Spivaek, M. A., *op. cit.*  
Van Krevelen, D. W., *op. cit.*, *loc. cit.*  
Vincent, P. I., *Plastics* (1964) **29**, 79.  
"1971-1972 Modern Plastics Encyclopedia," *loc. cit.*  
"Handbook of Chemistry and Physics," 52nd Edition, *loc. cit.*

#### SULF.

- Bassett, H. D., *SPE J.* (1967) **23** (5), 45.  
Bugel, T. E. and R. K. Walton, *Machine Design* (1965) 193.  
Macosco, C. W. and C. J. Brand, *Polym. Sci. Eng.* (1972) **12**, 444.  
Gotham, K. V., *Plastics Polym.* (1972) **40**, 59.  
Broutman, L. J. and R. S. Patil, *SPE Tech. Papers* (28th Ann. Tech. Conf.), (1970) **16**, 20.

#### PDMPO.

- Broutman, L. J. and R. S. Patil, *op. cit.*  
General Electric Corp., PPO product data sheet.  
Kambour, R. P. and G. A. Bernier, *Macromol.* (1968) **1**, 190.  
Nicolaï, L. and A. T. DiBenedetto, *J. Appl. Polym. Sci.* (1971) **15**, 1585.

#### ARSULF.

- Bringer, R. P. and G. A. Morneau, *Appl. Polym. Symp.* (1969) **11**, 189.

#### PAN.

- Andrews, R. D., K. Miyachi, and R. S. Doshi, *Polym. Preprints* (1972) **13**, 1168.

#### P(p-OXBz).

- "Ekonomol Engineered Compositions Properties, bulletin, The Carborundum Company, (1971).



*Literature Cited*

1. Aharoni, S. M., *J. Macromol. Sci.-Phys.* (1974) **B9**, 699.
2. Bartenev, G. M., Zuyev, Yu. S., "Strength and Failure of Visco-Elastic Materials" p. 33, (Pergamon Press, Oxford, 1968).
3. Aharoni, S. M., *J. Appl. Polymer Sci.* (1972) **16**, 3275.
4. Aharoni, S. M., *J. Polymer Sci. Symp.* (1973) **42**, 795.
5. Aharoni, S. M., *Wear* (1973) **25**, 309.
6. Aharoni, S. M., *Bull. Am. Phys. Soc., Ser. II* (1974) **19**, 239.

RECEIVED October 18, 1974.

# The Contribution of the Linear Viscoelastic Region to the Impact Properties of Thin Polymer Films

E. SACHER

IBM Corp., System Products Division, P.O. Box 6, Endicott, N. Y. 13760

*A linear relationship exists between the toughness (integrated stress-strain curve) and the dynamic mechanical dissipation factor. The types of materials that fit this relationship include glassy polymers, elastomers, and an impregnated fabric. The existence of this relationship indicates that toughness arises from the molecular motions which give rise to the dynamic mechanical properties.*

Although the difficulty in correlating dynamic mechanical and impact data has been noted (1, 2) because the former is measured in the linear viscoelastic region and the latter is measured presumably in the nonlinear region, it is nonetheless well documented (2-8) that various types of correlations do exist between these two measurements.

One of these studies (7) proposed that impact strength arose from a dynamic mechanical dissipation mechanism at the temperature and frequency of the impact. This raises a question: whether any one type of loss mechanism (*i.e.*, arising from main chain local mode motions) is better in this respect than another type (*i.e.*, arising from branch motions) as has been proposed (2), or whether the absolute magnitude of the loss at the temperature and frequency of the impact is the criterion. This assessment is the basis of the present study.

Although impact generally occurs at equivalent frequencies in the low kHz region (9), dynamic mechanical measurement instruments are generally confined to lower frequencies. Therefore it became necessary to extrapolate the low kHz data to a more conveniently measurable frequency. This was done in the following way: using the Toyo Rheovibron direct reading viscoelastometer DDV-II, dissipation factors were evaluated at the instrument frequencies of 3.5, 11, 35, and 110 Hz from

-100° to +100°C for the following materials: (a) 2.5-mil Dupont Fairprene polyurethane-impregnated nylon fabric, (b) 1-mil Dupont Kapton type H polyimide film, (c) 2-mil Dupont Tedlar type SG40TR poly(vinyl fluoride) film, (d) 2.5-mil Bayer Makrofol type KG polycarbonate film, and (e-g) 15-mil samples of Conap types 4541, 4546, and 4547 polyurethane elastomer coatings which were cast on Dupont Teflon sheet, cured according to manufacturer's directions, and stripped. Dynamic mechanical data indicated that samples (e-g) were elastomeric to temperatures substantially below those of interest here.

Within measurement precision ( $\pm 10\%$ ) the various peaks gave linear Arrhenius plots with activation energies between 15 and 40 kcal/mole. Assuming an average 25 kcal/mole, a reasonable 5 kHz impact frequency at room temperature (25°C) would extrapolate to *ca.* 10°C at 11 Hz, one of the Rheovibron measuring frequencies. Therefore the magnitude of the dissipation factor subsequently used for the correlation was 10°C, 11 Hz.

Several difficulties are presented in evaluating impact strength: the values determined on notched specimens (Charpy, Izod) depend on the notch size (8); those determined on unnotched specimens depend remarkably on strain rate (10). This latter study showed that an increased strain rate led to increases in strength and modulus and decreases in elongation and energy to break. Another finding is that falling weight impact strengths, which correlated well with those obtained on a high speed (8000 inch/min) tensile tester (10) also correlated well with the toughness (integrated stress-strain curve) obtained on an Instron at its highest crosshead speed (0.333 inch/sec) (11). In the present case, because of instrument availability and lack of sample rigidity, the toughness at 0.333 inch/sec at 25°C was used as a measure of impact strength.

The values of both toughness and dissipation factor are in Table I and are plotted in Figure 1. In spite of the approximations and momentarily excluding Tedlar, the correlation is good. The reason for the anomalous Tedlar results is found in the stress-strain curve in which the elongation was over 200% and in which the toughness at the yield stress accounted for less than 2% of the total. However when the total toughness for Tedlar is replaced by its toughness at the yield stress, the point falls almost on the line, whose equation is

$$\text{toughness (inch lb/inch}^3\text{)} = 1.606 \times 10^4 \tan \delta - 352 \quad (1)$$

One should not emphasize the values of the constants in Equation 1 since a change in measurement conditions (*i.e.*, the dissipation factor at the appropriate temperature at another experimentally measurable frequency) leads to different values, although the form is retained.

**Table I. Toughness and Dissipation Factor Values**

<i>Material</i>	<i>Toughness at 0.333 inch/sec, 25°C (inch lb/inch<sup>2</sup>)</i>	<i>Tan δ at 11 Hz, 10°C</i>
Fairprene UN 0001	1360 ± 378	0.12
Makrofol KG (machine direction)	2860 ± 356	0.18
Markofol KG (transverse direction)	2536 ± 240	0.18
DPPA 4541	627 ± 202	0.06
DPPA 4546	769 ± 351	0.10
DPPA 4547	769 ± 485	0.08
Kapton 100H	1350 ± 373	0.09
Tedlar 200SG40TR	1350 ± 33 (22.5 ± 4) <sup>a</sup>	0.01

<sup>a</sup> Toughness contribution taken to the yield stress.

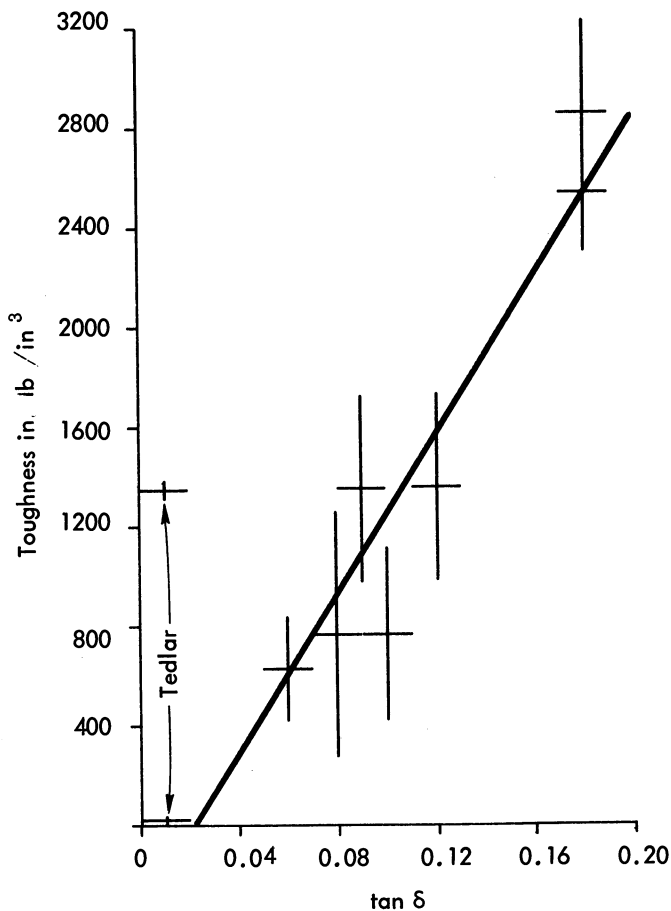


Figure 1. Toughness vs. dissipation factor

The existence of a non-zero intercept in Equation 1 is probably attributed less to experimental precision than to variable stress relaxation: although little stress relaxation generally occurs in high speed tensile measurements (12), the Tedlar data clearly demonstrate how extensive this may be. Even with the other materials, the toughness contribution from beyond the linear region, though small, differed from material to material. This variable contribution from beyond the linear region is considered the major reason for the nonzero intercept.

Since  $\tan \delta$  is equal to the ratio of the loss modulus to the storage modulus, one might expect a correlation of the toughness with the storage modulus. No such correlation was found—the plot appeared as scattered points—because at 10°C, 11 Hz, the loss moduli of the samples were neither negligible nor equal.

The correlation that exists between toughness and dissipation factor indicates that at high strain rates toughness (and impact strength) arise mainly from the linear viscoelastic region. Its generality is shown by its applicability to the wide range of materials studied here: glassy polymers, elastomers, and a polyurethane-impregnated nylon fabric. The limits of its applicability must be defined in terms of the extent of stress relaxation at high strain rates. As in the case of Tedlar, such an occurrence would increase toughness so that the correlation may be viewed as existing in the absence of stress relaxation, giving a minimum expected value of the toughness.

One may view Equation 1 as confirmation of the previously proposed theory (7) that impact energy is provided by a dynamic mechanical loss mechanism in the temperature and frequency range of the impact. Further it appears that the magnitude of the impact strength is directly related to that of the loss regardless of the source of the loss. Since it was previously noted (2) that losses arising from branch motions provided lower impact strengths than those arising from main chain motions, this finding must relate to their relative magnitudes at the temperature and frequency of impact.

One may also consider impact strength as a function of temperature. Polycarbonate for example has a high impact strength from  $-125^{\circ}\text{C}$  to at least  $+100^{\circ}\text{C}$  (2). It also has overlapping secondary losses in this temperature range (7). Recent work (8) showed that for several polymers temperature plots of impact strength (measured in the low kHz range) and dissipation factor (measured in the 30–300 Hz range) had similar peaks, *with those of the dissipation factor depressed 15°C below those of the impact strength*. This similarity in the temperature variation of both quantities suggests that impact strength over a wide temperature range arises from overlapping dissipation factor peaks whose main func-

tion is to provide dynamic mechanical losses at the temperatures and frequencies of the impact.

Finally one may speculate on how the structural motions that cause the dissipation factors dissipate the energy. A recent analysis of the structural motions giving rise to the three secondary losses in polycarbonate (13, 14) showed that their one distinguishing similarity is that they all involve large entities moving cooperatively, suggesting that the energy is dissipated through many degrees of freedom; that is, it is spread out so that no one bond is overstressed. This implies that impact strength may fall off at cryogenic temperatures where the losses are thought to involve either single entities or limited motions.

As both referees pointed out, other reasons have been offered for energy dissipation during impact. In each case however some energy dissipating mechanism must be provided. The present work indicates that, at least for the samples used, this mechanism is provided by the dynamic mechanical dissipation factor. This in turn is attributed to the fact that at the high strain rates of impact the linear viscoelastic region is the largest, if not the only, contributor to the dissipation process.

### *Acknowledgments*

The author thanks M. R. Palmer for carrying out most of the experimental work and both referees for their very helpful comments.

### *Literature Cited*

1. Vincent, P. I., *Polymer* (1960) **1**, 425.
2. Heijboer, J., *J. Polym. Sci., C* (1968) **16**, 3755.
3. Wada, Y., Kasahara, T., *J. Appl. Polym. Sci.* (1967) **11**, 1661.
4. Kohno, H., Nagata, Y., Koyama, K., Wada, E., Kanamaru, K., *Rep. Prog. Polym. Phys., Jap.* (1971) **14**, 337.
5. Koyama, K., Wada, E., Nagata, Y., Watanabe, Y., Futamura, H., *Rep. Prog. Polym. Phys., Jap.* (1972) **15**, 317.
6. Koyama, K., Nagata, Y., Okada, A., Wada, E., *Rep. Prog. Polym. Phys., Jap.* (1973) **16**, 375.
7. Sacher, E., *J. Macromol. Sci., Phys.* (1974) **9**, 167.
8. Vincent, P. I., *Polymer* (1974) **15**, 111.
9. Wolstenholme, W. E., *J. Appl. Polym. Sci.* (1962) **6**, 332.
10. Donnelly, P. I., Ralston, R. H., *Appl. Polym. Symp.* (1965) **1**, 71.
11. Evans, R. M., Nara, H. R., Bobalek, E. G., *Soc. Plast. Eng. J.* (1960) **40**, 76.
12. Lohr, J. J., *Appl. Polym. Symp.* (1965) **1**, 55.
13. Sacher, E., 1973 *Ann. Rept., Conf. Elect. Insul. Diel. Phenom.*, National Academy of Sciences, Washington, D. C., in press.
14. Sacher, E., *J. Macromol. Sci., Phys.* (1974) **10**, 319.

RECEIVED October 18, 1974.

## Contributory Phenomena to the Impact Wear of Polymers

R. G. BAYER, P. A. ENGEL, and E. SACHER

IBM Corp., System Products Division, P. O. Box 6, Endicott, N. Y. 13760

*Impact wear testing of several thin polymer films has shown that there is little or no correlation between impact strength and impact wear resistance. The impact wear of the films depended strongly on thermal conditions caused by the impact. It was found that through frictional heat generation, fretting motions during the impact can significantly influence the wear behavior of these materials.*

One application of thin polymer films is in high-speed electromechanical actuators. In these applications the thin films are frequently used to provide damping, a controlled air gap in a magnetic circuit, or protection to some surface. In such applications, they commonly experience repeated impacts. As a result of these impacts, material is progressively removed from the contact region of the film, and ultimately a hole may be produced through the film; this process may be termed impact wear. This paper reports on the initial results obtained in a study regarding the impact wear of thin polymer films.

### *Experimental*

The materials studied were (a) 5 mil Dupont Kapton type H polyimide film, (b) 2 mil Dupont Tedlar type SG 40TR poly(vinyl fluoride) film, and (c) 2.5 mil Bayer Makrofol type KG polycarbonate film. Specimens of these materials were mounted on smooth, flat steel substrates and fastened only on the periphery, the latter being far (several times the contact dimension) from the contact zone. The specimens were unlubricated.

Two types of pivotal steel hammers were used to provide repetitive impacts. One provided a 0.25-cm wide strike surface with a cylindrical radius of 63.5 cm. This was 1.4 cm long and had an effective mass of 7.8 gms. This hammer was operated at 40 Hz, providing  $31 \times 10^3$  ergs of impact energy at a velocity of 89 cm/sec. The second hammer had a

0.092-cm wide face with a 3.5 cm radius and was 0.3 cm long. It had an effective mass of 0.55 gm and a velocity range of 51–380 cm/sec. This results in a range of impact energies from 0.7–39  $\times 10^3$  ergs. This hammer was operated at 50 Hz. The latter hammering apparatus was used in prior impact wear studies of homogeneous, nonpolymeric surfaces (1). These units provided a variety of impact conditions.

Polymer samples were impacted for varying amounts, ranging from  $10^2$  to  $10^7$  impacts and with varying impact energies. Because of the different thicknesses of the three materials, several experiments were performed using multiple layers to give equivalent total thicknesses. It was found that for the range of thicknesses involved in this study, there was no significant dependence on thickness in terms of the relative wear behavior of the material and the nature of the damage produced.

### Results

Profilometer measurements of the impacted specimens revealed general distortion of the film in and around the region of impact. By profilometric measurements on both sides of the film, the amount of wear in the contact zone was estimated. This technique provided a comparison of wear behavior to within 15 or 20  $\mu\text{m}$ . In several cases the experiments were continued until the film was worn through. In such cases the number of impacts to failure also provided a means of comparing wear behavior. In terms of these techniques it was found that the poly(vinyl fluoride) had the best wear resistance, followed by the polyimide. For example, tests conducted with the larger hammer indicated that for the same thickness, the poly(vinyl fluoride) had approximately one-half the depth rate of wear exhibited by the polyimide.

The appearance of the impacted areas was significantly different for the three materials. For example, evidence of charring and flow was found in the impacted region of the polycarbonate (*see* Figure 1). Charring was not observed for the other two materials. However, flow was quite evident in the case of the poly(vinyl fluoride) while the polyimide exhibited a rougher, more brittle appearance (*see* Figure 2).

Infrared spectra of the impacted area of these materials were obtained on a Perkin-Elmer 521 grating infrared spectrophotometer. Comparison of these spectra with those obtained from unimpacted areas revealed definite changes in the structures of the poly(vinyl fluoride) and the polycarbonate materials, with indications of possible changes in the polyimide. Table I summarizes the changes noted for the poly(vinyl fluoride) and gives probable assignments.

These observations of char, flow, and structural change indicate significant temperature rises in the impacted zones of these materials, with the implication that thermal parameters are significant in the impact wear process. Consequently, a thermogravimetric analysis of these mate-



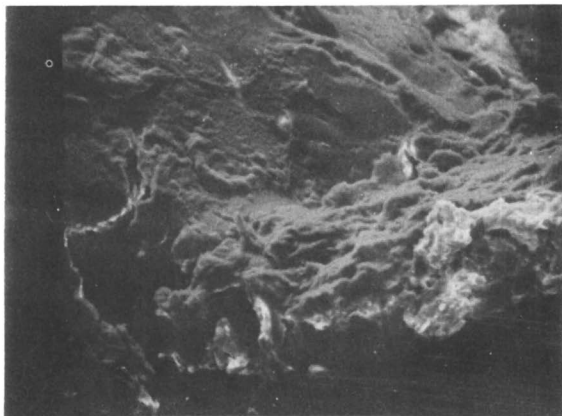


*Figure 1. A 130 $\times$  SEM photomicrograph of the flowing and charring of polycarbonate after  $11 \times 10^6$  impacts at 40 Hz at an energy level of  $31 \times 10^8$  ergs*



*Figure 2. A 84.5 $\times$  SEM photomicrograph of Kapton showing the brittle nature of the polyimide*

**Table I. Observed Changes in the Infrared Spectra of Poly(vinyl fluoride)**

Frequency ( $\text{cm}^{-1}$ )	Change	Probable Assignment
1710	formation	C=C stretch
1505	} doublet	C=CH <sub>2</sub> bending
1495		
760	formation (or increase)	C-F stretch
715	formation (or increase)	=C-H bending
		=C-H bending

rials was carried out so that the relative degree of thermal stability might be established. A Dupont 950 thermogravimetric analyzer was used at a heating rate of 20°C/min in air. The results of these tests are shown in Table II along with a summary of the observed natures of the impact areas of the three materials.

Table II also includes an estimate of the elevated temperatures reached in the contact areas. These estimates were developed on the basis of the TGA analysis as well as the IR data and appearance of the damage. Any evidence of thermal flow, charring, or chemical change in the impacted area of the film was taken as an indication that the T min of the TGA analysis was exceeded. As shown, these estimated local temperatures are quite high, and the question immediately arises as to their sources under impact conditions. There are three possible sources for this increase in temperature: (a) internal damping, (b) differential surface displacement resulting from contact, or (c) fretting motion at the interface induced by the impact.

### Discussion

The temperature rise caused by internal damping may be estimated in the following manner. The energy dissipated per unit volume per unit time,  $q$ , is approximately given by

$$q = \frac{nE''\epsilon^2}{2} \quad (1)$$

where  $n$  is the repetition rate of the impacts,  $E''$  the imaginary modulus at the temperature and frequency of the impact, and  $\epsilon$ , the peak strain in time, averaged over the contact area. Based on transducer measurements of the most severe impact used in this study,  $\epsilon$  is estimated to be around 15%. The imaginary modulus is estimated to be about  $5 \times 10^8$  dynes/cm<sup>2</sup>. Using these values and a repetition rate of 50 Hz,  $q \approx 4.8$  cal/cc-sec.

The associated temperature rise can be approximated by a one-dimensional thermal analysis, assuming an internal heat source with a strength of  $q$ . This analysis assumes constant heat rates, which implies constant viscoelastic properties.

The appropriate heat equation is, therefore:

$$\nabla^2 \delta T + \frac{q}{K} = \frac{\delta \dot{T}}{\kappa} \quad (2)$$

where  $K$  is the coefficient of thermal conductivity,  $\kappa$  is the diffusivity, and  $\delta T$  is the temperature rise. If we assume one surface of the polymer to be a perfect insulator (*i.e.*, no convection losses to the air) and the

**Table II. Summary of Impact Area Characteristics**

Sample	Results of Impact			TGA	
	Char	Flow	Roughness	Thin <sup>a</sup> (°C)	Combustion
Polyimide	no	no	yes	500	no
Poly (vinyl fluoride)	no	yes	no	300	no
Polycarbonate	yes	yes	no	400	yes

<sup>a</sup> Minimum temperature of which weight loss begins.

other to be in contact with a perfect heat sink (*i.e.*, the steel substrate), the equilibrium temperature rise can be shown to be given by the following equation:

$$\delta T = \frac{2qh^2}{K} \left[ \frac{x}{2h} - \left( \frac{x}{2h} \right)^2 \right] \quad (3)$$

where  $h$  is the sample thickness and  $x$  is the distance from the infinite sink. This expression shows the maximum temperature at the free surface—*i.e.*,  $x = h$ . If  $4 \times 10^{-4}$  cal cm<sup>2</sup>/cc sec °C is used for  $K$ , then the maximum temperature rise for a 2-mil ( $5 \times 10^{-3}$  cm) sample is *ca.* 0.3°C. This is several orders of magnitude smaller than the temperature actually attained.

One further point regarding this mechanism should be made: the temperature dependency of the viscoelastic properties. If the impact condition—*e.g.*, frequency and temperature—corresponds to an up-slope region of the loss peaks with temperature, then the temperature will continue to rise at an increasing rate, assuming no heat losses. However, examination of the loss peaks would indicate that the temperature rise caused by this effect should be less than 100°C since for these materials there is a negative slope above 70°–80°C.

Consequently, while the above analysis of temperature rises caused by internal friction (viscoelasticity) are approximate, they do indicate that it is improbable that this mechanism can be the source of the high temperatures (*e.g.*, several hundred degrees) required to produce the observed behavior.

The second proposed mechanism for the temperature rise is differential surface displacement. This results from the ability of the polymer surface to slip relative to the hammer surface during the impact. It has been shown (2) that for a cylindrical hammer the energy dissipated per impact per width of cylinder is:

$$U = \frac{f(\mu)E'b^4}{R^2} \quad (4)$$

**and Appropriate Material Characteristics**

<i>IR</i>		
<i>Chemical Change</i>	<i>Local<sup>b</sup> Temp (°C)</i>	<i>Coefficient of Friction</i>
possible but slight	< 500	.29
yes	> 300	.26
yes	> 400	.40

<sup>b</sup> Estimated.

where  $f(\mu)$  is a function of the coefficient of friction,  $\mu$ ,  $E'$  is the tensile modulus, and  $b$  is half the contact length of the cylinder and its radius,  $r$ . For  $\mu$  of 0.2,  $f(\mu)$  is about  $1 \times 10^{-3}$ . Further, it can be shown by impact analysis that  $b$  is about  $4 \times 10^{-2}$  cm for the more severe energy conditions with the smaller hammer. Assuming that  $E'$  is  $10^{10}$  dynes per  $\text{cm}^2$ ,  $U$  is estimated to be 1.6 erg/cm. For a hammer width of 0.09 cm, the energy dissipated per unit time for a 50-Hz repetition rate is 7 ergs/sec, which is approximately  $2 \times 10^{-7}$  cal/sec. This is an extremely small amount of power, and it therefore does not appear likely that this mechanism can explain the large temperatures associated with the observed phenomena.

The third possible mechanism results from the fretting action or small amplitude sliding between hammer and polymer induced as a result of vibrations in the impacting hammer. The surface temperature rise attributed to this effect may be estimated from (3):

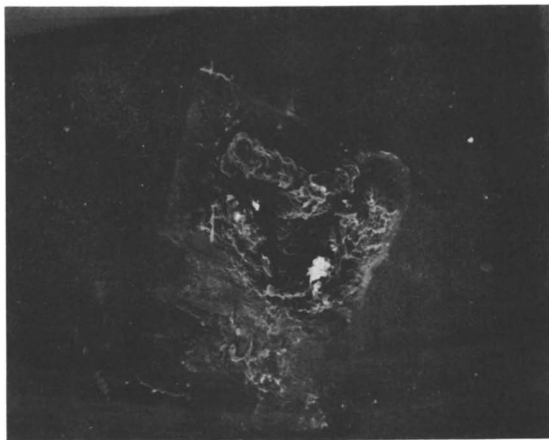
$$\delta T \approx \frac{2\mu P v}{3\pi a K} \quad (5)$$

where  $v$  is the average velocity of the tangential oscillation,  $a$  is the equivalent contact radius, and  $P$  is the peak force during impact. Utilizing a transducer-determined  $P$  value of  $2.7 \times 10^3$  dynes and an estimated average tangential velocity of 175 cm/sec, Equation 5 gives a temperature rise of  $3 \times 10^2$  to  $10^5$  °C for  $a$  and  $\mu$  values ranging from  $10^{-5}$  to  $10^{-2}$  cm and from 0.1 to 0.4, respectively. Clearly this surface friction mechanism could produce the large temperatures observed.

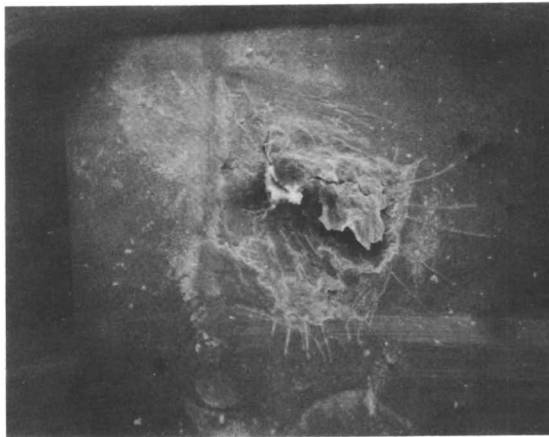
This conclusion is further substantiated by three other observations. First, when damping was applied to the larger hammer used in this study to reduce vibrations, the wear scars of the polymer films were substantially reduced as well. Secondly, friction measurements made against cold-rolled steel utilizing a standard friction sled (ASTM D1894) moving at 2 inches/min at 23°C and 40% RH tend to confirm the significance of surface friction in the impact wear of thin films. The friction values are also given in Table II and show that the lower the friction value, the

better the observed wear resistance. Finally, when the polycarbonate was coated with Mobay's E-397 low friction coating, the observed charring was considerably reduced (*see* Figure 3).

Since this source of heat depends on the friction coefficient, the estimate of the temperature achieved by the polyimide film may be fur-



*a*



*b*

*Figure 3. SEM photomicrograph at 26 $\times$  of (a) uncoated polycarbonate sample after  $3.3 \times 10^5$  impacts and (b) polycarbonate sample coated with Mobay's E-397 friction coating after  $4.5 \times 10^5$  impact. The same impact conditions were used in both tests. The surface friction was halved after coating. Note the presence of coating cracks.*

ther refined over that given in Table II. Since the impact condition and thermal constants for the polyimide and the poly(vinyl fluoride) are similar, as well as their coefficients of friction (*see* Table II), the peak temperatures should also be similar. Hence, the polyimide film should also have experienced a peak temperature near 300°C.

The large influence of surface friction effects observed in these impact wear tests indicates the significance of induced parasitic vibrations in polymer impact wear. Since it is quite likely that vibration will occur under most impact conditions, it is expected that there should be a strong relationship between polymer wear phenomena under sliding and impact conditions.

Since several different wear characteristics were noted for the materials tested (*e.g.*, charring, flow, and brittle behavior), it can be inferred that there is no unique mechanism associated with impact wear of polymer thin films. Further, because of this aspect and the probability that the same mechanisms do not occur under impact testing conditions (Charpy and Izod), it is reasonable to infer that there is little correlation between impact wear resistance and impact strength. This latter point may be illustrated by considering polycarbonate. Even though it has the highest impact strength of any unfilled polymer (4), it exhibits the poorest wear behavior in this study.

### **Conclusions**

(1) A strong correlation does not exist between impact strength and impact wear resistance.

(2) Temperatures generated at the surface of these films as a result of fretting motion strongly influence the wear process.

(3) Structural changes in the polymer films can occur as a result of repeated impacts.

### **Literature Cited**

1. Engel, P. A., Bayer, R. G., *J. Lub. Tech.* (1974) **96**, 595-604.
2. Engel, P. A., Conway, H. D., *IBM J. Res. Develop.* (1971) **15**, 116-122.
3. Holm, R., *J. Appl. Mech.* (1952) **19**, 369-374.
4. Sacher, E., *J. Macromol. Sci.* (1974) **B9**, 163-167.

RECEIVED October 18, 1974.

## Fatigue Crack Propagation in Polycarbonate

J. A. MANSON, R. W. HERTZBERG, S. L. KIM, and W. C. WU

Materials Research Center, Lehigh University, Bethlehem, Pa. 18015

*We investigated the effects of various material and fatigue parameters on crack-growth rate per cycle,  $da/dn$ , as a function of stress intensity factor range,  $\Delta K$ . In contrast to other common polymers the frequency (0.1–20 Hz) or wave form has little effect on fatigue crack propagation (FCP) of polycarbonate. However, mean stress is significant, with FCP curves shifted towards higher  $\Delta K$  values for higher mean stresses. Environment is also significant; water induces a discontinuity in the FCP curves. Thermal history is important; annealing at temperatures below  $T_g$  causes complex changes in FCP behavior. Some changes such as minima in plots of  $\Delta K$  at fracture and fracture energy as a function of annealing temperature can be correlated with calorimetric (DSC) data which suggest competitive ordering–disordering effects caused by annealing.*

As polymers become used to an increasing extent in engineering applications, a better understanding of failure characteristics is important to material selection and design. Since behavior under cyclic stresses (fatigue), though particularly important, has received relatively little attention (1–8), a program was begun in these laboratories to explore the range of fatigue crack propagation (FCP) in engineering plastics and to investigate the roles played by polymer structure and morphology.

During these studies polycarbonate (PC) was exceptionally resistant to fatigue crack propagation (at least in ¼-inch thick sheets at room temperature). In fact, a high level of toughness as measured by various criteria has long been known for PC, and various explanations were proposed (1, 7). Since few detailed studies of PC fatigue behavior have been conducted (1, 2, 3), we examined the roles of several structural and fracture parameters, including mean stress, thermal history, molecular weight, crazing, and fracture surface morphology. The study of thermal history effects is especially convenient in PC whose state can be

varied by suitable annealing procedures without introducing a detectable degree of crystallinity (9, 10, 11, 12, 13).

In this paper we review current research in this group on fatigue behavior of PC and discuss some recent results that demonstrate the roles of several external and material variables and thermal history. Careful attention was paid to the characterization of the PC specimens used—*e.g.*, by differential scanning calorimetry (DSC)—and that the work complements another detailed study of PC (12, 13).

### *Experimental*

Commercial polycarbonate sheet was used—Lexan,  $\frac{1}{4}$  inch thick;  $\bar{M}_v = 42,000$ ;  $d = 1.1970$  gm/cm<sup>3</sup>. Specimens were cut in one direction only to minimize the small degree of anisotropy present (*see* below). Annealing at temperatures above 25°C was effected in an oven at various temperatures,  $\theta$ : 48 hr for  $\theta = 80^\circ$  and 125°C; 60 hr for 150°C. For  $\theta = 150^\circ\text{C}$  rigorous vacuum drying (48 hr) was necessary prior to heating. It was shown previously that an annealing time of 48 hr was sufficient to reach equilibrium (12, 13). (Effects of time per se are currently under study.)

Fatigue tests were conducted using an MTS tester over a range of cyclic frequencies and either compact tensile ( $3 \times 3$  inch) or single-edge, notched ( $3 \times 12$  inch) specimens. Tests of annealed specimens were conducted at 10 Hz. An appropriate geometrical factor,  $Y$ , was used to calculate stress intensity factor ranges,  $\Delta K$ , according to the relation

$$\Delta K = Y \Delta \sigma \sqrt{a} \quad (1)$$

where  $\Delta \sigma$  is the range in applied stress, and  $a$  is the crack length (3). Crack extension readings were taken at appropriate intervals, and values of  $da/dn$ , the crack propagation rate per cycle, were analyzed and plotted as a function of  $\Delta K$  by a CDC 6400 computer. For environments other than laboratory air, an appropriate chamber was used. Two maximum  $\Delta K$  values were determined:  $\Delta K_{\text{mr}}$  (calculated from the crack length corresponding to the onset of catastrophic failure as observed directly on the fracture surface), and  $\Delta K_{\text{mr}}$  (calculated from the last observed crack length recorded during testing prior to failure. Stress strain curves (on two to four specimens for each value of  $\theta$ ) were obtained on an Instron tested using standard dumbbell specimens and a crosshead speed of 2 inches/min.

For differential scanning calorimetry (DSC), specimens ( $\sim 10$  mg) were punched out from thin (10–30 mil) machined films and were carefully weighed on a Perkin-Elmer autobalance model AD-1. Tests were run on a Perkin-Elmer differential scanning calorimeter model DSC-1B at 10°C/min using an empty tray as reference. With all specimens an endothermic peak (12, 13, 14) was observed close to the glass transition temperature  $T_g$ . To characterize the magnitude of the peak, which was observed to be a function of thermal history, an apparent energy of transition,  $Q_a$ , was calculated by the procedure given in the instrument manual, with the melt transition in indium as a reference. Although the



peak does not correspond to a true melting peak, correspondence to some kind of order-disorder transition has been proposed and supported by independent evidence (11, 12, 13). Densities were measured using a Tecam density gradient column but did not show any consistent changes on annealing.

### Results and Discussion

**FCP in Unannealed PC.** One objective in this study was to examine the FCP response of the unannealed polymer as affected by changes in mean stress, test frequency, wave form, environment, and specimen orientation. Initial studies were directed toward establishing any FCP anisotropy as a function of loading direction. For FCP tests conducted at room temperature and in a flowing nitrogen atmosphere a twofold difference in crack growth rate was noted at any given  $\Delta K$  level when  $R = 0.1$  ( $R = K_{\min}/K_{\max}$ ). When the mean stress level was increased such that  $R = 0.5$ , no difference in FCP was noted as a function of specimen orientation. Since a twofold change in crack growth rate is not very significant in terms of the analysis of FCP data, we concluded that specimen orientation exerts a minor influence on test results of the current material supply.

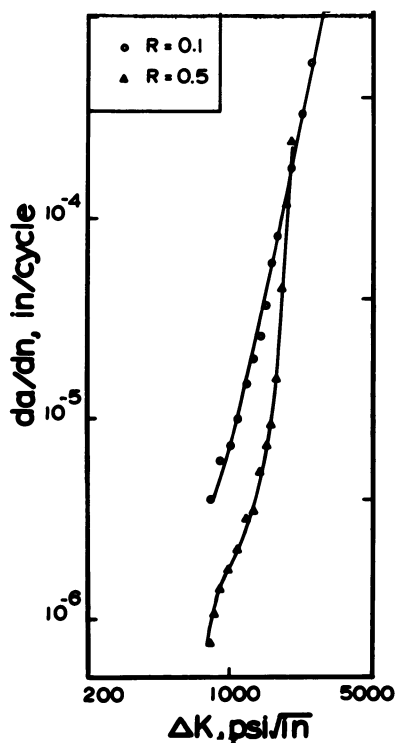


Figure 1. Effect of mean stress on FCP in PC

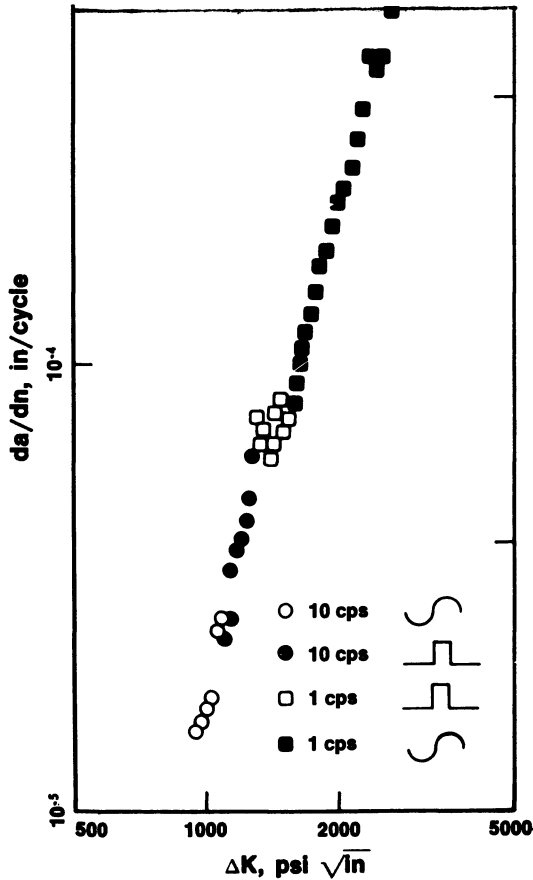


Figure 2. Effect of wave form on FCP in PC

By comparison, a change in mean stress substantially changed crack growth behavior in both directions. Surprisingly the FCP rate was reduced substantially (a four- to fivefold change at  $\Delta K = 800$  psi/in.) when the  $R$  ratio was increased from 0.1 to 0.5. In contrast an increased mean stress level in tests of metal alloys results in an increased crack growth rate. The increased slope of the  $da/dn-\Delta K$  plot with increasing mean stress (Figure 1), however, is comparable with the response in metals and, in the case of PC, produces a convergence of fatigue response at high  $\Delta K$  levels. It would appear then that an increase in mean stress causes the fatigue crack propagation rate in PC to be more sensitive to changes in  $\Delta K$  but at the same time produces a decrease in the magnitude of the pre-exponential constant  $A$  in the Paris relationship (15):

$$da/dn = A\Delta K^n \quad (2)$$

It is postulated that the reduction in  $A$  is related to an increase in molecular free volume associated with the higher mean stress level; this increase in free volume, in turn, is believed to enhance chain segmental movements responsible for fracture energy absorption and overall toughening.

Manson and Hertzberg (1) recently discussed the much lower frequency sensitivity of fatigue crack propagation in PC *vs.* that observed in PS, PVC, and PMMA. Additional tests conducted as part of this investigation from 0.1–20 Hz again showed little effect of frequency on FCP. Similarly, a negligible change in FCP was noted when the load profile was changed from sinusoidal to square wave form for tests conducted at 1 and 10 Hz (Figure 2).

A striking perturbation is seen in two of the  $da/dn$  *vs.*  $\Delta K$  plots for PC reported previously by Hertzberg, Nordberg, and Manson (Figure 3). One possible explanation for this pronounced shift in the material's response might be related to an interaction between the specimen and the

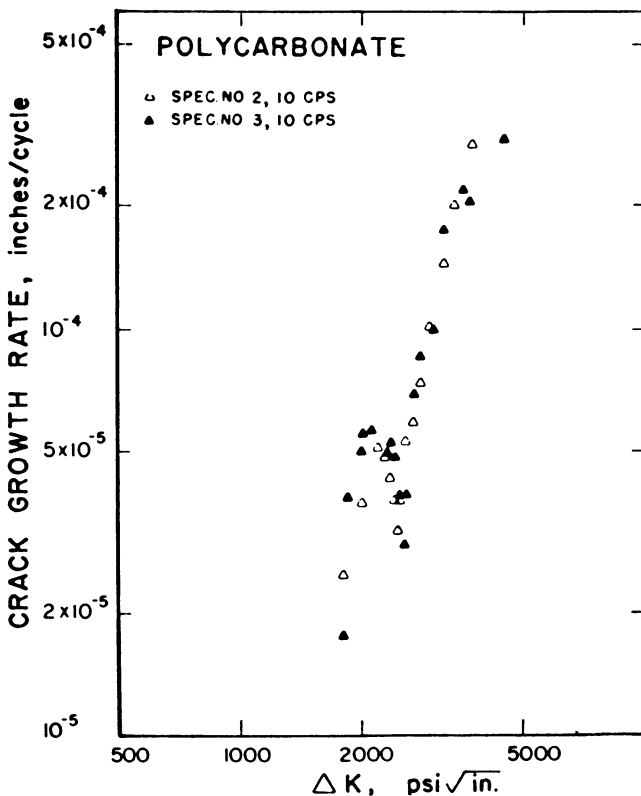


Figure 3. FCP in PC

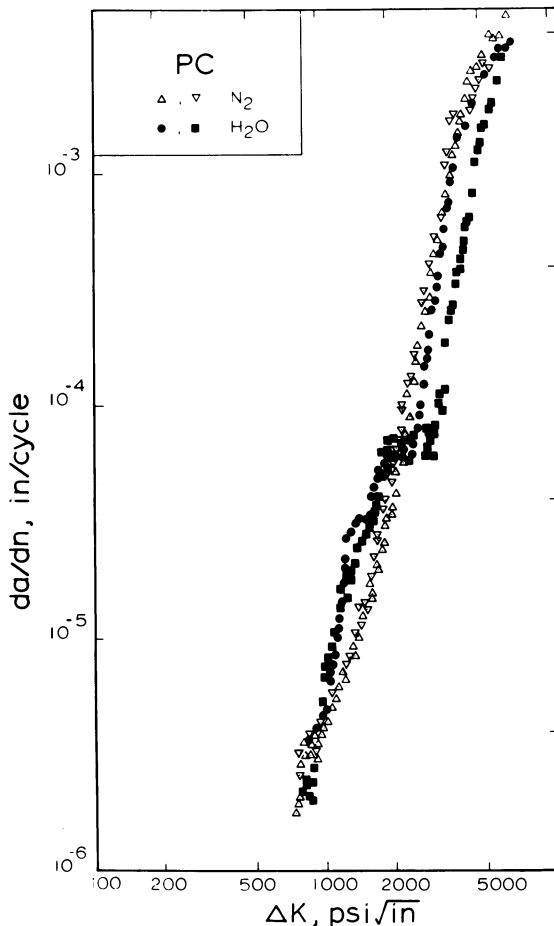


Figure 4. Environmental effects on FCP in PC

test environment. Since temperature and humidity conditions were not recorded for these two tests, additional experiments were conducted. First, specimens from the current material supply were tested in gaseous nitrogen, laboratory air, and water. From Figure 4 it is clear that water at the crack tip is responsible for the discontinuity noted in the fatigue behavior of this material. No significant difference in test results was found between laboratory air and gaseous nitrogen atmospheres. To ascertain whether the material tested previously by Hertzberg *et al.* (3) was also sensitive to water at the crack tip, additional tests were conducted on the original material. In agreement with the above findings an inflection was noted in test results from a specimen tested in water while none was observed with another sample tested in air (relative humidity, 55%).

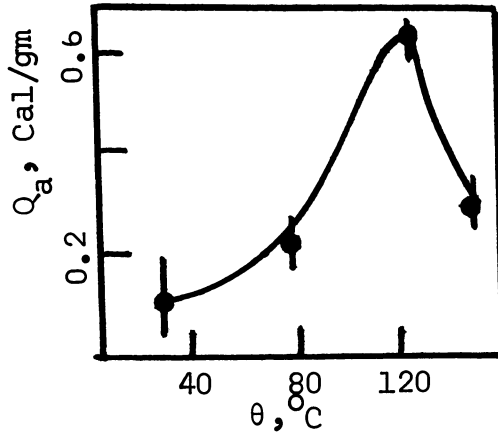


Figure 5.  $Q_a$  for annealed PC

Additional tests are planned to determine the effect of test frequency on the crack growth rate range where the transition occurs. On the basis of similar results in environmentally enhanced crack growth in metal alloys, the growth rate transition would be expected to decrease with increasing test frequency.

**Effects of Thermal History.** One of the most useful and fundamental parameters defining the state of a polymer is its enthalpy (or specific heat). Considerable evidence has been adduced to show that the thermal characteristics of glassy polymers such as PC are sensitive to thermal

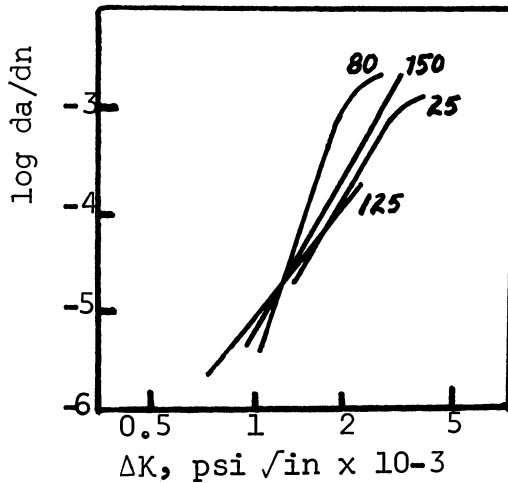


Figure 6. Fatigue crack growth of annealed PC

history (12, 13, 14). In particular when specimens are examined using DSC techniques, endothermic peaks (the intensity and position of which are relatable to annealing conditions) often appear at temperatures close to  $T_g$ . Although there is argument about the origin of these peaks (14), the fact they occur indicates that some alternation in state must occur on annealing. Consider Figure 5, which presents  $Q_a$  (corresponding to the magnitude of the endothermal peak and hypothetically to some kind of an order-disorder transition), as a function of  $\theta$ . Even if part of the contribution to  $Q_a$  may arise from a relaxation effect (14), the variation observed must surely reflect changes in the polymer (12, 13). Whatever these changes are (and they have been shown not to be associated with crystallinity) (11, 12, 13), they were most intense around  $\theta = 120^\circ\text{C}$  with the specimens used in this study.

Considering fatigue, we see from Figure 6 that temperatures up to  $T_g$  induce significant changes in several aspects of FCP behavior: the slope and shape of the fatigue curves and the maximum value of  $\Delta K$  recorded prior to failure. The fact that crossovers occur in the range of  $da/dn$  of interest in addition to curvature for  $\theta = 25^\circ$  and  $80^\circ\text{C}$  make it difficult to use  $\Delta K$  at an arbitrary value of  $da/dn$  to indicate relative toughness, as has been done successfully previously (1, 3). Since a maximum in the slope of the  $da/dn$ - $\Delta K$  plot occurs at *ca.*  $80^\circ\text{C}$  which does not correlate with a temperature corresponding to a maximum (or minimum) in any other property of PC—*e.g.*,  $Q_a$ , loss modulus, tensile behavior, etc. (9, 10, 12, 13)—elucidation of the full significance of the shapes and slopes of the FCP curves remains to be achieved. An anomaly in permeability was also noted by Conde (12, 13) for an annealing temperature of  $80^\circ\text{C}$ .

In spite of the yet unresolved ambiguity regarding fatigue response per se throughout the crack propagation stage, clear correlations are noted between ultimate behavior parameters and the observed values of  $Q_a$  (*see* Figures 7–9). First, values of  $\Delta K$  (maximum)—whether the last recorded value whose crack lengths were measured,  $\Delta K_{mr}$ , or whether the maximum determined by inspection of the fracture surface,  $\Delta K_{mf}$ —clearly pass through a minimum (Figure 7) at *ca.*  $\theta = 120^\circ\text{C}$ . (Note that  $\Delta K_{mf}$  should be comparable with  $K_c$ , static, the critical stress intensity factor for fracture.) Thus the fracture toughness of a notched specimen first decreases with  $\theta$  and then appears to rise a little as  $\theta$  approaches  $T_g$ . The position of the minimum of course is consistent with the position of the maximum in  $Q_a$ .

This behavior may be compared with the (unnotched) tensile fracture energy,  $T$ , on the same plot. Clearly, excellent consistency is obtained. Thus either the energy for crack propagation dominates the

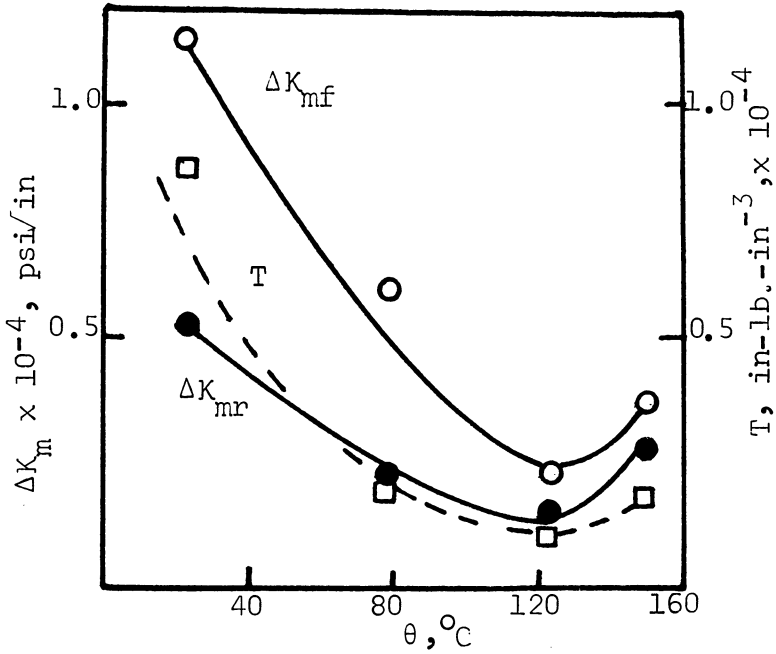


Figure 7. Tensile fracture energy ( $T$ ),  $\Delta K_{mf}$ , and  $\Delta K_{mr}$  for annealed PC

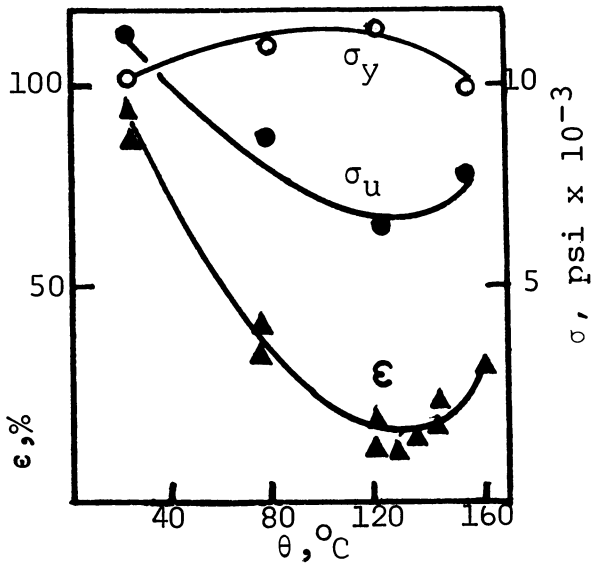


Figure 8. Tensile properties of annealed PC

picture, or more likely the form of the temperature dependence for both crack initiation and propagation is similar.

Similar maxima or minima are observed for other tensile properties, namely  $\sigma_y$  (the stress at the yield point),  $\epsilon$  (the elongation to break), and  $\sigma_u$  (the ultimate strength). As shown in Figure 8 the minimum position corresponds to  $\theta = 120^\circ\text{C}$ . The results are consistent with the decreases in  $T$ ,  $\Delta K_{mf}$ , and  $\Delta K_{mr}$ ; as  $\sigma_y$  increases, failure tends to intervene so that  $\sigma_u$  tends to decrease. The results are also consistent with results in the literature, though the latter do not extend to high enough values of  $\theta$  to exhibit a maximum or minimum (9, 10). Other properties may also depend strongly on  $\theta$ ; thus Conde (12, 13) found that the energy of activation for the permeation of water is at a minimum for  $\theta = 120^\circ\text{C}$ .

Finally Figure 9 shows an excellent correlation between  $\Delta K_{mf}$ , a measure of fracture energy, and  $Q_a$ , a measure of polymer state. A reason-

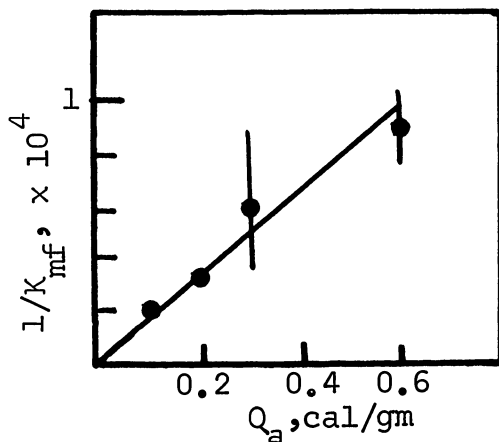


Figure 9. Relationship between  $\Delta K_{mf}$  and  $Q_a$  for annealed PC

able explanation may be proposed. The parameter  $Q_a$  should in some manner reflect the degree of ordering in PC. If so, one may hypothesize a competition between the ordering or close packing of small segments, facilitated by increasing  $\theta$ , and disordering caused by the onset of large segmental motions as  $T_g$  is approached. Such an effect is also consistent with observations of loss modulus and permeabilities (12, 13). Thus as ordering increases and free volume is decreased, the ability to relax within the time scale of a stress cycle and dissipate energy through plastic deformation is reduced. Further work in progress with fractography should test this proposal; the more closely packed polymers might show a tendency to craze more readily than yield, though in contrast it has



been suggested that cyclic softening may be easier for ordered specimens (7). Clearly the phenomenon of ordering merits further attention.

### *Acknowledgments*

The authors gratefully appreciate the general assistance from, and helpful discussions with, A. Conde and M. Skibo and technical assistance from E. Kozma.

### *Literature Cited*

1. Manson, J. A., Hertzberg, R. W., *Macromol. Sci.* (1973) **1**, 433.
2. Jacoby, G. H., ASTM Spec. Tech. Publ. 453, 147 (1969).
3. Hertzberg, R. W., Nordberg, H., Manson, J. A., *J. Mater. Sci.* (1970) **5**, 521.
4. Harris, J. S., Ward, I. M., *J. Mater. Sci.* (1973) **8**, 1655.
5. Hertzberg, R. W., Manson, J. A., *J. Mater. Sci.* (1973) **8**, 1554.
6. Manson, J. A., Hertzberg, R. W., *J. Polym. Sci., Polym. Phys. Ed.* (1973) **11**, 2483.
7. Rabinowitz, S., Beardmore, P., *J. Mater. Sci.* (1974) **9**, 81.
8. Crawford, R. J., Benham, P. P., *J. Mater. Sci.* (1974) **9**, 18.
9. Golden, J. H., Hammant, B. L., Hazell, E. A., *J. Appl. Polym. Sci.* (1967) **11**, 1571.
10. Legrand, D. G., *J. Appl. Polym. Sci.* (1969) **13**, 2129.
11. Siegmann, A., Geil, P. H., *J. Macromol. Sci.* (1970) **B4**, 557.
12. Conde, A., Ph.D. Thesis, Lehigh University, June 1974.
13. Conde, A., Manson, J. A., *Amer. Chem. Soc., Div. Polym. Chem., Preprints* (1974) **15** (2), 465.
14. Petrie, S. E. B., *J. Polym. Sci., Part A-2* (1972) **10**, 1255.
15. Paris, P. C., Proc. 10th Sagamore Army Mat. Res. Conf. (1964) 107.

RECEIVED October 18, 1974. Work supported in part by the Army Research Office (Durham) under Grant DAHCO4 7460010 and by the Pennsylvania Science and Engineering Foundation.

# Application of Group Theory Concepts to Polymer Blends, Grafts, and IPN's

L. H. SPERLING

Materials Research Center, Lehigh University, Bethlehem, Pa. 18015

*Some of the concepts of group theory have been applied to polymer blends, grafts, and interpenetrating polymer networks in an effort to classify the many materials already prepared and to offer a systematic approach for the synthesis of unknown materials. The first paper on group theory applications (14, 15) defined the operations: (M) addition of monomer, (P) polymerization, (G) grafting, and (C) cross-linking. Combinations of two polymers were considered. This paper broadens the first paper and considers combinations of  $n$  distinguishable polymers. Physical operations such as (S) dissolving, (A) annealing, (O) orientation, and (N) crystallization are introduced along with their inverses. Three distinguishable types of graft junctions are introduced: a line (L) junction, to represent a block copolymer, a T-junction, to represent grafting, which frequently appears during polymerization, and an X-junction, to represent the distinguishable structures often formed by post-polymerization grafting.*

Polymer blends, grafts, and interpenetrating polymer networks (IPN's) can be considered from several points of view:

- (1). The detail of their synthesis involving anionic, cationic, and free radical and condensation modes.
- (2). Their morphology which because of polymer-polymer incompatibility causes most of these materials to display two or more distinct phases.
- (3). Their non-linear and often synergistic mechanical behavior which arises from their above mentioned multiphase morphology. Thus, both impact resistant plastics and thermoplastic elastomers have been born.

(4). Their topology which can be described by the branch of mathematics known as group theory.

This paper focuses on the topology: the interrelationships among these several materials and some rules for future syntheses.

The experimental literature for polymer blends, grafts, blocks, and IPN's includes symposia collections by Ceresa (1), Burke and Weiss (2), Aggarwal (3), Molau (4), Gould (5), Platzer (6), Sperling (7), and a monograph by Manson and Sperling (8).

The basic aspects of group theory as applied to chemical problems are introduced by Cotton (9) and Davidson (10); Bruck (11) and Artin (12) discuss basic mathematical forms and theorems related to group theory. Perhaps the most famous application of group theory to chemical problems relates to crystal structure; 32 classes of crystals and exactly 230 distinguishable space lattices have been found (9, 10). Other important applications include orbital theory, ligand field theory, and molecular vibrations (9). Recently, group theory concepts have been applied to fibrous composites (13) and, in a preliminary way, to polymer blends, grafts, and IPN's (14, 15). This paper develops group theory concepts in polymeric mixtures (14, 15) and extends and generalizes the work from two-component systems to  $n$  polymer components.

### *Structure and Nomenclature*

The simplest mixture of two kinds of polymer molecules, polymer 1 and polymer 2, which can be achieved by mechanical blending, latex blending, or solvent cast blending, involves no chemical bonds between the two types of molecules (*see* Figure 1). Occasionally such blends may be described chemically as poly(1-m-2), where the  $m$  denotes "mechanical blend."

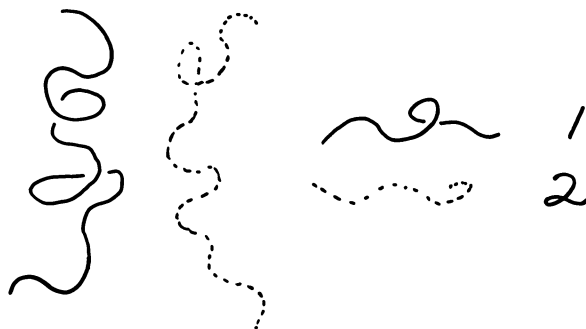
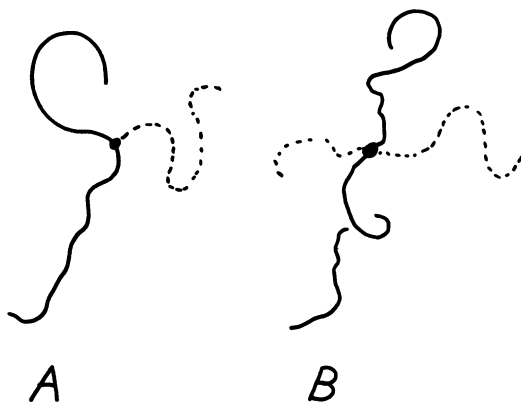


Figure 1. A schematic of a mechanical blend of polymer 1 and polymer 2



*Figure 2. Graft copolymers, poly(1-g-2). In this and succeeding figures, the solid line (polymer 1) is synthesized first, and the dotted line (polymer 2) is synthesized second. Black dots represent graft points. A represents a T-junction graft, and B represents an X-junction graft.*

If polymer 1 and polymer 2 are grafted together, the backbone structure and the grafted side chain are distinguished as poly(1-g-2)—2 as a graft on backbone 1 (*see* Figure 2). Further topological distinctions might be made between the T-junction in Figure 2A and the X-junction in Figure 2B which are usually brought about by different grafting mechanisms. Hydrogen abstraction or condensation mechanisms may lead to a T-junction, but polymerization through the double bond of a diene-mer that leads to an X-junction apparently does not occur (16, 17). X-junction materials often arise from post-polymerization grafting (*see* below). A special type of graft copolymer is formed when the grafts are situated at the end of the molecule. These materials are block copolymers (Figure 3). Poly(1-b-2) is depicted in Figure 3A. Block copolymers can be considered line (L) junctions, and often three or more blocks appear in the same molecule (*see* Figure 3B).

The polymer blends and grafts in Figures 1–3 usually have finite molecular weights and are soluble in appropriate solvents. When grafting is so extensive that covalently bonded molecules of macroscopic size are formed, insoluble networks arise. A simple homopolymer network is shown in Figure 4. When one or both polymers are involved in network structure, several subclassifications must be distinguished. (The following materials may be broadly denoted as graft copolymers because the synthetic procedure involves cases where monomer 2 is polymerized in the presence of polymer 1. This is an accepted generic nomenclature regardless of the presence, absence, or extent of the grafting involved.)

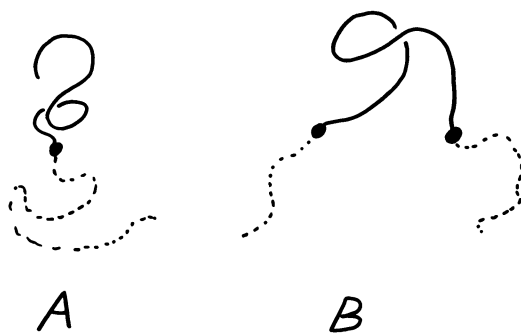


Figure 3. Representations of block copolymers: A, a diblock copolymer, poly(1-b-2); B, a triblock copolymer, poly(2-b-1-b-2). A block copolymer can be considered as an L-junction graft (L represents "line").

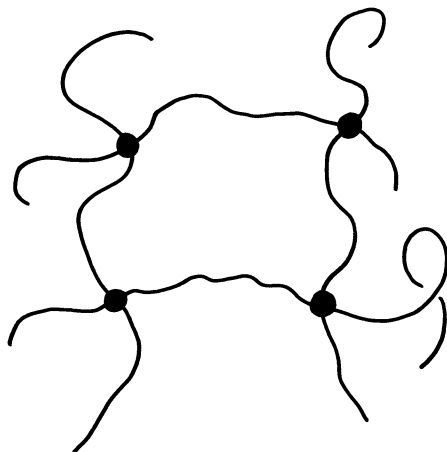


Figure 4. A polymer network, schematically portrayed. Black dots represent crosslink sites.

In the following, polymer 1 is formed first and polymer 2 is formed secondly.

When monomer 2 is swollen into network 1 and polymerized *in situ* to form a linear polymer, a semi-interpenetrating polymer network (semi-IPN) of the first kind arises (18, 19, 20, 21, 22). The "first kind" denotes that the first polymer synthesized forms the network (Figure 5A). A semi-IPN of the second kind denotes that the first synthesized polymer is linear and the second synthesized polymer is crosslinked (23-25). If polymer 1 is linear and polymer 2 is crosslinked, the structure in Figure 5B arises. In general, polymerizing 2 first and then 1, yields quite

different materials. These may be called an “inverse” syntheses. There are then four ways in which a semi-IPN can be formed from monomers 1 and 2, assuming that crosslinking and polymerization are simultaneous and that grafting occurs during the second polymerization.

If both 1 and 2 form networks, an IPN, designated as a full IPN, arises (26) as shown in Figure 6. This structure also has an inverse—that is, if 2 is synthesized first and then monomer 1 is swollen in and polymerized. A material may be considered an IPN rather than just a

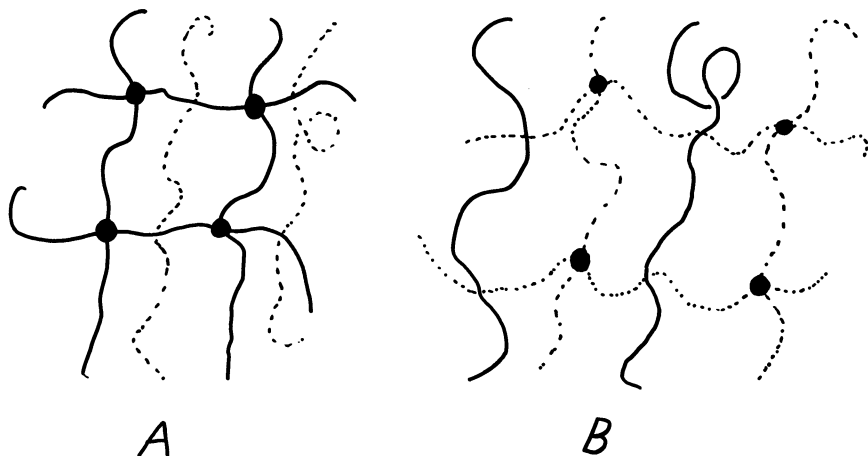


Figure 5. A schematic of semi-IPN's: A, a semi-IPN of the first kind; B, a semi-IPN of the second kind

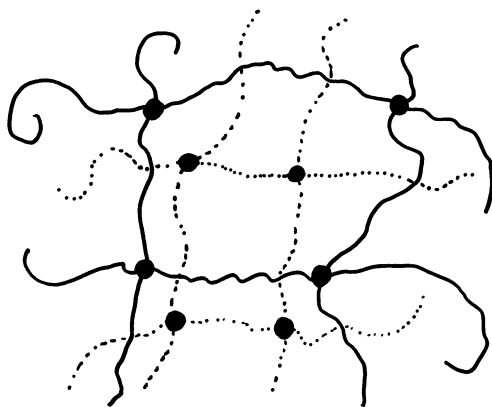


Figure 6. A schematic of a full-IPN (polymer 1 and polymer 2 are crosslinked). No graft sites are included.

graft copolymer when the intraspecies crosslinks are more numerous than the interspecies grafts and when the crosslinking is extensive enough to bind the molecules into a continuous network. If monomer 2 grafts to linear polymer 1 in such a way as to bind different polymer 1 molecules together, but not crosslink with itself, a series of AB crosslinked copolymers, sometimes called joined IPN's, arises. Simple joined IPN's are shown in Figure 7. Here we may distinguish between X-junction (27), Figure 7A and T-junction materials, Figure 7B (28), and also the inverse structures. In general, polymers with two or more of the several types of bonding may be deliberately prepared. The above polymers and a number of such combinations have already been prepared.

**Other Classification Criteria.** Other levels of classification should be superimposed on the above. These include latex, suspension, and bulk type syntheses, all of which result in different properties of the final materials. Uses of plastic-forming and elastomer-forming monomers and crystalline and amorphous structures must be distinguished. The tacticity of the polymers is sometimes important. Of course, the ratio of both polymer masses dictates the overall morphology. Physical operations such as swelling, annealing, and orienting must be considered in any complete treatment.

Another criteria for polymer blend classification involves compatibility. Although most polymer pairs are incompatible—*i.e.*, two distinct phases on a microscopic or submicroscopic level—some of the bonding modes in Figures 1–7 are truly compatible, and some exhibit semi-compatibility. Occasionally the compatibility or phase morphology can be substantially changed by selective solvent treatment or annealing. We may also distinguish between regular grafts, where substantially all the

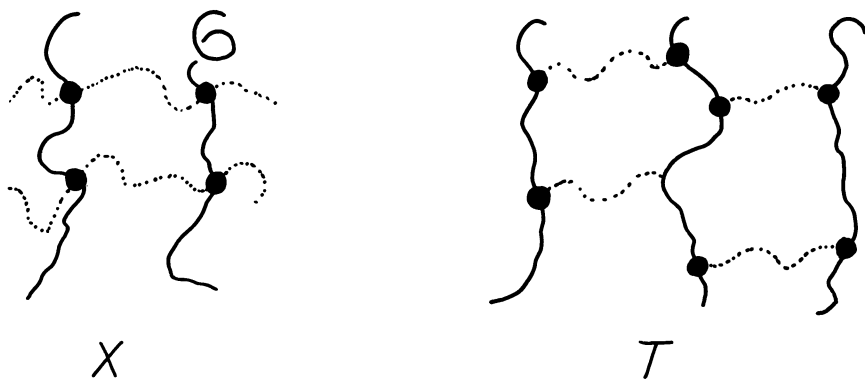


Figure 7. A schematic of AB-crosslinked polymers, or joined IPN's. X represents X-junction materials; T represents T-junction materials.

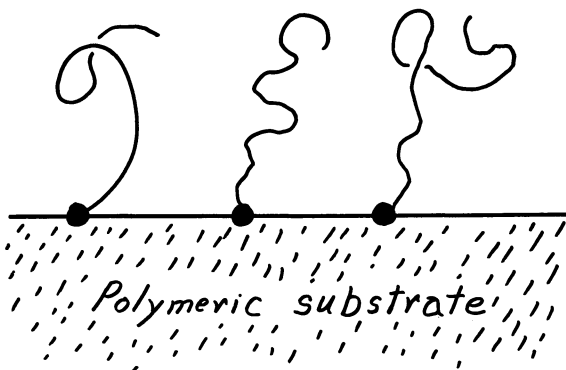


Figure 8. A schematic of a simple surface graft

molecules are grafted in some particular mode, and the irregular, occasional, or surface grafts, shown in Figure 8. Note that each of the above classifications results in significantly different and distinguishable physical and mechanical behavior. The state of the polymer and physical operations will also be discussed when necessary.

#### ***Application of Group Theory Concepts***

These descriptions are basic examples of polymer 1–polymer 2 combinations such as simple blends, grafts, blocks, and IPN's. Noting that there are over 100 distinguishable types of “graft copolymer” blends alone (14, 15), the current nomenclature is apparently inadequate; it does not adequately differentiate among the more complicated materials described in the literature, and it fails to suggest how new combinations of two or more polymer molecules might be conceived. Thus to supply a concise mathematical formulation, we use that branch of mathematics known as group theory (9, 10, 11, 12).

To form a group, four conditions must be met: (1) The set must be closed—*i.e.*, the combination of two operations also yields a member of the set. (2) The operations must include an identity which leaves the molecules unchanged. (3) The associative law of combination must hold. (4) Every operation must have an inverse.

In a formal sense, a group must meet certain criteria. Collections of sets and operations that meet some of the required criteria may meet the lesser demands of semi-groups or groupoids. The groupoids demand only a set and an operation between them (10). Conditions (1) and (3) will sometimes not be met (14, 15). Hence, even though our theory is incomplete, the definition of a groupoid most closely applies to the present study.



We consider monomer 1, monomer 2, . . . , monomer  $n$ , as basic elements which can be polymerized to form various polymers and copolymers. For the basic operations we designated P for polymerization, G for grafting, and C for crosslinking. Polymerization is assumed to be linear unless the operation C is specified. Most important, the present group is non-commutative, and the time sequence of events must be preserved; thus the order of the operations must be maintained. We found that we must increase our sensitivity to the order of the operations in more complex cases and not assume, for example, that crosslinking followed by grafting is identical to grafting followed by crosslinking.

The operations and the reactive units must be clearly distinguished. Capital and lower case letters differentiate between operations and the objects upon which the group operates. For example, the addition of monomer is designated as  $m$ . The addition of monomers which can induce grafting or crosslinking—*e.g.* divinylbenzene—are designated  $g$  and  $c$ . The operations of grafting and crosslinking, which may come much later in the reaction sequence, are specified by the capital letters. (The writer is indebted to N. W. Tschoegl of the California Institute of Technology for suggesting this notation which improves upon that (14, 15) previously used.)

Because the theory is primarily chemically oriented, we use a left-to-right notation. In mathematics the operation is written generally to the left of the symbol upon which it operates— $2X$  and  $(d/dy)X$ . Chemical notation usually reads from left to right— $HCl + NaOH = NaCl + H_2O$ . Thus  $mP$  indicates the addition of a monomer followed by its polymerization. The combination  $pC$  indicates taking a previously formed polymer and crosslinking it.

The fourth and most interesting condition needed to form a group, indicates that we should consider a series of inverse operations. Thus  $P^{-1}$  is introduced as depolymerization,  $G^{-1}$  as degrafting, and  $C^{-1}$  as decrosslinking. In this context  $C$  and  $C^{-1}$  are inverses;  $CC^{-1} = I$  where  $I$  represents the mathematical identity. In chemical terms, the reaction was reversed.

Simultaneous operations are placed in parentheses to distinguish them from sequential operations. Square brackets distinguish separate polymerizations where their products are later mixed and/or reacted. In a formal sense, the parentheses and brackets constitute operations in their own right.

The polymer molecule will be associated with the designated operation by subscripts 1, 2, etc. Thus  $P_1$  indicates polymerization of  $m_1$ . The operation  $G$  is specified by both subscripts, the order of the subscripts indicating the backbone and the branch side chain. (Identical subscripts could, of course, be used to indicate homopolymer branching.)

Grafting during polymerization that results in T-junctions is designated  $G_T$ . Post-polymerization grafting between equal partners which results in an X-junction is designated by the subscript X. Unless otherwise specified,  $G_{12}$ ,  $G_{21}$ ,  $G_{13}$ , etc., indicate T-junctions, which are more common, and  $G_X$  indicates X-junctions. To clarify multipolymer syntheses, T or X are followed by the numbers of the polymers involved. Thus  $G_{X(2,5)}$  indicates X-junction grafting between polymers 2 and 5. Again, a T-junction indicates one side chain only at the graft location, and an X-junction indicates continuity of both chains beyond the graft site (*see* A and B in Figure 2). In the general case, T- or X-junctions may be formed during or after the polymerization step, depending on the chemistry. For specialized applications, an additional symbol is the "box" (B) junction (B-junction). The B-junction will distinguish the AB-crosslinked polymers in Figure 7 from the graft copolymers in Figure 2. These grafts are designated  $G_B$ . In homopolymer nomenclature, branched and cross-linked structures are distinguished by the absence or presence of a continuous network. Introduction of this concept into graft copolymer terminology would simplify the nomenclature and eliminate the need for a specialized "B" junction. Graft copolymers could then be represented as  $G(b)$  or  $G(c)$  when necessary to distinguish between branched and crosslinked structures. While most of the graft copolymers considered herein constitute the counterpart of the branched homopolymers, it is clear that Bamford considers the crosslinked analog. In the above context, operation G is used as it is commonly designated in the graft copolymer literature regardless of the true extent of chemical grafting.

A few examples are in order. The combination

$$[m_1P_1] [m_1P_2] \quad (1)$$

represents a mixture of two linear polymers, as in a simple mechanical blend. A simple graft copolymer may be written

$$m_1P_1m_2(P_2G_{12}) \quad (2)$$

The combination

$$m_1(P_1C_1)m_2(P_2G_{12}) \quad (3)$$

refers to a simple semi-IPN of the first kind. Note that the order of the operations is important. For example,

$$m_1P_1m_2(P_2G_{12})C_1 \neq m_1(P_1C_1)m_2(P_2G_{12}) \quad (4)$$

the left side indicates a post-crosslinking operation for polymer 1; the

right side indicates that the crosslinks in polymer 1 are introduced during polymerization.

The finite collections of symbols described above are sometimes called "words." If we consider the permutations of all the operations, each considered once in a word, the number of possible structures may be arrived at. Some, of course, are physically impossible. If we add more operations, the number grows rapidly. Before assessing the total possible number of ways to prepare these materials, we include some refinements which will more clearly distinguish different subclasses of materials.

**Idempotent Operations.** A series of operations are termed idempotent (*II*) if repeating the given operation results in no further change. Thus,

$$m_1 P_1 P_1 P_1 \dots \quad (5)$$

is physically equivalent to  $m_1 P_1$  provided the  $P_1$  operations are the same. However, multifunctional monomers and polymers must be considered carefully. For example, a monomer like glycidyl methacrylate can react in two distinct ways which would need to be distinguished by proper subscripting.

**Grafting and Crosslinking Operations.** In Equations 2, 3, and 4, the grafting of polymer 2 chains to polymer 1 chains was considered simultaneous with operation  $P_2$ . The interpretation of the grafting operation can be broadened considerably, however, by also considering the addition of a monomer capable of being grafted. Thus a natural distinction arises between the introduction of grafting sites before polymerization,

$$\dots (m_n g_n) P_n \dots \quad (6)$$

the introduction of grafting during polymerization,

$$\dots P_m m_n (P_n G_{m n}) \dots \quad (7)$$

and a post-polymerization grafting (formation of ester bonds through heating, for example),

$$\dots P_m m_n P_n G_{\chi(m n)} \dots \quad (8)$$

Similarly, the crosslinking operation *C* may be broadened by also considering that it represents the addition of a monomer capable of being crosslinked in a later reaction. For example, when one of the polymers is crosslinked (semi-IPN's), the picture becomes interesting. Assuming first that  $G_{12}$  is simultaneous with  $P_2$ , as in Equation 7, a number of

different synthetic operations may still be used to prepare semi-IPN's, depending on whether a crosslinking monomer (such as divinylbenzene) is added with  $m$  or whether crosslinking is done during polymerization, as in radiation polymerization or post-polymerization cures, as with sulfur vulcanization. The subset of semi-IPN's of the first kind may be written:

$$(m_1c_1)P_1m_2(P_2G_{12}) \quad (9)$$

$$m_1(P_1C_1)m_2(P_2G_{12}) \quad (10)$$

$$m_1P_1C_1m_2(P_2G_{12}) \quad (11)$$

The corresponding subset of semi-IPN's of the second kind may be written:

$$m_1P_1(m_2c_2)(P_2G_{12}) \quad (12)$$

$$m_1P_1m_2(P_2C_2G_{12}) \quad (13)$$

$$m_1P_1m_2(P_2G_{12})C_2 \quad (14)$$

Note that by inverting the order of polymerization of 1 and 2, six additional materials may be prepared. By allowing for the various grafting possibilities (*see* Equations 6, 7, and 8), 72 possible semi-IPN's may be distinguished. If one considers semi-IPN formation without grafting (*e.g.*  $P_2$  as a condensation polymerization), 12 semi-IPN's are distinguished. Table I contains some semi-IPN, IPN, and related structures.

**Table I. Some IPN's and Related Materials**

<i>Classification</i>	<i>Description</i>	<i>Reference</i>
$m_1P_1C_1m_2(P_2G_{12})$	Semi-IPN	21
$(m_1c_1)P_1(m_2c_2)(P_2G_{12})$	IPN	24
$m_1P_1m_2(P_2G_{BT(1,2)})$	AB Crosslinked	25,26
$(m_1m_2c_1c_2)(P_1P_2G_{12}G_{21})$	SIN <sup>a</sup>	28-31
$[m_1P_1][m_2P_2]G_{BX(1,2)}$	Association Complex	22,32

<sup>a</sup> Simultaneous interpenetrating network.

In the following we add monomers capable of grafting ( $g_1, g_2, g_3, \dots, g_n$ ) or crosslinking ( $c_1, c_2, c_3, \dots, c_n$ ) and consider  $G$  and  $C$  as the operations of grafting or crosslinking. Again, remember to distinguish between capital and lower case notation.

### **Group Theory Theorems and Problems**

By understanding the theorems and mathematical relations used in group theory we can broaden our ability to synthesize polymer blends

and grafts. A theorem in group theory states that the inverse of a combination of two or more operations is equal to the combination of the inverses, in reverse order. [This theorem has broad implications in many areas of construction. For example, it gives the logical path to dismantle existing structures such as brick walls. The operation of constructing a brick wall may be written:

$$B_{11}B_{21}B_{31} \dots B_{(n-1)1}B_{n1}B_{12}B_{22}B_{32} \dots B_{nm} \quad (16)$$

where the first subscript represents the brick number within a row, and the second subscript the row number. To dismantle such a wall, the logical brick to remove first is the last brick laid,  $B_{nm}$ . Similar rules hold for houses built of cards. Removal of the cards in any but the prescribed order can result in an immediate collapse.] For the present context, this theorem relates to the decomposition of what was previously formed. Taking Equation 12 as an example,

$$[m_1P_1(m_2C_2)(P_2G_{12})]^{-1} = (P_2G_{12})^{-1}(m_2C_2)^{-1}P_1^{-1}m_1^{-1} \quad (15)$$

for the total removal of the material.

A widely used group theory operation is known as the similarity transformation. In general, if A and X are two operations of the group, then  $XAX^{-1}$  will be equal to some third operation of the group, B. This may be expressed:

$$XAX^{-1} = B \quad (17)$$

The quantities A and B are said to be conjugate. Every operation is conjugate with itself. This is always true for the trivial case where X equals the identity, E. A requirement for the similarity transform is that A and X commute, which in general is not true. Let us consider a few cases:

$$m_1m_2P_2m_1^{-1} = m_2P_2 \quad (18)$$

$m_1$  might be a monomer that does not react or a plasticizer. Upon removal of  $m_1$ , polymer 2 remains. In a broad sense, Equation 18 is not exactly true because  $m_1$  and  $m_2P_2$  do not commute, and reversing the order of the operations will not, in general, yield the same product. Although polymer morphology is not considered directly, it is obvious to the polymer chemist that the supermolecular structure of  $P_2$  (crystallinity, orientation, density, etc.) might differ. A simpler case is true, for instance,

$$m_1m_2m_1^{-1} = m_2 \quad (19)$$

Because of the commutation limitation, no important cases, within the narrow scope of the present paper, involved an operation or group of operations that yielded a well-defined, different conjugate product after undergoing the similarity transform. However, the similarity transform is widely used in the polymer industry. We may consider broadly the following useful examples:

(1.) Addition and removal of a solvent before and after polymerization (*see* Equation 18 where  $m_1$  represents the solvent).

(2.) Addition and removal of a polymerization inhibitor, as expressed by Equation 19.

(3.) In the use of shrink packaging where a polymer is oriented, wrapped around a package, and then heated to cause melting, shrinkage, and reduced orientation (*see* New Operations section, p. 174).

Group theory shows the potential strength of the inverse operations, particularly decrosslinking and degrafting, at intermediate stages in the synthesis of more complex materials. Some of these aspects were treated in detail earlier (14, 15). The use of inverse has caused some unresolved problems. For example, group theory implies that a series of operations may begin with any operation. Clearly, we may not begin a "word" with an inverse operation since this has no physical meaning. Mathematical consultants advised the writer to omit meaningless "words" which impede development of the theory. However, questions arise concerning the ability of the new theory to fit all the requirements of formal group theory. Hence the term "group theory concepts" has been used. Examination of semi-groups and groupoids reveals that the present theory fits best the definition of a groupoid (10).

### *Multi-mer Syntheses*

The previous papers (14, 15) considered polymer blends and grafts involving two polymers. At this time, we generalize the system to consider any number of monomers and polymers and the topologically distinct ways that they may be polymerized together. Consider a number ( $i$ ) of monomer units,  $m_1, m_2, m_3, \dots, m_i$ , ( $j$ ) crosslinkers,  $c_1, c_2, c_3, \dots, c_j$ , and ( $k$ ) grafting units,  $g_1, g_2, g_3, \dots, g_k$ , where the subscripts  $i, j$ , and  $k$  merely indicate numbers as large as required. The  $m$ 's,  $c$ 's, and  $g$ 's may be added as needed in any order in the following. Polymerization and related operations may then be performed.

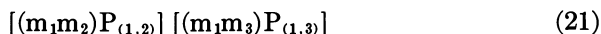
**Random Copolymers.** A simple random copolymer (36, 37) may be described:



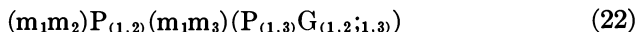
where the subscripts (1,2) on P indicate simultaneous reaction. For alternating copolymers (38, 39) the operation P may be subdivided into

P(R) and P(A) to distinguish between the random and alternating modes. As a side note, the random copolymers containing three or more monomer units that have been investigated have achieved importance in several areas—for example, in the paint industry (40).

**ABS and Related Materials.** The so-called ABS (acrylonitrile–butadiene–styrene—monomers 1, 2, and 3) materials comprise a class of compounds that consists of either blends or grafts (41). All have three monomers divided between two different polymers in a 1,2 and 1,3 combination mode. Blends of styrene–butadiene (1,2) random copolymers with styrene–acrylonitrile (1,3) random copolymers result in toughened plastics; the common-mer, styrene, improves compatibility. The material may be described:

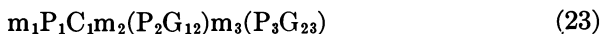


The emulsion polymerized graft copolymer, technically more important than the blend copolymer, may be written:



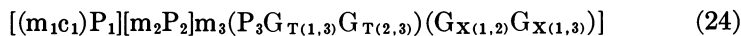
Note that latex paints (42) and materials relating to piezodialysis (24) may be composed of one copolymer in the latex and an ionic copolymer in the aqueous phase. (This last class of materials, mixtures of two polymers, was accidentally omitted from Refs. 14 and 15.)

**Multi-polymer Materials.** The literature for multi-polymer materials is extensive but is less than that for blends and grafts composed of two polymers. A ternary graft copolymer, semi-IPN is described by Rogers and Ostler (43, 44); an original crosslinked polyethylene graft–poly-(potassium acrylate) was swelled with styrene and radiation polymerized. The authors comment that most of the grafting of polymer 3 was on polymer 2, the poly(potassium acrylate). This reaction sequence can be described:



Some rather interesting, if complex, materials have been prepared by Vollmert (18). Previously we considered some of his materials composed of two polymers; now we will consider mixtures of three or more polymers. (Notations relating to mode of polymerization and state of the polymer (14, 15) are omitted for clarity.) Because the individual polymers, in most cases, are multi-mer random copolymers in their own right, one “monomer” will be considered per polymer for simplicity in the following. In his example 5, the Vollmert emulsion polymerized *n*-butyl acrylate, styrene, 1,4-butanediol monoacrylate, and 1,4-butanediol

diacrylate to form polymer 1. Separately, *n*-butyl acrylate, styrene, and acrylic acid are emulsion polymerized to form polymer 2. Polymers 1 and 2 were mixed, precipitated, washed, dried, and dissolved in styrene and acrylic acid; polymerization followed to form polymer 3. The material was then heated to induce grafting between polymers 1 and 2 and 1 and 3. The series of reactions may be written:



The T and X subscripts on G refer to T- and X-junctions. Note that  $P_1$  is crosslinked. In a similar polymerization (Vollmert's example 4) 1,4-butanediol is introduced along with monomer 3, and the last step in the synthesis involves a crosslinking of polymer 2. In his example 7, four different polymers are mixed. To conserve space, details are omitted.

In a more recent patent (45), Ryan prepared poly(*n*-butyl acrylate)/poly(methyl methacrylate) latex semi-IPN's of the first kind. These materials were then blended into linear poly(vinyl chloride) and became a ternary polymer mixture.

In a related patent (46) Amagi *et al.* synthesized a triple latex IPN. In brief, polymer 1 was a crosslinked SBR, polymer 2 was a crosslinked styrene-methyl methacrylate copolymer, and polymer 3 was a crosslinked poly(methyl methacrylate). All three were sequentially synthesized on the same latex particle. The latex material was then mechanically blended with linear poly(vinyl chloride). Also, Torvik (47) blended together four polymers that had different glass transition temperatures.

**Block Copolymers.** As illustrated in Figure 3, block copolymers represent a special kind of graft copolymer, *i.e.*, polymer  $n + 1$  is always attached at the end of polymer  $n$ . This mode of attachment will be designated as a line (L) junction. (The writer is indebted to Charles E. Rogers of Case Western Reserve University for suggesting "L-junction" nomenclature.) A simple, two-component block copolymer can then be represented by:



Note the progression in complexity and the relationships among the L-junction, the T-junction, and the X-junction that represent 2, 3, or 4 chain segments containing one or more segments of both polymer 1 and polymer 2 emanating from a graft site.

Block copolymers are sometimes prepared with several different kinds of polymers. For example, Fielding-Russell and Pillar (48) synthesized poly( $\alpha$ -methylstyrene-*b*-butadiene-*b*-styrene).

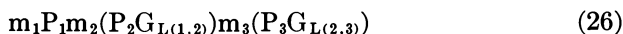




**Table II. Multicomponent Polymer Combinations**

<i>Classification</i>	<i>Description</i>	<i>Reference</i>
$m_1P_1C_1m_2(P_2G_{T(1,2)})m_3(P_3G_{T(2,3)})$ $[(m_1c_1)P_1][m_2P_2][m_3(P_3G_{T(1,3)}G_{T(2,3)})$ $(G_{X(1,2)}G_{X(1,3)})$	semi-IPN	40,41
$m_1P_1m_2(P_2G_{L(1,2)})m_3(P_3L_{(2,3)})$	block	45
$[(m_1c_1)P_1m_2(P_2G_{T(1,2)})][m_3P_3]$	semi-IPN	42
$[(m_1c_1)P_1(m_2c_2)P_2(m_3c_3)P_3][m_4P_4]$	triple-IPN	43
$[m_1P_1][m_2P_2][m_3P_3][m_4P_4]$	blend	44
$[m_1P_1][m_2P_2][m_1P_1m_2(P_2G_{L(1,2)})]$	blend	46

Kawai and Inoue (49) recently explored the mechanical blend of polystyrene/polyisoprene/poly(styrene-*b*-isoprene); polymer 1 and polymer 2 appear as both homopolymers and block components.

Although not exhaustive, the above descriptions merit appreciation. Table II summarizes additional interesting combinations containing three or more polymers.

### *New Operations*

In addition to the major operations P, G, and C, we will focus next on several new operations: chemical transformations and physical operations.

**Chemical Transformations.** Operations that modify a mer, such as saponifying poly(vinyl acetate) to poly(vinyl alcohol), should be considered. The introduction of chain transfer agents, I, which limit molecular weight, need consideration for many cases. The symbol *i* for initiator might be introduced. However, details of these operations are beyond the scope of the present work.

**Physical Operations.** Some of the physical operations ordinarily encountered in polymer processing are shown in Table III. The quantity  $A^{-1}$ , the inverse of annealing, indicates quenching. Operation S has two inverses (allowed by group theory): drying and precipitation, which need to be properly distinguished when necessary. Operation O indicates

**Table III. Physical Operations**

<i>Symbol</i>	<i>Operation</i>
S	Dissolving (solvating)
A	Annealing
O	Orienting
N	Crystallization <sup>a</sup>
Z	Blending (mechanical)

<sup>a</sup> In Refs. 14 and 15 we considered amorphous and crystalline states of matter; we now consider the transition.

polymer orientation;  $O^{-1}$  indicates disorientation or randomization of structure, *e.g.* a shrink film (50). Operation  $N$  is crystallization, and  $N^{-1}$  is melting.

Consider for example the manufacture of nylon fiber, described as:

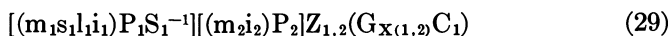


In the manufacture of graft copolymers, polymer 1 is often dissolved in monomer 2:



where the subscript 12 on  $S$  indicates "dissolve 1 in 2."

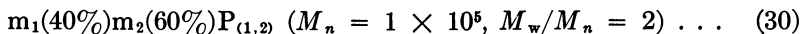
Returning to Vollmert's patent (18), we apply the more complete spectrum of operations to his example 1. In this case butyl acrylate and acrylic acid are dissolved in acetone with azoisobutyronitrile (initiator) and dodecyl mercaptan (chain transfer agent), polymerized, and the acetone is evaporated to form polymer 1. Separately, styrene and 1,4-butanediol monoacrylate are bead polymerized with benzoyl peroxide to form polymer 2. Polymers 1 and 2 are mechanically blended with the simultaneous addition of 1,4-butanediol followed by heating to promote grafting and crosslinking. These steps can be represented in some detail by:



Note that the final product is a semi-IPN. It is fairly obvious that different operations can be specified to give very great detail for the series of synthetic steps.

### **Quantitative Limitations**

The above symbolic approach to the representation and differentiation of polymer blend, graft, and IPN syntheses is largely qualitative. Operations such as  $P$  do not suggest the final molecular weight or molecular weight distribution,  $G_{12}$ , the actual extent of grafting, or  $A$  the annealing times and temperatures; all are obviously important to the final product. Although this paper and a previous work (14, 15) originated from the need to classify the numerous graft copolymers and to suggest a means of systematically synthesizing new materials, a word should be said about quantitative aspects. The exact conditions can be specified by the use of parentheses following the operation. For example,



can specify some of the details. A user of this group theory application may wish to keep the notation as simple and as brief as possible, consistent with his needs.

Other important factors include monomer sequence distribution, distribution of graft and crosslink sites along the chains, the occurrence of branching *per se*, and the general phenomena of side reactions. In addition, stirring rate, the detailed post-reaction "workup" procedure, the temperature history, subsequent processing and fabrication conditions, etc. must be considered since these have major effects on the nature of the product.

This presentation is limited, of course, to the major chemical and physical steps that determine the end product. The major emphasis is to describe the different topological ways in which two or more polymers can be placed in juxtaposition and is not intended as a comprehensive study of all possible variables.

### Reaction Networks

In the previous paper (14, 15), the problem of counting the total number of distinguishable blends, grafts, and IPN's was briefly considered. Limiting each operation combination arbitrarily to two identical sequences resulted in a finite, countable number of materials.

An alternate approach for counting the minimum number of distinguishable combinations generated with any specified set of restraints has been developed by Sellers (51, 52). For certain complex reactions, such as biochemical processes, a number of possible mechanisms may be involved. Sellers writes:

$$\mu = \rho - \sigma + K + 1 \quad (31)$$

where  $\mu$  represents the maximum number of linearly independent mechanisms for a given reaction;  $\rho$  is the number of elementary reactions;  $\sigma$  is the number of species, and  $K$  the number of components. Equation 31 is reminiscent of the Gibbs phase rule, and the quantities enumerated are the minimum number required to specify the material.

In the present case  $\mu$  indicates the maximum number of distinguishable topologies. Taking the operations required to form a semi-IPN, which specifies one linear and one crosslinked polymer, we have three elementary operations, P, G, and C, and m, which sometimes bears characteristics of an operation ( $\rho$ ); two species, polymer 1 and polymer 2, ( $\sigma$ ), and one independent degree of freedom, ( $K$ ). Specification of one of the polymer structures (*i.e.*, crosslinked) specifies the other. This predicts:

$$4 - 2 + 1 + 1 = 4 \quad (32)$$

The four materials are: (1) polymer 1 linear and polymer 2 crosslinked; (2) polymer 1 crosslinked and polymer 2 linear; (3) and (4) are obtained by interchanging polymers 1 and 2. In each case the second polymerized material is grafted to the first polymerized material. Equations 9–14 and the related discussion result in 72 possibilities. The difference lies in the counting or omission of the time sequence of events. The reaction network scheme does not consider the importance of the time-order of events. Thus Equation 31 yields the minimum number of distinguishable materials.

### *Acknowledgment*

This paper is dedicated to my friend, Murray Jelling, who through his association with Research Corp. and patent matters literally drove me off a cliff to find a quantitative way to distinguish among the many IPN and related structures.

### *Literature Cited*

1. "Block and Graft Copolymerization," Vol. 1, R. J. Ceresa, Ed., Wiley, New York, 1973.
2. "Block and Graft Copolymers," J. J. Burke, V. Weiss, Eds., Syracuse, 1973.
3. "Block Polymers," S. L. Aggarwal, Ed., Plenum, New York, 1970.
4. "Colloidal and Morphological Behavior of Block and Graft Copolymers," G. E. Molau, Ed., Plenum, New York, 1971.
5. *ADVAN. CHEM. SER.* (1971) 99.
6. *ADVAN. CHEM. SER.* (1975) 142.
7. "Recent Advances in Polymer Blends, Grafts, and Blocks," L. H. Sperling, Ed., Plenum, New York, in press.
8. Manson, J. A., Sperling, L. H., "Polymer Blends and Composites, Broadly Defined," Plenum, New York, in press.
9. Cotton, F. A., "Chemical Applications of Group Theory," 2nd ed., Wiley-Interscience, New York, 1971.
10. Baumslag, B., Chandler, B., "Theory and Problems of Group Theory," Chap. 2, McGraw-Hill, New York, 1968.
11. Bruck, R. H., in "Studies in Modern Algebra," Vol. 2, A. A. Albert, Ed., The Mathematical Association of America.
12. Artin, E., *Amer. Scientist* (1950) 38, 112.
13. Sperling, L. H., *Fibre Sci. Technol.* (1974) 7, 199.
14. "Recent Advances in Polymer Blends, Grafts, and Blocks," L. H. Sperling, Ed., Plenum, 1974.
15. Sperling, L. H., *Polym. Preprints* (1973) 14 (2) 958.
16. Kennedy, J. P., in "Recent Advances in Polymer Blends, Grafts, and Blocks," L. H. Sperling, Ed., Plenum, 1974.
17. Allen, P. V., Ayrey, G., Moore, C. G., Scanlan, J., *J. Polym. Sci.* (1959) 36, 55.
18. Vollmert, B., U.S. Patent 3,005,859 (1962).
19. Cuddihy, E. F., Moacanin, J., Walmsley, D. E., *Polym. Preprints* (1970) 11, No. 2, 498.

20. Allen, G., *et al.*, *Polymer* (1973) **14**, 597, 604.
21. *Ibid.* (1974) **15**, 13, 19, 28, 33.
22. Hatch, M., Dillon, J., Smith, H., *Ind. Eng. Chem.* (1957) **49**, 1812.
23. Donatelli, A. A., Thomas, D. A., Sperling, L. H., in Ref. 7.
24. Leitz, F. B., Sharr, J., "Research on Piezodialysis—Third Report to the Office of Saline Water, Report No. 775, May 1972.
25. Odian, G., Bernstein, B. S., *Nucleonics* (1963) **21**, 80.
26. Huelck, Volker, Thomas, D. A., Sperling, L. H., *Macromolecules* (1972) **5**, 340, 348.
27. Sperling, L. H., Sarge III, H. D., *J. Appl. Polym. Sci.* (1972) **16**, 3041.
28. Bamford, C. H., Eastmond, G. C., Whittle, D., *Polymer* (1971) **12**, 247.
29. Noshay, A., Robeson, L. M., *J. Polym. Sci., Part A-1* (1974) **12**, 689.
30. Frisch, K. C., Frisch, H. L., Klempner, D., German Patent **2,153,987** (1972).
31. Frisch, K. C., *et al.*, *J. Appl. Polym. Sci.* (1974) **18**, 683, 689.
32. Touhsaent, R. E., Thomas, D. A., Sperling, L. H., *J. Polym. Sci.* (1974) **46C**, 175.
33. Sperling, L. H., Arnts, R. R., *J. Appl. Polym. Sci.* (1971) **15**, 2371.
34. Eisenberg, A., King, M., *Macromolecules* (1971) **4**, 204.
35. Eisenberg, A., King, M., *Rubber Chem. Technol.* (1972) **45**, 908.
36. Battaerd, H. A. J., Tregear, G. W., "Graft Copolymers," Chap. 2, Interscience, New York, 1967.
37. Ceresa, R. J., "Block and Graft Copolymers," Nomenclature Section, Butterworths, London, 1962.
38. Furukawa, J., *Bull. Japan Petrol. Inst.* (1970) **12**, 40.
39. Furukawa, J., Iseda, Y., Kobayashi, E., *Polymer* (1971) **2**, 337.
40. Edwards, W. M., in "Technology of Paints, Varnishes, and Lacquers," Chap. 9, C. R. Martens, Ed., Reinhold, New York, 1968.
41. Kato, K., *Japan Plastics* (April, 1968) **2**, 6.
42. Martens, C. R., "Emulsion and Water-Soluble Paints and Coatings," Reinhold, New York, 1964.
43. Rogers, C. E., Ostler, M. I., *Amer. Chem. Soc., Div. Polym. Chem., Preprints* (1973) **14** (1), 587.
44. Rogers, C. E., Kupka, B., Yamada, S., Ostler, M. I., *Amer. Chem. Soc., Div. Coatings Plast., Preprints* (1974) **34** (1), 485.
45. Ryan, C. F., U.S. Patent **3,678,133** (1972).
46. Amagi, Y., Ohya, M., Shuki, Z., Yusa, H., U.S. Patent **3,671,610** (1972).
47. Torvik, P. J., *Tech. Rept., AFIT, TR71-2*, Wright Patterson Air Force Base, Ohio, May 1971.
48. Fielding-Russell, G. S., Pillar, P. S., *Polymer* (1974) **15**, 97.
49. Kawai, H., Inoue, T., *Japan Plast.* (July 1970) **4**, 12.
50. Rodriguez, F., "Principles of Polymer Systems," Chap. 12, McGraw-Hill, New York, 1970.
51. Sellers, P. H., *J. Franklin Inst.* (1970) **290**, 113.
52. Sellers, P. H., *SIAM J. Appl. Math.* (1967) **15**, 13.

RECEIVED October 21, 1974. Work supported by the National Science Foundation through grant GH-40645.

## Quantitative Studies of Toughening Mechanisms in ABS and ASA Polymers

C. B. BUCKNALL, C. J. PAGE, and V. O. YOUNG

Cranfield Institute of Technology, Cranfield, Bedford MK43 OAL, England

*The kinetics and mechanisms of tensile deformation in ASA and ABS polymers were studied using high accuracy creep tests. Crazeing was detected by volume strain measurements. In both polymers, creep of compression-molded specimens is caused mainly by crazeing, with shear processes accounting for less than 20% of the total time-dependent deformation. Crazeing is associated with an increasing creep rate and a substantial drop in modulus. The effects of stress upon creep rates are described by the Eyring equation, which also offers an explanation for the effects of rubber content upon creep kinetics. Hot-drawing reduces creep rates parallel to the draw direction and increases the relative importance of shear mechanisms.*

Acrylonitrile–butadiene–styrene (ABS) and acrylonitrile–styrene–acrylate (ASA) are rubber-toughened plastics based upon the styrene–acrylonitrile (SAN) copolymer matrix. The combination of the stiffness and toughness exhibited by these materials has made them increasingly attractive in engineering applications, and the activity of the patent literature testifies to a continuing interest in improving properties through modifications of structure. The aim of this paper is to discuss a quantitative approach to structure-property relationships in ABS and ASA polymers.

Electron microscope studies have shown that the toughness of ABS polymers is caused largely by multiple craze formation (1, 2). The rubber particles appear both to initiate and to control craze formation, so that impact energy is dissipated in the production of numerous small crazes (3). However, this theory does not exclude the possibility of contributions from other mechanisms. The observation that many ABS polymers tend to neck during a tensile test suggests that shear mechanisms are also significant.

The first quantitative study of deformation mechanisms in ABS polymers was made by Bucknall and Drinkwater, who used accurate extensometers to make simultaneous measurements of longitudinal and lateral strains during tensile creep tests (4). Volume strains calculated from these data were used to determine the extent of craze formation, and lateral strains were used to follow shear processes. Thus the tensile deformation was analyzed in terms of the two mechanisms, and the kinetics of each mechanism were studied separately. Bucknall and Drinkwater showed that both crazing and shear processes contribute significantly to the creep of Cyclic T—an ABS emulsion polymer—at room temperature and at relatively low stresses and strain rates.

The same techniques were used in the present work to study the effects of orientation and rubber content upon the creep behavior of rubber-toughened SAN polymers at room temperature. As in previous work, the tests were conducted at low strain rates and were terminated at longitudinal strains between 5 and 6%.

### Experimental

Two ASA polymers were studied: Luran S 757R and Luran S 776S; both were made by BASF. The polymers have similar SAN matrices but respectively contain *ca.* 30 and 40% of the acrylic rubber-toughening agent. The ABS polymer (ABS 500) was made by the Dow Chemical Co. It contained SAN-filled rubber particles *ca.* 1.0  $\mu\text{m}$  in diameter, suggesting that it was manufactured by bulk or suspension polymerization.

Dumbbell creep specimens with a parallel gage portion 40 mm long and 5 mm wide were milled from compression-molded sheet. Some of the ABS sheets were subjected to uniaxial hot-drawing at 116°C, and creep specimens were cut parallel to the draw direction. Creep tests were carried out at  $20^\circ \pm 0.5^\circ\text{C}$  using high accuracy lever-loading creep rigs developed by Darlington and Saunders (5) (*see* Figure 1).

Longitudinal strain  $e_3$  was measured in the central 20 mm of the specimen, and lateral strain  $e_1$  was measured simultaneously at the center of the gage portion;  $e_1$  is usually negative in a tensile test. The lateral strain  $e_2$  was not measured. In the calculations all specimens, including those cut from a drawn sheet, were assumed to be transversely isotropic—*i.e.*,  $e_1 = e_2$ . On the basis of this assumption the volume strain  $\Delta V/V$  was calculated from the expression:

$$\Delta V/V = (1 + e_3) (1 + e_1)^2 - 1 \quad (1)$$

Each long-term creep test was preceded by a loading-unloading program at successively increasing loads in order to obtain a 100 sec isochronous curve of tensile creep modulus against a 100 sec longitudinal strain within the low strain region. During this preliminary program stress levels were kept well below those used for long term testing. Long-term tests were terminated when  $e_3$  was *ca.* 5%; the specimen was then unloaded and allowed to recover. The unloading program was then re-

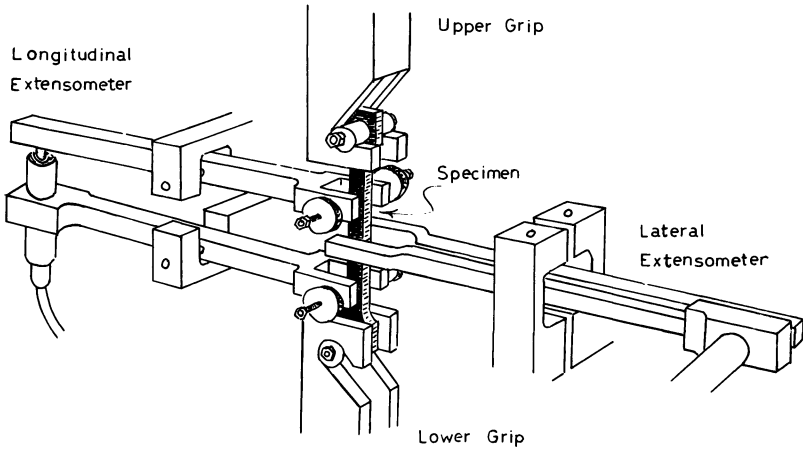


Figure 1. Darlington-Saunders creep apparatus

peated in order to obtain another 100 sec isochronous curve, to illustrate the effects of creep history on the polymer.

### Results

**ASA Polymers.** Creep tests were performed on Luran S 757R at stresses from 19–26 MN/m<sup>2</sup>. Over this range, the time to reach 5% ex-

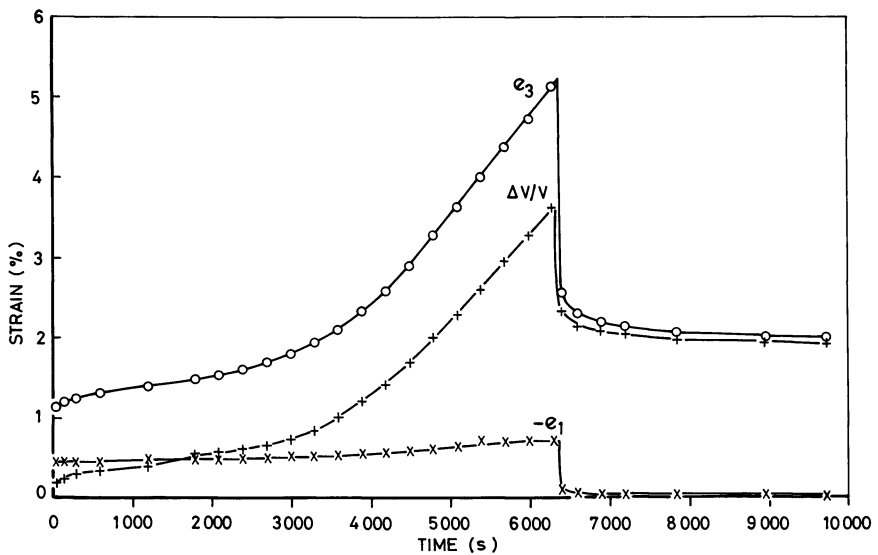


Figure 2. Creep and recovery of ASA polymer Luran S 757R: stress = 20 MN/m<sup>2</sup>



tension varied from 12,700 to 40 sec. A typical set of results is shown in Figure 2. The creep rate is low initially but increases at a strain of *ca.* 2% and then becomes approximately constant. After the initial deformation, the lateral strain  $-e_1$  changes comparatively slowly, whereas the volume strain  $\Delta V/V$  changes in a manner similar to that of the longitudinal strain  $e_3$ .

The creep behavior of Luran S 776S is similar to that of 757R, except that creep rates are higher. Tests were made at stresses between 19 and 24 MN/m<sup>2</sup>; the times to reach 5% extension varied from 4700 to 20 sec. Increased creep rates are to be expected in view of the higher rubber content of the polymer.

Elastic and viscoelastic deformation, crazing, and shear band formation all contribute to the tensile creep of rubber-toughened plastics. In order to separate the contributions of these various mechanisms, certain assumptions are needed. In the following analysis, it is assumed that the volume strain measured in the specimen at the time of the first strain determination is caused entirely by the elastic and viscoelastic response of the polymer to the hydrostatic component of stress and that all subsequent volume changes are caused by crazing. The duration of the creep tests is long compared with the time at which the first strain measurements are made, and the observed kinetics of crazing strongly suggest that very little crazing occurs during this initial period. The subsequent time-dependent volume changes are very large and can be explained only in terms of craze formation. Generalized volume relaxation effects, and any volume changes that might be associated with shear band formation, can be neglected. In support of this statement, it should be noted that creep occurs at constant volume in Cyclocac T grade ABS under a tensile stress of 26.5 MN/m<sup>2</sup> (4). At this stress, the polymer reaches a strain of 5% by elastic deformation and time-dependent shear processes only, showing no visible evidence of crazing and no further volume change after the initial elastic response to loading.

In discussing shear deformation, it is convenient to distinguish between the initial elastic and viscoelastic response of the polymer to the applied load and the subsequent time-dependent response. However, the distinction is somewhat arbitrary and is not as fundamental as that between elastic volume response and crazing. Viscoelastic shear deformation continues throughout the period under load. The observed time-dependence of lateral strain reflects both generalized viscoelastic relaxation and shear band formation. Since crazing consists simply of displacement in the tensile stress direction, it makes no contribution to lateral strain; therefore  $-e_1$  specifically measures deformation by shear processes.

The most convenient way to analyze the contributions of crazing and shear processes to creep is to plot the volume strain recorded at any given stage of the creep test against the corresponding longitudinal strain as shown for Luran S 757R in Figure 3. The slopes of the lines are 0.85 at 19 MN/m<sup>2</sup> and 0.89 at 22 MN/m<sup>2</sup>, indicating that crazing is responsible for 85–90% of the time-dependent part of the creep. If there were no contribution from crazing, the slope would be zero, whereas if crazing were the only deformation mechanism operating during the period of the measurements, the slope would be unity. Results for Luran S 776S are similar to those obtained for 757R.

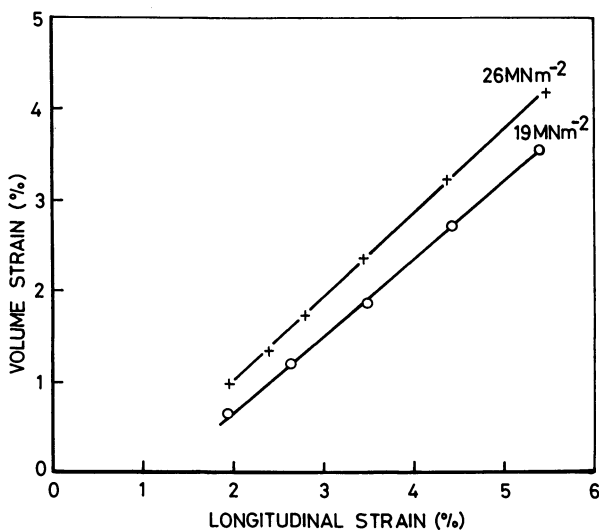


Figure 3. *Creep mechanisms in Luran S 757R*

Earlier work (4, 6) demonstrated that a high gradient in the volume strain–longitudinal strain curve is associated with a large drop in the modulus of the material. This is to be expected, as the crazes have much lower moduli than the material from which they were formed (7). As a result of the creep tests described above, the 100 sec tensile modulus of Luran S 757R at a strain of 0.5% fell from 1.99 to 1.30 GN/m<sup>2</sup>, and the modulus of Luran S 776S at a similar strain fell from 1.65 to 0.98 GN/m<sup>2</sup>.

The effect of stress upon the kinetics of crazing can be represented by two rate quantities obtainable from the creep data. The linear portion at the end of the volume strain–time curve defines a maximum rate of crazing,  $\frac{d}{dt} \frac{\Delta V}{V}_{\max}$ , and the beginning of this period of rapid creep defines

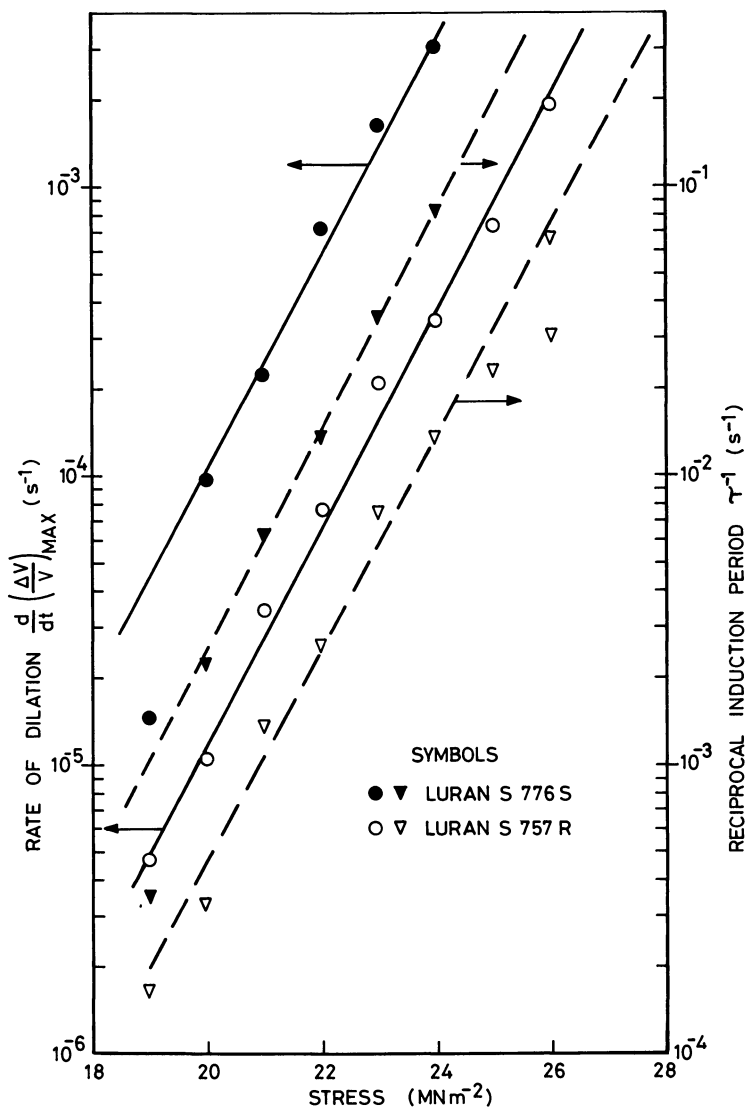


Figure 4. Eyring relationships for crazing

an induction period,  $\tau$ . Graphs of the logarithms of the maximum rate and of reciprocal induction period against stress are linear over the range of stresses used. This agrees with the Eyring equation:

$$\dot{\epsilon} = A \exp(\gamma v \sigma / kT) \quad (2)$$

where  $\dot{\epsilon}$  is the rate,  $A$  is a constant,  $\gamma$  is a stress concentration factor,  $v$  is the activation volume,  $\sigma$  is the stress,  $k$  is Boltzmann's constant, and

$T$  is the absolute temperature. These plots are shown in Figure 4 for both ASA polymers. Both rate quantities give approximately the same value, *ca.*  $3500\text{\AA}^3$ , for the apparent activation volume  $\gamma v$  for both polymers.

A similar graph can be plotted for the maximum lateral strain rate  $d/dt (-e_1)$  (see Figure 5); this gives an apparent activation volume of *ca.*  $3000\text{\AA}^3$  for the shear processes in both ASA polymers.

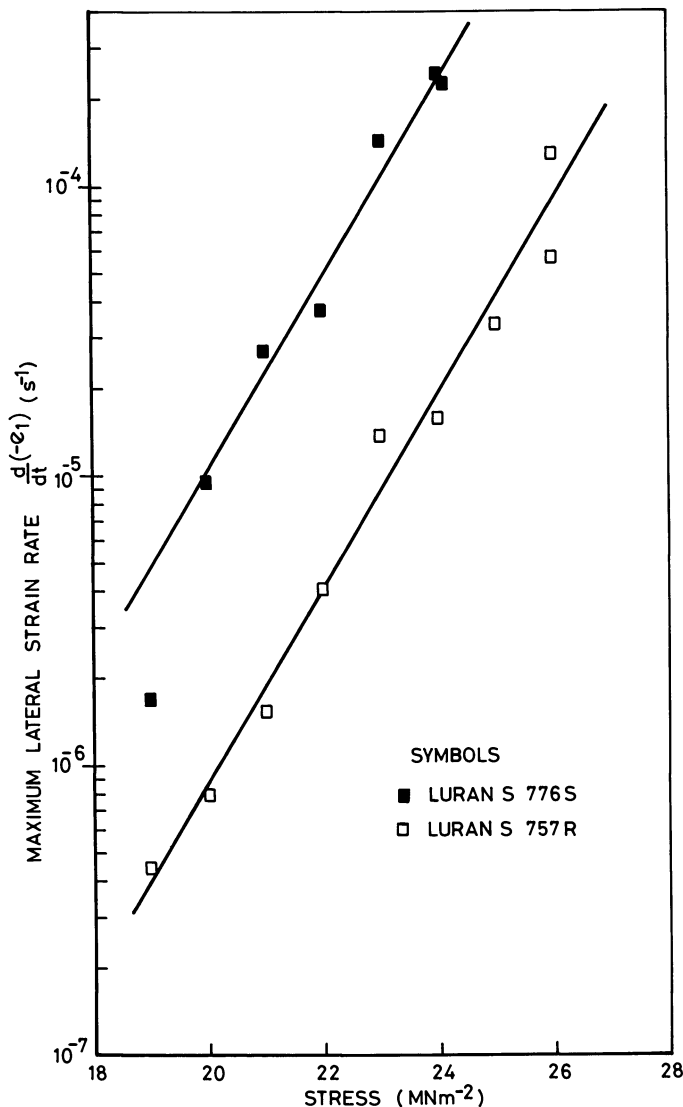


Figure 5. Eyring relationships for shear deformation

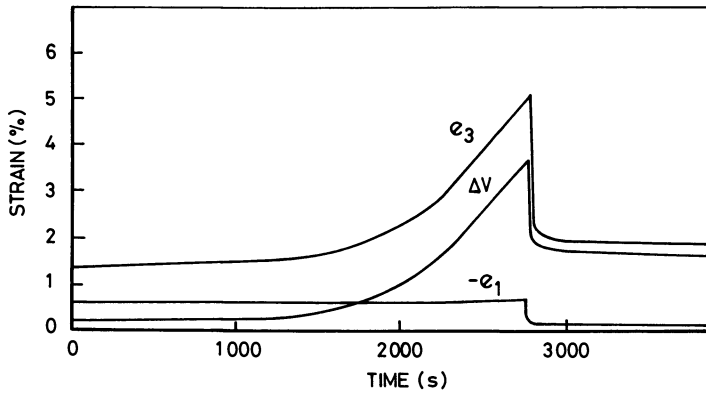


Figure 6. Isotropic Dow 500 ABS: creep at  $30.0 \text{ MN/m}^2$  and recovery

**Isotropic ABS Polymer.** Isotropic Dow 500 ABS polymer has the same general creep characteristics as the ASA polymers described above. Some typical results are shown in Figure 6. The longitudinal strain  $e_3$  increases relatively slowly at first, but then accelerates at a strain of *ca.* 2% and becomes approximately linear with time. Apart from the initial elastic response, most of the deformation is caused by crazing: the volume strain follows the same pattern as the longitudinal strain while the lateral strain remains almost constant throughout the test. The relationship between the volume strain and the longitudinal strain (*see* Figure 7) reinforces the conclusion that the creep of this grade of ABS polymer

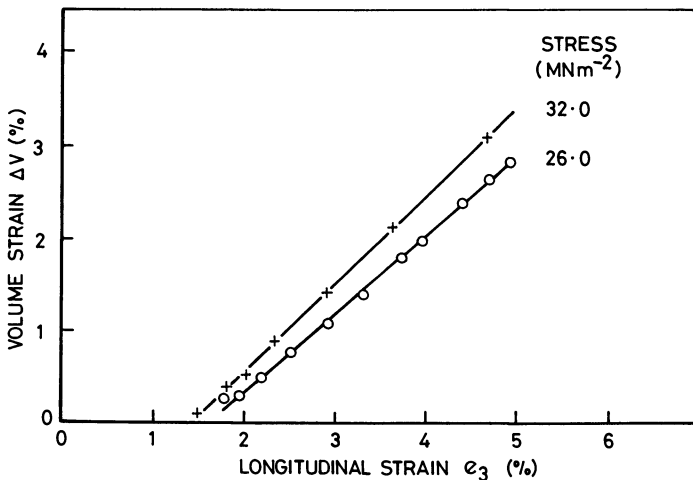


Figure 7. Creep mechanisms in isotropic Dow 500 ABS

is dominated by crazing. The slopes of the lines in Figure 7 are 0.84 at 26 MN/m<sup>2</sup> and 0.96 at 32 MN/m<sup>2</sup>. On unloading, the longitudinal strain falls to *ca.* 2%: the recovery, like the creep, is dominated by the volume strain associated with crazing. Again the formation of numerous crazes reduces the modulus. The 100 sec tensile modulus at 1% strain fell from 2.5 to 1.0 GN/m<sup>2</sup> as a result of the creep test.

**Hot-Drawn ABS Polymer.** Draw ratios were varied between 1.0 and 2.9. In order to determine the extent of orientation produced during drawing, specimens were sectioned and etched: the shapes of the initially spherical rubber particles are a measure of orientation (8). In general, the effective draw ratios calculated from particle shapes were close to the actual draw ratios.

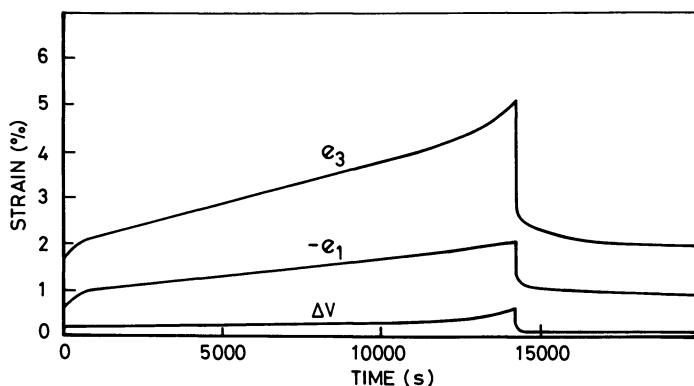


Figure 8. Hot-drawn Dow 500 ABS: draw ratio 1.8; creep at 42.0 MN/m<sup>2</sup> and recovery

With increasing draw ratio the pattern of creep behavior changed in three ways. Firstly, the creep rate at a given stress decreased, and it was necessary to use increasingly higher stresses in order to complete the experiments. Secondly, shear mechanisms made an increasingly important contribution to creep, and crazing became correspondingly less important. Thirdly, the relative importance of crazing and shear processes became more dependent upon stress level at any given draw ratio.

The increased contribution from shear processes causes a change in the shape of the creep curves. Whereas creep rates caused by crazing tend to increase during the test, rates of shear deformation tend to decrease or to remain constant. Thus with increasing draw ratio the upturn in the creep curves gradually disappears. This point is illustrated in Figure 8 which presents results obtained at a draw ratio of 1.8. Volume strain is almost constant for most of the test, showing only a small increase during the final stages, which is reflected in a slight upturn in the curve

of longitudinal strain *vs.* time. The main contribution to creep comes from shear processes; consequently the creep rate is almost constant. Unrecovered shear processes are largely responsible for the strains observed during the recovery stage of the test.

The change in mechanism with stress at an intermediate draw ratio of 1.47 is illustrated in Figure 9. At all three of the stresses studied there is little evidence of crazing until 2.2% strain. In the higher strain region, above 3% elongation, the contribution of crazing to creep increases with stress level. A similar increase in the importance of crazing with increasing stress is also observed at the higher draw ratios. By contrast, at a draw ratio of 1.24 crazing is the only significant deformation mechanism, and there is no change with stress.

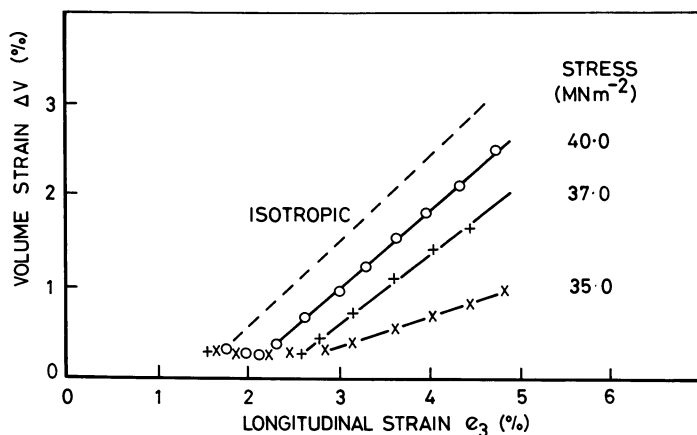


Figure 9. Creep mechanisms in Dow 500 ABS: draw ratio 1.47

The loss of modulus caused by crazing becomes less pronounced as the draw ratio is increased, especially in tests carried out at lower stress levels. This observation supports earlier conclusions drawn from creep studies on other rubber-toughened plastics (6): if the specimen can reach a strain of 5% largely or entirely by shear mechanisms, the loss of modulus resulting from the creep and recovery program is quite small; if, on the other hand, crazing is the dominant mechanism, the loss in modulus is large.

### Discussion

The creep behavior of the isotropic ASA and ABS polymers is similar to that previously reported for HIPS (9). The time-dependent part of the deformation is dominated by crazing which begins slowly, accelerates,

and reaches a steady high rate. This pattern of behavior can be represented by a simple model in which crazes are initiated at a constant rate, are propagated linearly at a constant rate from one rubber particle to a near neighbor, and are terminated when they meet the neighboring particle (9). According to this model the rate of crazing is constant when the rate of termination is equal to the rate of initiation. At this stage the population of active (propagating) crazes reaches a stable number and size distribution. Once this condition is fulfilled, the rate of craze termination (and therefore of craze initiation) controls the rate of increase in the total amount of craze material. Therefore the maximum rate of crazing is a measurement of the rate of initiation of crazes.

The reciprocal induction period  $\tau^{-1}$ , on the other hand, measures the rate of propagation of crazes. During the early stages of creep, there is no termination. New crazes are initiated, and existing ones grow so that the total rate of crazing increases. This period of acceleration ends when some of the crazes are large enough to terminate on reaching the rubber particles towards which they are propagating. Increasing the rate of propagation of crazes shortens this period—there is an inverse relationship between propagation rate and induction period.

Over the stress range studied the difference in rubber content between the two ASA polymers causes a difference of approximately a factor of 10 between the materials in all three rate quantities—*viz.*, maximum rate of crazing, reciprocal induction period, and rate of shear. There are at least two contributing factors. Firstly, at any given applied stress the stress concentrations around each individual rubber particle are higher at higher rubber contents. Secondly, the material that has more rubber particles contains more initiation sites for crazes and shear bands. Referring to the Eyring equation, the first factor affects the stress concentration parameter  $\gamma$ , whereas the second affects the pre-exponential factor  $A$ .

In principle, the effect of rubber content upon  $\gamma$  can be determined from the differences in apparent activation volume  $\gamma v$  obtained from Figure 4, since the true activation volume should be the same for both materials. In practice, the scatter in the results reduces the reliability of the estimate in the present work.

Stress concentrations around isolated spherical inclusions in an isotropic matrix have been calculated by Goodier (10), but apparently there is no satisfactory theory for the problem of concentrated dispersions. A simple approach would be to use Goodier's equation and to allow for the effect of the high concentration of rubber particles simply by adding the calculated stress concentrations that arise from neighboring particles.

Further work is required in this area. Preliminary examination suggests that the data presented in Figures 4 and 5 for the two ASA poly-



mers can be superposed by applying a scaling factor, related to  $\gamma$ , to the stress axis, together with a vertical shift to account for the difference in concentration of craze or shear band initiation sites. The rate of crazing is not related simply to the number of rubber particles, however, as the amount of crazed material generated from each initiation event becomes smaller as the interparticle spacing is reduced.

Over most of the stress range, the amount of shear deformation occurring in the ASA polymers is too small to affect the rate of crazing, but there are signs of some interaction at lower stresses, particularly in Lurans 776S at 19 MN/m<sup>2</sup>. At these lower stresses, the rates of crazing and reciprocal induction periods are lower than expected from an extrapolation of the line through the data for higher stresses. This type of interaction has already been noted in other rubber-toughened polymers (11).

An interaction between crazes and shear bands is also suggested in the data for drawn ABS. As the draw ratio increases, the rates of crazing and of shear deformation observed at any given applied stress drop. Both factors contribute to the fall in overall creep rate. The net effect is to increase the relative importance of shear deformation. Highly drawn ABS polymer reaches 5% strain without significant craze formation. This result agrees with previous observations that crazing is suppressed in highly drawn material. The interaction between crazes and shear bands has a similar origin—crazes do not propagate readily through the oriented polymer constituting a shear band. In hot-drawn ABS, rates of crazing are low both because of the difficulty of initiating and propagating crazes in the oriented SAN matrix and because the progressive formation of sheared zones during the creep experiment further hinders craze propagation.

### **Conclusion**

The results indicate how quantitative creep studies can help in understanding structure–property relationships in rubber-toughened plastics. This understanding is of value both to the materials scientist in developing improved materials, and to the engineer, in selecting and using toughened polymers. The data of most interest to the engineer are probably those presented in Figures 4 and 5 showing both the time  $\tau$  for the start of rapid crazing and the rate of shear deformation as functions of applied stress. The effects of orientation are also important. Since crazing leads to a major drop in modulus, the increasing participation of shear mechanisms in deformation, as the draw ratio is increased, leads to a reduction in the extent of strain damage under load.

Although the present study covers a range of strain rates, it is essentially restricted to slow tensile deformations. However the main interest in rubber-toughened plastics centers upon their behavior at high rates of strain, especially under impact loading, and the logical extension of the work involves applying the same techniques to deformation at very high rates of strain. It is difficult to measure strain accurately at higher strain rates, but considerable progress has been made in solving this problem. Both Cessna (12) and Fenelon and Wilson (13) measured volume changes in ABS during the tensile impact test by marking a grid on the specimen and recording longitudinal and lateral strains with a high-speed movie camera. Their results show that the crazing and shear deformation mechanisms observed at low strain rates also operate under impact loading. There is clearly scope for further work in this area.

### *Acknowledgments*

The authors thank the Science Research Council for a grant in support of this work, the Dow Chemical Co. for the gift of ABS, and BASF for the gift of ASA.

### *Literature Cited*

1. Matsuo, M., *Polymer* (1966) **7**, 421.
2. Michler, G., Gruber, K., Pohl, G., Kaestner, G., *Plaste Kautsch.* (1973) **20**, 756.
3. Bucknall, C. B., Street, D. G., *J. Appl. Polym. Sci.* (1968) **12**, 1311.
4. Bucknall, C. B., Drinkwater, I. C., *J. Mater. Sci.* (1973) **8**, 1800.
5. Darlington, M. W., Saunders, D. W., *J. Phys.* (1970) **E3**, 511.
6. Bucknall, C. B., Clayton, D., Keast, W. E., *J. Mater. Sci.* (1973) **8**, 514.
7. Kambour, R. P., Kopp, R. W., *J. Polym. Sci. A2* (1969) **7**, 183.
8. Bucknall, C. B., Drinkwater, I. C., Keast, W. E., *Polymer* (1972) **13**, 115.
9. Bucknall, C. B., Clayton, D., *J. Mater. Sci.* (1972) **7**, 202.
10. Goodier, J. N., *Trans. ASME* (1933) **55**, 39.
11. Bucknall, C. B., Clayton, D., Keast, W. E., *J. Mater. Sci.* (1972) **7**, 1443.
12. Cessna, L. C., *Polym. Eng. Sci.* (1974) **14**, 696.
13. Fenelon, P. J., Wilson, J. R., *Amer. Chem. Soc., Div. Org. Coatings Plastics Chem., Preprint 34* (2), 326 (1974).

RECEIVED October 18, 1974.

## The Role of Rubber Modification in Improving High Rate Impact Resistance

MARGARET E. ROYLANCE

Army Materials and Mechanics Research Center,  
Watertown, Mass. 02172

DAVID K. ROYLANCE and JACQUES N. SULTAN

Massachusetts Institute of Technology,  
Cambridge, Mass. 02139

*Prediction of response of a material to high rate impact involving wave propagation effects such as spallation requires computer analysis utilizing accurate mechanical property data. The rate sensitivity of these properties is significant in polymeric materials and must be characterized in an accurate model. Since rubber modification can suppress spallation, markedly improving high rate impact resistance, the rate and temperature sensitivity of the yield stress of a promising series of rubber modified acrylics was characterized as a function of rubber content. Apparent activation parameters were determined to elucidate the nature of the flow process. The yield criteria obtained help to explain the occurrence of a maximum in impact resistance with increasing rubber content and may be used in computer analysis to predict detailed response to impact.*

The use of polymeric materials to protect against high rate particle and projectile impacts is extensive and increasing rapidly. Since polymeric materials combine light weight with actual or potential transparency, their use in these applications is natural. However, the detailed nature of the response of polymeric materials to this type of impact (*i.e.*, impact conditions involving microsecond interaction times as compared with second interaction times in quasistatic loading or millisecond interaction time in conventional Izod impact loading) is not well understood. These differences arise from two sources. The first is the general rate sensitivity

of the mechanical properties of polymers, and the quantification of this rate sensitivity could explain several observed differences between Izod impact and high rate projectile impact (1). Another factor is the influence of such wave propagation effects as spallation which become important as the velocity of impact becomes comparable with the velocity of propagation of stress waves through the material. Spallation is discussed later in greater detail.

Analysis of these effects is difficult and time consuming. Much recent work has utilized two-dimensional, finite-difference computer codes which require as input extensive material properties, *e.g.*, yield and failure criteria, and constitutive laws. These codes solve the equations of motion for boundary conditions corresponding to given impact geometry and velocities. They have been widely and successfully used to predict the response of metals to high rate impact (2), but extension of this technique to polymeric materials has not been totally successful, partly because of the necessity to incorporate rate effects into the material properties. In this work we examined the strain rate and temperature sensitivity of the yield and fracture behavior of a series of rubber-modified acrylic materials. These materials have commercial and military importance for impact protection since as much as a twofold improvement in high rate impact resistance can be achieved with the proper rubber content. The objective of the study was to develop rate-sensitive yield and failure criteria in a form which could be incorporated into the computer codes. Other material properties (such as the influence of a hydrostatic pressure component on yield and failure and the relaxation spectra necessary to define viscoelastic wave propagation) are necessary before the material description is complete, but these areas will be left for later papers.

### **Experimental**

**Materials.** This study was directed primarily toward a series of American Cyanamid materials (3) with a terpolymer matrix of methyl methacrylate, styrene, and acrylonitrile modified by particles of butadiene rubber with a graft layer of matrix material to ensure good bonding between matrix and rubber. These particles were approximately 1000 Å (100 nm) in diameter but exhibited considerable agglomeration with diameters of particle clumps up to 5000 Å (*see* Figure 1). The American Cyanamid materials studied contained 0, 4, 10, and 13% rubber. Also included in the study for comparison purposes was a Goodyear Research material (4) also containing 13% rubber with the smaller rubber particles approximately 500 Å in diameter well dispersed in the matrix (*see* Figure 2). The matrix in the Goodyear material was also a glassy terpolymer.

At quasi-static rates of loading the effect of the rubber particle is twofold. First, the stress concentrations near the rubber particles induce

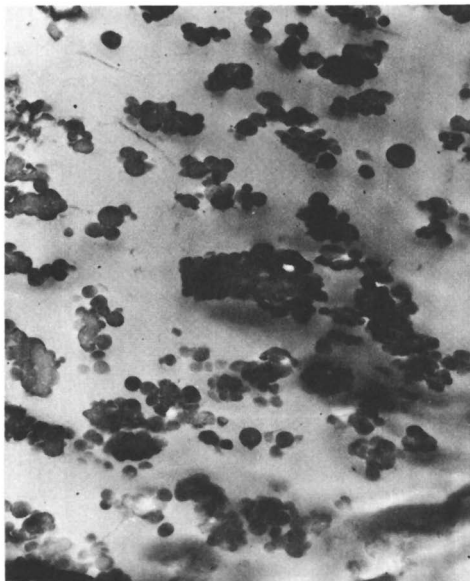


*Figure 1. Transmission electron micrograph (22,050 $\times$ ) of American Cyanamid rubber-modified acrylic with 16% butadiene rubber*

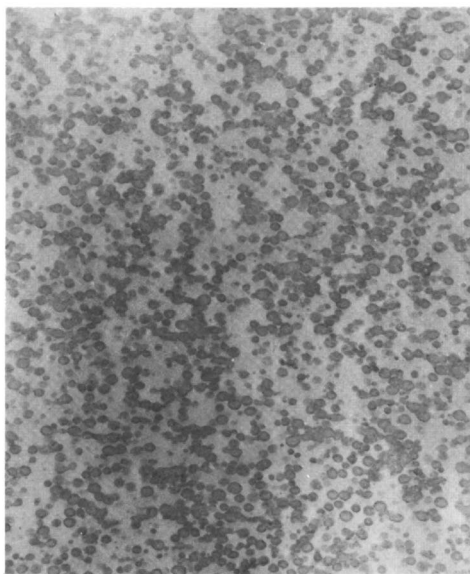


*Figure 2. Transmission electron micrograph (20,250 $\times$ ) of Goodyear rubber-modified acrylic with 13% butadiene rubber*

the material to yield locally. This yielding can be either dilational (crazing) or distortional (shear yielding). In these materials crazing predominates, but the occurrence of shear yielding cannot be ruled out, especially near the small rubber particles. The second effect of the rubber particles is to stabilize the crazes once they have initiated and thus prevent the formation of flaws which could propagate catastrophically to produce brittle fracture. This craze-crack mechanism is the process by which brittle fracture occurs in the unmodified matrix materials.

**Procedures.** The specimens were tested in an Instron Universal testing machine at 0°, 23°, 50°, and 75°C and at crosshead extension rates of 0.02, 0.2, 2.0, and 10.0 inches/min. Clip-on strain gage extensometers were used to record sample strain, and testing was done in an environmental chamber capable of maintaining the selected temperature to within  $\pm 0.5^\circ\text{C}$ . All samples were soaked at temperature for at least 30 min before testing.

### *The Role of Spallation in High Rate Impact*

At high rates of loading the brittle nature of the unmodified material is manifested by the occurrence of spallation (*see* Figure 3). Spallation

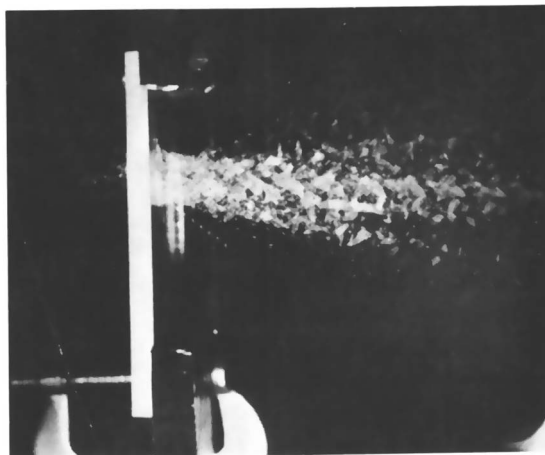


*Figure 3. Multiflash photograph of 1/4 inch plexiglas under ballistic impact. Projectile is moving from right to left.*

is fracture away from the impact point caused by dynamic tensile stresses which arise from interactions of the initial, compressive stress pulse with unloading waves from the free surfaces. Spallation results in particles with fairly high velocities being ejected from the rear surface, and it also decreases the effective thickness of the material resisting the impact. Occurrence of spallation significantly decreases the impact resistance of a polymeric material, and conversely, suppression of spallation by various

means is a very powerful method of enhancing impact resistance. If the material can be induced to yield rather than to fracture, spallation can be eliminated, and plug-like failure at the projectile occurs instead.

As is shown in Figure 4, spallation is suppressed by rubber modification. On the left are front and rear views of an unmodified matrix material which has been subjected to partial penetration by a metal projectile. Extensive spallation and radial cracking are apparent. The material on the right is the same matrix material modified by incorporating 16% rubber (*see* Figure 1). Figure 4 illustrates the response of this modified material to both partial and complete penetration. At a given rate of loading as the rubber content of the system is increased, spallation is eventually eliminated, and a maximum in impact resistance as a function of rubber content is achieved. Stress whitening replaces spall fracture. In these materials stress whitening accompanies crazing at quasi-static rates of loading. A measurable decrease in density in impacted samples indicates that crazing also occurs at high loading rates.

Additional evidence of crazing at high loading rates can be seen in Figure 5 which is a transmission electron micrograph of a section obtained from the stress-whitened area shown in the previous figure. The section was obtained using an ultramicrotome at liquid nitrogen temperature and subsequent staining with osmium tetroxide. This micrograph shows

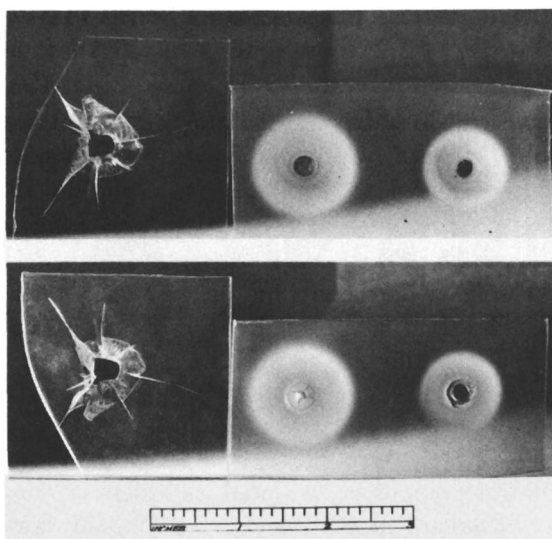


**Figure 4.** Front and rear views of American Cyanamid materials subjected to ballistic impact. Material on left is unmodified; material on right contains 16% rubber.

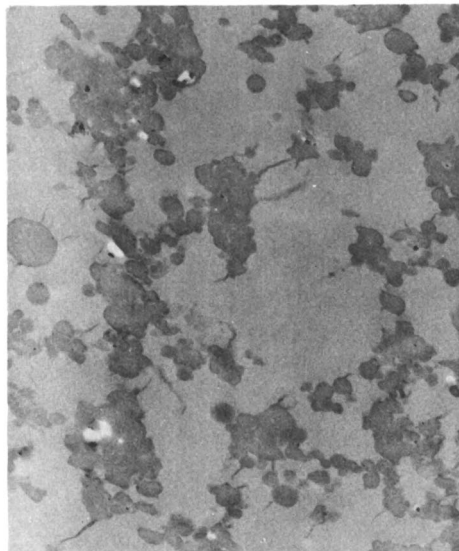


*Figure 5. Transmission electron micrograph (21,600 $\times$ ) of craze material produced by ballistic impact in American Cyanamid material with 16% rubber*

crazes that propagated outward into the glassy matrix from points of initiation at the particle–matrix interface. This provides experimental evidence that craze yielding is an important factor in the response of these materials to high rate impact. To quantify this response, especially in regard to spallation, one must quantify the rate dependence of yield by crazing in these materials.

#### *Choice of an Analytical Yield Criterion*

Simplicity is highly desirable in a yield criterion used in a wave propagation code since the numerical schemes are often only conditionally stable and since ease of implementation is desirable in any case. Simplicity is attained by assuming that the yield process is controlled by a single, thermally activated mechanism which can be described by the Eyring rate theory. Given  $d\sigma/dt = 0$ , satisfied during yield ( $\sigma$  is stress), a viscous flow process can be assumed to be occurring, produced under the action of an applied shear stress along a series of parallel layers in the stress direction. The basic process is a jump of a molecular patch from one equilibrium position to another; in glassy polymers this flow patch is a molecular segment. Assuming a symmetrical energy barrier of height  $E_0$  (attributed to the energy required to open a new equilibrium



position for the flow unit) which can be biased in the forward direction by the applied stress, the Eyring theory gives

$$\dot{\gamma} = \dot{\gamma}_0 \exp [-(E_0 - v\tau)/RT] \quad (1)$$

where  $\dot{\gamma}$  is the shear strain rate,  $\dot{\gamma}_0$  is a pre-exponential,  $v$  is an activation volume,  $\tau$  is the molecular shear stress,  $R$  is the gas constant, and  $T$  is the absolute temperature (5).

Since spallation is controlled by the response to tensile stress pulses, the measurements of yield behavior were performed in uniaxial tension rather than in shear, and a tensile yield stress criterion was required. Bouwens-Crowet *et al.* (6) rearranged Equation 1 to give an expression for the uniaxial-tension yield stress  $\sigma_y$  as follows:

$$(\sigma_y/T) = A [\ln \dot{\epsilon} + \ln B + (E_0/RT)] \quad (2)$$

where  $A$  and  $B$  are modified constants related to the molecular parameters  $v$  and  $\dot{\gamma}_0$ , and  $\dot{\epsilon}$  is the tensile strain rate. Yield data can be fit to this equation to give values of the apparent activation energy  $E_0$ , although  $A$  and  $B$  cannot be used directly to determine the activation volume and the pre-exponential. Although more complex forms of this equation are available, including for example the influence of multiple yielding mechanisms, we determined the applicability of this simple equation as a yield criterion by performing quasistatic tensile tests as a function of strain rate and temperature and by fitting these data to Equation 2.

### Results and Discussion

Representative stress-strain curves for the various materials, rates, and temperatures are shown in Figure 6. Tests were replicated from two to five times; in general these replications had very high reproducibility in yield values. Values at fracture, especially fracture strain, showed much more scatter. Accordingly the yield values of the unmodified material, which are really fracture values, also contained more scatter. (In the plots of yield values to follow, the data symbols lie over all of the replication values unless the values are sufficiently spaced to permit another symbol.)

Figure 6a shows the effect of rubber content on the stress-strain behavior of these materials. All the rubber-modified materials exhibited a load maximum under all testing conditions. In most tests the unmodified material failed before it exhibited a yield maximum, although the data were reduced in the same manner used for the other samples. In all cases the yield stress decreased as the rubber content was increased, but the

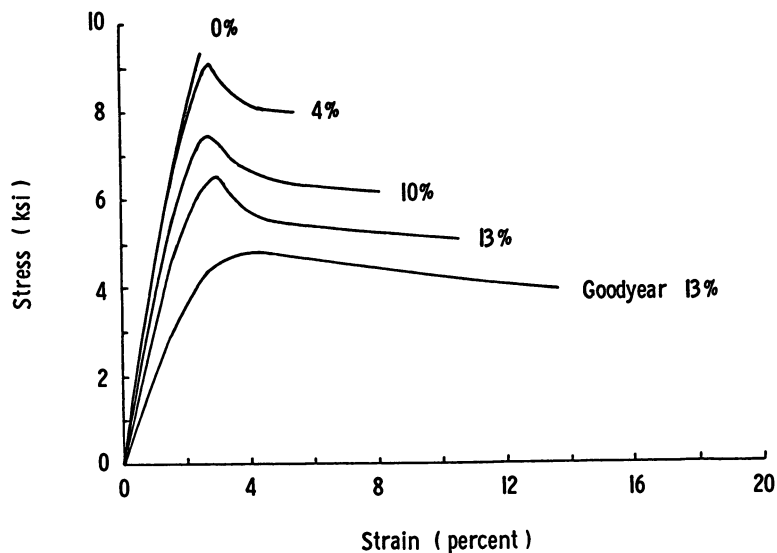


Figure 6a. Stress-strain curves for various rubber-modified acrylics at 0.2 inch/min and 23°C

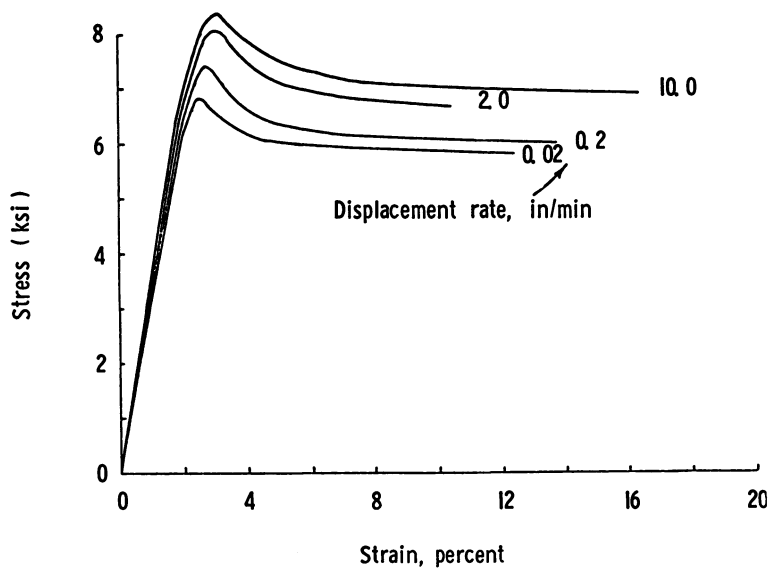


Figure 6b. Stress-strain curves for 10% American Cyanamid material at 23°C and various displacement rates

Goodyear material with the same rubber content as the 13% American Cyanamid material exhibited more ductile stress-strain behavior. Possible reasons for this difference will be discussed later in the paper. Figure 6b shows the effect of rate on the behavior of the 13% American Cyanamid material. The yield stress increases with strain rate as was the case in all materials tested. Figure 6c shows the effect of temperature on the behavior of the same material. Again, as was the case in all materials tested, the yield stress decreases as the temperature is increased.

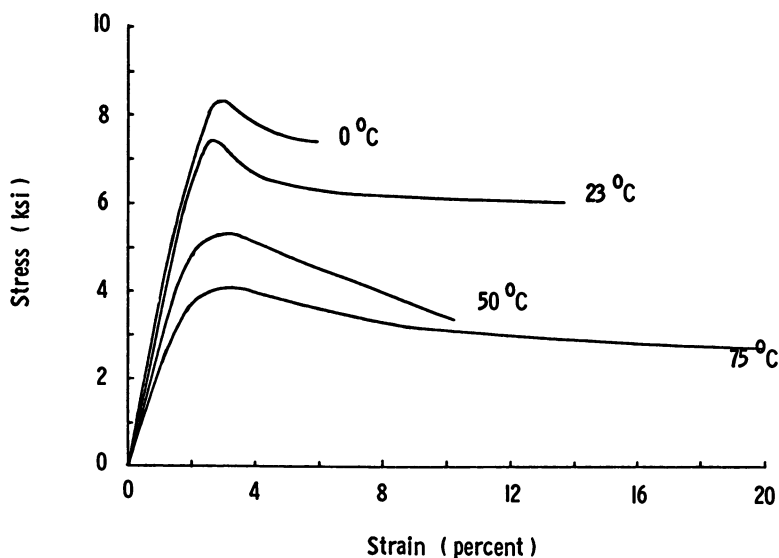


Figure 6c. Stress-strain curves for 10% American Cyanamid material at 0.2 inch/min and various temperatures

To determine the applicability of the Bauwens-Crowet criterion, these these data were plotted as  $\sigma_y/T$  vs.  $\log \dot{\epsilon}$  and  $1/T$ . Figure 7 shows the results for the 13% American Cyanamid material. As seen in Figure 7a, the behavior is linear at each temperature, and the slopes are the same except at 75°C. At 75°C yielding becomes localized, stress whitening diminishes, and the material appears to undergo a transition in its yield behavior. Since we were interested only in the high effective strain rate behavior, we used only the data obtained at 0°, room temperature, and 50°C to calculate the slope. A good least-squares linear fit was obtained from the data, and the slope obtained in these calculations can be used to determine the value of the constant  $A$  in the Bauwens-Crowet equation. As Figure 7b indicates, the yield behavior of the material is more sensitive to temperature than to strain rate. This illustrates the

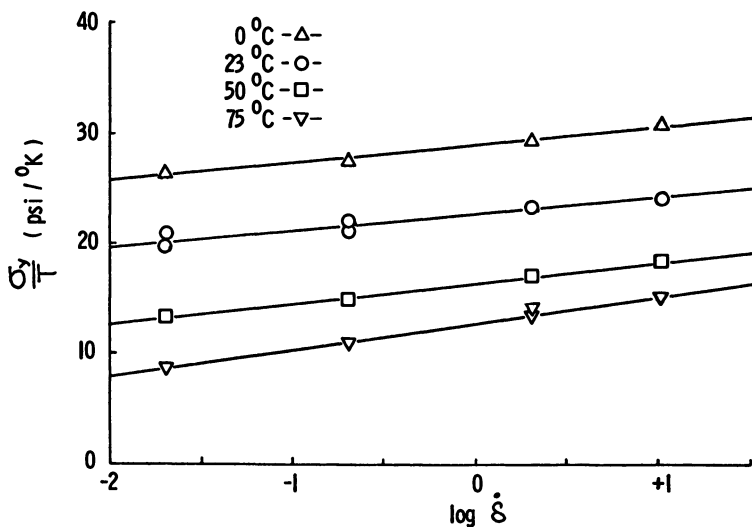


Figure 7a.  $\sigma_y/T$  vs.  $\log \dot{\delta}$  for 13% material

advantage of low temperature testing. If an equivalence between low temperature and high rate conditions can be established, details of the mechanical behavior can be studied much more easily at low temperatures than at high rates. The slope obtained by least-squares fit to the  $\sigma_y/T$  vs.  $1/T$  data, can be used along with the value of  $A$  to determine  $E_0$ .

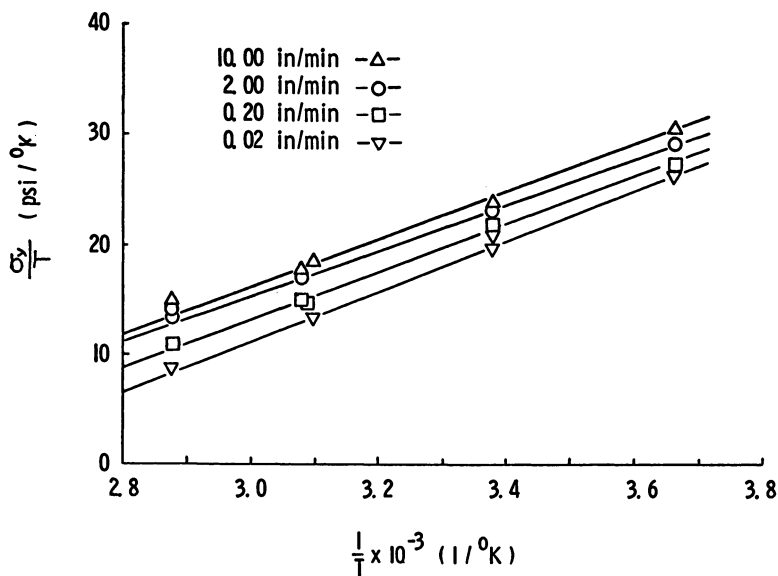


Figure 7b.  $\sigma_y/T$  vs.  $1/T$  for 13% material

**Table I. Constants from Bauwens–Crowet Equation for Various Materials**

Material	A	ln B	$E_0$
American Cyanamid 0%	1.25	29.6	40.2
American Cyanamid 4%	.98	36.2	63.6
American Cyanamid 10%	.90	30.1	56.0
American Cyanamid 13%	.75	32.5	59.3
Goodyear 13%	1.12	19.2	39.5

Table I shows the values of these activation parameters for the materials tested. A time–temperature superposition shift factor ( $\Delta$ ) can be calculated from Equation 2 as follows:

$$\Delta = \log a_T = E_0/R [(1/T) - (1/T_{ref})] \quad (3)$$

and this value of  $\Delta$  can be used to obtain master curves of  $\sigma_y/T$  against log effective strain rate. The fit of these shifted data to the Bauwens–Crowet equation is another test of the applicability of the Bauwens–Crowet criterion to these materials.

Using room temperature as a reference the shifted data for the American Cyanamid 13% material is shown in Figure 8. The fit to the Bauwens–Crowet equation represented by the solid line is excellent especially at high effective strain rates. The data obtained at 75°C are included in

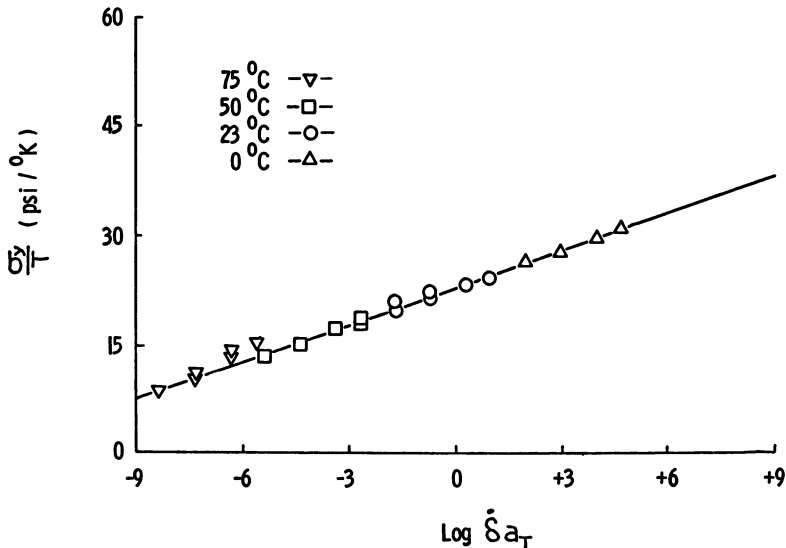


Figure 8.  $\sigma_y/T$  vs.  $\log \delta a_T$  for 13% material.  $T_{ref} = 23^\circ\text{C}$

this figure but were not used to calculate the contents for the Bauwens-Crowet equation. The fit to the Bauwens-Crowet equation was good at the high effective strain rate for all American Cyanamid materials tested, even the unmodified material.

Turning to Table I, values of the parameter  $B$  are essentially the same for all the American Cyanamid materials but differ for the Goodyear material. These values are calculated from the intercept of the  $\sigma_y/T$  vs.  $\log$  effective strain rate curve. This value reflects the pre-exponential in the Eyring equation and therefore depends on the basic frequency of the flow unit as modeling by Eyring. This value should be characteristic of the matrix since the actual flow process occurs in the matrix material. Therefore differences in matrix formulation between the American Cyanamid and Goodyear materials are indicated by the data. This conclusion is borne out by the fact that the Goodyear material undergoes a gradual transition in the effective strain rate range of the study manifested by an upward curvature in the data points around the line representing the Bauwens-Crowet equation. Roetling (7) reported yield data for pure PMMA which exhibits this same curvature. Analysis of data in a transition region requires the use of the more sophisticated Ree-Eyring model however, and activation parameters obtained from the simple Bauwens-Crowet equation are essentially meaningless. Since the simple Bauwens-Crowet equation seems a good model for the American Cyanamid materials, information about the basic nature of the yielding process in these materials may be obtained from examining the Bauwens-Crowet activation parameters. The values of  $E_0$ , apparent activation energy, are essentially the same for all the rubber modified American Cyanamid materials. Under all test conditions all these materials exhibited whitening at yield accompanied by a decrease in density. This indicates that crazing occurs extensively in all these materials and that *ca.* 60 kcal/mole is the appropriate apparent activation energy for this process; 40 kcal/mole, which is observed in the unmodified American Cyanamid material, represents the apparent activation energy for craze fracture and not that for craze yielding. Even though a yield point was not observed, the data were included in the analysis since crazing would still be involved in the fracture process. Although there is considerable scatter in the fracture data, it still behaves in a linear fashion describable by the Bauwens-Crowet equation indicating the thermally activated nature of this fracture process. The values of  $A$  listed in Table I are a measure of the sensitivity of the yield stress of each material to the applied strain rate. Also the Bauwens-Crowet constant  $A$  is inversely proportional to the apparent activation volume  $v$  in the Eyring equation. It can be seen from Table I that the rate sensitivity becomes less pronounced and the apparent activa-

tion volume increases as the rubber content increases. This may reflect the fact that increasing the amount of rubber induces a larger volume of matrix to undergo yield.

Figure 9 compares the master curves obtained for all the materials tested. At a given effective strain rate, which would correspond to a given impact velocity, the material with the lowest rubber content gives the highest yield stress. Barring spallation, the highest yield stress should correspond to the highest impact resistance since high speed photography of high rate impact indicates that strains during plug-flow under impact are essentially the same for all these materials. However if spallation occurs because of the material's inability to yield under dynamic tensile stresses, the impact resistance of the material is drastically reduced.

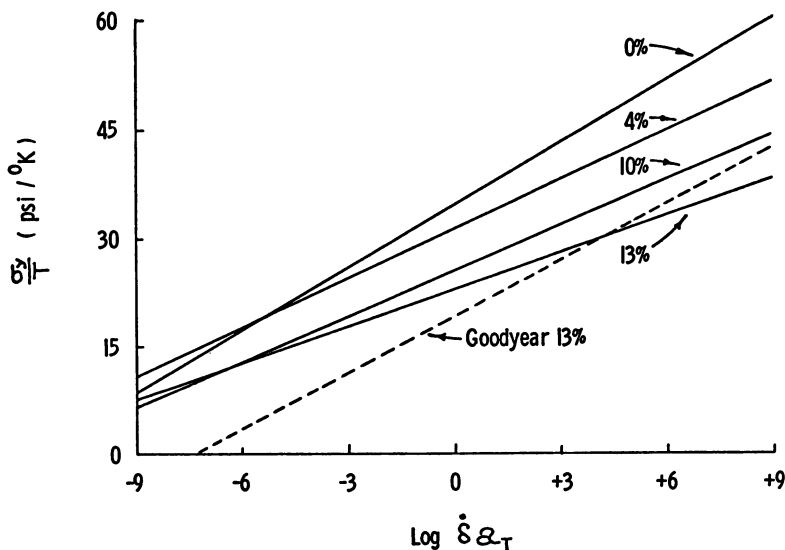


Figure 9. Comparison of shifted curves for various materials

Thus at a given rate the lowest rubber content which can induce ductility and suppress spallation will result in maximum energy absorption under impact. If this yield-spall transition coincides with the ductile-brittle transition which occurs in these tensile tests, the effective strain rate of the onset of spallation could be predicted by tests of this type. This ductile-brittle transition occurs at low effective strain rates for the unmodified material since it is brittle through the range of conditions used in these tests. For the 4% material at the highest effective strain rates achieved in these tests, the load maximum is just beginning to disappear. Thus, if rate-temperature equivalence holds, extension of these test to

lower temperatures should allow prediction of both yield stress and the occurrence of spallation as a function of rubber content and rate. By this means the optimum rubber content for a given strain rate or impact velocity could be predicted.

### **Conclusions**

First, the role of rubber modification in high rate impact is to suppress spallation by inducing the material to yield in the presence of dynamic tensile stresses arising from impact. Second, this yield-spall transition occurs at different strain rates for different rubber contents and may be predictable using quasistatic, low temperature tests of this type. These tests can also provide information concerning the basic nature of the yield process in these materials through the activation parameters which are obtained. Third, the Bauwens-Crowet equation seems to be a good model for the rate and temperature sensitive behavior of the American Cyanamid materials and is therefore a likely candidate for a yield criterion to use in the analytical code work on these materials which we hope to perform as a continuation of this work.

### **Literature Cited**

1. Roylance, M. E., Lewis, R. W., *Army Mater. Mech. Res. Center Rept., AMMRC TR 7223* (1972).
2. Wilkins, M. L., *Lawrence Livermore Lab. Rept. UCRL-7322* (1969).
3. Schmitt, J. M., *et al.*, U.S. Patent 3,354,238 (Nov. 21, 1967).
4. Baur, R. G., *et al.*, U.S. Patent 3,475,516 (Oct. 28, 1969).
5. Glasstone, S., Laidler, K. J., Eyring, H., "The Theory of Rate Processes," McGraw-Hill, New York, 1941.
6. Bauwens-Crowet, C., *et al.*, *J. Polym. Sci.* (1969) A27, 735.
7. Roetling, J. A., *Polymer* (1965) 6, 311.

RECEIVED October 18, 1974.



## Simultaneous Interpenetrating Networks Based on Epoxy/Acrylic Materials

R. E. TOUHAENT,<sup>1</sup> D. A. THOMAS, and L. H. SPERLING

Materials Research Center, Lehigh University, Bethlehem, Pa. 18015

*Simultaneous interpenetrating networks (SIN's) were prepared by simultaneously synthesizing crosslinked epoxy and poly(n-butyl acrylate) polymers. A two-phase morphology emerged with the dispersed rubber domains being 0.1–0.5  $\mu$  in diameter. The actual dimensions of the dispersed rubber phase domains and the extent of molecular mixing between the components depended on the relative polymerization rates or reaction gel times in relation to the time of phase separation. Although most molecular mixing occurred when the reactions were closest to simultaneity, better mechanical properties resulted when conditions were removed slightly from simultaneity. In some of the SIN's the main glass transition temperature was abnormally higher than that of the cured epoxy resin. Entrapment of low molecular weight epoxy in n-butyl acrylate phase domains was proposed as a cause.*

Two polymeric species can be combined in a variety of ways, each producing a distinctive material. Mechanical blends contain no appreciable interspecies bonds, while graft copolymers and block copolymers contain variable percentages of bonds joining the two components. In addition the two polymers may be either linear or crosslinked. Also, if the monomers are mixed before polymerization, different morphologies and mechanical behavior patterns will develop. Morphologies and properties may also vary if the polymerization reactions are run simultaneously or sequentially.

Simultaneous interpenetrating networks (SIN's) are produced by running two essentially independent and noninterfering, crosslinking

<sup>1</sup> Present address: Mobil Chemical Co., Plastics Division, Macedon, N. Y. 14502.

polymerizations simultaneously in the same container under the same conditions (1, 2). An example might be a condensation and an addition reaction. Ideal SIN's are produced if the polymerizations form entirely independent, crosslinked networks. However because of the nature of simultaneous polymerizations, some interaction between the two components is expected. As long as the crosslinking in each component is much greater than grafting between the components and copolymerization does not occur, the networks can be considered largely chemically (but not physically) independent as a first approximation. In the present work an epoxy resin serves as the condensation polymer, and poly(*n*-butyl acrylate) serves as the addition polymer.

Similar materials but with different topologies and mechanical behavior have been made by combining epoxy and vinyl or acrylic polymers by conventional graft polymerization. A vinyl or acrylic polymer with or without (3–60) active graft sites is added to an epoxy resin prepolymer, and the epoxy is cured with a greater or lesser extent of grafting to the vinyl polymer.

Nearly all polymer blends undergo phase separation to some extent because of the small entropy gained and usual positive heat of mixing. Phase separation is controlled by the change in the Gibbs free energy of mixing,  $\Delta F_m$ , which is:

$$\Delta F_m = \Delta H_m - T \Delta S_m \quad (1)$$

where  $\Delta H_m$  and  $\Delta S_m$  are the changes in enthalpy and entropy of mixing, and  $T$  is the absolute temperature at which mixing occurs. Complete mixing can occur if  $\Delta F_m$  is zero or negative. Because of their low initial molecular weight, the monomers, prepolymers, and crosslinking agents involved in simultaneous polymerization have a large entropy gain on mixing and hence are soluble in each other. At some point during simultaneous polymerization, as the molecular weight of each polymer increases,  $\Delta S_m$  decreases sufficiently so that a positive  $\Delta F_m$  results, and phase separation occurs. However it is thought that phase equilibrium may be kinetically hindered by the simultaneous polymerization of two networks. Specifically the chain entanglements and crosslinking associated with simultaneous polymerization would be expected to restrict mechanically phase separation. Maximum restriction of phase separation should result when the polymer begins to gel near or before the time at which  $\Delta F_m$  becomes positive and at which phase separation can first occur. Thus phase separation in a simultaneous polymerization is controlled by the relative times of gelation and phase separation.

Varying the relative rates of the two reactions in a simultaneous polymerization permits a great variety of synthetic detail. One component

can be allowed to react faster, slower, or at nearly the same rate as the other component. It is both convenient and of interest to study simultaneous polymerizations when their reaction rates and gel times are nearly equal. In addition the reaction rates can be varied slightly to produce reactions that are more or less simultaneous to study the effects on the microstructure and mechanical behavior of the materials produced.

**A Brief History of IPN's and SIN's.** Simultaneous interpenetrating networks (SIN's) constitute a subgroup of a larger class of materials which are known as interpenetrating polymer networks (IPN's). IPN's are unique types of graft copolymers because they consist of two cross-linked polymer networks that are intimately mixed but largely chemically independent. The first IPN's reported in the literature were prepared by Millar (61) who used swelling techniques to produce polystyrene/polystyrene IPN's, both components being equal. Polystyrene network I was swollen with styrene, initiator, and crosslinking agent and was polymerized *in situ* to form network II. Shibayama and Suzuki (62, 63) studied similar IPN compositions with both networks composed of polystyrene. Shibayama and Kodama (64, 65) using the same swelling technique synthesized IPN's with two chemically different plastic networks: one composed of polystyrene (PS) and the other composed of poly(methyl methacrylate) (PMMA). IPN's of the type made by Millar swelled less than the corresponding single networks with the same chemical crosslink density. The reason for the swelling restriction was the permanent deformation and reduced entropy imparted to network I by the swelling of monomer II.

Sperling and Frisch both reported distinguishable polyblend topologies composed of two different network polymers. Frisch's polyblends (66, 67) were designated as interpenetrating elastomeric networks (IEN's) because the original materials had two elastomeric components. The IEN's were made by mixing polyurethane (PU) and polyacrylate (PA) emulsions and by crosslinking after film formation. The PU was crosslinked by a triol, and the PA was crosslinked by allowing double bonds in the polymer to react with sulfur. Sperling and Friedman (68) however were the first to report making an interpenetrating polymer network with one network a plastic and the other a rubber component. Sperling and co-workers (68-81) used a swelling method similar to Millar's in an effort to obtain a polyblend with finely divided phases without mechanical mixing. In IPN's and IEN's components were chemically different; thus incompatibility and phase separation resulted. The phase structure was influenced largely by the compatibility of the two networks, the crosslink density, and the order in which they are formed. The phase domain size of the IEN's was controlled by the latex particle size.

When one polymer of an IPN was plastic and the other was rubber, the combination showed synergistic properties; reinforced rubbers, impact resistant plastics, or noise damping materials were reported. Because of the macroscopic network structure formed in IPN's, they are thermoset and cannot be molded. However IPN's have been made by emulsion polymerization so that each individual emulsion particle is an IPN in miniature form containing both networks (75, 76, 77, 78, 82, 83). Emulsion polymerization allows the molding of IPN's if the crosslink density of the "miniature" IPN's is not too high.

A novel approach to IPN synthesis was reported by Sperling and Arnst (1). They synthesized two polymer networks by simultaneous yet independent reactions in the same container at the same time. Complicated interactions were eliminated in the SIN's by combining free radical (acrylate) and condensation (epoxy) polymerization. The present work uses the basic technique of Sperling and Arnst.

Since work on this project was begun, several cases of simultaneous polymerization have been reported. Frisch *et al.* (82, 83, 84, 85, 86) studied simultaneous polymerizations that consisted of two crosslinked components: one a polyurethane and the other either a polyester, a polyacrylate, or an epoxy. They mixed the prepolymers with their respective crosslinking agents in solution or bulk and then cured them *in situ*. Allen *et al.* (90-95) studied a system combining free radical and condensation polymerization reactions. They mixed polyurethane elastomer prepolymers and catalysts with an addition type monomer, usually methyl methacrylate, and initiator. The polyurethane polymerization was always started at room temperature; later the free radical polymerization was begun at 50°-70°C. In all cases the polyurethane gelled before the free radical polymerization began because of the prereaction of the urethane and the induction time of the free radical polymerization. However the urethane polymerization was not complete when the free radical polymerization started. The materials of Allen *et al.* (90-95) may be designated semi-SIN's because only one component, the polyurethane, was crosslinked and the second component was linear. Several other examples of SIN's (93) and semi-SIN's (97-103) with similar topologies have also been reported in the literature (*see* Appendix).

### *Experimental*

**Synthesis.** The samples in this study were made by heating a low molecular weight epoxy prepolymer, Epon 828, Shell Chemical Co., to 120°C and adding with stirring 31.1 parts phthalic anhydride per 100 parts epoxy. After the epoxy mix prereacted for set times, *n*-butyl acrylate monomer was added along with di-*tert*-butyl peroxide initiator and crosslinking agent diethylene glycol dimethacrylate (DEGDM). Two percent

isoprene based on *n*-butyl acrylate was added to provide unsaturation in the polymer for osmium tetroxide staining. The reaction flask was purged with dry nitrogen and sealed. Stirring was continued at 120°C until the reaction mix became sufficiently viscous to prevent the lighter rubber component from rising to the surface and producing gross layering. The mix was then poured into heated glass plate molds. The reaction was run for at least three days at 120°C, which is above the glass transition temperature of the epoxy, so that the reaction was not hindered by vitrification (106, 107). The reaction was continued an additional day at 150°C to ensure full curing of the epoxy. The sample was then cooled and removed from the mold.

**Instrumental Technique.** The morphology and mechanical behavior of the SIN compositions were studied by electron microscopy, dynamic mechanical spectroscopy (DMS), and tensile and impact tests. Materials were prepared for electron microscopy by first drying pretrimmed samples in a vacuum oven for two days at 75°C. The samples were then stained in osmium tetroxide vapors (108, 109) for at least 19 hr. After staining, ultramicrotome sections *ca.* 700 Å thick were obtained using a diamond knife with a Sorval Porter-Blum ultramicrotome. Electron microscopy was done on a Philips model 300 transmission electron microscope. Dynamic mechanical spectroscopy was done with a Rheovibron model DDVII on vacuum-dried samples by increasing the temperature from *ca.* -150° to 150°C at about 1°C per min. Dynamic mechanical spectroscopy measured the storage modulus,  $E'$ , and the loss modulus,  $E''$ . The quantities  $E'$  and  $E''$  are related through the equation

$$E''/E' = \tan \delta \quad (8)$$

where  $\delta$  is the phase angle between  $E'$  and  $E''$ , the in-phase and out-of-phase components of the complex modulus. Tensile (Instron) and notched impact tests (Charpy) were made on at least four standard size samples from each action, and the averages were reported.

**Independent Variables.** Simultaneous synthesis of two polymer networks is a complex process. Many independent variables are available for study and not all could be explored in a limited investigation. The emphasis in the present study centers on those variables whose predominant effect is to influence the relative rates or gelation times of the reactions. Three independent variables were selected: (a) the concentration of di-*tert*-butyl peroxide initiator was changed to vary the rate of polymerization of *n*-butyl acrylate; (b) the epoxy mix was allowed to prereact for different lengths of time before the acrylate mix was added, and (c) the amount of DEGDM added to the acrylate mix was varied to control the gel time of the acrylate without significantly affecting its rate of polymerization.

Experiments were centered around conditions that would result in simultaneous polymerization or simultaneous gelation of the two components. Reactions off center resulted in one reaction or the other proceeding faster. Thus a range of properties at or near simultaneous gelation could be systematically observed. The range of the initiator concentration was 0.18–0.46% (based on *n*-butyl acrylate). The epoxy was prereacted from one to eleven hours before the acrylate mix was added.

The length of time the epoxy could prereact was limited at the high end by the gel time of the epoxy which was about 14 hr. The concentration of DEGDM was varied between 0 and 1.6% based on *n*-butyl acrylate. (Note that 0% DEGDM content produces a semi-SIN.) The ranges of all variables were preselected so that the reactions were most nearly simultaneous in rate when the variables were at the midpoint of their experimental ranges. The experimental conditions are given in Table I.

**Table I. Experimental Conditions Levels of the Independent Variables**

<i>Experiment Number</i>	<i>Initiator Concentration (%)</i>	<i>Epoxy Prereaction Time (hr)</i>	<i>DEGDM Concentration (%)</i>
1	0.40	9	1.28
2	0.40	9	0.32
3	0.24	9	1.28
4	0.24	9	0.32
5	0.40	3	1.28
6	0.40	3	0.32
7	0.24	3	1.28
8	0.24	3	0.32
9	0.32	6	0.00
10	0.32	6	1.60
11	0.32	1	0.80
12	0.32	11	0.80
13	0.18	6	0.80
14	0.46	6	0.80
15	0.32	6	0.80
16	0.32	6	0.80
17	0.32	6	0.80
18	0.32	6	0.80
19	0.32	6	0.80

**Dependent Variables.** Electron microscopy revealed the size and shape of the phase domains, and DMS gave complementary information about the extent of molecular mixing and phase continuity. The stress-strain and impact studies revealed the extent of toughness of the materials.

The quantitative data used from DMS and electron microscopy in the computer study included: (a) the average length and width of the discontinuous (*n*-butyl acrylate) phase; (b) the glass transition temperature of the continuous epoxy rich phase ( $T_{g1}$ ), (c) the glass transition temperature of the discontinuous poly(*n*-butyl acrylate)-rich phase ( $T_{g2}$ ), and the height of the low temperature loss modulus peak caused by the acrylic glass transition ( $HT_{g2}$ ). The glass transitions are defined in the present work as the temperatures at which the corresponding loss moduli have maxima. Other dependent variables included impact strength, ultimate tensile strength, elongation at break, and toughness, denoted by the area under the stress-strain curve. In addition the gel time of the reaction mix was estimated roughly by the viscosity of the mix and was taken as the time when stirring was stopped and when the material was poured in the mold.

**Computer Program.** Because of the complexity of the problem stemming from the many variables, computer programs were used to assist in the analysis. The experiments were designed in such a way that more information could be obtained from fewer experiments than is the case with traditional noncomputer-related experimentation. The experimental design used was a rotatable central composite design developed by Box and Wilson (110) and described by others (111, 112, 113). In the rotatable designs all experimental points were at a constant distance from a central experimental point. A rotatable design was ideal for the experiments because it revealed how the properties varied from simultaneous conditions with three independent variables.

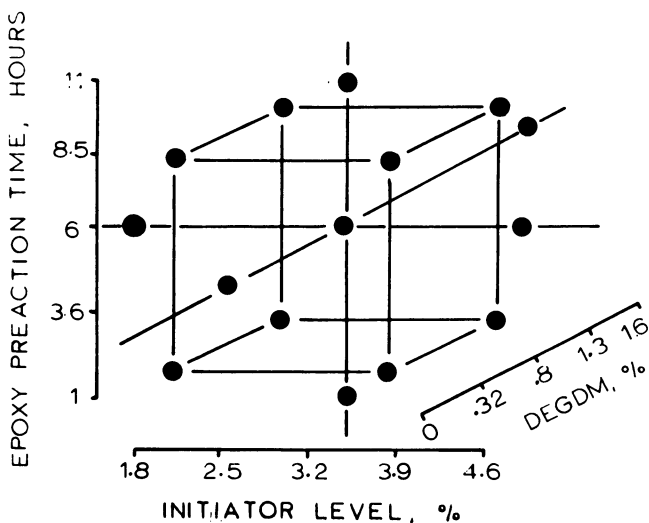


Figure 1. Rotatable central composite experimental design

The center of the experimental design was chosen as the point thought to give simultaneous gelation with both reactions proceeding at a moderate rate. Since the experiments included three independent variables, initiator concentration, epoxy prereaction time, and DEGDM concentration, the design was set up in three dimensions. Experiments were conducted on and around the center point of a cube as shown in Figure 1. There were eight experiments around the center point on the corners of the cube. Six additional experimental points an equal distance from the center were found along axes through the centers of the faces of the cube. In addition, the center point was replicated so that the experimental error could be found. The experiments were conducted in random order so that any time trends would tend to average out and not favor any one direction. Also the experiments were carried out in two blocks so that no direction would be favored by variables such as the machining of the samples.

Mathematical models that represented the relationships between the dependent and independent variables were developed. Once the model

was developed, the relationships between the dependent and independent variables could be represented by a response surface. It was convenient to display the response surfaces by contour graphs developed by a computer program. Holding one independent variable constant, the experimental conditions were described by the  $x$  and  $y$  coordinates representing the other two independent variables. The response surface was indicated in the third dimension by iso-valued contour lines.

The entire response surface could be predicted from the few experiments performed because the rotatable design had equal predictability in all directions. If we assume that the responses are functions of the independent variables' levels:

$$Y = f(\chi_1, \chi_2, \chi_3) \quad (9)$$

where  $Y$  is the measured response and  $\chi_1$ ,  $\chi_2$ , and  $\chi_3$  are the independent variables, a mathematical model can be used to describe the response surface. In the present case, there was evidence from preliminary experiments that the response surface was not planar, and a second-order model was used to describe the surface:

$$Y = B_0\chi_0 + B_1\chi_1 + B_2\chi_2 + B_3\chi_3 + B_{11}\chi_1^2 + B_{22}\chi_2^2 + B_{33}\chi_3^2 + B_{12}\chi_1\chi_2 + B_{13}\chi_1\chi_3 + B_{23}\chi_2\chi_3 + E \quad (10)$$

where  $\chi_0$  is a constant always equal to unity, and the  $B$ 's are coefficients determined by the method of least squares, a method which minimizes the sum of squares of the error  $E$ . In practice, the coefficients are determined by a computer program which conducts a stepwise regression analysis of the data by the method of least squares. Statistical tests were then used to determine if the model was valid. When it was found that the model was valid, the response surface could be plotted by the computer.

## Results

**General.** Because of intense light-scattering effects, the samples produced were various shades of blue-white. Some samples were opaque, while others were nearly clear. The milky appearance of these materials indicated a two-phase morphology. The SIN materials were also all significantly tougher than the epoxy homopolymer. For example, during cutting and trimming operations related to sample preparation, epoxy homopolymers responded in a brittle manner and required heating to the glass temperature before cutting. The SIN materials were tough and could be cut at room temperature with scissors without special precautions.

**Electron Microscopy.** Electron microscopy illustrates the two-phased nature of the SIN's directly by showing their microstructure. In all cases



there was a discontinuous minor phase, presumed to be primarily the poly(*n*-butyl acrylate) component. The poly(*n*-butyl acrylate)-rich phase domains tended to be slightly elliptical in shape, or irregular. Some typical electron micrographs are shown in Figures 2 to 5. Particle diameters ranged from less than one-tenth micron to several tenths micron. Some of the samples had a bimodal particle size distribution. The bimodal characteristics are illustrated by plotting frequency *vs.* particle size (Figure 6).

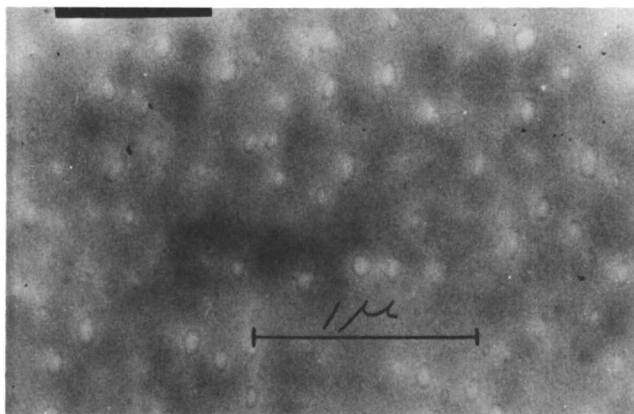


*Figure 2. Electron micrograph of sample 5. This sample phase separated after gelation and therefore has small and nearly spherical phase domains.*

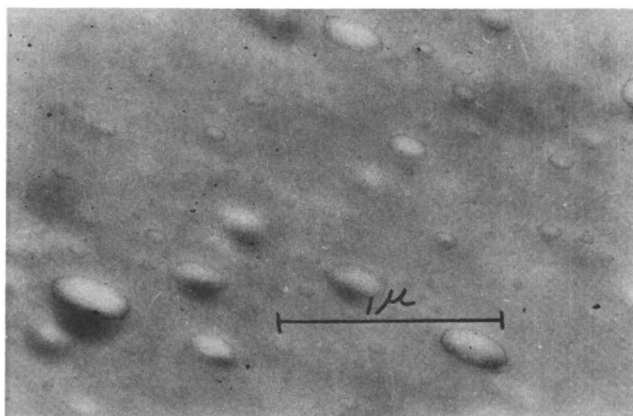


*Figure 3. Electron micrograph of sample 8. Phase separation occurred near but before gelation while the sample was being stirred; thus the rubber phase domains are slightly elliptical.*

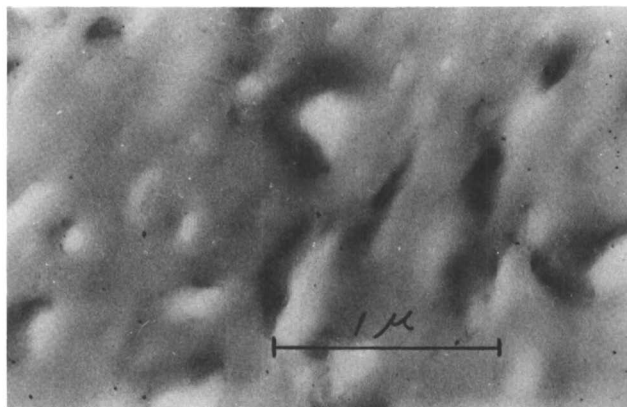


*Figure 4. Electron micrograph of sample 10. Phase separation occurred before gelation while the sample was being stirred which resulted in larger and more elongated and irregular rubber phase domains.*

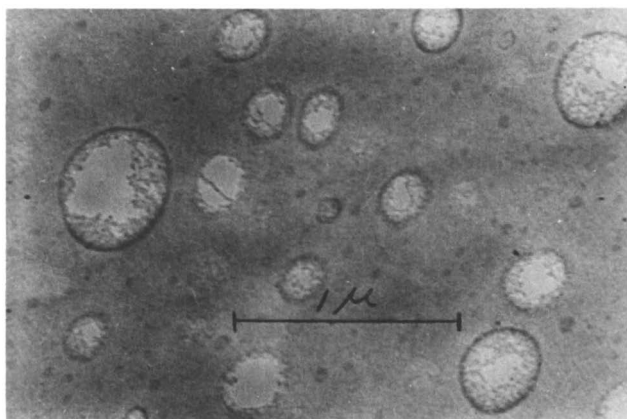


*Figure 5. Electron micrograph of sample 9. Phase separation occurred before gelation while stirring which resulted in larger phase domains. Phase domains are nearly spherical because there was no DEGDM in this sample. The phase domain size distribution is noticeably bimodal; the smaller phase domains are believed to result from a secondary phase separation after gelation.*

Similar to our earlier study (2) some of the materials had a dark band at the phase interface which is believed to be rich in the isoprene component. This phenomenon arises from the slow rate of copolymerization of the isoprene monomer with the *n*-butyl acrylate. The major experimental results of this and succeeding sections are summarized in Table II which shows phase domain dimensions for the several samples.

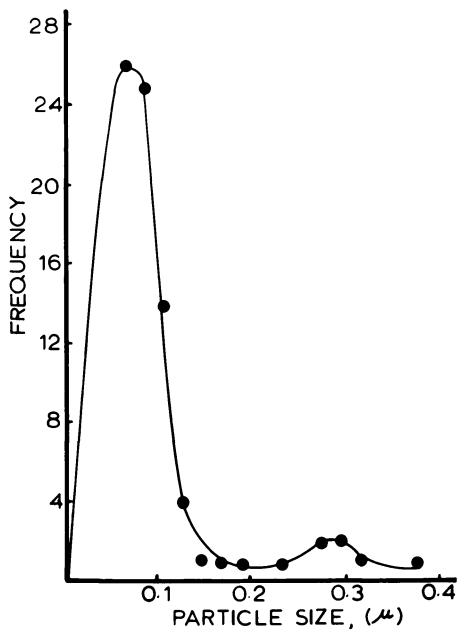


Figure 6. Particle size distribution of sample 8

Table II.

Experiment (Table I)	$T_{g1}$ ( $^{\circ}\text{C}$ )	$T_{g2}$ ( $^{\circ}\text{C}$ )	$\text{HT}_{g2}$ ( $\text{dyne}/\text{cm}^2$ $\times 10^{-8}$ )	Tensile Strength ( $\text{psi}$ )	Elongation (%)
1	113	-54	9.7	6973	5.03
2	112	-48	13.0	6427	4.76
3	104	-54	8.9	8292	5.80
4	105	-54	9.2	8689	6.34
5	111	-50	7.7	8930	6.63
6	110	-51	8.8	8094	5.61
7	96	-50	6.9	7596	5.22
8	101	-55	8.2	8187	5.70
9	104	-59	9.2	8269	6.11
10	105	-54	9.1	8116	6.67
11	97	-55	8.4	7267	4.84
12	115	-57	9.7	8013	5.74
13	107	-53	10.9	6781	4.69
14	108	-53	10.1	7508	5.36
15	104	-58	8.8	7685	5.53
16	105	-55	9.0	7520	5.48
17	106	-51	10.4	6547	4.80
18	105	-54	9.5	7664	5.79
19	108	-53	9.2	7640	6.10

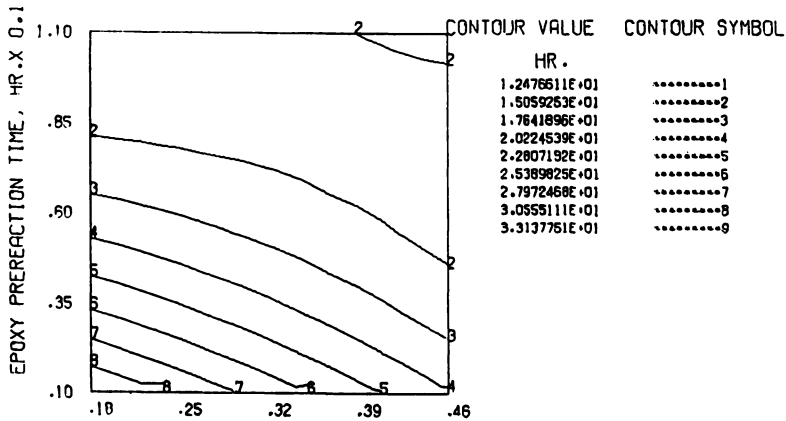


Figure 7. Contour plot of the gel time, holding DEGDM constant

**Gel Point and Phase Separation.** Depending on epoxy prereaction time, a 20 wt % addition of rubber would be expected to increase the gel time of the epoxy from 14 hr to a maximum of *ca.* 19 hr just by a dilution effect. In many cases the gel time of the reaction is longer than expected by simple dilution, probably because the *n*-butyl acrylate hinders the epoxy reaction. If phase separation occurs before gelation, hindrance

### Experimental Results

Toughness (psi-%)	Gel Time (hrs)	Rubber Phase Length (units)	Rubber Phase Width (units)	<i>l/w</i>
197	17	0.246	0.152	2.22
170	14	0.276	0.149	2.40
272	18	0.239	0.136	1.77
337	15	0.62	0.281	2.21
359	27.5	0.100	0.63	1.59
275	14	0.282	0.116	2.43
226	30	0.087	0.070	1.24
270	25	0.092	0.060	1.53
295	21	0.089	0.064	1.38
346	18.5	0.289	0.144	2.01
193	25	0.206	0.108	1.91
268	14	0.209	0.136	1.54
179	15	0.486	0.334	1.45
240	13	0.205	0.117	1.75
242	18.5	0.179	0.137	1.31
242	16	0.407	0.196	2.08
176	17	0.324	0.126	2.57
265	16	0.353	0.169	2.09
279	17	0.344	0.150	2.29

is less important and, if phase separation is near or after the gel point, the gel time is up to 30 hr longer than expected. The hindrance is believed to be caused by the grafting of *n*-butyl acrylate to hydroxyls on the epoxy which lowers the rate of polymerization of the epoxy (2). However if phase separation occurs before gelation, the dilution effect is partly lost, and grafting is reduced because of its limitation to interfacial regions; thus the gel time is more nearly that expected. Therefore, the gel time of the SIN depends upon when phase separation occurs.

Generally there were larger increases in gel time for samples with low epoxy prereaction times and low initiator concentrations (Figure 7). The increase in gel time probably occurred because the reactions are homogeneous for longer times. Unexpectedly, increasing the concentration of DEGDM tended to increase the gel time, especially when the gel time was already long. The gel time may be increased by DEGDM because DEGDM forms grafts much more readily than *n*-butyl acrylate because of its double reactivity.

**Dynamic Mechanical Spectroscopy.** Dynamic mechanical spectroscopy was used to study the loss and storage moduli and  $\tan \delta$  of the several materials from  $-150^\circ$  to  $+150^\circ\text{C}$ . Thus we obtained information

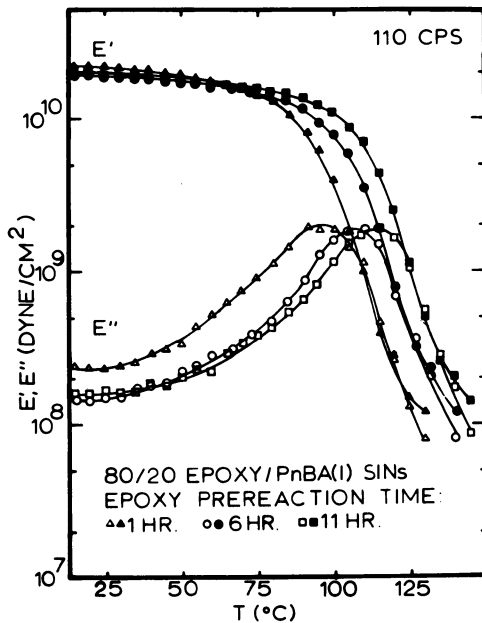


Figure 8. Dynamic mechanical spectroscopy on samples 11, 12, and 15 showing the increase in glass transition temperature with increased epoxy prereaction time

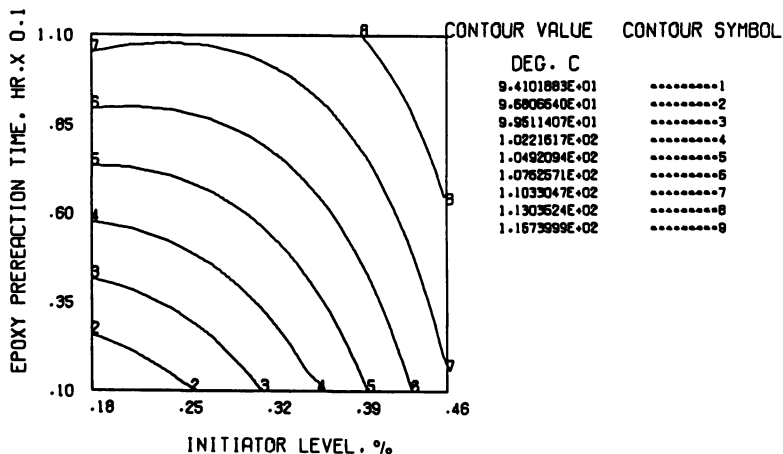


Figure 9. Contour plot of  $T_{g1}$  holding DEGDM constant

about the glass transition behavior, extent of molecular mixing, and phase continuity.

The most important results were observed in the glass transition behavior of the materials where increasing the epoxy prereaction time increased the glass transition of the epoxy-rich phase (Figure 8). At an epoxy prereaction time of about 1 hr,  $T_{g1}$  was 97°C which was lower than the glass transition of the pure epoxy, 105°C. However when the epoxy prereaction time was increased,  $T_{g1}$  also increased. When the epoxy prereacted for 6 hr, the SIN's  $T_{g1}$  was 105°C or nearly the same as that of the epoxy homopolymer. Surprisingly, for eleven hours prereaction time the SIN's  $T_{g1}$  was 115°C or higher than that of the pure epoxy. The differences in  $T_{g1}$  from 97° to 115°C could not readily be accounted for by experimental error. Replication of the center point showed that the experimental error was only about  $\pm 2^\circ\text{C}$ .

A complete picture of how the independent variables affect  $T_{g1}$  can be obtained from examining a contour plot of the predicted response surface of  $T_{g1}$  at constant DEGDM level; DEGDM was held constant because it had little effect on  $T_{g1}$  (Figure 9). It is evident from the contours that  $T_{g1}$  is increased not only by increased epoxy prereaction time but also by increased initiator concentration. The lowest values for  $T_{g1}$  are found with low epoxy prereaction times and low initiator concentrations, independent of DEGDM concentration.

The glass transition of the phase rich in poly(*n*-butyl acrylate),  $T_{g2}$ , ranged from  $-59^\circ$  to  $-48^\circ\text{C}$ . However the estimated experimental error ( $\pm 4^\circ\text{C}$ ) was fairly large compared with the range of  $T_{g2}$ ,  $12^\circ\text{C}$ . When the contour plots of  $T_{g2}$  were analyzed, no trends were significant

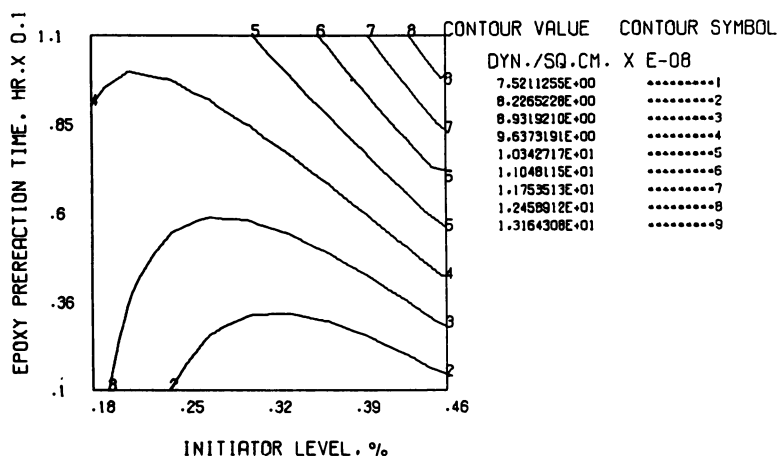


Figure 10. Contour plot of  $HT_{g2}$  holding DEGDM constant

compared with the experimental error. However the height of the poly-(*n*-butyl acrylate) damping peak at its maximum  $HT_{g2}$  did show significant trends. Figure 10 shows the predicted response surface of  $HT_{g2}$  to varying initiator concentration and epoxy prereaction times at a constant DEGDM concentration. The quantity  $HT_{g2}$  rises at high initiator concentrations and epoxy prereaction times and is lower in other cases. Again the level of DEGDM does not greatly affect the behavior, although  $HT_{g2}$  generally increases slightly with increasing amounts of DEGDM.

**Stress-Strain Studies.** Stress-strain analysis showed that most SIN samples had tensile strengths greater than that of the epoxy homopolymer (Figure 11). The pure epoxy resin has a tensile strength of *ca.* 6700 psi, and the tensile strength for the SIN's ranged from *ca.* 6400–8900 psi.

The predicted response surfaces for tensile strength at three different levels of DEGDM are given in Figures 12, 13, and 14 which show epoxy prereaction time and percent initiator level as variables. The surfaces are saddle contours with maxima and minima in alternating corners of the graphs. High tensile strengths are found in the corner with low initiator concentration and high epoxy prereaction time and in the corner with high initiator concentration and low epoxy prereaction time. The lowest tensile strengths are found in the other two corners of the graphs where prereaction time and initiator concentration are either both high or both low. Thus, less simultaneous reaction conditions produced materials that were stronger than those synthesized with more simultaneous conditions.

Computer-generated contour plots of the elongation at break and the toughness, measured by the area under the stress-strain curve, exhibit

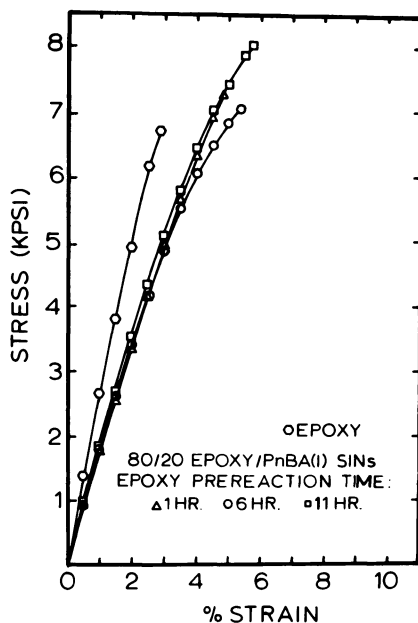


Figure 11. Stress-strain curves for samples 11, 12, and 15

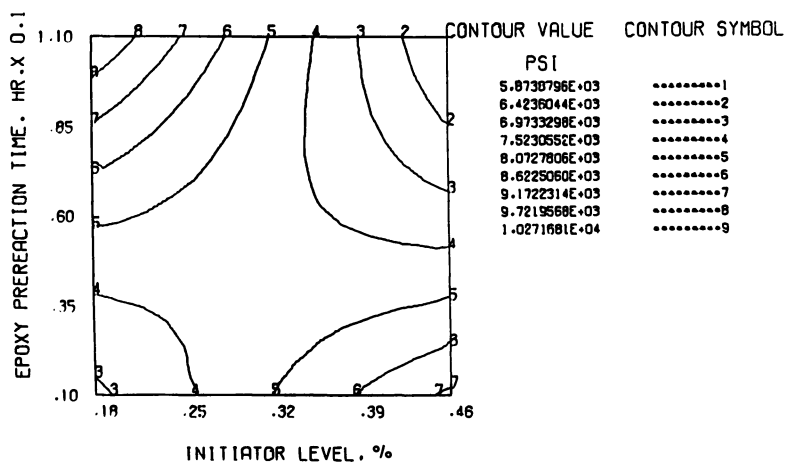


Figure 12. Contour plot of tensile strength holding DEGDM constant at 0.32%



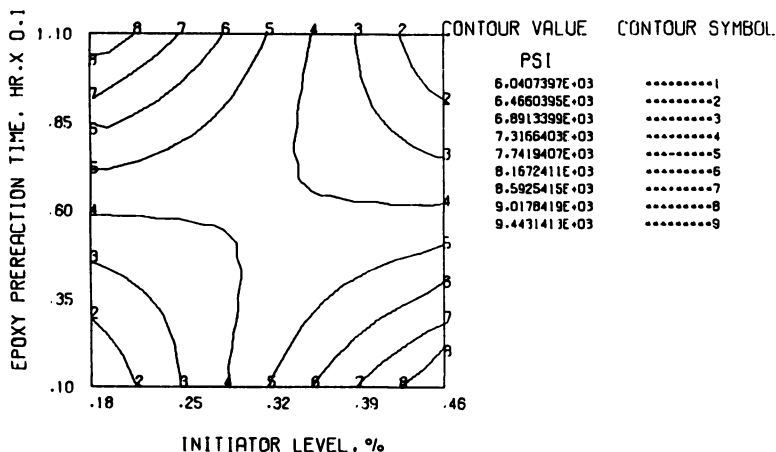


Figure 13. Contour plot of tensile strength holding DEGDM constant at 0.80%. The diagonal from lower left to upper right represents the reaction conditions believed to be "most" simultaneous.

essentially the same features as the contour plots of tensile strength with the less simultaneous reactions yielding better mechanical specimens than the more simultaneous reactions. The values of elongation and toughness for the SIN's may also be favorably compared with those of pure epoxy. Epon 828 cured with phthalic anhydride has an elongation of less than three percent and a toughness of *ca.* 110 psi %, while the range of elongations for the SIN's is 4.8–6.6%, and the range of toughness is 170–360 psi %.

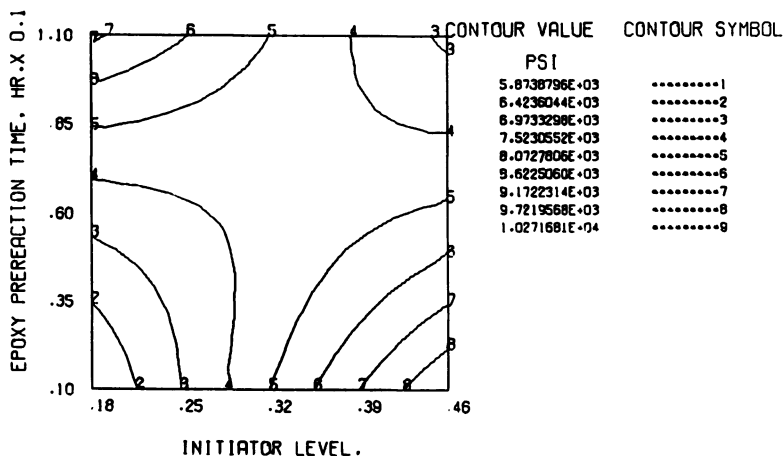


Figure 14. Contour plot of tensile strength holding DEGDM constant at 1.28%

The regions in which the tensile strengths show maxima have the conditions that are the least simultaneous. The experimental point where the experimental conditions are most simultaneous and where both reactions have medium reaction rates is in the center point of Figure 13. Along the diagonal running from lower left to upper right in Figure 13 the experimental conditions are such that the reactions are still simultaneous, but the gel times of the reactions are longer or shorter than at the center. Above the line the reactions are less simultaneous—the epoxy gels faster than the acrylate. Increasing the DEGDM concentration in this region (Figure 14) tends to make the reaction more simultaneous. Below the line reactions are less simultaneous—the acrylate reacts faster than the epoxy. Decreasing the DEGDM concentration (Figure 12) in this region makes the reaction more simultaneous. Reaction conditions which are less simultaneous tend to give samples with greater tensile strength.

**Impact Tests.** High speed mechanical impact causes the rapid growth of crazes and cracks in a plastic, resulting ultimately in fracture. The incorporation of a rubber phase increases impact strength because the rubber causes the generation of many small crazes or cracks rather than a few large ones, thus distributing the energy of the impact.

The SIN's all exhibited modest increases in impact strengths. The impact strength for the pure epoxy was 0.16 ft-lbs/in., while the impact strength of the SIN's ranged from 0.21–0.33 ft-lbs/in. However experimental error was significant when compared with the range of the impact strength for the SIN. Consequently no valid trends could be established other than the modest increases already described.

### *Discussion*

**Rubber Phase Domain Size and Shape.** Phase domain size seems to be controlled in part by the time of phase separation in relationship to the gel time of the reaction. Smaller phases are generally produced when phase separation is delayed until near or after the gel point of the total reaction. It is possible to tell if phase separation has occurred near the gel point by the clarity of the mix. If phase separation has occurred, the mix is cloudy or milky. In addition the bimodal distribution of phase domain sizes found in some samples is evidence that the reactions are truly simultaneous because the larger domains are probably formed before gelation and smaller domains by continued phase separation after gelation.

The variation in rubber phase domain shape appears to be determined more strongly than expected by the time of phase separation and the amount of DEGDM crosslinking agent. The ratio of length to width or elongation increases substantially at the higher levels of DEGDM.

When phase separation occurs before gelation and while the mix is still being stirred, the discontinuous acrylate phases tend to be elongated by the stirring. When DEGDM crosslinks the *n*-butyl acrylate before stirring is stopped, the elongation persists because of network formation. Thus the irregular or elongated shapes of the rubber domains are locked in as a result of crosslinking attributed to the presence of DEGDM. For example in sample 10 (Figure 4) phase separation occurred before gelation while the sample was still being stirred. This resulted in large, elongated, irregular rubber phase domains. However in sample 9 (Figure 5), although phase separation occurred before gelation, there was no DEGDM present, and large but nearly spherical domains resulted. In sample 8 (Figure 3) phase separation occurred near but before gelation while the sample was still being stirred; thus the rubber phase domains are slightly elliptical. On the other hand phase separation occurred after gelation in sample 5 (Figure 2), and small and nearly spherical domains resulted.

**Phase Composition and Simultaneous Polymerization.** Theoretically the phase composition of the SIN's should not be determined by the true solubility of one polymer in the other. Even though the true solubility of one polymer in the other is low because the components of the SIN's are incompatible, simultaneous polymerization and gelation are expected to cause entrapment of one component in the other. The degree of entrapment presumably will be controlled by the relative rates of the two reactions and their degree of simultaneity. The phase composition is reflected in the glass transition behavior of the material. Thus a close look at the dynamic mechanical spectra of the SIN's is necessary to determine the effect of simultaneous polymerization on phase composition.

The most striking feature of the dynamic mechanical spectra is the increase of the major glass transition ( $T_{g1}$ ) above the glass transition temperature of the homopolymer epoxy. While the exact cause for the increase in  $T_{g1}$  is unknown, the following factors were considered. First, increased crosslinking may increase  $T_{g1}$ . The crosslinking in the SIN may be increased either by chemical means or physical entanglements and promoted by a greater mobility in the epoxy phase attributed to the presence of the acrylic monomer and polymer (114, 115, 116, 117). However measurements of the modulus above the glass transition showed that changes in the density of chemical and physical crosslinks as determined by the equation

$$G = nRT \quad (11)$$

where  $G$  is the shear modulus and  $n$  is the crosslink density, were not very large or consistent with changes in the glass transition behavior of the SIN's (Table III). Secondly, the rubber may fill the free volume of

**Table III. The Effect of Shear Modulus with Changes in the Glass Transition Temperature**

Experiment Number	$T_{g1}$ ( $^{\circ}\text{C}$ )	$\beta G(10)$ dynes/cm <sup>2</sup>
11	97	$1.0 \times 10^8$
16	105	$9.6 \times 10^7$
12	115	$1.2 \times 10^8$

the epoxy so that the glass transition of the epoxy is raised. Examples of the filling of the free volume of a polymer with low molecular weight compounds are found in the literature; the process is called antiplasticization. However antiplasticization is not entirely analogous to the phenomena found with SIN's. In antiplasticization, described by Jackson and Caldwell (118, 119), Robeson (120, 121), and others (122-124), low molecular weight molecules are added to a polymer with a low temperature transition. The low molecular weight compound fills the free volume and depresses or eliminates the low temperature transition. Thus the modulus of the polymer does not change at low temperatures in association with the low temperature transition. The storage modulus remains at a higher level until the principal glass transition temperature. As a result the storage modulus of the polymer above the low temperature damping peak and below the glass transition is higher when the polymer is antiplasticized. However the principal glass transition temperature is lowered with the addition of antiplasticizer, and the material softens at a lower temperature. Thus antiplasticization cannot explain the increase in  $T_{g1}$  and  $HT_{g2}$  found in the SIN's.

Another explanation for an abnormal increase in  $T_{g1}$  in polymer blends has been proposed by Manabe, Murakami, and Takayanagi (125). They used a three-layered shell model, which accounts for interaction between the dispersed and continuous phases of the blend. Abnormal increases in the glass transition of polystyrene in blends with various rubbers were explained by thermal stresses which arise from the difference in thermal expansion coefficients of the component polymers. However shifts in the glass transition temperatures of the SIN's do not appear to arise from differences in the expansion coefficients of the components because samples with the same overall composition and almost identical microstructures have significantly different glass transition temperatures.

Another explanation of the increase in the major glass transition (126) of SIN's relates to the retention of low molecular weight polymer of one component by the other phase. In this case low molecular weight fractions of the epoxy may be trapped in the rubber. When the epoxy is at its gel point, there is still much low molecular weight epoxy resin that has not reacted. At the point when the *n*-butyl acrylate is still mostly

monomer and when the epoxy is near gel formation, the low molecular weight fractions of the epoxy are still soluble in the acrylic phase. This low molecular weight epoxy component will tend to remain and be trapped in the acrylic phase as it polymerizes. The low molecular weight fraction thus trapped in the rubber phase cannot act as a plasticizer for the epoxy as it normally would; therefore the glass transition temperature of the epoxy is increased.

The glass transition temperature of a polymer varies with the molecular weight. A low molecular weight component decreases the glass temperature. Its removal by fractionation raises the glass temperature. The present mixing process might cause such a fractionation. Expressed mathematically (127, 128):

$$T_{g1} = T_{g1\infty} - \frac{K'}{M_n} \quad (12)$$

where  $T_{g1\infty}$  = the maximum transition temperature,  $K'$  is a constant, and  $M_n$  is the number average molecular weight (the inverse of  $M_n$  is proportional to the concentration of end groups). Thus  $T_{g1}$  is increased by a decrease in the concentration of end groups. Roovers and Toporowski (129) showed by studying star polymers that an increase in endgroups from branching decreases the glass transition temperature even when the molecular weight is constant. The number of endgroups in the completely reacted SIN's is controlled by the excess amount of epoxy groups in the formulation. If a low molecular weight fraction of the epoxy is trapped in the *n*-butyl acrylate phase, the endgroup concentration of the epoxy phase may be decreased, and therefore  $T_{g1}$  increases while the overall crosslink density in the material remains nearly the same.

If the rise in  $T_{g1}$  is caused by the entrapment of low molecular fractions of the epoxy in the acrylate, we expect several trends:

(a) the samples should become more brittle because the low molecular weight epoxy trapped in the acrylate will not be available to plasticize the epoxy phase;

(b) entrapment of low molecular weight epoxy in the *n*-butyl acrylate phase should increase the volume of the acrylate phase and therefore increase  $HT_{g2}$  with  $T_{g1}$ ;

(c) the highest values of  $T_{g1}$  should result when the reactions are simultaneous and fastest (high epoxy prereaction time and initiator concentration) because these conditions favor entrapment.

In fact these trends do occur, and therefore the entrapment of low molecular weight in the acrylic phase is consistent with the experimental results and is the favored explanation for the observed rise in  $T_{g1}$ .

On the other hand, when epoxy prereaction time and initiator concentration are low,  $T_{g1}$  is decreased. This decrease in  $T_{g1}$  is more com-

mon in polyblends. The decrease in  $T_{g1}$  probably arises from the entrapment of the acrylate polymer molecules in the epoxy phase. Theoretically, if the acrylate is trapped in the epoxy phase causing  $T_{g1}$  to decrease,  $HT_{g2}$  should decrease because the volume of the acrylic phase domains would be decreased. Entrapment of the acrylic polymer in the epoxy at low epoxy prereaction times and initiator concentrations is enhanced by the longer time of reaction before phase separation which encourages grafting of the acrylate to the epoxy especially at the hydroxyl groups on the epoxy (2). Experimentally,  $HT_{g2}$  does not tend to decrease when  $T_{g1}$  decreases (compare Figure 9 with Figure 10). Thus the entrapment of rubber in the epoxy at low initiator concentrations and epoxy prereaction times causes a decrease in  $T_{g1}$  while the entrapment of low molecular weight epoxy in rubber at high initiator concentrations and prereaction time causes an increase in  $T_{g1}$ .

The entrapment of rubber in the epoxy at low initiator concentrations and epoxy prereaction times promoted by grafting causes a decrease in  $T_{g1}$ ; the entrapment of low molecular weight epoxy in the rubber at high initiator concentrations and prereaction times causes an increase in  $T_{g1}$ . Both types of entrapment occur at the same time, and their effect on  $T_{g1}$  is in the opposite direction accounting for the rather small changes in  $T_{g1}$ . However one or the other type of entrapment may predominate depending on the reaction conditions, especially the reaction rates or gel times and the time phase separation occurs. With low initiator concentrations and prereaction times, grafting causes entrapment of the acrylate in the epoxy phase to dominate, and  $T_{g1}$  is lowered. When both reactions are fast, phase separation occurs early in the reaction, and grafting is limited to the interface. Also the *n*-butyl acrylate monomer is more mobile than the higher molecular weight epoxy prepolymer which makes entrapment of the epoxy in the acrylate predominate when the gel times are shorter and when there is less time for phase separation to occur.

It is not surprising that entrapment of one component in the other is significant when the epoxy prereaction time and the initiator concentrations are both high or both low because in these cases the two polymerizations are more simultaneous than if one variable were high and one low. Although the reaction conditions were chosen so that the reaction would be most simultaneous when the independent variables were at the middle of their ranges, changing both the epoxy prereaction time and the initiator concentration together changes the rate of both polymerizations, thus keeping the reactions close to simultaneity. When the reactions are less simultaneous, the two types of entrapment probably occur to a lesser extent and may result in improved properties. Entrapment of the rubber in the epoxy could offset the brittleness caused by entrapment of the low molecular weight epoxy fractions in the acrylic phase domain. The

result is a material with a higher softening point, decreased brittleness, and greater tensile strength.

Ideally, a simultaneous interpenetrating network should have extensive mixing at the molecular level, even to the extent of forming one uniform phase. As with other polymer blends, blocks, and grafts, SIN's exhibit phase separation attributed to the low entropy of mixing of two polymers which limits interpenetration in the real case. Thus there is an apparent discrepancy between theory and practice; however, the pursuit of the ideal has led to a new understanding of the ways that supermolecular structure can be controlled, and new understanding of the relationship between polymer structure and properties.

### *Conclusions*

Simultaneous interpenetrating networks of 80/20, epoxy/acrylate systems have resulted in polyblends with novel behavior. However interesting it may have been to control the reaction components so that they reached gelation simultaneously, experimental results show that better properties are obtained with the present system when the two gelations are less simultaneous in time. The present simultaneous polymerizations produced materials with a discontinuous, acrylic rubber-rich phase in a continuous epoxy-rich phase. The discontinuity of the acrylic phase is a result of its being present only to a level of 20%. The discontinuous phase size and shape was changed by the relative times of phase separation and gelation and mixing conditions. Phase composition determined the mechanical properties of the SIN's to a greater extent than expected. The formation of two incompatible crosslinked polymers simultaneously from a homogenous solution of their monomers hindered complete phase separation of the polymers and promoted entrapment of a minor amount of one component in the phase domains of the other. Entrapment by a minor amount of one polymer in the other was controlled by the relative polymerization rates and gel times of the two polymerizations. Both entrapment of the acrylic in the epoxy phase and entrapment of epoxy in the acrylic phase domains occurred to some extent. The glass transition of the epoxy rich phase was increased over that of the epoxy homopolymer as the initiator concentration and epoxy prereaction time were increased. The increase in the glass transition may have been caused by entrapment of low molecular weight portions of the epoxy in the acrylate. On the other hand at low initiator concentrations and epoxy prereaction times the glass transition of the epoxy was lowered from that of the epoxy homopolymer probably because of entrapment of rubber in the epoxy phase. Samples made with more simultaneous reactions tended to have lower tensile strengths and toughnesses than those whose reactions were

not as simultaneous. Samples made with less simultaneous reactions tended to have greater tensile strengths and higher glass transition temperature than the epoxy polymerized above.

### *Appendix*

**Application of Group Theory Concepts.** The above descriptive approach has indicated some basic examples of polymer combinations. Noting that there are in fact over 100 distinguishable types of graft-copolymers alone, several of which involve simultaneous polymerizations, it becomes immediately apparent that the nomenclature used to date is inadequate. Besides inadequately differentiating among the more complicated materials described in the literature, the nomenclature system fails to suggest how new combinations of two or more polymer molecules might be conceived. To supply the need for a concise mathematical formulation we make use of that branch of mathematics known as group theory (104, 105).

To form a group four conditions must be met: (a) The set must be closed—*i.e.*, the combination of two operations also yields a member of the set. (b) The operations must include an identity which leaves the molecules unchanged. (c) The associative law of combination must hold. (d) Every operation must have an inverse.

In a formal sense a group must meet all of these criteria. Collections of sets and operations meeting some but not all of the required criteria may meet the lesser demands of semi-groups or groupoids. The groupoids demand only a set and an operation between them. Conditions (a) and (c) will sometimes not be met. Hence although the theory we present below is incomplete, the definition of a groupoid most closely applies to it.

As basic elements we consider monomer 1, monomer 2, . . . . , monomer  $n$ , that can be polymerized to form various polymers and copolymers. As the basic operations we designate the following symbols: P (polymerization), G (grafting), and C (crosslinking). Polymerization will be assumed to be linear unless operation C is specified. Most important the present group is noncommutative, and the time sequence of events must be preserved. Thus the order of the operations must be maintained.

The operations and the reactive units must be clearly distinguished. Capital and lower case letters will differentiate between operations and the objects upon which the group operates. For example the addition of a monomer will be designated as  $m$ . The addition of monomers capable of inducing grafting or crosslinking, *e.g.* divinyl benzene, will be designated by  $g$  and  $c$ . The operations of grafting and crosslinking, which may come much later in the reaction sequence, will be specified by the capital



letters. Parentheses indicate simultaneous operations, and brackets indicate operations carried out separately with the products later mixed or allowed to react. Different components are denoted by the subscripts 1, 2, . . . , n .

With the aid of group theory concepts the different IPN's and SIN's may be written in mathematical form. For example a graft copolymer with polymer 2 crosslinked (11-22) (designated a semi-IPN of the second kind (18) may be written:

$$m_1P_1m_2c_2(P_2G_{12}) \quad (2)$$

where  $G_{12}$  represents grafting of the second monomer to the backbone of the first polymer. The Millar type (61) IPN's could be written:

$$(m_1c_1)P_1(m_1c_1)P_1 \quad (3)$$

Note that the first and second polymerizations involve identical polymers as crosslinking agents. Sequential (bulk) IPN's could be written (68-81):

$$(m_1c_1)P_1(m_2c_2)(P_2G_{12}) \quad (4)$$

For simultaneous polymerizations note this case of two linear polymers:

$$(m_1m_2)(P_1P_2G_{12}G_{21}) \quad (5)$$

When one polymer is linear and one is crosslinked (90-95, 97-103) the synthesis may be written:

$$(m_1c_1m_2)(P_1P_2G_{12}G_{21}) \quad (6)$$

This product is designated as a semi-SIN. The SIN's may be written (1, 2, 84-89, 96):

$$(m_1c_1m_2c_2)(P_1P_2G_{12}G_{21}) \quad (7)$$

where both polymers are crosslinked. Thus group theory concepts help to delineate the similarities and differences among the various IPN's and SIN's.

### Literature Cited

1. Sperling, L. H., Arnts, R. R., *J. Appl. Polym. Sci.* (1971) **15**, 2317.
2. Touhsaent, R. E., Thomas, D. A., Sperling, L. H., "Epoxy/Acrylic Simultaneous Networks," *J. Polym. Sci.* (1974) **46**, 175-190.
3. Rowe, E. H., Siebert, A. R., Drake, R. S., *Mod. Plast.* (August 1970) **47**, 110.
4. Soldatos, A. C., Burhans, A. S., "Multicomponent Polymer Systems," *ADVAN. CHEM. SER.* (1971) **99**, 531.

5. Kalfoglou, N. K., Leverne Williams, H., *J. Appl. Polym. Sci.* (1973) **17**, 1377.
6. McGarry, F. J., Willner, A. M., Sultan, J. N., "Toughening of Glassy Crosslinked Polymers with Elastomeric Inclusions," R 69-35, July 1, 1969, Massachusetts Institute of Technology (1969).
7. Sultan, J. N., McGarry, F. J., "Microstructures Characteristic of Toughened Thermoset Plastics," R 69-59, October 1, 1969, Massachusetts Institute of Technology (1969).
8. Sultan, J. N., Taible, R. C., McGarry, F. G., *Appl. Polym. Symp.* (1971) **16**, 127.
9. Siebert, A. R., Rien, C. K., *Amer. Chem. Soc., Div. Org. Coatings Plastics Chem., Preprint* **31**, 555 (1971).
10. Noshay, A., Robeson, L. M., *J. Polym. Sci.* (1974) **12**, 689.
11. Ball, A., Hayes, B. J., Matthews, A. J., U.S. Patent **3,641,195** (1972).
12. Garnish, E. W., U.S. Patent **3,634,169** (1972).
13. DeCosta, J. B., U.S. Patent **3,579,616** (1971).
14. Jeffery, J. J., Rohrbacker, F., Jr., U.S. Patent **3,505,269** (1970).
15. Chadwick, A. C., Hocker, R. W., U.S. Patent **3,501,434** (1970).
16. Czerwinski, R. W., U.S. Patent **3,496,250** (1970).
17. Russel, D. H., U.S. Patent **3,464,948** (1969).
18. Garling, R. A., Hausch, W. R., U.S. Patent **3,383,337** (1968).
19. Howerton, W. W., U.S. Patent **3,291,857** (1966).
20. Carter, R. J., Causens, R. H., Osmund, D. W. J., U.S. Patent **3,261,788** (1966).
21. Newey, H. A., U.S. Patent **2,795,565** (1957).
22. Safford, M. M., U.S. Patent **2,843,557** (1958).
23. Fellers, J. F., Newman, S., U.S. Patent **3,652,723** (1972).
24. Muny, R. P., Wilson, D. W., U.S. Patent **3,699,500** (1972).
25. Dunion, Jr., P. F., Tsukamoto, A., U.S. Patent **3,542,902** (1970).
26. Davis, Jr., L., Larson, P. A., U.S. Patent **3,538,185** (1970).
27. Holup, F. F., Evans, S., Evans, M. L., U.S. Patent **3,535,403** (1970).
28. Marion, D. L., Hall, R. H., U.S. Patent **3,528,935** (1970).
29. Edwards, D. C., U.S. Patent **3,529,036** (1970).
30. Rohrbacker, Jr., F., U.S. Patent **3,509,086** (1970).
31. Clarke, J. A., U.S. Patent **3,509,230** (1970).
32. Baker, I., Robins, C., U.S. Patent **3,506,603** (1970).
33. Farber, H. A., Saffranski, J. C., U.S. Patent **3,501,434** (1970).
34. Hicks, D. D., U.S. Patent **3,467,730** (1969).
35. McCarthy, W. J., U.S. Patent **3,465,058** (1969).
36. Verdox, J. A., Gower, B. G., U.S. Patent **3,429,946** (1969).
37. Windemuth, E., Braun, G., U.S. Patent **3,399,247** (1968).
38. Tanaka, S., Minami, T., U.S. Patent **3,378,601** (1968).
39. Applegath, D. D., Klumb, G. A., U.S. Patent **3,361,842** (1968).
40. Kelly, D. J., U.S. Patent **3,310,603** (1967).
41. Hicks, D. D., U.S. Patent **3,305,601** (1967).
42. Gaske, J. E., Brown, W. H., U.S. Patent **3,301,801** (1967).
43. Wolff, N., Pitrolffy-Szabo, T. B., U.S. Patent **3,238,170** (1966).
44. Murdock, J. D., U.S. Patent **3,222,418** (1965).
45. Heppollette, R. L., U.S. Patent **3,222,420** (1965).
46. Lombardi, L. J., Wright, H. J., Westfall, P. F., U.S. Patent **3,215,756** (1965).
47. Zimmerman, R. L., Lee, L., U.S. Patent **3,207,718** (1965).
48. Clemens, D. H., U.S. Patent **3,183,281** (1965).
49. Brockman, F. J., Segal, G. H., U.S. Patent **3,179,714** (1965).
50. Nix, V. G., U.S. Patent **3,129,198** (1964).
51. Schwarzer, C. G., U.S. Patent **3,113,036** (1963).
52. Touner, F. I., Dison, G. F., U.S. Patent **3,107,336** (1963).

53. Roeser, G. P., U.S. Patent 3,070,564 (1962).
54. Vasta, J. A., U.S. Patent 3,065,195 (1962).
55. Fang, J. C., U.S. Patent 3,048,552 (1962).
56. Lombarde, L. J., Wright, H. J., Westfall, P. F., U.S. Patent 3,030,332 (1962).
57. Fry, J. S., U.S. Patent 3,008,914 (1961).
58. Segall, G. H., Cameron, J. L., U.S. Patent 2,798,861 (1957).
59. Wentworth, O. C., U.S. Patent 2,662,870 (1953).
60. Zimmerman, R. L., Lyons, C. E., U.S. Patent 3,342,896 (1967).
61. Millar, J. R., *J. Chem. Soc.* (1960) 1311.
62. Shibayama, K., Suzuki, Y., *Kobunshi Kagaku* (1966) 23 (249), 24.
63. Shibayama, K., Suzuki, Y., *Rubber Chem. Technol.* (1967) 40, 476.
64. Shibayama, K., Kodama, M., *Kobunshi Kagaku* (1967) 24, 1.
65. *Ibid.* (1967) 24, 104.
66. Frisch, H. L., Klempner, D., Frisch, K. C., *Polym. Lett.* (1969) 7, 775.
67. Klempner, D., Frisch, H. L., Frisch, K. C., *J. Polym. Sci.* (1970) A-2 (8), 921.
68. Sperling, L. H., Friedman, D. W., *J. Polym. Sci., Part A-2* (1969) 7, 425.
69. Sperling, L.H., Taylor, D. W., Kirkpatrick, M. L., George, H. F., Bardman, D. R., *J. Appl. Polym. Sci.* (1970) 14, 73.
70. Sperling, L. H., George, H. F., Huelck, V., Thomas, D. A., *J. Polym. Sci.* (1970) 14, 2815.
71. Sperling, L. H., Huelck, V., Thomas, D. A., in "Polymer Networks: Structure and Mechanical Properties," S. Newman, A. J. Chomppff, Eds., Plenum, 1971.
72. Sperling, L. H., George, H. F., Huelck, V., Thomas, D. A., *Amer. Chem. Soc., Div. Polym. Chem., Preprint* 11, 477 (1970).
73. Huelck, V., Thomas, D. A., Sperling, L. H., *Macromolecules* (1972) 5, 340, 348.
74. Sperling, L. H., Sarge III, H. D., *J. Appl. Polym. Sci.* (1972) 16, 3041.
75. Sperling, L. H., Chiu, Tai-Woo, Thomas, D. A., *J. Polym. Sci.* (1973) 17, 2443.
76. Sperling, L. H., Chiu, Tai-Woo, Hartman, C. P., Thomas, D. A., *Int. J. Polym. Mater.* (1972) 1, 333.
77. Sperling, L. H., Chiu, Tai-Woo, Gramlich, R. G., Thomas, D. A., *J. Paint Technol.* (1974) 46, 47.
78. Sperling, L. H., Thomas, D. A., U.S. Patent 3,833,404 (1974).
79. Curtius, A. J., Covitch, M. J., Thomas, D. A., Sperling, L. H., *Polym. Eng. Sci.* (1972) 12 (2), 101.
80. Sperling, L. H., Mihalakis, E. N., *J. Appl. Polym. Sci.* (1973) 17, 3811.
81. Donatelli, A. A., Thomas, D. A., Sperling, L. H., in "Recent Advances in Polymer Blends, Grafts, and Blocks," L. H. Sperling, Ed., Plenum Press, New York, 1974.
82. Ryan, C. F., Crochowski, F. J., U.S. Patent 3,426,101 (1969).
83. Amagi, Y., Obya, M., Shiiki, Z., Yusa, H., U.S. Patent 3,671,610 (1972).
84. Frisch, K. C., Klempner, D., Frisch, H. L., Ghiradella, H., in "Recent Advances in Polymer Blends, Grafts, and Blocks," L. H. Sperling, Ed., p. 395, Plenum, New York, 1974.
85. Frisch, K. C., Klempner, D., Migdal, S., Frisch, H. L., Ghiradella, H., *Polym. Eng. Sci.* (1974) 14, 76.
86. Frisch, K. C., Klempner, D., Antczak, T., Frisch, H. L., *J. Appl. Polym. Sci.* (1974) 18, 683.
87. Frisch, K. C., Klempner, D., Migdal, S., Frisch, H. L., *J. Polym. Sci., Polym. Chem. Ed.* (1974) 12, 885.
88. Frisch, K. C., Klempner, D., Mukherjee, S. K., Frisch, H. L., *J. Appl. Polym. Sci.* (1974) 18, 689.
89. Frisch, K. C., Klempner, D., German Patent 2,153,987 (1972).

90. Allen, G., Bowden, M. J., Blundell, D. J., Hutchinson, F. G., Jeffs, G. M., Vyvoda, J., *Polymer* (1973) **14**, 597.
91. Allen, G., Bowden, M. J., Blundell, D. J., Jeffs, G. M., Vyvoda, J., White, T., *Polymer* (1973) **14**, 604.
92. Allen, G., Bowden, M. J., Lewis, G., Blundell, D. J., Jeffs, G. M., *Polymer* (1974) **15**, 13.
93. Allen, G., Bowden, M. J., Lewis, G., Blundell, D. J., Jeffs, G. M., Vyvoda, J., *Polymer* (1974) **15**, 19.
94. Allen, G., Bowden, M. J., Todd, S. M., Blundell, D. J., Jeffs, G. M., Davis, W. E. A., *Polymer* (1974) **15**, 28.
95. Blundell, D. J., Longman, G. W., Wignall, G. D., Bowden, M. J., *Polymer* (1974) **15**, 33.
96. Teffan, A. J., U.S. Patent 3,305,514 (1967).
97. Pennino, C. J., U.S. Patent 3,293,322 (1966).
98. Foster, N. C., U.S. Patent 3,099,638 (1963).
99. Ramscheidt, G. E., U.S. Patent 2,939,859 (1960).
100. Parker, E. D., U.S. Patent 2,890,202 (1959).
101. Eirich, F. R., U.S. Patent 2,848,433 (1958).
102. Armitage, F., Trace, L. G., U.S. Patent 2,846,410 (1958).
103. Speitel, R., Hegnauer, M. R., U.S. Patent 3,657,381 (1972).
104. Sperling, L. H., in "Recent Advances in Polymer Blends, Grafts, and Blocks," Plenum Press, New York, 1974.
105. Sperling, L. H., *ADVAN. CHEM. SER.* (1975) **154**, 159.
106. Babayevsky, P. G., Gillham, J. K., *J. Appl. Polym. Sci.* (1973) **17**, 2067.
107. Gillham, J. K., Benci, J. A., Noshay, A., *J. Appl. Polym. Sci.* (1974) **18**, 951.
108. Kato, K., *Jap. Plast.* (April 1968) **2**, 6.
109. Matsuo, M., *Jap. Plast.* (July 1968) **2**, 6.
110. Box, G. E. P., Wilson, K. B., *J. Roy. Stat. Soc., Sect. B* (1951) **13**, 1.
111. Hill, W. J., Hunter, W. G., *Technometrics* (1966) **8** (4), 571.
112. Hicks, C. R., "Fundamental Concepts in the Design of Experiments," p. 233, Holt, Rinehart, and Winston, New York, 1964.
113. Davies, O. L., "Design and Analysis of Industrial Experiments," p. 449, Hafner Pub. Co., New York, 1956.
114. Gibbs, J. H., DiMarzio, E. A., *J. Chem. Phys.* (1958) **28**, 373, 807.
115. Gibbs, J. H., DiMarzio, E. A., *J. Polym. Sci.* (1959) **40**, 121.
116. Ueberreiter, K., Kanig, G., *J. Chem. Phys.* (1950) **18**, 399.
117. Loshack, S., *J. Polym. Sci.* (1955) **15**, 391.
118. Jackson, Jr., W. J., Caldwell, J. R., *Amer. Chem. Soc., Div. Org. Coatings Plastics, Preprint* **26** (2), 160, 170 (1966).
119. Jackson, Jr., W. J., Caldwell, J. R., *ADVAN. CHEM. SER.* (1965) **48**, 185.
120. Robeson, L. M., *Polym. Eng. Sci.* (1969) **9** (4), 277.
121. Robeson, L. M., Faucher, J. A., *J. Polym. Sci., Part B* (1960) **7** (1), 35.
122. Robertson, R. E., Joynson, C. W., *J. Appl. Polym. Sci.* (1972) **16** (3), 733.
123. Wyzgoski, M. G., Yeh, G. S. Y., *Polym. J.* (1973) **4** (1), 29-34.
124. Kinjo, N., *Jap. Plast.* (1973) **7** (8), 6.
125. Manabe, S., Murakami, R., Takayanagi, M., *Int. J. Polym. Mater.* (1971) **1**, 47.
126. Robeson, L. M., Union Carbide Corp., Bound Brook, N. J., May 2, 1974, personal communication.
127. Fox, T. G., Flory, P. J., *J. Appl. Phys.* (1950) **21**, 581.
128. Fox, T. G., Flory, P. J., *J. Polym. Sci.* (1954) **14**, 315.
129. Roovers, J. E. L., Toporowski, P. M., *J. Appl. Polym. Sci.* (1974) **18**, 1685.

RECEIVED October 18, 1974. This work was supported through the National Science Foundation grant GH-40645.

## The Impact Strength of Styrene–Butadiene Block Copolymer and Its Dependence on the Continuous Phase

R. J. ANGELO and R. M. IKEDA

E. I. du Pont de Nemours & Co., Inc., Film Research Laboratory,  
Experimental Station, Wilmington, Del. 19898

M. L. WALLACH

E. I. du Pont de Nemours & Co., Inc., Photo Products Research Laboratory,  
Experimental Station, Wilmington, Del. 19898

*The pneumatic impact strengths of a series of well-characterized styrene–butadiene triblock copolymers (B/S/B) were measured and compared with torsion pendulum  $\tan \delta$  measurements. Instead of a linear log–log impact strength– $\tan \delta$  correlation, an S-shaped curve was observed. The latter is interpreted in terms of the two-phase structures revealed by electron microscopy.*

A few years ago, T. P. Yin (1) correlated the internal friction and tensile impact strength measurements for several series of homogeneous and heterogeneous elastomeric polyblends. With each series, a linear log–log plot was obtained which was attributed to the invariance of the crack propagation energy, rubbery reinforcement, geometrical factors, etc., in the series and to a simple dependence of the impact strength on the dissipative vibrational energy ( $\tan \delta$ ). In view of this work, we examined  $\tan \delta$  and pneumatic impact strength information gathered on our series of styrene/butadiene block copolymers.

### *Experimental*

The styrene/butadiene block polymers were synthesized in tetrahydrofuran by the Szwarc anionic living polymerization technique (2, 3, 4). Details of the polymerization, as well as extensive characterization

**Table I. Polymer Characterization Data**

Polymer Designation	Vol % S <sup>a</sup>	[ $\eta$ ]		$M_w/M_n$	$T_g(B)^b$ ( $^{\circ}C$ )	$T_g(S)^b$ ( $^{\circ}C$ )
		Benzene dl/g	$M_n \times 10^{-5}$			
S	100	0.49	0.609	1.17	—	111
S/B <sub>1</sub>	81	0.71	1.05	—	-4	100
S/B <sub>2</sub>	67	0.76	1.02	1.22	-1	104
S/B <sub>3</sub>	55	0.82	0.845	—	-2	100
S/B <sub>4</sub>	48	1.06	1.28	—	2	103
S/B <sub>5</sub>	28	2.85	3.14	—	0	99
B	0	1.19	0.914	1.08	-1	—
B/S	85	1.69	1.85	—	-2	105

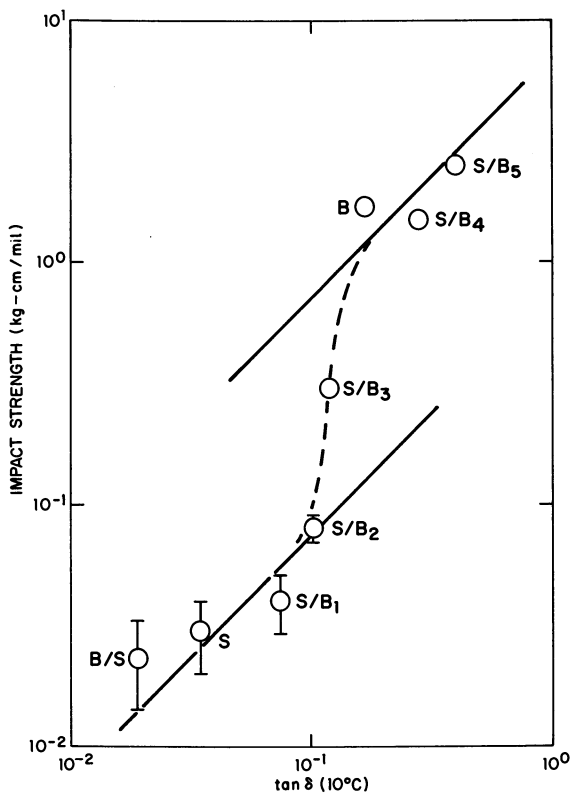
<sup>a</sup> Based on NMR.<sup>b</sup> DSC values (heating rate: 30 $^{\circ}C$ /min).

Figure 1. Impact Strength vs.  $\tan \delta$ . For samples S/B<sub>3</sub>, S/B<sub>4</sub>, S/B<sub>5</sub>, and B, the range of impact strength values are enclosed by the circles.

information, have been reported (5, 6). Infrared analysis showed the polybutadiene segments to be 90% 1,2- and 10% *trans*-1,4-butadiene.

The samples used in this study are listed in Table I with selected characterization data. Also given are our notations for the samples. S and B represent polystyrene and polybutadiene, respectively. The block polymers are denoted S/B<sub>1</sub>, S/B<sub>2</sub>, etc. The letters identify the polymer components with the first letter indicating the center segment. The polymers were isolated from the polymerization solution by precipitation into cold (0°C), well-stirred methanol. After careful drying in a vacuum oven (25°C), film samples were prepared by melt pressing at temperatures ranging from 25°C for homopolybutadiene to 150°C for homopolystyrene.

Details of the torsion pendulum analyses were given previously (5). Pneumatic impact strengths were determined by a well-known method (7).

Electron microscopy samples were prepared by techniques similar to that of Kato (8). Film samples were fixed with OsO<sub>4</sub>, potted in polymethyl methacrylate and then microtomed into thin sections (~100 nm) for transmission examination using a Philips 100B electron microscope.

### Results and Discussion

The torsion pendulum determinations were made at low frequency (~1 Hz) while the duration of the impact strength measurements is on the order of 1 msec. To correct for this frequency difference, we used the WLF equation (9) and found that the 10°C (1 Hz) tan δ information should approximately correspond to the impact measurements taken at room temperature. In Figure 1, we plot the impact strengths vs. tan δ (10°C). A single linear correlation does not exist, but the tan δ values predict that the S sample would have a higher impact strength than the B/S sample and that the B sample, at the other extreme, would have a lower impact strength than the S/B<sub>5</sub> specimen. Most models would favor

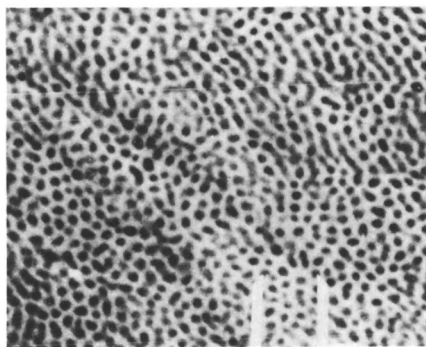
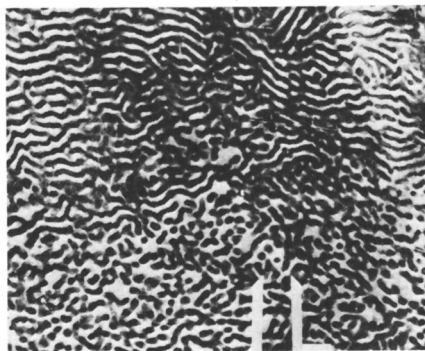


Figure 2. Electron micrograph of samples S/B<sub>1</sub>. OsO<sub>4</sub> staining results in dark polybutadiene phases. Markers indicate 1 μM.



*Figure 3. Electron micrograph of sample S/B<sub>3</sub>. OsO<sub>4</sub> staining results in dark polybutadiene phases. Markers indicate 1  $\mu$ M.*

placing the compositional extremes at the correlation extremities. The straight lines were expected on the basis of Yin's work. We interpret the two lines as indicating a change in failure mechanism with a change in continuous phase. With polystyrene as the continuous phase, we obtain a characteristic low impact strength with modest increases (straight line) accompanying the incorporation of the soft filler. When polybutadiene becomes the continuous phase, we get a tenfold increase in the impact strength which then modestly increases further with a decrease in the hard segment content. The composition at which the impact strengths switch from one mechanism to the other ( $\sim 50$  vol %) is reasonable for this hypothesis and, indeed, electron microscopy studies provide evidence for this switch in continuous phase.

Our OsO<sub>4</sub> staining techniques and the subsequent observation of the two phases are similar to that found by a number of workers (10, 11). Figures 2 and 3 are representative examples of our observations. The butadiene domains appear dark in these micrographs from the incorporation of the osmium. Near the compositional extremities [B/S (85% S), S/B<sub>1</sub> (81% S), and S/B<sub>5</sub> (28% S)], the minor component appears in spherical domains dispersed in the continuous second matrix. Figure 2, a micrograph of S/B<sub>1</sub>, is illustrative, showing a continuous styrene matrix with dispersed, spherical polybutadiene domains. For the middle compositions [S/B<sub>2</sub> (67% S), S/B<sub>3</sub> (55% S), and S/B<sub>4</sub> (48% S)], the shapes of the domains are rodlike or, possibly, platelike. In these cases, a clear choice of the continuous phase is difficult although S/B<sub>2</sub> appeared to have a continuous polystyrene phase and S/B<sub>4</sub> a continuous polybutadiene phase. Figure 3, a photomicrograph of S/B<sub>3</sub>, illustrates the structures usually seen. In parts of Figure 3, polystyrene is the continuous



matrix. In other areas, polybutadiene predominates. The absence of a single continuous phase in this sample, S/B<sub>3</sub>, agrees with its transitory position between the two straight line portions in Figure 1.

The possible effect of crosslinking upon the impact strength of this copolymer series was not examined. Although the butadiene-rich polymers showed a tendency to crosslink slightly during film fabrication, the extent of crosslinking was considered insufficient to account for the shape of the curve in Figure 1.

### *Acknowledgment*

We thank Mr. E. N. Buckley for obtaining the electron micrographs used in this study.

### *Literature Cited*

1. Yin, T. P., private communication.
2. Szwarc, M., *Nature* (1956) **178**, 116B.
3. Szwarc, M., Levy, M., Milkovich, R., *J. Am. Chem. Soc.* (1956) **78**, 2656.
4. Szwarc, M., Rembaum, A., *J. Polymer Sci.* (1956) **22**, 189.
5. Angelo, R. J., Ikeda, R. M., Wallach, M. L., *Polymer* (1965) **6**, 141.
6. Ikeda, R. M., Wallach, M. L., Angelo, R. J., "Block Polymers," p. 43, Plenum Press, New York, 1970.
7. Spangler, R. D., Cooper, E. B., Amer. Soc. Test Mat. Method D3099, *J. Apply. Phys.* (1957) **28**, 329.
8. Kato, K., *J. Electron Microscopy* (1965) **14**, 220.
9. Ferry, J. D., "Viscoelastic Properties of Polymers," p. 228, Wiley, New York, 1961.
10. Inoue, T., Soen, T., Hashimoto, T., Kawai, H., *J. Polymer Sci., A-2* (1969) **7**, 1283.
11. Bradford, E. B., Vanzo, E., *J. Polymer Sci., A-1* (1968) **6**, 1661.

RECEIVED October 18, 1974.

# Super High Impact Polystyrene Based on Polystyrene and Butadiene–Styrene Block Polymer Blends

R. R. DURST, R. M. GRIFFITH, A. J. URBANIC, and W. J. VAN ESSEN

General Tire and Rubber Co., Research and Development Division,  
Akron, Ohio 44329

*A blend of a rubbery styrene–butadiene block polymer and commercial polystyrene has been prepared which can be injection molded into articles having high impact strength and most of the other desirable properties of high quality ABS. The impact strength of the molded articles depends on the particle size of the rubbery block polymer component, its composition, and molecular weight. Impact strength reaches a maximum when the average particle size of the rubbery compound is near 1  $\mu\text{m}$  and when the styrene content of the block polymer is preferably in the range  $50 \pm 10\%$ . A relatively high molecular weight, preferably ca. 250,000  $M_n$ , is required to process successfully the blend while retaining the impact strength. When molecular weight is below 150,000  $M_n$ , impact strength decreases with increased processing. Articles molded from this polymer blend have an impact strength, flexural modulus, heat distortion, hardness, and appearance comparable with high quality ABS.*

Attempts to improve the impact strength or to toughen polystyrene are not new. Some early attempts to improve the impact strength by blending butadiene rubber with polystyrene failed because of the poor bond between the separate phases (1, 2, 3, 4).

Commercial high impact polystyrene (HIPS), having rubber present during the polymerization of the styrene, will reach an Izod impact of 2.2 ft-lbs/inch compared with 0.2 ft-lbs/inch for unmodified polystyrene. Styrene grafts on the rubber were sufficient to improve the bond between phases; this resulted in the higher impact (5, 6, 7, 8, 9). The commercial

HIPS products however do not have sufficient impact strength for many uses. Skilled researchers agree that HIPS with impact strength approaching 7.5 ft-lbs/inch notch can be prepared by adding more rubber. However the hardness, flexural modulus, tensile, and heat distortion temperatures are then drastically reduced.

Van Henten, at the Shell Plastic Laboratories (11), showed that styrene-butadiene block polymers can be blended with commercial HIPS to upgrade its impact strength to 5.8 ft-lbs/inch. Childers, at Phillips Petroleum (12), blended commercial polystyrene with block polymers in a Brabender plastograph. To control rubber particle size he added a peroxide during the blending operation, thereby creating crosslinks. With this technique he achieved an impact strength of 5.9 ft-lbs/inch.

Here we describe work which led to a high impact polystyrene blend, designated as PS/SBS, with a notched Izod impact of *ca.* 7.5 ft-lbs/inch. This product was obtained by mechanically or solution blending crystal polystyrene with a proprietary, unbranched graded styrene-butadiene-styrene block polymer. The blend has impact strength, flexural modulus, heat distortion, hardness, and molded appearance more equal to a high quality ABS resin than other polystyrene blends reported. The morphology, processing, and properties of the PS/SBS are briefly discussed and compared with those of commercial HIPS and ABS resin.

### *Development of PS/SBS Blend*

Initially various rubbery butadiene and styrene-butadiene block polymers were screened as impact-modifying agents for polystyrene. Commercial polystyrene and various rubbers were blended by dissolving the polymers in benzene and by subsequently precipitating them with isopropyl alcohol. The solid polymer blends were dried and molded into test bars. Laboratory and commercial polybutadiene and polystyrene were used in several combinations with the block polymer prepared in our laboratory.

A preliminary screening indicated that excellent impact could be obtained using 15–20 wt % butadiene based on the total polymer blend. At #20 wt % butadiene, several block polymers were screened for optimum impact and overall balance of properties. Two-component systems (block polymer-polystyrene) and three-component systems (block polymer-polybutadiene-polystyrene) were tried. The impact varied with the styrene content of the block polymer in both two- and three-component systems as shown in Figure 1. Subsequent work showed that the best overall balance of impact, flexural modulus, and heat distortion was obtained at 15% butadiene.

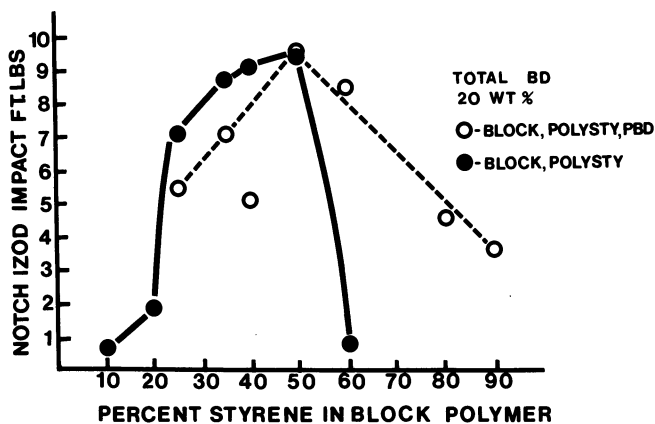


Figure 1. Impact strength vs. composition

For economic reasons we achieved the same quality blends by mechanically mixing commercial polystyrene with the block polymers. Good quality products were obtained from two-roll mills, the Brabender plastograph, the Banbury mixer, and continuous high intensity mixers.

With high shear mixing equipment such as the Banbury or continuous mixer, the use of block polymers with a number average molecular weight ( $M_n$ ) below 150,000 did not give the expected improvement in impact over polystyrene. This anomalous behavior occurred because the particle size of the discrete rubber phase averaged less than  $0.2 \mu\text{m}$  compared with an average of  $1 \mu\text{m}$  for blends with optimum impact obtained in the solution blends.

We attempted to prevent excessive dispersal of rubber particles by blending at a higher temperature which decreases the viscosity of the mix and reduces the shear experienced by the rubber. This technique slightly improved the impact strength, but the product still failed to match the solution blended polymers.

Block polymers of a higher molecular weight, around 250,000  $M_n$ , dispersed into particles in the  $1 \mu\text{m}$  range even in the intensive mixing units. The use of higher molecular weight block polymers resulted in polymer blends with properties equal to the best achieved by the solution blending technique. These blends retained their high impact during fabrication and in reprocessing operations.

After the molecular weight and composition of the block polymer were fixed at appropriate levels, mechanical blending was scaled-up to both larger and continuous dispersion mixers. An acceptable and reproducible product was made at all levels up to the highest output tried, e.g., 1000 lbs/hr.

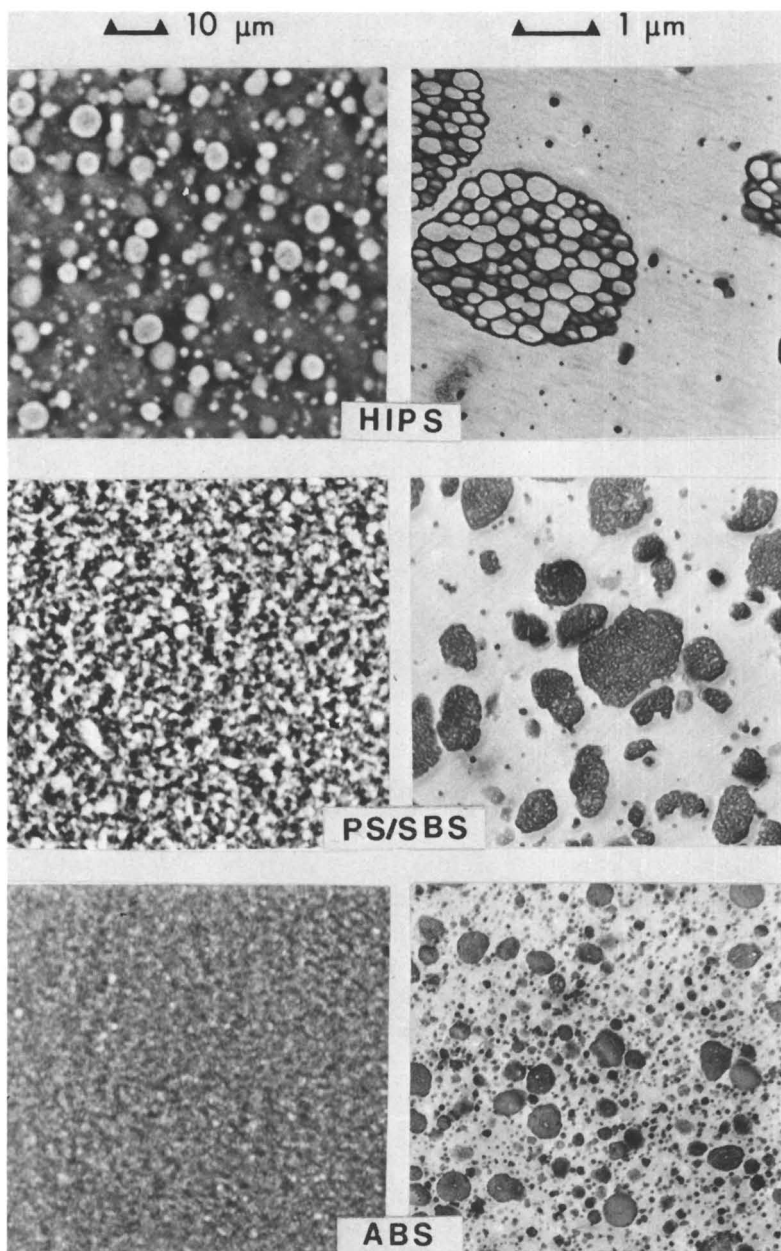


*Figure 2. Phase contrast photomicrographs of HIPS, PS/SBS, and ABS*

*Figure 3. Transmission electron micrographs of HIPS, PS/SBS, and ABS*

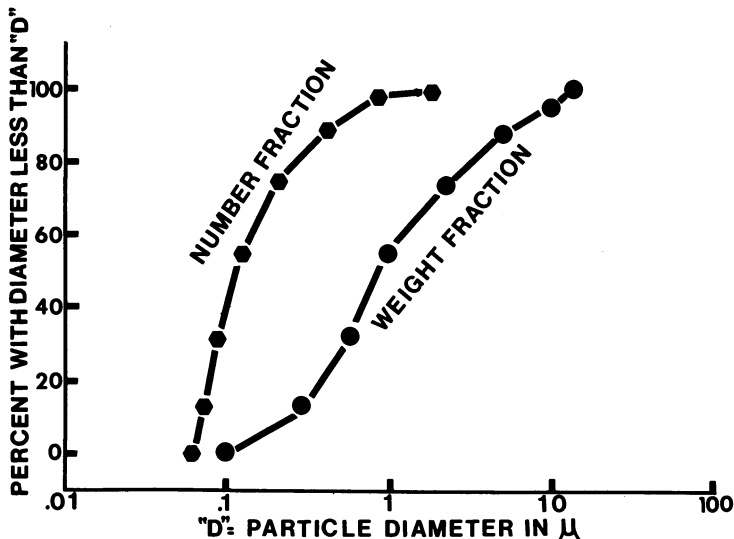


Figure 4. Size distribution of rubber particles in PS/SBS by thin section microscopy

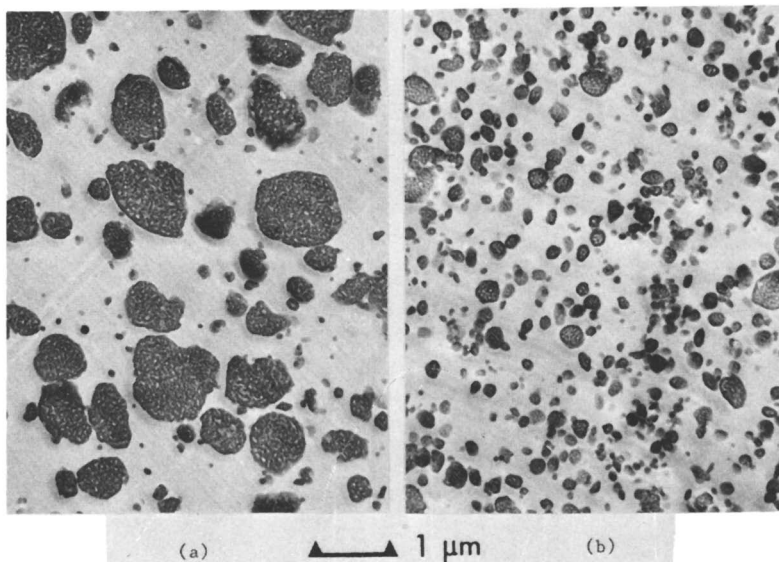


Figure 5. Effect of molecular weight of the block polymer on its particle size and blend impact strength in mechanical dispersions in polystyrene

Photograph	Mol Wt ( $M_n$ )	Av Particle Diam ( $\mu\text{m}$ )	Notched Izod Impact (ft-lb/inch) J/m	
(a)	250,000	1	7.5	400
(b)	165,000	0.2	1.0	53

Blends contain constant composition, styrene-butadiene block copolymer

### Morphology of PS/SBS Blend

Rubber particle size has been recognized as an important structural parameter in HIPS and ABS polymers (10). The dispersed phase in PS/SBS has been examined and compared with that in HIPS and ABS. Figure 2 shows thin section phase contrast photomicrographs of samples of PS/SBS, HIPS, and ABS resin. Figure 3 shows the transmission electron micrographs of the same materials. In HIPS one finds predominantly 1–10  $\mu\text{m}$  rubber particles (8, 10). In PS/SBS the rubber particles resemble those in ABS, but the average particle size is near 1  $\mu\text{m}$  in diameter in contrast to ABS with an 0.3–0.5  $\mu\text{m}$  average particle size. The ABS particle size range agrees with observations in the literature (10). The weight fractions of various particle sizes in PS/SBS were estimated from phase contrast and electron micrographs. The broad distribution (see Figure 4) was expected from mechanical blending.

The effect of the molecular weight of the block polymer on the size of the rubber particle and on the impact strength of the PS/SBS samples made under the same high shear mixing conditions is shown in Figure 5. The higher molecular weight results in a larger average particle size for the rubbery phase and in a higher impact strength for the PS/SBS.

### Properties of PS/SBS Blend

PS/SBS can be injection molded into test specimens and commercial articles on both laboratory- and commercial-size equipment. Processing conditions and cycles recommended for HIPS and ABS were acceptable for PS/SBS.

The properties of PS/SBS are compared with HIPS and ABS in Tables I and II. PS/SBS is similar to HIP in color, hardness, tensile strength and flexural strength and to ABS in impact strength, stiffness, and heat resistance. PS/SBS is intermediate between ABS and HIPS in tensile creep, gloss, and chemical resistance. Normal finishing methods

Table I. Physical Properties of PS/SBS, HIPS, and ABS

Property	Units	Polymer		
		PS/SBS	HIPS	ABS
Color	—	white	white	yellow
Gloss, 60°		70–86	70	90
Melt flow	g/10 min (condition g)	1.0	3.5	1.7
Rockwell "R"	—	103	103	105
Gardner impact	J/mm	9.9	0.9	11.8
	in.-lbs/mil	2.2	0.2	2.6

Table II. Physical Properties of PS/SBS, HIPS, and ABS

Property	Units	Polymer		
		PS/SBS	HIPS	ABS
Unnotched, Izod impact	} J/m } ft-lbs/in.	1185	747	1334
		22	14	25
Notched, Izod impact	} J/m } ft-lbs/in.	400	117	374
		7.5	2.2	7.0
Tensile yield strength	} MPa } psi	29.4	19.6	41.2
		4200	2800	5880
Elongation	%	28	38	30
Flexural modulus $\times 10^{-5}$	} MPa } psi	0.021	0.019	0.020
		3.0	2.7	2.8
Flexural strength	} MPa } psi	46	30	62
		6600	4300	8800
Deflection temp (Unannealed 1.82 MPa (264 psi) Annealed 2 hr at 73°C)		87	75	88
		93	82	94

can be used with PS/SBS. It can be painted, solvent welded, vacuum metallized, and hot stamped.

### Summary

Commercial polystyrene can be efficiently and reproducibly toughened by mechanical blending with a styrene-butadiene rubbery block polymer of specific composition. It is not necessary for this rubber to be crosslinked, but it must have sufficiently high molecular weight to resist particle size breakdown during processing of the blend into finished articles. The particle size distribution may be broad, but the diameter of most rubber particles must average  $1 \mu\text{m}$  for optimum impact strength and other physical properties. The end result of this work has been a high impact, rubber-modified polystyrene blend which has processibility and end use properties much closer to ABS than any polystyrene blend previously reported.

### Acknowledgment

This paper is published with permission of the General Tire and Rubber Co. The authors gratefully acknowledge the contributions made by R. T. Giuffria, V. M. Bauer, and H. F. Oswald for the phase contrast photomicrographs and transmission electron micrographs and S. L. Aggarwal, R. A. Livigni, and R. E. Bingham for valuable advice on polymer preparation and characterization.



**Literature Cited**

1. Turley, S. G., *J. Polym. Sci.* (1963) **C1**, 101.
2. Willersinn, H., *Makromol. Chem.* (1967) **101**, 297.
3. Simmons, P., *Rubber Plast. Age* (1967) **48**, 442.
4. Rosen, S. L., *Polym. Eng. Sci.* (1967) **7**, 115.
5. Wagner, E. R., Robeson, L. M., *Rubber Chem. Technol.* (1970) **43**, 1129.
6. Keskkula, H., *Appl. Polym. Symp.* (1970) **15**, 51.
7. Fettes, E. M., Maclay, W. N., *Appl. Polym. Symp.* (1968) **7**, 3.
8. Skeist, I., *Rubber World* (May 1967) 89.
9. Deland, D. L., Purdon, J. R., Schöneman, D. P., *Chem. Eng. Prog.* (1967) **63**, (No. 7), 118.
10. Bucknall, C. B., Drinkwater, I. C., *J. Mater. Sci.* (1973) **8**, 1800.
11. van Henten, J., *Plastica* (1972) **25**, 4, 144.
12. Childers, C. W., U.S. Patent **3,429,951** (1969).

RECEIVED October 18, 1976.

## Evaluating Mechanisms of Toughening in Impact Thermoplastics

P. J. FENELON and J. R. WILSON

Borg-Warner Chemicals, P.O. Box 68, Washington, W. Va. 26181

*Mechanisms of toughening in three experimental ABS polymers were studied at various impact strain rates at 25°C. The three experimental polymers formed a series of increasing polydiene content. Photographic analysis of high speed tensile deformation was used to measure simultaneously longitudinal and lateral strains and their respective strain distributions along gage lengths of test specimens. The extent of localization of deformation was determined, and true engineering stress-strain properties were quantified. Toughening mechanisms were divided into two main groups: cavitation mechanisms, i.e., crazing and other density reducing processes, and shear mechanisms, i.e., shear band formation and cold drawing.*

It has been reported by several workers (1, 2, 3, 4, 5, 6, 7, 8, 9) that when thermoplastics are subjected to tensile stresses they deform by shear and cavitation mechanisms. These processes are capable of absorbing substantial quantities of energy. Commercial impact thermoplastics, including rubber-toughened thermoplastics such as high impact polystyrene (HIPS) and acrylonitrile-butadiene-styrene polymers (ABS), owe their toughness to molecular motions and interactions which allow these deformation mechanisms to operate. It is important that the material scientist not only quantify the relative contributions of the above processes but also establish their rate, stress, and environmental dependence. Such quantization will allow more detailed studies of relationships between structure and mechanical properties and will provide better judgment on the suitability of deformation theories, i.e., elastic, plastic, elasto-plastic, etc., for predicting multiaxial material response from simple uniaxial tensile behavior.

Following the procedures used by Bucknall *et al.* (6, 7, 8) for analyzing low strain rate deformation mechanisms, toughening in three ABS

polymers ABS 1, ABS 2, and ABS 3 was studied at impact strain rates at 25°C. The three polymers formed a series of increasing polydiene content. Photographic analyses of high speed tensile deformation was employed simultaneously to measure longitudinal and lateral strains, together with their respective strain distributions, along gage lengths of test specimens. In this way, localization of material deformation, true engineering stress-strain properties and volume strain *vs.* longitudinal strain were determined. Volume strains were calculated, based on the assumption that the deformation in thickness and width was isotropic. Toughening mechanisms were divided into two main processes: cavitation mechanisms, *i.e.*, crazing and other density reducing processes, and shear mechanisms, *i.e.*, shear band formation and cold drawing. It is assumed that during deformation bulk modulus of uncrazed material does not alter and that shear mechanisms obey constant volume relationships. Respective contributions of cavitation and shear to overall deformation were quantified by comparing experimental volume strain *vs.* longitudinal strain curves with theoretically determined curves for pure cavitation and pure shear. These contributions were determined throughout the complete tensile deformation, *i.e.*, up to and including fracture. Analyses of results showed that the relative contribution of shearing to the total deformation becomes more dominant at higher strains, that cavitation persists even after the material has traversed its engineering yield point, and that the influence of increasing polydiene content is to increase fracture strain rather than change the relative contributions of the various processes giving rise to toughening.

### ***Experimental Details and Results***

**Materials and Specimen Preparation.** ABS 2 and ABS 3 were prepared by dry and melt blending of ABS 1 with a rigid polySAN. The styrene/acrylonitrile ratio of the polySAN used for blending was the same as that present in the parent ABS 1. Polydiene contents are in the order ABS 1 > ABS 2 > ABS 3.

Extruded compounded pellets were converted into strips (1 in. × 0.05 in.) using a 3/4 in. Brabender laboratory extruder. ASTM-D 638 Type I 0.05 ± 0.005 in. tensile specimens were tensile cut from the extruded strips. Extrusion conditions used were typical for this class of materials. Extrusion take-off rates were controlled to minimize orientation in the extruded strips. Annealing experiments showed shrinkage to be approximately 2% in the longitudinal direction.

**High Speed Movie and Tensile Testing.** High speed force-elongation material properties were measured on a model 581 Plastechon high speed tester. Experimental details have been described previously (10). Figure 1 shows a typical force-elongation trace obtained for this class of materials.

A Hycam 16 mm high speed movie camera with a variable framing rate of up to 11,000 frames/sec. was used to film the high speed tensile

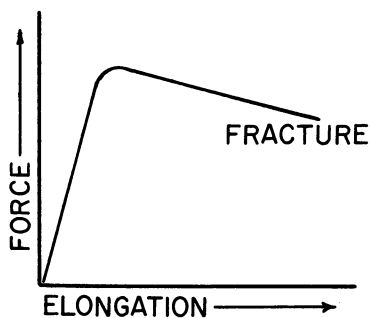


Figure 1. Typical force-elongation plot

deformations. Specimen index marks approximately 0.1 in. apart were used to allow measurement of incremental longitudinal strain over the total length of specimen during deformation. In this way, localization of material deformation—*i.e.*, variation of material strain within the specimen gage length—was quantified. Figure 2 shows a schematic of localized deformation. Figure 3 shows actual variation of longitudinal strain along the gage length of a specimen of ABS 1 at fracture. The degree of strain localization is substantial. This points out the uncertainty associated with selecting constant gage lengths for converting force-elongation traces into stress-strain curves for thermoplastic materials. Specimen edge markings were used to provide suitable photographic contrast for measurement of lateral strains during specimen deformation.

**True Tensile Stress-Strain.** As indicated above, analysis of high speed motion pictures of material deformation during tensile testing provides a measure of maximum strain change in cross-sectional area and

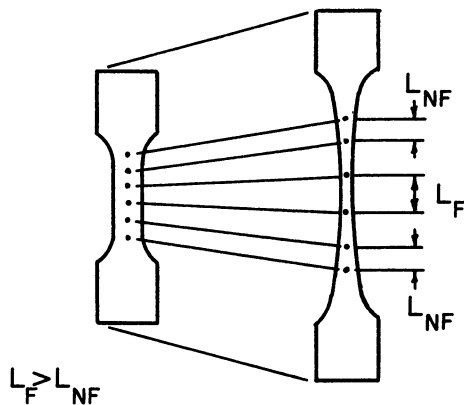


Figure 2. Schematic of variation of material deformation along the length of a specimen

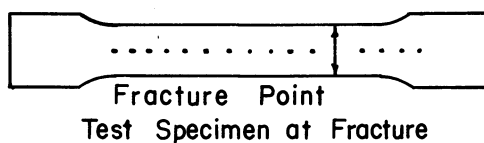
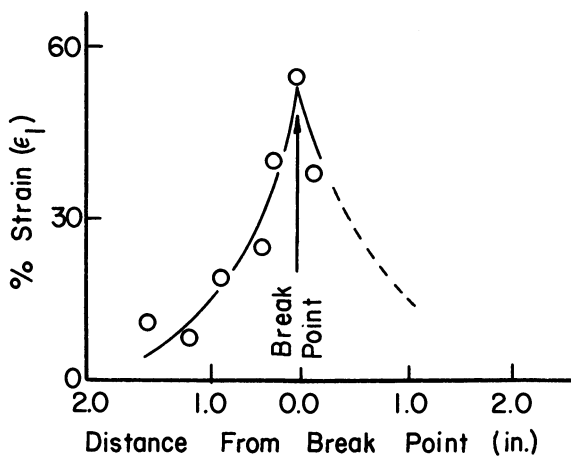


Figure 3. Variation of strain along length of specimen at time of fracture

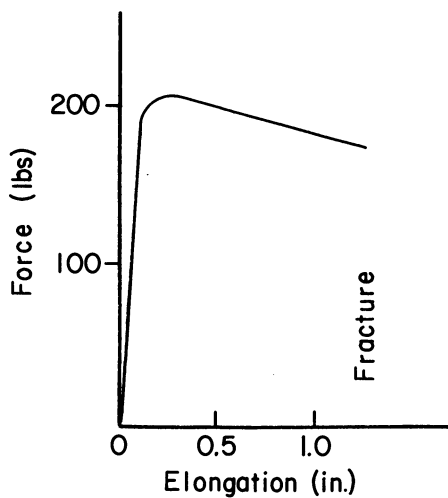


Figure 4. Force-elongation for ABS 1 at 10,000 in./min.

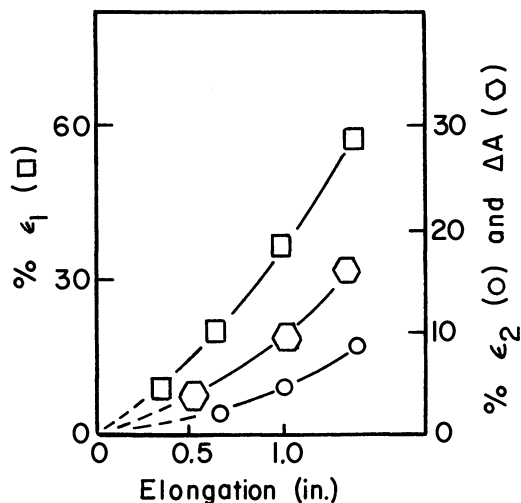


Figure 5. Local maximum elongation ( $\epsilon_1$ ), lateral ( $\epsilon_2$ ), and cross-sectional area ( $\Delta A$ ) strains vs. elongation for ABS 1 at 10,000 in./min.

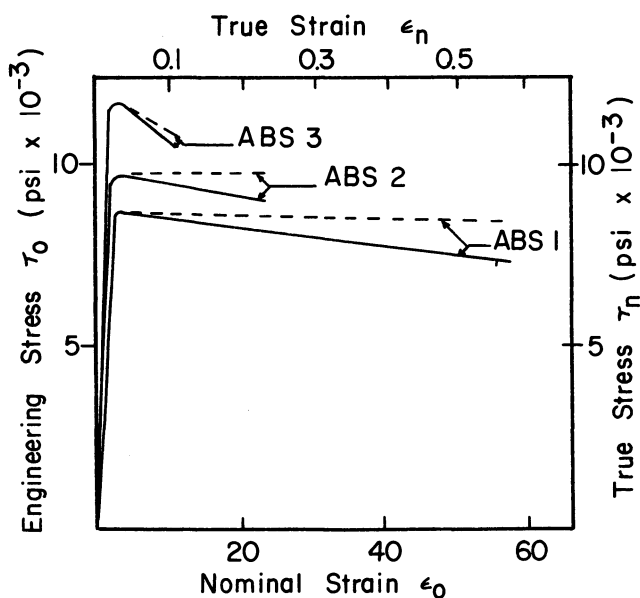


Figure 6. Engineering stress ( $\tau_0$ ) vs. nominal strain ( $\epsilon_0$ ) and true stress ( $\tau_n$ ) vs. true strain ( $\epsilon_n$ ) for ABS 1, 2, and 3 at 10,000 in./min

length as a function of deformation. Figure 4 shows a force–elongation trace obtained for ABS 1 at 10,000 in./min. Figure 5 shows maximum longitudinal, lateral, and cross sectional area strains *vs.* deformation for ABS 1. These curves were generated by photographic analyses. Cross-sectional area strains were calculated on the assumption that specimens deform isotropically in width and thickness. The data in Figures 4 and 5 are combined to yield true stress–strain curves through use of the following relationships:

$$\tau_n = \frac{\text{instantaneous force}}{\text{instantaneous cross-section area}} = \frac{F_t}{A_t} \quad (1)$$

$$\epsilon_n = \frac{\text{sum of incremental changes in length}}{\text{instantaneous lengths}} = \int_{L_0}^L \frac{dL}{L} = \ln(1 + \epsilon_0) \quad (2)$$

where  $\tau_n$ ,  $\epsilon_n$ , and  $\epsilon_0$  are true stress, true strain, and nominal strain, respectively. Figure 6 shows a comparison of true stress *vs.* true strain and nominal stress *vs.* nominal strain for ABS 1, ABS 2, and ABS 3 in the vicinity of maximum deformation.

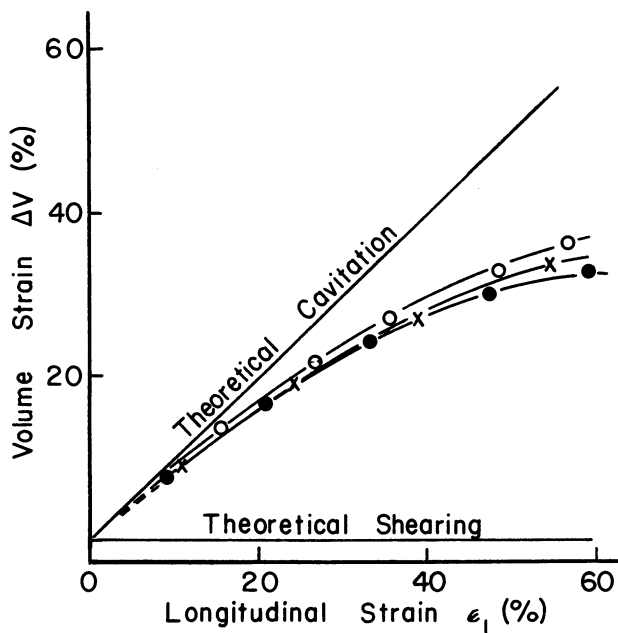


Figure 7. Volume strain *vs.* longitudinal strain curves for three specimens of ABS 1 at 10,000 in./min. Theoretical cavitation and shear curves are also included.

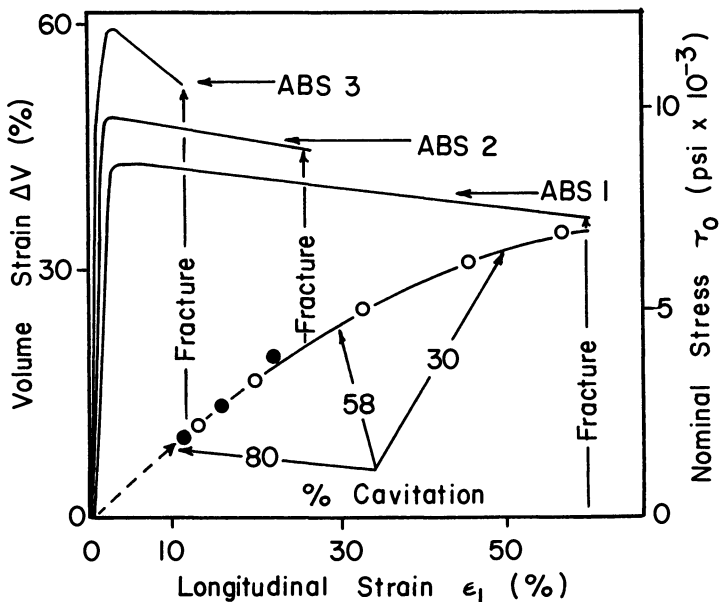


Figure 8. Volume strain ( $\Delta V$ ) and nominal stress ( $\tau_0$ ) vs. longitudinal strain ( $\epsilon_1$ ) for ABS 1, 2, and 3 at 10,000 in./min

**Volume Strain Vs. Longitudinal Strain.** Volume strains ( $\Delta V/V_0$ ) were calculated from longitudinal strain  $\epsilon_1$  and lateral strain  $\epsilon_2$  by use of the following expression:

$$\frac{\Delta V}{V_0} = (1 + \epsilon_1)(1 + \epsilon_2)^2 - 1 \quad (3)$$

The  $(1 + \epsilon_2)^2$  term arises from the assumption that specimens deform isotropically in width and thickness. Volume strain vs. longitudinal strain curves are shown for three specimens of ABS 1 in Figure 7. For comparison, theoretical curves for total cavitation, *i.e.*,  $\epsilon_2 = 0$ , and pure shear, *i.e.*,  $\Delta V = 0$ , are also shown. Volume strain vs. longitudinal strain curves, together with nominal stress vs. nominal strain curves, for ABS 1, ABS 2, and ABS 3 are shown in Figure 8. Because of the size of the strains involved, it is not possible to approximate Equation 3 with an expression which contains only first-order powers of strain when calculating volume strains.

### Discussion

The change of mechanical properties with applied external forces, *i.e.*, stress-strain relationships, is of practical importance in structural



applications of thermoplastics. Since theory is of little use in predicting these relationships, it is necessary to resort to experimental procedures. The uniqueness of combining photographic analyses with high speed tensile testing for defining the stress-strain properties of thermoplastics at impact strain rates is demonstrated in the accompanying graphs. Indeed, for materials which deform locally, *i.e.*, thermoplastics in general, it is impractical to determine these relationships by other experimental procedures. The significance of defining real material properties under conditions that simulate end use has been shown (11) to be of practical value. In particular, areas under true stress-true strain curves, such as those shown in Figure 6, have been related to end use impact performance of finished articles. Photographic analysis not only provides a means of generating engineering properties but also allows macroscopic observation of material changes which take place during deformation. Such changes include onset of stress whitening, necking, and tearing. Determining the strains at which such phenomena take place may provide better judgment in selecting thermoplastics for specific applications in the future.

Volume strain *vs.* longitudinal strain curves shown in Figure 7 and 8 clearly indicate that combinations of shearing and cavitation take place during tensile deformation for this series of materials at the test speed studied. In particular, cavitation predominates at low strains and accounts for > 95% of the total deformation up to the engineering yield point, *i.e.*, 2-3% strain. The change in ratio of cavitation to shearing with longitudinal strain is smooth and changes from > 95% cavitation at low strains to > 80% shearing at fracture strain for ABS 1. Percentage cavitation with deformation for this material is listed in Figure 7. Volume strain *vs.* longitudinal strain curves for the ABS series shown in Figure 8 indicate that the influence of increasing polydiene content is to increase fracture strains. It does not change the shape of a volume strain *vs.* longitudinal strain curve, *i.e.*, the strain dependence of the various processes giving rise to toughening is unchanged. These results demonstrate that impact modification through dispersing a discrete elastomeric phase in a rigid matrix is achieved by allowing cavitation and shearing mechanisms to operate. Furthermore they provide a means of quantifying these mechanisms.

The observed results shown in Figures 7 and 8 are in general agreement with the predictions of Buknall and Drinkwater (8). They suggested, based on the influence of stress on the creep behavior of ABS polymers that crazing (cavitation) should be the dominant factor under impact conditions. Their predictions were based on low strain ( $\leq 5\%$ ) observations and are clearly substantiated by the data shown in Figures 7 and 8.

Cessna (9) carried out similar experiments as those reported here on several commercial impact thermoplastics over a range of strain rates. His work suggested that the classes of impact plastics studied exhibit a similar transition from volume-conserving to cavitation-controlled deformation processes as deformation rates are increased or temperature decreased. The present work supports those findings, as do the predictions of Bucknall and Drinkwater. Unlike Cessna, in no case did we find evidence of closure of cavities by shear yielding after cavitation.

### Conclusions

This work has shown that the use of photographic analysis of material deformation allows true engineering stress-strain properties, extent of localization of material deformation, volume strains, and other macroscopic material changes, *e.g.*, necking, whitening, and tearing, to be determined. Volume strain *vs.* longitudinal strain relationships may be used to quantify the extent of cavitation and volume conserving deformation mechanisms. In particular, for a series of increasing polydiene ABS polymers, the relative contribution of shearing to the total deformation becomes more dominant at higher strains, and the major influence of increasing polydiene content is to increase fracture strain and not to change the strain dependence of the various processes giving rise to toughening.

This work has been extended to include other polymer systems over a range of deformation rates (12).

### Acknowledgments

The permission of Borg-Warner Chemicals to publish this paper is gratefully acknowledged.

### Literature Cited

1. Bucknall, C. B., Smith, R. P., *Polymer* (1965) **6**, 437.
2. Matsuo, M., *Poly. Eng. Sci.* (1969) **9**, 206.
3. Kambour, R. P., Russell, R. P., *Polymer* (1971) **12**, 237.
4. Schmitt, J. A., *J. Appl. Polym. Sci.* (1965) **12**, 533.
5. Newman, S., Strella, S., *J. Appl. Polym. Sci.* (1965) **9**, 2297.
6. Bucknall, C. B., Clayton, D., Keast, W., *J. Mater. Sci.* (1972) **1**, 1443.
7. Bucknall, C. B., Clayton, D., *J. Mater. Sci.* (1972) **7**, 202.
8. Bucknall, C. B., Drinkwater, I. C., *J. Mater. Sci.* (1973) **8**, 1800.
9. Cessna, L. C., *Poly. Eng. Sci.* (1974) **14**, 696.
10. Malpass, V. E., Paul, L. A., Fenelon, P. J., 31st SPE ANTEC, Montreal, 1973.
11. Fenelon, P. J., *Polym. Eng. Sci.* (1975) **15**, 538.
12. Fenelon, P. J., Wilson, J. R., unpublished data.

RECEIVED October 18, 1974.

## Carbon Black Embrittlement of ABS

RUDOLPH D. DEANIN and KALIDAS R. PATEL

Plastics Department, University of Lowell, Lowell, Mass. 01854

*The addition of carbon black to ABS resin improves its hardness, modulus of rigidity, heat deflection temperature, and ultraviolet stability but reduces its ultimate strength, particularly its impact strength. Fine particle size and high structure carbon blacks have the greatest effects.*

Commercial ABS generally combines the rigidity, strength, and heat and chemical resistance of a continuous styrene/acrylonitrile (SAN) copolymer matrix with the impact resistance gained from small dispersed butadiene rubber particles (1). Carbon black reinforces the strength and the resistance of butadiene rubbers against tearing, abrasion, and chemical attack (2, 3); a similar reinforcement in plastics is rarely observed (4, 5). This study investigates if butadiene rubber in ABS makes it susceptible to carbon black reinforcement.

### *Experimental*

Two commercial grades of ABS were used: Goodrich Abson 89140 and 89110 (Table I) which represent "soft" and "hard" grades presumably made with high and low rubber contents (6). Four commercial grades of carbon black were used (Table II) which represent fine and coarse particle size and low and high "structure." ABS was blended with 0–20 phr (parts per hundred of resin) carbon black by masticating the blends for 10 min at 152°C on 6 × 12 in. two-roll, differential-speed mills and by pressing for 10 min at 174°C to form 1/8 × 6 × 6 in. sheets. These were machined into standard 1/8 × 1/2 × 5 in. test bars, and properties were measured according to standard ASTM methods. Results are presented in Tables III–X.

### *Discussion*

The addition of carbon black to ABS markedly increased its rigidity both at room temperature (Tables III–V) and at elevated temperature

Table I. Description of ABS<sup>a</sup>

Goodrich Abson grade	89140	89110
General type	"soft"	"hard"
Shore D hardness	76	85
Barcol hardness	58	70
Flexural modulus, 10 <sup>6</sup> psi	2.62	3.52
Flexural strength, 10 <sup>3</sup> psi	9.1	10.9
Izod notched impact strength, fpi	4.2	1.5
Heat deflection temperature, 264 psi, °C	99	96
Melt flow, 250°C, 5000 g, g/10 min	18.5	6.8
Burning rate, ASTM D635, inch/min	1.7	1.3

<sup>a</sup>Experimental data from present study

Table II. Description of Carbon Blacks (7)

Type	Medium Color		Low Color	
	Black Pearls	Black Pearls	Sterling	Regal
Cabot Grade	700	800	SO	SRF-S
Particle size	fine	fine	coarse	coarse
Structure	high	low	high	low
Av. particle diam., m $\mu$	18	16	41	60
DBP absorption, cc/100 g	115	60	120	62
Density, lb/cu ft	21	30	22	29

Table III. Shore Durometer (D) Hardness—ASTM D2240

Carbon Blacks	Amount, phr	ABS-89140	ABS-89110
Black Pearls 700	0	76	85
	3	79	86
	10	81	86
	20	84	87
Black Pearls 800	0	76	85
	3	78	86
	10	79	85
	20	84	87
Sterling SO	0	76	85
	3	79	83
	10	81	84
	20	82	87
Regal SRF-S	0	76	85
	3	79	84
	10	81	85
	20	82	86

**Table IV. Barcol Hardness—ASTM D2583**

<i>Carbon Blacks</i>	<i>Amount, phr</i>	<i>ABS-89140</i>	<i>ABS-89110</i>
Black Pearls 700	0	58	70
	3	58	73
	10	62	74
	20	66	79
Black Pearls 800	0	58	70
	3	57	72
	10	62	75
	20	70	85
Sterling SO	0	58	70
	3	58	72
	10	62	75
	20	67	79
Regal SRF-S	0	58	70
	3	61	73
	10	63	76
	20	65	79

**Table V. Flexural Modulus—ASTM D790 (psi)**

<i>Carbon Blacks</i>	<i>Amount, phr</i>	<i>ABS-89140</i>	<i>ABS-89110</i>
Black Pearls 700	0	262,000	352,000
	3	277,000	379,000
	10	293,000	410,000
	20	372,000	458,000
Black Pearls 800	0	262,000	352,000
	3	294,000	374,000
	10	344,000	392,000
	20	427,000	451,000
Sterling SO	0	262,000	352,000
	3	278,000	373,000
	10	300,000	432,000
	20	346,000	467,000
Regal SRF-S	0	262,000	352,000
	3	274,000	397,000
	10	298,000	417,000
	20	350,000	468,000

(Table VIII). Fine particle carbon black was somewhat more effective than the coarse grade. Such "hardening" effects usually occur when inorganic fillers are added to organic polymers, particularly thermoplastics. In this study, the effects might be more pronounced for two reasons: (1). The carbon black probably concentrated in the rubber domains where it reached loadings as high as 200 parts carbon black per 100 parts polybutadiene; this greatly reduced the "softening" effect of the rubber on the SAN matrix. (2). The high surface area of the carbon

blacks could immobilize more polymer molecules than the coarser inorganic fillers such as clay and calcium carbonate. Thus carbon black could increase the hardness, modulus, and heat deflection temperature of ABS in applications where the butadiene rubber had detracted too much from the inherent properties of SAN.

However, the addition of carbon black reduced ultimate strength properties both in low-speed flexure (Table VI) and in high-speed impact (Table VII). Fine particle size carbon black had the greatest effect

**Table VI. Flexural Strength—ASTM D790 (psi)**

<i>Carbon Blacks</i>	<i>Amount, phr</i>	<i>ABS-89140</i>	<i>ABS-89110</i>
Black Pearls 700	0	9100	10,900
	3	8900	11,100
	10	7700	9400
	20	4500	6700
Black Pearls 800	0	9100	10,900
	3	8600	10,600
	10	8100	8800
	20	6900	6800
Sterling SO	0	9100	10,900
	3	9000	11,600
	10	8700	10,900
	20	7900	9700
Regal SRF-S	0	9100	10,900
	3	9100	11,600
	10	8600	10,500
	20	6700	9600

**Table VII. Izod Notched Impact Strength—ASTM D256 (fpi)**

<i>Carbon Blacks</i>	<i>Amount, phr</i>	<i>ABS-89140</i>	<i>ABS-89110</i>
Black Pearls 700	0	4.2	1.5
	3	1.9	1.1
	10	1.0	0.8
	20	0.8	0.8
Black Pearls 800	0	4.2	1.5
	3	1.4	1.0
	10	1.0	0.8
	20	0.7	0.8
Sterling SO	0	4.2	1.5
	3	2.8	1.0
	10	1.2	0.9
	20	1.0	0.8
Regal SRF-S	0	4.2	1.5
	3	2.7	1.0
	10	1.4	1.0
	20	1.0	0.8

**Table VIII. Heat Deflection Temperature—ASTM D648  
(264 psi), (°C)**

<i>Carbon Blacks</i>	<i>Amount, phr</i>	<i>ABS-89140</i>	<i>ABS-89110</i>
Black Pearls 700	0	99	96
	3	101	97
	10	103	99
	20	106	101
Black Pearls 800	0	99	96
	3	101	97
	10	103	99
	20	106	103
Sterling SO	0	99	96
	3	100	98
	10	102	98
	20	103	98
Regal SRF-S	0	99	96
	3	100	97
	10	102	98
	20	102	99

**Table IX. Melt Flow—ASTM D1238 (250°C, 5000 g, g/10 Min)**

<i>Carbon Blacks</i>	<i>Amount, phr</i>	<i>ABS-89140</i>	<i>ABS-89110</i>
Black Pearls 700	0	18.5	6.8
	3	8.2	5.2
	10	2.0	3.9
	20	0.0	0.6
Black Pearls 800	0	18.5	6.8
	3	8.9	4.4
	10	2.1	3.1
	20	0.1	0.7
Sterling SO	0	18.5	6.8
	3	17.7	7.8
	10	10.1	3.1
	20	0.9	2.7
Regal SRF-S	0	18.5	6.8
	3	18.4	5.5
	10	11.3	5.0
	20	5.9	4.1

on flexural strength. This probably arose from the carbon black acting as an impurity or flaw which initiated the failure in the SAN matrix. Also the carbon black in the rubber particles might reduce their ability to promote ductility and impact resistance. Thus carbon black may sacrifice much of the impact improvement which the rubber originally produced. Earlier studies show that even the small amounts of carbon black used for ultraviolet stabilization may produce some brittleness (8).

Note that in recent studies the embrittlement of ABS by fillers was alleviated by reducing interfacial adhesion (9).

Also carbon black markedly reduced melt processability (Table IX), particularly when fine particle size was used in "soft" ABS. This might be caused by the bonding between carbon black surfaces and polymer molecules or by the adsorption of low molecular weight lubricants on the carbon black surface. This suggests that coarse carbon black, especially low structure grades, should be used for the least loss of processability.

Finally, carbon black did reduce burning rate somewhat, especially when high structure grades were used (Table X), but not sufficiently to act as a sole flame-retardant—only as an assistant to more conventional flame-retardant additives. The importance of char and free radicals in burning mechanisms (10) and the relationship of char and free radicals to carbon black should prompt further exploratory studies of this property—*viz.*, carbon black's synergistic combination with conventional flame retardants.

**Table X. Burning Rate—ASTM D635 ( $\frac{1}{8}$  In., In./Min)**

<i>Carbon Blacks</i>	<i>Amount, phr</i>	<i>ABS-89140</i>	<i>ABS-89110</i>
Black Pearls 700	0	1.7	1.3
	3	1.6	1.2
	10	1.6	1.1
	20	1.3	1.0
Black Pearls 800	0	1.7	1.3
	3	2.0	1.6
	10	1.7	1.3
	20	1.6	1.3
Sterling SO	0	1.7	1.3
	3	1.5	1.0
	10	1.5	1.0
	20	1.3	0.9
Regal SRF-S	0	1.7	1.3
	3	1.7	1.2
	10	1.7	1.1
	20	1.5	1.1

### **Conclusions**

The addition of carbon black to ABS improves its hardness, modulus of rigidity, heat deflection temperature, and ultraviolet stability but reduces its ultimate strength, particularly its impact strength; recent surface treatment techniques might alleviate this. Theoretically it could contribute to flame retardance, but this would require further studies of its synergism.



*Literature Cited*

1. Saxe, J. P., Pokigo, F. J., *Mod. Plast. Encyc.* (1973) 50 (10A), 16.
2. Kraus, G., "Reinforcement of Elastomers," Interscience, New York, 1965.
3. Boonstra, B. B., "Rubber Technology," M. Morton, Ed., Chap. 3, Van Nostrand Reinhold, New York, 1973.
4. Brydson, J. A., "Plastics Materials," pp. 118, 181, 390, 424, 442, 474, Van Nostrand, New York, 1966.
5. Boonstra, B. B., in "Reinforcement of Elastomers," G. Kraus, Ed., Chap. 16, Interscience, New York, 1965.
6. Goodrich Chemical Co., technical bulletins on Abson ABS.
7. Cabot Corp., technical bulletins on carbon blacks.
8. Deanin, R. D., Cebula, D. R. *Soc. Plast. Eng. ANTEC.* (1973) 19, 700.
9. Sperti, W. M., Jenkins, C. F., *Amer. Chem. Soc., Div. Org. Coatings Plast. Chem., Preprints* (1973) 33 (2), 152.
10. Lyons, J. W., "The Chemistry and Uses of Fire Retardants," pp. 14-20, Wiley, New York, 1970.

RECEIVED October 18, 1974. Taken from an MS thesis submitted by K. R. Patel.

# Transparent, Impact-Resistant, Styrene/ Methyl Methacrylate Copolymer Grafted onto Polybutadiene

BERNARD BAUM, WILLIAM H. HOLLEY, HAROLD STISKIN,  
ROY A. WHITE, and PAUL B. WILLIS

DeBell & Richardson, Inc., Enfield, Conn. 06082

ANTHONY F. WILDE

Army Materials and Mechanics Research Center, Watertown, Mass. 02172

*A series of impact- and ballistic-resistant, rubber-modified, transparent polymers based on styrene/methyl methacrylate copolymer grafted onto polybutadiene were developed for Army Materials and Mechanics Research Center (AMMRC). The refractive index of the copolymer matched that of polybutadiene. Variables that were investigated included the particle size of the polybutadiene latex, the degree of grafting, the particle content, and the degree of dispersion of the graft constituent. The highest ballistic impact was for a graft polymer based on 300 A rubber (polybutadiene) latex containing 15% rubber and a high degree of grafting and dispersion.*

The objective of this research program was to produce a series of transparent, rubber-modified polymers designed for investigating ballistic resistance and possessing good optical properties over as maximum a temperature range as possible. AMMRC had previously specified the types and general ranges of the rubber particle variations to be investigated. Based on laboratory impact testing we determined what clear thermoplastics to use, even though ballistic resistance cannot be correlated to standard impact testing. The size, shape, and speed of a projectile and the projectile's effect on ballistic resistance of a thermoplastic are factors that cannot be accurately predicted.

We used a matrix copolymer system consisting of methyl methacrylate (MMA) and styrene (St) grafted on polybutadiene rubber. The variables investigated were latex particle size (360, 2000, and 5000 Å), degree of grafting, rubber content, and the degree of particle dispersion. The following variables must be considered when a transparent impact polymer is prepared.

**Impact Properties. CHEMICAL NATURE OF THE RUBBER.** If the rubber is too compatible with the matrix, it will dissolve in the rigid material and disperse on a molecular scale. Little or no reinforcement will occur since the rubber particles become smaller than the radius of the tip of a stress-induced propagating crack. However if it is highly incompatible, good adhesion between rubber and matrix cannot be obtained. For example polybutadiene rubber adheres poorly to a styrene/acrylonitrile copolymer, but a nitrile rubber adheres well to the SAN copolymer. If grafting techniques are used however, compatibility is less of a problem since the rubber is chemically bonded to the matrix.

**ENERGY ABSORPTION BY THE RUBBER.** For the rubber phase to work effectively it must be able to absorb energy by elongating in the face of a propagating crack and redistribute the stress to the surrounding matrix, thus dissipating the energy that causes the crack to propagate (1). In general a rubber with the lowest possible glass transition temperature is required for good impact (2, 3). As with commercial elastomers the degree of crosslinking in the rubber particles (*i.e.*, the amount of macrogel crosslinked rubber and microgel highly branched chains) greatly affects the strength, toughness, and resiliency of the rubber, with an optimum degree of crosslinking necessary for maximum toughness in the final product.

**AMOUNT OF RUBBER.** Generally the impact strength of rubber-modified plastics increases with an increase in rubber content. Although the impact improves, it is usually at the sacrifice of other properties such as strength, modulus, heat distortion, weather resistance, and creep.

**RUBBER PARTICLE SIZE AND DISPERSION.** Particle size is important for impact. If the size distribution is wide—*i.e.*, 1–20 microns—the large particles represent a less efficient use of the toughness of the rubber and tend to reduce tensile strength and to give poorer surface finish when compared with a narrow particle size distribution—*i.e.*, 1–5 microns (4).

If the rubber is evenly dispersed throughout the polystyrene matrix, cracks which form under stress soon encounter a rubber particle during propagation through the material; thus further progress of the crack is hindered by the energy absorbing properties of the rubber.

The degree of dispersion depends on the degree of grafting, where the graft acts almost as a surface-active agent to keep the rubber in a colloidal dispersion in the matrix. The effectiveness of the graft appears

to depend more on the thickness of the graft layer than on the weight percent used. Below a certain thickness of graft on the particles (*e.g.* 100 Å), the rubber tends to aggregate badly (5).

**ADHESION OF RUBBER TO THE MATRIX.** Another important variable for impact properties is how well the rubber adheres to the plastic continuum (6). Without sufficient adhesion the energy of a propagating crack can tear a rubber particle from the matrix, and the crack will effectively bypass the particle. The most commonly used method to adhere rubber to a matrix is grafting. Grafting has the advantage of using rubbers which are only moderately compatible with the plastic matrix because the chemical bonding achieves adhesion. Grafting can be performed in bulk or suspension, but for better control of rubber particle size it is usually done in an emulsion. The rubber is usually swollen, at least in the outer layer of the particle, with a monomer, and then the monomer is polymerized with free-radical initiators such as peroxides or persulfate.

Grafting is achieved by chain transfer of the growing polymer chains to the rubber molecules. For unsaturated rubbers such as polybutadiene grafting probably occurs at allylic carbons or at pendant double bonds.

**PLASTIC MATRIX.** To ensure good impact properties the plastic matrix should have a medium to high molecular weight. On a commercial basis this generally means a melt flow (ASTM D 1238) of one to five or an inherent viscosity (7) greater than one.

**Optical Properties. MATCHED REFRACTIVE INDEXES.** Of all the variables, the most important to optical properties is the refractive indexes of the continuous and dispersed phases. The effects of semicompatible polyblending on optical properties are generally undesirable. Since each incompatible phase has its own refractive index, light traveling through such a semicompatible polyblend is refracted and dispersed many times as it enters and leaves the dispersed phase in its journey through the continuous phase. Thus most semicompatible polyblends are translucent to opaque. One way to overcome this problem is to match the refractive index of the plastic matrix to that of the rubbers (8, 9). Most rubbers have refractive indexes of *ca.* 1.52, and this is closely matched by styrene/methyl methacrylate copolymers.

**PARTICLE SIZE.** Another method to produce transparency is to make the particle size of the rubber phase smaller than the wavelength of light (*i.e.*, less than 4000 Å). Although the technique is effective, these small particle sizes are difficult to achieve on a commercial basis and may have an adverse effect on the impact properties of the final product.

**COMPOSITION OF THE CONTINUOUS PHASE.** To ensure a haze-free plastic, the continuous phase, if a copolymer, must have a consistent composition. If the monomers react in the same ratio as they are added, there

is no problem. However if one monomer reacts preferentially to the other and this is not taken into account during monomer addition, the material can gradually change in composition during the polymerization reaction and can result in a mixture of molecules of different comonomer content.

### *Experimental*

**Laboratory.** Methyl methacrylate/styrene copolymer, polybutadiene latex, and a graft combination of the two were synthesized in returnable-type soda bottles. To produce polybutadiene latex, water, surfactant, and initiator were charged to the bottle followed by butadiene (de-inhibited by distilling through aqueous sodium hydroxide) at specific time intervals using a hypodermic syringe to inject the monomer and/or surfactant through a resealable cap. No mercaptan, chain transfer agent, was used with 360 A latex formulations. Larger particle sizes generally required mercaptan to yield a more linear, less crosslinked, more rubbery polymer structure.

For some grafting runs, distilled water, surfactant, polybutadiene latex, styrene/MMA monomers, and initiator were all injected into the bottle. The bottle was then purged with nitrogen, sealed, and rotated in a water bath at 60°C for 16 hr. In other grafting runs, preswelling in the absence of initiator was carried out by adding all the ingredients except the initiator to the bottle. The bottle was purged with nitrogen, sealed, and rotated inside the water bath at 50°C for 2 hr to swell the rubber slightly in the monomer. The bottle was removed from the bath, cooled, and initiator was added. It was then repurged with nitrogen and was resealed and rotated inside a 60°C bath for 16 hr.

After grafting, the latex was coagulated in and washed thoroughly with methanol and was filtered. During washing Irganox 1010, an antioxidant, was added to prevent degradation of the rubber during subsequent drying. The graft polymer was dried in a circulating air oven at 60°C overnight and was compounded on a steam-heated, two-roll mill at 315°F for 10 min with 0.1% Irganox 1010. Films used to evaluate clarity and impact were prepared by compression molding at 350°F using a hydraulic press equipped with electrically heated platens.

**Pilot Plant Scale-Up.** All of the pilot plant polymerizations to produce a rubber latex or a graft polymer were carried out in a 10-gal, glass-lined Pfaudler kettle. A 50-gal, glass-lined kettle was used to prepare MMA/St copolymer. EDTA was used in all pilot plant runs to sequester iron.

The first pilot plant grafting that was run with the commercial 2000 A latex from B. F. Goodrich coagulated. We switched Run 17B formulation with the pentamine/peroxide initiator system to the persulfate initiator system, Run 26 (Table VII). Based on tensile impact data, No. 26 had almost the same impact resistance as No. 17B.

For the 5000 A latex, scale-up in the 10-gal, glass-lined kettle required 64 hr polymerization at 60°C. After each addition of butadiene, initiator, surfactant, and/or mercaptan, an additional 16 hrs of polymerization was needed. Four separate additions were needed to grow the 2000 A polybutadiene latex to 5000 A. The final latex had a solids content of 25.3%

and was calculated to be 80% converted. This latex was used to make the 5000 A graft.

The ballistic performance of these materials was determined by a standard projectile impact test. This performance is characterized by the average impact velocity at which the projectile barely penetrates the test specimen. Accordingly the higher the characteristic velocity, the better is the ballistic performance or the ballistic impact resistance of the specimen. The data are presented in arbitrary units.

### Discussion

**Graft Polymer Studies on "Model" System.** Methyl methacrylate/styrene ratio, chain transfer agent level, and type of initiator system were evaluated in graft polymer using Firestone 2004 polybutadiene latex as a model.

**CLARITY OF GRAFT POLYMERS WITH VARYING METHYL METHACRYLATE/STYRENE RATIOS.** Refractive index considerations (7, 8) and general state of the art considerations (8) favor methyl methacrylate (MMA) over styrene (St) as the major monomer portion of the matrix. With this in mind, we selected MMA/St ratios from 62/38 to 80/20 (wt %). Using a commercial Firestone butadiene latex (2004) to supply the 15% rubber graft, polymerization runs were made as outlined in Table I.

After the resultant polymers had been worked up, an evaluation was made based on clarity. At 73° and 140°F the 80/20 MMA/St polymer (Run 5) had the best clarity, but at -4°F the 67/33 MMA/St (Run 2)

**Table I. Clarity of Graft Polymers with Varying MMA/St Ratios**

Formulation <sup>a</sup>	Run No.				
	1	2	3	4	5
Distilled water, total	180.0	180.0	180.0	180.0	180.0
2004 butadiene latex, (2500 A) solids basis	15.0	15.0	15.0	15.0	15.0
Methyl methacrylate					
MMA	52.8	56.9	59.5	63.8	68.0
Styrene	32.2	28.1	25.5	21.2	17.0
Sodium stearate	5.0	5.0	5.0	5.0	5.0
Na <sub>3</sub> PO <sub>4</sub> · 12 H <sub>2</sub> O	0.5	0.5	0.5	0.5	0.5
K <sub>2</sub> S <sub>2</sub> O <sub>8</sub>	0.3	0.3	0.3	0.3	0.3
Yield, %	99.5	98.5	98.8	97.8	99.5
Clarity <sup>b</sup> @ 140°F	5	4	3	2	1
Clarity @ 73°F	5	4	3	2	1
Clarity @ -4°F	5	1	2	3	4
MMA/St based upon					
100 Monomer	62/38	67/33	70/30	75/25	80/20

<sup>a</sup> All formulations are based on 85 parts by weight monomer (MMA/St) and 15 parts by weight rubber solids.

<sup>b</sup> Rated from 1-5 (1 is best and 5 is worst).

**Table II. Effect of Level of Chain Transfer Agent on Impact of Graft Polymer**

Formulation <sup>a</sup>	Run No.			
	6	6A <sup>b</sup>	9	10
<i>tert</i> -Dodecyl mercaptan	0.3	0.5	0.7	0.9
Melt index, g/10 min	1.4	—	1.7	4.3
Tensile impact, ft-lbs/in. <sup>2</sup>	6	6	7	brittle
Clarity	slt. haze	clear	clear	clear

<sup>a</sup> H<sub>2</sub>O-180 parts, butadiene latex-15, MMA-65.5, styrene-19.5, sodium stearate-5, Na<sub>3</sub>PO<sub>4</sub>·12 H<sub>2</sub>O-0.6, and K<sub>2</sub>S<sub>2</sub>O<sub>8</sub>-0.3.

<sup>b</sup> Pre-swelled for 2 hrs @ 50°C without K<sub>2</sub>S<sub>2</sub>O<sub>8</sub>; K<sub>2</sub>S<sub>2</sub>O<sub>8</sub> added and polymerized for 16 hrs. @ 60°C.

ratio was superior, and the 80/20 was rated next to the worst. As a compromise the 77/23 MMA/St was chosen for the remaining experiments.

EFFECT OF CHAIN TRANSFER AGENT CONCENTRATION ON IMPACT OF GRAFT POLYMER. With the MMA/St ratio at 77/23, 15% rubber grafts were made using Firestone butadiene latex and different levels of the chain transfer agent (*tert*-dodecyl mercaptan) to lower the molecular weight of the polymer so that it can be readily processed. Our first attempt, without mercaptan, yielded a difficult to process, almost intractable material. At low mercaptan levels the high molecular weight polymer caused haze (Table II). Run 10 with 0.9 part mercaptan lowered the molecular weight to a point where the specimen produced was brittle. We choose 0.5 part mercaptan as the working level for the remainder of the project.

**Table III. Effect of Initiator Systems on Impact of Graft Polymers**

Formulation	Run No.		
	6A	13	14
Distilled water, total	180.0	180.0	180.0
2004 butadiene latex, solids basis	15.0	15.0	15.0
MMA	65.5	65.5	65.5
Styrene	19.5	19.5	19.5
Sodium stearate	5.0	5.0	5.0
Na <sub>3</sub> PO <sub>4</sub> ·12 H <sub>2</sub> O	0.6	0.6	0.6
<i>tert</i> -Dodecyl mercaptan	0.5	0.5	0.5
K <sub>2</sub> S <sub>2</sub> O <sub>8</sub>	0.3	—	—
Cumene hydroperoxide	—	0.170	—
Tetraethylene pentamine	—	0.085	0.170
<i>tert</i> -Butyl hydroperoxide	0	—	0.153
EDTA, 30% solids	—	0.017	0.017
Tensile impact, ft-lbs/in. <sup>2</sup>	6	14	19

**Table IV. Polymerization of Methyl Methacrylate/Styrene Copolymer**

Formulation	Run No.			
	7	11	11A	12
Distilled water	180.0	180.0	180.0	180.0
Na <sub>3</sub> PO <sub>4</sub> · 12 H <sub>2</sub> O	0.6	0.6	0.6	0.6
MMA	77	77	77	77
Styrene	23	23	23	23
Sodium stearate	5.0	5.0	5.0	5.0
K <sub>2</sub> S <sub>2</sub> O <sub>8</sub>	0.3	0.3	0.3	0.3
<i>tert</i> -Dodecyl mercaptan	0.5	0.6	0.65	0.7
Melt index, g/10 min	3.1	3.9	4.8	7.8
Clarity	haze	sl. haze	clear	v. clear
Yield, %	98.8	—	—	—

**Table V. Polymerization of 360-A Latex**

Formulation	Run No.		
	8 <sup>a</sup>	8A <sup>a</sup>	8B <sup>b</sup>
Distilled water	75	71	71
Butadiene monomer	25	25	25
Na <sub>3</sub> PO <sub>4</sub> · 12 H <sub>2</sub> O	0.075	0.035	0.035
Dupanol ME	5.0	—	—
Dowfax 2A1, 45% solids	—	6.68	6.68
K <sub>2</sub> S <sub>2</sub> O <sub>8</sub>	0.075	0.075	0.075
Rubber particle size, A	880	135	360
Solids, %	23.8	26.7	21.7

<sup>a</sup> All ingredients charged to reaction vessel together.

<sup>b</sup> Butadiene charged to reaction vessel at the following time intervals: 4% initially; 36% after 1 hr; 60% after 2½ hrs.

**EFFECT OF INITIATOR SYSTEMS ON IMPACT STRENGTH OF GRAFT POLYMERS.** Table III contains the formulations and tensile impact data of grafting runs made with various initiator systems. Run 13 contains tetraethylenepentamine with cumene hydroperoxide; Run 14 has the same amine but in conjunction with *tert*-butyl hydroperoxide. The pentamine/*tert*-butyl hydroperoxide system (Run 14) produced a polymer with higher impact. Both runs (13 and 14) gave much higher tensile impact than the potassium persulfate system. This higher impact could be related to the higher degree of grafting of Run 14 vs. 6A (Table VIII).

**Latex Particle Size and Grafting.** The bulk of the program involved the preparation of monodisperse, polybutadiene latexes of 360, 2000, and 5000 A particle sizes and the grafting of these latexes with methyl methacrylate/styrene.

**PREPARATION OF 360 A LATEX AND GRAFTING.** Attempts to make a 360 A latex are outlined in Table V. Runs 8 and 8A are identical in procedure but vary in the type of surfactant used. Run 8B which gave a



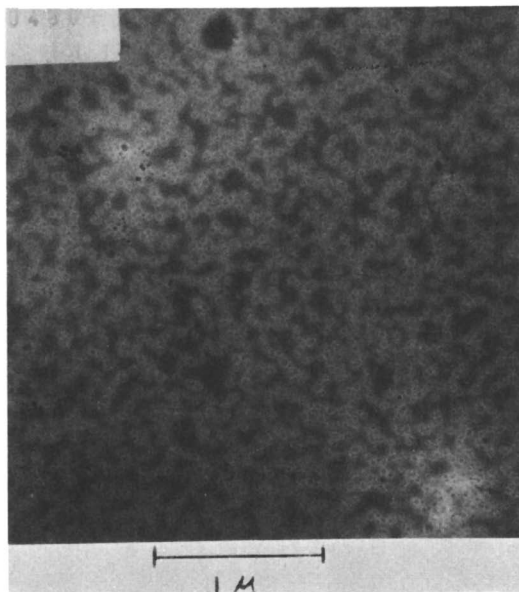


Figure 1. Electron micrograph of 360-A rubber particles in Run 8B latex (22,160  $\times$ )

360 A latex has the identical formulation to Run 8A, but the butadiene was injected into the bottle at specific intervals. Runs 8 and 8A were made by injecting everything into the bottle at once.

Photographing the rubber particles by using the SEM stage of an electron microscope was unsatisfactory. However, by using the TEM

Table VI. Preparation of Rubber Graft Polymer Using 360-A Monodisperse Latex

Formulation	Run No.	
	32	33 <sup>a</sup>
Distilled water, total	180.0	180.0
Run 8B 360-A latex, solids basis	15.0	15.0
Na <sub>3</sub> PO <sub>4</sub> · 12 H <sub>2</sub> O	0.6	0.6
Sodium stearate	5.0	5.0
MMA	65.5	65.5
Styrene	19.5	19.5
<i>tert</i> -Dodecyl mercaptan	0.625	0.5
EDTA, 30% solids	0.017	—
Tetraethylenepentamine	0.170	—
<i>tert</i> -Butyl hydroperoxide	0.153	—
K <sub>2</sub> S <sub>2</sub> O <sub>8</sub>	—	0.3
Tensile impact, ft-lbs/in. <sup>2</sup>	18	35

<sup>a</sup> 2 hrs @ 50°C without K<sub>2</sub>S<sub>2</sub>O<sub>8</sub>; add K<sub>2</sub>S<sub>2</sub>O<sub>8</sub> and polymerize 16 hrs @ 60°C.

stage and polyvinyl alcohol to hold the particles apart, satisfactory pictures were obtained. A photograph of the 360 A rubber particles produced in the Run 8B latex reveals its monodispersity (Figure 1). Runs 8 and 8A gave polydisperse latex as well as the wrong particle size, indicating the importance of both the type of surfactant and the need for continuous addition of butadiene monomer.

Table VI shows the grafting experiments made with 360-A latices. Grafting runs (32 and 33) which were made from latex 8B (360 A) again showed that the initiator system has a significant part in the properties of the grafted polymer. The persulfate system produced a polymer with almost twice the tensile impact as the pentamine/peroxide system. Run 33 was scaled-up in the pilot plant.

**GRAFTING EXPERIMENTS USING A COMMERCIAL 2000-A LATEX.** A commercial, monodisperse (*see* Figure 2) 2000 A latex (B. F. Goodrich Hycar 1870X3) was used for the grafting experiments. Run 17 (Table VII) shows the effects of standard type formulations with the pentamine/peroxide initiator system. All ingredients were charged to the reaction vessel initially; our yield was only 53%, and the polymer was difficult to process because of its high molecular weight. In Run 17A the pentamine was injected last into the reaction bottle which was agitated during the addi-

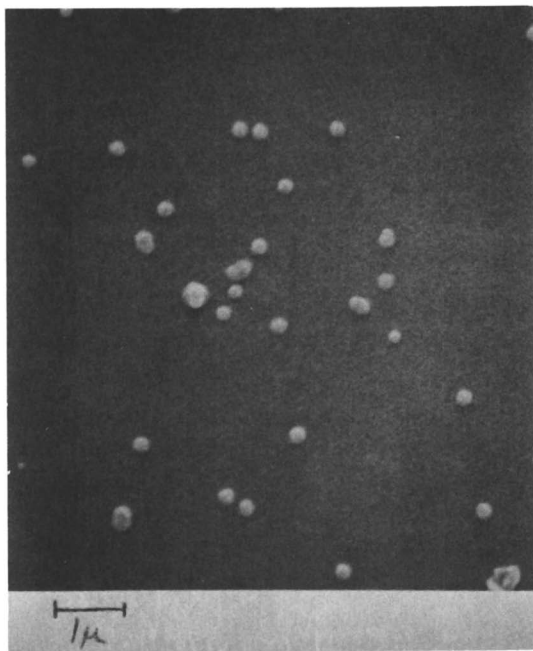


Figure 2. Electron micrograph of 2000-A rubber particles in B. F. Goodrich 1870X 3 latex (8000  $\times$ )

**Table VII. Preparation of Rubber Graft Polymer Using a 2000-A Latex**

Formulation <sup>a</sup>	Run No.			
	17 <sup>b</sup>	17A <sup>c</sup>	17B <sup>c</sup>	26 <sup>d</sup>
Na <sub>3</sub> PO <sub>4</sub> ·12 H <sub>2</sub> O	0.6	0.6	0.6	0.6
Sodium stearate	5.0	5.0	5.0	5.0
MMA	65.5	65.5	65.5	65.5
Styrene	19.5	19.5	19.5	19.5
<i>tert</i> -Dodecyl mercaptan	0.5	0.5	0.625	0.5
EDTA, 30% solids	0.017	0.017	0.017	—
Tetraethylenepentamine	0.170	0.170	0.340	—
<i>tert</i> -Butyl hydroperoxide	0.153	0.153	0.306	—
K <sub>2</sub> S <sub>2</sub> O <sub>8</sub>	—	—	—	0.3
Yield, %	53.0	98.5	98.8	98.8
Processability	very difficult	difficult	normal	normal
Tensile impact, ft-lb/in. <sup>2</sup>	—	—	36	33

<sup>a</sup> H<sub>2</sub>O—180 parts, Hycar 1870X3 latex—15, MMA—65.5, styrene—19.5, Sodium stearate—5, Na<sub>3</sub>PO<sub>4</sub>·12 H<sub>2</sub>O—0.6.

<sup>b</sup> All ingredients charged to reaction vessel initially.

<sup>c</sup> Tetraethylenepentamine charged last to reactor under agitation.

<sup>d</sup> 2 hrs @ 50°C without K<sub>2</sub>S<sub>2</sub>O<sub>8</sub>; add K<sub>2</sub>S<sub>2</sub>O<sub>8</sub> and polymerize 16 hrs @ 60°C.

tion. The yield was now 98.5%, but the resultant polymer still had too high a molecular weight and was difficult to process.

In Run 17B we increased the mercaptan level by 25% and doubled the pentamine/peroxide initiator levels. This produced a tough polymer. Run 17B had a slightly higher impact resistance than the polymer made in Run 26 which was made with the persulfate initiator system. Run 17B was scaled-up in the pilot plant.

**PREPARATION OF A 5000-A MONODISPERSE LATEX.** The most common method to prepare a monodispersed latex (*i.e.*, with a narrow distribution of particle sizes) is the seed latex technique. In this process a polymer emulsion of uniform particle diameters is prepared by polymerizing a small amount of monomer (10–20%) with a slight excess of surfactant and by running the reaction to high conversion. The resulting latex has a narrow range of particle sizes. This latex is used to “seed” a subsequent reaction in which additional monomer, catalyst, and surfactant are added continuously and polymerized until the desired particle diameter is achieved. A seeded reaction must be carefully controlled; also the quantity of fresh surfactant added is important since the rate of addition of surfactant, with respect to the progress of the reaction, is a nonlinear function. As the reaction proceeds, the growing particles require additional emulsifier to protect the rapidly expanding surface area. If the surfactant is added too slowly, there may be an insufficient quantity adsorbed on the

particles to prevent aggregation or coagulation. If it is added rapidly, the excess of surfactant will form new micelles (above the critical micelle concentration) and will initiate new polymer particles of small diameters, thereby creating a dispersity.

The best choice for seeding the 5000-A latex reaction was the B. F. Goodrich monodisperse 2000-A latex. Preliminary calculations were necessary to determine the quantity of monomer required to grow the particles to the desired diameter. A simple multiplication factor was determined from a ratio of the volume of the initial seed particle to the volume of the final particle. If the volume of a sphere =  $V = 4/3 \pi r^3$

$$\frac{V_2}{V_1} = \frac{4/3\pi r_2^3}{4/3\pi r_1^3} = \left[ \frac{r_2^3}{r_1^3} \right] = \left[ \frac{0.25\mu}{0.1\mu} \right]^3 = 15.6 \quad (1)$$

$V_2; r_2$  = volume and radius of the 5000-A particle,  $V_1; r_1$  = volume and radius of the 2000-A particle, and  $1 \mu = 10,000 \text{ \AA}$ .

Since density is a factorable constant in the above equation, the ratio also indicates the necessary increase in weight required by each particle. The factor was increased to an even 16 to leave a 3% margin for completion of the reaction. It is possible to add additional catalyst to force the reaction to 100% conversion, but this leads to an undesirably high degree of crosslinking which reduces the impact strength of the rubber.

Growing the 2000-A latex by multiple additions involving surfactant, monomer, catalyst, and a chain transfer agent to control the molecular weight was successful. Each increment was added every 26 hr for three increments from the start of the polymerization. The first two additions consisted of fresh monomer (not exceeding a 2:1 monomer to polymer ratio) with 0.25 phm each of catalyst and chain transfer agent. The first addition also included half of the total surfactant used; the second and third had catalyst alone.

After the reaction terminated the latex was post-stabilized with 0.5 phr Triton X-202 (Rohm and Haas surfactant) to inhibit aggregation and was stored at 40°F under dry nitrogen. No antioxidant could be added at this time because it would destroy the catalyst necessary for the final grafting polymerization.

Preliminary examination of the latex involved centrifugation and optical microscopy. Only a marginal tendency to fractionate was noticed after 2 hr of centrifuging several 10-ml samples. The approximate diameter of particles separable by normal centrifuging was near 0.5  $\mu$ . An optical microscope was equipped with an oil immersion lens (1000 $\times$ ) and a phase contrast stage. The polymer particles were noticeable but only marginally visible. Their diameters were near the threshold of reso-

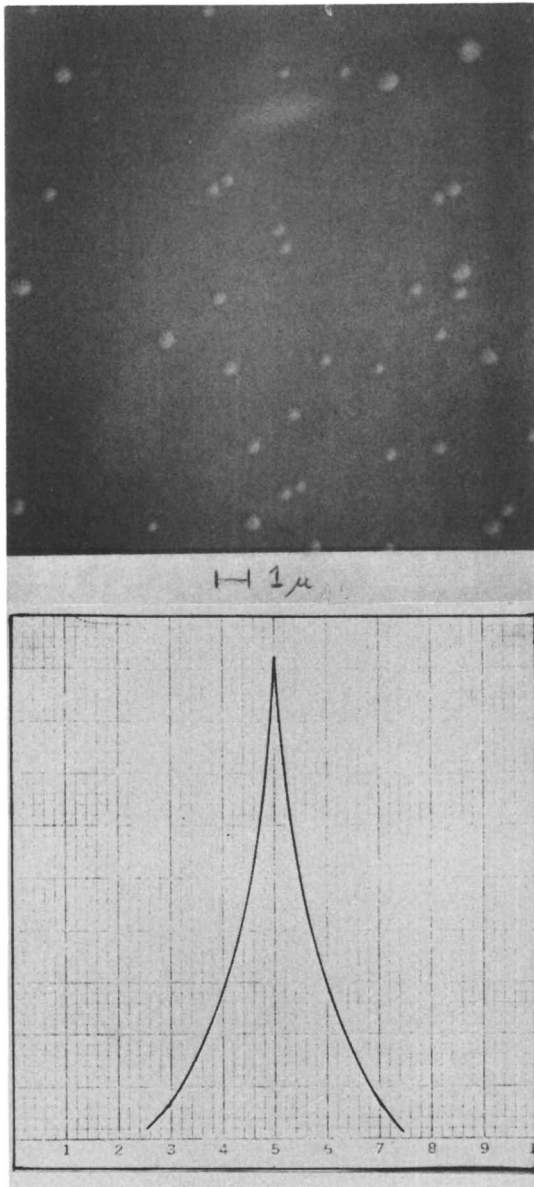


*Figure 3. Electron micrograph (4000 ×) of typical latex section (top) and latex dispersity graph (bottom). 5000-A latex characterization (Run A-32).*

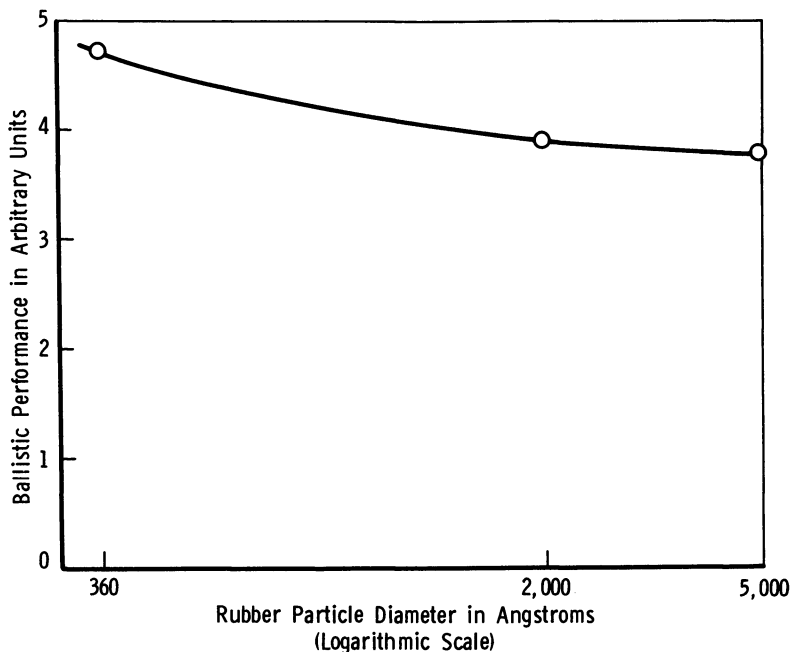


Figure 4. Latex particle diameter vs. ballistic impact of graft polymer made from these latexes

lution about  $0.5 \mu$ . Microphotography was difficult, but electron microscopy photographs gave excellent results (Figure 3).

Visual examination with the help of calipers revealed that the average particle diameter was  $5000 \pm 100$  A. No aggregates were discovered. After measuring the sizes and numbers of particles at different diameters, we plotted the dispersity. As the graph shows, only about 15% of the particles are outside 4000–6000 A; nearly 50% are between 4800–5200 A.

**PREPARATION OF BLENDS OF GRAFTED POLYMERS.** The individual 360-, 2000- and 5000-A polymers were worked up, compounded, and compression molded into sheets. Blends of the three particle size polymers were made according to the following proportions based on percent rubber. The total rubber content in the blends remained at 15%.

5% 360 A + 10% 2000 A  
 10% 360 A + 5% 2000 A  
 5% 360 A + 10% 5000 A  
 10% 360 A + 5% 5000 A  
 5% 2000 A + 10% 5000 A  
 10% 2000 A + 5% 5000 A

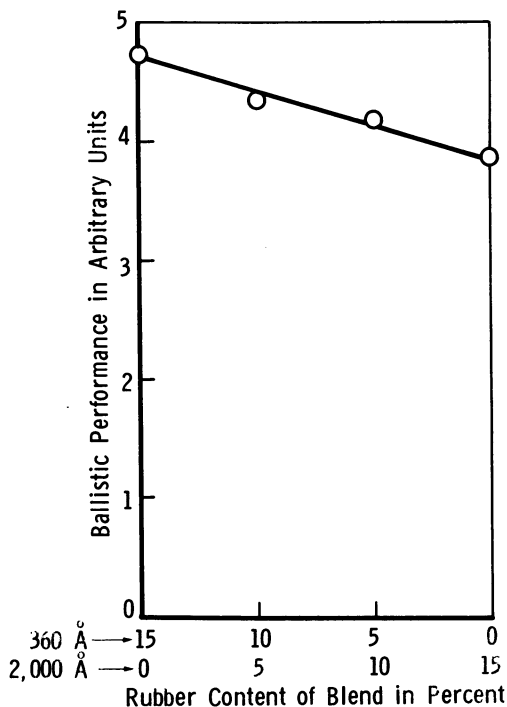


Figure 5. Ballistic impact of blends of graft polymers made from 360- and 2000-A polybutadiene latexes

The above blends were mixed in powder form prior to compounding on the roll mills. The resultant compounds were compression molded into sheets and were delivered along with the single particle size compounds to AMMRC for ballistic impact evaluation.

**BALLISTIC EVALUATION OF GRAFT POLYMERS MADE WITH VARYING PARTICLE SIZE LATEXES.** In Figures 4–7 the rubber graft polymers examined by AMMRC for ballistic impact were based on 15% rubber content and had a high degree of graft and dispersion of the rubber particles in the MMA/St matrix. Because of security requirements, ballistic performance is given in arbitrary units. Ballistic impact resistance is plotted *vs.* rubber latex particle diameter or *vs.* the percent of each blend of the graft polymer. The ballistic impact resistance of the graft polymer increases as the latex particle diameter decreases (Figure 4). The graft polymer blending study indicates again that the graft polymer made from the smallest (360 Å) particle diameter latex has the highest ballistic impact resistance.

**Degree of Grafting vs. Tensile Impact.** Only a percentage of the monomer that polymerized in the presence of rubber is actually attached or grafted to the rubber. An accepted measure of how well a graft is made is the resultant tensile impact of the polymer. Generally the higher the tensile impact, the higher the degree of graft (10).

A quantitative method to determine the amount of graft was to dissolve-disperse a known amount of the polymer in MEK (methyl ethyl ketone), which is a solvent for the matrix copolymer only. The rubber plus the graft remained undissolved and was recovered, washed, dried, and weighed. Since we knew the initial amounts of rubbers and monomers and the percent conversion, we could calculate the amount of graft on the rubber.

Table VIII lists the parts of graft per 100 parts of rubber for some laboratory runs as well as the latex particle size and tensile impact. The correlation of the degree of grafting to tensile impact still holds—*i.e.*, within each latex system the higher the degree of grafting, the greater the impact. This condition however does not hold from latex to latex. A higher level of graft in one latex does not necessarily produce a higher

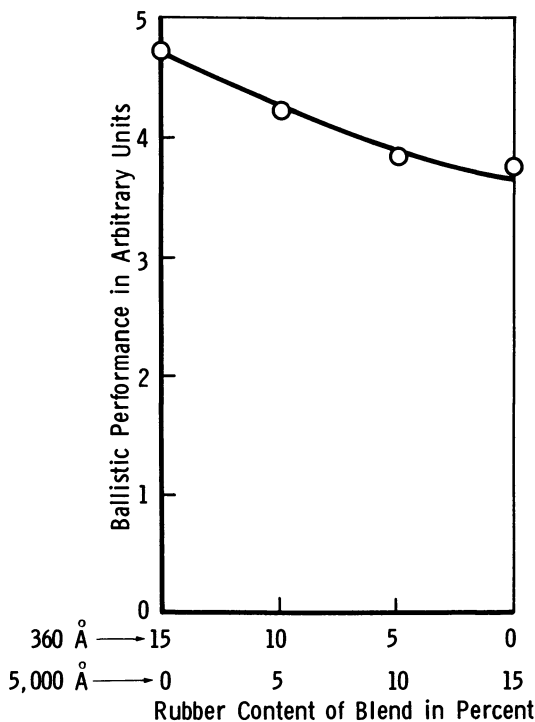


Figure 6. Ballistic impact of blends of graft polymers made from 360- and 5000-Å latexes



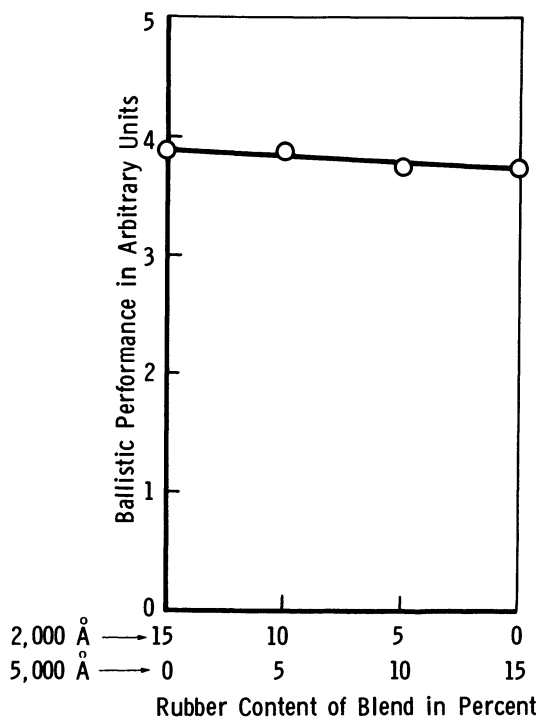


Figure 7. Ballistic impact of blends of graft polymers made from 2000- and 5000-Å polybutadiene latexes

Table VIII. Quantitative Measurement of Degree of Grafting and Its Correlation with Tensile Impact

Run No.	Latex Particle Size, Å	Tensile Impact, ft-lb/in. <sup>2</sup>	Parts Graft per 100 Parts Rubber
33	360	35	238
22A	880	39	108
18A	880	54	283
15	1000	12	115
16C	1000	21	256
26	2000	33	82
17B	2000	37	151
6A	2500	6	95
14	2500	19	167
21A	2500	34	113
20A	2500	42	203

**Table IX.** Preparation of Graft Polymer<sup>a</sup> with a Medium Degree of Graft

<i>Formulation</i>	<i>Run No.</i>	
	45	46
Distilled water, total	245.0	245.0
Modified Run 8B latex, solids basis	70.0	70.0
Na <sub>3</sub> PO <sub>4</sub> · 12 H <sub>2</sub> O	0.6	0.3
Sodium stearate	5.0	—
Aerosol A-196, 85% solids	—	1.8
MMA	23.1	23.1
Styrene	6.9	6.9
<i>tert</i> -Dodecyl mercaptan	0.15	0.15
K <sub>2</sub> S <sub>2</sub> O <sub>8</sub>	0.15	0.15
Tensile impact, ft-lb/in <sup>2</sup>	17.6	20.4

<sup>a</sup> 2 hrs @ 50°C without K<sub>2</sub>S<sub>2</sub>O<sub>8</sub>; add K<sub>2</sub>S<sub>2</sub>O<sub>8</sub> and polymerize 16 hrs at 60°C; based on 360-A polybutadiene latex.

tensile impact than a lower level of grafting in another latex. The manner in which each latex reacts to its initiator and the particle size of the rubber all contribute to vary the tensile impact of the polymer.

Within each latex system tensile impact improves with the degree of grafting. The graft polymers evaluated so far by AMMRC had a high degree of grafting. To complete the correlation of degree of grafting *vs.* ballistic impact, graft polymers with a low and medium graft content were prepared. AMMRC evaluation of the three-particle-size polymers and their blends showed that the 360-A polymer had higher ballistic impact resistance than the others tested.

We prepared a 360-A polymer with a low degree of grafting by blending latexes. The 360-A latex blended with the copolymer latex gave a 15% rubber content with no graft. The resultant latex blend was freeze-coagulated and was treated the same as the previous specimens.

A graft polymer made with 360-A latex which had a medium degree of grafting was made by changing the ratio of rubber to copolymer from 15/85 to 70/30. Since only about 15% of the monomer was expected to graft on the rubber, less graft was expected. Different surfactant systems were also investigated (Table IX) since it was difficult to wash the residual sodium stearate from the previously made polymers; another surfactant which was more water soluble and which would give results comparable with those of sodium stearate would be desirable.

Based on the tensile impact data in Table IX, we used Run 46 with Aerosol A-196 surfactant to scale up in the pilot plant. We took the 70/30 rubber to copolymer material and diluted it with copolymer to lower the final rubber content to 15% of the polymer; this was done during milling.

The differences between low, medium, and high degree of grafting are:

<i>Degree of Grafting</i>	<i>Parts Graft per 100 Parts Rubber</i>	<i>Monomer Level</i>	<i>Rubber Level</i>	<i>Method of Preparation</i>
Low	0	85	15	latex blending
Medium	87	30	70	polymerization
High	238	85	15	polymerization

The AMMRC tests (Figure 8) reveal a direct correlation between degree of graft and ballistic impact resistance.

**Rubber Content.** To analyze the effect of rubber content we made a graft polymer with 25% polybutadiene rubber and a high degree of graft using the 360-A polybutadiene latex. Essentially the same procedure that developed the 15% rubber graft was followed. The rubber/monomer ratio was changed to 25/75, and three surfactant systems were evaluated (Table X).

The scale-up of Run 43 was made in the 10-gal kettle. The latex was freeze-coagulated and worked up in the same manner as the other grafts.

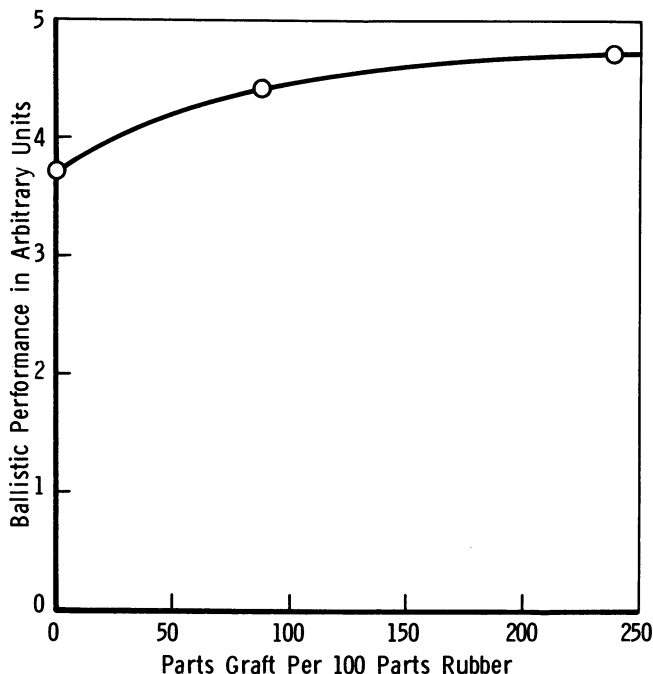


Figure 8. Degree of graft vs. ballistic impact

**Table X. Preparation<sup>a</sup> of 25% Rubber Graft Using 360-A Latex**

<i>Formulation</i>	<i>Run No.</i>		
	<i>42</i>	<i>43</i>	<i>44</i>
Distilled water, total	180.0	180.0	180.0
Run 8B latex, solids basis	25.0	25.0	25.0
Na <sub>3</sub> PO <sub>4</sub> ·12 H <sub>2</sub> O	0.6	0.3	0.3
Sodium stearate	5.0	—	—
Sodium propyl phosphate, 20% solids	—	4.0	—
Aerosol A-196, 85% solids	—	—	1.685
MMA	57.75	57.75	57.75
Styrene	17.25	17.25	17.25
<i>tert</i> -Dodecyl mercaptan	0.5	0.5	0.5
K <sub>2</sub> S <sub>2</sub> O <sub>8</sub>	0.3	0.3	0.3
Tensile impact, ft-lb/in. <sup>2</sup>	56	80	75

<sup>a</sup> 2 hrs @ 50°C without K<sub>2</sub>S<sub>2</sub>O<sub>8</sub>; add K<sub>2</sub>S<sub>2</sub>O<sub>8</sub> and polymerize 16 hrs @ 60°C.

The 25% rubber graft was compounded and compression molded into sheets. The same 25% graft was cut during milling with copolymer to reduce the rubber content to 20%. This same technique was used to cut the 15% rubber graft previously made to 10 and 5% rubber content. Copolymer alone was compounded and molded into sheets to give a 0% rubber content material.

The tensile impact data below show that the 25% rubber polymers have much higher impact resistance than the 15% rubber polymers. Comparing the highest tensile impact obtained at the 25% rubber level, we find that it is over 125% higher than the tensile impact at the 15% rubber level (80 vs. 35 ft-lb/in.<sup>2</sup>).

<i>% Rubber</i> <i>(360 A Latex)</i>	<i>Tensile Impact</i> <i>(ft-lb/in.<sup>2</sup>)</i>	<i>Ballistic</i> <i>Impact</i>
15	35	4.75
25	80	4.55

Figure 9 indicates that, in agreement with the tensile impact data, ballistic impact resistance improves with increasing rubber content. However ballistic impact, unlike tensile impact, decreases above 15% rubber content.

**Degree of Dispersion.** The graft polymers examined had a high degree of rubber particle dispersion. A batch was now made with a low degree of dispersion at 15% rubber and a high graft content using 360-A latex. Taking the recovered, dried, 15% rubber graft polymer, we dissolved the ungrafted copolymer in MEK. This left us with a rubber and graft prepared with a high degree of grafting.

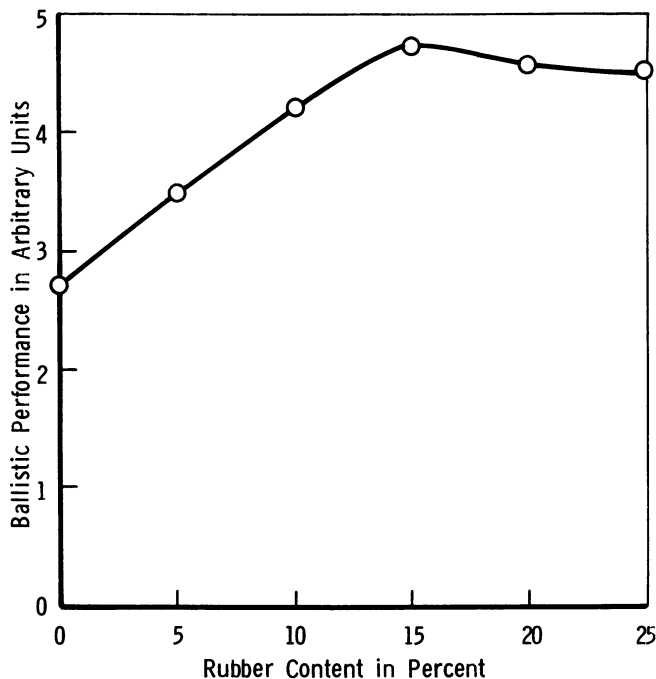


Figure 9. Rubber content of graft polymer vs. ballistic impact

Because we knew the amount of polymer, we carefully weighed and used the rubber and graft that remained; we could easily calculate the amount of rubber. The recovered rubber/graft mixture was compounded into copolymer on a two-roll mill at a sufficient amount to give a final rubber content of 15%. The compounding was just long enough (2 min) to blend the materials. It has been our experience in plastics processing that 10 min of compounding gives an extremely high degree of dispersion and that 2 min gives a poor dispersion. As expected, ballistic data reveals that the higher degree of rubber dispersion gives a higher impact resistance (Figure 10).

### Conclusion

This research program has produced a series of transparent rubber-modified polymers that were designed to investigate ballistic resistance and that had good optical properties over a maximum temperature range. Of the variables studied, a 360-A particle size polybutadiene latex with a high degree of methyl methacrylate/styrene copolymer grafting and high dispersion was optimum at the 15% rubber level.

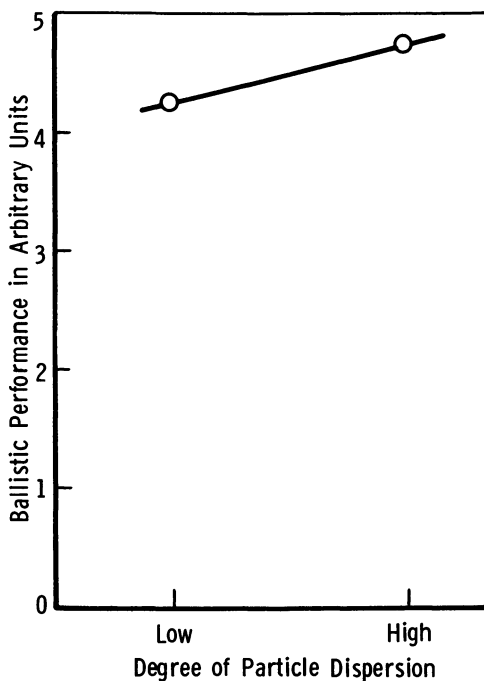


Figure 10. Degree of rubber particle dispersion vs. ballistic impact

### Literature Cited

1. Bragaw, C. C., "The Theory of Rubber Toughening of Polymers," *ADVAN. CHEM. SER.* (1971) 99, 86.
2. "Encyclopedia of Polymer Science and Technology," Vol. 5, H. F. Mark, Ed., p. 443, Interscience, New York, 1966.
3. "Polymer Handbook," J. Brandrup *et al.*, Eds., Interscience, New York, 1966.
4. "Encyclopedia of Polymer Science and Technology," Vol. 7, H. F. Mark *et al.*, Eds., p. 613, Interscience, New York, 1967.
5. Huguet, M. G. *et al.*, *Amer. Chem. Soc., Div. Polym. Chem., Preprints*, 11 (2), 548-552 (Chicago, September 1970).
6. Frazer, W. J., *Chem. Ind.* (1966) 33, 1399.
7. Sorenson, W. *et al.*, "Preparative Methods of Polymer Chemistry," pp. 34-42, Interscience, New York, 1961.
8. *Mod. Plas. Encyclo.* (1969-1970) 46 (10A), 968-985.
9. Lange, N. A., Ed., "Lange's Handbook of Chemistry," 10th ed., p. 875, McGraw-Hill, New York, 1967.
10. Steinberg, M., Kukacka, L. E., Colombo, P., Auskern, A., Manowitz, B., Dikeou, J. T., Backstrom, J. E., Hickey, K. B., Rubinstein, S., Jones, C. W., *Brookhaven Natl. Lab. Rept.* 50218 (T-560), REC OCE 70-1 (Dec. 1969).

RECEIVED November 11, 1974. Work supported under Contract DAAG 46-73-C-0127.

## A Strength–Morphology Study of Transparent Two-Phase Polymers

R. G. BAUER and P. S. PILLAI

The Goodyear Tire & Rubber Co., Research Division,  
142 Goodyear Blvd., Akron, Ohio 44316

*ABS and high impact polystyrene are two-phase composites comprising dispersions of rubber particles in a rigid glassy matrix of SAN or polystyrene. Because of their transparency, the MBS, MBAS, SA, and similar clear impact plastics are useful variations of these rubber-modified polymers. The investigation of two-phase morphology has been expanded using laser light scattering, a convenient, non-destructive method to characterize domains of super-molecular size which give the outstanding impact resistance characteristics of these heterogeneous two-phase systems. The laser light scattering technique is most valuable when used to determine the morphology of the new transparent plastics containing saturated elastomers which are not readily stained by osmium tetroxide and similar oxidizing agents for electron microscopy studies.*

The physical properties of rubber-modified impact plastics depend on the morphology, the nature, and extent of the inhomogeneity in the blend. Light scattering is a convenient method to characterize domains of the size commonly found in these thermoplastics. Laser light scattering has been used to study the structure of SBS block copolymers (1) and to examine the phase structure of an MBAS plastic as a function of the graft rubber concentration (2). In this investigation the authors used this method to study the domain sizes in several transparent impact plastics and attempted to make some correlation between their morphology and strength.

### **Experimental and Procedure**

**Material.** Optically clear films (about 5 mils thick) of three SA (saturated acrylic) plastics (3) that contained 25, 33, and 50% of an acrylic graft rubber (referred to as SA-1, SA-2, and SA-3) were compression molded. The acrylic graft rubber latices were latex blended with a resin latex composed primarily of methyl methacrylate, and the blend was coagulated. The compositions of these three polymers are as follows: SA-1, 79/17/4 wt %—methyl methacrylate/butyl acrylate/styrene; SA-2, 72/23/5 wt %—methyl methacrylate/butyl acrylate/styrene; SA-3, 59/34/7 wt %—methyl methacrylate/butyl acrylate/styrene. All three graft rubbers contained low levels of a crosslinking comonomer (less than 1.0 wt %).

**Apparatus.** Impact strengths were measured by the notched Izod procedure. These tests were run using a TMI autographic impact tester. Tensile strengths were run using an Instron tensiometer. Samples were elongated at 0.2 and 2.0 inches/min. For laser light scattering a He-Ne Laser ( $\lambda = 6328 \text{ \AA}$ ) was the source, and an RCA 7265 photomultiplier tube was the detector. This was mounted on a rotating arm with the sample axis as the center. The output voltage was amplified by a Sanborn amplifier and then was fed into a recorder.

Each of the impact plastic films was supported independently, and the scattered intensity ( $I$ ) was measured as a function of angle by a previously described method ( $I$ ).

### **Results and Discussion**

It is well known that systems like polystyrene or polystyrene-acrylonitrile—generally considered brittle materials—have a remarkable increase in toughness and resistance to impact when polyblended with finely dispersed, crosslinked, but partly compatible, rubber particles. These particles are generally 0.1–10  $\mu$  in size and frequently consist of butadiene which has been grafted with monomers of similar composition to the matrix or continuous phase.

Typically, electron microscopy has been used to determine rubber particle size and overall domain sizes in polyblends. For most systems containing polybutadiene or similar diene elastomers, it is possible to stain the rubber phase satisfactorily with a suitable oxidizing agent such as bromine or osmium tetroxide to provide a density gradient for detection. Since the graft rubber used in this investigation had no double bonds, these samples could not be stained; hence the electron micrographs had poor quality with no discernible phase structure. Electron microscopy requires ultrathin sections for examination which must be sectioned by ultramicrotoming.

A procedure ( $I$ ) was described to examine the size of these rubber particles and the interparticle distance using laser light scattering which is uniquely applicable to transparent polyblends. This procedure is best



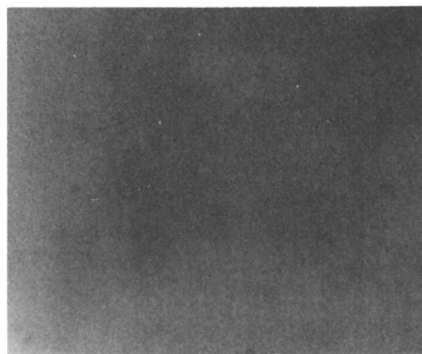


Figure 1. Electron micrograph of SA-1 (75,000  $\times$ )

used to examine the phases in transparent polyblends containing saturated elastomers which cannot be readily oxidized. Figure 1 shows an electron photomicrograph of a saturated, acrylic, rubber-modified polyblend. The difficulty in measuring rubber particle size or interparticle domain sizes in this polymer is apparent. By contrast Figure 2 is an electron photomicrograph of a polybutadiene rubber-modified polyblend; the structural features are more clearly seen.

Laser light scattering was described by one of us (2) for measuring the phase structure of an MBAS plastic as a function of graft rubber concentration. The data were analyzed with the Debye-Bueche expression (1, 2)

$$I = CV\eta^{-2}\pi^{3/2}a^3\exp[-4\pi^2\sin^2(\theta/2)a^2/\lambda^2] \quad (1)$$

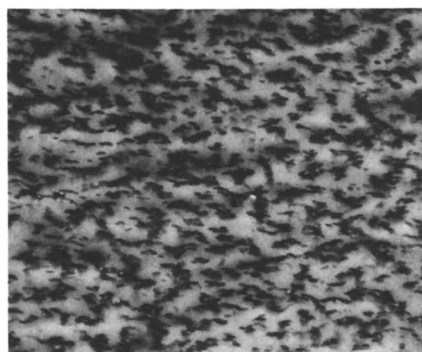


Figure 2. Electron micrograph of MBAS-1 (15,000  $\times$ )

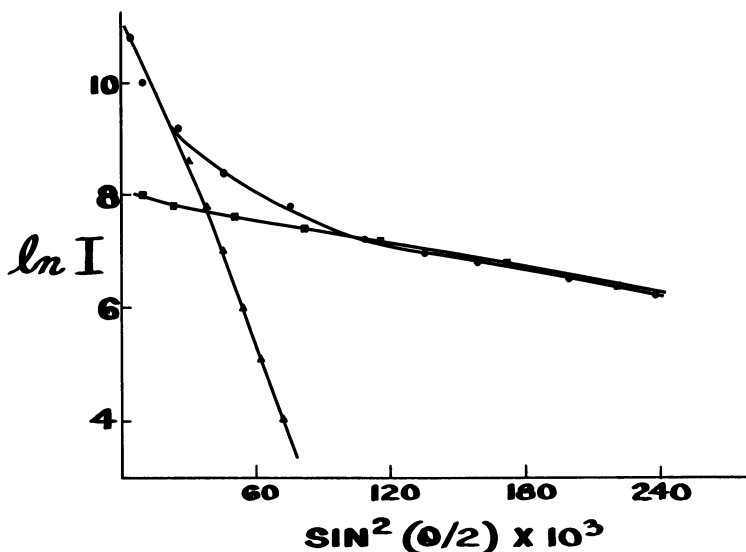


Figure 3. Log intensity vs.  $\sin^2(\theta/2)$  plot—SA-3

where  $C$  = constant,  $V$  = scattering volume,  $\bar{\eta}^2$  = mean scattering power,  $a$  = domain size (radius),  $\theta$  = scattering angle, and  $\lambda$  = wavelength in the medium.

Plots of  $\ln I$  as a function of  $\sin^2(\theta/2)$  were made by a computer for all of the films studied. One such plot for an SA-modified PMMA is shown in Figure 3. The initial and tail portions have different slopes. The mean sizes  $a_1$  and  $a_2$  of the scattering domains were calculated from these slopes and are given in Table I.

Table I shows that the size  $a_1$  is constant ( $\approx 0.26 \mu$ ) for all three samples, and  $a_2$  decreases from 1.05 to 0.78 as the graft rubber content increases from 25 to 50%. The same rubber latex was used for all three samples. Therefore the smaller dimension  $a_1$  is attributed to the size of the filler domain. The large dimension  $a_2$  varies inversely with the filler content and hence is considered as an interparticle separation distance.

Table I. Characteristic Dimensions of Domain Sizes and Interdomain Distances

Sample	Domain Radius		Separation Distance
	$a_1(\mu)$	$a_2(\mu)$	
SA-1	0.26	1.05	
SA-2	0.25	0.85	
SA-3	0.27	0.78	

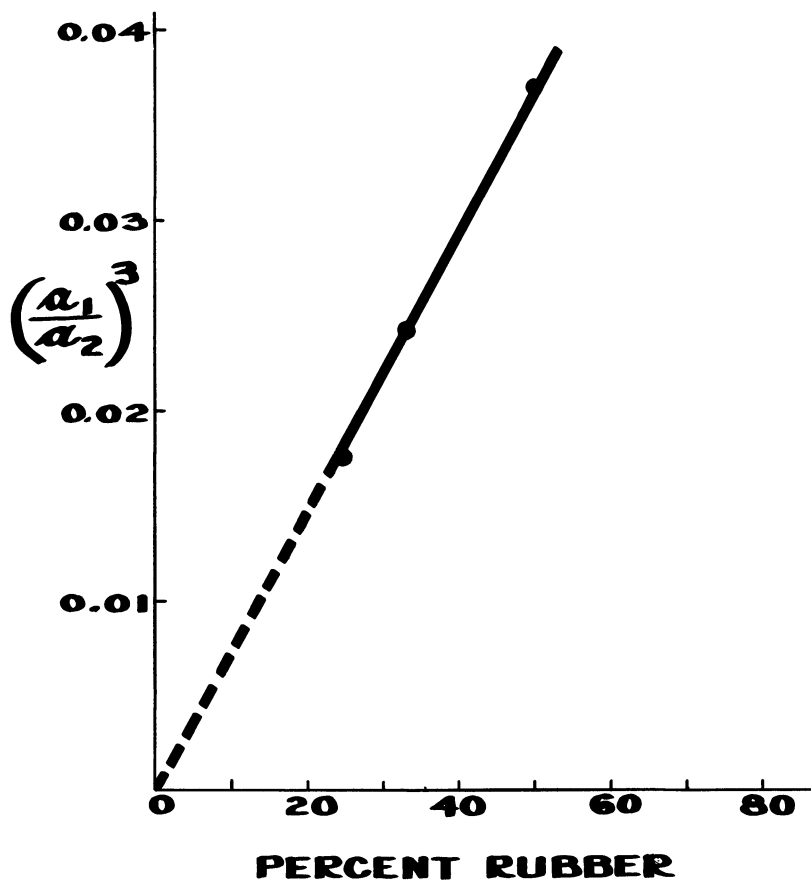


Figure 4.  $(a_1/a_2)$  vs. rubber concentration

The physical significance attached to the  $a_1$  and  $a_2$  dimensions in this study is identical to that which we obtained for a series of MBAS impact plastics (2) containing butadiene rubber where rubber latex particle size was determined independently. We found that both laser light scattering and electron microscopy results agreed.

The above conclusion was verified by checking whether the  $a_1$  and  $a_2$  values were consistent with the composition of the rubber in the plastic matrix (2). The volume of one scattering particle ( $v$ ) is  $4/3\pi a_1^3$ . If there are  $n$  such scatterers in the correlation volume ( $V$ ) given by  $4/3\pi a_2^3$  and if  $c$  is the percentage of the rubber filler, then

$$Vc = nv \quad (2)$$

$$\text{i.e., } (a_1/a_2)^3 = kc \quad (2a)$$

A plot of  $(a_1/a_2)^3$  vs.  $c$  should be a straight line going through the origin (2) (see Figure 4). The straight line nature of this graph agrees with Equation 2a, thus confirming the physical significance attached to the dimensions  $a_1$  and  $a_2$ . These results indicate a two-phase structure in which the rubber particles are dispersed in the plastic matrix.

Figure 5 depicts the dimensions of the  $a_1$  and  $a_2$  parameters measured by the light scattering method. The ratio  $(a_2/a_1)$  gives an approximation of the relative matrix size for different loadings of graft rubber. A plot of this function vs. impact strength or tensile behavior for various rubber loadings indicates the efficiency of a given type of rubber to improve impact strength. Figure 6 shows two curves of this type: one for the saturated acrylic plastic (from  $a_1$  and  $a_2$  values in Table I) and the other for the MBAS plastic (data from Ref. 2). These curves have the same shape, indicating an exponential relationship between rubber content and impact strength. This coincides with the experimental data reported for other types of rubber used to improve the impact strength of glassy resins (4). A similar examination can be made of the tensile strength variation with elastomer content for these two types of rubber (see Figure 7).

The graft rubber particle sizes for these MBAS and SA impact polymers are nearly equivalent; hence they can be compared directly. Other variables which may affect strength properties such as the craze size of the resin matrix, the interphase adhesion, molecular weights and

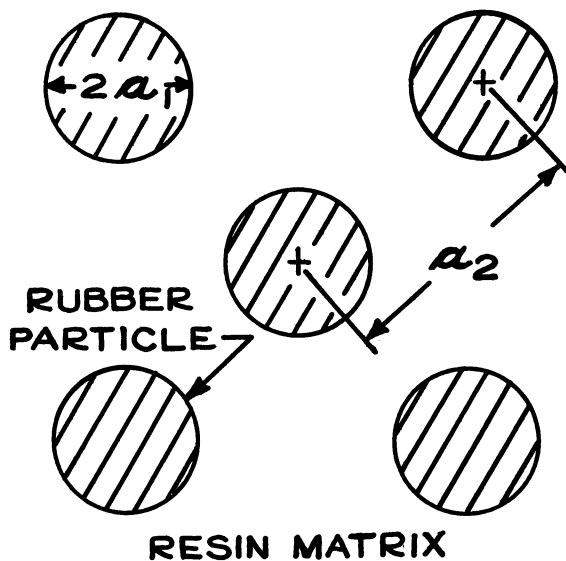


Figure 5. One-dimensional, rubber-resin array showing  $a_1$  and  $a_2$  distances

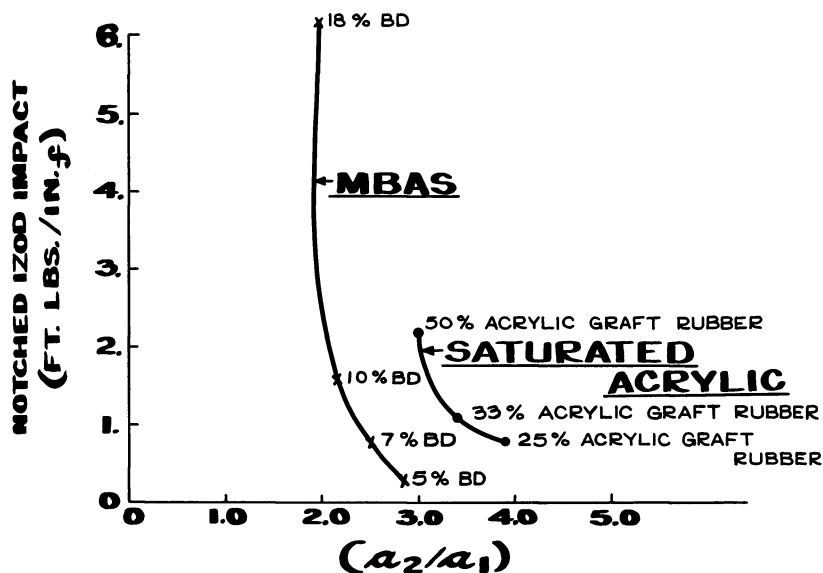


Figure 6. Impact strength vs.  $(a_2/a_1)$

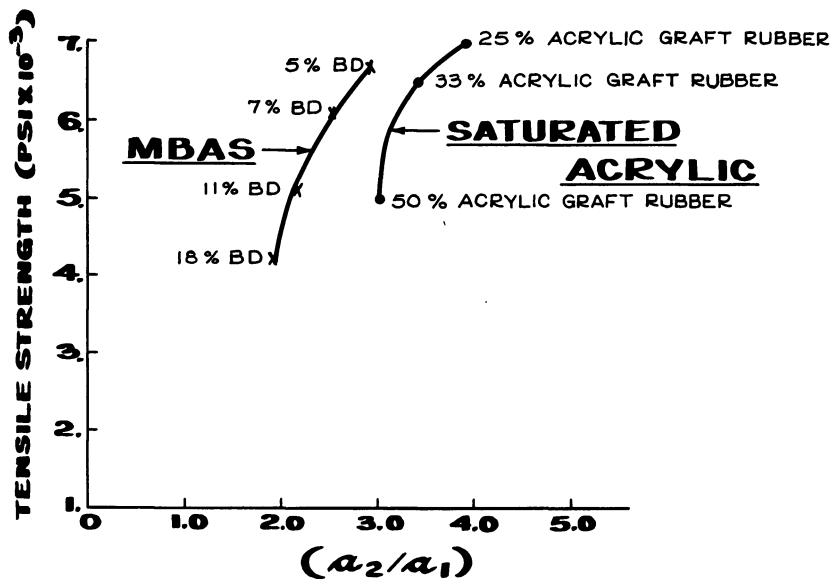


Figure 7. Tensile strength vs.  $(a_2/a_1)$

molecular weight distributions of the resin and rubber, and the graft type and level were not included; however the data suggest that the diene rubber in the MBAS plastic increases notched Izod impact strength more efficiently than the acrylic rubber in the saturated acrylic plastic although the tensile strengths of the latter seem less dramatically reduced by rubber modification.

Experiments—previously impossible without laser light scattering technology—suggested by this work involve studying the effect on physical properties of varying particle size for different types of elastomers.

### *Conclusion*

The application of laser light scattering technology to the study of the morphology and physical behavior of transparent impact plastics has been introduced. This procedure is an excellent means of studying saturated elastomer impact modifiers which have not been amenable to examination by other procedures, *e.g.*, electron microscopy.

The SA polymer exhibited a two-phase structure in which the filler particles of radius *ca.*  $0.26\ \mu$  are dispersed in the plastic matrix. The impact and tensile behavior of this polyblend was compared with that of an MBAS polyblend (graft diene rubber approximately the same size) which was examined previously by the laser light scattering technique.

### *Acknowledgments*

The authors thank M. E. Testa for the electron microscopy, J. D. Strang for light scattering measurements, and the Goodyear Tire & Rubber Co. for permission to publish this work.

### *Literature Cited*

1. Pillai, P. S., Livingston, D. I., Strang, J. D., *Rubber Chem. Technol.* (1972) **45**, 241.
2. Pillai, P. S., Livingston, D. I., Strang, J. D., *Indian J. Technol.* (Dec. 1974).
3. Bauer, R. G., Pierson, R. M., Mast, W. C., Bletso, N. C., Shepherd, L., *ADVAN. CHEM. SER.* (1971) **99**, 251.
4. Bragaw, C. G., *ADVAN. CHEM. SER.* (1971) **99**, 100.

RECEIVED October 18, 1974. Goodyear Contribution No. 538.

## Relationship of Morphology to Mechanical Properties of Rapidly Polymerizing Acrylic Dispersions

F. F. KOBLITZ, S. D. STEEN, P. R. KULP,  
R. C. GILL and J. F. GLENN

Dentsply International Inc., 550 West College Ave., York, Pa. 17404

*Dispersions of acrylic polymer beads in rapidly polymerizable liquids are used extensively in biomedical applications. Their utility and durability depend on their resistance to impact and to flexural stresses under bioconditions. Resistance to impact was investigated by an instrumented Izod method which also determined the time scale of events occurring during impact. Flexural strengths and moduli were determined under simulated oral conditions (37°C in water). The morphological features responsible for the mechanical behavior of polymerized dispersions were examined by polarized light and scanning electron microscopy. The microstructure and mechanical properties were dependent on the volume fraction of dispersed acrylic beads, impact modifiers, and barium sulfate filler and on the molecular weight and volume fraction of crosslinkers and dissolved polymers in the continuous phase.*

Dispersions of acrylic polymer beads in rapidly polymerizable liquids are important biomaterials (1, 2). The biocompatibility and functionality of dental restoratives, dental prostheses, and surgical prostheses depend on the mechanical properties of these biopolymers as well as on their physical and chemical constitution. This investigation was part of a continuing program to determine the influence of microstructural parameters on the mechanical properties of these multiphase systems. The effects of the volume fractions of dispersed phase and matrix, molecular weight of the matrix, chain length and concentration of crosslinkers, impact modifiers, and filler were studied in terms of microstructure, hard-

ness, flexural properties, impact resistance, and fracture characteristics to find methods to improve the function and durability of dental and surgical materials.

### **Experimental**

**Experimental Design.** Model dispersions were prepared consisting of 60% (by volume) dispersed phase and 40% polymerizable matrix to simulate commercial denture base resins and surgical cements. Volume concentration effects were observed by comparing these with a dispersion with 67% dispersed phase. Effects of crosslinker chain length were observed by substituting ethylene dimethacrylate, triethylene glycol dimethacrylate, or tetraethylene glycol dimethacrylate for methyl methacrylate in the matrix. Effects of crosslinker concentration were observed at 0, 5, 10, and 15% crosslinker concentration in the matrix—that is, 0, 2, 4, and 6% of the total dispersion volume using ethylene dimethacrylate and triethylene glycol dimethacrylate as the crosslinkers.

Effects of additives in the matrix were observed by substituting for methyl methacrylate a poly(methyl methacrylate) homopolymer with a solution molecular weight of 950,000, a vinylidene fluoride copolymer (Pennwalt's Kynar 7201), and a methacrylate-butadiene-styrene impact modifier (Marbon's Blendex BTA IIIN). Concentrations were 2% on the total dispersion volume. The same additives were studied at the same volume concentration in the dispersed phase. Barium sulfate (Whittaker, Clark, and Daniels' Barytes No. 91), a commonly used additive for radiopacity, was also studied in the dispersed phase. Responses were observed by the test methods described below.

**Test Methods.** All dispersions were prepared by twin shell blending of the dispersed phase followed by thorough stir-in mixing of the dispersed phase into the liquid matrix. Polymerization was in silicone molds in a thermostated pressure reactor at 20 psi for 1 hr at 60°C. Sample preparation was by the method of American Dental Association Specification 12.

ASTM D790-71 was used to obtain flexural strengths and tangent moduli. The tests were performed in water at 37°C on specimens preconditioned in water 50 hr at 37°C to approximate bioconditions. Comparative fracture energies were calculated from the flexural stress-deflection curves by taking the area under the curves.

The standard Izod test apparatus of ASTM D256 was modified to permit simultaneous Izod and dynamic impact studies. A special vise with built-in strain gages was used to detect the stress-strain behavior of samples during fracture. The output from the strain gages was amplified by a bridge amplifier (BAM-1) and displayed on a storage oscilloscope (Tektronix, type 564) as a stress *vs.* time curve. The memory display was photographed for later study of the phenomena occurring during fracture. The impact studies were made on specimens preconditioned in water 50 hr at 37°C followed by 24 hr in water at 23°C.

Rockwell hardnesses and recoveries were determined by the method of American Dental Association Specification 15. Samples were conditioned 50 hr in water at 37°C and 72 hr at 23°C. Tests were run in water at 23°C. Loads were 15 kg on a ½ in. ball.



Polarized light microscopy studies were done on a Leitz Ortholux metallographic microscope. All observations were by transmitted 3200°K unfiltered light. Scanning electron microscopy studies were done on a Cambridge Stereoscan microscope.

**Materials.** The dispersed phase of the dispersions contained, by weight: 98.07% acrylic polymer beads, 0.8% benzoyl peroxide (98% active), 1% red acetate fibers, 0.03% red pigments, and 0.1% TiO<sub>2</sub> pigment. The acrylic polymer beads were a 50/50 wt/wt blend of two suspension polymerized poly(methyl methacrylate) polymers with solution molecular weights of 160,000 and 950,000. Additives to the dispersed phase were those described above. The polymers were each reduced 1 vol % on the total dispersion volume to compensate for the additives.

The liquid phase of the dispersions contained, by weight, 99% methyl methacrylate, 0.5% distilled dimethyl-*p*-toluidine, and 0.5% ultraviolet absorber. Matrices used for volume concentration effects contained 5% ethylene dimethacrylate and 10% methyl methacrylate-ethyl methacrylate copolymer with methyl methacrylate monomer reduced to 84%. Matrices containing 5% additives (described above) contained 15% triethylene glycol dimethacrylate with methyl methacrylate reduced to 79%.

### Results and Discussion

Table I shows the effect of crosslinker chain length and concentration on mechanical properties. Contrary to expectations, both flexural and impact properties increased slightly with increasing ethylene dimethacrylate (EDMA) content up to 10%. The crosslinker had a relatively slight effect on the stiffness and brittleness of the cured dispersions up to 15 vol %. Triethylene glycol dimethacrylate (TEDMA) behaved similarly but had a less favorable effect on impact strength. The 5 to 10% improvements in all mechanical properties at the 10% EDMA level compared with uncrosslinked dispersion might well offer a substantial improvement in functionality and durability under bioconditions if combined with other dispersion technology (1, 2).

Table I. Effect of Crosslinker

	<i>No Crosslinker</i>
Flex strength, psi <sup>b</sup>	7800
Flex modulus, 10 <sup>5</sup> psi <sup>b</sup>	3.0
Unnotched Izod impact strength, ft-lb/in.	3.0
Rockwell indentation, mm	0.056
Recovery, %	79
Comparative fracture energy, ft-lb <sup>c</sup>	0.128

<sup>a</sup> EDMA: ethylene dimethacrylate.

TEDMA: triethylene glycol dimethacrylate.

Fracture surfaces of impact and flexural specimens indicated increased toughness at 5 and 10% EDMA in the matrix but brittleness with 12% tetraethylene glycol dimethacrylate (4EDMA) (Figures 1 to 6). Flexing (hinging) effects in the samples became increasingly prominent at 5 to 10% EDMA while 4EDMA caused glassy multiple fractures with reduced ability to bend. Fracture of the polymerized dispersions occurred by a combination of cracking through and around the dispersed

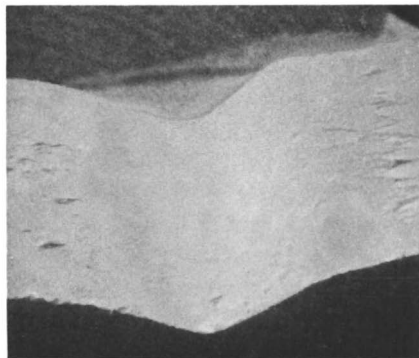


Figure 1. Impact fracture surface of polymerized acrylic dispersion, no dimethacrylate, SEM 17.5 $\times$

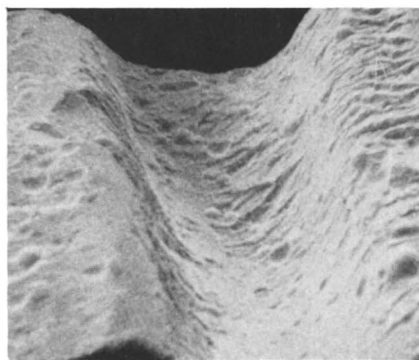


Figure 2. Impact fracture surface of polymerized acrylic dispersion containing 5% ethylene dimethacrylate, SEM 19 $\times$

#### Type<sup>a</sup> and Concentration

5% Crosslinker		10% Crosslinker		15% Crosslinker	
EDMA	TEDMA	EDMA	TEDMA	EDMA	TEDMA
8200	8150	8600	8450	8200	8050
3.1	3.3	3.2	3.2	3.1	3.2
3.0	2.9	3.3	2.9	3.1	2.8
0.058	0.054	0.052	0.055	0.055	0.057
78	79	83	78	78	77
0.139	0.144	0.143	0.140	0.150	0.143

<sup>b</sup> ASTM D790-71.

<sup>c</sup> Area under flexural stress-strain curve.

*Figure 3. Impact fracture surface of polymerized acrylic dispersion containing 10% ethylene dimethacrylate, SEM 17.5×*

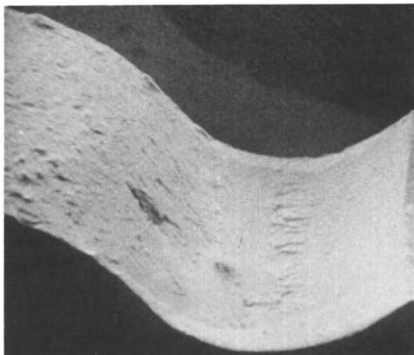


*Figure 4. Impact fracture surface of polymerized acrylic dispersion containing 12% tetraethylene glycol dimethacrylate, SEM 19×*

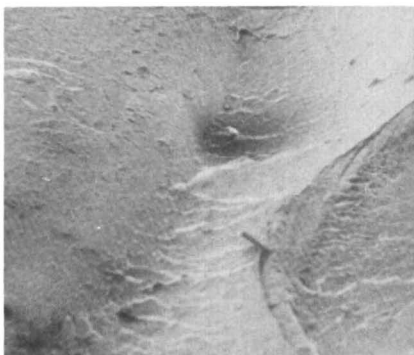
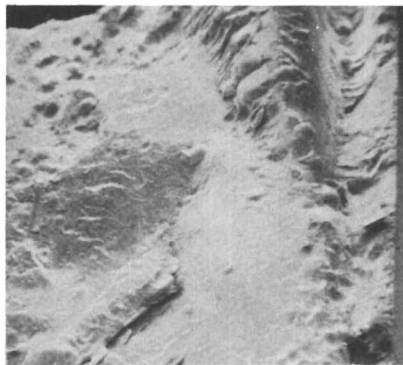


*Figure 5. Flexural (0.05 in./min) fracture surface of polymerized acrylic dispersion containing 10% ethylene dimethacrylate, SEM 17.5×*



beads. Increased flexural strength and impact resistance were accompanied by increased cracking around the beads, possibly caused by increased load bearing ability of the matrix with increased failure at the diffused interface of the beads and matrix.

Figure 7 shows the hinging effect in the beads and cracking around a bead in the model dispersion (5% EDMA) in a denture bonded to an acrylic artificial tooth. The typical hyperbolic crack propagation pattern

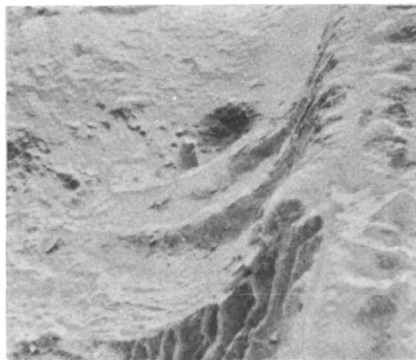


*Figure 6. Flexural (0.05 in./min) fracture surface of polymerized acrylic dispersion containing 12% tetraethylene glycol dimethacrylate, SEM 16 $\times$*

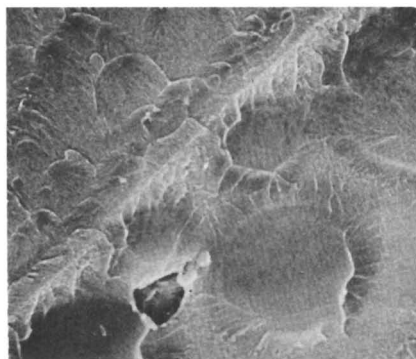


*Figure 7. Fracture surface of the interface of a molded acrylic artificial tooth with polymerized acrylic dispersion (60 vol % beads), SEM 850 $\times$*

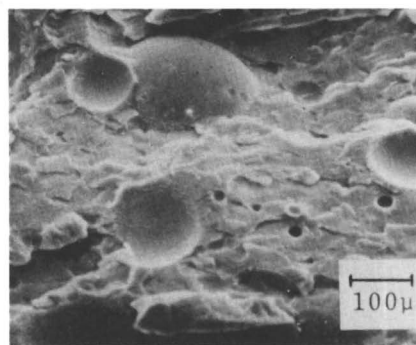


*Figure 8. Fracture surface of polymerized acrylic dispersion (67 vol % beads), SEM 250 $\times$*

of molded poly(methyl methacrylate) (3) is evident in the tooth. The diffused interface between matrix and beads is marked by the transition from parallel striations to a relatively smooth featureless topography.

Increasing the volume fraction of dispersed phase from 60 to 67% increased the proportion of crack propagation around the beads instead of through them (Figure 8). Decreasing the volume of relatively lower molecular weight matrix apparently increased the load borne by the inter-

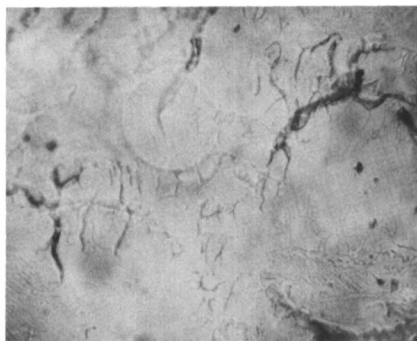


*Figure 9. Fracture surface of polymerized acrylic dispersion (67 vol % beads), polarized transmitted light microscopy 68 $\times$*

facial regions resulting in a shift to interfacial failure. Figure 9 shows the modes of crack initiation and propagation through and around the dispersed beads. Black and white photographs showed the stress concentration areas in the interfacial region as lighter than surrounding lower stressed areas. Color photography showed these stress concentrations as bright, yellowish birefringence. Cracks were generated in both the body of the matrix and in the interphase, but no crack initiation was observed within the beads. The stress patterns indicated the ability of the matrix to distribute stress to the interface, but this region apparently lacked the toughness of the higher molecular weight beads and so generated cracks preferentially to deformation of the beads. Reducing the volume of the matrix or increasing its toughness should be reflected in increased fracture energy (4), and this was the general behavior observed (Table I). Crack initiation and propagation followed a characteristic pattern of generation of tiny cracks at critical stress concentration points. These microcracks gathered to form larger cracks which then propagated relatively rapidly through the specimens.

Occasionally debonding was observed at the interface (Figure 8) producing smooth, dewetted surfaces on the beads. This bead-matrix adhesion failure made a relatively minor contribution to the overall fracture mode and was limited to beads larger than about 150  $\mu\text{m}$  diameter. A critical diameter range for stress distribution at the interface may exist for certain matrix compositions and volume concentrations.

These debonding effects were rate sensitive, as were the other failure phenomena. Fracture surfaces of samples broken slowly in flexure showed more crack propagation around beads and more bead dewetting than impact fracture surfaces which exhibited more brittle behavior. Even in impact specimens, however, the surface topography reflected the rate of crack propagation. The leading edge of the specimens, where crack propagation was somewhat slower than in the middle and hinging areas, exhibited an overall tougher fracture pattern.

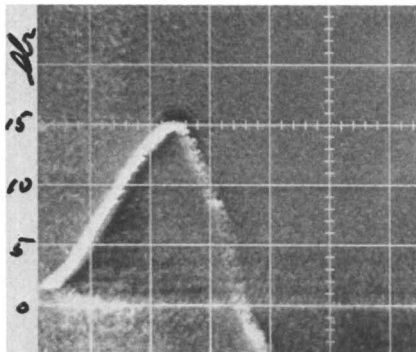


Figure 10. Oscilloscope trace of impact fracture B/double window glass; time scale = 20  $\mu$ sec per division

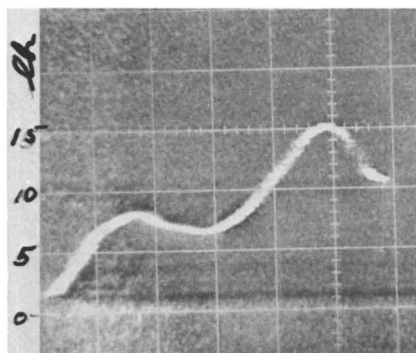


Figure 11. Oscilloscope trace of impact fracture of cast acrylic sheet; time scale = 20  $\mu$ sec per division

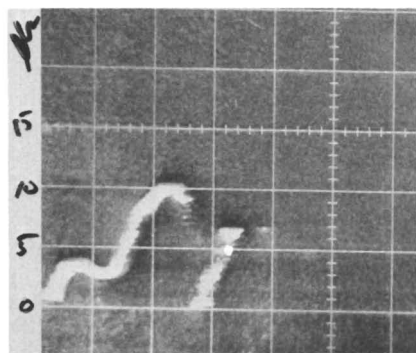


Figure 12. Oscilloscope trace of impact fracture of polymerized acrylic dispersion; time scale = 50  $\mu$ sec per division

The oscilloscope traces (Figures 10, 11, 12) indicated a time span of about 100 to 300  $\mu$ sec for the fracture events during impact of standard depth Izod specimens. Glass control specimens, which were half the depth, broke in 50  $\mu$ sec, yielding the expected elastic stress vs. time curve. The curves for cast methacrylate sheet and the 60 vol % dispersion showed a similar elastic region, a region involving plastic deformation or tearing or compressive phenomena, a final region of elastic deformation, and an unloading region. Some not yet defined ringing or rebound phe-

**Table II. Effect**  
*pMMA*

	<i>No Additives</i>	<i>Dispersed Phase</i>	<i>Matrix</i>
Flex strength, psi	8050	8150	7750
Flex modulus, 10 <sup>5</sup> psi <sup>b</sup>	3.2	3.1	3.3
Unnotched Izod impact strength, ft-lb/in.	2.8	3.0	2.7
Rockwell indentation, mm	0.057	0.056	0.056
Recovery, %	77	78	78
Comparative fracture energy, ft-lb <sup>c</sup>	0.143	0.147	0.125

<sup>a</sup> Modifiers added at 2 vol % on total volume. All matrices contained 6 vol % triethylene glycol dimethacrylate.

nomena were observed after specimen failure. An approximate correlation of deformation with time was made by considering the deformation to be qualitatively related to stress divided by tangent modulus of elasticity. Deformations on the order of .05% per 100  $\mu$ sec were calculated.

The effects of additives on the mechanical properties of the dispersion system are shown in Table II. None of the additives either in the dispersed phase or the matrix significantly improved any of the mechanical properties. The MBS modifier reduced the flexural strength and impact resistance when used as a dispersed phase additive as did the very high molecular weight pMMA in the matrix. The mechanical properties were much less sensitive to this low volume loading of additives than to similar volumes of crosslinkers.

### **Conclusions**

The mechanical properties of rapidly polymerizing acrylic dispersions, in simulated bioconditions, were directly related to microstructural characteristics. The volume fraction of matrix, the crosslinker volume in the matrix, the particle size distribution of the dispersed phase, and polymeric additives in the matrix or dispersed phase were important microstructural factors. The mechanical properties were most sensitive to volume fraction of crosslinker. Ten percent (vol) of ethylene dimethacrylate produced a significant improvement in flexural strength and impact resistance. Qualitative dynamic impact studies provided some insight into the fracture mechanics of the system. A time scale for the elastic, plastic, and failure phenomena in Izod impact specimens was qualitatively established. The time scale and rate sensitivity of the phenomena were correlated with the fracture surface topography and fracture geometry in impact and flexural samples.

of Modifiers<sup>a</sup>

<i>Fluoropolymer</i>		<i>MBS Modifier</i>		<i>Barytes Dispersed Phase</i>
<i>Dispersed Phase</i>	<i>Matrix</i>	<i>Dispersed Phase</i>	<i>Matrix</i>	
8000	7900	7650	7650	7950
2.9	3.0	3.2	3.0	3.2
3.0	2.9	2.6	2.9	2.6
0.056	0.055	0.057	0.055	0.054
80	79	78	79	80
0.148	0.133	0.126	0.123	0.131

<sup>b</sup> Tangent modulus of elasticity, ASTM D790-71.

<sup>c</sup> Area under flexural stress-deflection curve.

**Acknowledgment**

The authors thank K. L. DeVries, University of Utah and Phylisse D. Quickel, deceased, for their technical assistance in planning and conducting tests for this paper.

**Literature Cited**

1. Koblitz, F. F., Steen, S. D., Smith, R. A., Glenn, J. F., *Abstracts, 51st General Session, Intern. Assoco. Dental Res.* (1973).
2. Koblitz, F. F., Steen, S. D., Glenn, J. F., *Preprints, 166th Meeting, Amer. Chem. Soc., Div. Org. Coatings Plastics Chem.* (1973) 33 (2), 357.
3. Aharoni, S. M., *Bull. Amer. Phys. Soc.* (1974) 19 (3), 239.
4. Speri, W. M., Jenkins, C. F., *Polym. Eng. Sci.* (1973) 13, 409-414.

RECEIVED October 18, 1974.



## Impact Modification of Polysulfone with Polysulfone/Poly(dimethylsiloxane) Block Copolymers

A. NOSHAY, M. MATZNER, B. P. BARTH, and R. K. WALTON

Research and Development Department, Chemicals and Plastics,  
Union Carbide Corp., Bound Brook, N. J. 08805

*Polysulfone/poly(dimethylsiloxane) block copolymers (PSF/PSX) of controlled structure and composition are very effective additives for increasing the notched impact strength of polysulfone. This is attributed to a unique combination of PSF/PSX characteristics: morphology, compatibility, elastomeric nature, and thermal stability. The optimum effect is achieved with copolymers containing 5000  $\bar{M}_n$  PSF and PSX blocks at block copolymer concentrations of 5 wt % and with blending conditions that produce a PSF/PSX maximum particle size of 0.5–3.0  $\mu$ . Under these conditions good quality injection molded parts can be produced with notched Izod impact strengths as high as 22.0 ft-lbs/inch, compared with 1.3 ft-lbs/inch for unmodified polysulfone. The other properties of polysulfone are affected to only a minor extent by this modification.*

The impact strength of thermoplastic resins can be improved by blending with flexible polymeric additives or by synthesizing the resin in the presence of a rubber modifier to produce an *in-situ* graft copolymer. Since the latter technique is more amenable to addition polymers such as polystyrene (1) than to step-growth condensation polymers, impact modification of polysulfone was investigated *via* the additive blending approach. Polysulfone/poly(dimethylsiloxane) block copolymers are ideal additives for this purpose. Other block copolymers have also been reported as useful additives to improve the properties of the corresponding homopolymers. For example styrene/butadiene block copolymers, especially when used with peroxide crosslinking agents, improve the impact

strength of polystyrene (2), and polycarbonate/siloxane block copolymers reduce the wettability and frictional properties of polycarbonate resins (3).

Polysulfone is a high performance engineering thermoplastic which displays good toughness in the form of flat sheets. However it is notch sensitive—*i.e.*, it displays reduced toughness in molded items containing sharp corners, holes, etc. The notched Izod impact strength has been improved from 1.3 ft-lbs/inch to as high as 22.0 ft-lbs/inch by incorporating 5% of a polysulfone/poly(dimethylsiloxane) block copolymer (hereafter abbreviated as PSF/PSX). This improvement has been achieved without appreciably sacrificing processability and physical properties because of the unique morphology, compatibility, elastomeric nature, and thermal stability of PSF/PSX block copolymers. Many other additives including dimethylsiloxane homopolymers were investigated and found to be inferior to PSF/PSX because of the absence of one or more of these characteristics. This paper successfully demonstrates the concept of impact modification of a thermoplastic resin *via* the tailoring of a block copolymer structure designed to achieve a difficult combination of requirements.

### Experimental

The synthesis of polysulfone/poly(dimethylsiloxane) block copolymers was reported earlier (4, 5). Blends of the block copolymer with

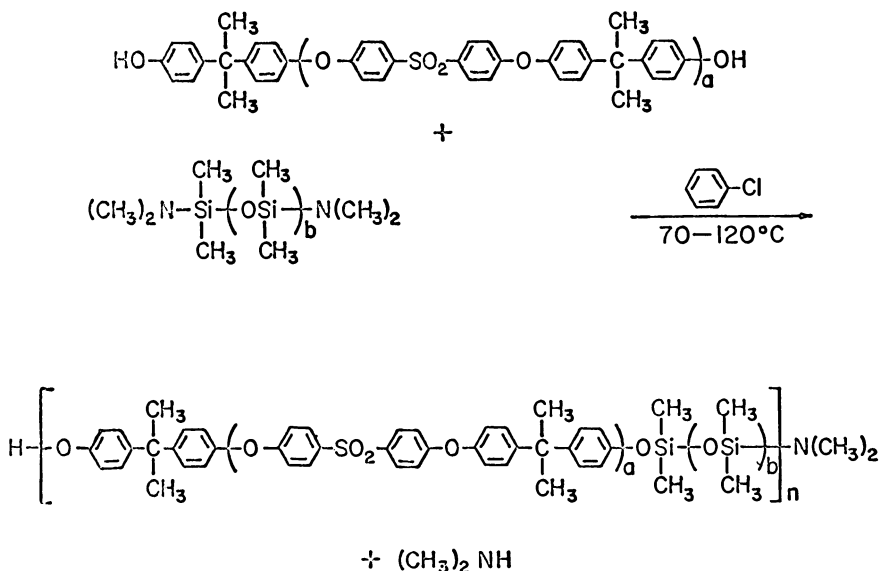


Figure 1. Synthesis of polysulfone-poly(dimethylsiloxane) block copolymers

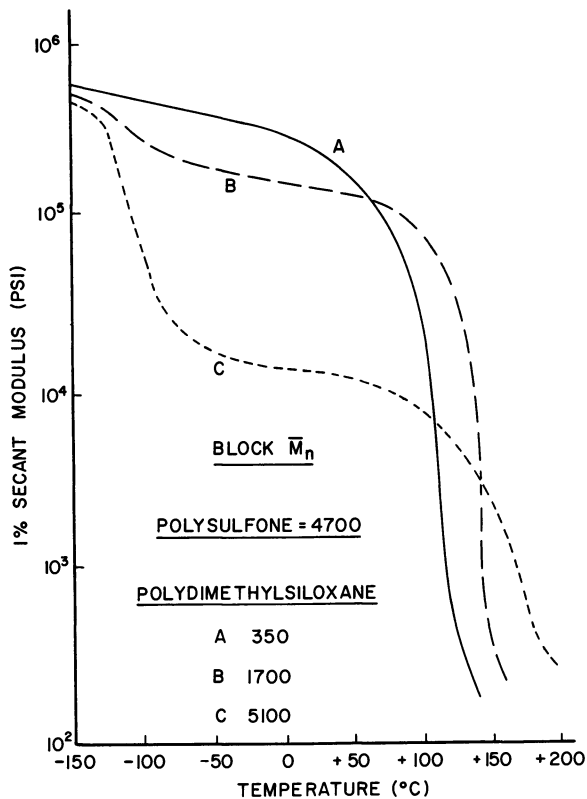


Figure 2. Temperature-modulus curves

polysulfone were prepared by solid or solution blending techniques. Solid blending was carried out for 5–10 min in a Brabender plastograph at  $\sim 280^\circ\text{C}$  or in a steam-heated Banbury mixer. Solution blending was carried out in a Marshall mill to mix and to strip off the solvent simultaneously. Compression molding was carried out at  $290^\circ\text{C}$ , and injection molding was performed at  $315^\circ\text{--}370^\circ\text{C}$ . Tensile properties, notched Izod impact strengths, and tensile impact strengths were determined *via* ASTM Methods D638, D256, and D1822.

### Discussion

The synthesis of PSF/PSX block copolymers described earlier (4) is carried out by the interaction of hydroxyl-terminated polysulfone oligomers with dimethylamino-terminated poly(dimethylsiloxane) oligomers (*see* Figure 1). The length of the PSF and PSX blocks in the copolymer, which are controlled by varying the molecular weight of the oligomers, greatly influences the composition and thus the properties of the block

copolymer (4, 5, 6, 7, 8). Copolymers of short block length display single phase morphology, but those with block molecular weights ( $\bar{M}_n$ ) of 5000 or greater display two-phase morphology. This is demonstrated by the presence of two glass transitions in the two-phase systems characteristic of each of the segments (*see* Figure 2). Mechanical properties, which depend on the weight fraction of the segments in the copolymer, are summarized in Table I. Compositions ranging from rigid to elastomeric can be achieved by varying the PSX content from 10–79 wt %. The elastomeric nature of the high PSX-content materials is attributed to a physical network which is an outgrowth of the two-phase morphology of the systems (4, 5, 6, 7, 8). The preferred compositions for impact modification of polysulfone are those containing 5000  $\bar{M}_n$  PSF and PSX blocks since they exhibit the best balance of required properties.

A proper degree of additive compatibility with a matrix resin is necessary to achieve optimum impact modification (9). Excessive compatibility reduces energy absorbing capacity and therefore causes poor impact strength. On the other hand gross incompatibility leads to “cheezy” blends and inefficient utilization of the impact modifier. The PSF/PSX block copolymers display just the proper degree of compatibility with PSF homopolymer. The PSX segments are highly incompatible with the polysulfone matrix resin because of a large difference in their solubility parameters, 7.3 and 10.6 (8). However the PSF segments of the block copolymers are of course soluble in the chemically identical polysulfone matrix resin. This provides an ideal mechanism for achieving a high degree of additive dispersion and adhesion between the resulting dispersed particles and the surrounding matrix resin. This is shown schematically in Figure 3. As a result, the PSF/PSX block copolymer disperses very easily in polysulfone when compounded *via* solid or solution blending techniques. These blends, after molding, contain PSF/PSX particles ranging from  $< 0.5 \mu$  to  $8.0 \mu$  (*see* Figure 4). By way of comparison, the optimum particle size in impact modified polystyrene is  $1\text{--}5 \mu$  (1).

**Table I.** Effect of Block  $\bar{M}_n$  on Block Copolymer Properties

Block $\bar{M}_n$		Wt % Siloxane	Tensile Modulus (psi)	Tensile Strength (psi)	Elonga- tion (%)	$T_g$ (°C)
Poly- sulfone	Poly(di- methyl- siloxane)					
4,700	350	10	240,000	6,000	5	+125
4,700	1,700	28	170,000	4,700	12	+140
9,300	4,900	41	29,000	2,700	150	-110; +170
4,700	5,100	55	20,000	2,400	350	-120; +160
4,700	9,200	67	2,000	1,300	500	-120; +160
6,500	25,000	79	300	900	550	-120; +160

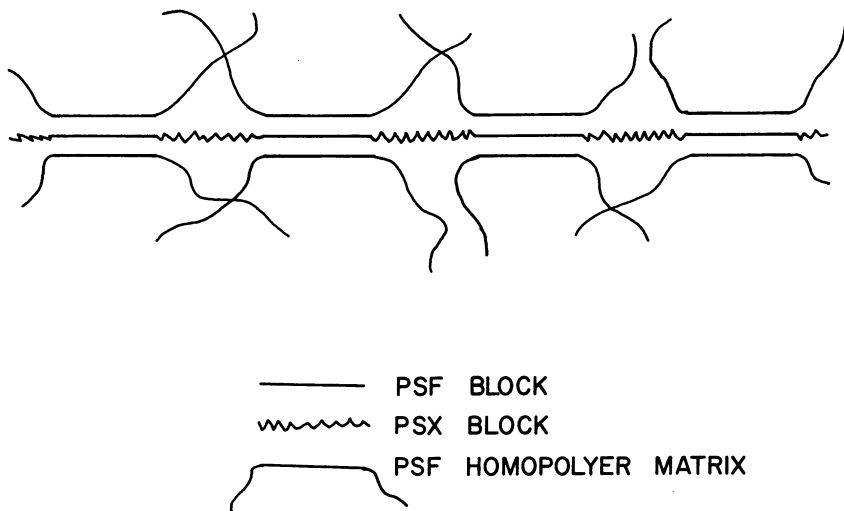


Figure 3. Compatibility of PSF blocks with PSF matrix

Another attribute that makes the PSF/PSX block copolymer a good impact modifier for polysulfone is its highly elastic nature. This arises from the unique rheological behavior of the material. Its melt viscosity and melt elasticity are so high that it cannot be extruded into filaments even at temperatures (*e.g.*,  $> 300^{\circ}\text{C}$ ) that are well above the glass transition temperature of the PSF segment ( $160^{\circ}\text{C}$ ). This unusual behavior for linear, soluble polymers is believed to arise from an extraordinarily stable physical network structure which persists even in the melt. This, in turn, is attributed to the high degree of phase separation in the PSF/PSX block copolymer which results from the large differential ( $\Delta$ ) in segment solubility parameter (8). All attempts to extrude the block copolymer led to extreme melt fracture resulting in “fluffy” extrudates similar in appear-

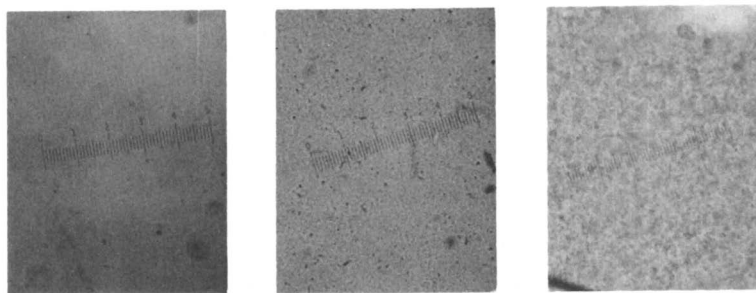


Figure 4. PSF/PSX dispersion in polysulfone (5% injection-molded blend observed at  $172\times$ )

Left:  $< 0.5 \mu$ ; Middle:  $< 3.0 \mu$ ; Right:  $< 8.0$

ance to the material before extrusion (*see* Figure 5). These rheological characteristics however do not adversely affect the melt processability of blends of PSF/PSX with polysulfone since the block copolymer is present in the dispersed phase. On the other hand the high melt viscosity and elasticity within the dispersed particles of linear PSF/PSX block copolymer results in rheological behavior which is similar to that displayed by the crosslinked grafted rubber modifiers present in impact-modified polystyrene. An important consequence of this behavior is retention of particle size integrity during high shear melt processing.

Since polysulfone is often melt processed at high temperatures (up to 370°C), another requirement of a successful impact modifier is that it display adequate thermal stability at these temperatures. As expected from the known good thermal stability of polysulfone and silicones (10, 11), the PSF/PSX block copolymer displays excellent thermal stability. This is illustrated by the thermogravimetric analysis curves shown in Figure 6.

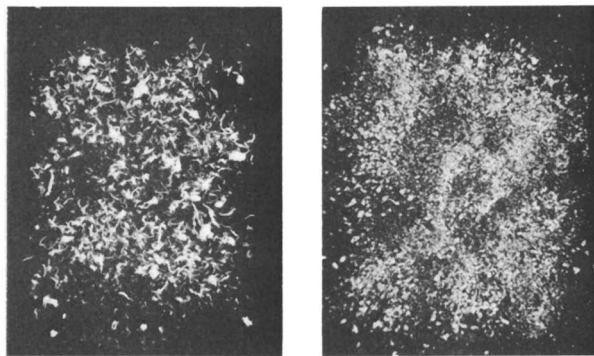


Figure 5. Highly melt-fractured extrudate of PSF/PSX. Left: before extrusion; right: after extrusion at 340°C.

Impact strength and melt processability are affected by the composition, concentration, and molecular weight of the PSF/PSX block copolymer. Low notched Izod impact values were obtained with 5% concentrations of high modulus block copolymers that contained short PSX blocks (*e.g.*,  $\bar{M}_n = 1700$ ). However uniformly high values (16–20 ft-lbs/inch) were obtained with copolymers containing 5000–10,000  $\bar{M}_n$  PSF and PSX blocks (*see* Table II). Although some copolymers had high impact strengths at 3% concentration levels, the 5% level provided consistently high values (*see* Table III). The range of PSF/PSX block copolymer molecular weight capable of producing high impact strengths is quite broad, covering reduced viscosity levels of 0.5–1.3 (*see* Table IV).

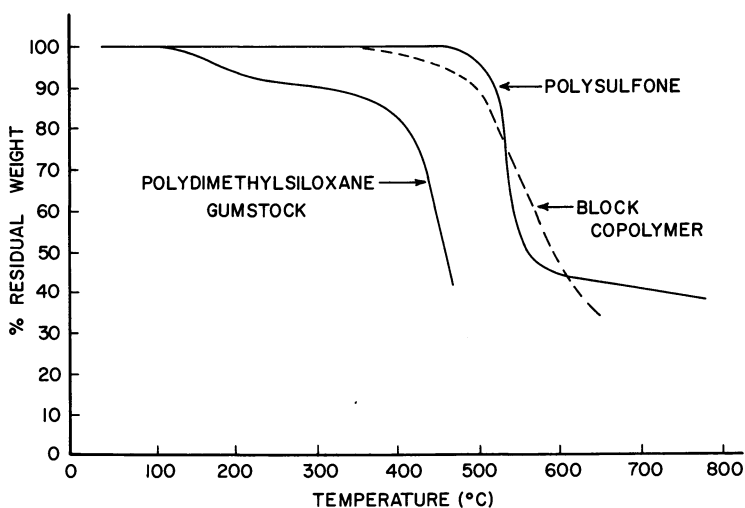


Figure 6. TGA of polysulfone-poly(dimethylsiloxane) block copolymers and homopolymers (in nitrogen at  $10^{\circ}\text{C}/\text{min}$ )

Table II. Effect of PSF/PSX Composition on Impact Strength

Block $\bar{M}_n$		Wt % PSX	Notched Izod Impact Strength <sup>a</sup> of 5% Blend (ft-lbs/inch)
PSF	PSX		
6,600	1,700	20	1.6
5,000	5,000	50	20.4
5,000	10,000	67	20.5
10,000	5,000	33	15.9
10,000	10,000	50	18.6

<sup>a</sup> Compression molded specimens.

Table III. Effect of PSF/PSX Concentration on Impact Strength

% PSF/PSX Concentration	Notched Izod Impact Strength <sup>a</sup> (ft-lbs/inch)	
	5,000/5,000 PSF/PSX	10,000/10,000 PSF/PSX
3	11.0	2.0
4	16.0	3.1
5	20.4	18.6

<sup>a</sup> Compression molded specimens.

**Table IV. Effect of PSF and PSF/PSX Molecular Weight**

<i>PSF Melt Flow (dgm/min 44 psi @ 343°C)</i>	<i>5,000/5,000 PSF/PSX Reduced Viscosity (0.2% Soln in CH<sub>2</sub>Cl<sub>2</sub>)</i>	<i>Notched Izod Impact Strength<sup>a</sup> of 5% Blend (ft-lbs/inch)</i>
7	0.3	1.7
7	0.5	17.6
7	1.0	17.8
7	1.3	18.5
17	1.0	17.4

<sup>a</sup> Injection molded specimens.

**Table V. Effect of PSF/PSX Degree of Dispersion**

<i>5,000/5,000 PSF/PSX Maximum Particle Size<sup>a</sup> in Molded 5% Blend (μ)</i>	<i>Injection Molded Notched Izod Impact Strength (ft-lb/inch)</i>	<i>Injection Molding Performance</i>
<0.5	1.5	Good
<3.0	18.5	Good
<8.0	16.5	Fair-Poor

<sup>a</sup> Observed in light microscope at 430X.

**Table VI. Reprocessability**

<i>Number of Times Molded</i>	<i>Notched Izod Impact Strength (5% Blend)</i>	<i>Injection Molding Performance</i>
1	18.4	Good
2	17.1	Good
3	16.0	Good

Lower molecular weight PSF/PSX did not give high impact strengths presumably because of an insufficient number of segments in the copolymer to produce a stable physical network. The molecular weight of the polysulfone matrix resin did not have an appreciable effect on impact strength, at least at the two levels investigated—*i.e.*, melt index = 7 and 17 (*see* Table IV).

Variations in blending conditions produced differences in PSF/PSX particle size. Low impact strengths were obtained when the maximum particle size in the molded part was less than 0.5 μ, but high values were obtained at the < 8.0 μ level (*see* Table V). However injection molding performance—*i.e.*, molding pressure required and molded part appearance—was adversely affected by particles greater than ~ 3.0 μ. An optimum balance appears to be achieved when the maximum particle size is 0.5–3.0 μ.



Table VII. Typical Thermal and Mechanical Properties

Property	PSF	5% PSF/PSX
		(5,000/5,000) +95% PSF
HDT (°C)	173	166-171
Tensile strength (psi)	10,200	9,200-9,400
Tensile modulus (psi)	360,000	320,000-340,000
Elongation at break (%)	50-100	10-100
Tensile impact strength (ft-lbs/inch <sup>3</sup> )	425	370-500
Notched Izod impact strength (ft-lbs/inch)	1.3	14-20

Impact strength was not greatly affected by reprocessing of the blends (*see* Table VI). This demonstrates two of the important properties of PSF/PSX referred to above: (a) excellent thermal stability and (b) high melt viscosity and elasticity within the dispersed particles.

The improved notched impact strength obtained in a 5%, 5000/5000, PSF/PSX block copolymer blend is achieved with minimal sacrifice in polysulfone properties. The data in Table VII indicate that heat distortion temperature is reduced by only  $\sim 5^\circ\text{C}$ . Tensile strength and modulus are reduced by *ca.* 10%, and elongation and tensile impact strength (unnotched) are essentially unchanged.

### Conclusions

PSF/PSX block copolymers of controlled structure and composition are effective additives for increasing the notched impact strength of polysulfone. This is attributed to a unique combination of PSF/PSX characteristics: morphology, compatibility, elastomeric nature, and thermal stability. The optimum effect is achieved with copolymers containing 5000  $\bar{M}_n$  PSF/PSX blocks at block copolymer concentrations of 5 wt % and with blending conditions which produce a PSF/PSX maximum particle size of 0.5-3.0  $\mu$ . Under these conditions good quality injection molded parts can be produced with notched Izod impact strengths as high as 22.0 ft-lbs/inch compared with 1.3 ft-lbs/inch for unmodified polysulfone. The other properties of polysulfone are only slightly affected by this modification.

### Literature Cited

- Lannon, D. A., in "Encyclopedia of Polymer Science and Technology," Vol. 7, p. 606, Interscience, New York, 1967.
- Childers, C. W., Kraus, G., Gruver, J. T., Clark, E., *Amer. Chem. Soc., Div. Polym. Chem., Preprints* (1970) 11 (2), 553.
- Legrand, D. G., Gaines, G. L., *Amer. Chem. Soc., Div. Polym. Chem., Preprints* (1970) 11 (2), 442.

4. Noshay, A., Matzner, M., Merriam, C. N., *J. Polym. Sci., Part A-1* (1971) **9**, 3147.
5. Noshay, A., Matzner, M., Williams, T. C., *Ind. Eng. Chem. Prod. Res. Develop.* (1973) **12** (4), 268.
6. Robeson, L. M., Noshay, A., Matzner, M., Merriam, C. N., *Angew. Makromol. Chem.* (1973) **29/30**, 47.
7. Matzner, M., Noshay, A., Robeson, L. M., Merriam, C. N., Barclay, R., Jr., McGrath, J. E., *Appl. Polym. Symp.* (1973) **22**, 143.
8. Matzner, M., Noshay, A., McGrath, J. E., *Amer. Chem. Soc., Div. Polym. Chem., Preprints* (1973) **14** (1), 68.
9. Brighton, C. A., in "Encyclopedia of Polymer Science and Technology," Vol. 7, p. 574, Interscience, New York, 1967.
10. Johnson, R. N., in "Encyclopedia of Polymer Science and Technology," Vol. 11, p. 447, Interscience, New York, 1969.
11. Meals, R. N., Lewis, F. M., "Silicones," Reinhold, New York, 1959.

RECEIVED October 18, 1974.

# Toughness Enhancement by Introduction of Silicone Blocks into Polycarbonates of Bisphenol Acetone and Bisphenol Fluorenone

R. P. KAMBOUR, D. FAULKNER, E. E. KAMPF, S. MILLER,  
G. E. NIZNIK, and A. R. SHULTZ

General Electric Co., P.O. Box 8, Schenectady, N.Y. 12301

*Two families of transparent polycarbonate-silicone multi-block polymers based on the polycarbonates of bisphenol acetone (BPA) and bisphenol fluorenone (BPF) were synthesized. Incorporation of a 25% silicone block in BPA polycarbonate lowers by 100°C the ductile-brittle transition temperature of notched specimens at all strain rates; silicone block incorporation also converts BPF polycarbonate into a ductile plastic. At the ductile-brittle transition two competing failure modes are balanced—shear yielding and craze fracture. The yield stress in each family decreases with silicone content. The ability of rubber to sustain hydrostatic stress appears responsible for the fact that craze resistance is not lowered in proportion to shear resistance. Thus, the shear biasing effects of rubber domains should be a general toughening mechanism applicable to many plastics.*

**B**oth resin families are polymerized by copolycondensation in which a dimethylsiloxane oligomer capped on each end with bisphenol is mixed with additional bisphenol and then phosgenated. The synthesis of the block polymers based on bisphenol acetone (BPA) has been described elsewhere (1).

**BPF Polycarbonate.** The synthesis of bisphenol fluorenone polycarbonate was first reported by Morgan (2). As in that study, the BPF carbonate family reported here was made by an aqueous caustic/organic liquid interfacial polymerization. In our case the monosodium salt of

BPF, which has low solubility in both water and organic liquids, was used. Phosgene was bubbled into the chloroform/water/salt slurry, and sodium hydroxide was added at a rate to maintain pH 10.5. Gel permeation chromatograms of these polymers showed a bimodal distribution; the smaller peak was attributable to cyclic carbonates (1–10%). Soxhlet extraction with dimethoxymethane reduced these to 1% or less, and subsequent to extraction  $\bar{M}_w/\bar{M}_n = 2.5\text{--}3.5$ ; apparent  $\bar{M}_n$ 's (based on a polystyrene GPC calibration) were 25,000–50,000. (Corresponding osmometric molecular weights are roughly one-third greater.)

**BPF Carbonate-Silicones.** The dichlorosilane fluids were first capped with BPF using a fourfold excess of the bisphenol to avoid coupling the silicone oligomers. The hydrochloric acid produced in the condensation was neutralized with ammonia. The interfacial copolycondensation was run at pH 10–10.5. (The aryloxy–silicon bond appeared stable to at least pH 11.)  $\bar{M}_n = 30,000\text{--}100,000$  by osmometry. Extraction with dimethoxymethane removed 2% cyclics and a small fraction of the silicone present largely as cyclic silicones in the original silicone fluid. The resultant polymers contained 7–27% silicone as blocks with number average degree of polymerization of 8 to 35 siloxy units depending on design conditions. All polymers could be cast into water-clear films from chloroform solutions. Residual chloroform lowered yield stress and increased ductility; however it could be removed by vacuum drying at 200°C overnight.

### *Viscoelastic Properties*

The relaxation behavior of the BPA carbonate–siloxane block polymers over the whole range of silicone content is reported elsewhere in detail (3). As seen in Figures 1–3 the behavior of the BPF family is similar to that of the BPA family except for two important differences. First, the modulus of BPF polycarbonate is higher than that of BPA polycarbonate by about 70,000 psi ( $5 \times 10^9$  dynes/cm<sup>2</sup>) at moderate and low temperatures; these differences also have their counterparts in the two block polymer families. Secondly, the  $T_g$  of BPF polycarbonate is 275°C by DSC scanning calorimetry *vs.* 150°C for BPA polycarbonate; consequently large differences between the thermo–mechanical behavior of the two families are seen at high temperature. The low temperature modulus dispersion in both families reflects the polycarbonate  $\beta$  relaxation and the glass-to-rubber relaxation of the silicone microdomains. The dispersions at high temperatures in each family depend on the polycarbonate block length but are independent of polycarbonate content. The 125°C difference in  $T_g$ 's of the homopolymers carries through in the block polymers as long as the families are compared in terms of block lengths rather than block molecular weights (which differ for equal length in the ratio  $M_{\text{BPFc}}/M_{\text{BPAC}} = 376/254$ ).

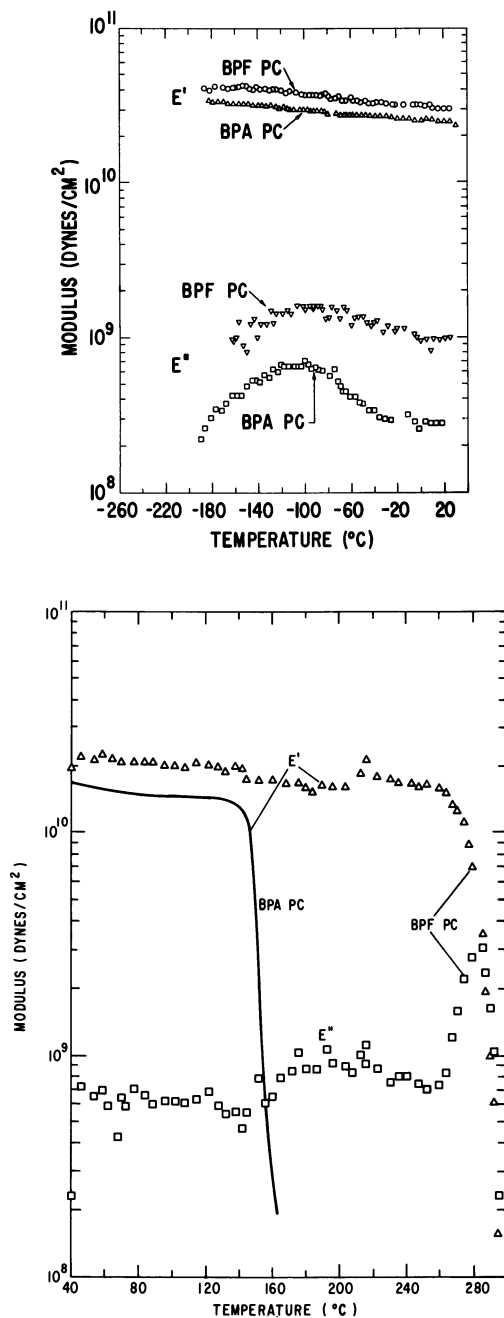


Figure 1. Storage and loss moduli ( $E'$  and  $E''$ ) for the homopolycarbonates of BPA and BPF at 110 Hz

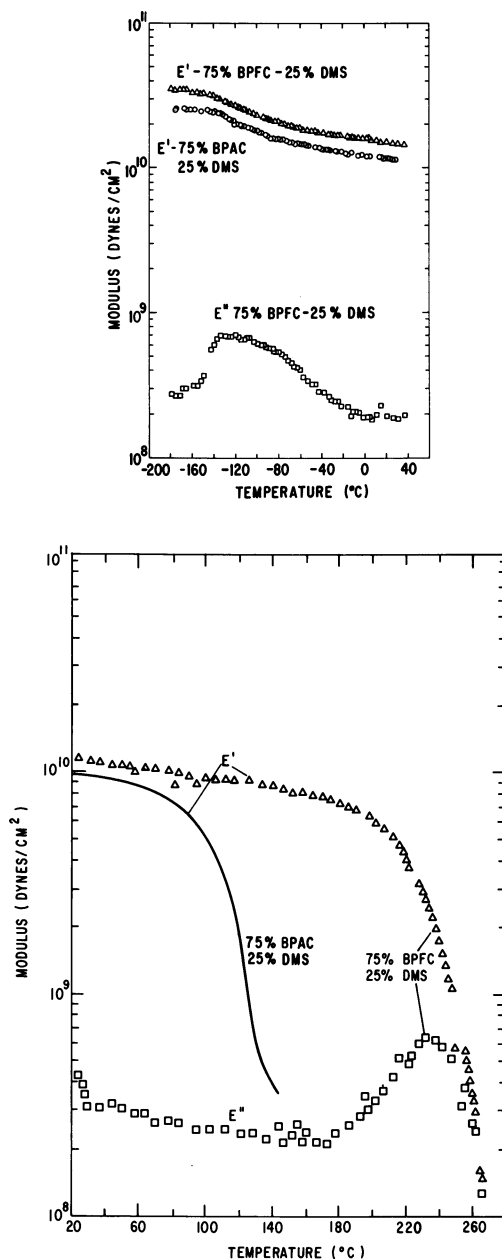


Figure 2. Storage moduli  $E'$  for silicone block polymers of BPA carbonate and BPF carbonate. Silicone content = 25%. Loss modulus  $E''$  for BPF polymer also shown. Silicone  $\overline{DP}_n = 20$ . Data at 110 Hz. Solid line-torsion pendulum results from Ref. 3.

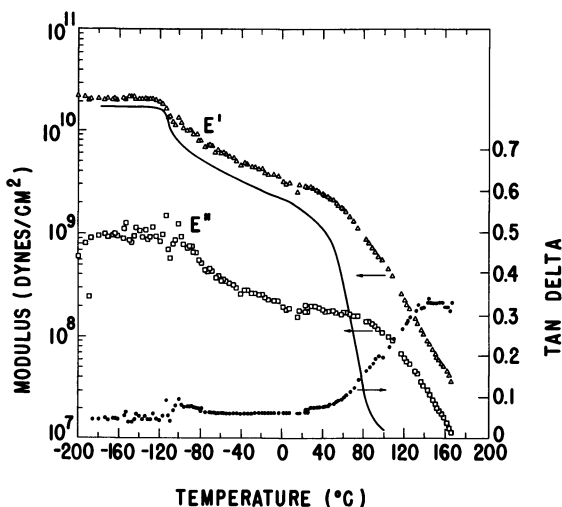


Figure 3. Storage and loss moduli and  $\tan \delta$  for BPF carbonate-silicone block polymer of 55% silicone of  $\overline{DP}_n = 20$ . Solid line: storage modulus of BPA carbonate block polymer of 50% silicone of average block length = 20 SiO units.

### Ductile and Brittle Failure in Notched Izod Specimens of BPA Carbonate Polymers

**Impact Failure.** Standard notched Izod impact measurements have been made over wide temperature ranges on specimens cut from compression molded  $\frac{1}{8}$ -inch thick sheets of BPA polycarbonate and two BPA carbonate-silicone block polymers (Figure 4) (see Table I for compositions and properties). In the homopolymer a ductile-brittle transition occurs at  $0^\circ$  to  $-15^\circ\text{C}$ , as reported previously (4, 5). Introduction of 15 and 25% silicone lowers the transition to  $-45^\circ$  and  $-110^\circ\text{C}$  (block polymers A and B). As indicated in Table I, this increase in toughness at low temperature is accompanied by the reduction of modulus and yield stress.

**Instron Three-Point Bending Failure.** Three-point bending tests have also been conducted on notched Izod specimens at crosshead rates of 0.02–20 inches/min (Figure 5). Plots of work to break obtained from the areas under the Instron force-displacement traces show abrupt ductile-brittle transitions; these are displaced to lower temperatures as the test rate is decreased. However the temperature interval between ductile-brittle transitions of the two materials remains about the same. The force-displacement trace for each specimen shows a yield point with a ductile failure but a sharp termination when the sample breaks in a brittle fashion.

**Table I. Composition and Properties of BPA Polycarbonate and BPA Carbonate-Silicone Block Polymers A and B**

	$(\eta)$ (dl/g)	BPAC <sup>a</sup> $T_g$ ( $^{\circ}$ C)	Wt, % DMS <sup>b</sup>	$\frac{DMS^b}{DP_n}$	$E^c$ (ksi)	$\sigma_y^d$ (ksi)
BPA Polycarbonate	0.55	150	0	—	340	9
Silicone—BPA Carbonate Block Polymer—A	0.8	135 <sup>e</sup>	15	20	270	7.6
Silicone—BPA Carbonate Block Polymer—B	0.6	120	25	20	150	5

<sup>a</sup> BPAC = Bisphenol-A-carbonate.

<sup>b</sup> DMS = Dimethylsiloxane block.

<sup>c</sup>  $E$  = Tensile modulus.

<sup>d</sup>  $\sigma_y$  = Tensile yield stress.

<sup>e</sup> Estimated from composition and block length using Figure 7 (3).

With the homopolymer the yield point in the force-displacement trace occurs when the yield zone (discussed below) has already advanced into the specimen.

**Failure Morphologies.** Ductile failure of notched polycarbonate specimens has long been recognized to occur with shear yielding from the notch tip (6). This occurs for the block polymers for all rates of test. Hull and Owen (5) recently reported from micrographic studies of impact fracture surfaces that the brittle failure of polycarbonate involves the formation and breakdown of a craze at the notch tip. The ductile-

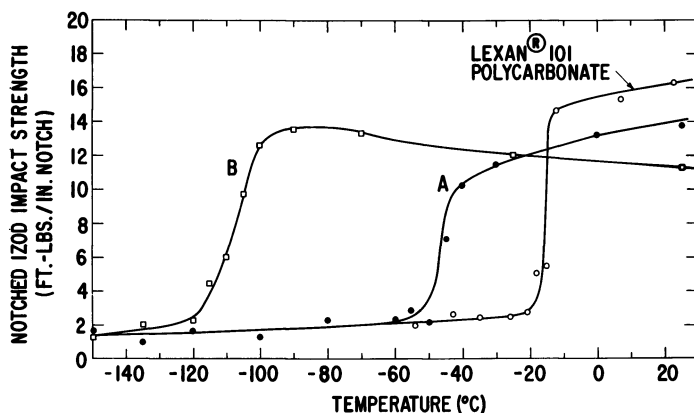


Figure 4. Temperature dependence of impact energy for  $\frac{1}{8}$  inch thick notched Izod specimens cut from compression molded sheets of BPA polycarbonate and two of its block polymers. A: 15% silicone, B: 25% silicone. Silicone  $DP_n = 20$ .



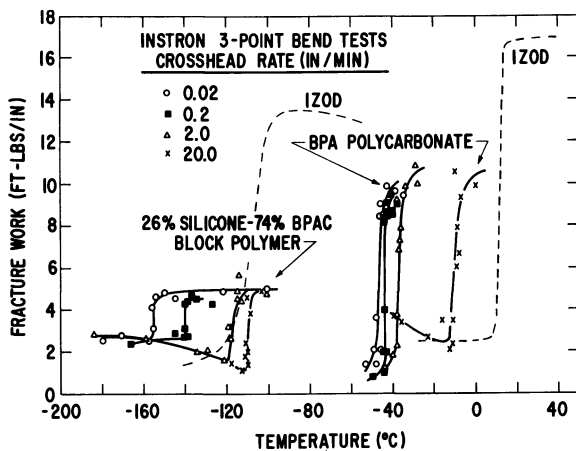


Figure 5. Failure energies of  $\frac{1}{8}$  inch notched Izod bars of BPA polycarbonate and block polymer B (Figure 4) tested in three-point bending compared with impact results. Crosshead rates as shown. Span = 2 inches.

brittle transition involves competition between shear yielding and craze formation and breakdown.

Our findings for the BPA homopolymer generally agree with those of Hull and Owen—brittle fracture surfaces show mirror areas centered midway through the bar close to the notch tip. In three-point bending tests conducted in an environmental chamber craze initiation can be observed using a cathetometer focused through the chamber window; the specimen can then be unloaded before failure and removed from the chamber, and the craze can be examined. With a wedge technique described previously (7) for empty crazes the critical angle for total internal reflection has been measured; from it the refractive index was calculated to be 1.26, in close agreement with the value obtained for the dried-out solvent craze. The craze is best examined microscopically by sectioning the specimen parallel to and above the craze plane; with collimated incident monochromatic light the craze acts as an interference wedge that permits its planar shape and thickness profile to be constructed (8). We found that the craze was always separated from the root of the notch by a section of unvoided material *ca.* 0.01 inch thick and also from the sides of the specimen by 0.02 inch or more (Figure 6). These separations are believed to exist because the stresses in these peripheral regions do not have a sufficient triaxial component. That is, the craze is initiated inside the specimen midway between the sides and removed from the notch root where the triaxial component of stress is understood to be

greatest; the craze then grows forward and toward the sides only in areas of sufficient triaxial tension.

The plane stress yield zones that spread from the root of the notch envelope, distort, and "neutralize" the craze. At temperatures just below the ductile–brittle transition temperature the shear flow begins at the notch, but the craze breaks before the shear zones have grown enough to encompass the craze.

Using the cathetometer the force at initiation was measured on notched bars of  $\frac{1}{8}$  inch thick extruded Lexan polycarbonate sheet over the widest temperature range possible at one rate of deformation. These initiation forces and the forces at failure are shown in Figure 7a. Brittle failure parallels craze initiation in its temperature dependence. Yield force has a greater temperature dependence—one that approximately parallels the measured values of yield stress in linear tensile tests (data

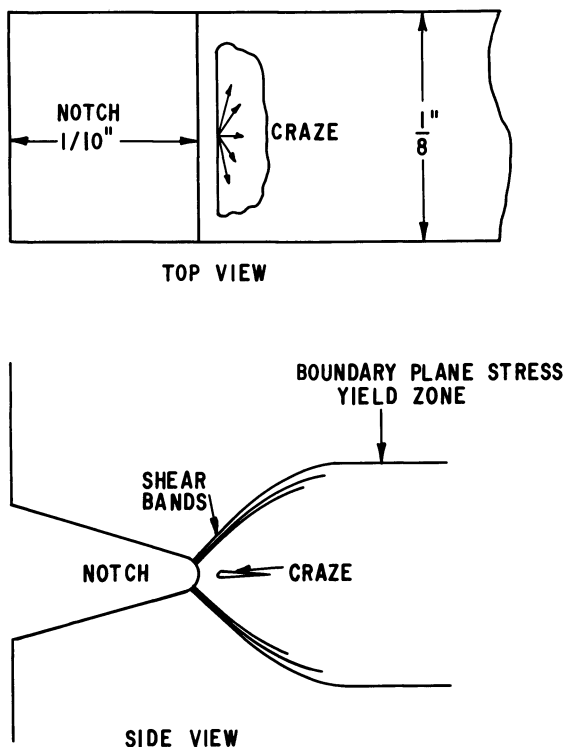


Figure 6. Diagrams of planar shape and thickness profile of full grown craze and shear zone beyond root of notch in BPA polycarbonate specimen. Shear bands initiate from positions of maximum shear stress at root. Arrows indicate craze growth directions.

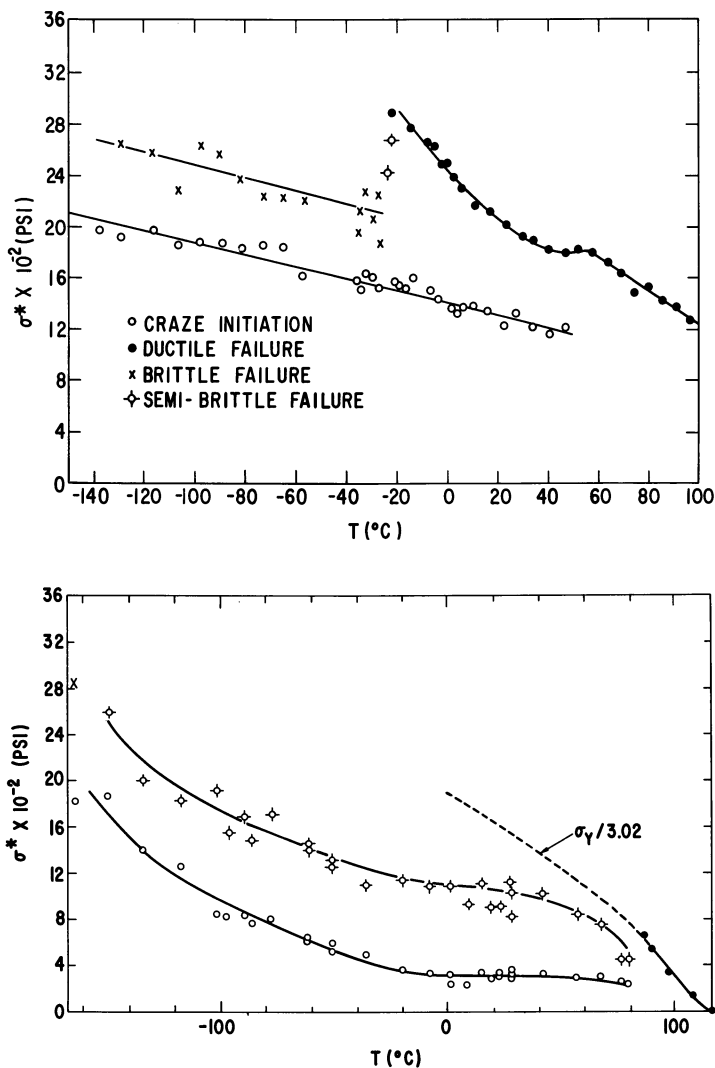


Figure 7. Temperature dependence of failure stresses in Instron three-point bend tests on  $\frac{1}{8}$  inch notched Izod bars cut from (a) extruded polycarbonate sheet and (b) compression molded block polymer B. Crosshead rate = 0.02 inch/min. Span = 2 inches.  $\sigma^*$  = net section stress = force/net cross-section at notch root.  $\circ$ , Craze initiation;  $\bullet$ , ductile failure;  $\times$ , brittle failure;  $\diamond$ , semi-brittle failure.  $\sigma_y$  = tensile yield stress.

not shown). Note however the discontinuity at 50°C from which a stress concentration effect caused by pre-yield crazing is inferred.)

Block polymer B differs substantially in its failure characteristics from BPA polycarbonate. For the block polymer a mixed failure mode predominates in three-point bend tests of notched specimens from -100°-90°C. In the mixed mode craze breakdown and plane strain fracture occur first inside the specimen; subsequently shear failure occurs in the surface regions of the specimen. Shear lips (11) are formed as a result. Shear lips are also found on the notched Izod impact fracture surfaces of block polymer B, implying that the same mixed mode of failure occurs under high speed loading conditions.

A comparison of Figures 7a and 7b shows that the resistance to craze initiation is lowered more than the resistance to plane strain crack initiation (*i.e.*, craze breakdown) by introducing silicone blocks into BPA polycarbonate.

**Kinetics of Yielding.** Tensile yield stresses were measured at several Instron rates for block polymer B. These results and those of Bauwens-Crowet *et al.* (9) for BPA polycarbonate were analyzed in the framework of the Rhee-Eyring stress bias activation theory for comparison purposes. Yield stress of the block polymer is roughly half that of the homopolymer at a given temperature. The apparent activation volume for the block polymer is double that of the homopolymer at each temperature. Activation energies at zero stress are essentially the same (60 kcal/mole for the block polymer *vs.* 70 kcal/mole for BPA polycarbonate above -50°C).

The modulus and yield kinetic parameters of the block polymer B can be related to those of the homopolymer in terms of a microcomposite model in which the silicone domains are assumed capable of bearing no shear load. Following Nielsen (10) we successfully applied the Halpin-Tsai equations to calculate the ratio of moduli for the two materials. This ratio of 2 is the same as the ratio of the apparent activation volumes. Our interpretation is that the silicone microdomains introduce shear stress concentrations on the micro scale that cause the polycarbonate block continuum to yield at a macroscopic stress that is half as large as that for the homopolymer. The fact that the activation energies are the same however indicates that aside from this geometric effect the rubber domains have little influence on the yield mechanism.

From these results and those in Figures 7a and 7b the following can be concluded about the effects of silicone block introduction: at intermediate temperatures the resistance to craze initiation is reduced by 60-70%, the resistance to shear deformation by 40-50%, and the resistance to craze fracture by about 40%. Thus both modes of plastic deformation are made easy relative to brittle failure. The origins of

these relative changes may lie in the sizes of the silicone domains (*e.g.*, 40 Å) relative to the diameters of the fibrils in the craze (*e.g.*, 100–200 Å) (12). The stress concentrations at the boundaries of the initially spheroidal silicone domains bring about easy shear flow and cavitation. However the drawing out of material into long fibrils during the maturing of the structure of the craze (12) very likely reduces the stress concentration drastically at the boundaries of the now highly oriented silicone domains. Thus the strength of the craze in the block polymer is reduced less than is the resistance to its initiation.

### *Ultimate Properties of BPF Polycarbonate and Silicone-BPF Carbonate Block Polymers (BPFC-DMS)*

**Tensile Yield Stresses of Cast Films.** At room temperature all of the BPFC-DMS polymers investigated (with one exception) reached their yield stresses before fracturing. BPF polycarbonate on the other hand is brittle, breaking at about 11,000 psi. Traces of residual chloroform make the homopolymer ductile; however the yield stress decreased linearly with chloroform content. Extrapolation of these results to a dry polymer gives a yield stress of 14,000 psi.

Each BPF polymer has a yield stress  $\sigma_y$  that decreases linearly with temperature, extrapolating to zero somewhat above the respective BPF carbonate  $T_g$ . At room temperature—far removed from the whole group of  $T_g$ 's—the effects of these differences are slight. Here the yield stress

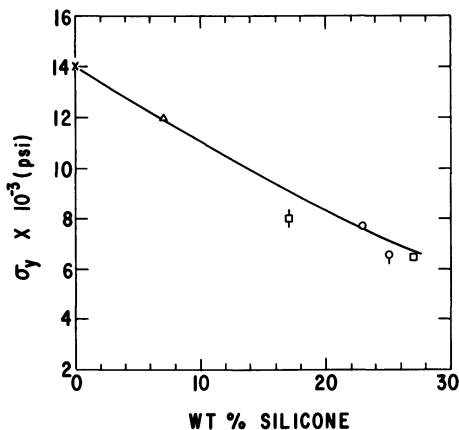


Figure 8. Dependence of yield stress on silicone content of BPF carbonate-silicone block polymers. Line is calculated from Halpin-Tsai equations for moduli of composite of rigid matrix containing soft spherical inclusions.

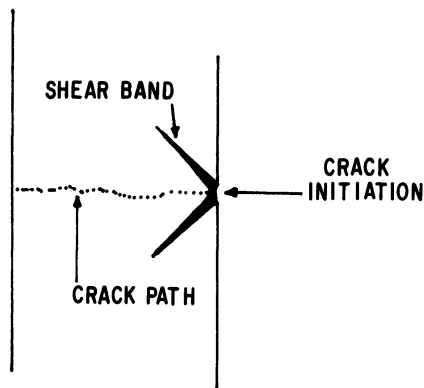


Figure 9. Failure morphology of BPF-C-DMS block polymer

depends on composition, not on block length (Figure 8). The composition dependence of yield stress is well fitted by the equation

$$\sigma_y \text{ (psi)} = 14,000 [G(c)/G(0)] \quad (1)$$

where  $G(c)/G(0)$  is the ratio of shear modulus of the block polymer to that of BPF polycarbonate calculated from the Halpin-Tsai equations.

**Failure Mechanisms.** BPF polycarbonate develops crazes at ascending stresses and fractures in a pseudo-brittle manner similar to polystyrene or PMMA. At room temperature the block polymers develop few separate crazes. As the yield is approached, shear bands grow from the edges. Fracture initiates at an edge from a point where the two shear bands initiated. When a neck forms, the plastic strain in the neck is *ca.* 80%; however fracture occurs shortly after the neck is formed so that the ultimate elongation of the specimen is only 10 or 12%. The shear bands and necks show some stress whitening (Figure 9).

**Effects of Hot Stretching on Ultimate Elongation.** Films of some of the polymers were uniaxially stretched under dead load just above their  $T_g$ 's and then were quenched. Hot stretching did not change the elongation of the BPF polycarbonate but improved the block polymers considerably. Figure 10 shows room temperature stress-strain curves after several degrees of hot stretch on one of these polymers. Hot-stretching increased the strain hardening so that the plastic strain in the neck was reduced (note decreasing size of post-yield load drop); this increased the cross-sectional area and thus decreased the true drawing stress. Also crazing and stress whitening were eliminated. These two effects counteract the rise in yield stress and engineering drawing stress so that the neck was better able to sustain load during drawing. The result was higher elongations.

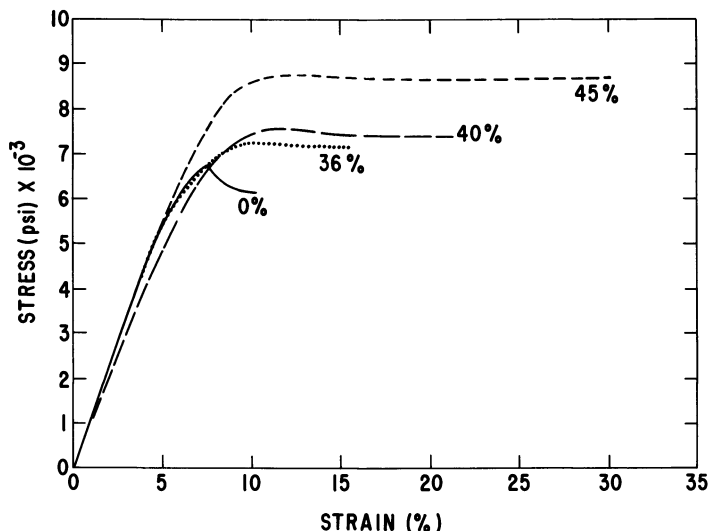


Figure 10. Effect of hot-stretching on subsequent room temperature Instron stress strain curves of one BPFC-DMS block polymer. 27% silicone of  $DP_n = 36$ .

Thus the combination of pre-orientation to suppress crazing and to reduce the natural draw ratio and rubber block introduction to bias the deformation response toward yielding has converted a brittle polymer to a moderately ductile one. Although the BPFC domain  $T_g$  has been reduced by roughly  $30^\circ\text{C}$ , the improved balance of mechanical properties makes this sacrifice worthwhile.

### Conclusions

Chronologically the implications for enhanced shear ductility in Figure 4 prodded us to convert BPF polycarbonate—a transparent but brittle and useless polymer—into a transparent, tough, and potentially useful material. The results of the efforts on both families of resins indicate a general recipe for toughening that does not compromise the transparency of plastics.

### Acknowledgments

We are grateful to C. Bersch and S. W. Kantor for many helpful suggestions.

### Literature Cited

1. Vaughn, H. A., *J. Polym. Sci., Part B* (1969) 7, 569.
2. Morgan, P. W., *Macromolecules* (1970) 3, 536.

3. Kambour, R. P., in "Block Polymers," S. L. Aggarwal, Ed., p. 263, Plenum, New York, 1970.
4. Merlon Engineering Handbook, Mobay Chemical Co., 1966.
5. Hull, D., Owen, T., *J. Polym. Sci., Polym. Phys. Ed.* (1973) **11**, 2039.
6. LeGrand, D. G., *J. Appl. Polym. Sci.* (1969) **13**, 2129.
7. Kambour, R. P., *Polymer* (1964) **5**, 143.
8. Kambour, R. P., *J. Polym. Sci., Part A-2* (1966) **4**, 349.
9. Bauwens-Crowet, C., Bauwens, J. C., Homes, G., *J. Mater. Sci.* (1972) **7**, 176.
10. Nielsen, L. E., "Morphology and the Elastic Modulus of Block Polymers and Polyblends," Report No. HPC71-144, Monsanto Res. Corp., St. Louis, Mo., Sept. 1972.
11. Tetelman, A. S., McEvily, A. J., Jr., "Fracture of Structural Materials," p. 136, Wiley, New York, 1967.
12. Kambour, R. P., *J. Polym. Sci., Part D, Rev.* (1974) **7**, 1.

RECEIVED October 18, 1974.



## Rubber Toughened Thermosets

C. K. RIEW, E. H. ROWE, and A. R. SIEBERT

B. F. Goodrich Co., Research and Development Center, Brecksville, Ohio 44141

*Epoxy resins are toughened with functionally terminated liquid polymers. Small rubbery domains of a definite size and shape are formed in situ during cure. The selectivity and reactivity of the functional groups of liquid polymers are critical for the in situ formation of rubber particles. These systems show marked increases in impact and crack resistance. Shear deformations are dominant in resins toughened with small particles ( $< 0.5 \mu\text{m}$ ). Crazeing is associated with microvoid development around the rubber particles in resins toughened with large particles ( $1\text{--}5 \mu\text{m}$ ). Maximum toughness is obtained under conditions of combined shear and craze deformations. This condition is obtainable when there is bimodal distribution of particle sizes in the rubber toughened resins. Criteria for rubber toughening of brittle resins and failure mechanisms are discussed. These criteria are based on chemical and morphological observations.*

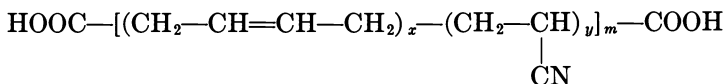
A small amount of rubber in the form of discrete particles in a glassy thermoset resin, such as epoxy resin, can greatly improve its crack resistance and impact strength. This improvement is achieved without significantly decreasing thermal or mechanical properties. McGarry with his co-workers (1, 2) and Rowe *et al.* (3), emphasized using Hycar CTBN (liquid carboxyl terminated butadiene–acrylonitrile copolymer) as a toughener for epoxy resins. They determined the effects of composition, molecular weight of the CTBN, and particle size of the rubber phase on fracture energy improvement in epoxy resin systems.

Siebert and Riew (4) described the chemistry of the *in situ* particle formation. They proposed that the composition of the particle is a mixture of linear CTBN–epoxy copolymers and crosslinked epoxy resin. The polymer morphology of the CTBN toughened epoxy systems was investigated by Rowe (5) using transmission electron microscopy by carbon replication of fracture surfaces. Riew and Smith (6) supported the

character of the discrete rubbery phase using a new osmium staining technique. Rowe and Riew (7) suggested deformation mechanisms based on morphology. They observed shear bands and/or crazes depending on the particle sizes in CTBN toughened epoxy systems. The experiments described above were confined to CTBN toughened epoxy resins. However we believe that the technology should apply to thermoplastics or other thermosets. In this paper we show how the chemistry, physics, and morphology of the CTBN toughened epoxy resins relate to the thermal-mechanical properties of these systems.

### Experimental

**Materials.** Hycar CTBN is a registered trade name of a carboxyl-terminated, liquid copolymer of butadiene and acrylonitrile (B. F. Goodrich Chemical Co.). For most purposes it can be represented structurally as:



where averaged  $x = 5$ ,  $y = 1$ , and  $m = 10$ . Cure agent D is 2-ethylhexanoic acid salt of DMP-30 (Shell Chemical Co.). DMP-30 is tris-(*N,N*-dimethylaminomethylene) phenol (Rohm and Haas). Piperidine was used as received (Fisher Scientific Co.). Epon 828 is the liquid diglycidyl ether of bisphenol-A resin (DGEBA) (Shell Chemical Co.). Bisphenol A is the trade name of 4,4'-isopropylidene diphenol. It has a melting point of 152°–153°C and a molecular weight of 228.3 (Dow Chemical Co.).

#### Procedures. PREPARATION OF CAST DOUBLE-CANTILEVER CLEAVAGE TEST SPECIMENS.

**CAST SAMPLE.** This material consisted of 100 parts DGEBA resin (Epon 828), five parts Hycar CTBN, and five parts piperidine (or DMP-30). For the following procedure we used a 15 × 25 cm tray. Proceed as follows. Place Epon 828 (285.7 g, *ca.* 0.76 mole) and the Hycar CTBN (14.3 g, *ca.* 0.04 mole) in a 500-ml beaker. Stir the mixture mechanically for at least 5 min at room temperature or at an elevated temperature. The mixture is usually turbid with normal Hycar CTBN (acrylonitrile content, 17–18%). Add piperidine (14.3 g, 0.17 mole) in one portion with stirring. Continue the stirring another 5 min. The mixture becomes clear. Pour the mixture into a Teflon-coated metal tray which has been leveled and preheated at 120°C in an oven. The mixture has a working life of at least 2 hr. Cure at 120°C for 16 hr. Cool the sample gradually to avoid warpage, and remove it from the tray. Cut into three double cantilever specimens (3.8 × 23 cm) for fracture energy test.

**HYCAR CTBN-BISPHENOL A-EPON 828 CAST SAMPLES.** A standard recipe follows: 100 parts DGEBA resins (Epon 828), 24 parts bisphenol A, five parts liquid rubber (CTBN), and five parts piperidine. It is often desirable to have a stock mixture of bisphenol A and Epon 828. Since the shelf stability of the mixture is poor at room temperature, it should be refrigerated. Melt the bisphenol A in Epon 828 with stirring

at 120°C using an oil bath for *ca.* 20 min. Use essentially the same procedure to prepare cast samples according to the preceding section.

**FRACTURE SURFACE ENERGY CALCULATION: BERRY'S METHOD (8).** The dimensions of double cantilever test specimen and techniques are illustrated in Ref. 3. We determined the surface work by substituting the measured quantities from the cleavage tests into Griffith's equation. Three cantilever bars were used.

The fracture surface work,  $\gamma$  (hJ/m<sup>2</sup>), is given by:

$$\gamma = - \frac{n}{4} \cdot \frac{F\delta}{wl}$$

where  $F$  = applied force, kgf;  $\delta$  = deflection of one cantilever, m;  $w$  = crack width, m;  $l$  = crack length, m;  $n$  = experimental constant.

**TENSILE TESTS.** After a sample has been tested for fracture energy, the cleaved bars are used for further mechanical testing. Three of the bars are cut into tensile specimens according to ASTM D-638 test methods.

**GARDNER IMPACT.** A single bar remaining from the cleavage test is used for impact resistance. We used a Gardner impact tester and determined an average weight times drop height for a dart of 1.27 cm radius.

**HEAT DISTORTION TEST.** Two remaining bars from the cleavage tests are used to determine heat distortion temperature in accordance with ASTM D-621 test methods. These thermal-mechanical tests are necessary to determine whether a brittle resin has been truly toughened or whether it has been merely flexibilized. The morphology of the resin also effectively describes a true toughening situation and can aid immeasurably in explaining departures from true toughening.

**ELECTRON MICROSCOPY.** We replicated the surfaces developed from the double cantilever cleavage test and the surface developed from the tensile test specimen. Replicas are first taken with a gelatin solution from the fracture surface (9). A typical electron micrograph of a CTBN-epoxy system is shown in Figure 1. This micrograph is from a surface of a fractured cantilever cleavage specimen. It shows a uniformly dispersed rubber phase in a brittle epoxy matrix.

## Results and Discussion

Epoxy resins toughened with reactive liquid polymers consist of a continuous rigid epoxy resin phase and a dispersed rubber phase. The rubber phase is formed *in situ* during the early stage of the cure reaction. We do not know the precise chemical composition of the particles. We propose that the particle composition is a mixture of linear copolymers of CTBN-epoxy resin and homopolymers of epoxy resin (4). The rubbery domains impart some ductility which in turn improves the toughness or crack resistance by absorbing strain energy. We have demonstrated a technique by which a two-phase thermoset system is produced to form a toughened system. Also we will describe how the toughening mechanism is related to the chemistry and morphology of these toughened epoxy resin systems.

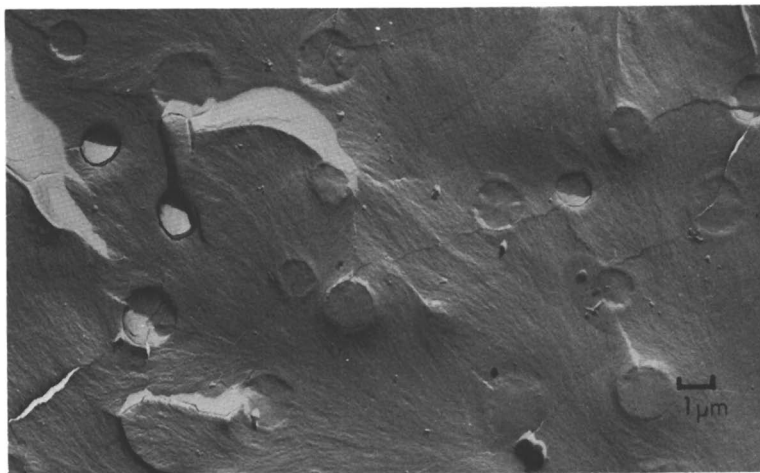
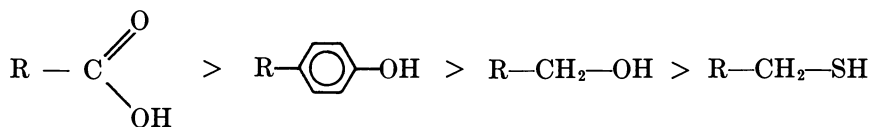
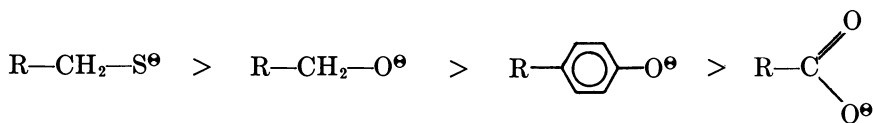


Figure 1. Typical electron micrograph of a CTBN-toughened epoxy resin ( $\times 4400$ )

**Effect of the Selectivity and Reactivity of Functional Groups.** The acidic functional end groups such as carboxylic, phenolic, hydroxylic, etc. are highly selective in forming anions with amine catalysts. The order of selectivity is (10):



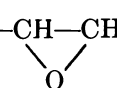
The order of reactivity of functional groups (anions) toward the epoxy group is:



The polymerization in the discrete phase is an anionic addition between the difunctional liquid rubber and the epoxy resin which gives a linear block copolymer. Thus the selectivity and reactivity of the end groups of the liquid rubber are critical.

Table I shows the fracture energies for epoxy resin which have been toughened by liquid polymers with different functional groups. Clearly the selectivity of the functional groups is more important than the reactivity. MTBN, with the most reactive mercaptan end groups, had the least improvement in fracture energy; the cured material is trans-

**Table I. Effect of Functional End Groups on Fracture Energy<sup>a</sup>**

Liquid Acrylonitrile-Butadiene Copolymer	Type of Functional End Groups	Fracture Energy, hJ/m <sup>2</sup>	Second Phase	
			Rubbery Domain	Domain Size, μm
Hycar CTBN	carboxyl; $-\text{R}-\overset{\text{O}}{\parallel}{\text{C}}-\text{OH}$	28	yes	1-5
PTBN <sup>b</sup>	phenol; $-\text{R}-\text{C}_6\text{H}_4-\text{OH}$	26-30	yes	1-5
ETBN <sup>b</sup>	epoxy; $-\text{R}-\text{CH}-\text{CH}_2$ 	18-26	yes	<1
HTBN <sup>b</sup>	hydroxyl; $-\text{R}-\text{CH}_2\text{OH}$	9-26	yes	1-5
MTBN <sup>b</sup>	mercaptan; $-\text{R}-\text{CH}_2/\text{SH}$	2-4	?	<1 × 10 <sup>-2</sup>

<sup>a</sup> Epon 828 (100 parts), liquid rubber (5 parts), and piperidine (5 parts); cured at 120°C, for 16 hr.

<sup>b</sup> These liquid polymers are experimental materials.

parent. MTBN is probably dissolved throughout the matrix. The gelation apparently proceeds under the dissolved state where MTBN reacts rapidly with epoxy resin; thus it will not precipitate. Also heat distortion temperature and other mechanical properties have been degraded. This is a system that flexibilized rather than toughened (11).

**Effect of Reactive Functional Groups.** Table II shows that maximum fracture energy is obtained from liquid polymers that contain approximately two reactive end groups. With random, reactive, end groups on the liquid copolymer (PBAN), less improvement in fracture energy is obtained. With neither reactive end groups nor random groups (Hycar 1312) there is a slight improvement in fracture energy even though *in situ* particles are present.

**Table II. Effect of Functionality and Terminal vs. Pendant Reactive Groups on Fracture Energy<sup>a</sup>**

Liquid Acrylonitrile-Butadiene Copolymer	Func-tionality	Position of -COOH		Fracture Energy hJ/m <sup>2</sup>	Rubbery Domain
		Terminal	Pendent		
None	—	—	—	1.75	no
Hycar 1312	0	no	no	3.5	yes
PBAN	>2	no	yes	7.9	yes
Hycar CTBNX	>2	yes	yes	17.5	yes
Hycar CTBN	≈2	yes	no	28.0	yes

<sup>a</sup> Epon 828 (100 parts), liquid rubber (5 parts), and piperidine (5 parts); cured at 120°C for 16 hr.

We believe that the Hycar 1312 is not cured. In these systems there exist only the van der Waals attractive and/or hydrogen bonding type forces between the epoxy matrix and the liquid rubber particles. In such two-phase systems the liquid rubber merely acts as a diluent and will show physical properties analogous to mechanical mixtures of two different polymers.

Table II shows that the chemical bonding between the epoxy matrix and the rubbery phase is important. The terminal reactive groups are more effective than the pendant groups in toughening epoxy resins.

**Effect of Molecular Structure.** Table III shows the effects of the molecular structure of the liquid polymer on the fracture energy of toughened systems. The CTIN is a carboxyl terminated isoprene-acrylonitrile copolymer; CTBS is a carboxyl terminated butadiene and styrene copolymer, and CTA is a copolymer of ethyl acrylate-butyl acrylate.

We demonstrated previously that the elastic character of the rubbery domain is an important factor (4) in toughening epoxy resins. However the moduli of these liquid polymers when cured with a stoichiometric amount of epoxy resin (Epon 828) all have similar values (2.8–4.1 MPa at 300–500% elongation).

**Table III. Effect of Molecular Structure of Liquid Polymers on Fracture Energy of Epoxy Resin<sup>a</sup>**

<i>Liquid Polymer<sup>b</sup></i>	<i>Fracture Energy hJ/m<sup>2</sup></i>	<i>Rubbery Domain</i>
CTB	8.8	(incompatible)
CTBN	28.8	yes
CTBNX	17.5	yes
CTIN	22.8	yes
CTBS	5.3	(incompatible)
CTA	22.8	yes

<sup>a</sup> Epon 828 (100 parts), liquid rubber (5 phr), and piperidine (5 phr); cured at 120°C for 16 hr.

<sup>b</sup> CT (carboxyl terminated), B (butadiene), N (acrylonitrile), X (pendant-COOH group), I (isoprene), S (styrene), A (acrylate).

The solubility of CTBN in epoxy resin increases directly with the acrylonitrile content (3). Systems toughened with CTB and CTBS have the least improvement in fracture energy. This probably arises from the poor solubility of the polymers in epoxy resin; however the solubility of CTA is very good. Although the particle sizes from acrylate polymers are rather small, the improvement in fracture energy is very good.

The initial solubility of a reactive liquid polymer in epoxy resins before cure is a critical condition not only for chemical reactions but also for the *in situ* formation of rubbery domains. A good initial solubility

**Table IV. Effect of Level of Piperidine on Mechanical Properties<sup>a</sup>**

	A	B	C	D
Epon 828, parts	100	100	100	100
CTBN, parts	0	10	10	10
Piperidine, parts	5	5	7.5	10
Second phase:				
rubbery domain	No	Yes	Yes	Yes
domain size, $\mu\text{m}$	—	1-5	1-5	1-5
Tensile strength, M Pa	65.8	58.4	54.9	54.3
Fracture energy, $\text{hJ/m}^2$	1.75	33.3	40.3	49.0
Gardner impact, J (0.635 cm thick specimen)	5.7	7.7	6.1	7.2
Heat distortion temp, $^{\circ}\text{C}$	80	74	73	66
Molar ratio; piperidine/Epon 828	0.11	0.11	0.17	0.22

<sup>a</sup> Cured at 120 $^{\circ}\text{C}$  for 16 hr.

with good reactivity results normally in a system with small rubbery domains.

**Effect of Level of Piperidine.** Infrared analyses of a system cured with piperidine show a steady increase in hydroxyl content (steps II and III in Figure 4). The hydroxyl content increases markedly after the esterification is complete. The increase in the hydroxyl content lessens at a point during the etherification (steps II and IV in Figure 4). It increases again to the final hydroxyl concentration. Gel permeation chromatographic analyses are consistent with the results of infrared analyses. Thus initial molecular weight increase is minimal during the esterification; it becomes moderate during phase separation (linear etherification) and then drastic during final gelation (crosslinking etherification).

Table IV shows test results of samples with various levels of piperidine and a constant amount of Hycar CTBN. The data on fracture energy in the table show conclusively an increase in crack resistance with increasing amounts of piperidine, but there is no corresponding increase in the Gardner impact. This system shows a rate sensitivity. The slow rate cleavage test for fracture energy improves although a fast rate impact test does not. Also there is a greater deterioration of mechanical properties when the additional piperidine is used.

The morphology of these systems with the additional piperidine indicates that more of the particles become less distinct in the matrix. The particle boundaries are less well defined, and the fracture surface of the particles becomes similar to the matrix—*i.e.*, the striations in the matrix will carry over within the particle boundaries. We believe that the additional piperidine enhances linear copolymerization to give the characteristics of flexibilization to the resin. This brings the modulus of

the matrix closer to that of the domain. The optimum concentration of piperidine seems to be five parts per hundred parts of resin by weight. At this concentration it gives a reasonable fracture energy with minimal sacrifice in other mechanical properties. The molar ratio of 1:10 for the amine to epoxy appears optimum for both DMP 30 and piperidine.

**Effect of Level of CTBN.** In Table V we varied the level of CTBN at a constant amount of piperidine. At 20 parts of CTBN we find a fourfold increase in impact strength with an 11°C loss of heat distortion temperature. This loss of thermal properties suggests that some of the CTBN flexibilizes the epoxy matrix. The morphology of these systems all shows about the same particle size. However electron micrographs of the fracture surface of the system with 20 parts CTBN show that the particles are somewhat larger and more diffuse.

**Effect of Bisphenol A Addition: Two-Particle Size Systems.** If we modify the Hycar CTBN-epoxy resin system so as to produce a two-particle size system, we can produce the toughest epoxy resins. We modified the CTBN-epoxy resin system by adding bisphenol A. A manyfold improvement in fracture energy is obtained when Hycar CTBN is used with bisphenol A and epoxy resin. The maximum improvement, when 5 phr Hycar CTBN is used, is at a bisphenol A concentration of 24 parts per hundred parts of epoxy resin. Typical data describing the properties of these systems are shown in Table VI.

We conclude from our morphology observations and the properties listed in Table VI that at low bisphenol A content the system shows the same appearance and therefore the same properties as the CTBN-epoxy system. As the bisphenol A is increased to an optimum of 24 phr, the particles decrease in size, a two-particle size population develops, and multiple failure sites appear. An example of the bisphenol A modified system is shown in Figure 2 in which the fractograph shows one family of small particles < 0.1  $\mu\text{m}$  diameter and another family of larger particles 1-5  $\mu\text{m}$  diameter. Another feature shown in this micrograph are multiple

**Table V. Mechanical Properties at Various Levels of CTBN<sup>a</sup>**

	A	B	C	D	E
Epon 828, parts	100	100	100	100	100
CTBN, parts	0	5	10	15	20
Tensile strength, MPa	65.8	62.8	58.4	51.4	47.2
Elongation at break, %	4.8	4.6	6.2	8.9	12.0
Modulus, GPa	2.8	2.5	2.3	2.1	2.2
Fracture energy, hJ/m <sup>2</sup>	1.75	26.3	33.3	47.3	33.3
Gardner impact, J	5.7	7.9	7.7	7.7	24.6
Heat distortion temp, °C	80	76	74	71	69

<sup>a</sup> Cured with 5 parts of piperidine at 120°C for 16 hr.



**Table VI. Effect of Bisphenol A Concentration on Thermal-Mechanical Properties<sup>a</sup>**

<i>Amount of Bisphenol A</i>	<i>Fracture Energy hJ/m<sup>2</sup></i>	<i>Gardner Impact, J</i>	<i>Heat Distortion Temperature, °C</i>
0	21	9	78
3.25	16	7	—
6	21	6	83
12	33	7	78
24	86	32	82
36	37	7	74
45	7	2	71

<sup>a</sup> Epon 828 (100 parts), CTBN (5 parts), piperidine (5 parts), bisphenol A (parts); cured at 120°C for 16 hr.

failure initiation sites. These multiple failure sites indicate that much more surface is created during failure. This greater surface development extends the energy absorption volume by a large amount. We believe that these features give rate insensitivity to the modified Hycar CTBN-epoxy system. The two-particle size feature of this material is shown in Figure 3 also. This is an OsO<sub>4</sub> stained microsection of the sample and shows both the large and small particles. At higher levels of bisphenol A, the particles get smaller, and the toughening properties are decreased.

The thermal-mechanical properties and toughness data on this system are described in Table VII. From the data it can be seen that in the bisphenol A modified system there is no loss in thermal (HDT) or mechanical properties. In addition there is a further improvement in

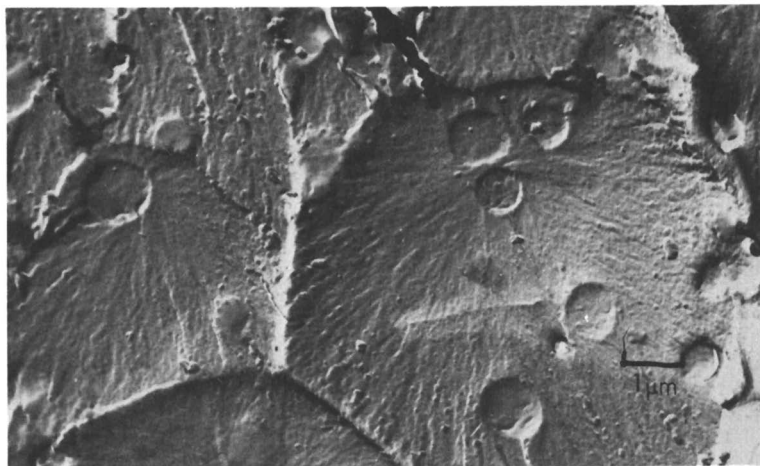


**Figure 2. Electron micrograph of a bisphenol A modified CTBN-toughened epoxy resin ( $\times 8000$ )**

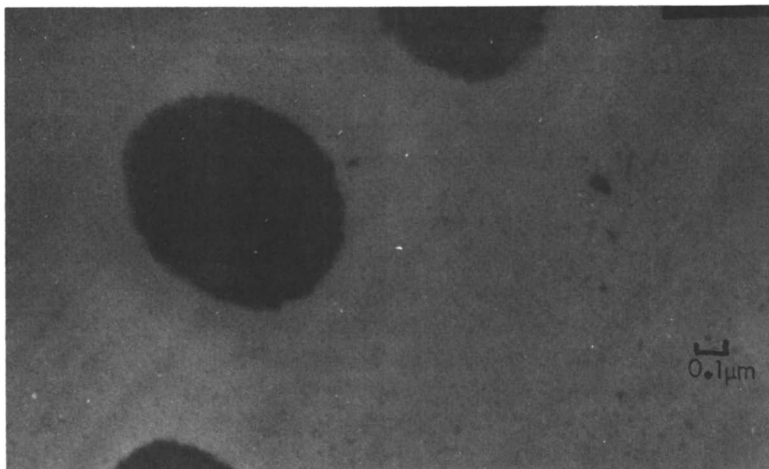


Figure 3. Electron micrograph of an  $\text{OsO}_4$  stained microsection of a bisphenol A modified CTBN-toughened epoxy resin ( $\times 34,000$ )

fracture energy and Gardner impact strength and a significant improvement in Izod impact strength. The Izod impact test is a high rate of loading test. We also show in this table high-speed tensile tests (6.35 m/sec). The new toughened system shows an increase in both tensile strength and elongation. This high speed test shows that the bisphenol A modified systems are less flaw sensitive than the unmodified epoxy resins.

**Chemistry of *in situ* Discrete Phase Formation.** We propose a reaction mechanism involving CTBN and epoxy resin in the presence of piperidine as a curing agent. We include the role of bisphenol A in this mechanism. The schematic reaction steps are summarized in Figure 4.

Table VII. Thermal-Mechanical Properties of Bisphenol A Modified CTBN-Epoxy System

		Unmodified Epoxy Resin System (Control)	Bisphenol A Modified CTBN- Epoxy System
Tensile strength MPa	} 0.12 mm/sec	65.5	64.1
Elongation at break, %		4.8	9.0
Modulus, GPa		2.8	2.7
Tensile strength, MPa	} 6.35 m/sec	73.1	95.8
Elongation at break, %		7.3	11.3
Heat distortion temp, °C		83	83
Fracture energy, $\text{kJ/m}^2$		1.75	53-88
Gardner impact <sup>a</sup> , J		6	23-34
Izod impact, J/m of notch		0.68	3.5

<sup>a</sup> Nominal 0.635 cm thick samples.

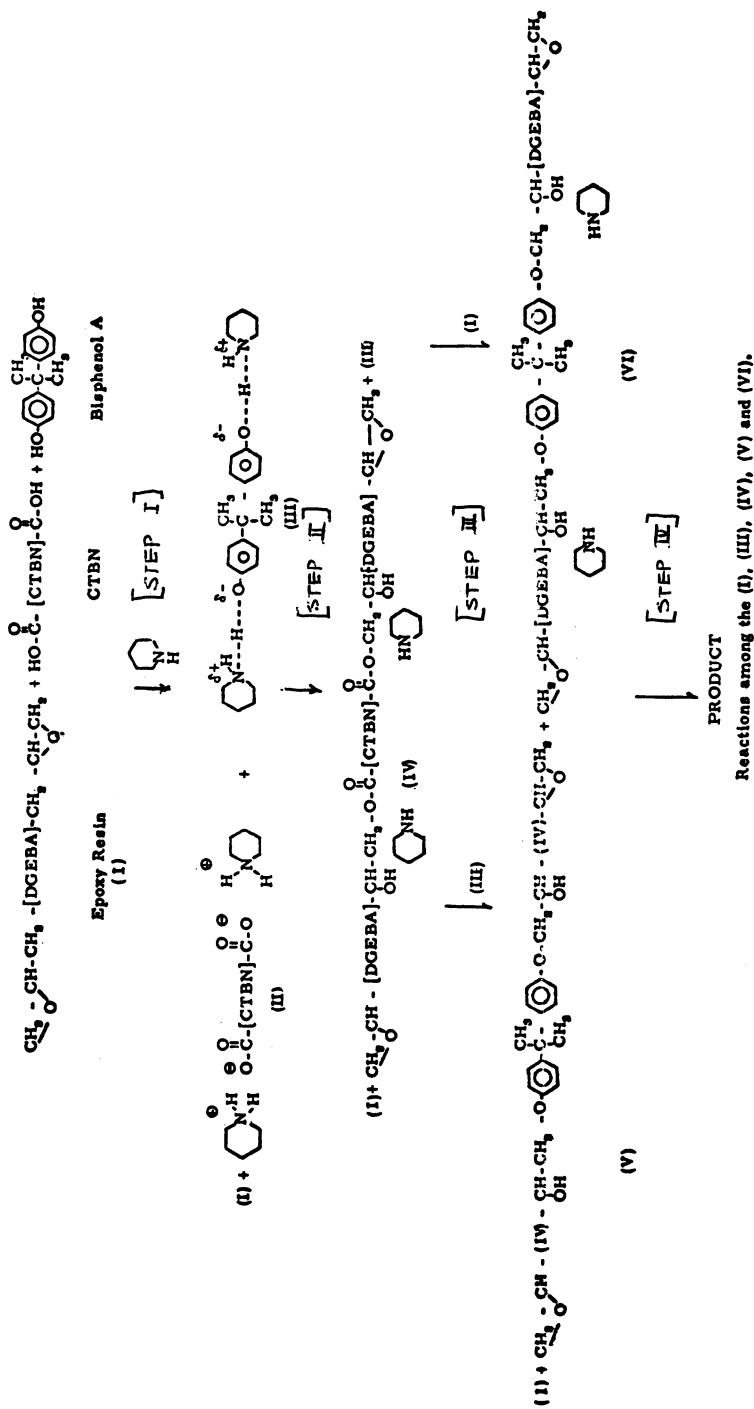


Figure 4. Schematic reaction steps in bisphenol A modified CTBN-epoxy systems

**SALT FORMATION.** In our typical formulations, the equivalent molar ratio of CTBN (Ephr; 0.054, 5 phr), bisphenol A (24 phr), and piperidine (5 phr) is about 1:70:20. According to the selectivity of the carboxylic and phenolic groups (10), all the carboxylic groups and about one-third of the phenolic groups can possibly form the salts (II) and (III) in Figure 4. Infrared spectra of the mixture showed that the salt formation of bisphenol A is not very pronounced, whereas the carbonyl band ( $1710\text{ cm}^{-1}$ ) of the carboxyl group shifted completely to  $1550\text{ cm}^{-1}$  indicating total carboxyl salt formation.

**ESTERIFICATION.** Infrared spectra showed that the carboxylate salts of CTBN form ester groups first by opening the epoxy groups. The product should be the linear chain extended product (IV), Figure 4. Consequently while the esterification proceeds, etherification by the phenoxide ions of bisphenol A may also take place to form product (VI), Figure 4. However, the more selective carboxyl groups control the reaction so that the major product is (IV) (*see* Figure 4 for the various products).

**ETHERIFICATION.** After most of the esterification is completed, *i.e.*, all the CTBN has reacted, the phenoxide ion controls the reaction. The diphenoxide ion of bisphenol A couples either compounds (IV) to form compound (V) or part of epoxy resin (I) to form compounds (VI). As the less selective phenol groups are consumed, active reaction among the epoxy groups takes place by the liberated piperidine from the piperidinium salts. This is the stage at which gelation begins. The gelation reduces the solubility of product (V). Therefore product (V) or its aggregate would precipitate first as large particles. Product (IV) or its aggregate, the least chain extended molecules, would precipitate as small particles mainly because of a greater solubility than product (V).

In the CTBN-epoxy resin system without bisphenol A we believe product (IV) type may be dissolved and distributed throughout the matrix. Because the solubility parameter difference between product (IV) and the epoxy resin matrix is less than with the bisphenol A modified epoxy resin matrix, we do not observe the second small particle size in this system.

**GELATION (COMPATIBILITY).** Phase separation occurs during the incipient gelation step but without growth in particle sizes or increase in the number of particles. The particles are formed simultaneously at an early stage of gelation.

Chemically, gelation is a process of crosslinking after the completion of esterification (*see* Figure 4). Physically, it is a process of continuously increasing the viscosity of a polymer solution with time, depending on the nature of the polymer solvent system and on the temperature. The

final result is solidification of the entire system into a three-dimensional network.

A peculiarity of a polymer solution is that under certain conditions the system does not separate into two phases. For example if we add more than 10 phr of DMP 30 in the system (100 parts Epon 828 and 5 phr CTBN), the cured product is a transparent material. This occurs when the critical solubility of a polymer can be varied by adding to the solution a small quantity of a good solvent, *e.g.*, DMP 30.

**Polymer Morphology and Failure Mechanisms.** A failed tensile bar of unmodified piperidine-cured epoxy resin shows shear deformation before tensile failure when strained slowly (0.127 cm/sec). We could not produce stable crazes in specimens of unmodified epoxy resins. At all stress levels, temperatures, and conditions of annealing only fracture occurred after shear band formation. The failure to observe crazes in unmodified epoxy resins may be explained by a fast equilibrium condition which exists between crazing on loading and recovery on unloading.

Berry (12) found a large discrepancy between observed ( $\sim 4 \times 10^5$  ergs/cm<sup>2</sup>) and calculated ( $\sim 10^3$  ergs/cm<sup>2</sup>) fracture surface energy for poly(methyl methacrylate). The calculated value was computed from the energy required to rupture the chemical bonds in unit area of cross-section, assuming perfect orientation. To explain the discrepancy of fracture surface energy he proposed an orientation hypothesis of polymer molecules. He raised the possibility that a brittle crack involved plastic flow on a molecular scale at the crack tip. To produce the extent of orientation necessary to give the interference effects, a considerable amount of energy is required to orient the molecule prior to the brittle failure.

Kambour (13) elucidated the nature of crazes and differentiated the crazes from cracks by observing optical properties of polycarbonate. He noted that a craze can bear a tensile load and heal under heat. The crazes in the glassy polymers studied to date are 40–60% void (14, 15, 16). In essence the crazing was seen as a process of polymer rarefaction involving the conversion of strain energy to surface free energy. He also suggested that craze is different from cold drawing which appears to involve elongation by shearing at 45° to the tensile stress with no change in material density.

An electron micrograph of a fracture surface of a CTBN-toughened epoxy resin is shown in Figure 5. This CTBN is particular in that the *in situ* formed particles are less than 0.5  $\mu$ m in diameter. A tensile bar of this system also shows shear deformation which indicate that the small particles have not interfered with the shear deformation characteristic of the unmodified resin. The deformation bands are nearly parallel to the planes of maximum shear stress—*i.e.*, roughly at 45° to the principal

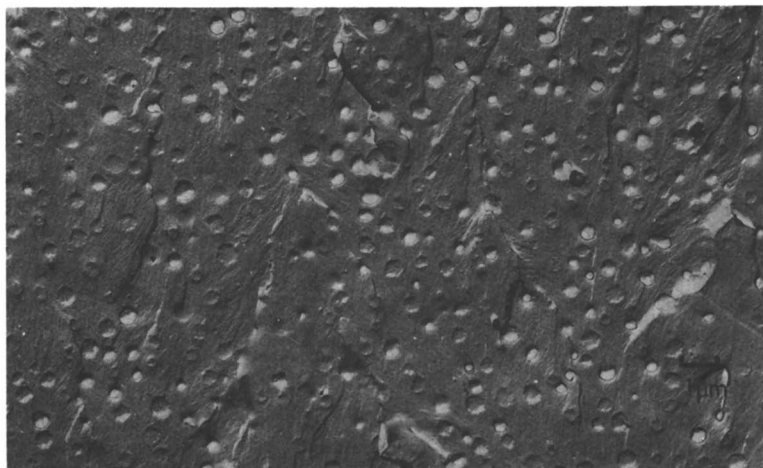


*Figure 5. Electron micrograph of a CTBN-toughened epoxy resin with small particles ( $\times 4400$ )*

axis of deformation. Once a deformation band forms and attains a certain width, it grows only in length. According to the electron micrograph, the deformation is a true uniform plastic shear without any sign of fracture.

The morphology of a small particle size, toughened system has been further explored by examining the fracture surfaces of the stressed tensile bars. An electron photomicrograph of a replica of this surface showed a deformation band extending diagonally (Figure 6). The rubber par-

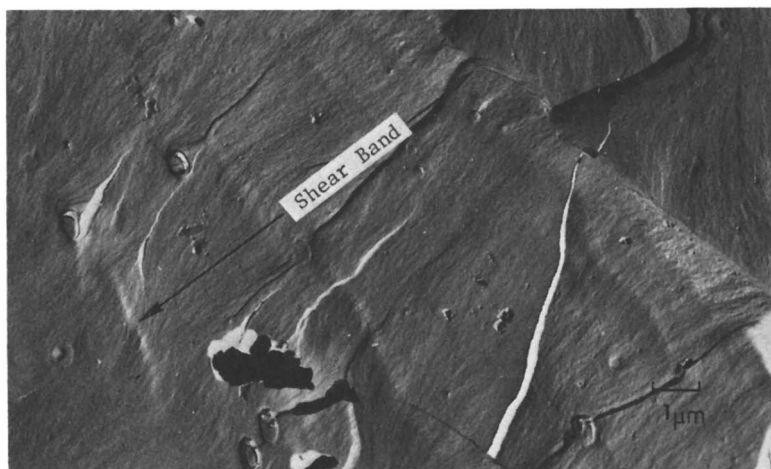


*Figure 6. Electron micrograph of a CTBN-toughened epoxy resin with small particles—fracture through a shear band ( $\times 5200$ )*

ticles within this band are distorted in the direction of the shear deformation. The band widths are generally 5–50  $\mu\text{m}$ .

However if we examine a tensile bar made from a toughened system containing large particles, we find that the material deformation arises entirely from crazing. A failed tensile bar of this system has no shear deformation or necking throughout the length of the sample. Crazing during stress is observed as whitening in the strained section of the sample. There is also a corresponding increase in the sample volume. Shear deformation does not produce whitening, and there is no increase in sample volume. The crazes occur in a direction perpendicular to the principal tensile stress axis. Both the shear bands and crazes disappear when the sample is heated above the glass transition temperature.

We observed in crazed tensile samples that particles are elongated in the direction of the tensile stress field and show what appears to be a microvoid associated with each of the large particles (Figure 7). We did not observe the fibrous crazes reported elsewhere (14, 15, 16) for the thermoplastics.

Bucknall and Smith (17) concluded that crazing is the dominant mechanism to toughen high impact polystyrene and related polymers. One important function of the rubber particles is to serve as craze initiators and stabilizers in the glassy matrix. However Newman and Strella (18) concluded from optical microscope studies that cold drawing is responsible for toughness in ABS.

The question arises as to whether our observed phenomenon which we call "microvoids" is truly a microvoid associated with the particles or

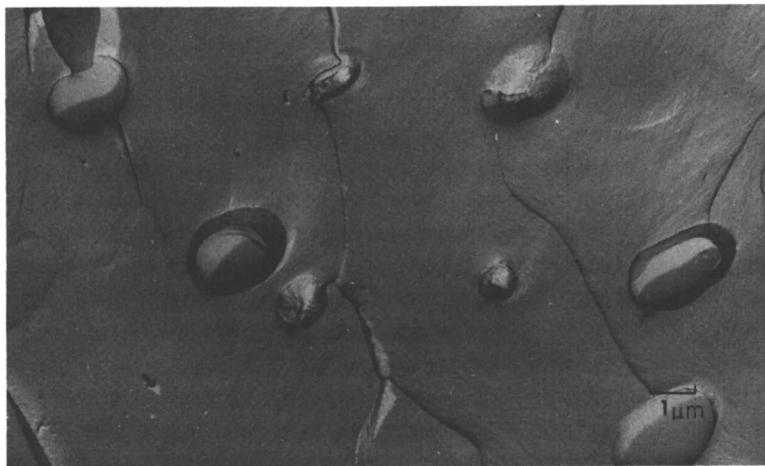


Figure 7. Electron micrograph of a CTBN-toughened epoxy resin with large particles—fracture through a craze volume ( $\times 5200$ )

an artifact produced by the fracture surface development process. We offer three reasons for proposing actual microvoids. First, the phenomenon is not observed in normal rapid cleavage surface development. Second, the craze lines extend only to the void surface and do not terminate (initiate) at the particle (Figure 7). Third, we found that a crazed tensile specimen that shows whitening (and volume increase) will shrink to its original size, and the whitening will disappear when heated above the HDT of the sample. The morphology of this heated sample showed that the microvoid evidence disappeared. Additional evidence was obtained by an  $\text{OsO}_4$  stained microsection of the stressed and heat-treated material. The particles (stained) are of the same size as in the original unstressed sample.

Next we looked at the microvoid situation in a bisphenol A modified CTBN–epoxy system. This sample had the highest toughening properties that we developed in the epoxy system because of a two-particle size rubber population that uniquely gives a combination of shear deformation and tensile crazing. Only some of the large particles had microvoid development. Consequently the whitening was much less than when only crazing occurs. The multiple failure sites were still evident.

Recently McGarry (19) suggested that toughness may be enhanced by the interaction of crazes and shear bands in a system with a bidistribution of particle sizes. He (20) later showed the effect of rubber particle size on deformation mechanisms in CTBN toughened epoxy system—a shear mechanism is enhanced by the presence of particles a few hundred Angstroms in diameter; whereas crazing appears as the predominant flow mechanism under tensile stress with larger particles (1.5–5  $\mu\text{m}$  diameter). Bucknall *et al.* (21, 22) supported McGarry's observations for shear bands and crazes in rubber modified polyphenylene oxide. He found that HIPS/PPO blends deformed by a combination of crazing and shear band formation; whereas the HIPS deformed almost entirely by crazing. The results in Table VII show conclusively that there is a synergistic benefit gained in the two-particle size system in toughened properties. This benefit arises from the dual energy-absorbing mechanisms of combined shear deformation and crazing.

### **Conclusions**

We conclude that: (a) Shear deformations are dominant in resins toughened with small rubbery particles. (b) Crazing associated with polymer whitening and microvoid development is dominant in resins toughened with large particles. (c) Maximum toughening is obtained under conditions of combined shear and craze deformations. This condition is obtainable when both large and small particles are present.



(d) Conditions of maximum toughening also show multiple failure sites in fractured surfaces. These sites allow for a greatly increased surface development, and (e) from the present study and our previous findings a toughened system must meet the following criteria:

**Chemical Criteria.** (a) The liquid polymer should have at least two functional end-groups. (b) The functional group must have a selectivity to form a salt with an amine cure agent. Also it should have a reactivity which enables it to undergo initial linear chain extension with a difunctional epoxy resin. The selectivity and reactivity of the functional group are necessary to form chemical bonds between the rubbery particles and the epoxy matrix. (c) The liquid polymers should have some degree of solubility in the epoxy resin without phase separation or agglomeration before gelation.

**Morphological Criteria.** It must show a second particulate rubbery phase. The second phase must have a definite size and shape and the domains must be dispersed throughout the matrix.

**Thermal-Mechanical Criteria.** The thermal and mechanical properties must not be degraded. The toughness properties (crack and impact resistance) must be improved, and the system should be rather insensitive to the rate of loading (or temperature) of a given test.

### *Acknowledgments*

The authors thank the B. F. Goodrich Co. for permission to publish this paper.

### *Literature Cited*

1. McGarry, F. J., Willner, A. M., "Toughening of an Epoxy Resins by an Elastomeric Second Phase," *Res. Rept. R68-8*, School of Engineering, Massachusetts Institute of Technology, Cambridge, Mass. (1968).
2. Sultan, J. N., McGarry, F. J., "Microstructural Characteristics of Toughened Thermoset Polymers," *Ibid.* R69-59 (1969).
3. Rowe, E. H., Siebert, A. R., Drake, R. S., *Mod. Plast.* (1970) 417, 110.
4. Siebert, A. R., Riew, C. K., "The Chemistry of Rubber Toughened Epoxy Resins I," *161st National Meetg., ACS, Org. Coatings Plast. Div.* (March 1971).
5. Rowe, E. H., "Fractography of Thermoset Resins Toughened with Hycar CTBN," *26th Ann. Tech. Conf., Reinforced Plast. Composites Inst., SPI, Section 2-D* (1971).
6. Riew, C. K., Smith, R. W., *J. Polym. Sci., Part A-1* (1971) 9, 2737.
7. Rowe, E. H., Riew, C. K., "What Failure Mechanisms Tell about Toughened Epoxy Resins," *Plast. Eng.* (March 1975) 45-47.
8. Berry, J. P., "Determination of Fracture Surface Energy by a Cleavage Technique," American Physical Society Meeting, Baltimore, Md. (April 1962).
9. Andrews, E. H., Walsh, A., *Nature* (1957) 179, 729.

10. Riew, C. K., Rowe, E. H., Siebert, A. R., Lipiec, J. M., "ABE Thermosets for Structural Plastics," *27th Ann. Tech. Conf., Reinforced Plast. Composites Inst., SPI*, Section 2-D (1972).
11. Siebert, A. R., Rowe, E. H., Riew, C. K., Lipiec, J. M., "Toughness vs. Flexibility in Epoxy Resins," *28th Ann. Tech. Conf., Reinforced Plast. Composites Inst., SPI*, Section 1-A (1973).
12. Berry, J. P., *Nature* (1960) 185, 91.
13. Kambour, R. P., *Nature* (1962) 195, 1299.
14. Kambour, R. P., *Polymer* (1964) 5, 143.
15. Kambour, R. P., *J. Polym. Sci., Part A* (1964) 2, 4159.
16. Kambour, R. P., *Polym. Eng. Sci.* (1968) 8, 281.
17. Bucknall, C. B., Smith, R. R., *Polymer* (1965) 6, 437.
18. Newman, S., Strella, S., *J. Appl. Polym. Sci.* (1965) 9, 2297.
19. McGarry, F. J., *Proc. Roy. Soc., A* (1970) 319, 59.
20. Sultan, J. N., McGarry, F. J., *Polym. Eng. Sci.* (1973) 13, 29.
21. Bucknall, C. B., Clayton, D., Keast, W. E., *J. Mater. Sci.* (1972) 7, 1443.
22. *Ibid.* (1973) 8, 514.

RECEIVED October 18, 1974.

## Motionless Mixer Blending of Styrene/ Acrylonitrile Copolymer and Nitrile Rubber to Form ABS

NICK R. SCHOTT and DILIP DHABALIA

Department of Plastics Technology, University of Lowell, Lowell, Mass. 01854

*An SAN resin in pellet form and a nitrile rubber powder were melt blended in a single screw extruder and a two port motionless mixer to produce an ABS type resin. The compounded extrudate was compression molded and formed into samples for mechanical testing. Both impact and tensile properties were measured to characterize the degree of mixing. It was found that the impact and tensile strength of the physical blend fell within the range of values reported for ABS terpolymer resins. A toughness index defined as the area under the tensile stress-strain curve indicated that the energy required to break a sample could be correlated with the rubber content, the degree of mixing in the motionless mixer, and the number of mixing elements.*

**M**ixing and compounding of plastic resins and additives such as plasticizers, fillers, colorants, and reinforcements form an important part of plastics processing. Few, if any resins are used in their original unmodified state as they are manufactured during polymerization. The base resins are modified by additives to give either improved physical and chemical properties or a dilution of the resin by the addition of extenders that reduce the overall cost. Polymer systems are difficult to mix because the materials are very viscous and thus require a high power input per unit mass to achieve the desired degree of homogeneity. Two types of mixing are possible: simple and dispersive (1). The main objective of any simple mixing is to alter and to randomize the original spatial distribution of a component. The non-random, segregated particles are redistributed into a more random state without reduction of size of individual particles. Dispersive mixing, on the other hand, aims

at reducing the particle size in addition to randomizing the distribution of components. This action increases the probability of finding a particle of any one component at any particular point. An acceptable spatial probability distribution is achieved when the sample appears uniform at a specified scale of examination (2).

This study (3) was done to produce an ABS type resin by dry and melt blending SAN and a nitrile rubber in a motionless mixer. In polyblends of two semicompatible polymers, the particle size of the dispersed phase is an important factor concerning final properties, particularly if a rubber is dispersed to improve impact strength. Motionless mixers should give precise control over the final particle size since for laminar flow the number of fluid layers and the striation thickness can be predicted mathematically. The hypothesis that the impact strength should peak out at a precise number of mixing elements was thus investigated.

### Experimental

**Mixers.** Two-port motionless mixers similar to the one reported by Chen and Fan (4) were used in this study. These mixing devices consist of right- and left-hand helices which are inserted into a tubular housing (5). The leading and trailing edges of two adjoining helices are welded together perpendicularly. A total of six right- and left-hand helices were welded into a 2.0 inch diameter stainless steel pipe for the dry blending mixer. Each helix had a 1.5:1 L/D ratio, and the total length of the mixer was 20.5 inches. A stream of solid particles flowing through the tube is split into two streams and twisted clockwise by the first helix. At the entrance to the second helix each split stream is split again and mixed with the split from the other stream. Simultaneously the mixed streams are twisted counterclockwise in this helix. This behavior is repeated for each two helices in the mixer housing. A similar mixer for melt blending was attached to a Brabender  $\frac{3}{4}$ -inch 24:1 L/D extruder just before the die as shown in Figure 1. This mixer had a  $\frac{3}{4}$ -inch diameter housing into which 0, 4, 6, or 10 elements could be placed. When a polymer melt passes through the mixer, the fixed geometric design produces unique flow patterns of flow division and radial mixing simultaneously. At the leading edge of each element the flow divides and follows the semicircular channel created by the element shape. At each succeeding element intersection the two flows are further divided to give an exponential growth of flow division. The number of layers formed is given as:

$$S = 2^n \quad (1)$$

where  $S$  is the number of striations produced, and  $n$  is the number of elements in the unit. For laminar mixing the degree of mixedness is related to the striation thickness. The smaller the striation thickness, the more interfacial area between the mixture components and hence the better the mixing. The striation thickness,  $d$ , is defined as:

$$d = D/2^n \quad (2)$$

where  $D$  is the inside diameter of the mixer housing.

**Resin.** A styrene/acrylonitrile (SAN) copolymer, Tyril 870, manufactured by the Dow Chemical Co. was used. The resin came as  $\frac{1}{8}$ -inch pellets and had a reported tensile strength of 9500 psi and an Izod impact strength of 0.35 ft-lb/inch of notch.

**Rubber.** Hycar 1442  $\times$  110 manufactured by B. F. Goodrich Co. was used. Properties reported by the company include: specific gravity 1.0 to 3.0, tensile strength 3000–4000 psi, and a maximum service temperature of 250°–300°F. The rubber came as a powder and was sifted in Tyler screens; only the largest (20–40 mesh) particles were blended with the styrene/acrylonitrile.

**Mixing and Sample Molding.** Blends of 10, 20, and 30% rubber were made by subjecting the two components to the processing scheme of Figure 1. The extrudate emerged from the melt blending as a strand which was pelletized. The material was dried overnight at 150°F and then compression molded. A sheet 6"  $\times$  6"  $\times$   $\frac{1}{8}$ " was formed. Molding conditions were as follows: 2 min preheat at 350°F with low pressure and 4 min at 350°F with 3000 psi. Cooling was done at room temperature and low pressure for 3 min in a second press.

## Results

**Impact and Tensile Testing.** A number of mechanical tests were carried out on test bars cut from the molded sheets. For the impact tests six sample bars were cut for each mixing and composition condition while for the tensile tests four test specimens were prepared. The reported results are average values as determined from that number of test bars. The tensile tests were run at a crosshead speed of 0.2 inch/min. Table I lists the results for the impact and tensile tests of the dry blended mate-

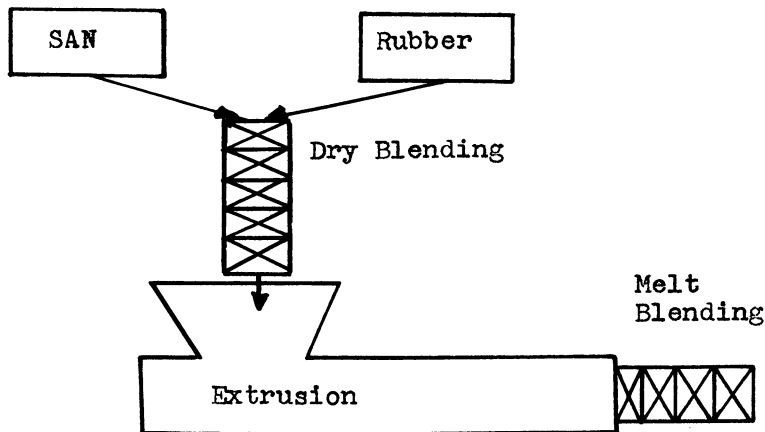


Figure 1. Schematic for dry and melt blending of SAN and rubber

**Table I. Dry Blend Properties**

<i>Percent Rubber</i>	<i>Izod Impact Strength, ft-lb/inch of Notch</i>	<i>Tensile Strength, psi</i>
0	.35 <sup>a</sup>	9500 <sup>a</sup>
10	.70	5440
20	.99	3350
30	1.74	1990

<sup>a</sup> Values from company literature.

rial in which the 1/8-inch SAN pellets were mixed with the 20-mesh (0.0328-inch) rubber powder. As expected, the impact strength increased with rubber content while the tensile strength decreased. The results represent property values for a simple mixing case. That is, in the dry blending operation the particle size is not reduced, and hence the SAN to rubber particle size is approximately 0.125/0.0328, or 3.8 to 1 on a diameter basis. Table II lists the same properties after the components had been melt blended in the extruder and 10 mixing elements. Again note the trends in decreased tensile strength and increased impact strength. In addition, no significant improvement in either the impact strength or the tensile strength was observed although the particle size of the minor component is markedly different from the previous case.

**Table II. Melt Blend Properties (10 Elements)**

<i>Percent Rubber</i>	<i>Izod Impact Strength, ft-lb/inch of Notch</i>	<i>Tensile Strength, psi</i>
0	.35 <sup>a</sup>	9500 <sup>a</sup>
10	.85	4450
20	1.12	5340
30	1.60	2920

<sup>a</sup> Values from company literature.

**Toughness Index Correlation.** The above observation suggested that a toughness index, defined as the area under the tensile test curve, may correlate directly with the number of mixing elements (implying degree of mixing and ultimate particle size) and the rubber content. The significance of this index can be visualized as the amount of energy that is stored in the material in a deformation process prior to failure. Table III

**Table III. Toughness Index**

<i>Percent Rubber</i>	<i>Four Elements</i>	<i>Six Elements</i>	<i>10 Elements</i>
10	33.0	30.0	27.0
20	40.5	47.4	46.0
30	28.5	30.0	36.85

shows the toughness index for the blends as a function of rubber composition and the number of mixing elements. A 20% rubber content gave the best toughness index. Also, more mixing elements are required as the rubber content is increased to produce the maximum toughness index for a given rubber content. For the 10% rubber a toughness index of 33 is obtained with four elements, for 20% rubber it takes six elements to obtain an index of 47.4, and for the 30% rubber it takes 10 elements to obtain an index of 36.9.

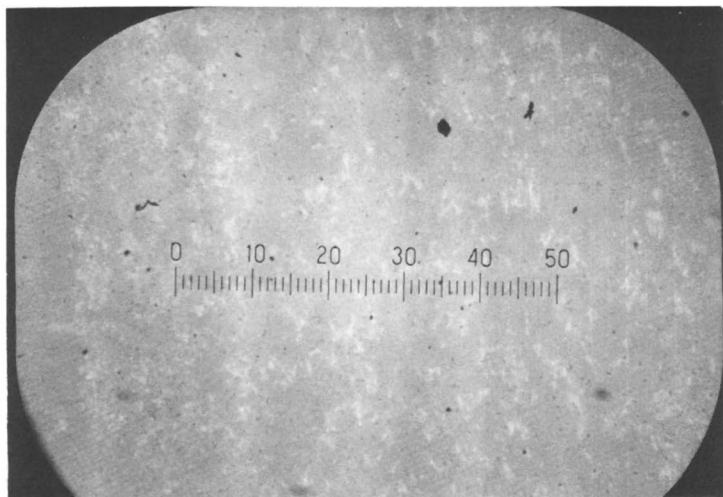
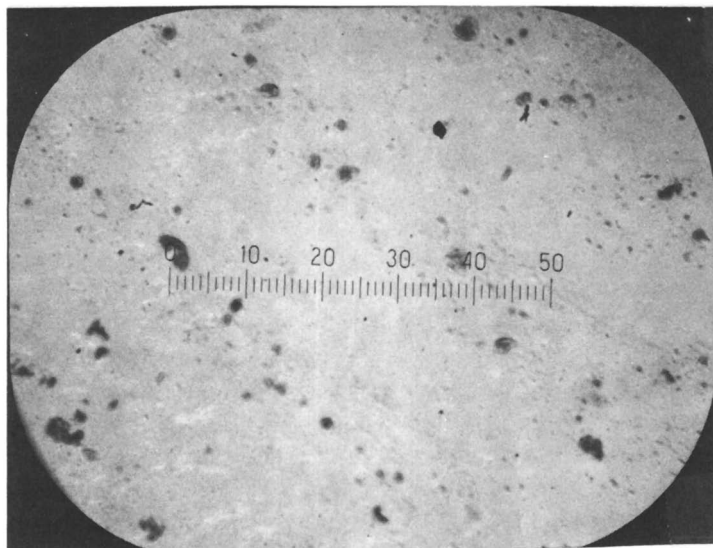
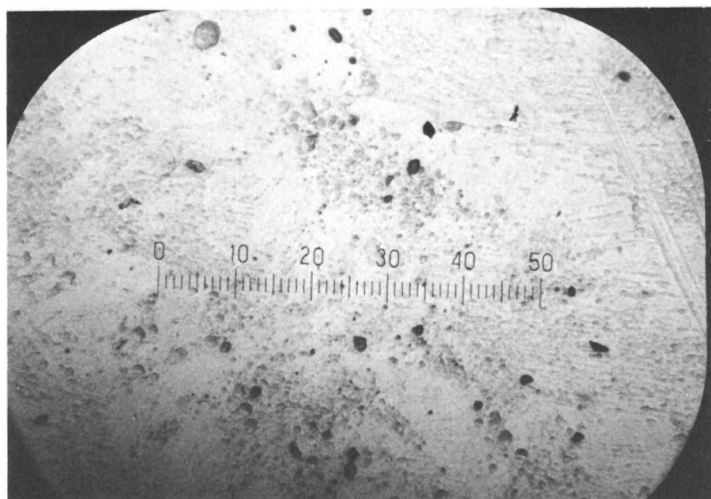


Figure 2. Microstructure of 10% rubber-90% SAN (75 $\times$  magnification, four elements)

**Striation Thickness and Ultimate Particle Size.** Striation thickness can be used to infer the particle size reduction as the components are melt blended. A certain amount of dispersion takes place in the extrusion process, but this is constant in all cases (assuming constant extrusion conditions). The extruder has by far the higher shear rates (100  $\text{sec}^{-1}$  or greater), and most of the particle size reduction occurs in the extruder. However, the motionless mixer radially homogenizes the melt from the extruder which has been subjected to a non-uniform shear field. Also an additional degree of dispersive mixing is imparted as the melt passes through the motionless mixer. The ultimate particle size calculated according to Equation 2 is 0.0468, 0.0117, and 0.00073 inches for four, six, and 10 elements. Microscopic examination was done in the material extruded and passed through four mixing elements. A magnification of 75 $\times$  was used. Figures 2, 3, and 4 show typical microstructures. No large rubber particles remain for the 10 percent rubber content. Rubber is the dark phase. In all cases most of the rubber has been effectively



**Figure 3.** *Microstructure of 20% rubber-80% SAN (75 $\times$  magnification, four elements)*



**Figure 4.** *Microstructure of 30% rubber-70% SAN (75 $\times$  magnification, four elements)*



dispersed (if one takes the relative areas of dark rubber and light SAN resin into account). For the 20 and 30% rubber-content sample a certain number of large rubber particles remain; this result agrees with the observation that the ultimate toughness index for those conditions required more mixing elements. It is estimated that the width of the field is approximately 0.0007 inch at this magnification which leads to a corresponding largest particle size of 0.0003 inch (for Figure 4) and an estimated average particle size of  $10^{-5}$  inch. Thus, the ultimate particle size for the optimum toughness index falls below  $10^{-5}$  inch.

### *Conclusions and Recommendations*

The impact strength values of ABS as reported in the literature (6) vary from 1 to 10 ft-lb/inch of notch for extrusion grade material. The experimentally determined average impact strength for the material formulated by physical melt blending was 1.5 ft-lb/inch of notch. The calculated average tensile strength of the same material is 5000 psi which falls between the values of 4000 and 7000 psi reported for the extrusion grade. The physical melt blend of the SAN and nitrile rubber had properties which fall within the reported range of values for the copolymerized material. A toughness index which represents energy stored in a sample during deformation correlated with both the rubber content and the degree of mixing. The impact strength and the tensile strength are independent of the particle size range under consideration in this investigation while the toughness index depended on the ultimate particle size. The optimum toughness index is obtained at 20% rubber content. For a constant rubber content the toughness index varied with the degree of mixing (number of mixing elements). The degree of mixing must be increased with increasing rubber content. It is estimated that the ultimate particle size of the dispersed rubber phase is less than  $10^{-5}$  inch. It is recommended that further work concerning the ultimate particle size and particle size distribution in the physical blend be carried out to obtain the optimum impact and tensile properties by means of the proper degree of melt mixing.

### *Acknowledgment*

The authors gratefully acknowledge the loan of the mixing devices from the Kenics Corp., Danvers, Mass.

### *Literature Cited*

1. Ho, F. C., Kwong, A., *Chem. Eng.* (July 23, 1973) 80, 94.
2. Bernhardt, E. C., Ed., "Processing of Thermoplastic Materials," p. 135, Reinhold, New York, 1959.

3. Dhabalia, D., Masters Thesis, University of Lowell, Lowell, Mass. (May 1974).
4. Chen, S. J., Fan, L. T., *J. Food Sci.* (1971) **36**, 688.
5. *Kenics Corp. Bulletin*, Kenics Corp., One Southside Road, Danvers, Mass. 01923.
6. "Modern Plastics Encyclopedia," plastics properties chart (1970).

RECEIVED October 18, 1974.

## Crack Propagation Resistance of Random Fiber Composites

S. K. GAGGAR and L. J. BROUTMAN

Department of Metallurgical and Materials Engineering  
Illinois Institute of Technology, Chicago, Ill. 60616

*The random arrangement of glass fibers in resin matrices produces composite materials which have planar isotropy and are of great importance to many structural and engineering applications. Random fiber composites offer a good combination of mechanical properties and are extensively used in various industries. This study deals with the characterization of strength and fracture behavior of random glass fiber reinforced polyester composites. The concepts of linear elastic fracture mechanics (LEFM) have been applied to these composites to obtain meaningful toughness parameters. Substantial slow crack growth occurs prior to unstable fracture and the total fracture behavior of the material should be studied by applying the concepts of crack growth resistance curves (R-curves).*

The incorporation of brittle glass fibers into brittle resins results in composite materials stronger and tougher than its constituent materials. The random arrangement of glass fibers in resin matrices produces composite materials which have planar isotropy and are very important to many structural and engineering applications. Random fiber composites offer a good combination of mechanical properties and are used extensively in industry. The properties of aligned discontinuous fiber composites have been studied to some extent but only a limited amount of information exists on the fundamental properties of random fiber composites. After the work of Wu (1), a number of papers have been published in recent years dealing with the application of linear elastic fracture mechanics (LEFM) to predict fracture properties of composites. Wu considered the case of a unidirectional glass reinforced

epoxy resin with a crack parallel to the direction of the fibers and reported that the critical stress intensity factor,  $K_{Ic}$ , did not vary significantly with the crack length. Konish *et al.* (2) studied a wide variety of composites and concluded that the failure mechanism of the specimens tested was crack dominated in most cases and the procedures of linear elastic fracture mechanics (LEFM) could be applied even where the overt failure mechanism was not so obviously dominated by the starter crack. Recently, Owen and Bishop (3) have carried out fracture toughness tests on a polyester resin containing various forms of glass reinforcement. The  $K_{Ic}$  values in most cases were not independent of crack size, but a method similar to the plastic zone correction in metals can be used to obtain  $K_{Ic}$  values independent of the crack length. Ellis and Harris (4) studied the effect of specimen size and other test variables on the fracture properties of some fiber reinforced epoxy resins. The work of fracture values depended on the dimensions of the test specimen, crack length, and type of fracture test. Beaumont and Phillips (5) investigated random glass fiber polyester composites with respect to application of LEFM and the effect of strain rate, crack length, and test method on fracture properties. The stress intensity factor did not vary significantly with the crack length when the specimens were fractured in a three-point bending mode. More recently, Mandell *et al.* (6) have shown that the candidate stress intensity factor ( $K_{Ic}$ ) is almost completely insensitive to the thickness of the specimen for the roving mat type of composites. In the present study, the principles of LEFM and the concept of crack growth resistance ( $R$ -curves) have been applied to a random fiber polyester composite to characterize the fracture behavior.

### Experimental

A polyester resin P-43 (Rohm and Haas) was selected as a matrix material. The glass fiber reinforcement was in the form of a chopped strand mat (M 700) weighing  $1\frac{1}{2}$  oz/sq ft bonded together with a high solubility polyester resin. The chopped fibers were about 2 in. long and the fiber diameter was about 0.0004 in.

In order to produce test specimens, 10 in.  $\times$  5 in. composite plates were first molded. The volume fraction of fibers was varied by varying the number of glass fiber mat layers or by varying the thickness of the final composite plate. Benzoyl peroxide (1.5 wt %) was used as a curing agent. The curing agent was dissolved in styrene (10 wt %) and the resulting solution was added to polyester resin (100 wt %). The cast mixture thus prepared was poured over the fiber mat layers which were placed in a mold. The mold was then placed in a vacuum chamber for about 1 hr to drive off the air bubbles entrapped in the material during the mixing and pouring process. The resin impregnated mat layers were then transferred to a larger mold (10 in.  $\times$  10 in.) which was placed on

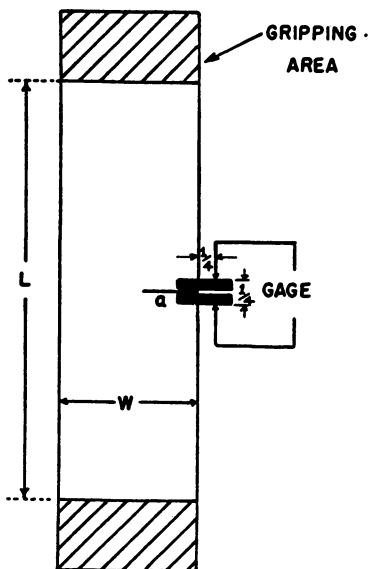


Figure 1. SEN test specimen

a hot plate (150°F). Burlap strips were placed around the mat layers and the resin was slowly squeezed out using a flat knife. The squeezing process was continued until there were no visible air bubbles in the resin which was removed. The mold was transferred to a compression press and a top plate was placed on the mold. The curing cycle required 2 hr at 220°F.

The composite plates thus prepared were quite clear and transparent at low volume fractions ( $v_f < 25\%$ ). At higher fiber volume fractions the plates became translucent because of the close packing of fibers and larger interface surface area.

Flexure and tension tests were conducted on an Instron testing machine at a crosshead speed of 0.05 in./min. Single edge notch (SEN) fracture tests were conducted at a crosshead speed of 0.1 in./min. Figure 1 shows the SEN specimen configuration. The width and thickness of the specimen are 1 in. and 0.090 in., respectively. The notches were machined on a milling machine using a jeweler's saw (6 mil) which produced a square notch as shown in Figure 1. Two small strips ( $\frac{1}{8}$ -in. square pieces cut from a unidirectional glass fiber composite plate) were bonded to the specimen using Eastman 910 adhesive on both sides of the crack as shown in Figure 1. These strips were bonded to the specimen to accommodate a strain gage extensometer to monitor the crack mouth opening displacement during the fracture test. An Instron transverse strain sensor (G 57-12) was used to monitor the crack mouth displacement. The strain sensor is quite sensitive and displacement values up to  $1 \times 10^{-4}$  in. could easily be measured from the chart recorder. The load displacement records were analyzed in accordance with the procedure recommended in Method ASTM E 399-71 (7). The candidate stress intensity factor  $K_Q$  was calculated using the following K-equation (8).

$$K_Q = Y \frac{P_Q a^{1/2}}{tw} \quad (1)$$

where  $t$  is the thickness of test specimen

$Y$  is a calibration factor

$P_Q$  is the load as obtained from load displacement records

$a$  is the initial crack length

$w$  is the width of the specimen.

### Results

The flexural and tensile properties of polyester composites at various fiber volume fractions are listed in Table I. Strength values increase up to a fiber volume fraction of about 40% but then decrease with increased fiber volume fraction. This is caused by the poor wetting and extensive fiber damage which occurs at higher volume fractions because of compaction and close packing of the fibers. The ultimate flexural strain shows a similar trend. The modulus values increase almost linearly with fiber volume fraction.

**Table I. Tensile and Flexural Properties of Polyester Composite (9)**

$v_f$	Flexural Properties			Tensile Properties		
	Strength, psi	Modulus, $\times 10^6$ psi	Strain, %	Strength, psi	Modulus, $\times 10^6$ psi	Strain, %
0	13,000	0.6	2.4	6,000	0.6	0.9
20	30,000	1.5	2.75	14,500	1.33	1.75
30	38,000	1.95	2.85	19,000	1.75	1.90
40	50,000	2.40	2.60	27,000	2.06	1.84
50	40,000	2.85	1.75	24,000	2.4	1.96

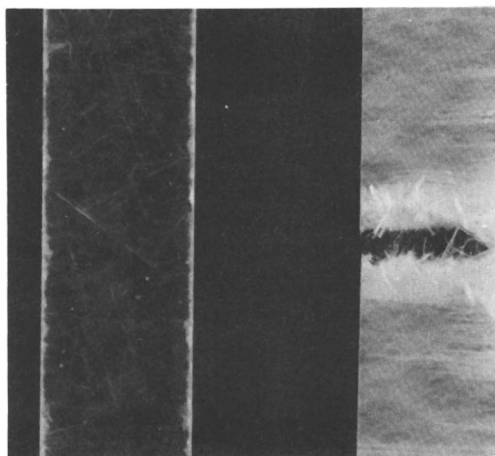


**Figure 2. Tensile specimen before and after failure**

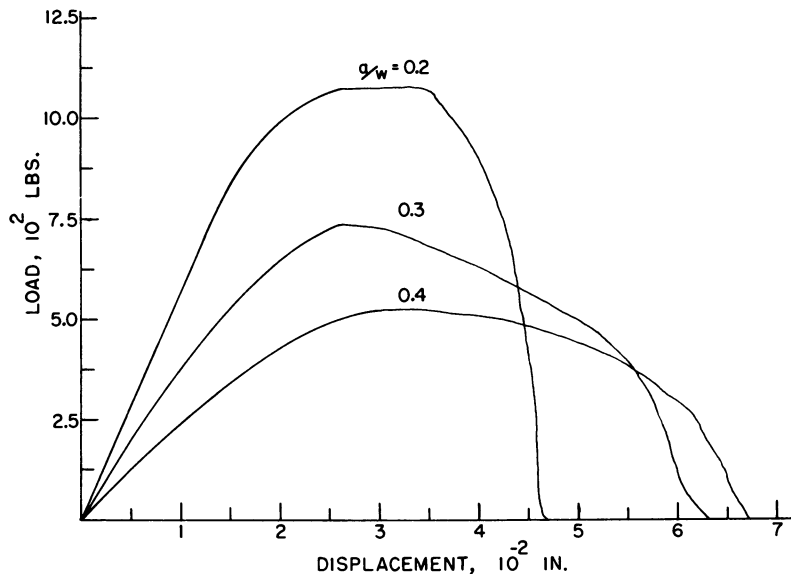


Figure 3. Load displacement curves at various crack lengths

Massive debonding of the fibers occurred prior to catastrophic failure of the test specimen. Figure 2 shows a tensile specimen before and after failure. The initially transparent specimen becomes translucent when loaded in tension. Some transverse cracks begin to appear on the surface of the specimen at about 30–40% of the failure load values. The density of these cracks increased as the load on the specimen was increased. Owen and Duke (10) reported that the debonding in polyester composites started as early as 30% of maximum load. Thus, the debonding in these materials starts occurring along the transverse fibers and then spreads to fibers which are at progressively smaller angles to the load direction. The onset of debonding can thus be considered to be the crack initiation mode in these materials.

**Fracture Results.** The polyester resin specimen (SEN) fails in a brittle manner. The average value of candidate stress intensity factor for polyester resin as calculated from Equation 1 is 1.97 ksi-in.<sup>1/2</sup>. The load displacement records for the composite ( $\nu_t \approx 0.29$ ) at various crack lengths are shown in Figure 3 and the  $K_Q$  values as a function of crack length are shown in Figure 4. A minimum of four specimens were tested at each crack length. The results indicate that the  $K_Q$  values increase as the initial crack is increased. The method of determination of load  $P_Q$  from the load displacement record is recommended for crack length to width ratios greater than 0.45, and thus the load  $P_Q$  obtained at smaller crack lengths may be somewhat erroneous. In other words, the value of

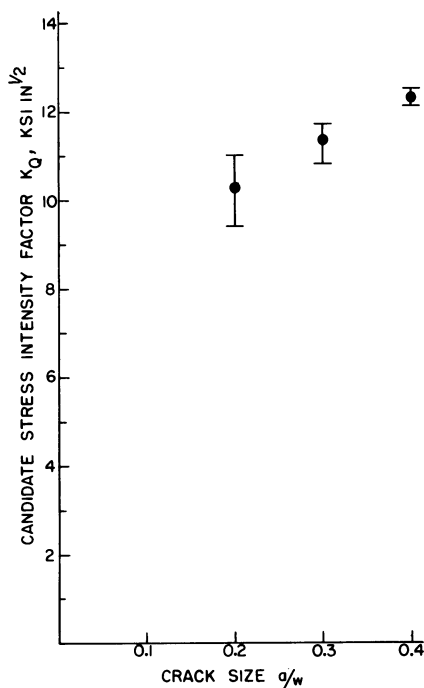


Figure 4. Variation of  $K_Q$  with crack size

$P_Q$  obtained at smaller crack lengths may not correspond to the same crack growth stage as for large crack lengths. At smaller crack lengths, the constraint at the crack tip is more severe and thus the material undergoes less deformation or less debonding takes place at the crack tip. This results in smaller values of material resistance to crack propagation.

Table II lists the  $K_Q$  values,  $K_I$  values based on maximum load and initial crack length, and  $K_R$  values based on maximum load and instantaneous crack length at that load.  $K_R$  values are much higher than  $K_Q$  and  $K_I$  values. This indicates that the crack growth resistance of the material increases as the crack extension occurs in the material. The instantaneous crack lengths were obtained using the following procedure.

A compliance crack detection curve as shown in Figure 5 was first constructed using the load displacement records obtained from the fracture tests. This compliance is based on the crack mouth opening displacement and is thus not to be confused with the compliance of the

Table II. Various Stress Intensity Factors for Polyester Composite

$a/w$	Average $K_Q$ , ksi-in. <sup>1/2</sup>	Average $K_I$ , ksi-in. <sup>1/2</sup>	Average $K_R$ , ksi-in. <sup>1/2</sup>
0.2	10.3	11.80	16.85
0.3	11.3	13.05	16.70
0.4	12.2	14.05	—



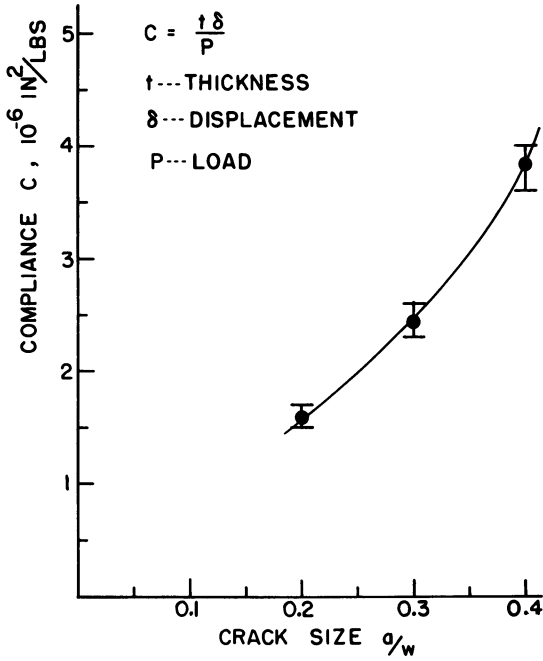


Figure 5. Compliance vs. crack size

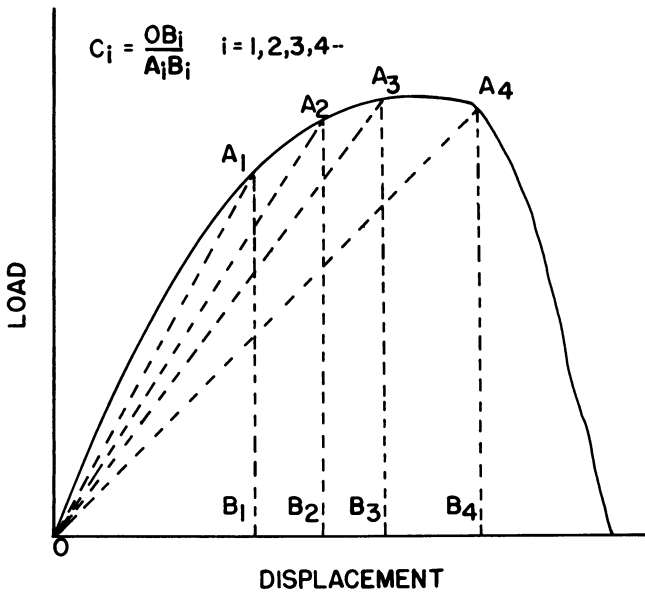


Figure 6. Compliance determination at various stages of fracture process

specimen. Initial straight line portions of the load displacement record at various initial notch lengths were used to calculate the compliance and these compliance values at various notch lengths were plotted to get the crack detection curve shown in Figure 5. If, during a crack propagation test, the compliance at any load value is measured, then the crack length corresponding to that load can be determined from Figure 5.

From the results presented in Table II, the resistance of the material increases as crack growth occurs in the material. It is thus necessary to calculate the material resistance values as a function of crack length if the fracture behavior of the material is to be fully characterized. This type of approach known as the R-curve approach has been used to study the fracture behavior of many metallic materials. The R-curve concept has been completely reviewed (11).

A load displacement record obtained from the fracture test can be used to develop the R-curve for the material. The procedure used for establishing the R-curve for the material is described below.

(1) A straight line is drawn from the origin to a point on the load displacement record as shown in Figure 6. The compliance is the reciprocal of the slope of this line.

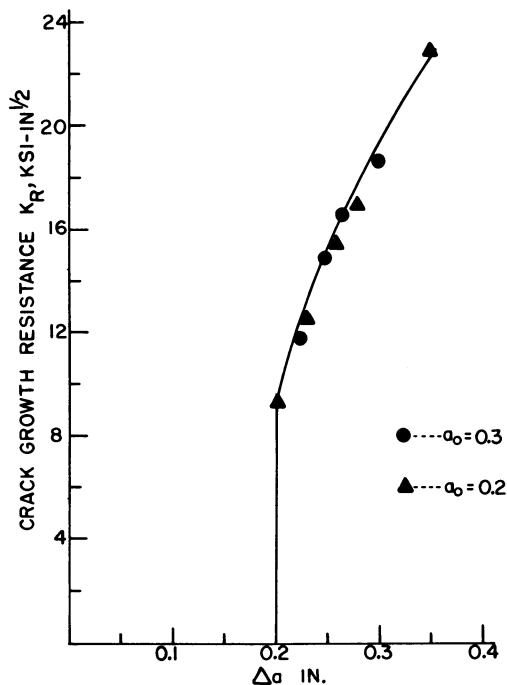


Figure 7. Crack growth resistance curve of two initial crack lengths

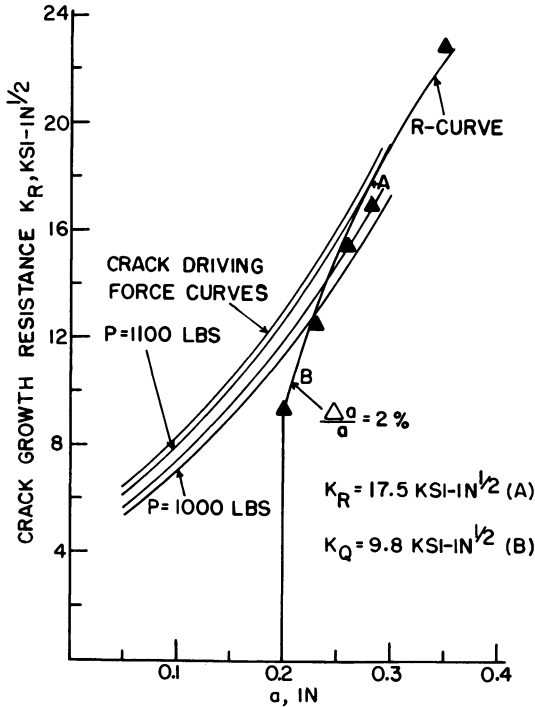
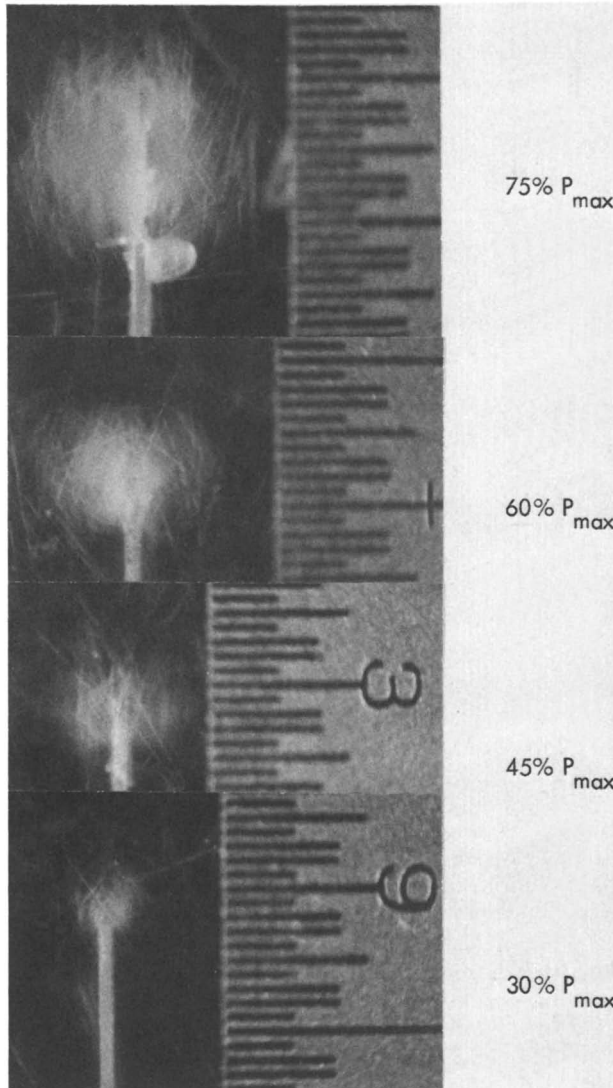


Figure 8. Determination of crack instability point from R-curve

(2) From the compliance *vs.* crack length curve (Figure 5) the instantaneous crack length (*a*) is obtained. The instantaneous crack length minus the initial crack length (*a* - *a*<sub>0</sub>) corresponding to the point on the load displacement curve is then the amount of crack extension ( $\Delta a$ ).

(3) The stress intensity factor  $K_R$  is calculated using this load and the corresponding crack length. This procedure is followed for a number of points on the load displacement record.

Figure 7 shows the R-curve for the polyester resin composite. The data points for two initial crack lengths are quite close to each other, indicating that the R-curve for the materials is independent of initial crack length. The R-curve shown in Figure 7 can be used to predict the crack instability point and the  $K_Q$  values as shown in Figure 8. Crack driving force curves have been plotted at various load values using the *K*-equation, *i.e.*,  $K = Y(Pa^{1/2}/tw)$ . The point of instability is defined as the point where the crack driving force is equal to resistance of the material. The point of tangency between the R-curve and crack driving force curve thus determines the point of instability. From Figure 8, the material resistance at the point of instability is about 17.5 ksi in.<sup>1/2</sup>. To



*Figure 9. Development of the debonded zone at the crack tip (each small division is 0.01 in.)*

calculate the candidate stress intensity factor, a crack extension of 2% has been used by Jones and Brown (12) for some metallic materials. For many metallic materials, the determination of load  $P_Q$  from the load displacement records using the method described in ASTM E 399-71 corresponds to a crack extension of about 2%. Using the R-curve approach, the  $K_Q$  value obtained from the polyester composite from the

**Table III. Predicted and Experimentally Observed Debonded Zone Sizes (13)**

Applied Load, % of Max Load	Stress Intensity Factor, $\text{ksi-in.}^{1/2}$	Debonding Stress, $\sigma_D$ psi	Observed Debonded Zone Size, in.	Predicted Zone Size, in.	
				Plane Strain	Plane Stress
30	1.95	3300	0.020	0.0186	0.054
45	2.92	3300	0.039	0.0416	0.12
60	3.90	3300	0.067	0.0745	0.225
75	4.88	3300	0.083	0.116	0.348

International Journal of Fracture Mechanics

R-curve is about  $9.8 \text{ ksi-in.}^{1/2}$ , in good agreement with the average value of  $K_Q$  (at  $a/w = 0.2$ ) obtained earlier. The  $K_Q$  value obtained from the R-curve is smaller than the  $K_Q$  values at larger crack lengths, indicating that the load  $P_Q$  determined from the load displacement records for  $K_Q$  calculations at higher crack lengths probably corresponded to larger crack extensions. This is possible because a large amount of slow crack growth in the form of debonding occurs near the crack tip before unstable fracture in these composites.

Figure 9 shows the debonding at the crack tip at various fractions of maximum applied load in a three point notch bend test. The debonding at the crack tip starts at loads less than 30% of maximum load. The size of the damage zone can be predicted using a fracture mechanics approach. Table III lists the comparison of measured damage zone size to the theoretically predicted values. The correlation between experimen-

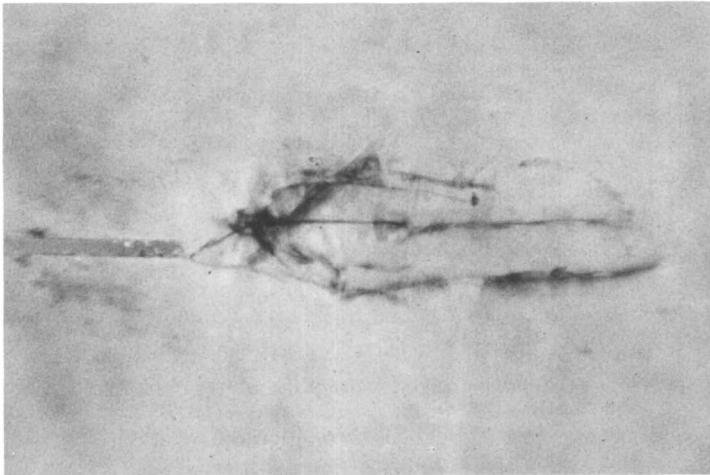


Figure 10. Transverse cracks at crack tip (75% of maximum fracture load)

tally measured and predicted values is quite good up to 60% of the maximum load values. At 75% of the maximum load, a crack has initiated from the notch and thus the debonded zone size cannot increase behind the crack tip. This results in poor correlation of measured and predicted values for debonded zone size.

Figure 10 shows the notch tip zone in a SEN test specimen loaded to about 75% of maximum load. The transverse cracks are easily seen in this photograph. These cracks even occur at some distance away from the notch plane and the final fracture plane. These micrographs indicate that considerable damage occurs in the polyester composites prior to unstable fracture. It is thus important that the R-curve concept should be applied to these materials if their total fracture behavior is to be characterized.

### Conclusion

Linear elastic fracture mechanics (LEFM) approach can be used to characterize the fracture behavior of random fiber composites. The methods of LEFM should be used with utmost care for obtaining meaningful fracture parameters. The analysis of load displacement records as recommended in method ASTM E 399-71 may be subject to some errors caused by the massive debonding that occurs prior to catastrophic failure of these composites. By using the R-curve concept, the fracture behavior of these materials can be more accurately characterized. The K-equations developed for isotropic materials can be used to calculate stress intensity factor for these materials.

### Literature Cited

1. Wu, E. M., #8, "Composite Materials Workshop," p. 20, Technomic Publishing Co., Inc., New York, 1968.
2. Konish, M. J., Swedlow, J. L., Cruse, T. A., *J. Comp. Mat.* (1972) **6**, 114.
3. Owen, M. J., Bishop, P. T., *J. Comp. Mat.* (1973) **7**, 146.
4. Ellis, C. D., Harris, B. H., *J. Comp. Mat.* (1973) **7**, 76.
5. Beaumont, P. W. R., Phillips, D. C., *J. Mater. Sci.* (1972) **7**, 682.
6. Mandell, J. F., McGary, F. J., Kashihare, R., Bishop, W. R., "Engineering Aspects of Fracture Toughness: Fiber Reinforced Laminates," 29th Annual Technical Conf., SPE (1974) 17-D.
7. ASTM E 299-71, Standard Method of Test for Plane-Strain Fracture Toughness of Metallic Materials.
8. Brown, W. F., Srawley, J. E., ASTM STP 410, ASTM Philadelphia, 1966.
9. Gaggar, S. K., Ph.D. Thesis, Illinois Institute of Technology, Chicago.
10. Owen, M. J., Dukes, R., *J. Strain Analysis* (1967) **2**, 4.
11. Heyer, R. H., Fracture Toughness Evaluation by R-Curve Methods, ASTM STP 527, ASTM Philadelphia, 1973.
12. Jones, M. H., Brown, W. F., ASTM STP 463, ASTM Philadelphia, 1970.
13. Gaggar, S. K., Broutman, L. J., *Inter. J. Fracture Mech.*, Dec. 1974.

RECEIVED October 18, 1974.

## Retarded Necking in Continuous Nylon-Fiber Reinforced Polypropylene

M. R. KANTZ and R. D. CORNELIUSSEN

Department of Materials Engineering, Drexel University,  
Philadelphia, Pa. 19104

*The tensile properties of isotactic polypropylene materials reinforced with continuous nylon fibers were measured. Less than 10 vol % of the fibers leads to an increased yield strength and yield elongation. As little as 3 vol % of the nylon fibers increased the elongation at necking from 10 to 20%. This retarded necking arises from the fiber-matrix debonding which delocalizes the microscopic yielding processes.*

**R**einforcement of metallic and polymeric materials with high modulus fibers and particles generally leads to reduced tensile elongation or ductility. According to Nielsen (1) the reduction in the ultimate elongation of the composite varies systematically with the volume fraction of reinforcing particles,  $V_r$ , for particulate reinforced materials in which the adhesion between the two phases is "perfect." This relationship is given as:

$$\frac{\epsilon_c}{\epsilon_m} = (1 - V_r^{1/3}) \quad (1)$$

where  $\epsilon_c$  and  $\epsilon_m$  are the ultimate elongations of the composite and matrix. The validity of this model has been demonstrated for certain glass-bead reinforced thermoplastic and thermosetting resins (2, 3, 4). It has been reported (2), however, that increasing the adhesion between glass beads and an epoxy matrix using a coupling agent gave higher values of  $\epsilon_c$  than predicted by Nielsen (1). In recent work involving glass-bead filled amorphous thermoplastics such as polystyrene, styrene/acrylonitrile copolymers, and polyphenylene oxide, the elongation of the composite was greater than the elongation of the matrix when the tensile test was carried

out above the brittle-ductile transition temperature (3, 4). This behavior was attributed to debonding, craze nucleation, and subsequent termination of craze propagation by notch blunting at weak phase boundaries (4).

During our study of the tensile behavior of isotactic polypropylene containing low volume fractions ( $< 10\%$ ) of continuous thermoplastic fibers we found that the composite yield strength ( $\sigma_c$ ), yield elongation ( $\epsilon_{c,y}$ ), and toughness vary strongly with volume fraction while the elastic modulus remains essentially constant (5, 6). As in the work cited above for glass-filled systems, the observation of increased rather than decreased elongation at yield was entirely unexpected. This paper examines the basis for increased yield elongation behavior in this crystalline polymer composite system.

### *Experimental*

Polypropylene (PP) composites containing monofilament nylon were prepared by compression molding at  $230^\circ\text{C}$  under a pressure of 1200 psi. The fibers were wound tightly onto a picture frame mold using a lathe and then were sandwiched between premolded 0.010–0.030 in. thick polypropylene 5520 (PP) sheets (Shell). Composites containing continuous glass fibers (glass tow, PPG Industries) were prepared by hand layup between the premolded polymer sheets and compression molded as above.

Following a minimum aging period of 48 hr, specimens were cut so that the fibers were parallel to the long or tensile axis. Conventional 1.5-inch dogbone tensile specimens (1 inch gage length) were tested at 0.2 inch/min on an Instron testing machine.

Specimens sufficiently thin (0.002–0.010 inch) for detailed observation of deformation by optical microscopy were prepared by simply repressing the tensile specimens. The thin specimens were strained manually on the microscope stage using a Siemens x-ray diffraction fiber holder.

### *Results*

The dependence of  $\epsilon_{c,y}/\epsilon_{m,y}$  on fiber volume fraction for the PP-nylon system is linear as shown in Figure 1. A least-squares fit of these data gives the relationship,

$$\frac{\epsilon_{c,y}}{\epsilon_{m,y}} = 1 + 36.4V_f \quad (2)$$

Thus, reinforcement of polypropylene with as little as 3 vol % of nylon fibers increases the elongation at which necking and stress whitening occur from 10% for the unreinforced matrix to 20% for the composite. We call this phenomenon "retarded necking."



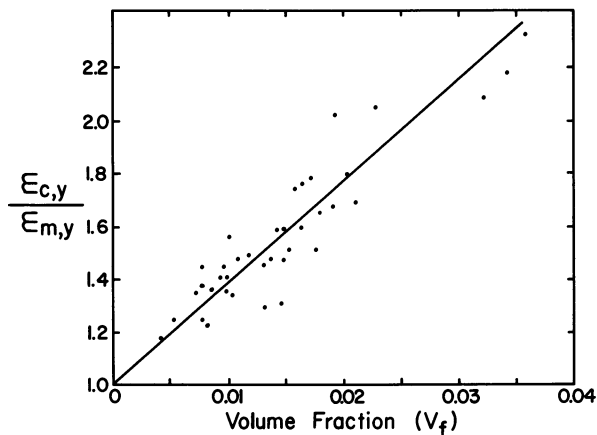


Figure 1. Normalized elongation behavior of PP-nylon composites as a function of fiber volume fraction

In contrast to the retarded yielding behavior exhibited by the PP-nylon system, the PP-glass fiber system undergoes the expected reduction in composite yield elongation. Figure 2 shows that the data for the PP-glass fiber system follow a modified Nielsen prediction as follows:

$$\frac{\epsilon_{c,y}}{\epsilon_{m,y}} = (1 - 1.5V_f^{1/3}) \quad (3)$$

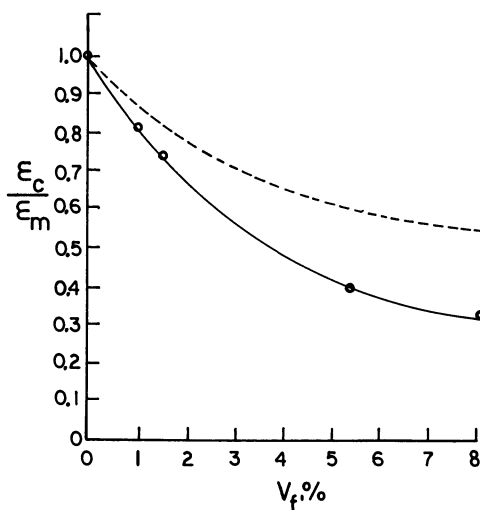
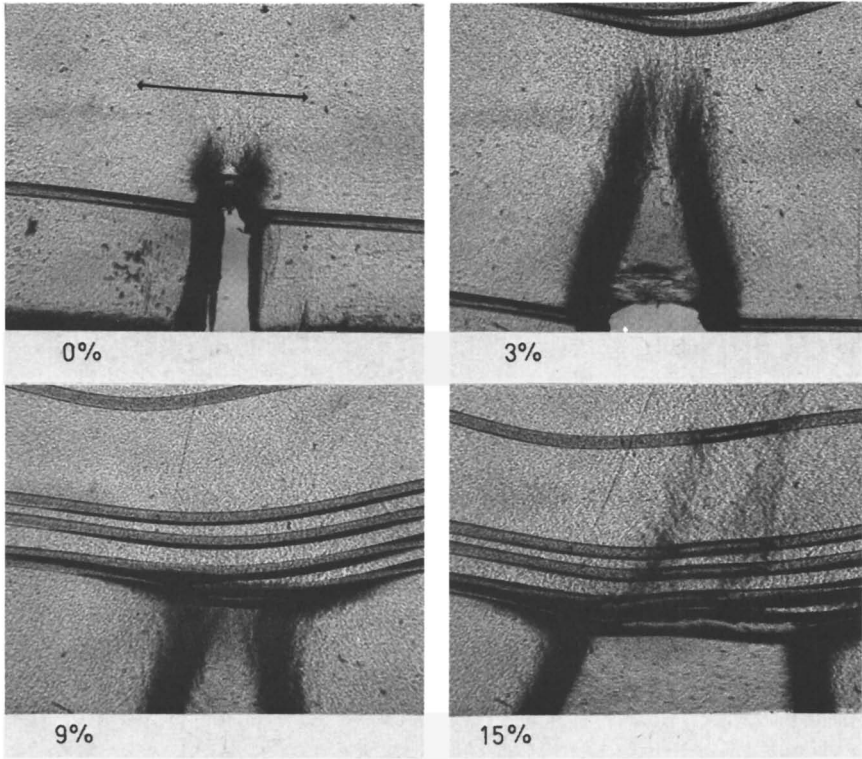
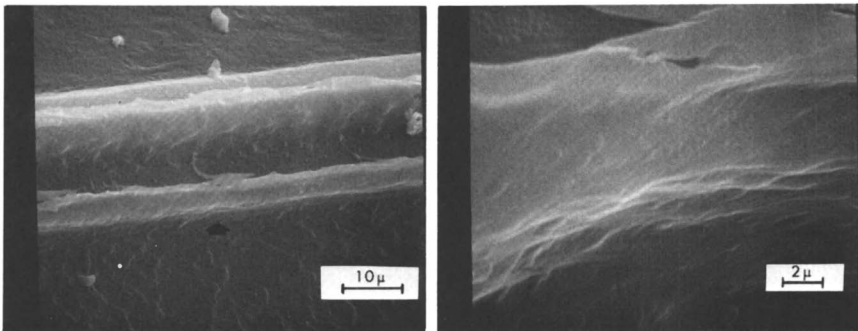


Figure 2. Normalized elongation behavior of PP-glass composites as a function of fiber volume fraction. Dashed curve represents the Nielsen prediction.



**Figure 3.** Uniaxial deformation behavior of a thin film PP-nylon composite. See text for the description of the sequence.



**Figure 4.** Scanning electron micrographs illustrating drawing of the spherulites in the matrix-fiber interface. The arrow in the left micrograph shows the location of the more detailed fibrillar features shown in the right micrograph.

Optical microscopy during uniaxial stretching of PP-nylon and PP-glass thin film composites revealed for the former system that debonding occurs at elongations as low as 2%, followed by drawing of the spherulites at the interface. No debonding occurs for the latter system. The glass simply fractures, and the diameter of the void channel left by the glass fiber is less than the diameter of the fiber itself. This indicates that the radial stress at the interface was compressive. On the other hand, debonding in the PP-nylon composite suggests a reversed Poisson effect —*i.e.*, the radial stress was tensile. For PP, the Poisson's ratio is 0.33 *vs.* 0.23 for glass. The photomicrographs in Figure 3 illustrate the following steps in the retarded yielding process in the PP-nylon composite system:

(a) Unstrained specimen showing slight prestress at the notch root (black lobes caused by internal reflection from cavitation voids). The specimen was notched to localize necking.

(b) Neck propagation after 3% elongation. Debonding of the fibers is shown at the top of the micrograph.

(c) Deflection of the yield front in the axial direction at the interface following 9% elongation.

(d) Fiber rupture at 15% elongation.

The appearance of the interfacial zone shown in the bottom two micrographs suggests that the debonded portion of matrix adjacent to unbroken fibers should be fibrillar to reflect the cold drawing of the PP spherulites at the interface. This is indeed the case as illustrated by the scanning electron micrographs in Figure 4. These micrographs were obtained from the shoulder of the neck in an Instron tensile specimen that was ground, polished, and subsequently etched in a  $\text{CrO}_3\text{-H}_2\text{SO}_4$  glassware cleaning solution for 72 hr at 70°C. Etching was done to remove the fibers and to enhance the details of the crystalline morphology of the matrix. The lower third of the left micrograph shows the base of a fiber channel and a portion of one of the "walls" (circled) of the channel. The right micrograph shows the fibrillar or cold drawn morphology of the circled portion of wall shown in left photo in greater detail.

### Discussion

The results shown in Figures 3 and 4 illustrate that the retarded necking phenomenon, just as the increased ultimate elongations observed by Nicolais *et al.* (4), arises from matrix-fiber debonding with the consequent formation of a third phase. Just as the weak interface causes lateral spreading or blunting of a crack during the operation of the Cook-Gordon mechanism, the debonded regions in the PP-nylon system cause progressive local yielding to occur parallel to the tensile axis for some macroscopic strain increment rather than transverse to the axis as

would ordinarily be expected. The microyielding in the axial rather than transverse direction permits more homogeneous distribution and dissipation of local strain energy throughout a larger volume of the specimen gage length than would be observed for the matrix alone. Thus, the onset of necking instability is retarded by strain demagnification (delocalization) where energy dissipation is achieved by drawing of the crystalline matrix in the debonded region. The extent of local strain demagnification is reflected by the experimental result given by Equation 2. The direct dependence of  $\epsilon_{c,y}/\epsilon_{m,y}$  on the volume fraction of fibers is understandable on the basis that the larger the available surface area present as sites for interface separation, the more homogeneous the microyielding process. There must be a limit to the extent of retarded yielding; however, this is assumed to be the ultimate elongation of the nylon fibers which is 20–22%. In the case of the PP–glass system, the compressive radial stress gives rise to strain magnification. This is reflected by the experimental result given by Equation 3.

It is now pertinent to examine the significance of the coefficients in Equations 2 and 3. As noted earlier, the Nielsen prediction given by Equation 1 is based on particulate inclusions in a matrix. For the reinforced PP, we assume that there is reasonably good adhesion since the radial stress at the interface is compressive. Despite the fact that this work deals with continuous fibrous inclusions rather than with particulate ones, we see that the basic form of the Nielsen prediction is obeyed except for the coefficient of 1.5. The origin of this factor can be rationalized by construction of a model composite comprised of a matrix containing continuous linear assemblies of spheres. If instead of spheres along a given axis we substitute a fiber having a diameter equivalent to that of the sphere, it can be shown readily that the fraction of volume occupied by the fiber ( $V_f$ ) is 1.5 times greater than that occupied by the assembly of spheres ( $V_s$ ). Thus, it appears that the coefficient in Equation 3 is a form factor that accounts for continuous fiber reinforcement rather than (spherical) particle reinforcement.

The PP–nylon system can be treated similarly. If the debonded region between the fiber and the matrix is viewed as an assembly of contiguous voids but having a volume fraction corresponding to a hypothetical cylinder (fiber) surrounding the voids, the modified form of Kerner's expression (7) for foams and polyblends can be shown to give a result in excellent agreement with Equation 2.

### *Acknowledgments*

We thank Larry Cessna (Hercules Corp.) for helpful suggestions during the writing of this paper. One of us (MRK) also expresses his

appreciation to Charles Garber for the use of his SEM facility (Structure Probe, Inc.).

### *Literature Cited*

1. Nielsen, L. E., *J. Appl. Polym. Sci.* (1966) **10**, 97.
2. Kenyon, A. S., Duffey, H. J., *Polym. Eng. Sci.* (July 1967) p. 189.
3. Lavengood, R. E., Nicolais, L., Narkis, M., *J. Appl. Polym. Sci.* (1973) **17**, 1173.
4. Nicolais, L., Droili, E., Landel, R. F., *Polymer* (1973) **14**, 21.
5. Kantz, M. R., Corneliussen, R. D., *J. Polym. Sci., Part B* (1973) **11**, 279.
6. Kantz, M. R., Corneliussen, R. D., "The Mechanical Properties of Organic Fiber Reinforced Polypropylene Composites," *Am. Chem. Soc., Div. Polym. Chem., Preprints* (1973) **14**(1), 447.
7. Kerner, E. H., *Proc. Phys. Soc., London* (1956) **69B**, 808.

RECEIVED October 18, 1974. Work supported in part by a Department Grant from the National Science Foundation.

## Tough–Brittle Transition of Glass Fiber Composites by Impact Testing

HIDEMITSU HOJO, YUKIO OKADA, and TOSHIO MAEDA

Department of Chemical Engineering, Tokyo Institute of Technology, Ookayama, Meguro-ku, Tokyo, Japan

*Charpy impact tests were made to show the effects of temperature and specimen size on the impact strength and fracture mode of glass–polyester composites. The tough–brittle transition depended on temperature and was controlled by the weaker intrinsic strength of the materials. The law of similarity for size effects held for all materials when the fracture mode was unchanged, and a clear transition of fracture mode occurred for cloth laminates. This transition occurred at the critical size ratio depending on temperature. Consequently we could predict the impact behavior over a wide range of temperature, independent of specimen size, by using standard specimens.*

Numerous studies have been made of the mechanical properties of fibrous composites; these include recently published papers on impact properties by Izod (1, 2, 3, 4) and Charpy (5, 6) and drop weight (7) tests. We reported the Charpy impact fracture behavior of various glass–polyester composites regarding the effects of temperature (8, 9, 10), specimen size (8), and fiber orientation (10). This paper describes the effects of the tough–brittle transition in the impact behavior of glass–polyester composites which occurs with a variation of temperature and specimen size.

### *Materials and Test Procedure*

The materials tested were mainly unidirectional and bidirectional satin cloth laminate. Unsaturated polyester resin was used as a matrix. The tensile strength ratio of longitudinal fiber to transverse fiber was

6.6 to 1.0 for the unidirectional laminate and almost unity for the bidirectional laminate; their glass contents (GC) were 62 and 60 wt %.

ASTM E 23-66 was applied for the dimensions of standard specimens except that the mat reinforced specimen (GC: 33 wt %) used ASTM D 256-56. Specimens were taken from a molded plate along the longitudinal fiber direction, and V notches were cut edgewise, perpendicular to both fiber direction and molding surface. Occasionally a specimen notched on the molding surface (flatwise) was used. Tests were performed with an instrumented Charpy impact tester (10) with a 30 kg-m or 150 kg-cm capacity. Test temperatures were varied from  $-196^{\circ}$ – $250^{\circ}$ C.

### *Transition of Fracture Mode Depending on Temperature*

Four typical impact fracture modes—tensile, compressive shear, compressive buckling, and interlaminar shear—were recognized from the broken specimens (9) and load-time curves (10). Among these four the tensile fracture had the lowest absorbed energy and behaved as a brittle material; compressive shear fracture had higher absorbed energy and behaved as a tough material. A mixed mode of fracture was often observed except for buckling failure at high temperature.

The temperature dependence of the absorbed energy for standard specimens is shown in Figure 1. Impact behaviors and fracture modes of edge notched specimens depending on temperature were reported elsewhere (9, 10). In edge notched specimens of unidirectional roving reinforced material (GC: 68 wt %), cloth laminates, and mat reinforced material the fracture mode changed with temperature; all materials re-

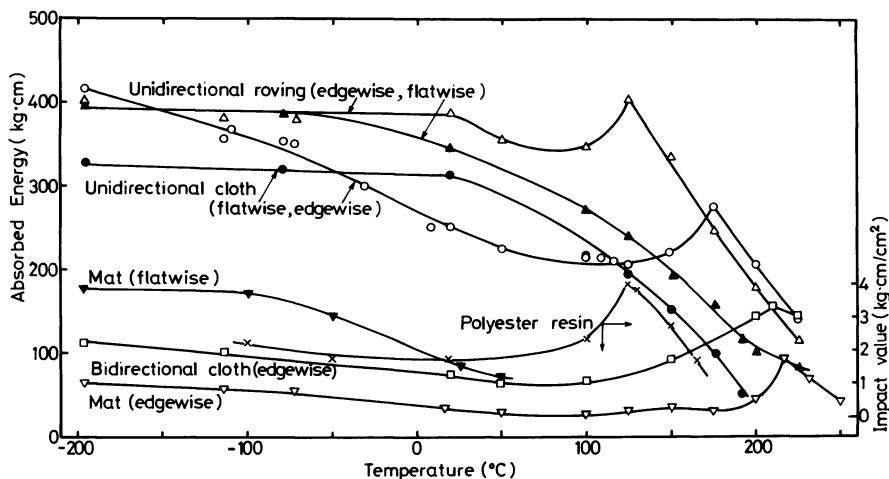


Figure 1. Effect of temperature on impact strength of glass fiber composites

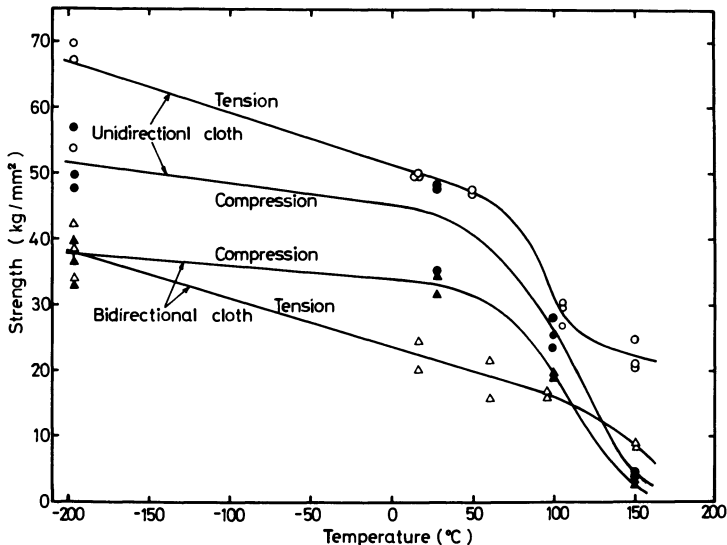


Figure 2. Variation of static tensile and compressive strength of cloth laminates with temperature

vealed sharp peaks at high temperatures which seemed to correspond with the glass transition temperature in impact testing. After reaching the peak the specimens buckled by compressive load along the longitudinal direction.

In unidirectional cloth specimens the fracture mode was essentially compressive; there was compressive shear at lower temperatures and buckling after the peak, but tensile fracture apparently became dominant at moderate temperatures. For bidirectional cloth specimens the fracture is almost controlled by tension but it shifts to compressive shear and then to buckling at higher temperatures.

Local indentation at the point of impact may contribute to picking in absorbed energy with increasing temperatures. There was clear indentation for unidirectional roving reinforced specimens that seemed to increase with increasing temperatures. For cloth specimens a slight indentation was observed above 100°C.

In specimens notched flatwise the absorbed energy is constant at lower temperatures and decreases with increasing temperatures. Fracture is caused almost entirely by interlaminar shear, and the number of delaminated layers is reduced at higher temperatures; however in mat specimens tensile fracture is added to interlaminar shear, and there is no clear transition of fracture mode in these cases.

Therefore the clear, tough-brittle transition exists, with reference to the temperature variation, when the notch was cut on the edge of



cloth specimens. To evaluate these results static tensile and compressive strength data were obtained as a function of temperature (*see* Figure 2). This behavior in static strength coincides with that of dynamic strength obtained by the load–time curve (10) and the transition of fracture mode in Figure 1. In unidirectional cloth laminate compressive strength is weaker than tensile strength for the temperature range tested, but at 100°C the difference between both strengths becomes smallest; in this point the fracture area ratio of tension to compression is maximum (10). For bidirectional cloth laminate, the weaker strength changes at 110°C, corresponding to the change of fracture mode from tension to compression. Consequently the fracture mode is controlled by the weaker intrinsic strength of the materials at the test temperature.

### *Effect of Specimen Size*

To clarify the relation between absorbed energy and specimen size, tests were made with various specimen widths ( $b$ ) and thicknesses under the notch—*i.e.*, remaining depth ( $h$ ).

**Law of Similarity.** An example of size effects is shown in Figure 3. The absorbed energy increases linearly with an increase in width and continuously increases with an increase in remaining depth for unidirectional cloth notched flatwise. The same behavior occurred for other specimen sizes. Figure 4 shows a logarithmic plot of absorbed energy and the remaining depth for resin and various composites at room temperature. The law of similarity, Equation 1, held for all the materials between absorbed energy ( $E$ ) and specimen size when the same fracture mode was maintained regardless of specimen size.

$$E = Cb^m h^n \quad (1)$$

where  $C$ ,  $m$ , and  $n$  are the material constants;  $m$  is unity for most cases, and  $n$  varies from 1.0 to 2.0.  $C$  depends on the temperature and fracture mode, and  $m$  and  $n$  are constant and independent of temperature when specimens have the same fracture mode. The total absorbed energy ( $E$ ) consists of  $E_1$  (proportional to the sectional area  $bh$ ) and  $E_2$  (proportional to the volume  $bh^2$ ). Therefore  $E$  is given in the form

$$E = E_1 + E_2 = C_1bh + C_2bh^2 \approx Cbh^n \quad (2)$$

**Tough–Brittle Transition in Cloth Laminates.** For cloth specimens notched edgewise transition of fracture mode occurred with a variation of specimen size although the law of similarity held for each region having the same fracture mode. Figure 5 shows this transition for bidirectional cloth specimens at room temperature. With the increase of remain-

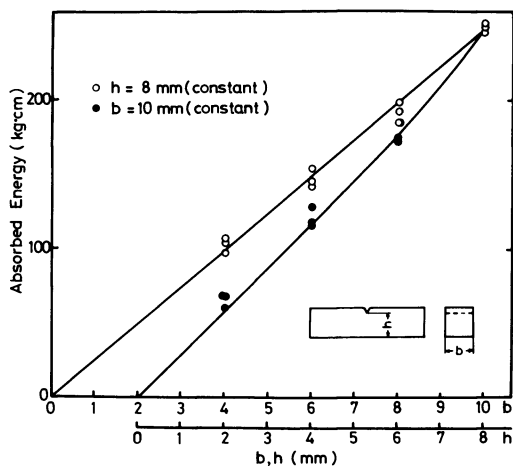


Figure 3. Effect of specimen size on absorbed energy of unidirectional cloth specimen notched flatwise at room temperature

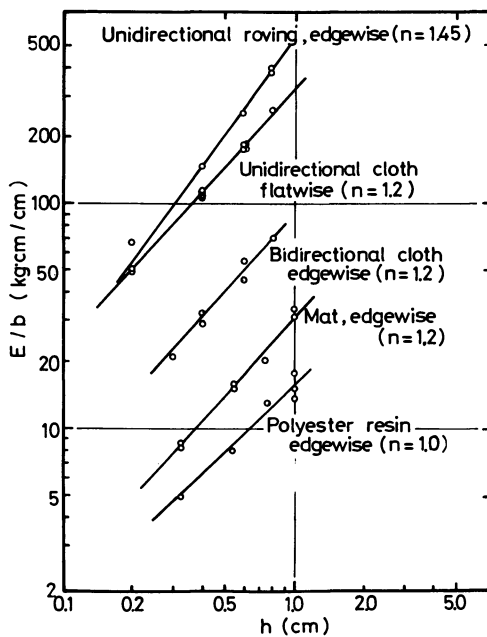


Figure 4. Absorbed energy vs. specimen size relationship for various glass fiber composites at room temperature

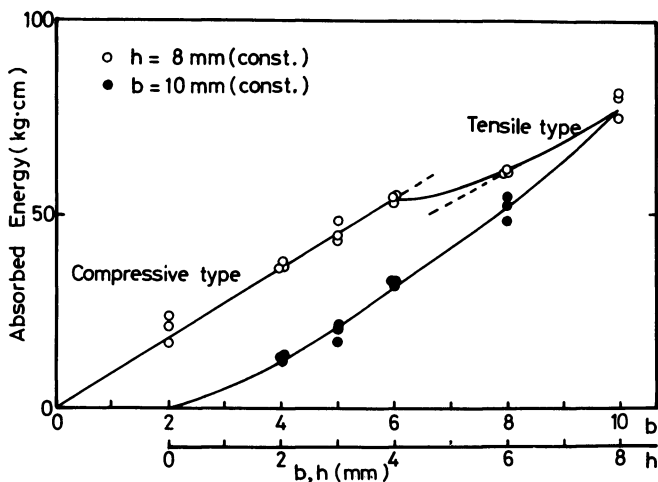


Figure 5. Effect of specimen size on absorbed energy of bidirectional cloth laminate at room temperature

ing depth at constant width ( $b = 10$  mm), the absorbed energy increases continuously although an abrupt transition from compressive to tensile type occurs with increasing width at a constant remaining depth ( $h = 8$  mm).

The fracture transition from compressive to tensile type occurred at a fixed size ratio—at a critical size ratio  $(b/h)_c$  at constant temperature

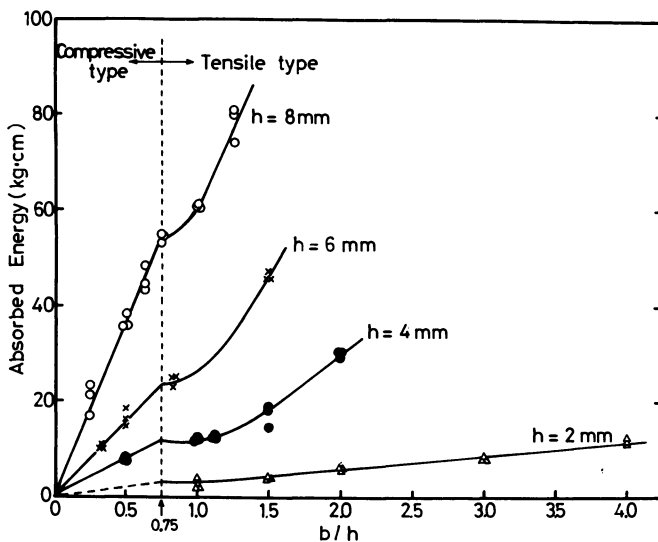


Figure 6. Relationship between transition in fracture mode and critical size ratio

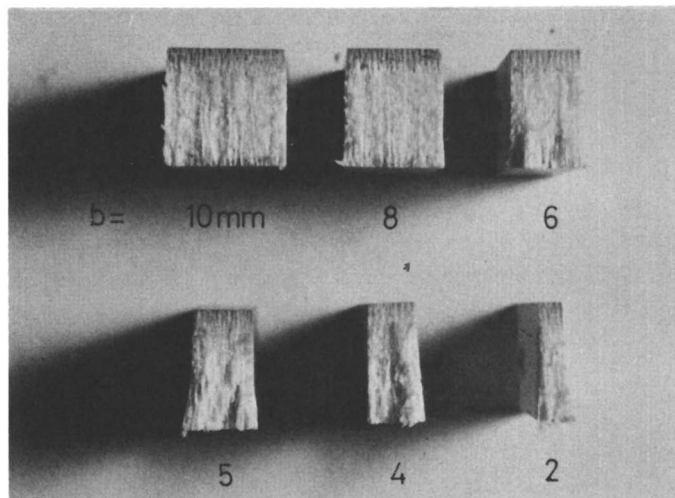


Figure 7. Appearance of fracture surface with variation of specimen width for bidirectional cloth laminate

(see Figure 6). At room temperature the transition points appeared at  $(b/h)_c = 0.75$ . Figure 7 shows the appearance of the fracture surface with the variation of specimen width at  $h = 8$  mm and fracture mode changes at  $b = 6$  mm. Compressive type fracture arose from shear fracture which always was preceded by local buckling failure. With decreasing specimen width the glass cloth layers limited near the striking zone tended to buckle toward the outside on each side by direct impact load without bending. The mechanism of this type of transition may be considered in the following way. Euler's equation on the critical buckling stress ( $\sigma_c$ ) induced in a slender column subjected to compressive load ( $W$ ) is given by

$$\sigma_c = \frac{\pi^2 E}{4} \left( \frac{k}{L} \right)^2 \quad (3)$$

where  $E$  is Young's modulus,  $k$  is the radius of gyration  $= \sqrt{I/A}$  ( $I$ : moment of inertia;  $A$ : cross-sectional area), and  $L$  is height of the column. If we consider a hypothetical, small rectangular column at the striking zone with a cross-sectional area  $bl/2$  ( $l$ : length of local buckled layers along a longitudinal direction) and a height  $h$  subjected to compressive load  $W/2$  and substitute these values in Equation 3, the critical buckling stress can be expressed as

$$\sigma_c = AE \left( \frac{b}{h} \right)^2 \quad (4)$$

where  $A$  is constant. Therefore Equation 4 implies that the local buckling failure will occur at the critical size ratio  $(b/h)_c$ . We only assumed that the column height was  $h$  in place of specimen thickness  $t$  ( $h +$  notch depth), and Figure 6 seemed to prove our assumption; for unnotched specimens the transition occurred at the same critical size ratio with notched specimens when the size ratio was taken as  $b/t$ .

For unidirectional cloth specimens notched edgewise, the effects of specimen size at room temperature are shown in Figure 8. Although the fracture mode is unchanged for the variation of specimen width, it changes gradually from tensile to compressive shear type with increasing remaining depth at constant width ( $b = 10$  mm)—a change different from the bidirectional one. From the examination of the fracture surface, the area ratio of tension to compression in fracture surface varied continuously with the following relations. Figure 9 shows the variation of tensile fracture area represented as the depth under notch  $a$  to the specimen width at room temperature. The depth in tensile fracture is proportional to specimen width. Figure 10 shows the relationship between depth in tensile fracture and remaining depth. The depth in tensile fracture is constant and independent of the remaining depth. The same relations as those shown in Figures 9 and 10 were obtained for other sizes and temperatures. These relations are expressed as follows:

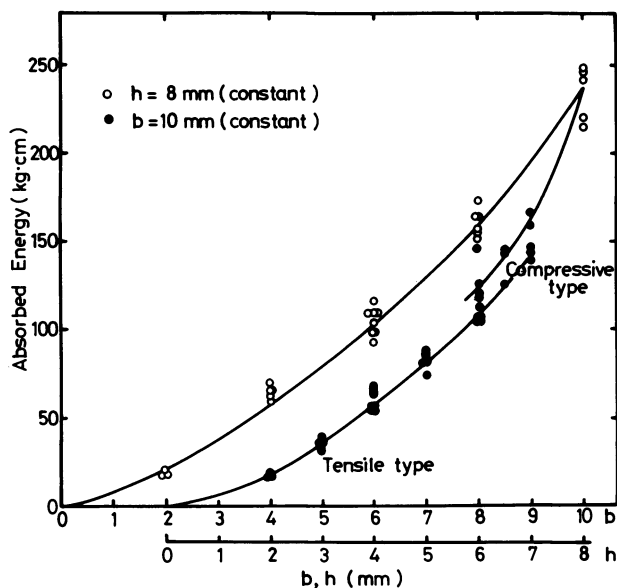


Figure 8. Effect of specimen size on absorbed energy of unidirectional cloth laminate at room temperature

$$a = Kb \quad (5)$$

At the transition point the tensile-to-compressive area ratio becomes unity; then

$$a_c = \frac{1}{2} h_c \quad (6)$$

By combining Equations 5 and 6, the critical size ratio becomes

$$(h/b)_c = 2K = \text{constant} \quad (7)$$

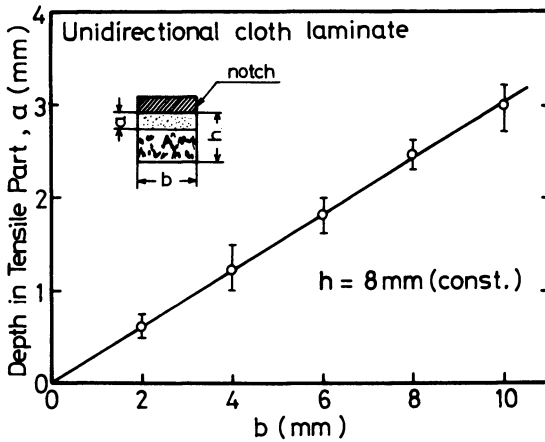


Figure 9. Depth in tensile fracture part vs. specimen width

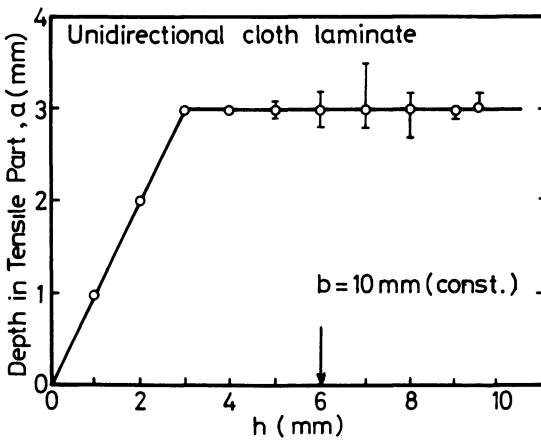


Figure 10. Depth in tensile fracture part vs. remaining depth

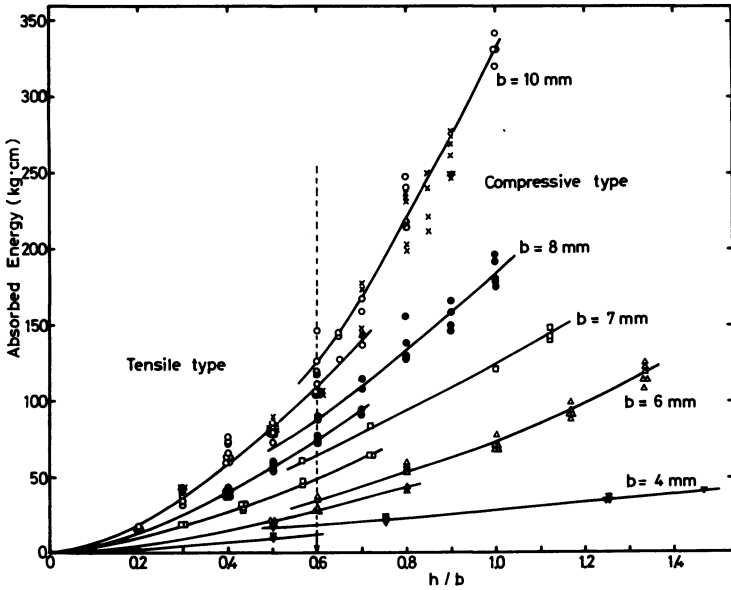


Figure 11. Relationship between transition in fracture mode and critical size ratio for unidirectional cloth laminate

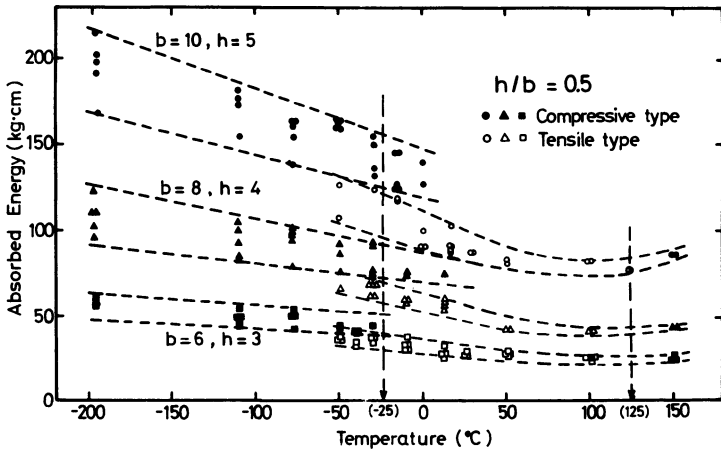


Figure 12. Relationship between transition in fracture mode and temperature at constant size ratio ( $h/b = 0.5$ ) for unidirectional cloth laminate

where  $K$  is a material constant that depends on temperature. At room temperature [ $2K = (h/b)_c$ ] equals 0.6 ( $a_c = 3$  mm;  $b = 10$  mm). Therefore the transition point should occur at  $(h/b)_c = 0.6$  at room temperature. The validity of this conclusion is presented in Figure 11. The

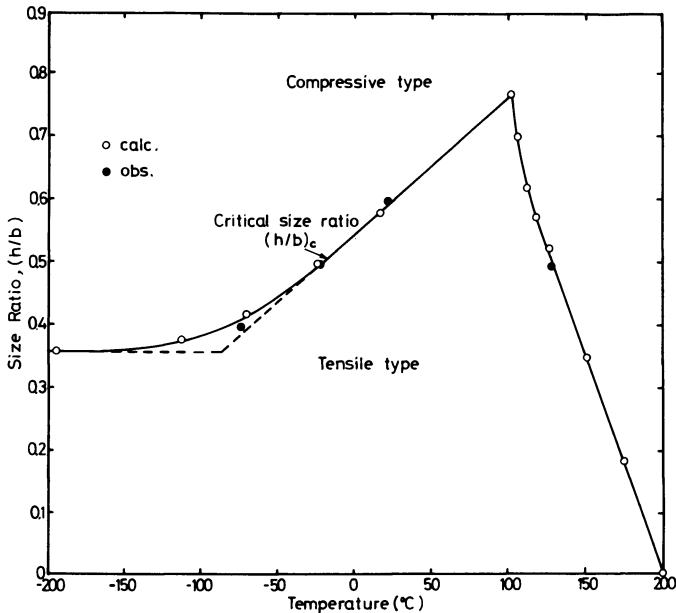


Figure 13. Size ratio-temperature-fracture mode diagram

same result was obtained by using various notch depths at a constant width (*see* X in Figure 11). If the specimen size ratio ( $h/b$ ) is constant, the transition point occurs at the same temperature (*see* Figure 12); there are two transition temperatures of  $-25^{\circ}$  and  $125^{\circ}\text{C}$  at  $(h/b) = 0.5$ .

As a result of analysis using Equations 5-7 and measuring the depth in tensile fracture of standard specimens at various test temperatures, we determined the temperature dependence of critical size ratio (*see* Figure 13). The critical size ratio maintains approximately a constant value up to  $-90^{\circ}\text{C}$ ; it increases linearly with increasing temperature, but after a peak at  $100^{\circ}\text{C}$  it decreases markedly. Calculated values coincide well with observed values (Figure 12 and Ref. 8) obtained with various sized specimens. The upper region from the line of critical size ratio corresponds to compressive fracture, and the material behaves in a tough manner; however in the lower region the specimen breaks with tensile fracture mode and behaves in a brittle manner. At over  $200^{\circ}\text{C}$  failure occurs by buckling completely.

### Conclusion

We can predict the impact behavior, namely impact strength and fracture mode, over a wide range of temperatures independent of specimen size by using standard specimens.



**Literature Cited**

1. Chamis, C. C., Hanson, M. P., Serafini, T. T., *NASA Tech. Note D-6463* (August, 1971).
2. Hancox, N. L., *Composites* (1971) **2**, 41.
3. Hancox, N. L., Wells, H., *Composites* (1973) **3**, 26.
4. Simon, R. A., *28th Ann. Tech. Conf. RP/C Inst., SPI, 17-C* (1973).
5. Barker, A. J., *Proc. Intern. Conf. Carbon Fibers, London, Feb. 1971*, paper 20.
6. Ellis, C. D., Harris, B., *J. Compos. Mater.* (1973) **7**, 76.
7. Broutman, L. J., Rotem, A., *28th Ann. Tech. Conf. RP/C Inst., SPI, 17-B* (1973).
8. Suezawa, Y., Hojo, H., Nakamura, K., *Kagaku Kogaku (J. Soc. Chem. Eng., Japan)* (1969) **33**, 1051.
9. Hojo, H., Saito, Y., *J. Inst. Soc. High Pressure Gas Eng., Japan* (1971) **8**, 72.
10. Hojo, H., Okada, Y., Nakamura, K., *Proc. Jap. Congr. Mater. Res., 17th* (1974) 167.

RECEIVED November 11, 1974.

## Polyester Fiber: An Impact Reinforcement in Polystyrene

T-W SHI<sup>1</sup> and A. CRUGNOLA

Department of Plastics Technology, University of Lowell,  
Lowell, Mass. 01854

*Two polystyrene plastics were reinforced with polyester fibers, and the mechanical/physical properties of the resulting composites were determined. One of the plastics was then reinforced alternately with asbestos and glass fiber ¼ inch long, equal to that of one of the polyester fibers. The properties of these latter structures were compared with those of the polyester reinforced structures. It was observed that certain fibers selectively improved particular properties (i.e., glass improved the strength and modulus; asbestos improved heat deflection temperature; polyester improved impact strength). A mathematical model was proposed to predict quantitatively the property values of multifiber reinforced plastics. The model forecast the observed property values of several fabricated multifiber composites to a good level of agreement.*

The 1973 output of reinforced thermoplastics has been estimated at 200 million pounds. This represents a 700% growth from the production level of 1967. The obvious reason for this massive increase is the possibility of attaining adequate/acceptable structural properties in these materials with the convenience and economy of thermoplastic processing methods.

Currently glass fiber is the overwhelmingly dominant reinforcement (90–95%) used for thermoplastics. Various other materials make up the remaining 5–10% with perhaps asbestos running a far distant second. The use of synthetic, organic fiber reinforcements on the other hand has been very limited. Although isolated applications document their utiliza-

<sup>1</sup> Present address: Union Industrial Research Institute of Taiwan, Republic of China.

tion in thermosetting resins (nylon fabric in electrical laminates and nylon fibers in polyester shower stalls), virtually nothing has been reported concerning the reinforcing effects of these fibers in thermoplastics.

Our study is outlined in five parts. (a) Two polystyrene plastics were reinforced at different fiber contents alternately with polyester, asbestos, and glass fibers. (b) The mechanical/physical properties of the resultant monofiber-reinforced plastics were determined and compared. (c) Combinations of fibers were then used to fabricate multifiber-reinforced structures to exploit simultaneously the particular advantages of the different reinforcements. (d) The effect of each fabrication stage on the molecular weight and molecular weight distribution of the matrix plastics was established and (e) a linear mathematical model was formulated to predict the properties of multifiber structures and forecasted values compared with corresponding values experimentally obtained from (c) above.

### **Experimental**

**Materials.** Plastics used were Foster-Grant Fostarene polystyrene 50D3  $\bar{M}_w = 315,000$  and Foster-Grant Fostarene polystyrene 817D9 high flow  $\bar{M}_w = 232,800$  containing approximately 10% of low molecular weight modifier. Fibers used were DuPont Dacron polyester type 54 staple 1.5 denier, 0.25 inch length, Beaunit Vycron polyester type flock 3.0 denier, 0.03 inch length, Johns Manville asbestos type Paperbestos No. 1 0.25 inch length (well opened), Johns Manville asbestos type Plastibest No. 20 0.125-0.188 inch length (not well opened), Pittsburgh Plate fiber glass type 3129 0.25 inch length, 0.00038 inch diameter, and Pittsburgh Plate Fiber Glass type 3129 0.125 inch length, 0.00038 inch diameter.

**Procedure.** SPECIMEN FABRICATION. The reinforcements were mixed into the polystyrene melt on a Farrell two-roll mill at 320°F. It was necessary to dry the asbestos fibers for 24 hr at 250°F prior to mixing to ensure the breakup of bundle aggregates. The milling/fluxing time was held to 8 min for all samples. The sheets obtained in milling were cut, crossplied, and compression molded in an open frame on a Wabash press. After they reached the platen temperature the material was held at 330°F and 2000 psi for 6 min. The frame was then transferred to a cold press, and the sample was cooled under the same pressure. The test specimens were cut from 1/8-inch thick plates prepared in the foregoing manner.

**TESTING.** The physical/mechanical testing was carried out in a fairly standard method. The tensile properties of modulus, breaking stress, and breaking strain were determined at a 10% per minute strain rate. Izod notched impact ASTM D256 and Shore D hardnesses were also obtained as were the heat deflection temperatures (HDT) according to ASTM D648 under 264 psi. The molecular weight and molecular weight distributions were determined with a Waters' model 200 gel permeation chromatograph (GPC). Each sample was run at a concentration of

**Table I. Mechanical/Physical Properties of Polyester Fiber-Reinforced Polystyrene<sup>a</sup>**

Fiber length	0.25 inch		0.03 inch		
	0	15%	30%	15%	30%
Fiber content	0	15%	30%	15%	30%
Tensile strength (psi) <sup>b</sup>	4250	4210	3500	4300	3900
Elongation at break (%)	2.30	2.30	2.00	2.20	2.00
Tensile modulus (1% strain, psi)	233,000	241,000	242,000	234,000	235,000
Impact strength (ft-lb/inch notched)	0.30	1.29	3.08	0.42	0.57
Hardness (Shore-D)	84	83	83	84	84
Heat deflection temperature, °C	63	75	77	74	77

<sup>a</sup> Foster-Grant 50D3.<sup>b</sup> Strain rate 10%/min.

0.25% in dimethyl formamide. The rate of flow and the temperature of the GPC columns were 1 cc/min and 50°C. The processed plastics were separated from the fibers by dissolution in toluene and subsequent filtration.

### Results and Discussion

**Polyester Reinforcement.** The data in Tables I and II reveal the following:

(a) Tensile strength is somewhat reduced—a maximum of 15% at a 30 wt % content of 0.25 inch fiber but only one half that much by the 0.03 inch fiber.

(b) Elongation to break is barely affected; at most it is slightly reduced.

(c) Tensile modulus is increased slightly (4%) by the longer fiber but not altered by the short flock.

**Table II. Mechanical/Physical Properties of Polyester Fiber-Reinforced Polystyrene<sup>a</sup>**

Fiber length	0.25 inch		0.03 inch		
	0	15%	30%	15%	30%
Fiber content	0	15%	30%	15%	30%
Tensile strength (psi) <sup>b</sup>	3160	3150	2900	3200	3300
Elongation at break (%)	2.40	2.30	2.30	1.90	1.80
Tensile modulus (1% strain psi)	195,000	196,000	198,000	220,000	232,000
Impact strength (ft-lb/inch notched)	0.30	1.28	3.08	0.40	0.57
Hardness (Shore-D)	84	84	84	84	84
Heat deflection temperature, °C	61	74	76	65	71

<sup>a</sup> Foster-Grant 817D9 high flow (10% modifiers, lubricants).<sup>b</sup> Strain rate 10%/min.

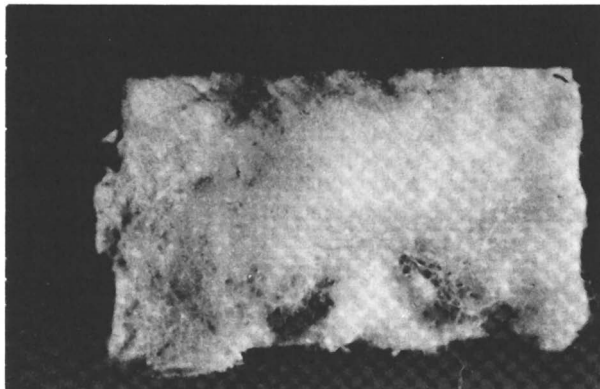


*Figure 1. Fracture surface polystyrene reinforced with 1/4-inch polyester fiber*

(d) Impact strength is the property most dramatically affected by the polyester fiber. The inclusion of 30% 0.25 inch fiber brings about a tenfold increase in notched Izod but only modest increases are registered with the 0.03 inch fiber.

(e) Hardness values are virtually unaffected by these reinforcements.

(f) Heat deflection temperatures are increased significantly (from 63°C to 77°C at 30% fiber). The length of the reinforcement does not appear to be a factor.

The foregoing analysis summarizes the results obtained with the 50D3 polystyrene plastic. With the 817D9 material, although the impact

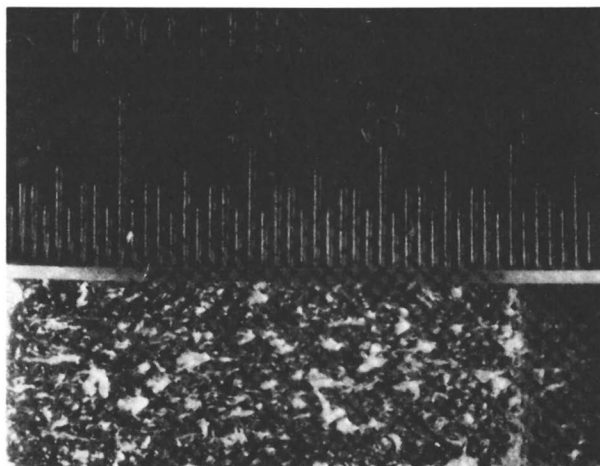


*Figure 2. Fracture surface of rigid polyvinyl chloride reinforced with No. 1 asbestos*

strength and hardness modifications are identical (*see* Table II) to those of 50D3 (*see* Table I), some differences are observed with the tensile properties and the HTD results. Here the tensile strengths are only slightly reduced (8% at 30% for 0.25 inch fiber) or even improved as by the flock. The elongation to break, though not effected by the longer fibers, is somewhat reduced by the shorter. The modulus, though not altered by adding 0.25-inch fiber, is increased significantly (20%) by adding flock fiber.

The spectacular increase in impact strength is of particular interest. Figure 1 is a photograph of the fracture surface of a polystyrene reinforced with  $\frac{1}{4}$  inch polyester fiber. Figures 2 and 3 are similar photographs of a rigid polyvinyl chloride (PVC) reinforced alternately with the No. 1 and No. 20 asbestos. These are taken from a previous study by one of us (1) and are in apparent agreement with Cameron (2) who reported that the impact strength of an asbestos-reinforced polyvinyl chloride depended on the "bundle integrity" of the asbestos fibers. The originally less well opened No. 20 fiber retained its bundle integrity much more than the No. 1 fiber. This is evidenced by the lack of complete fiber wetting. A similar argument may be applicable to the huge increase in impact strength observed with the polyester fibers. Certainly Figure 1 reveals that much of the fiber has not been wet out.

However the foregoing only shows that good impact behavior accompanies incomplete fiber wetting. It does not suggest how this condition increases impact. A mechanism for this increase was proposed by Crugnola and Litman (1) for asbestos fibers in PVC. They stated that:

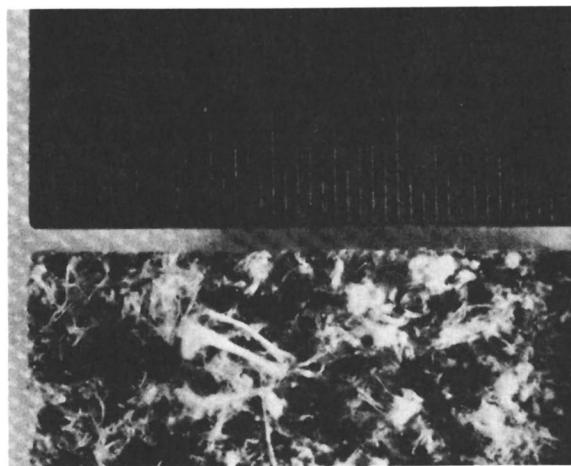


Figure 3. Fracture surface of rigid polyvinyl chloride reinforced with No. 20 asbestos

**Table III. Mechanical/Physical Properties of Asbestos-Reinforced Polystyrene<sup>a</sup>**

Type		<i>Paperbestos No. 1</i>		<i>Plastibest No. 20</i>	
Content	0	15%	30%	15%	30%
Tensile strength (psi) <sup>b</sup>	4250	4250	4250	4100	4000
Elongation at break (%)	2.30	2.30	2.30	2.30	2.20
Tensile modulus (1% strain psi)	233,000	245,000	258,000	240,000	250,000
Impact strength (ft-lb/inch notched)	0.30	0.49	0.59	1.07	1.12
Hardness (Shore D)	84	85	86	87	88
Heat deflection temperature, °C	61	82	86	82	85

<sup>a</sup> Foster-Grant 50D3.<sup>b</sup> Strain rate 10%/min.**Table IV. Mechanical/Physical Properties of Asbestos-Reinforced Polystyrene<sup>a</sup>**

Type		<i>Paperbestos No. 1</i>		<i>Plastibest No. 20</i>	
Content	0	15%	30%	15%	30%
Tensile strength (psi) <sup>b</sup>	3160	3250	3200	3500	3450
Elongation at break (%)	2.40	2.10	1.70	1.80	1.80
Tensile modulus (1% strain psi)	195,000	233,000	233,000	205,000	230,000
Impact strength (ft-lb/inch notched)	0.30	0.47	0.60	0.54	0.60
Hardness (Shore D)	84	86	87	86	87
Heat deflection temperature, °C	61	71	73	72	73

<sup>a</sup> Foster-Grant 817D9.<sup>b</sup> Strain rate 10%/min.**Table V. Mechanical/Physical Properties of Glass Fiber-Reinforced Polystyrene<sup>a</sup>**

Fiber length		<i>0.25 inch</i>		<i>0.125 inch</i>	
Fiber content	0	15%	30%	15%	30%
Tensile strength (psi) <sup>b</sup>	4250	5300	5580	4600	5400
Elongation at break (%)	2.30	2.20	2.00	2.10	2.10
Tensile modulus (1% strain psi)	233,000	265,000	325,000	238,000	340,000
Impact strength (ft-lb/inch notched)	0.30	0.85	1.48	0.80	1.41
Hardness (Shore D)	84	89	90	87	89
Heat deflection temperature, °C	63	82	83	82	83

<sup>a</sup> Foster-Grant 50D3.<sup>b</sup> Strain rate 10%/min.

**Table VI. Mechanical/Physical Properties of Glass Fiber-Reinforced Polystyrene<sup>a</sup>**

Fiber length	0.25 inch		0.125 inch		
	0	15%	30%	15%	30%
Fiber content	0	15%	30%	15%	30%
Tensile strength (psi) <sup>b</sup>	3160	5000	5100	4950	5000
Elongation at break (%)	2.40	2.40	2.30	2.40	2.30
Tensile modulus (1% strain psi)	195,000	280,000	326,000	260,000	265,000
Impact strength (ft-lb/inch notched)	0.30	0.64	1.14	0.58	1.13
Hardness (Shore D)	84	87	89	87	87
Heat deflection temperature, °C	61	70	71	70	71

<sup>a</sup> Foster-Grant 817D9.<sup>b</sup> Strain rate 10%/min.**Table VII. Comparison of the Reinforcing Effects of Polyester, Asbestos, and Glass Fiber in Polystyrene<sup>a</sup>**

	<i>Nonre-</i> <i>inforced</i>	<i>Polyester</i>	<i>Asbestos</i>	<i>Glass</i>
Tensile strength (psi) <sup>b</sup>	4250	3500	4250	5580
Elongation break (%)	2.30	2.00	2.30	2.00
Tensile modulus (1% strain)	233,000	242,000	258,000	325,000
Impact strength (ft-lb/inch notched)	0.30	3.08	0.59	1.48
Hardness (Shore-D)	84	83	86	89
Heat deflection temperature, °C	63	77	86	83

<sup>a</sup> One quarter inch fibers at 30% content in Foster-Grant 50D3 polystyrene.<sup>b</sup> Strain rate 10%/min.**Table VIII. Molecular Weight and Molecular Weight Distributions**

	<i>Polystyrene 50D3</i>		
	$\overline{M}_w^a$	$\overline{M}_N^b$	$\overline{M}_w/\overline{M}_N^c$
Original as received	315,500	131,200	2.41
Original after dissolving in toluene	301,400	126,500	2.38
After milling (without fiber)	248,300	116,000	2.14
After molding (without fiber)	256,000	121,000	2.12
After milling (with 30% 0.25 inch polyester fiber)	259,600	119,800	2.17
After molding (with 30% 0.25 inch polyester fiber)	286,500	121,600	2.36

<sup>a</sup>  $\overline{M}_w$  = weight average molecular weight.<sup>b</sup>  $\overline{M}_N$  = number average molecular weight.



Considerable energy must be involved in pulling apart the asbestos fibers during the impact: energy used in overcoming frictional type forces, forces required to pull individual fibers away and past others. The extent of this mechanism is dependent on the asbestos fiber bundles not being thoroughly wet by the matrix since the better wet open fibers are fractured at the matrix fracture surface.

With the polyester fiber one must consider the added positive effect of its substantial elongation to break (here 30–40%).

**Comparison with Asbestos and Glass.** Tables III, IV, V, and VI catalog the properties obtained when the two polystyrenes were reinforced with asbestos and glass. Table VII compares the reinforcing effects of the several fibers studied at 30 wt %. The data show that particular fibers improve particular properties. The tensile modulus and tensile strength are most improved by glass; the heat deflection is most improved by asbestos, and the impact strength is most improved by polyester.

**Changes in the Fibers.** Samples of fibers were collected after each processing stage, milling, and molding by dissolution of the polystyrene in toluene. None of the three fibers (polyester, asbestos, and glass) were measurably shortened by either fabrication step. The polyester (0.25 inch) fiber increased in density after milling and after molding—original 1.3706 g/cm<sup>3</sup>, after milling 1.3769 g/cm<sup>3</sup>, and after molding 1.3807 g/cm<sup>3</sup>. On a percent volume crystallinity these densities correspond to 33, 38, and 42%.

**Molecular Weight and Molecular Weight Distributions.** The results of the molecular weight determinations appear in Table VIII. They show that the molecular weight of the polystyrene was somewhat decreased by the processing. Milling without the fiber lowered the weight average molecular weight  $\bar{M}_w$  of 50D3 by *ca.* 20%. The subsequent compression molding operation had little further effect; if anything the molecular weight averages were slightly increased. When the reinforcing

#### of Polystyrenes 50D3 and 817D9 before and after Processing

##### *Polystyrene 817D9*

$\bar{M}_w$	$\bar{M}_N$	$\bar{M}_w/\bar{M}_N$
232,800	111,000	2.10
216,900	108,800	2.00
214,300	105,700	2.03
200,500	105,200	1.91
185,800	100,400	1.85
181,000	99,300	1.82

\*  $\bar{M}_w/\bar{M}_N$  = polydispersity.

**Table IX. Comparison of Experimental**

	<i>D/G (15/15)</i>	
	<i>Experimental</i>	<i>Predicted</i>
Tensile strength (psi) <sup>b</sup>	4850	5300
Elongation at break (%)	1.80	
Tensile modulus (1% strain psi)	315,000	273,000
Impact strength (ft-lb/inch notched)	1.74	1.62
Hardness (Shore-D)	87	
Heat deflection temperature, °C	83	

<sup>a</sup> Foster-Grant 50D3 polystyrene.

<sup>b</sup> Strain rate 10%/min.

polyester fiber was present, the same milling operation dropped the  $\bar{M}_w$  somewhat less (15%); the molding operation again caused an increase over the milled value. The molecular weight distribution as reflected in the polydispersity ratio  $\bar{M}_w:M_n$  appears to have been slightly narrowed as a result of the processing. The results obtained with the other polystyrene (817D9) are not in one-to-one agreement with those obtained with the 50D3. These observations may have been complicated by the low molecular weight fraction in this particular plastic (*see* materials description above). Nevertheless there is general agreement in that processing does lower the molecular weight and narrow the molecular weight distribution. The decreases caused by milling are probably the consequence of chain scission induced by the high shearing forces to which the polymer melt is subjected in the mill. The increases in molding could arise from a recombination of some of the free radicals formed in milling.

$$P_c = P_0 + (P_1 - P_0) \frac{C_1}{X_1} + (P_2 - P_0) \frac{C_2}{X_2} + \dots$$

WHERE

$P_c$  = VALUE OF A PARTICULAR PROPERTY IN THE MULTIFIBER COMPOSITE

$P_0$  = VALUE OF THE PROPERTY FOR THE NON-REINFORCED PLASTIC

$P_1, P_2, \dots$  = VALUE OF THE PROPERTY FOR THE SINGLE FIBER COMPOSITE

$C_1$  = VOLUME RATIO OF FIBER 1 IN THE MULTIFIBER COMPOSITE

≡ VOLUME FIBER 1/(VOLUME FIBER 1 + VOLUME OF PLASTIC IN MULTIFIBER COMPOSITE)

$X_1$  = VOLUME FRACTION OF FIBER 1 IN THE SINGLE FIBER COMPOSITE

≡ VOLUME FIBER 1/(VOLUME FIBER 1 + VOLUME OF PLASTIC IN SINGLE FIBER COMPOSITE)

*Figure 4. Mathematical model—multifiber-reinforced thermoplastic*

and Predicted Composite Properties<sup>a</sup>

<i>D/A (15/15)</i>		<i>D/G/A (10/10/10)<sup>c</sup></i>	
<i>Experimental</i>	<i>Predicted</i>	<i>Experimental</i>	<i>Predicted</i>
4200	4220	4900	4970
1.80		1.90	
286,000	252,000	310,000	269,000
1.35	1.23	1.41	1.32
86		87	
81		83	

<sup>a</sup> D-Polyester 0.25 inch; G-Glass 0.25 inch; A-Asbestos 0.25 inch.

MS FORTRAN (4.2) / MSOS

08/16/74

```

PROGRAM SHI
DIMENSION P(10),D(10),A(10),G(10)
READ (60,1) (P(I),I=1,4)
READ (60,1) (D(I),I=1,4)
READ (60,1) (A(I),I=1,4)
READ (60,1) (G(I),I=1,4)
C1=30./1.37
C2=30./2.5
C3=30./2.5
C4=70./1.05
N1=C1+1
N2=C2+1
N3=C3+1
DO 10 I=1,4
DO 20 K1=1,N1
K=K1-1
DO 30 J1=1,N2
J=J1-1
DO 40 M1=1,N3
M=M1-1
Q=P(1)+(D(1)-P(1))-P(1)*(K*(C1+C4))/(C1*(K+C4))+A(1)-P(1))*(J*(C2+C4))
1/(C2*(J+C4))+G(1)-P(1))*(M*(C3+C4))/(C3*(M+C4))
50 FORMAT (4F20.5,3I10,F20.5)
WRITE (61,50) P(1),D(1),A(1),G(1),K,J,M,Q
40 CONTINUE
30 CONTINUE
20 CONTINUE
10 CONTINUE
1 FORMAT (4F10.2)
STOP
END FORTRAN DIAGNOSTIC RESULTS FOR SHI

NO ERRORS
LOAD,56
RUN,

```

Figure 5. Fortran program of the mathematical model

**Multifiber Composites.** Table IX, under *Experimental*, catalogs the results obtained when the three fibers are combined in several ways. The different fibers appear to reinforce in combination as they reinforce when acting individually.

Figure 4 presents the mathematical model which quantitatively forecasts the individual property values obtained by combining the different fibers in a single reinforced structure. The model is a linear one; it presupposes that a fiber when incorporated in a plastic with other fibers contributes to the improvement of a particular property in the same way as it did when incorporated alone. In keeping with the well known "rule of mixtures" the equation utilizes volume percentage rather than weight percentage. Further, as indicated in Figure 4, the use of the model requires a previous evaluation of the individual fibers at some one level of concentration.

Table IX also catalogs the values of the several multifiber composites predicted by the model. Agreement with the property values actually obtained appears to be good: tensile strength 4%, impact strength 6%, and modulus 12%. A Fortran program for the model appears in Figure 5.

### Conclusions

(a) For the polyester reinforcement at 30%, the tensile strength decreased by 15%, the tensile modulus increased by 5%, the impact strength increased tenfold, the hardness was not affected, and the HDT increased from 63° to 77°C.

(b) The particular fibers improved particular properties—the glass improved tensile strength and tensile modulus, the asbestos improved HDT, and the polyester improved impact strength.

(c) The three fibers when combined in multifiber composites appeared to reinforce as they did individually.

(d) The linear mathematical model proposed predicted the experimentally observed multifiber structure properties to a good level of agreement.

### Literature Cited

1. Crugnola, A., Litman, A., *ADVAN. CHEM. SER.* (1974) 134, 29.
2. Cameron, A. B., Heron, G., Wicker, G., *SPI 28th Annual Conf. Reinforced Plastics/Comp. Inst.* 1973, 11-B.
3. Litman, A., Crugnola, A., *Amer. Chem. Soc., Div. Org. Coatings Plastics Chem., Preprints* 33 (2), 152 (1973).
4. Baum, B., *Amer. Chem. Soc., Div. Org. Coatings Plastics Chem., Preprints* 33 (2), 80 (1973).

RECEIVED October 18, 1974.

# INDEX

A	
ABS	
acrylonitrile-butadiene-styrene	
polymers	247
and ASA polymers, quantitative studies of toughening mechanisms in	179
carbon black embrittlement of	256
motionless mixer blending of styrene/acrylonitrile copolymer and nitrile rubber to form	344
polymer, hot-drawn	187
polymer, isotropic	186
and related materials	172
soft	261
Absorbed energy	377
Acetone and bisphenol fluorenone, toughness enhancement	312
Acrylic	
dispersions, rapidly polymerizing	292
materials, fracture behavior of rubber-modified	193
materials, simultaneous interpenetrating networks based on epoxy/	206
polymer beads, dispersions of	292
rubber modified polyblend	286
Acrylonitrile-butadiene-styrene polymers (ABS)	247
Acrylonitrile copolymer), CTBN (liquid carboxyl terminated butadiene-	326
Acrylonitrile copolymer and nitrile rubber to form ABS, motionless mixer blending of styrene/	344
Acrylonitrile (SAN) styrene/	256
Action, fretting	143
Activation energy, apparent	198, 203
Activation energy for the glass transition	123
Adhesion of rubber to matrix	265
Analysis, one-dimensional thermal	141
Angle, orientation	39
Angle x-ray scattering, small-	12
Anisotropic failure properties	46
Anisotropic matrix	55
Anisotropic tensile strengths	55
Anisotropy	36, 104, 148
Annealing	3, 5
Apparent activation energy	198, 203
Applied external forces	253

Applied strain rate	203
Approach, R-curve	362
Areas, mirror	318
ASA polymers, quantitative studies of toughening mechanisms in	179
Asbestos	386
Asymptotic yield stress	104
Axial stress	101

## B

Ballistic evaluation of graft polymers	276, 280
Ballistic resistance of a thermoplastic	263
Banded and nonbanded spherulitic morphology	121
Banding of polymer spherulites	115
Bands, interaction between crazes and shear	190
Bands, shear	108
Bauwens-Crowet criterion	200
Bead reinforced thermoplastic and thermosetting resins, glass-	367
Beads, dispersions of acrylic polymer	292
Behavior, glass transition	219
Bending failure, Instron three-point	316
Bending, three-point	356
Biaxial strip test for polymeric materials	100
Bisphenol acetone (BPA)	312
Blend(s)	305
classification of	161
of grafted polymers	275
grafts, and IPN's, application of group concepts to polymer	159
HIPS/PPO	341
morphology of PS/SBS	244
polymer	161
PS/SBS	240, 244
super high impact polystyrene based on polystyrene and butadiene-styrene block polymer	239
Blending, mechanical	241
Blending of styrene/acrylonitrile copolymer and nitrile rubber to form ABS, motionless mixer	344
Block copolymer(s)	161
and its dependence on the continuous phase, impact strength of styrene-butadiene	234

Block copolymer(s) ( <i>Continued</i> )			
polysulfone/poly(dimethylsiloxane) . . . . .	302		
Block polymer blends, super high impact polystyrene based on polystyrene and butadiene-styrene . . . . .	239		
Block polymers, BPA carbonate-siloxane . . . . .	313		
Blocks into polycarbonates of bisphenol acetone and bisphenol fluorenone, toughness enhancement by introduction of silicone . . . . .	312		
BPA (bisphenol acetone) carbonate polymers, ductile and brittle failure in . . . . .	316		
carbonate-siloxane block polymers . . . . .	313		
Brittle			
behavior of a semicrystalline polyester by control of morphology, ductile to . . . . .	112		
-ductile transition . . . . .	112, 368		
failure in BPA carbonate polymers, ductile and . . . . .	316		
failure, stress concentration for . . . . .	125		
polymers, stress-strain curve of . . . . .	127		
polymers under compressive shear stresses, ductile failure of . . . . .	123		
transition in cloth laminates, tough- . . . . .	377		
transition, ductile- . . . . .	97, 204, 319		
transition of glass fiber composites by impact testing, tough- . . . . .	374		
Brittleness in glassy polymers, thermodynamic aspects of . . . . .	3		
Brittleness of plastics, plane strain and . . . . .	97		
Brittleness of polymer glasses and composites, structural parameters affecting the . . . . .	8		
Buckling failure, local . . . . .	380		
Buckling stress, critical . . . . .	380		
Bueche expression, Debye- . . . . .	286		
Butadiene-acrylonitrile copolymer, CTBN (liquid carboxyl terminated) . . . . .	326		
Butadiene block copolymer and its dependence on the continuous phase, impact strength of styrene- . . . . .	234		
Butadiene-styrene block polymer blends, super high impact polystyrene based on polystyrene and . . . . .	239		
Butadiene-styrene polymers (ABS), acrylonitrile- . . . . .	247		
			<b>C</b>
		Calorimetry (DSC), differential scanning . . . . .	6, 147
		Carbon black embrittlement of ABS . . . . .	256
		Carbonate polymers, ductile and brittle failure in BPA . . . . .	316
		Carbonate-siloxane block polymers, BPA . . . . .	313
		Carboxyl terminated butadiene-acrylonitrile copolymer, CTBN (liquid . . . . .	326
		Cast polymer glasses, solution- . . . . .	13
		Cavitation-controlled deformation processes . . . . .	255
		Chain motions, main . . . . .	136
		Chain segments, parallel . . . . .	11
		Chain transfer agent concentration on impact of graft polymer, effect of . . . . .	268
		Clarity of graft polymers . . . . .	267
		Classification of blends . . . . .	161
		Cloth laminates . . . . .	375
		tough-brittle transition in . . . . .	377
		Cohesive failure . . . . .	108
		Compatibility . . . . .	303
		Complex formation and fracture surface morphology of a highly doubly oriented nylon 66 rod . . . . .	17
		Complexed samples, doubly oriented . . . . .	26
		Composites	
		crack propagation resistance of random fiber . . . . .	355
		discontinuous fiber . . . . .	355
		flexural and tensile properties of polyester . . . . .	358
		by impact testing, tough-brittle transition of glass fiber . . . . .	374
		structural parameters affecting the brittleness of polymer glasses and . . . . .	8
		Composition and simultaneous polymerization phase . . . . .	224
		Compressive shear . . . . .	376
		ductile failure of brittle polymers under . . . . .	123
		Concentration	
		critical stress . . . . .	57, 298
		for ductile failure . . . . .	123, 125
		of piperidine, optimum . . . . .	333
		Concepts, group theory . . . . .	171
		Conditions on crazing, effects of environmental . . . . .	74
		Conditions, simulated oral . . . . .	292
		Continuous nylon-fiber reinforced polypropylene, retarded necking in . . . . .	367
		Continuous phase, impact strength of styrene-butadiene block copolymer and its dependence on the . . . . .	234
		Cook-Gordon mechanism . . . . .	371

- Copolymer(s)  
 block ..... 161  
 CTBN (liquid carboxyl terminated butadiene-acrylonitrile) ..... 326  
 and its dependence on the continuous phase, impact strength of styrene-butadiene block ..... 234  
 graft ..... 161  
 impact modification of polysulfone/poly(dimethylsiloxane) block ..... 302  
 and nitrile rubber to form ABS, motionless mixer blending of styrene/acrylonitrile ..... 344  
 polysulfone/poly(dimethylsiloxane) block ..... 302  
 random ..... 171  
 Correlation, toughness index ..... 347  
 Correlations, structure-frequency ..... 27  
 Crack  
 driving force ..... 363  
 growth ..... 95  
 rate ..... 149  
 initiation ..... 298  
 instability point ..... 363  
 length ..... 356  
 mouth opening ..... 360  
 propagation ..... 94, 296  
 in polycarbonate, fatigue ..... 146  
 resistance of random fiber composites ..... 355  
 nucleation and propagation of .. 72  
 stress-induced propagating ..... 264  
 Craze ..... 69, 318  
 formation, multiple ..... 179  
 layer, strain in ..... 63, 67  
 polystyrene ..... 65  
 strain ..... 69  
 stress ..... 64, 70  
 termination, rate of ..... 189  
 wedge, measurement of the refractive index in a ..... 65  
 Crazes and shear bands, interaction between ..... 190  
 Crazes, laser diffraction of polymer ..... 72  
 Crazing ..... 182  
 development of ..... 78  
 effect of environmental conditions on ..... 74  
 effect of stress upon the kinetics of ..... 183  
 multiplicity of ..... 95  
 of non-crystalline polymers, fibrillar morphologies in ... 18  
 subsidiary ..... 95  
 Creep, tensile ..... 182  
 Criterion  
 Bauwens-Crowet ..... 200  
 pressure-modified von Mises-yield ..... 98  
 strain energy as the strength ... 4  
 Criterion (*Continued*)  
 Tresca yield ..... 101  
 yield ..... 197  
 Critical  
 buckling stress ..... 380  
 draw ratio ..... 51  
 stress concentration ..... 57  
 stress intensity factor ..... 356  
 Crosslinking operations, grafting and ..... 168  
 Crowet criterion, Bauwens- ..... 200  
 Crystallinity, percent ..... 117  
 Crystallization rate ..... 113  
 Crystallographic planes ..... 20  
 CTBN, effect of level of ..... 333  
 CTBN (liquid carboxyl terminated butadiene-acrylonitrile copolymer) ..... 326  
 CTBN-toughened epoxy resin .... 338  
 Curve approach, R- ..... 362  
 Curve of brittle polymers, stress-strain ..... 127  
 Curves, stress-strain ..... 116, 323  
 Curves, true stress-strain ..... 252
- D**
- Davidenkov-Orowan hypothesis, Ludwik- ..... 112  
 Debonding, matrix-fiber ..... 371  
 Debye-Bueche expression ..... 286  
 Decrosslinking ..... 166  
 Deformation ..... 119  
 cavitation-controlled ..... 255  
 initial ..... 182  
 mechanisms, low strain rate ... 247  
 shear ..... 190  
 viscoelastic shear ..... 182  
 Degrafting ..... 166  
 Degree of dispersion ..... 281  
 Degree of mixing ..... 350  
 Depolymerization ..... 166  
 Dewetting ..... 298  
 Differential scanning calorimetry (DSC) ..... 6, 147  
 Diffraction  
 line, vertical ..... 86  
 patterns, laser ..... 80  
 of polymer crazes, laser ..... 72  
 technique, laser ..... 73  
 Dilution, stress-induced ..... 5  
 Discontinuous fiber composites ... 355  
 Discrete phase formation ..... 335  
 Discrete rubber phase ..... 241  
 Dispersion, degree of ..... 281  
 Dispersions of acrylic polymer beads ..... 292  
 Dispersions, rapid polymerizing acrylic ..... 292  
 Dispersive mixing ..... 344  
 Dissipative vibrational energy ... 234  
 Dissipation factor ..... 134

Domain size and shape, rubber phase .....	223	Epoxy prereaction time, low .....	220
Domain sizes, interparticle .....	286	Epoxy resin, CTBN-toughened ...	338
Domains, spherical polybutadiene .	237	Equation	
Double-oriented samples, morphology of .....	20	Debye-Bueche .....	286
Doubly oriented complexed samples .....	26	Euler's .....	380
Draw ratio, critical .....	51	Eyring .....	184
Draw ratio, fixed .....	54	Lorenz-Lorentz .....	67
Drawing .....	3	WLF .....	5
orientation effects by .....	45	Esterification .....	337
Drawn ABS polymer, hot- .....	187	Etherification .....	337
Driving force, crack .....	363	Euler's equation .....	380
Ductile and brittle failure in BPA carbonate polymers .....	316	External forces, applied .....	253
Ductile-brittle transition .....	97, 112, 204, 368	Eyring equation .....	184
temperature .....	319		
Ductile failure of brittle polymers under compressive shear stresses .....	123	<b>F</b>	
Ductile failure, stress concentration factor for .....	123	Factor, critical stress intensity ...	356
Dynamic mechanical spectroscopy	218	Factor, dissipation .....	134
		Factor for ductile failure, stress concentration .....	123
<b>E</b>		Failure	
Effect, Poisson .....	371	in BPA carbonate polymers, ductile and brittle .....	316
Elastic fracture mechanics, linear .	355	of brittle polymers under compressive shear stresses, ductile .....	123
Elasticity, melt viscosity and .....	307	cohesive .....	108
Elastomeric nature .....	303	impact .....	316
Ellipse, orientations of the .....	43	Instron three-point bending ...	316
Elliptic flaw, stress concentration from an .....	37	local buckling .....	380
Elongation, effects of hot stretching on ultimate .....	323	mechanisms .....	323
Embrittlement of ABS, carbon black .....	256	polymer morphology and .....	338
Embrittlement of polycarbonate ..	10	morphologies .....	317
Embrittlement of polymer glasses .	9	number of impacts to .....	138
Energies, fracture .....	94	properties, anisotropic .....	46
Energy		sites, multiple .....	334
absorbed .....	377	stress concentration factor for brittle .....	125
apparent activation .....	198, 203	stress concentration factor for ductile .....	123
dissipative vibrational .....	234	Fatigue crack propagation in polycarbonate .....	146
fracture .....	89	FCP anisotropy .....	148
effect of molecular structure of liquid polymer on ...	331	Fiber	
of low molecular weight fractions of polystyrene .	89	composites, crack propagation resistance of random .....	355
method for measuring .....	91	composites, discontinuous .....	355
of polystyrene .....	95	composites by impact testing, tough-brittle transition of glass .....	374
for the glass transition, activation of mixing, Gibbs free .....	123, 207	debonding, matrix- .....	371
as the strength criterion, strain .	4	impact reinforcement in polystyrene, polyester .....	386
tensile fracture .....	153	reinforced polypropylene, retarded necking in continuous nylon- .....	367
Environmental conditions on crazing effects of .....	74	volume fraction .....	368
Epoxy/acrylic materials, simultaneous interpenetrating networks based on .....	206	wetting .....	390
Epoxy phase, entrapment of rubber in the .....	228	Fibrillar morphologies in crazing of non-crystalline polymers ..	18
		Field, shear .....	348
		Filler frictional effects, polymer- ..	15
		Filler, rubber .....	288



Films, contribution of the linear viscoelastic region to the impact properties of thin polymer ..... 133

Films, impact wear of thin polymer ..... 138

Fixed draw ratio ..... 54

Flaw(s) ..... 13

    distributions ..... 45

    spectrum theory for multiple flaw failure in solid polymers ... 35

    stress concentration from an elliptic ..... 37

Flexural and tensile properties of polyester composites ..... 358

Flexure, polymer specimens subjected to rapid tension or . 97

Flow ..... 9

Fluorenone, toughness enhancement by introduction of silicone blocks into polycarbonates of bisphenol acetone and bisphenol ..... 312

Force, crack driving ..... 363

Forces, applied external ..... 253

Forces, van der Waals ..... 331

Formation, discrete phase ..... 335

Formation, multiple craze ..... 179

Fortran program ..... 395

Fraction, fiber volume ..... 368

Fractional free volume ..... 6

Fractions of polystyrene, narrow molecular weight ..... 90

Fracture ..... 248

    behavior of rubber-modified acrylic materials ..... 193

    energy ..... 89, 94

    effect of molecular structure of liquid polymer on ..... 331

    of low molecular weight fractions of polystyrene . 89

    method for measuring ..... 91

    of polystyrene ..... 95

    tensile ..... 153

    mechanics, linear elastic ..... 355

    mode of ..... 25

    modes, impact ..... 375

    morphology, layered ..... 24

    surface ..... 153

    morphology of a highly doubly oriented nylon 66 rod, complex formation and .. 17

    topography studies ..... 10

Free energy of mixing, Gibbs ... 207

Free volume, fractional ..... 6

Frequency correlations, structure- 27

Fretting action ..... 143

Friction ..... 126

    internal ..... 142

    polymer-filler ..... 15

**G**

Gel point ..... 217

Gelation ..... 337

Geometrical changes of the sample 29

Gibbs free energy of mixing ..... 207

Glass(es) ..... 386

    -bead reinforced thermoplastic and thermosetting resins ... 367

    and composites, structural parameters affecting the brittleness of polymer ..... 8

    embrittlement of polymer ..... 9

    fiber composites by impact testing, tough-brittle transition of ..... 374

    microvoid formation during sample preparation of polymer ..... 13

    solution-cast polymer ..... 13

    transition, activation energy for . 123

    transition behavior ..... 219

    transitions, secondary ..... 9

Glassy polymers, thermodynamic aspects of brittleness in ..... 3

Gordon mechanism, Cook- ..... 371

Graft(s)

    vs. ballistic impact, degree of .. 280

    copolymers ..... 161

    and IPN's, application of group theory concepts to polymer blends ..... 159

    polymer, effect of chain transfer agent concentration on impact of ..... 268

    polymers, ballistic evaluation of ..... 276

    polymers, clarity of ..... 267

    rubber particle size ..... 289

    rubber particle size ..... 289

Grafted polymers, blends of ..... 275

Grafted onto polybutadiene, transparent, impact-resistant styrene/methyl methacrylate copolymer ..... 263

Grafted-rubber reinforced polymer systems ..... 109

Grafting and crosslinking ..... 168

Grafting, latex particle size and ... 269

Group theory concepts ..... 160, 171

    application of ..... 159, 229

Groupoids .. ..... 165

Growth, crack ..... 95

    rate ..... 149

Gyration, radius of ..... 380

**H**

Hardness ..... 389

Haze-free plastic ..... 265

High impact polystyrene (HIPS) ..... 239, 247

High rate impact resistance, role of rubber modification in improving ..... 192

High rate impact, role of spallation in ..... 195

High-speed tensile tests ..... 335

HIPS (high impact polystyrene) ..... 239, 247



- Load profile ..... 150  
 Loading, Izod impact ..... 192  
 Local buckling failure ..... 380  
 Longitudinal strain, relationship  
   between volume strain and .. 186  
 Longitudinal strain, volume  
   strain vs. .... 253  
 Lorenz-Lorentz equation ..... 67  
 Low epoxy prereaction time .... 220  
 Low molecular weight fractions of  
   polystyrene, fracture energy of 89  
 Low strain rate deformation  
   mechanisms ..... 247  
 Ludwik-Davidenkov-Orowan  
   hypothesis ..... 112
- M**
- Main chain motions ..... 136  
 Materials  
   ABS and related ..... 172  
   biaxial strip test for polymeric .. 100  
   fracture behavior of rubber-  
     modified acrylic ..... 193  
   multi-polymer ..... 172  
   simultaneous interpenetrating  
     networks based on epoxy/  
     acrylic ..... 206  
 Mathematical model ..... 387  
 Matrix  
   adhesion of rubber to ..... 265  
   anisotropic ..... 55  
   -fiber debonding ..... 371  
   plastic ..... 265  
   SAN ..... 260  
 Measurements, light scattering ... 20  
 Measuring fracture energy,  
   method for ..... 91  
 Mechanical blending ..... 241  
 Mechanical properties ..... 292  
 Mechanical spectroscopy, dynamic 218  
 Mechanically stressed polystyrene . 84  
 Mechanics, linear elastic fracture . 355  
 Mechanism(s)  
   Cook-Gordon ..... 371  
   failure ..... 323  
   low strain rate deformation ... 247  
   polymer morphology and failure 338  
   toughening ..... 248  
   of toughening in impact thermo-  
     plastics, evaluating ..... 247  
 Melt viscosity and elasticity ..... 307  
 MEPS (poly-2-methyl-2-ethyl-  
   propylene sebacate) ..... 113  
 Methyl methacrylate copolymer  
   grafted onto polybutadiene,  
   transparent, impact-resistant,  
   styrene/ ..... 263  
 Microdomains, silicone ..... 321  
 Microvoids ..... 340  
   formed during sample  
   preparation of polymer  
   glasses ..... 13  
 Mirror areas ..... 318
- Mixer blending of styrene/  
   acrylonitrile copolymer and  
   nitrile rubber to form ABS  
   motionless ..... 344  
 Mixing  
   degree of ..... 350  
   dispersive ..... 344  
   Gibbs free energy of ..... 207  
 Mixtures, rule of ..... 395  
 Mode of fracture ..... 25, 375  
 Model, mathematical ..... 387  
 Models, property-texture ..... 25  
 Modification, impact ..... 302  
 Modification in improving high  
   rate impact resistance, role  
   of rubber ..... 192  
 Modification of polysulfone with  
   polysulfone/poly (dimethyl-  
   siloxane) block copolymers,  
   impact ..... 302  
 Modified polyblend, acrylic rubber 286  
 Modifier, impact ..... 4  
 Modulus, shear ..... 224  
 Modulus, tensile ..... 393  
 Molecular structure of liquid  
   polymer on fracture energy,  
   effect of ..... 331  
 Molecular weight distributions ... 393  
 Molecular weight fractions of  
   polystyrene, low ..... 89, 90  
 Molecules, tie ..... 121  
 Monodispersity ..... 271  
 Morphologies in crazing of non-  
   crystalline polymers, fibrillar . 18  
 Morphologies, failure ..... 317  
 Morphology ..... 292, 303  
   banded and nonbanded  
     spherulitic ..... 121  
   ductile to brittle behavior of a  
     semicrystalline polyester  
     by control of ..... 112  
   and failure mechanisms, polymer 338  
   fracture surface ..... 18  
   layered fracture ..... 24  
   of a highly doubly oriented nylon  
     66 rod, complex formation  
     and fracture surface ..... 17  
   of double-oriented samples ... 20  
   of PS/SBS blend ..... 244  
   of transparent two-phase  
     polymers, strength ..... 284  
   two-phase ..... 305  
 Motionless mixer blending of  
   styrene/acrylonitrile copolymer  
   and nitrile rubber to form ABS 344  
 Motions, main chain ..... 136  
 Mouth opening, crack ..... 360  
 Multi-mer syntheses ..... 171  
 Multiple craze formation ..... 179  
 Multiple failure sites ..... 334  
 Multiple flaw failure in solid  
   polymers, flaw spectrum  
   theory for ..... 35

Multiplicity of crazing ..... 95  
 Multi-polymer materials ..... 172

### N

Narrow molecular weight fractions  
 of polystyrene ..... 90  
 Nature, elastomeric ..... 303  
 Necking in continuous nylon-fiber  
 reinforced polypropylene,  
 retarded ..... 367, 368  
 Network, simple homopolymer ... 161  
 Networks based on epoxy/acrylic  
 materials, simultaneous  
 interpenetrating ..... 206  
 Networks (IPN's), inter-  
 penetration polymer ..... 159  
 Networks (SIN's), simultaneous  
 interpenetrating ..... 206  
 Nitrile rubber to form ABS,  
 motionless mixer blending of  
 styrene/acrylonitrile copolymer  
 and ..... 344  
 Nodular structure in polycarbonate 12  
 Nonbanded spherulitic morphology,  
 banded and ..... 121  
 Non-crystalline polymers, fibrillar  
 morphologies in crazing of .... 18  
 Notation, left-to-right ..... 166  
 Notation, quantitative limitations  
 of symbolic ..... 175  
 Notched Izod impact strength ... 97, 316  
 Nucleation and propagation of  
 cracks ..... 72  
 Number of impacts to failure .... 138  
 Nylon-fiber reinforced polypropy-  
 lene, retarded necking in  
 continuous ..... 367  
 Nylon 66 rod, complex formation  
 and fracture surface morph-  
 ology of a highly doubly  
 oriented ..... 17

### O

One-dimensional thermal analysis . 141  
 Opening, crack mouth ..... 360  
 Operations, grafting and  
 crosslinking ..... 168  
 Operations, idempotent ..... 168  
 Optimum concentration of  
 piperidine ..... 333  
 Orientation ..... 187  
 angle ..... 39  
 effects by drawing ..... 45  
 of the ellipse ..... 43  
 Orowan hypothesis, Ludwik-  
 Davidenkov- ..... 112  
 Osmium staining technique .... 237, 327

### P

Parallel chain segments ..... 11  
 Parameters affecting the brittleness  
 of polymer glasses and  
 composites, structural ..... 8  
 Paris relationship ..... 149  
 Particle size ..... 264  
 graft rubber ..... 289  
 and grafting, latex ..... 269  
 ultimate ..... 348  
 Patterns, laser diffraction ..... 80  
 Percent crystallinity ..... 117  
 Phase  
 composition and simultaneous  
 polymerization ..... 224  
 discrete rubber ..... 241  
 domain size and shape, rubber . 223  
 entrapment of rubber in the  
 epoxy ..... 228  
 formation, discrete ..... 335  
 impact strength of styrene-  
 butadiene block copolymer  
 and its dependence on the  
 continuous ..... 234  
 morphology, two- ..... 305  
 nature of SIN's, two- ..... 213  
 polymers, strength-morphology  
 of transparent two- ..... 284  
 separation ..... 207  
 thermoset system, two- ..... 328  
 Piperidine, optimum concentration  
 of ..... 333  
 Plane, slip ..... 23  
 Plane strain and the brittleness  
 of plastics ..... 97  
 Plane-stress-to-plane-strain  
 transition ..... 98  
 Plastic, haze-free ..... 265  
 Plastic matrix ..... 265  
 Plastics, plane strain and the  
 brittleness of ..... 97  
 Point bending, three- ..... 356  
 Point, crack instability ..... 363  
 Point, gel ..... 217  
 Poisson effect ..... 371  
 Poisson ratio ..... 4, 99  
 Polyblend, acrylic rubber modified 286  
 Polyblends, transparent ..... 285  
 Polybutadiene domains, spherical . 237  
 Polybutadiene, transparent, impact-  
 resistant, styrene/methyl  
 methacrylate copolymer  
 grafted onto ..... 263  
 Polycarbonate  
 of bisphenol acetone and  
 bisphenol fluorenone ..... 312  
 embrittlement of ..... 10  
 fatigue crack propagation in ... 146  
 nodular structure in ..... 12  
 secondary losses in ..... 137  
 Poly(dimethylsiloxane) block  
 copolymers, polysulfone/ .... 302

- Polyester by control of morphology, ductile to brittle behavior of a semicrystalline ..... 112
- Polyester composites, flexural and tensile properties of ..... 358
- Polyester reinforcement ..... 388
- Poly(hexamethylene sebacate) (HMS) ..... 113
- Polymer
- beads, dispersions of acrylic ... 292
  - blends ..... 161
  - grafts, and IPN's, application of group theory concepts to ..... 159
  - super high impact polystyrene based on polystyrene and butadiene-styrene block . 239
  - crazes, laser diffraction of ..... 72
  - effect of chain transfer agent concentration on impact of graft ..... 268
  - filler frictional effects ..... 15
  - films, contribution of the linear viscoelastic region to the impact properties of thin .. 133
  - films, impact wear of thin ..... 138
  - on fracture energy, effect of molecular structure of liquid glasses ..... 331
  - and composites, structural parameters affecting the brittleness of ..... 8
  - embrittlement of ..... 9
  - microvoid formation during sample preparation of ... 13
  - solution-cast ..... 13
  - hot-drawn ABS ..... 187
  - isotropic ABS ..... 186
  - materials, multi-morphology and failure mechanisms ..... 338
  - networks (IPN's), interpenetrating ..... 159
  - rich skin effect ..... 15
  - spherulites, banding of ..... 115
- Polymeric materials, biaxial strip test for ..... 100
- Polymerization, phase composition and simultaneous ..... 224
- Polymerizing acrylic dispersions, rapid ..... 292
- Polymers
- ABS (acrylonitrile-butadiene-styrene) ..... 247
  - ballistic evaluation of graft ... 276
  - blends of grafted ..... 275
  - BPA carbonate-siloxane block .. 313
  - clarity of graft ..... 267
  - contributory phenomena to the impact wear of ..... 138
  - ductile and brittle failure in BPA carbonate ..... 316
  - flaw spectrum theory for multiple flaw failure in solid ..... 35
- Polymers (*Continued*)
- grafted-rubber reinforced ..... 109
  - quantitative studies of toughening mechanisms in ABS and ASA ..... 179
  - semicrystalline ..... 115
  - strength-morphology of transparent two-phase .... 284
  - stress-strain curve of brittle ... 127
  - subjected to rapid tension or flexure ..... 97
  - thermodynamic aspects of brittleness in glassy ..... 3
  - under compressive shear stresses, ductile failure of brittle ... 123
- Poly-2-methyl-2-ethylpropylene sebacate, (MEPS) ..... 113
- Polyphenylene oxide ..... 367
- Polypropylene, retarded necking in continuous nylon-fiber reinforced ..... 367
- Polystyrene ..... 239, 367
- craze layer, strain in a ..... 63, 65
  - fracture energy of ..... 95
  - fracture energy of low molecular weight fractions of ..... 89
  - HIPS (high impact) ..... 239, 247
  - mechanically stressed ..... 84
  - narrow molecular weight fractions of ..... 90
  - polyester fiber: an impact reinforcement in ..... 386
- Polysulfone ..... 302
- /poly(dimethylsiloxane) block copolymers ..... 302
- PP-nylon system ..... 369
- PPO blends, HIPS/ ..... 341
- Preparation of polymer glasses, microvoid formation during sample ..... 13
- Prereaction time, low epoxy ..... 220
- Pressure-modified von Mises-yield criterion ..... 98
- Process, deformation ..... 119
- Processes, cavitation-controlled deformation ..... 255
- Profile, load ..... 150
- Propagation, crack ..... 94, 264, 296
- and nucleation ..... 72
  - in polycarbonate ..... 146
  - resistance of random fiber composites ..... 355
- Properties, anisotropic failure ... 46
- Properties of PS/SBS blend ..... 244
- Properties, temperature dependency of the viscoelastic ..... 142
- Property-texture models ..... 25
- PS/SBS blend ..... 240, 244
- Q**
- Quadrant, tension-tension ..... 109
- Quantitative studies of toughening mechanisms in TBS and ASA polymers ..... 179

## R

Radius of gyration .....	380
Random copolymers .....	171
Random fiber composites, crack propagation resistance of ....	355
Rapid polymerizing acrylic dispersions .....	292
Rapid tension or flexure, polymer specimens subjected to .....	97
Rate(s)	
applied strain .....	203
crack growth .....	149
crystallization .....	113
deformation mechanisms, low strain .....	247
impact resistance, role of rubber modification in improving high .....	192
impact, role of spallation in high shear .....	195
strain .....	348
Ratio, critical draw .....	51
Ratio, Poisson .....	4, 99
Refractive index .....	65
in a craze wedge, measurement of the .....	65
Reinforced	
polymer systems, grafted-rubber polypropylene, retarded necking in continuous nylon-fiber ..	109
thermoplastic and thermosetting resins, glass-bead .....	367
thermoplastics .....	386
Reinforcement, polyester .....	388
Reinforcement in polystyrene, polyester fiber: an impact ...	386
Relative toughness .....	153
Relaxation time under strain, shift of .....	4
Resin, CTBN-toughened epoxy ...	338
Resins, glass-bead reinforced thermoplastic and thermosetting .....	367
Resistance of random fiber composites, crack propagation	355
Resistance, role of rubber modification in improving high rate impact .....	192
Resistance of a thermoplastic, ballistic .....	263
Retarded necking in continuous nylon-fiber reinforced polypropylene .....	367
Retarded yielding .....	372
Rich skin effect, polymer- .....	15
Rigidity, sample .....	134
R-curve approach .....	362
Rubber	
in the epoxy phase, entrapment of .....	228
filler .....	288

Rubber (*Continued*)

to form ABS, motionless mixer blending of styrene/acrylonitrile copolymer and nitrile .....	344
to matrix, adhesion of .....	265
modification in improving high rate impact resistance, role of .....	192
-modified acrylic materials, fracture behavior of .....	193
modified polyblend, acrylic ...	286
particle size, graft .....	289
phase, discrete .....	241
phase domain size and shape ..	223
reinforced polymer systems, grafted- .....	109
softening effect of .....	258
toughened thermosets .....	326
Rule of mixtures .....	395

## S

Sample preparation of polymer glasses, microvoid formation during .....	13
Sample rigidity .....	134
SAN, (styrene/acrylonitrile) ...	256
matrix .....	260
SBS blend, PS/ .....	240
morphology and properties of ..	244
Scanning calorimetry (DSC), differential .....	6, 147
Scattering, laser light .....	288
Scattering, small-angle x-ray .....	12
Secondary glass transitions .....	9
Secondary losses in polycarbonate .	137
Seed latex technique .....	272
Segments, parallel chain .....	11
Semicrystalline polyester by control of morphology, ductile to brittle behavior of a .....	112
Semicrystalline polymer .....	115
Semi-groups .....	165
Separation, phase .....	207
Shape, rubber phase domain size and .....	223
Shear	
bands .....	108
interaction between crazes and compressive .....	190
deformation .....	376
viscoelastic .....	190
field .....	182
interlaminar .....	348
modulus .....	375
rates .....	224
strain rate .....	348
stresses .....	198
ductile failure of brittle polymers under compressive .....	41
compressive .....	123
Shift of relaxation time under strain	4

- Silicone blocks into polycarbonates  
of bisphenol acetone and bisphenol fluorenone, toughness enhancement by introduction of ..... 312
- Silicone microdomains ..... 321
- Siloxane block polymers, BPA carbonate- ..... 313
- Similarity, law of ..... 377
- Simple homopolymer network .... 161
- Simultaneous interpenetrating networks (SIN's) ..... 206
- history of IPN's and ..... 208
- two-phased nature of ..... 213
- Simultaneous polymerization, phase composition and ..... 224
- Sites, multiple failure ..... 334
- Size(s)
- graft rubber particle ..... 289
- and grafting, latex particle ..... 269
- interparticle domain ..... 286
- particle ..... 264
- and shape, rubber phase domain ..... 223
- ultimate particle ..... 348
- Skin effect, polymer-rich ..... 15
- Slip plane ..... 23
- Small angle x-ray scattering ..... 12
- Small main-chain motions ..... 9
- Soft ABS ..... 261
- Softening effect of rubber ..... 258
- Solid polymers, flaw spectrum theory for multiple flaw failure in ..... 35
- Solution-cast polymer glasses .... 13
- Spallation in high rate impact, role of ..... 195
- Specimens, notched Izod ..... 316
- Specimens subjected to rapid tension or flexure, polymer .. 97
- Spectroscopy, dynamic mechanical ..... 218
- Spectrum approach, flaw ..... 37
- Spectrum theory for multiple flaw failure in solid polymers, flaw ..... 35
- Spherical polybutadiene domains . 237
- Spherulites, banding of polymer .. 115
- Spherulitic morphology, banded and nonbanded ..... 121
- Stability, thermal ..... 303
- Staining technique, osmium ... 237, 327
- State of stress ..... 39
- Strain
- and the brittleness of plastics, plane ..... 97
- in the craze layer ..... 67, 69
- curves, stress- ..... 127, 252, 323
- energy as the strength criterion . 4
- lateral ..... 182
- vs. longitudinal strain, volume .1, 253
- in a polystyrene craze layer .... 63
- rate ..... 10
- applied ..... 203
- deformation mechanisms, low shear ..... 198
- Strain (*Continued*)
- relationship between volume strain and longitudinal .... 186
- shift of relaxation time under .. 4
- studies, stress- ..... 220
- transition, plane-stress-to-plane- vector ..... 99
- Strength(s) ..... 259
- anisotropic tensile ..... 55
- criterion, strain energy as the .. 4
- impact ..... 273, 302, 347, 390
- as a function of temperature . 136
- Izod ..... 97, 335
- morphology of transparent two-phase polymers ..... 284
- of styrene-butadiene block copolymer and its dependence on the continuous phase, impact ..... 234
- tensile ..... 347, 393
- Stress(es)
- asymptotic yield ..... 104
- axial ..... 101
- concentration(s) ..... 298
- for brittle failure ..... 125
- critical ..... 57
- from an elliptic flaw ..... 37
- factor for ductile failure .... 123
- craze ..... 64, 70
- critical buckling ..... 380
- ductile failure of brittle polymers under compressive shear ... 123
- induced dilatation ..... 5
- induced propagating crack ... 264
- intensity factor, critical ..... 356
- to-plane-strain transition, plane-shear ..... 41
- state of ..... 39
- strain curve(s) ..... 116
- of brittle polymers ..... 127
- strain studies ..... 220
- upon the kinetics of crazing, effect of ..... 183
- variation, tensile yield ..... 101
- whitening ..... 368
- Stressed polystyrene, mechanically ..... 84
- Stretching on ultimate elongation, effects of hot ..... 323
- Striation thickness ..... 345
- Strip test for polymeric materials, biaxial ..... 100
- Structural parameters affecting the brittleness of polymer glasses and composites ..... 8
- Structure-frequency correlation .. 27
- Structure of liquid polymer on fracture energy, effect of molecular ..... 331
- Structure in polycarbonate, nodular ..... 12
- Studies, fracture topography ..... 10
- Studies, stress-strain ..... 220
- Styrene/acrylonitrile (SAN) ..... 256
- and nitrile rubber to form ABS, motionless mixer blending of 344

- Styrene block polymer blends, super high impact polystyrene based on polystyrene and butadiene- . . . . . 239
- Styrene-butadiene block copolymer and its dependence on the continuous phase, impact strength of . . . . . 234
- Styrene/methyl methacrylate copolymer grafted onto polybutadiene, transparent, impact-resistant . . . . . 263
- Styrene polymers (ABS), acrylonitrile-butadiene- . . . . . 247
- Subsidiary crazing . . . . . 95
- Surface, fracture . . . . . 153
- Symbolic notation, quantitative limitations of . . . . . 175
- Syntheses, inverse . . . . . 163
- Syntheses, multi-mer . . . . . 171
- System, two-phase thermoset . . . . . 328
- Systems, grafted-rubber reinforced polymer . . . . . 109
- T**
- Technique, laser diffraction . . . . . 73
- Technique, osmium staining . . . . . 237, 327
- Technique, seed latex . . . . . 272
- TEDMA (triethylene glycol dimethylacrylate) . . . . . 294
- Temperature dependency of the viscoelastic properties . . . . . 142
- Temperature, ductile-brittle transition . . . . . 319
- Temperature, impact strength as a function of . . . . . 136
- Tensile
- creep . . . . . 182
  - fracture energy . . . . . 153
  - impact . . . . . 281
  - modulus . . . . . 393
  - properties of polyester composites, flexural and . . . . . 358
  - strength . . . . . 347, 393
  - anisotropic . . . . . 55
  - testing . . . . . 335, 346
  - yield stress variation . . . . . 101
- Tension or flexure, polymer specimens subjected to rapid . . . . . 97
- Tension-tension quadrant . . . . . 109
- Tension, triaxial . . . . . 98
- Tension, uniaxial . . . . . 41
- Termination, rate of craze . . . . . 189
- Test for polymeric materials, biaxial strip . . . . . 100
- Testing, impact and tensile . . . . . 346
- Testing, tough-brittle transition of glass fiber composites by impact . . . . . 374
- Tests, high-speed tensile . . . . . 335
- Tests, impact . . . . . 223
- Texture models, property- . . . . . 25
- Theory concepts, group . . . . . 160, 171
- application of . . . . . 159, 229
- Thermal analysis, one-dimensional . . . . . 141
- Thermal history, effects of . . . . . 152
- Thermal stability . . . . . 303
- Thermodynamic aspects of brittleness in glassy polymers . . . . . 3
- Thermoplastics . . . . . 258, 263, 367
- evaluating mechanisms of toughening in impact . . . . . 247
  - reinforced . . . . . 386
- Thermoset system, two-phase . . . . . 328
- Thermosetting resins, glass-bead reinforced thermoplastic and . . . . . 367
- Thermosets, rubber toughened . . . . . 326
- Thickness, striation . . . . . 345
- Thin polymer films, contribution of the linear viscoelastic region to the impact properties of . . . . . 133
- Thin polymer films, impact wear of . . . . . 138
- Three-point bending . . . . . 316, 356
- Tie molecules . . . . . 121
- Time, low epoxy prereaction . . . . . 220
- Time under strain, shift of relaxation . . . . . 4
- Topography studies, fracture . . . . . 10
- Topology . . . . . 160
- Tough-brittle transition in cloth laminates . . . . . 377
- Tough-brittle transition of glass fiber composites by impact testing . . . . . 374
- Toughened epoxy resin, CTBN- . . . . . 338
- Toughened thermosets, rubber . . . . . 326
- Toughening . . . . . 248
- in impact thermoplastics, evaluating mechanisms of . . . . . 247
  - on ABS and ASA polymers . . . . . 179
- Toughness . . . . . 146, 368
- enhancement by introduction of silicone blocks into polycarbonates of bisphenol acetone and bisphenol fluorenone . . . . . 312
  - index correlation . . . . . 347
  - relative . . . . . 153
- Transition
- brittle-ductile . . . . . 368
  - in cloth laminates, tough-brittle . . . . . 377
  - ductile-brittle . . . . . 97, 204
  - glass . . . . . 123, 219
  - of glass fiber composites by impact testing, tough-brittle . . . . . 374
  - secondary glass . . . . . 9
  - temperature, ductile-brittle . . . . . 319
- Transparent, impact-resistant, styrene/methyl methacrylate copolymer grafted onto polybutadiene . . . . . 263
- Transparent polyblends . . . . . 285
- Transparent two-phase polymers, strength-morphology of . . . . . 284
- Tresca yield criterion . . . . . 101



Triaxial tension .....	98	Volume strain and longitudinal strain, relationship between ..	186
Triethylene glycol dimethacrylate (TEDMA) .....	294	Von Mises-yield criterion, pressure-modified .....	98
Two-phase morphology .....	305		
Two-phase polymers, strength-morphology of transparent ...	284	<b>W</b>	
Two-phase thermoset system .....	328	Wear of polymers, contributory phenomena to the impact ...	138
Two-phased nature of SIN's .....	213	Wedge, measurement of the refractive index in a craze ...	65
		Weight distributions, molecular ..	393
<b>U</b>		Wetting, fiber .....	390
Ultimate particle size .....	348	Whitening, stress .....	368
Uniaxial tension .....	41	WLF equation .....	5
<b>V</b>		<b>X</b>	
Van der Waals forces .....	331	X-ray scattering, small-angle .....	12
Variation, tensile yield stress .....	101		
Vector, strain .....	99	<b>Y</b>	
Vertical diffraction line .....	86	Yield criterion .....	197
Vibrational energy, dissipative ...	234	Yield criterion, pressure-modified von Mises- .....	98
Viscoelastic properties, temperature dependency of the .....	142	Tresca .....	101
Viscoelastic region to the impact properties of thin polymer films, contribution of the linear	133	Yield stress .....	10
Viscoelastic shear deformation ...	182	asymptotic .....	104
Viscosity and elasticity, melt .....	307	variation, tensile .....	101
Volume fraction, fiber .....	368	Yielding, kinetics of .....	321
Volume, fractional free .....	6	Yielding, retarded .....	372
Volume strain vs. longitudinal strain	253		

*The text of this book is set in 10 point Caledonia with two points of leading. The chapter numerals are set in 30 point Garamond; the chapter titles are set in 18 point Garamond Bold.*

*The book is printed in offset on Text White Opaque, 50-pound. The cover is Joanna Book Binding blue linen.*

*Jacket design is by Linda Mattingly.  
 Editing and production by Mary Rakow.*

*The book was composed by Service Composition Co., Baltimore, Md.,  
 printed and bound by The Maple Press Co., York, Pa.*